Examining the climate drivers of phytoplankton variation along the Chilean coast

Felipe Andrés Tornquist Pérez

The University OF Sheffield
Department of Geography

PhD thesis
A thesis submitted in partial fulfilment of the requirement for the degree of Doctor of Philosophy

Supervisors: Prof Grant R. Bigg
                 Dr Robert R. Bryant

January 2022

Abstract.

The South American east coast is a very productive region, with more than 10% of the worldwide marine fish catch, especially along the Chilean shores. The base of this production is the phytoplankton that can be easily measured by the MODIS-aqua satellite through its chlorophyll (Chl). The Chl concentration depends on specific parameters such as precipitation rate (PR), surface sea temperature (SST), or wind direction (U, V), obtained by ERA5. These parameters have a different impact along the extensive Chilean coast, having different climates. Additionally, they are forced by climate drivers such as El Niño Southern Oscillation (ENSO), the Antarctic Oscillation (AAO), the Southern Pacific Subtropical Anticyclone (SPSA), and the Pacific Decadal Oscillation (PDO) obtained by NOAA.

The study area was split into ten subsections, grouped into three Zones (the Northern, Central and Southern Zone). The Chl and physical parameters were studied in each subsection from 2002 to 2018. The analysis revealed that the southerly winds driven by the presence of the SPSA and the shelf size are the main triggers for the phytoplankton bloom. Therefore, the most productive region is the middle Central Zone having a broad shelf. However, despite its extreme aridity and low southerly winds, the Northern Zone's extreme subsection (1N) had a significant Chl signal. In contrast, although the Southern Zone had high PR and predominant westerly winds leading to stratification, its production was significant, with a slightly lower concentration further south (3S). Thus, these regions need a deeper analysis.

Composites were created selecting the years when the climate drivers were either strongly positive or negative to understand their influence on the different parameters. The study period was extended towards 1979 to have enough years in the composite samples. Nonetheless, the Chl is only available from 2002 onwards. The Chl dataset from the long pre-MODIS period was reconstructed by Canonical Correlation Analysis (CCA), based on another parameter with a significant correlation with Chl. All the variables were tested, having better results with SST. This analysis concludes that AAO and ENSO are the predominant climate drivers that modulate the SPSA. The Chl's impact from El Niño was significant in the Southern Zone during the summer, while the Northern Zone was not significantly affected. Although AAO altered the PR patterns significantly, the Chl activity did not show a response.

Three case studies per Zone were selected to understand better the mechanisms that trigger the Chl increment. Also, a heavy dust storm and a significant red tide episode in the Northern and Southern Zone were added to determine these external factors' effects. The results confirmed that the southerly winds are the main trigger for these cases. Although this was straightforward in the Central Zone, it was less clear in the other Zones. The Chl blooms and the wind patterns showed slight gaps in location in the Northern Zone. The Southern Zone cases occurred when the southerly winds were dominant, and the PR was low at the same time. These conditions were driven when the SPSA was moved southwards by El Niño, and the positive AAO blocked the fronts coming from the Southern Ocean.

This thesis demonstrates the importance of longshore winds driven by the SPSA and the shelf width in ocean fertilisation, increasing the phytoplankton. Thus, the middle Central Zone is the most productive, where both variables are present. Due to its high PR and low southerly winds, these fluxes are more predominant in the Southern Zone leading to stratification. However, it reached an equilibrium when El Niño moved the SPSA southwards, and the positive AAO occurred. 1N and 3S's Chl signal is linked to a more significant presence of undercurrents Equatorial Subsurface Water (ESSW) and Antarctic Intermediate Water (AAIW), respectively.

Acknowledgements.

I would like to thank my supervisors, Prof. Grant Bigg and Dr Robert Bryant, for all your support, guidance and corrections, especially Grant for accepting me as his student even when this was not my speciality. Also, I would like to thank Becas Chile for funding this project.

My work would not have been possible without all the love, support and patience of my dear wife, Paola Bravo. You are everything to me. I missed you a lot when you were not here. It was a torture to come here and leave you in Chile. I do not have enough words to express my gratitude for your positive vibe and support in this complex process, believing in me this whole time. "Te Amo con todo mi corazón mi Poshi-Poshi, gracias por hacerme crecer y darme la noticia más bella del mundo, y esa es que seamos padres."

I also want to thank my parents, Andrés and Juany, for helping me pursue my dream of doing a PhD and supporting me in getting in here, especially my father, who was always interested in my topic. Also, I would like to thank my grandparents, who are not here but always in my heart, particularly my Abuelito Juan Luis. I send you a big hug to heaven.

Finally, this thesis is dedicated to our little angel Bastian that always be in our hearts "Te amamos a pesar de corto tiempo que estuviste con nosotros".

Thank you all for everything

Content.

Figure List.

Table List.

Acronyms List.

~: correlation notation
+AAO: positive Antarctic Oscillation
AAIW: Antarctic Intermediate Water
AAO: Antarctic Oscillation
-AAO: negative Antarctic Oscillation
ACC: Antarctic Circumpolar Current
C: Central Zone
C3S: Copernicus Climate Change Service
CCA: Canonical Correlation Analysis
CCC: Chile Coastal Current
C_d: Drag coefficient
CHC: Cape Horn Current
Chl: Chlorophyll-α band concentration (mg m^{-3})
CONAMA: National Commission for the Environment
CR2: Centre for Climate and Resilience Research
DGA: General Directorate of Water Management
DINEOF: Data Interpolating Empirical Orthogonal Function
DMC: Meteorological Directorate of Chile
EBUS: Eastern Boundary Upwelling System
ECMWF: European Centre for Medium-Range Weather Forecast
ENSO: El Niño Southern Oscillation
EOF: Empirical Orthogonal Function
EP: Ekman Pumping
ERA5: ECMWF ReAnalysis fifth generation
ESSW: Equatorial Subsurface Water
GES DISC: Goddard Earth Sciences Data and Information Services Centre
GIOVANNI: GES DISC Interactive Online Visualization and Analysis Infrastructure
GU: Gunther Undercurrent
HC: Humboldt Current
HCS: Humboldt Current System
HNLC: High Nutrient-Low Chlorophyll zone
LSEOF: Least-Squares Empirical Orthogonal Functions
MAE: Mean Absolute Error
MBL: Marine Boundary Layer
MERRA-2: Modern-Era Retrospective analysis for Research Application, version 2
MODIS: Moderate Resolution Imaging Spectro-radiometer
N: Northern Zone
NaN: Not a Number
NASA: National Aeronautics and Space Administration
NCEP: National Centre for Environmental Prediction
NetCDF: Network Common Data Form
NOAA: National Oceanic and Atmospheric Administration
O: Oceanic Strip
OMZ: Oxygen Minimum Zone
PCC: Peruvian Coast Current
PCCC: Peruvian-Chilean Countercurrent
PDO: Pacific Decadal Oscillation
PR: Precipitation Rate (mm mth^{-1})
Rc: Canonical Correlation
Rho: R used for Spearman correlations

RMS: Root Mean Square
RMSE: Root Mean Square Error
RPS: Recruitments Per Spawning biomass
RSEOF: Recursively Subtracted Empirical Orthogonal Functions
S: Southern Zone
SD: Standard Deviation
SeaDAS: SeaWiFS Data Analysis System
SeaWiFS: Sea-viewing Wide Field-of-view Sensor
SEC: Southern Equatorial Current
Sernageomin: National Geology and Mining Service
Sernapesca: National Fisheries and Aquaculture Service
SLP: Sea Level Pressure (kPa)
SMA: Chilean Superintendency of the Environment
SOI: Southern Oscillation Index
SPSA: Southeast Pacific Subtropical Anticyclone
SST: Surface Sea Temperature(°C)
SVD: Singular Value Decomposition
T: Coastal strip
TMPA: Multi-satellite Precipitation Analysis
TRMM: Tropical Rainfall Measuring Mission
UW: Westerly winds (m s^{-1})
VW: Southerly winds (m s^{-1})
W: Wind vector (m s^{-1})
WS: Wind stress (kg m^{-1} s^{-2})
WWD: West Wind Drift current
ZET: Zonal Ekman Transport

1. Introduction.

Phytoplankton makes a vital contribution to the ocean. It is the base of the marine trophic web and a key element in the biogeochemical cycles, owing to its photosynthesis. Hence, it is essential to understand its behaviour (Vergara et al., 2017). Phytoplankton requires light conditions, nutrient availability and adequate temperature. Phytoplankton fixes c.40% of carbon dioxide absorbed per year by plants, oxygenating the first ocean layer (Falkowski, 1994). This process allows the inorganic carbon to be reintroduced into the carbon cycle, transforming it into organic matter. The oxygen dissolved in the ocean permits many heterotrophic species to live in this layer, such as aerobic bacteria, zooplankton, fish, and others, which have a vital role in the biogeochemical cycles (Falkowski, 1994; Bigg, 2003; Vergara et al., 2017).

The phytoplankton phenology is studied by considering indices, such as the initiation and termination of its annual cycle, duration and intensity (Corredor-Acosta et al., 2015). In general, phytoplankton bloom is in spring, and there may be a second bloom in autumn while light levels are still enough to produce photosynthesis (Figure 1.1). To keep a high production in summer, a mechanism that introduces new nutrients is required (Bigg, 2003). Chlorophyll is one of the main phytoplankton components, and it is used in the photosynthesis process (Falkowski, 1994). Many studies use remote sensing to track phytoplankton. It is measured indirectly by chlorophyll pigment concentration (Chl; Miloslavich et al., 2011; Vergara et al., 2017; Gómez et al., 2017).
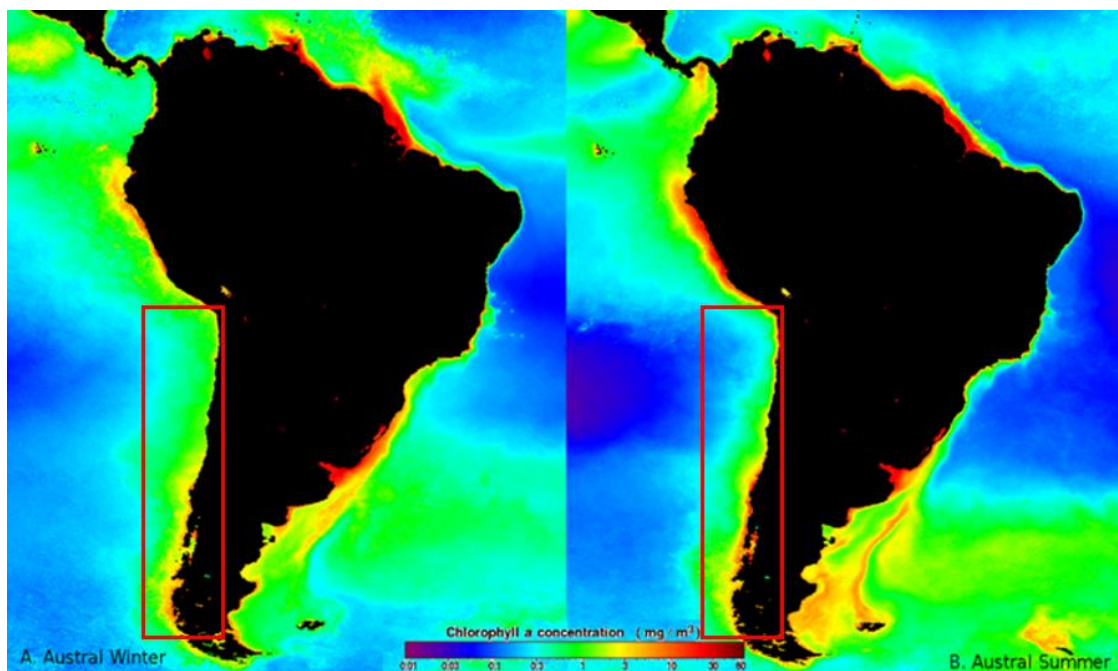
FIGURE 1.1. MAP OF CHLOROPHYLL-A CONCENTRATION (CHL) AROUND SOUTH AMERICA USING REMOTE SENSING. CHL IS USED TO KNOW THE PHYTOPLANKTON ACTIVITY INDIRECTLY. THE RED SQUARES MARK THE LOCATION OF THE CHILEAN COAST. SECTION A SHOWS AUSTRAL WINTER AND B AUSTRAL SUMMER, SHOWING A SLIGHT SEASONAL INCREMENT IN CHILE WITH A MORE SIGNIFICANT INCREASE IN THE SOUTH (MILOSLAVICH ET AL., 2011).

Phytoplankton lives in the euphotic layer (first 100 m) due to the light requirements of photosynthesis (Thiel et al., 2007). For this process, phytoplankton must absorb essential nutrients like nitrate (NO_3^-), nitrite (NO_2^-) and ammonium (NH_4^+; Bigg, 2003; Dortch, 1990). NO_2^- needs a significant effort to reduce over NH_4^+. For that reason, phytoplankton may

prefer NO_3^- and NH_4^+ as a second option. However, this depends on the quantity of light and N availability (Dortch, 1990). The organism primarily absorbs P from phosphate ions (PO_4^{-2}; Bigg, 2003; Vergara et al., 2017).

The deep layers contain more nutrients, primarily N and P (Mogollón and Calil, 2017; Falkowski, 1994). These nutrients come from the dead marine organism remains or living organism excreta, particularly zooplankton. This material is known as detritus (Bigg, 2003). Detritus sinks to the bottom depth of the ocean at different speeds, depending on its size (Gómez et al., 2017; Vergara et al., 2017). Aerobic bacteria remineralise detritus in the upper layers, and anaerobic bacteria in the deepest layers, where there is little or no oxygen (Thiel et al., 2007; Falkowski, 1994; Mogollón and Calil, 2017). The biogeochemical cycles that are affected in this process are C, O N, P, and S. The whole process is determined by many factors that could occur over a few hours to days or take several thousands of years (Bigg, 2003). Once nutrients are available again at depth, they could be brought back up owing to physical mechanisms such as upwelling (Bigg, 2003; Echevin et al., 2014). Therefore, the euphotic layer has more nutrients in regions with significant upwelling. Thus, phytoplankton increases its production and hence, fish populations (Gómez et al., 2012).

Eastern Boundary Upwelling Systems (EBUS) are considered the most productive zones of the world's oceans. They are dominated by seasonally-regulated upwelling episodes linked to alongshore winds (Mogollón and Calil, 2017; Vergara et al., 2017). These winds force the surface waters offshore to be replaced with deep water rich in nutrients. This phenomenon is the Zonal Ekman Transport (ZET; Yuras et al., 2005; Corredor-Acosta et al., 2015; Echevin et al., 2014; Gómez et al., 2012). There are many EBUSs, such as California, Morocco, and Namibia, but the most productive is in the Peru-Chilean region (Figure 1.1), owing to the Southeast Pacific Subtropical Anticyclone (SPSA) and Humboldt Current System (HCS). The SPSA creates favourable winds for upwelling, while HCS causes the water to be even colder (Ancapichun and Garcés, 2015; Yuras et al., 2005; Gómez et al., 2017). As a result, the annual cycle of phytoplankton and primary production are significant, making the Peru-Chile coast responsible for more than ten percent of the worldwide marine fisheries (Vergara et al., 2017; Mongollón and Calil, 2017; Corredor-Acosta et al., 2015; Gómez et al., 2012; Yuras et al., 2005). However, phytoplankton productivity could be limited by micronutrients such as Fe in the Southern Ocean, subarctic North Pacific and Equatorial Pacific (Bigg, 2003). This phenomenon leads to a high nutrient low chlorophyll zone (HNLC), and it occurs when some specific nutrients are missing, usually Fe, Si or, in some cases, PO_4^{-2} and NO_3^- (Vergara et al., 2017; Dezileau et al., 2004).

Fe and Si are also essential nutrients required by phytoplankton. These are supplied by dust deposition, sediment mobilisation and riverine input (Dezileau et al., 2004; Chase et al., 2002). This deposition and mobilisation happen continuously in arid regions (Echevin et al., 2014; Dansie et al., 2018). Meanwhile, there could be glacial/iceberg meltwater in the coldest areas. Glacial sediments typically contain significant quantities of Fe nanoparticles, of which a substantial part is bioavailable. The amounts of Fe here are even more bioavailable than the Fe present in typical atmospheric dust (Raiswell, 2011). This is because Fe required must be dissolved involving the hydroxyl ion (OH^-; Bigg, 2003). Some particles or colloids, along with deep-sea sources of Fe, such as lithogenic material, do exist in the ocean, but it is not always dissolved, while that from the glaciers is more likely to be suspended (Dezileau et al., 2004; Chase et al., 2002; Braun et al., 2019).

Once HNLC areas are enriched with the limiting nutrient, phytoplankton increases rapidly over 5-15 days, and it disappears when the limiting elements are consumed (Boyd et al., 2004). Coastal waters are typically iron- and silicon-rich compared to the open ocean (Chase et al., 2002; Dezileau et al., 2004). This is because the coast is shallower and closer to

terrestrial sources. Therefore, upwelling of deep water along the coast tends to reduce its Fe concentration as it imports water from offshore (Chase et al., 2002).

Phytoplankton variation is essential because it forms the main diet of zooplankton, the food for pelagic fish (Gómez et al., 2017). The fish populations are linked directly to phytoplankton concentration and conditions that affect it (Gómez et al., 2012). Gómez et al. (2012) studied the annual relationship between the recruitment of sardines (R) and the recruitment per spawning biomass (RPS) with phytoplankton concentration for the period 1991-2004 in the Central Zone of Chile (36°-39°S). The fish populations were calculated by a stock assessment model that estimates fish survival and catches, while phytoplankton was determined by remote sensing (Figure 1.2).
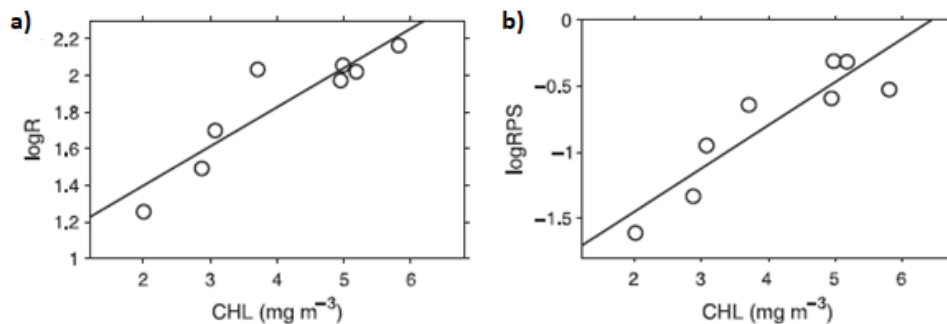
FIGURE 1.2. LINEAR REGRESSION MODELS WITH LOGR AND LOGRPS AGAINST THE CHL. THE R^2 IN BOTH CASES IS 0.92, SHOWING A STRONG RELATIONSHIP (GÓMEZ ET AL., 2012).

Despite the importance of this topic in understanding fisheries, the impact of forced intraseasonal variability on coastal primary production is poorly investigated for many reasons: First, it is hard to determine its implications from observations (Echevin et al., 2014). Second, it is difficult to forecast the impact of the weather and oceanic phenomena on the ecosystem from the few coastal moorings because of the intrinsic random variability. These relationships are not clear (Echevin et al., 2014). Complex models are used along with satellite information to understand these processes. In general, two types of models are needed. An oceanic model is required to understand the current movements along with its physical changes, while a biochemical model is used to comprehend phytoplankton development (Vergara et al., 2017; Mongollón and Calil, 2017; Corredor-Acosta et al., 2015; Gómez et al., 2017; Echevin et al., 2014).

In the case of Chile, previous studies have mainly covered specific zones located in the Central-Southern Zone (Vergara et al., 2017; Corredor-Acosta et al., 2015; Gómez et al., 2017). This leaves much of the long and varied Chilean coast unstudied. This is very important because, as Figure 1.1 demonstrates, there is an evident multi-zone character to the Chilean coastline, from experiencing the southern end of the Peruvian high productivity through a region with rather less production and less extensive to a more upper production region in the Southern Zone. Therefore, a first production study in the whole territory will help to understand which regions are more productive and how they are affected by climate drivers. This information is also valuable as a first stage for developing better fisheries strategies.

1.1. Aim and Objectives.

This research aims to investigate the spatial and temporal variability of phytoplankton behaviour along the Chilean coast, considering the influence of climate drivers (e.g., SPSA and HCS) and external factors (e.g., rivers, glaciers, rainfall, and dust deposition).

The following objectives are necessary to fulfil the aim.

O.1. Determination of the trends in seasonal, interannual and spatial variability for parameters that affect phytoplankton production.

This objective will define what parameters are more relevant to phytoplankton per Zone and their possible relationships. Anomalies per Zone will be identified, as well.

O.2. Understanding how climate drivers contribute to phytoplankton production.

This objective will estimate the impact of climate drivers on the physical parameters and the phytoplankton.

O.3. Determine specific mechanisms for an increase of phytoplankton in Case Study events.

This objective will clarify the triggers that produce a particular case study. Thus, it will be possible to understand better what happened in each extreme event, plus some external factors.

2. Setting the Scene – the Climate Environment and Coastal Biology.

2.1 Climate Variables.

2.1.1 Winds.

Winds are caused by the density differences existing between two regions. When the air is heated up, it tends to rise due to its density decrease. Another layer of air fills that space. The higher the difference in density, the faster the movement. This movement generates a vertical and horizontal pressure difference (Barreiro,2013). Consequently, the pressure difference leads to the formation of both horizontal and vertical winds. Horizontal-wise, winds move through the isobars. In the oceanic context, this process also produces in part, the movement of the currents by the planetary winds (Barreiro, 2013).

As the Earth receives more energy from the sun in the Equator than in the Poles, the warmer air moves polewards to maintain the energy balance forming a cell per Hemisphere. However, as the Earth is tilted, the heat varies in each region across the year, affecting air movements (Pinet, 2009; Colling, 2001). Additionally, the direction of the winds is also affected by the Earth's rotation, causing it to be deviated to the right in the Northern Hemisphere and left in the Southern Hemisphere; this phenomenon is called the Coriolis effect. The deviation magnitude depends on the latitude. So, its rate goes from zero at the Equator to the maximum at the poles (Barreiro, 2013; Pinet, 2009).

Due to the angular momentum and friction acting on the surface re-circulation path, each Hemisphere has three meridional cells instead of one: the Hadley, Ferrel, and Polar cells (Figure 2.1). Each cell has one ascending branch and another descending (Barreiro, 2013; Pinet, 2009). At the same time, these cells are affected internally by the Coriolis effect (Barreiro, 2013; Pinet, 2009). For example, the upper-level branches flow poleward in the Hadley cells but are diverted to the east in both Hemispheres generating the midlatitude upper-tropospheric winds. On the other hand, the Coriolis effect affects the air descending near 30°S latitude in each Hemisphere. Part of this air returns towards the Equator, travelling near the surface and deviating westward, forming the well-known Trade winds due to Coriolis being cero here. The other amount of air that descends at that same point moves to the Poles on the surface and is deflected to the east, leading to the lower-tropospheric westerlies (Barreiro, 2013).
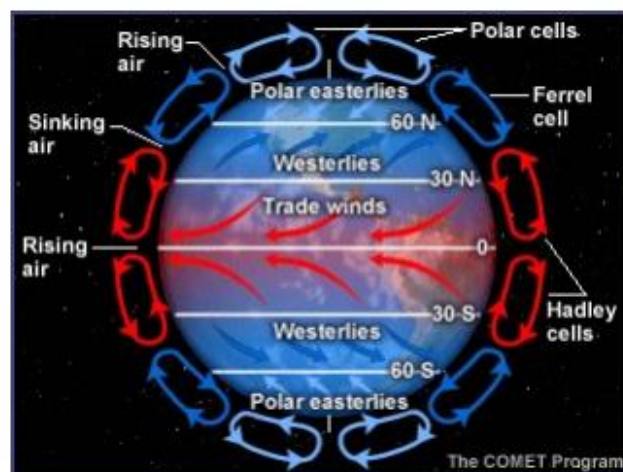
FIGURE 2.1. AVERAGE CIRCULATION CELLS IN THE EARTH'S ATMOSPHERE (BARREIRO, 2013).

The rising air in the Equator (0°) and the high latitudes (60°) form a low-pressure area, while the sinking air in the midlatitudes (30°) creates a high-pressure region defined in the Ferrel cell. Figure 2.2 shows the location of these low- and high-pressure systems, better defined in the Southern Hemisphere because the Northern Hemisphere contains more land that disrupts the winds (Colling, 2001; Barreiro, 2013). Vortices are formed around the pressure centres due to the Coriolis effect. The low-pressure centres converge the winds ascending in the centre, whereas the high-pressure centres diverge, known as cyclones and anticyclones, respectively (Colling, 2001). This happens because the planetary winds are affected by the resistance that surface roughness produces, slowing down the flow and changing its direction from the isobars (Barreiro, 2013). The circulation around the cyclone is anticlockwise in the Northern Hemisphere and clockwise in the Southern. Meanwhile, the anticyclone is clockwise in the Northern and anticlockwise in the Southern Hemisphere (Colling, 2001). The low-pressure areas lead to unstable conditions producing heavy rains, while the high-pressure zones are characterised by high evaporation, leading to arid conditions. Therefore, anticyclones are associated with dry conditions, while cyclones are humid (Colling, 2001; Bigg, 2003).
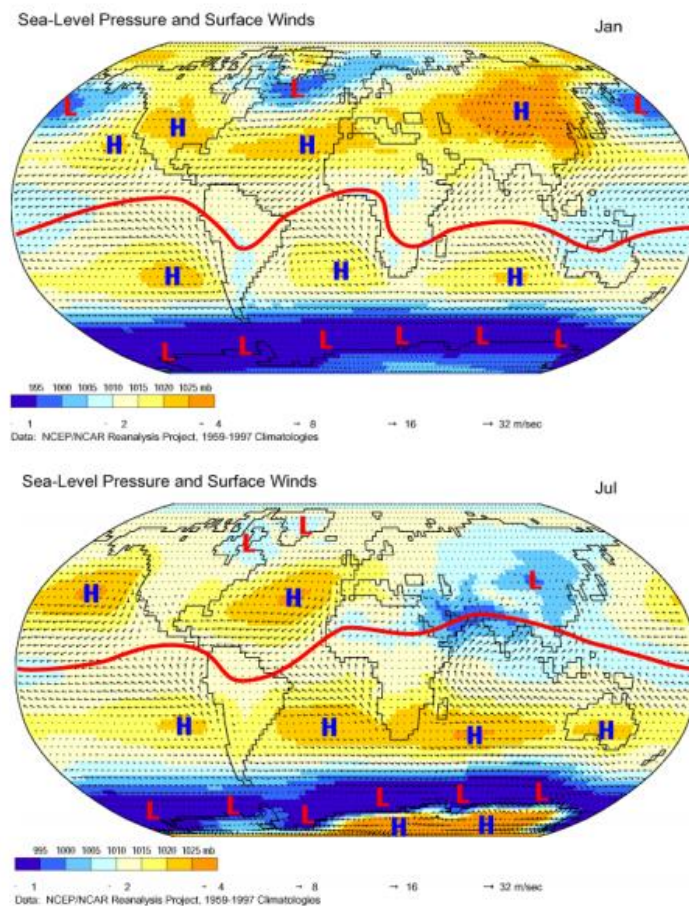
FIGURE 2.2. ATMOSPHERIC PRESSURE AT SEA LEVEL AND SURFACE WINDS IN JANUARY (ABOVE) AND JULY (BELOW). THE RED LINE ROUGHLY MARKS THE RISE ZONE OF HADLEY'S CELL, WHILE THE LETTERS H AND L DENOTE AREA HIGH AND LOW SURFACE PRESSURE AREAS, RESPECTIVELY (BARREIRO, 2013).

Due to the excessive energy for the sinking and ascending of the air, westerly jet streams are produced in the tropopause of the Ferrel cell limits, which are at 60° and 30°, known as Polar and subtropical jet streams, respectively (Bigg, 2003). Jet streams, which are approximately located at heights over 10 km, reaching more than 200 km h^{-1}, define the boundary of the high- and low-pressure zones, known as a warm and cold front, respectively (Colling, 2001). These limits or fronts constantly change due to heat variation across the year (Figure 2.2) and the Coriolis effect (Colling, 2001).

As it was mentioned, the Coriolis effect alters the wind and front directions depending on the latitude. Hence, polar jet streams present a higher undulation due to their location at high latitudes, allowing cold fronts to enter midlatitudes. However, warm fronts can also penetrate the high latitudes, but their motion is less wavy and more stable (Colling 2001). These front interactions can develop sporadic anticyclones and cyclones that are split for the border, or even isolated fronts (cut-off) can move more profoundly in the opposite region (Figure 2.3). These front interactions reduce their energy, so they are short-lived. When the fronts are combined, the result is an occluded front. Therefore, a sporadic low-pressure system can be seen in the midlatitudes or vice versa (Colling, 2001). The extended high-pressure regions are known as ridges, while the low-pressure regions are called troughs or lows (Barreiro, 2013; Pinet, 2009).
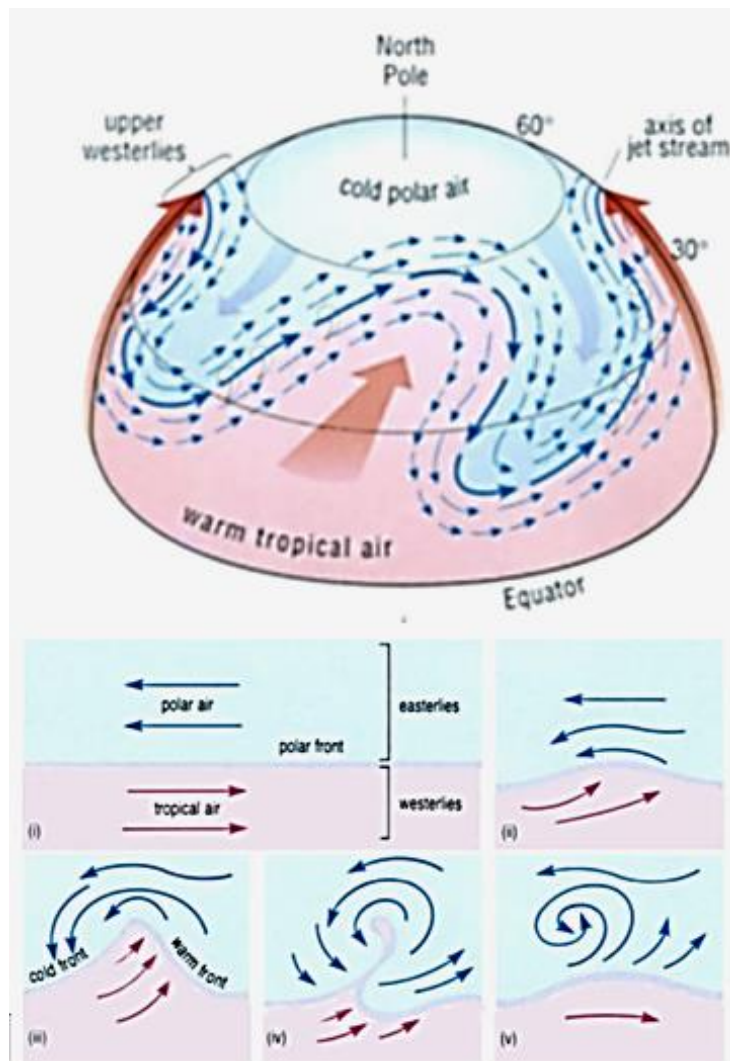
FIGURE 2.3. POLAR JET STREAM'S UNDULATION IN THE NORTHERN HEMISPHERE MIXING COLD AND WARM FRONTS (TOP PANEL). THE BOTTOM PANEL SHOWS HOW THE FRONT COLLISION CAN SWIRL, FORMING CYCLONES (V) OR ISOLATED PRESSURE SYSTEMS (IV) (COLLING, 2001).

2.1.2 Currents.

The current movement can be divided into two major components: The wind's forced circulation and the thermohaline circulation (Colling, 2001). The first is due to surface winds that guide the currents. In contrast, the second term refers to the very large-scale circulation created by the density differences between the water masses due to their temperature or salinity differences (Pinet, 2009). This is particularly important because the sunlight does not

penetrate to great depths heating only the ocean surface and forming thermoclines (Barreiro, 2013; Bigg, 2003).

These salinity differences are produced by adding or extracting water in a particular place. Precipitation, evaporation and river discharges are the mechanisms that control this water fluctuation. In the Polar regions, ice melting and frozen water also produce these fluctuations (Colling, 2001).
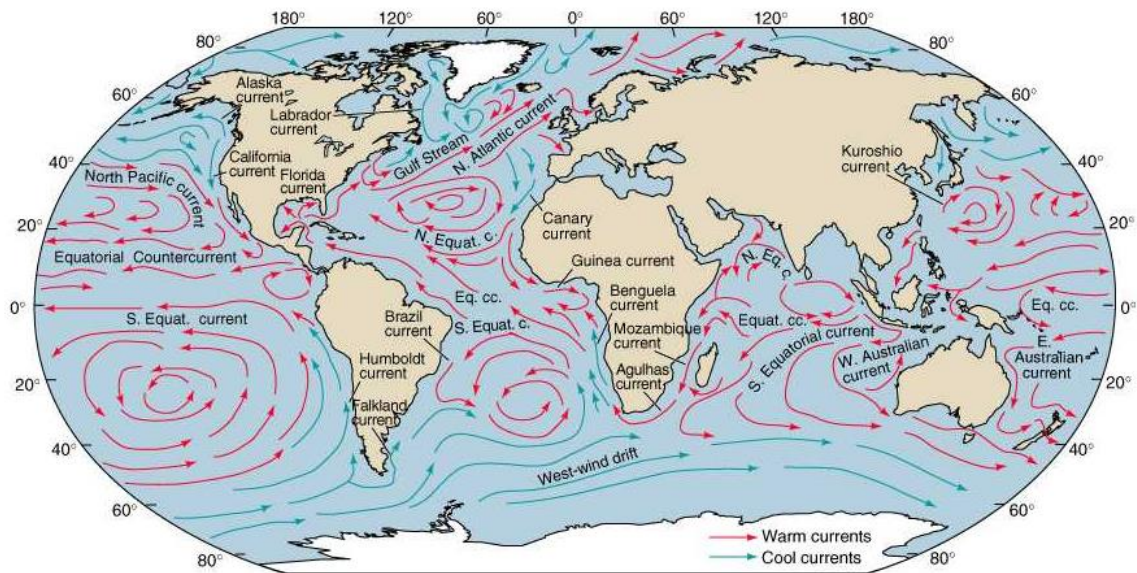
FIGURE 2.4. OCEAN SURFACE CURRENTS (BARREIRO, 2013).

Similarly to the winds, the Coriolis effect affects the currents, forming a deflection that increases towards the poles while the Equator is Zero. In the ocean, this motion creates waves that are capable of transporting energy to other regions (Pinet, 2009). The equatorial Kelvin waves are long-wave types that propagate eastward and only exist on the Equator (Bigg, 2003). These can then feed into coastal Kelvin waves, which are the energy that follows the Equator's coastline polewards, opposing the surface currents, such as in South America. The Rossby waves are another type of wave that travels westwards. This wave is much slower than the Kelvin because they react to variations in the Coriolis effect with the latitude, forming curves. Thus, the curves are more pronounced in the high latitudes (von der Heydt, 2016; Bigg, 2003), leading to westward currents along the Equator and eastward currents in midlatitudes give rise to the subtropical ocean gyres driven by the cyclones and anticyclones in the Pacific and Atlantic Oceans subpolar gyres that are shown in Figure 2.4 (Barreiro, 2013).

Comparing Figures 2.4 with 2.2 shows that the surface currents follow the typical wind patterns, sharing the direction and speed. However, the gyres are asymmetrical and do not fit perfectly with the wind patterns (Pinet, 2009; Barreiro, 2013). This distortion results from how the currents are formed by ocean friction with wind, which generates a response in the upper part of the water column, about 30-70 m. This zone is called the Ekman layer, where there is a balance of forces between friction and Coriolis, forming a spiral; it has a lower speed as it goes down in the water column. On the surface, the current forms at 45° in the wind direction. The Northern Hemisphere goes to the right, while the Southern Hemisphere goes in the opposite direction. This spiral leads to the Zonal Ekman Transport (ZET; Barreiro, 2013; Corredor-Acosta et al., 2015; Gómez et al., 2012). Another factor influencing these differences is the geographic land configuration that blocks the current motion (Bigg, 2003).

In general, the western boundary currents are intense and deep as the Gulf Stream and Kuroshio in the Northern Hemisphere, and to a lesser extent, the current of Brazil and that of the Agulhas in the Southern Hemisphere. On the contrary, the currents along the eastern boundaries are weaker, helping to form more upwelling systems in the East (Barreiro, 2013).

Eastern Boundary Upwelling Systems (EBUS) are considered the most productive zones of the world's oceans. They are dominated by extreme seasonally-regulated upwelling episodes linked to alongshore winds, advecting water equatorwards due to coastal Kelvin waves, also known as coastal-trapped waves. These winds force an offshore surface slope forming a flow that drags surface waters offshore (Figure 2.5). An upward flow of cold waters boosts this flow by the ZET (section 2.1.2.1; Vergara et al., 2017; Mongollón and Calil, 2017; Corredor-Acosta et al., 2015; Barrero, 2013; Ancapichun and Garcés, 2015; Yuras et al., 2005). Extreme seasonally-regulated upwelling episodes dominate them. Additionally, Kelvin wave allows upwelling to propagate beyond the region where the alongshore winds occur, and Ekman transport gives upwelling.
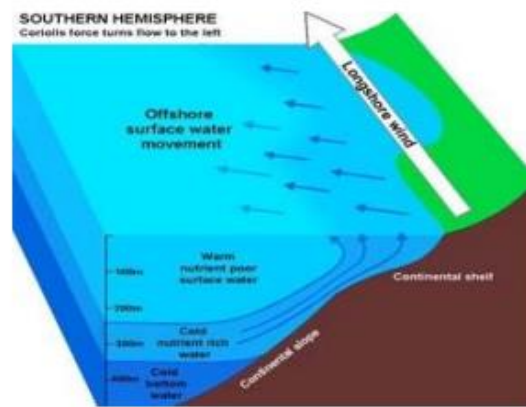
FIGURE 2.5. BOUNDARY UPWELLING SYSTEM IN THE SOUTHERN HEMISPHERE (BARREIRO, 2013).

The nutrients brought by the upwelling are primarily N and P, which come from the decomposition of marine organisms' remnants known as detritus (Mogollón and Calil, 2017; Falkowski, 1994). Detritus sinks to the bottom depth of the ocean at different speeds, depending on its size (Gómez et al., 2017; Vergara et al., 2017). Aerobic bacteria demineralise detritus in the upper layers, and anaerobic bacteria in the deepest layers, with little or no oxygen (Thiel et al., 2007; Falkowski, 1994; Mogollón and Calil, 2017). The biogeochemical cycles affected in this process are C, O N, P, and S. The whole process is determined by many factors that could occur over a few hours to days or take several thousands of years (Bigg, 2003).

2.1.2.1 Ekman Transport.

The ZET can be calculated to estimate the upwelling and define how much nutrients are supplied to the surface. ZET depends on the meridional wind stress (WS_y). Wind stress is the force that wind produces on the ocean surface. Although this variable is not obtained by satellite imaging, it can be derived from wind speed using the following equation (Gómez et al., 2012).

$$WS_y = \rho_a \cdot C_d \cdot |V| \cdot v \tag{2.1}$$

Where ρ_a is air density (1.2 kg m^{-3}), C_d is the drag coefficient (0.0012) based on observational data for winds below 10 m s^{-1}, $|V|$ is the wind speed, and v is the meridional wind component. Then, the ZET is calculated (Ancapichun and Garcés, 2015; Gómez et al., 2012;

Liao et al., 2016). Here it was considered that the geostrophic transport is negligible (Liao et al., 2016).

$$ZET = \frac{WS_y}{\rho_w f} \tag{2.2}$$

Where ρ_w is the seawater density (1026.97 kg m^{-3}), and f is the Coriolis effect. The Coriolis effect can be easily estimated by $2\Omega sin\theta$; where Ω is the Earth's angular velocity (7.292·10^{-5} s^{-1}) and θ is the latitude of the study area. Negative ZET values imply offshore transport or the opposite if it is positive (Ancapichun and Garcés, 2015; Gómez et al., 2012). Then the Ekman layer depth can be estimated using Eq. 2.3, where 3.2 combined other constants as C_d, ρ_a and ρ_w (Liao et al., 2016).

$$D = \frac{3.2\, V}{\sqrt{\sin \theta}} \tag{2.3}$$

The vertical speed of the ZET determines the speed of upwelling or downwelling, denominating the Ekman pumping (EP) and is defined by the following equations (Ancapichun and Garcés, 2015; Ancapichun, 2012; Bravo et al., 2016).

$$EP = \frac{Curl(WS)}{\rho_w f} + \frac{\beta \cdot WS_x}{\rho_w f^2} \tag{2.4}$$

$$Curl(WS) = \frac{WS_y}{\partial x} + \frac{WS_x}{\partial y} \tag{2.5}$$

The second term of Eq. 2.4 is generally rejected because β represents the rate of variation of the Coriolis between the latitudes in the Ekman transport, which are insignificant (Bravo et al., 2016). The Curl represents Ekman's spiral spin (Bigg, 2003). Finally, any nutrient concentration (mmol m^{-1} s^{-1}) supply can be obtained as total vertical transport multiplied by the concentration of that nutrient (Liao et al., 2016).

$$N_{supply} = ZET \cdot [N_D]_{Rossby} + EP \cdot [N_D]_{coastal\,band} \tag{2.6}$$

The nutrient concentrations added come from the values located at a depth of the Ekman layer estimated by Eq. 2.3. The concentration multiplied by the ZET is at the coast but with a Rossby radius deformation product of the Coriolis variation along the latitude. Therefore, the radius will be shorter at higher latitudes; for example, the Rossby radius is 60 Km at 15°S, while at 19°S is 55 km. In comparison, the EP is also multiplied by concentration at depth D but on the coastal edge defined by the shelf width (Liao et al., 2016).

2.2 Main Climate Drivers that affect the South America West Coast.

The South American west coast is a very productive region, with more than 10% of the worldwide marine fish catch, especially in the Peru-Chile current system (Vergara et al., 2017; Barrero, 2003; Salvatteci et al., 2017). This high production is related to the Southeast Pacific Subtropical Anticyclone (SPSA) and Humboldt Current System (HCS), which will be explained in more detail in this section. Other climate signals that affect the SPSA and HCS are the El Niño Southern Oscillation (ENSO) and Pacific Decadal Oscillation (PDO; Corredor-Acosta et al., 2015; Ancapichun and Garcés, 2015). Finally, the Antarctic Oscillation (AAO) presents a relevant impact in the southern part of South America (Ancapichun and Garcés, 2015). Other climate drivers that focus on the South Atlantic are blocked by the Andes (CONAMA, 2008; Quintana and Aceituno, 2011).

2.2.1 Southern Pacific Subtropical Anticyclone (SPSA).

The SPSA is the main atmospheric circulation component in the South Pacific Ocean, affecting from 0° to 42°S with a higher-pressure system (anticyclonic conditions) centred at 30°S. This area includes the coast of Ecuador, Peru, and the Northern toward the Central part of Chile (Ancapichun and Garcés, 2015). On the other hand, Antarctica presents a low-pressure system (cyclonic conditions) in the Amundsen and Bellingshausen Seas. Both systems are linked, forming the South Pacific dipole (Figure 2.2; Garreaud et al.,2020).

As section 2.1.1 mentioned, anticyclones in the Southern Hemisphere are vortices where the air sinks and spreads outwards anticlockwise, producing arid conditions (Colling, 2001). Hence, the SPSA leads southerly winds from 18° to 40°S, creating coastal upwelling because this South American region has a relatively straight meridionally oriented coastline (Thiel et al., 2007). The Andes mountains restrain the SPSA and block atmospheric frontal systems from the southwest, leading to particularly intense and dry winds (Barrett et al., 2009; Shultz et al., 2011). However, if the winds are too intense, they can produce turbulence. This turbulence disperses the nutrients and the plankton itself (Thiel et al., 2007). For that reason, optimal conditions are driven by winds with medium speeds, which are often found in this EBUS, especially in the Central Zone (30°-40°S) of Chile, where the SPSA centre is located (Gómez et al., 2012; Salvetteci et al., 2017; Thiel et al., 2007). Additionally, longshore winds around 5-6m s^{-1} have shown an increment in the pelagic fish population. Velocities over this, the flux becomes more turbulent, harming larval transport and affecting adequate nutrient motion through the surface (Gómez et al., 2012; Thiel et al., 2007). In Southern Chile (40°-56°S), the westerly winds prevail due to the low-pressure located further south (Garreaud et al., 2020).
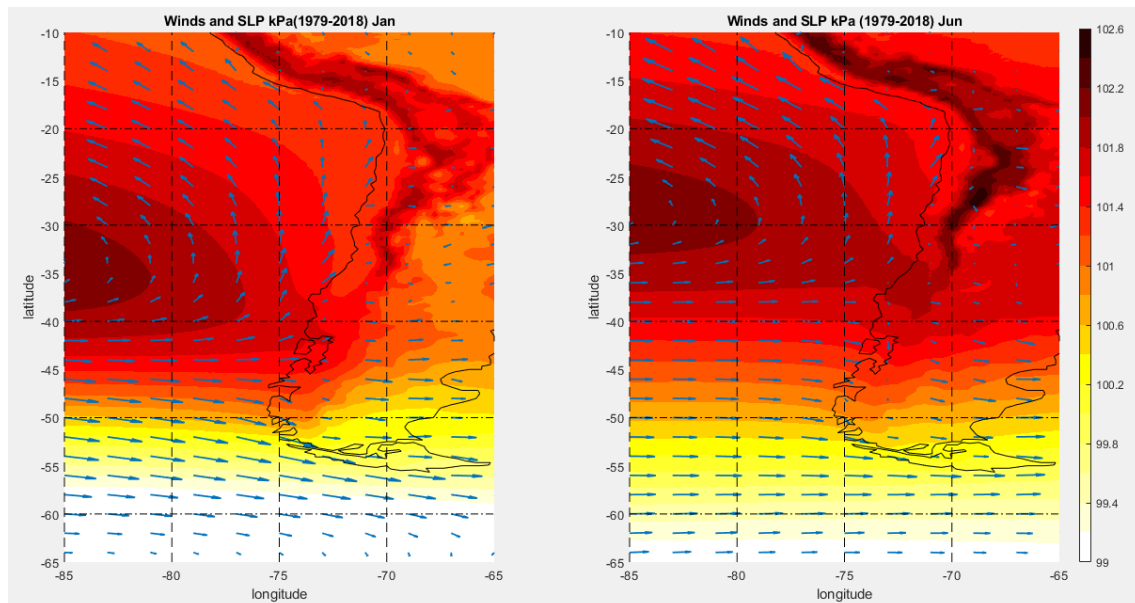
FIGURE 2.6. MONTHLY AVERAGED SEA LEVEL PRESSURE (SLP) AND WINDS FROM 1979 TO 2018, USING THE ERA5 DATASET. THE PANELS SHOW HOW THE HIGH-PRESSURE CENTRE VARIES FROM JANUARY (LEFT) TO JUNE (RIGHT) AND HOW THESE AFFECT THE WIND DIRECTION.

The SPSA has seasonal, interannual and interdecadal cycles. These cycles cause wind fluctuations in direction and intensity, disrupting normal conditions (Ancapichun and Garcés, 2015). Seasonally, the SPSA's core moves southwards during the Austral summer to 35°S, leading to southerly winds until 42°S; meanwhile, it moves to the Equator in the Austral winter (Figure 2.6). This produces a high wind variation between 35° to 42°S (Rahn, 2012; Ancapichun and Garcés, 2015; Aguirre et al., 2021). Due to this, cold fronts arrive in the Central Zone during the winter from the south, producing westerly winds, intense precipitation episodes and downwelling conditions. Meanwhile, from 40 to 42°S experience dry summers (Ancapichun and Garcés, 2015; Rahn, 2012; Quintana and Aceituno, 2011). The

winds in the section between 18° to 28°S do not change their direction, but they experience weak winds (Ancapichun and Garcés, 2015; Rahn, 2012; Aguirre et al., 2021).

On the interannual scale, SPSA variation is driven by ENSO and AAO altering the South Pacific dipole (Ancapichun and Garcés, 2015; Garreaud et al., 2020). In the case of its interdecadal range, it is altered by the PDO (Quintana and Aceituno, 2001; Ancapichun and Garcés, 2015), which will be discussed in the following sections. Finally, several studies have shown a wind intensification in this region, along with EBUS of California and Benguela over the recent years, owing to global warming (Salvetteci et al., 2017).

2.2.2 Humboldt Current System (HCS).

The longshore winds formed by the SPSA and the opposing Coriolis effect given by Ekman transport offshore drag the water oceanwards. This mass transport is balanced with the upwelling of cold waters, resulting in a set of cold currents mainly flowing northward along the South American coast, passing through Chile from 42°S, Peru and Ecuador (Thiel et al., 2007; Bigg, 2003; Colling 2001). The sea surface temperatures (SST) are 5 to 10 °C colder than out in the open ocean (CONAMA, 2008). The more chilled waters are a mix of surface waters originating from subantarctic areas and deeper subcurrents from the Equator that contains more nutrients (NO_3^- and PO_4^{-2}), feeding the phytoplankton that reproduces quickly (Mongollón and Calil, 2017; Corredor-Acosta et al., 2015; Thiel et al., 2007). Zooplankton is attracted by phytoplankton, and the fish feed on these.

Part of these cold and relatively fresh waters are a branch of the Antarctic Circumpolar Current (ACC) that flows around the Antarctic and becomes part of the West Wind Drift current (WWD). The formation of the HCS is driven by the diversion of the WWD at 35 to 40°S during the Austral winter and 42°S in summer due to SPSA movement (Figure 2.7; Colling, 2001; Thiel et al., 2007; Marchant et al., 2007; Aracena et al., 2011). In that limit, the currents split into two branches that flow in opposite directions (CONAMA, 2008). The equatorward flow begins the HCS while the second joins the Cape Horn Current (CHC), which flows along the coastline to the south into the Drake Passage, joining the ACC (Thiel et al., 2007; Strub et al., 2019; CONAMA, 2008; Marchant et al., 2007; Frenger et al., 2015). Although the ACC does not enter directly to the Chilean coast as it does to the Argentinian side, sub-antarctic waters flow towards the Equator at 400 to 1200m depth with a lower depth in the further south 50-100 m (42°-56°S); this is known as Antarctic Intermediate Water (AAIW; Marchant et al., 2007; Frenger et al., 2015). At the northern end of western South America, the poleward Equatorial Subsurface Water (ESSW; aka Gunther Undercurrent) from the Equator flows between 100 to 400m depth over the continental slope until the 55°S (CONAMA, 2008; Sievers and Silva, 2008). The ESSW approaches the surface in places owing to the upwelling, primarily until 35°S. However, the AAIW also appears at the surface during intense wind periods (Marchant et al., 2007). The upwelling water delivers nutrient-rich, saline and low-oxygen water (Thiel et al., 2007).

The Humboldt Current (HC) is the primary current of the HCS. It is 300 to 400 km offshore and goes to the north until the Equator, joining the Southeast Equatorial Current (SEC). SEC is a westward surface current forced by the trade winds (Figure 2.7; CONAMA, 2008; Bigg, 2003). The Chile Coastal Current (CCC), located lower than 100 km off the coast at the surface, is driven by local winds. This branch flows primarily towards the Equator (Thiel et al., 2007; Marchant et al., 2007). This current is called the Peruvian Coastal Current (PCC) along the coast of Peru. The poleward Peru-Chilean Countercurrent (PCCC) between the HC and CCC flows transports subtropical water to Southern Chile (Marchant et al., 2007; CONAMA, 2008).

The upwellings and downwellings mainly occur in the CCC, becoming the most crucial current (Marchant et al., 2007). The flow direction that the CCC takes depends on the coastal wind patterns that seasonally change (section 2.3.1). Therefore, the CCC does not change course in northern Chile (18°-24°S). Beyond this region, the CCC is poleward flowing during the winter, especially from 35°S to the end of HCS (Thiel et al., 2007).

HCS's nutrients and oxygen levels are susceptible to equatorial ocean variations, such as ENSO altering the cold-rich water flux (Mogollón and Calil, 2017; Thiel et al., 2007). For example, the increasing organic life leads to oxygen consumption that, along with weak aeration, forms minimum oxygen zones (OMZ) in surface waters (Mongollón and Calil, 2017). The OMZ affects the plankton predators' mobility to deeper waters. On the other hand, the OMZ is where the anaerobic nutrient degradation process occurs. Areas affected by this phenomenon increase the size of the OMZ region during the warm phase of ENSO (Thiel et al., 2007; Mogollón and Calil., 2017). If ENSO is too severe, it could produce eutrophication, leading to red tides in Southern Chile (Ménesguen and Lacroix, 2018; Wells, 1997).
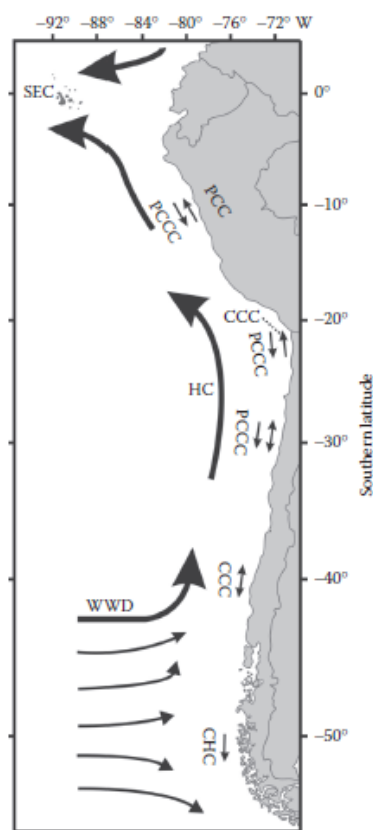
FIGURE 2.7. SURFACE HCS SCHEMA SHOWS THE DIRECTIONS OF THE CURRENTS, WHERE WWD ALSO GOES DIRECTLY TO THE ACC CURRENT (THIEL ET AL., 2007).

2.2.3 El Niño Southern Oscillation (ENSO).

The ENSO is an ocean-atmosphere system perturbation in the Pacific basin that occurs with a 2-7 year periodicity and typically starts in December-March (CONAMA, 2008). The name ENSO comes from the Southern Oscillation, of which El Niño is part. The Southern Oscillation is the variation between the sea level pressure (SLP) over the tropical indo-pacific region. Its index quantifies the pressure differences in the Pacific Basin's west and east coast (Bigg, 2003). The places usually used are the Darwin and Tahiti stations, called the Southern Oscillation Index (SOI; Colling, 2001).

The ENSO phenomenon alters the SLP differences on the west and east coast of the Pacific, modifying the Walker atmospheric circulation located over the equatorial Pacific Ocean

(Figure 2.8). Typically, the trade winds create a high sea level in the west and a low sea level in the east. This creates an opposite slope in the thermocline as the warm water is in the west (Figure 2.8). During El Niño conditions, the trade winds are reduced or change direction. This produces a relaxation of the sea level in the west, flattening the thermocline (Bigg, 2003). Thus, the South American East coast waters have become warmer for two reasons. The relaxed equatorial current brings warm water that propagates due to Kelvin waves, and the reduced upwelling in South America brings less cold water to the surface due to the deepening of the thermocline (Ancapichun and Garcés, 2015; Schollaert Uz et al., 2017; Echevin et al., 2014). El Niño leads to increases between 1 to 4°C on SST along the whole Chilean coast (Gómez et al., 2012; Ancapichun and Garcés, 2015; Saldías et al., 2016). Also, The SST and atmospheric temperature increase produced low-pressure systems arriving in the east Pacific midlatitudes, increasing the precipitations and reducing the longshore winds (Cordero et al., 2019; Garreaud et al., 2020 Vicente-Serrano et al., 2016). Thus, the warm waters are lower in nutrients as a result of the deeper thermocline and upwelled water coming from shallower depths due to weaker upwelling winds, reducing the pacific coast's primary production (Mogollón and Calil, 2017).
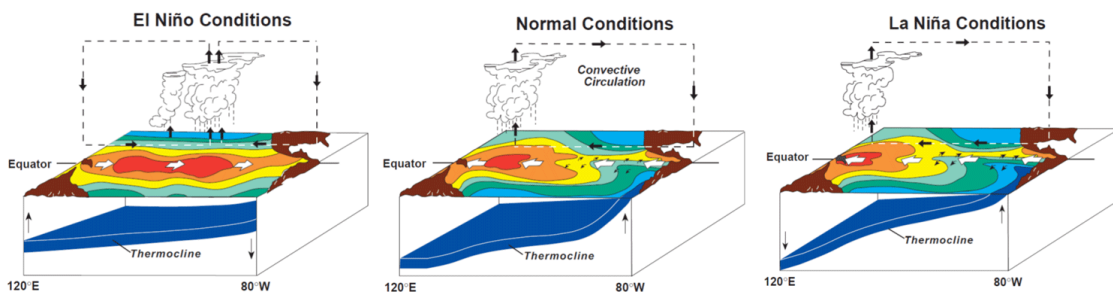
FIGURE 2.8. THE WALKER CIRCULATION'S SST, WINDS, AND THE THERMOCLINE (BLUE SURFACE) VARIATIONS DURING EL NIÑO, NORMAL, AND LA NIÑA CONDITIONS (CONAMA, 2008).

La Niña is the ENSO cold phase. In La Niña, the SST drops below 1-2°C in the Equatorial Pacific (NOAA, 2019). This variation increases the upwelling process due to stronger easterly winds that produce a higher sea level in the west (Mogollón and Calil, 2017; Gómez et al., 2012; Ancapichun and Garcés, 2015; Saldías et al., 2016; Rahn, 2012; Schollaert Uz et al., 2017). Therefore, La Niña increases the nutrient supply owing to the rise of deeper cold water (Schollaert Uz et al., 2017). On the other hand, La Niña enhances the SPSA effect intensifying the pressure difference on the South Pacific dipole, producing drought winters in the midlatitudes (Garreaud et al., 2020).

El Niño duration varies from nine months to two years because each event is unique in intensity and duration (CONAMA, 2008; Bigg, 2003). In extreme cases, a secondary intensification appears, extending El Niño for more than a year, as was seen in 1958, 1973, and 1983. These conditions finish when colder surface waters appear in the central Pacific. Sometimes, the trade winds increase too much, forming a La Niña event almost immediately. These happened in 1954, 1974 and 1998 (Bigg, 2003). La Niña could last one to three years. Recent strong El Niño years were 1997-98 and 2015-16, while La Niña were 1998-00, 2007-08, and 2010-11 (NOAA, 2019).

ENSO not only affects the Pacific east coast, but the western side and the Atlantic also exhibited extensive droughts during El Niño, especially in the tropical region (Amaya and Foltz, 2014). Other regions are also affected by ENSO due to its links with the Indian Monsoon. For that reason, droughts in Africa and Asia have been detected during El Niño (Bigg, 2003). In an extreme El Niño event, cyclones are formed in French Polynesia, and the number of storms in North America has increased, while in La Niña, the opposite effect is

seen (Colling, 2001; Bigg, 2003). Whether El Niño has strengthened or diminished in the last decades is debatable (Cordero et al., 2019; Colling, 2001).

Some authors have described a new ENSO variant, called ENSO modoki, where the warmest (coldest) SST is in the middle of the Walker cells during the El Niño (La Niña) event, which is still unclear why it happens (Preethi et al., 2016; Cordero et al., 2019; Amaya and Foltz, 2014). Their impacts are slightly different; for instance, reducing the SST in the northeastern tropical, while the rest of the Atlantic is not affected (Amaya and Foltz, 2014). The central east Pacific presents drought, while the south has similar precipitation patterns as El Niño but further south (DMC, 2018). ENSO modoki years were 1986, 1990, 1991, 1994, 2002 and 2004 (Ashok et al., 2007). The years when ENSO and the other climate drivers were more intense will be discussed in chapter 5.

2.2.4   Pacific Decadal Oscillation (PDO).
The PDO is a cycle of ocean-atmosphere climate variability centred on the midlatitudes of the North Pacific Basin with an extension to the South Pacific (Ancapichun and Garcés, 2015). The PDO cycles over twenty to thirty years and has a warm and cold phase like ENSO (Quintana and Aceituno, 2011; Corredor-Acosta et al., 2015). Other studies mentioned that PDO could even have a second cycle every seventy years (Colling et al., 2001). In general, ENSO variation has been well studied over the last century; PDO had not been documented before 1960 because of the lack of reliable data (Linsley et al., 2015). Considering the time PDO cycles take, current information is not of sufficient duration to understand PDO fully. However, NOAA (2019) uses statistical methods to reconstruct SST in a 2x2° grid to extend the PDO record from 1854 until now.

The PDO positive or warm phase produces positive SST anomalies in the North and South Pacific central subtropical gyres and a warmer equatorial western Pacific. Meanwhile, SSTs decay in the Eastern tropical Pacific (Linsley et al., 2015). As a result, the westerly winds in the central North Pacific are strengthened (Ancapichun and Garcés 2015). The opposite effect is seen during the PDO's negative or cold phase (Linsley et al., 2015). These phases affect the SST, precipitation, wind patterns, and SLP (Ancapichun and Garcés, 2015; Linsley et al., 2015).

PDO and ENSO produce similar SST patterns with some exceptions. PDO presents a more extensive latitudinal range in the east part of the Pacific and a bigger amplitude in the midlatitudes than in the tropics (Linsley et al., 2015). Due to ENSO and PDO similarities but with different time scales. Thus, a positive PDO intensifies the consequences of El Niño, while a negative PDO enhances the impacts of La Niña (Quintana and Aceituno, 2011; Corredor-Acosta et al., 2015). For instance, a phytoplankton reduction was observed in the upwelling system, especially in Central-South Chile, during El Niño events coinciding with positive PDO phases (Corredor-Acosta et al., 2015). The PDO has been positive from the mid-seventies until 1999, with brief negative periods. In 1990, 1999-2002, and 2007-2014 PDO was negative, which means PDO has been more negative lately (Garreund et al., 2020). It is worth mentioning that the late intense ENSO episodes, such as El Niños 1997-98 and 2015-16 as La Niñas 1998-00, 2007-08, and 2010-11 were enhanced by the PDO.

2.2.5   Antarctic Oscillation (AAO).
AAO, aka the Southern Annular Mode, is an oscillation with interannual and interdecadal variability, affecting the Southern Ocean. AAO is a large-scale atmospheric pressure alteration between the low-pressure system in Antarctica and the high-pressure at the midlatitudes (Stammerjohn et al., 2008). These anomalies are linked to the polar jet stream motion between the Polar and Ferrel cells in the Southern Hemisphere, located in Antarctica and the ocean's midlatitudes. The polar jet stream lower in the atmosphere is where strong

westerly winds and storm systems occur (Rahn, 2012; Quintana and Aceituno, 2011; Colling, 2001). AAO is present the whole year with a high variation due to Rossby waves, with significant activity during the Austral spring (Silvestri and Vera, 2003; Colling, 2001).

AAO has three stages: neutral, positive, and negative. These phases have a time scale of two weeks but could last longer (Hendon, 2007). In its positive phase, the SLP declines in the area close to Antarctica. This intensifies the dipole's SLP differences, leading to positive SLP anomalies in the midlatitudes that generate more intense longshore winds and aridity (Quintana and Aceituno, 2011; Ancapichun and Garcés, 2015; Garreund et al., 2020). In contrast, in the negative AAO, the dipole is inverted, resulting in low-pressure systems being displaced to the midlatitudes by the high-pressure anomaly in Antarctica (Ancapichun and Garcés, 2015, Rahn 2012; Stammerjohn et al., 2008).
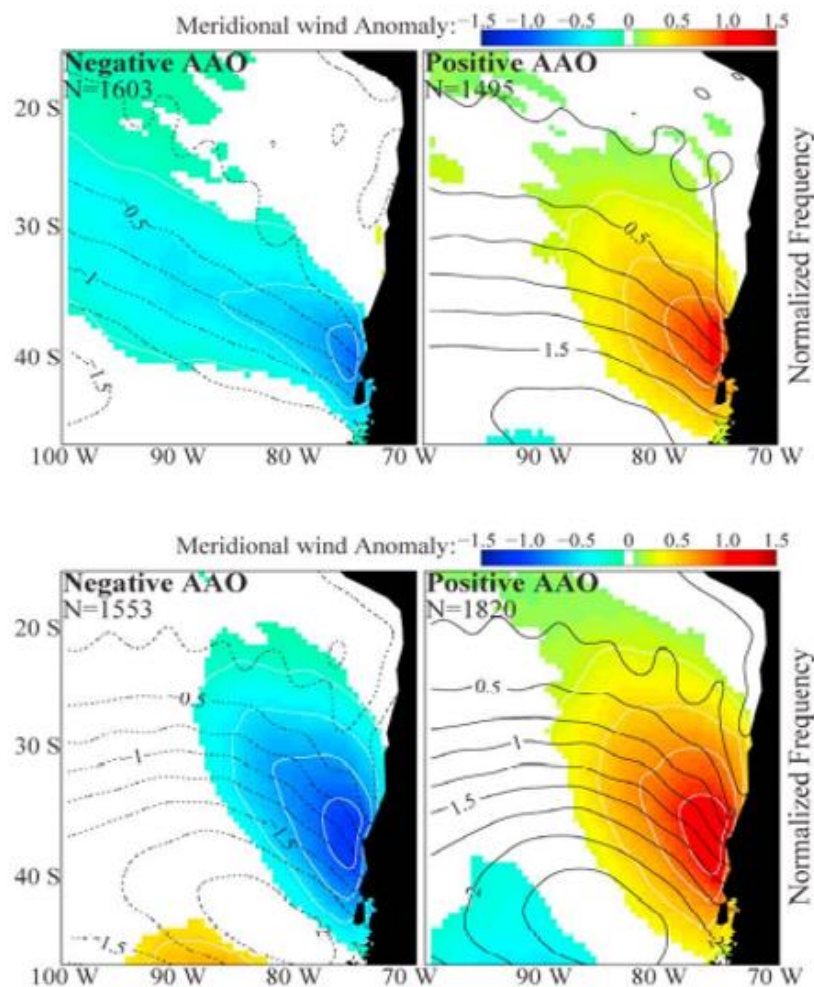
FIGURE 2.9. AAO COMPOSITES OF SLP ANOMALIES (HPA, BLACK CONTOURS) AND SIGNIFICANT LONGSHORE WIND ANOMALIES FOR SPRING-SUMMER (TOP) AND AUTUMN-WINTER (BOTTOM; RAHN, 2012).

The stronger westerly winds that AAO generates in the negative phase increase the precipitation in Australia, South America, and South Africa (Hendon, 2007). They also produce a higher sea-ice concentration and SST reduction in Antarctica (González-Reyes and Muñoz, 2013; Aravena and Luckman, 2009; Stammerjohn et al., 2008). In the case of Chile, the positive AAO increases the southerly winds and reduces the precipitation in the region around 34°S to 45°S, but especially in 40°S (Figure 2.9), retrieving the cold fronts to Antarctica. While in the negative, these fronts moved toward midlatitudes, becoming one of the precipitation sources for these latitudes (Aguayo et al., 2021, Ancapichun and Garcés, 2015, Rahn, 2012). The AAO effect is exceptionally high toward the end of Austral summer

and autumn's beginning (December to April; Figure 2.9; Cai et al., 2003; González-Reyes and Muñoz, 2013; Aravena and Luckman, 2009; Sen Gupta and McNeil, 2012; Rahn 2012). As the AAO index measures the pressure variability between mid and high latitudes in the whole Southern Hemisphere. Thus, its index does not necessarily indicate if Chile is influenced or not by the AAO (DMC, 2018).

Although the AAO changes constantly, it has a clear interdecadal tendency. AAO had shown a slightly negative tendency during the 1980s and a more positive one until now, especially in the last decade (Stammerjohn et al., 2008; NOAA, 2019). However, this more positive than negative tendency has been shown in the most recent fifty years, owing to a knock-on effect from the rise of CO_2 and Ozone depletion, leading to drier conditions in 40-45°S during that period (Cai et al., 2003; González-Reyes and Muñoz, 2013; Hendon, 2007; Cordero et al., 2019; Aguayo et al., 2021; DMC, 2018).

2.3 Plankton.

Plankton is defined as small organisms living in the ocean with weak or null swimming abilities. Thus, their motion is limited and heavily influenced by the current flow (Pinet, 2009). It is considered the base of the marine trophic web that could be divided into zooplankton and phytoplankton (Bigg, 2003).

2.3.1   Phytoplankton.

Phytoplankton is classed as algae and cyanobacteria that share the ability to photosynthesise, playing a vital role in ocean biogeochemical cycles influencing the concentration of certain atmospheric gases and aerosols. It absorbs CO_2 to form organic matter, so it is crucial to understand their behaviour (Vergara et al., 2017; Bigg, 2003).

Many species are classified as phytoplankton with different characteristics. However, the most important in terms of total biomass are diatoms and flagellates. Diatoms are the most abundant taxonomic groups that play an essential role in organic matter export to the deep sea and are classified as large with 5 µm–0.5 mm. Flagellate belongs to several classes, including both unicellular and colonial forms, with one, two, four, or eight flagella, with or without cell walls. They usually have a small size compared with diatoms (2-20µm; Bigg, 2003; Sospedra et al., 2018). Phytoplankton requires light conditions, nutrient availability, and adequate temperature for photosynthesis and then produces carbohydrates plus proteins and lipids. The proportion of products depends on environmental conditions and the type of phytoplankton. The following Eq. can summarise the process (Bigg, 2003; Echevin et al., 2014; Sospedra et al., 2018; Mogollón and Calil, 2017; Nakada and Nozaki, 2015).

$$nCO_2 + 2nH_2O \leftrightarrow nO_2 + nH_2O + n(CH_2O) \qquad (2.7)$$
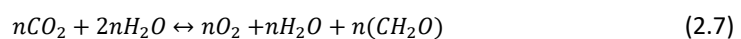
The ocean rapidly absorbs solar radiation, and only a little energy is left at a depth of 100m (euphotic layer). Thus, the section of maximum photosynthesis is below the surface, where the radiation is enough, but at the same time, they are protected from UV exposure. These characteristics and annual and daily variation in the intensity of phytoplankton energy sources affect their phenology (Bigg, 2003). Phenology studies the relationship between vegetative growth and the environment, often concerning seasonal changes in vegetative growth and decline. These periods are studied in terms of duration and intensity of the bloom per year by indices (Corredor-Acosta et al., 2015). Many phenological changes can be monitored by remote sensing due to their difference in appearance and structure in their period. The Wavelet Analysis is a way to understand phytoplankton's phenology because it allows observing its evolution, identifying changes and periodic behaviours where plants

experience chemical, physical and biological changes known as senescence (Corredor-Acosta et al., 2015; Campbell, 2002).

The macronutrients required by phytoplankton are N and P. These elements are necessary to create new cells, and both are part of the DNA structure. Some algae species can fix N as N_2, but oceanic species usually absorb NO_3^-, NO_2^- and NH_4^+ (Bigg, 2003; Dortch, 1990). NO_2^- needs a significant effort to reduce over NH_4^+. For that reason, phytoplankton may prefer NH_4^+. However, this depends on the quantity of light, N availability and the phytoplankton species (Iriarte et al., 2012). Some studies have shown that NH_4^+ is not taken if its concentration is considerably lower than NO_2^- (Dortch, 1990). The organism primarily absorbs P from PO_4^{-2} (Bigg, 2003; Vergara et al., 2017).

The light is also a critical limitation factor; for that reason, plankton production drastically decreases during the winter. Nevertheless, even when phytoplankton light requirements are satisfied, it could be limited by NO_3^- or PO_4^{-2} (Bigg, 2003). Hence, the interaction of these factors mainly marks phytoplankton behaviour. Zooplankton depends on phytoplankton because they feed on it. Consequently, these factors affect zooplankton as well. The phytoplankton bloom in spring and maybe a second in the autumn when the mixed layer begins to deepen, nutrients become available again, and the light is not limiting yet. (Corredor-Acosta et al., 2015; Bigg, 2003). To keep a high production in summer, a mechanism for renewing nutrients is required (Bigg, 2003). In the same way, the persistence of phytoplankton in that period is also related to the number of predators, such as zooplankton or even zooplankton's predators (Thiel et al., 2007).

The nutrient concentration in the euphotic layer depends on factors such as a combination of coastal aerosols (Nox, dust; Vergara et al., 2017). In particular, rivers deliver various dissolved and particulate elements to shelf waters and limit diffusion beneath the thermocline. Nutrients, organic and inorganic carbon, trace metals, pollutants and sediments, water column effects, and the diverse nature of coastal benthic substrates have a significant part in the biogeochemistry of the coastal ocean (Ikema et al., 2013; Saldías et al., 2016; Vergara et al., 2017). Bacteria also provide nutrients by decomposing dead organisms or living organisms' excreta, especially zooplankton. They can secrete enzymes that react chemically with the detrital material (dead organisms and remains of shells from plankton). This process is called remineralisation, and its speed is determined by many factors that could occur over a few hours to days or take several thousands of years (Bigg, 2003). These nutrients can return to the euphotic layer by upwelling (Gómez et al., 2017; Vergara et al., 2017).

The temperature, pH, salinity, carbon availability, and nutrients like Fe and Si are also critical in phytoplankton growth. Fe and Si may act as limiting factors for species, such as Si for diatoms (Bigg, 2003). The Fe required by phytoplankton is supplied by dust deposition and sediment mobilisation, which happens the whole time (Echevin et al., 2014). Because coastal waters are closer to shelf sediment, terrestrial sources are typically more iron-rich than the open ocean. Therefore, deep water upwelling along the coast tends to reduce their Fe concentration (Chase et al., 2002; Dezileau et al., 2004). However, the Fe required must be dissolved involving the hydroxyl ion (OH^-; Bigg, 2003). Then, some particles or colloids and deep-sea sources of Fe, such as lithogenic material, exist but are not permanently dissolved, leading to a weaker fertilisation effect. Although the particles may dissolve by photolysis at 300-400nm, this process might be complicated in winter (Chase et al., 2002; Dezileau et al., 2004; Bigg, 2003).

Si has a similar function to N for some species, like diatoms, which require as much Si as N and P for their development (De La Torre, 2016; Iriarte et al., 2012). In general, flagellates do not require Si. Silicate (SiO_4^{-2}) is a common component in the soil, which comes from

dissolved clays inside the dust (Sospedra et al., 2018). Although dust is the main fertilisation process in some particular locations, such as the Sahara desert, the primary delivery of these elements through the global ocean is by continental fluvial systems. Such as rivers (60%), the particulate matter that is dissolved in the river (20%) and groundwater discharges (7%; Ridame et al., 2014; Sospedra et al., 2018). These fluvial sediment alterations and atmospheric depositions provide the remaining SiO_4^{-2} into seawater. Thus, SiO_4^{-2} is more abundant on the coast in the same way as Fe. Diatoms have a productive life in that area, or they appear only during the spring bloom when the winter supply of entrained SiO_4^{-2} is still relatively abundant (Bigg, 2003; Sospedra et al., 2018). Hence, diatoms are more abundant in places where the river discharges are significant, while flagellates tend to appear in oceanic water where the NO_3^- and PO_4^{-2} are more concentrated (De la Torre, 2016). Additionally, dinoflagellates are superior competitors when reduced N is dominant in the water, such as NH_4^+ and organic N (Iriarte et al., 2012).

The Fe highly limits the productivity in the Southern Ocean, subarctic North Pacific and Equatorial Pacific. In the case of Peru, upwelling systems have shown Fe limits in winter, while summer phytoplankton experiences NO_3^- and SiO_4^{-2} limitations. This phenomenon is called high nutrient-low chlorophyll zones (HNLC) and occurs when some specific nutrients are missing, usually P, Fe or Si (Dezileau et al., 2004; Chase et al., 2002). Another possible explanation for HNLC is a high grazing pressure by herbivores such as zooplankton preventing phytoplankton blooms (Harris et al., 2000). The lack of Fe provokes the bloom of silicified chain-forming diatoms sinking very fast. Iron-stress diatoms consume the SiO_4^{-2} in the surface water before they deplete NO_3^-. This produces a rapid consumption of SiO_4^{-2}. Thus, Diatoms need significant levels of Si and Fe (Vergara et al., 2017; Chase et al., 2002; Echevin et al., 2014; Iriarte et al., 2012).

Contrarily, if these nutrients' abundance is satisfied, it may stimulate a rapid phytoplankton and zooplankton increase. These also may produce a significant proliferation of higher forms of plants living, such as green macroalgae on beaches, known as green tides or some phytoplanktonic species in coastal with red colour that is toxic, called red tides, which are common when only reduced forms of N are available such as NH_4^+ (Ménesguen and Lacroix, 2018; Wells, 1997; Iriarte et al., 2012). The consequences are several undesirable disorders in the marine ecosystem, such as a variation in flora and fauna, affecting their entire biodiversity, and depleting oxygen due to respiration. The lack of oxygen will provoke an anoxic zone in the bottom water, causing fish and other species' death. This process is called Eutrophication, and in many circumstances, the overcharge of nutrients is an anthropic effect, but it is also possible to be produced by natural conditions or both (Ménesguen and Lacroix, 2018).

The oceanic concentration of carbon is two or three times greater than NO_3^- or PO_4^{-2}. CO_2 transformation by photosynthesis is crucial for this conversion. Although atmospheric levels of CO_2 seem high enough, it does not limit phytoplankton growth, but low oceanic partial pressures may hinder cell growth. The temperature works as a regulator of growth speed rather than a limiting factor (Bigg, 2003).

2.3.2   Zooplankton.
Zooplankton can be differentiated from phytoplankton either based on morphology or mode of nutrition, autotrophic or heterotrophic. In general, they are considered microscopic animals. Therefore, all species have developed movements to change their vertical position but are not strong enough to overcome the currents and turbulence. Nonetheless, this mechanism helps to transfer carbon and nutrients in the water column (Harris et al., 2000; Bigg, 2003).

The term zooplankton considers various organisms with thousands of species. They usually are classified by their size, splitting into five classes (Harris et al., 2000). Nanoflagellates feeding on bacteria belongs to Nanozooplankton (2-20 μm), while ciliates and protozoans are Microzooplankton (20-200 μm). This class includes crustacean plankton and meroplankton in their early stages. Mesozooplankton (0.2-20 mm) more common species are small hydromedusa, ctenophores, Chaetognatha, appendicularians, doliolids, final stages of crustacean plankton and meroplankton larvae. The following two size categories, macrozooplankton (2-20 cm) and megazooplankton are not crucial because they do not contain many species (Harris et al., 2000).

Copepods are the most valuable specimen, which in their early-stage (copepodite), their size is 0.2μm, while in their mature stage form parts of the mesozooplankton group. They are a type of shellfish and the dominant species in the samples for their biomass. Since the 2000s, the importance of copepods has become a relevant issue, particularly the feeding impact on phytoplankton and the contribution to organic matter fluxes and the Si present in the benthos due to their silica-rich shells (Lo et al., 2004; Harris et al., 2000). Ciliates also accomplish that function. They are specialised protozoa with particular features. The most important is their cilia, short hair-like appendices with different uses like feeding or moving. Ciliates are very sensitive to changes in phytoplankton variations. For that reason, they are considered a bioindicator: thus, they react immediately to algal growth (Thorp and Rogers, 2016; Harris et al., 2000).

Zooplankton is the phytoplankton predator, which transfers their organic energy to higher trophic levels. Therefore, plankton biomass fluctuations are essential due to their effect on higher trophic levels, especially pelagic fish. Their availability is vital during the first feeding period of fish larvae (Harris et al., 2000).

3. Study Area and Data.

In general terms, Chile is a large and narrow country located in South America between the 18-and 56°S latitude and in the middle of 70°W longitude. It borders Peru in the North, the Drake Passage in the South, the Andes in the east, and the Pacific in the west. The coastline is more than 4300 km, while its width is 180 km on average (CONAMA, 2008). The shelf is very narrow in the Northern Zone (18°-30°S), less than 10 km, while the Central Zone (30°-40°S) is broader but variable, reaching a maximum width of 70 km. The Southern Zone presents a more extended shelf over 100 km wide further south of 46°S, with many fjords, adding extra complexity. The shelf edge has an approximate depth of 120 to 150 m (Thiel et al., 2007; Marchant et al., 2007; Figure 3.1).

Due to these particular geographic features, Chile contains markedly different climates across its territory, where the atmospheric temperatures slowly decrease and the rainfall increase southwards (CONAMA, 2008). These are driven mainly by SPSA and the HCS, which PDO, ENSO and AAO intermittently perturb (section 2.2; Mogollón and Calil, 2017; Ancapichun and Garcés, 2015). The SPSA generates a high-pressure system around the coast that compresses and heats the descending air mass. Then, the HCS chills that air rapidly, creating a cold layer in the bottom, forming a temperature inversion, which defines the marine boundary layer (MBL) that is more pronounced in the Northern Zone (18°-30°S). This negative temperature gradient creates stability conditions with weak winds and low-level stratocumulus that also contribute to coastal upwelling (CONAMA, 2008; Shultz et al., 2011). Another factor is the Andes, whose high elevations over 5,000 m (Figure 3.1) have snowpacks in their peaks, the rivers' primary freshwater source (Cordero et al., 2019). Additionally, the Andes constrains the SPSA, enhancing its effectiveness and leading to dry weather in Chile and wet in the Amazon basin (Barrett et al., 2009; Shultz et al., 2011; Garreaud, 2009).
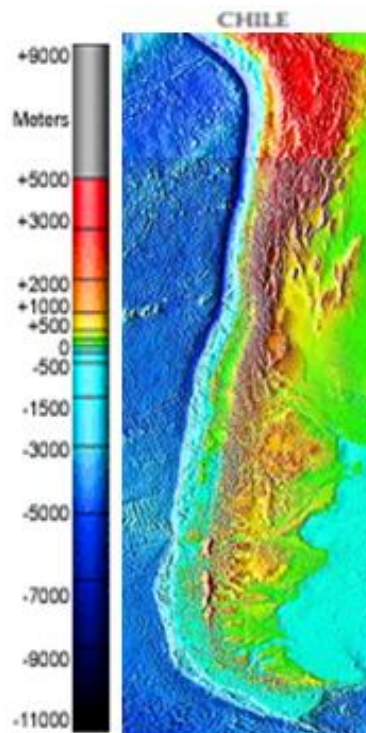
FIGURE 3.1. CHILEAN OCEAN GEOLOGY GENERATED BY COMPUTERS BASED ON REAL DATA AT A RESOLUTION OF 3,300x2,000 PIXELS (NOAA, 2000).

These climates are generally grouped into three Zones: The Northern (18°-30°S), Central (30°-40°S) and Southern Zone (40°-56°S; Thiel et al., 2007; CONAMA, 2008). The Northern Zone climate is extremely arid, with almost no precipitation (Shultz et al., 2011). The Central Zone is a Mediterranean-like climate, where most of the precipitation occurs during a few winter storms (Garreaud et al., 2020). Finally, the Southern Zone is considered a hyper-humid climate (Aguayo et al., 2021). These Zones will be discussed in more detail in the following section.

The Northern and Central Zone coastlines are relatively straight (Figure 3.1). However, the topography produces current variations that are hard to predict (Thiel et al., 2007). This leads to the formation of complex bays systems with counterrotating gyres that could affect the plankton dynamics. At the same time, along the Chilean coast exist areas with strong upwellings due to their topographic capes forming eddies and filaments. These are in Mejillones-Antofagasta (23.1°-23.6°S), Coquimbo (30°S), Valparaiso (33°S) and Concepción (36.8°S; Figure 3.2; Table 3.4; Thiel et al., 2007; Gómez et al., 2012).
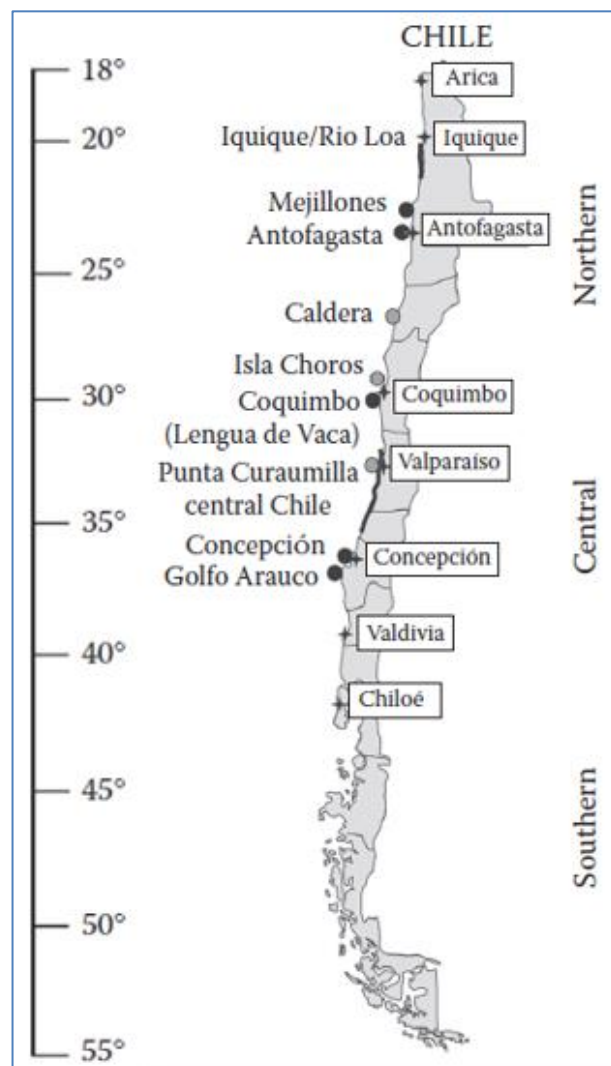
FIGURE 3.2. STUDY AREA WITH THE PRINCIPAL UPWELLING REGIONS LOCATED, THE GREY POINTS ARE ZONE WITH FREQUENT UPWELLING, WHILE THE BLACK DOTS ARE THE MAIN UPWELLING FILAMENTS ZONES. FINALLY, THE BLACK LINES SHOW THE COASTAL SECTIONS WITH OCCASIONAL UPWELLING (THIEL ET AL., 2007).

Chile has experienced an essential variation in marine productivity in the last decade due to changes in weather patterns related to climate change (Dacre et al., 2018). Besides the mentioned SST increase, climate change also has produced additional threats, such as the 10-20% snow receding in the Andes in the last decade and a big drought from 2010 to 2018 in

the whole territory with a higher impact in the Central Zone (Garreaud et al., 2020; Cordero et al., 2019; Aguayo et al., 2021). The main factors that influenced the rainfall in Chile are ENSO and AAO. El Niño increases the precipitation and consequently the snow in the Andes. However, El Niño has reduced its impact from 18°-34°S, while the AAO has been more positive, diminishing the rains from 34°-45°S in recent years (Cordero et al., 2019; Aguayo et al., 2021). The AAO's tendency is linked to CO_2 increment (Cai et al., 2003), raising ocean acidification (Ikema et al., 2013). According to Garreaud et al. (2020), the big drought was driven mainly by the SST rise in the last decades, increasing the SLP anomalies in the Central Zone and reducing the ENSO effect. Other notorious global warming effects are the Southern and Central Zone increasing wildfires (Dacre et al., 2018) and red tides (Buschmann et al., 2016).

3.1. Regional Summary.

3.1.1. Northern Zone of Chile (18°-30°S).

This Zone presents constant southerly winds from 18° to 28°S with a low variability owing to the SPSA presence the whole year and a low MBL with low-level stratocumulus (Ancapichun and Garcés, 2015; Yuras et al., 2005; Shultz et al., 2011; Garreund, 2009; Quezada et al., 2010). However, these winds are weaker than in the rest of Chile, especially from 18 to 23°S, leading to an almost aseasonal equatorwards CCC in this region with a slight increase during the autumn (Thiel et al., 2007; Aguirre et al., 2021). These winds also produce a constant upwelling system with a formation of higher upwelling filaments with relatively high NO_3^- and PO_4^{-2} in the euphotic layer close to the coast in Mejillones, Antofagasta and Coquimbo due to their topography (Figure 3.2; Thiel et al., 2007). These capes occasionally retain part of the CCC flow (squirt), chilling the coastal waters even more. Coquimbo bay tends to have more squirts (Thiel et al., 2007).

Studies in the south of Peru and north of Chile have shown that Fe is limiting, making it a HNLC Zone (Dezileau et al., 2004). The reason for that is the very narrow continental shelf, lower than 10km with a depth inferior to 100 m in some areas, and the region's aridity owing to the SPSA presence (Dezileau et al., 2004; Ancapichun and Garcés, 2015; Thiel et al., 2007). Regions with a narrow shelf have a thin OMZ, limiting the natural biological degradation of organic matter that regenerates the nutrient supply (Thiel et al., 2007; Mogollón and Calil., 2017). In contrast, the northern Peruvian coast shelf is over 100 km wide with seasonal precipitation, strong winds, along with low Coriolis. These factors lead to a constant Ekman transport that delivers a continuous nutrient supply in Peru that is transported by the poleward current ESSW (Echevin et al., 2014; Thiel et al., 2007). Effectively the Chilean region near Peru (18°-22°S) has a NO_3^- concentration of 2μM on average with a better defined OMZ region and, consequently, a more robust denitrification process (Thiel et al., 2007).

The excessive aridity makes the Northern Zone one of the driest places in the world, with meagre precipitation along with high solar radiation (Shultz et al., 2011; Garreaud, 2009; Quezada et al., 2010). The precipitation maximum fluctuates between 0.5 and 78 mm yr^{-1} (Thiel et al., 2007). Thus, riverine and atmospheric inputs are insignificant (Dezileau et al., 2004; Thiel et al., 2007). Waters with significant upwelling contribution and no freshwater discharges have a Si deficit (De la Torre, 2016), contributing to a higher predominance of small flagellates (Iriarte et al., 2000; Barlow et al., 2018). This is the situation in the Northern Zone except for Coquimbo, whose coastal waters interact with rivers (Thiel et al., 2007).

Nevertheless, the Fe limitation is more intense in the winter because episodic rainfall appears in the Andes during the summer further north 18-23°S (150 -300 mm yr^{-1}) due to convective storms related to the high radiation, which is required to become the Fe available

(Thiel et al., 2007; DiTullio et al., 2005). These rain events are significant during La Niña, whereas they are absent during El Niño (Garreaud, 2009). The precipitation of the rest of this Zone occurs during the winter, which turns into snow due to the height of the Andes (CONAMA, 2008; Dezileau et al., 2004; Garreaud, 2009). The few rivers later transport the melted snow during the Austral summer-spring, delivering Fe and Si to the ocean. These sediment inputs' intensifications should drive higher local ocean productivity (Dezileau et al., 2004). However, the river fluxes have reduced even more in the last decade (Cordero et al., 2019).
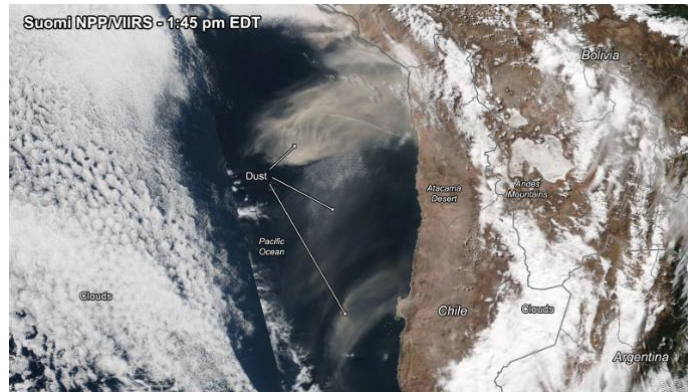
FIGURE 3.3. SUOMI NATIONAL POLAR-ORBITING PARTNERSHIP SATELLITE VIEW OF ATACAMA DUST PLUME TAKEN ON THE AFTERNOON OF 8TH JULY 2016 (SUTHERLAND, 2016).

The Atacama Desert, known as the driest region with 15 mm yr^{-1}, is a high source of dust rich in Fe and Si that could be transported to the ocean (Delizileau et al., 2004; Thiel et al., 2007). For instance, an enormous dust storm occurred in the Atacama Desert on 8th July 2016 (Figure 3.3). This storm moved along the north coast by the easterly low jet stream from the Andes (Sutherland, 2016). This thin stream moves between 100 and 20,000 m over the Earth's surface with a speed of around 10 to 15 m s^{-1} (Aceituno and Quezada, 2003). These events do not frequently happen because this region is not windy and flows westerly due to the Andes blocking the winds in the opposite direction. Indeed, they are more frequent in the Atlantic, and they are not completely clear why they happen (Sutherland, 2016; Reyers et al., 2019). Therefore, they have not been studied enough (Aceituno et al., 2015). However, their frequency has increased in recent years. For instance, similar events with lower intensity have been reported in the Northern Zone between June to September 2015, 2016, and 2018-2020 (24-horas 2015; Chilevision, 2018; Araya, 2020).

The phytoplankton concentration and the oceanic features in this Zone have not been well documented, but a few studies mention that it has a weak seasonality, with a slight increase in the winter due to more constant weather conditions, being HNLC and having a narrow shelf of 5 km on average that it does not extend over 10 km wide (Yuras et al., 2005; Thiel et al., 2007; Marchant et al., 2007). In-situ data have shown that in this area, higher Chlorophyll (Chl) concentrations are 2 mg m^{-3}; they are limited to 30 km or less from the coast (Yuras et al., 2005). Despite this generally low response, phytoplankton tends to be higher in Antofagasta, Mejillones and Coquimbo bays owing to the mentioned filaments and the fact that the capes restrict the phytoplankton. Another region with a high response is Arica-Iquique (18.5°-20.2°S, Figure 3.2), owing to a permanent nutrient supply by the poleward ESSW from Peru (Thiel et al., 2007, Echevin et al., 2014). Thus, this region has had more fisheries since the 1960s (Camus and Hajek, 1998).

El Niño increases the SST and weakens the southerly winds in this Zone during the Austral spring-summer leading to a primary production reduction of 11 to 48% compared to a regular year (Iriarte et al., 2000; DMC, 2018). These effects are higher during El Niño Modoki (DMC, 2018). As La Niña strengthens the SPSA, the phytoplankton is enhanced. Nonetheless,

these impacts are minimal compared to the ENSO effects on the Central and Southern Zones (Thiel et al., 2007).

In terms of anthropogenic activities that could harm the phytoplankton, this Zone is known for its copper mining industry, which is the main economic activity of Chile (Jara et al., 2014; Camus and Hajek, 1998). However, this activity generates significant trace metal levels in their tailings, which were often discharged into the sea or rivers for decades in the past (Camus and Hajek, 1998). Also, this industry requires large quantities of water, reducing the volume of the few rivers that exist in this region (Camus and Haje, 1998). Antofagasta to Valparaiso (Figure 3.2) is where the copper minings are concentrated, but Chañaral (26.3°S; Table 3.4) was the most affected by dumping tailings into the coast from 1938 to 1990 due to the lack of environmental policies to improve the Chilean economy (Lee and Correa, 2005; Camus and Hajek, 1998). Studies reported significant Fe, Cu and Cr levels in Chañaral, bioaccumulated by molluscs (Jara et al., 2014; Lee and Correa, 2005). Lee and Correa (2005) found that the zooplankton was lower on the Chañaral coasts, particularly harming copepods. Caldera (27.1°S) and Huasco (28.5°S) showed a high concentration of Cr with similar effects to the previous case (Jara et al., 2014; Table 3.4).

Mejillones, which has one of the most significant upwelling filaments in this Zone, is another city severely polluted because it is one of the most industrial developed in the north, with thermoelectric plants, coal loading docks, acid transfer plants for mining and fisheries located across the bay (Valdez, 2012). Thiel et al. (2007) and Valdez (2012) reported moderate Pb, Cu, Ni, Co, Zn and Cd levels in the water column and sediments in Mejillones bay (Figure 3.2 and Table 3.4). Finally, anthropogenic activities have not severely affected Coquimbo Bay (Thiel et al., 2007).

3.1.2. Central Zone of Chile (30°-40°S).

This area presents an evident seasonal coastal upwelling during the Austral spring-summer and downwelling during the autumn-winter due to the wind direction in that period driven by the SPSA movement, giving a Mediterranean-like climate (CONAMA, 2008; Ancapichun and Garcés, 2015; Garreaud et al., 2020). Therefore, the maximum precipitation occurs during the Austral winter produced by cold fronts, increasing the number of nutrients (Quintana and Aceintuno, 2002; Delizileau et al., 2004; Garreaud et al., 2020). However, the annual precipitation varies drastically southward, from 100 mm at 30°S to 2000 mm at 38°S, driven by SPSA motion (Garreaud et al., 2020; CONAMA, 2008). Due to these significant differences, the northern region 30°-32°S has a semiarid climate, whereas the Southern-Central Zone is semihumid to humid 36°-40°S (CONAMA, 2008). The Central Zone has suffered a precipitation decline since the late 1970s. For that reason, this region was the most affected by the 2010-2018 big drought, with a 25 to 45% deficit (Garreaud et al., 2020).

Coastal lows temporarily change the typical wind direction for a few days. These events are frequent, especially during the winter (Garreaud et al., 2002). The coastal lows are low-pressure systems in the area between 27° to 35°S, triggered when a high-altitude anticyclone appears further south of 40°S, migrating from the west to the east (Garreaud et al., 2002; Aguirre et al., 2021). Coastal lows initiate easterly winds from the Andes that dissipate the typical cloudiness from the north, increasing coastal atmospheric temperatures in the whole mentioned region. Once the coastal low is well established, westerly winds appear in the north pressure border (27°S), bringing back the cloudiness and cooling to that area, while in the south border (35°S), the sunny conditions prevail until the low-pressure vanishes in a couple of days (Garreaud et al., 2002).

Coastal lows culmination sometimes leads to short-lived southerly coastal low-level jets over 10 m s^{-1} in the Central Zone (30°-37°S) with more frequency in the spring-summer (Garreaud

et al., 2002; Aguirre et al., 2021; Garreaud and Muñoz., 2005). Although these jets are 100-150 m above the surface at 200 to 300 km from the coast, they significantly enhance the upwelling of the coastline. Even occasionally, these jets reach the coast, increasing even more the upwelling (Aguirre et al., 2021; Garreaud and Muñoz, 2005). These strong winds are followed by weak southerly or northerly winds (Aguirre et al., 2021). Coastal low-level jets episodes have increased in the last decade owing to SPSA intensification (Salvadecci et al., 2017; Aguirre et al., 2021; Garreaud and Muñoz., 2005).

A strong kinetic eddy centred at 30°S is driven by the SPSA, enhancing the upwelling along the coast from 30°S to 37°S (Lengua de Vaca to Punta Lavapié) during the warm season and downwelling in the cold season, becoming the most studied Zone in Chile (Figure 3.2; Thiel et al., 2007). This means the CCC flows equatorwards during the upwelling season with a more latitudinal direction from 35° to 40°S. Meanwhile, its flow goes opposite the rest of the time (Thiel et al., 2007). The ESSW that delivers nutrients during upwelling has a reduced impact over 35°S. Here, AAIW has a more significant role (Thiel et al., 2007; Marchant et al., 2007). Additionally, this Zone has a shelf below 10 km wide until 35°S. Then, its width southwards until the end varies from 40 to 70 km, except for the Arauco Peninsula (37-38°S), which reduces to 12 km (Thiel et al., 2007; Marchant et al., 2007).

The upwelling conditions directly influence the phytoplankton, with a bloom in the Austral spring-summer with a minimum production in autumn-winter (Corredor-Acosta et al., 2015; Gómez et al., 2017; Yuras et al., 2005). This is more significant southward 33°S, particularly in Valparaiso and Concepción (Figure 3.2 and Table 3.4), due to its capes forming filament spots (Thiel et al., 2007). Indeed, this region (33°-36.5°S) presents higher phytoplankton rates with a Chl range of 3.8 to 26 mg m^{-3} in the summer in comparison to the winter 1.0 to 2.5 mg m^{-3} due to more adequate longshore winds and many well-spaced rivers that add nutrients to the mixed layer, such as NO_3^- (5-15 µM), PO_4^{-2} (0.5-1 µM) and SiO_4^{-2} (5-8 µM; Masotti et al., 2018; Thiel et al., 2007). Examples of these rivers are Maipo (33.72°S), Mataquito (34.98°S) and Maule Rivers (35.41°S), but the most relevant are the Itata (36.47°S) and Biobio Rivers (36.84°S; Figures 3.4 and 3.5; Vergara et al., 2017; Masotti et al., 2018). The NO_3^- and PO_4^{-2} added by these rivers vary from 0.01 to 10.5 and 0.005 to 0.98 mg L^{-1}, respectively, in a plume area of 0.29 to 0.77 km^2 (Masotti et al., 2018). At the same time, these also provide significant quantities of organic matter and trace metals in sediments, reducing the light levels (Saldías et al., 2016). Additionally, they tend to produce coastal stratification, even during the Austral summer when the precipitation is low (Thiel et al., 2007). This limits the depth of the turbulent mixing, which is necessary to exchange nutrients in the euphotic layer where the phytoplankton grows (Aguayo et al., 2021; Silva et al., 2009). Thus, these inputs could positively or negatively impact phytoplankton blooms (Saldías et al., 2016). However, the Fe bioavailability of rivers is limited due to its poor solubility (Raiswell, 2011). This is compensated by a vast number of streams (Saldías et al., 2016). During the big drought (2010-2018), the stream discharge through the ocean decreased by 90% due to its direct relationship with the amount of precipitation (Figure 3.5; Garreaud et al., 2020; Masotti et al., 2018). This region is also well studied in comparison to others because near the Itata River, there is Station 18 (37.5°S), where the nutrients are continuously measured (Figure 3.4; Masotti et al., 2018).

El Niño produces above-average precipitation and river runoff in Central Chile (33°-38°S) during the winter and spring-summer (Gómez et al., 2017; Ancapichun and Garcés, 2015; Corredor-Acosta et al., 2015). Additionally, the atmospheric temperatures slightly decrease due to the cloudiness at 35-36.5°S during the spring-summer, which becomes a shorter and weaker duration of phytoplankton development in that region (DMC, 2018). On the other hand, during the La Niña years, the opposite effect is seen (Gómez et al., 2017; Ancapichun and Garcés, 2015). Hence, ENSO may modulate the Fe supply by rivers in the sea in those

periods (Dezileau et al., 2004). El Niño Modiki precipitation patterns are similar to the El Niño, but they are slightly lower and start at 35°S (DMC, 2018).

Although this Zone does not present as many industrial activities as the Northern Zone, Ventanas (32.7°S) is the exception, with oil and copper refineries polluting the ocean with heavy metals like Ni, V, Pb, Cr, Cu, Hg, As and Se (Table 3.4). Minor copper and molybdenum mines are other sources of contamination, discharging their residuals into the rivers (Jara et al., 2014; Camus and Haje, 1998). Quintero bay (32.8°S) exhibited high Cr, Mo, and Cd levels in the water, while Cr was present in molluscs tissues there (Jara et al., 2014; Table 3.4). The sewage waters may also be relevant, considering that 70% of the Chilean population lives in this Zone (Garreaud et al., 2020).

FIGURE 3.4. LOCATION OF MAIPO, MATAQUITO, MAULE, ITATA AND BIOBIO RIVERS AND STATION 18 USING TERRA-MODIS IMAGE IN THE BACKGROUND. STATION 18 IS THE ONLY PLACE WHERE CHEMICAL PARAMETERS ARE MONITORED (MASOTTI ET AL., 2018).
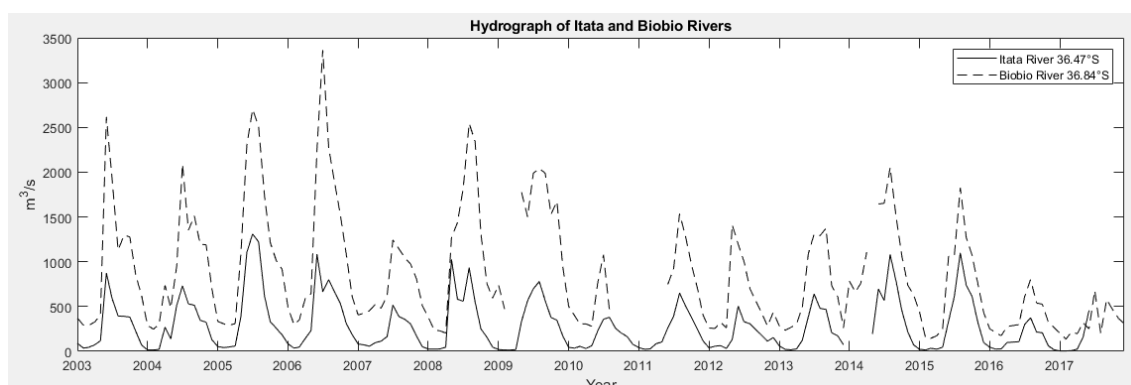
FIGURE 3.5. HYDROGRAPH OF ITATA AND BIOBIO RIVERS, MEASURED BY THE GENERAL DIRECTORATE OF WATER MANAGEMENT (DGA). THE FLUXES WERE NOT MEASURED ON SOME OCCASIONS OWING TO CLIMATIC CONDITIONS OR INSTRUMENTAL PROBLEMS. THIS FIGURE SHOWS HOW THE FLUXES HAVE DECREASED IN THE LATE YEARS (CR2, 2018).

3.1.3. Southern Zone of Chile (40°-56°S).

This Zone is characterised by intricate geography with many archipelagos and fjords mainly located south of Chiloe Island but with a shelf over 70 km wide and reaching more than 100 km at 46°S (Figures 3.6 and 3.8; Strub et al., 2019; Thiel et al., 2007; Marchant et al., 2007). This Zone marks the diversion of WWD transporting, forming the equatorward HCS and poleward CHC at 37°S in the autumn-winter and 48°S in the spring-summer, with some

equatorwards currents at 51°S in the summer (Strub et al., 2019; Aracena et al., 2011). Similarly, the SPSA impacts around 40° to 45°S, depending on the season (Thiel et al., 2007).
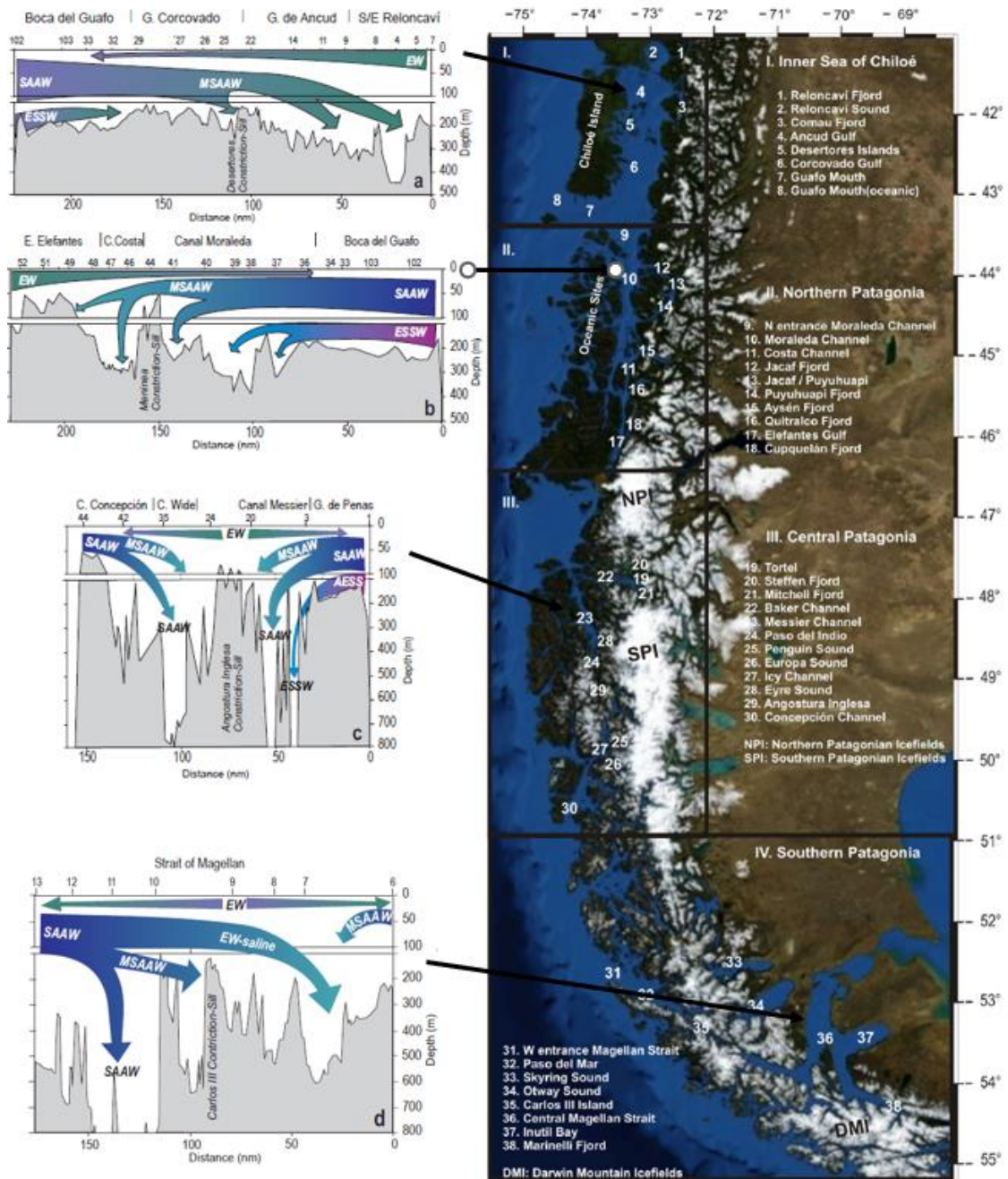
FIGURE 3.6. SCHEMATIC OF THE VERTICAL CIRCULATION FOR THE INNER SEA OF CHILOE, NORTHERN, CENTRAL AND SOUTHERN PATAGONIA, WHERE EW (ESTUARINE WATER), SAAW (SUB-ANTARCTIC WATERS AKA AAIW); MSAAW IS MODIFIED SAAW BY FRESHWATER (Sievers and Silva, 2008).

The channels and fjords have the AAIW, which is rich in nutrients that generally move equatorwards between the surface and 150 m depth, while at 150 to 300 m depth are remnants of ESSW, changing direction in some of them, such as Northern Patagonia (Figure 3.6; Sievers and Silva, 2008). These currents' interaction, along with the complex submarine geography such as submarine constrictions such as Desertores (42.5°S), Meninea (44°S), Angostura Inglesa (48.2°S) and Carlos III (53.8°S) tend to form eddies and curls (Figure 3.6; Aracena et al., 2011; Sievers and Silva, 2008). These eddies are anticyclonic during the summer or spring and cyclonic in the winter, leading to upwelling and downwelling conditions (Strub et al., 2019; Aracena et al., 2011).

From 42°S polewards, this Zone is more influenced by the AAO, with higher precipitation (2,000-5,000 mm yr^{-1}), along with top flow rivers (100-600 m^3 s^{-1}) and glaciers inputs (Lara et al., 2010; Landaeta et al., 2011), giving this region a colder climate with maximum precipitation (7000 mm yr^{-1}) and westerly winds around 50°S (Aracena et al., 2011). The Central Zone also has some glaciers, but there are a lot more in the Southern Zone, especially in Patagonia. Patagonian glaciers are divided into three systems: The Northern (46-47°S), the Southern (48-52°S) and the Darwin Mountains in Tierra del Fuego (54-55°S), with a total surface of 16,000 km^2 (Figure 3.6; Aracena et al., 2011). These are among the fastest retreating glaciers in South America (Braun et al., 2019; Castillo et al., 2016). Their input goes to the ocean through the rivers. However, their exact contribution has been poorly studied (Braun et al., 2019).
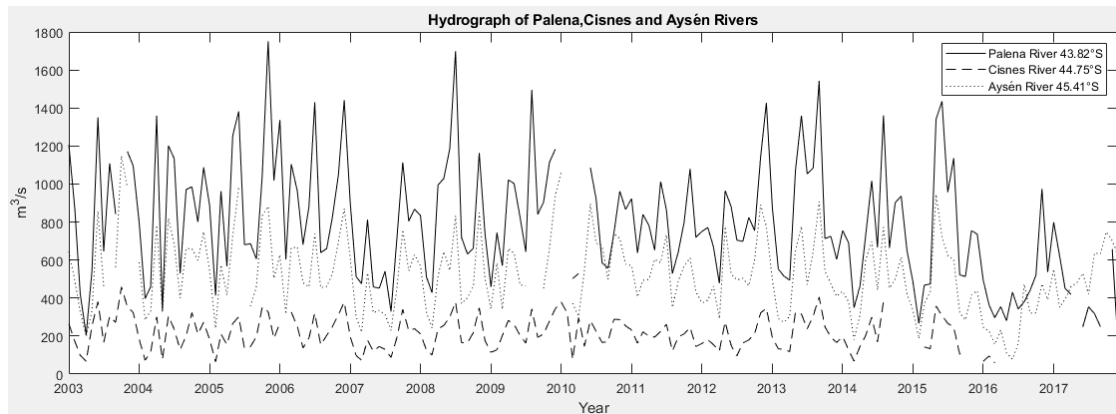
FIGURE 3.7. HYDROGRAPH OF PALENA, CISNES AND AYSÉN RIVERS, MEASURED BY DGA. THE FLUXES WERE NOT MEASURED ON SOME OCCASIONS OWING TO CLIMATIC CONDITIONS OR INSTRUMENTAL PROBLEMS (CR2, 2018).
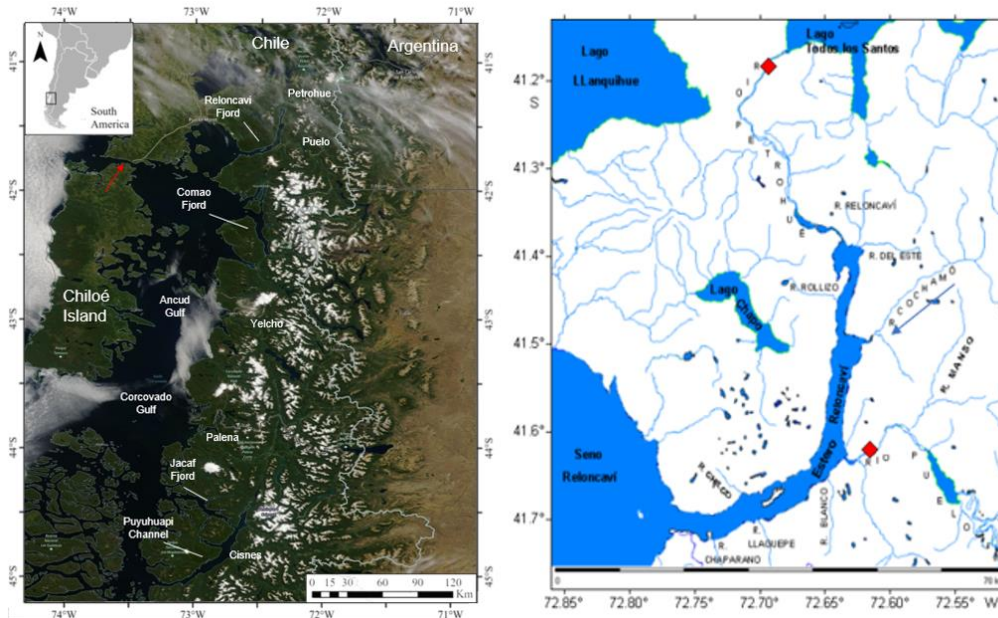
FIGURE 3.8. THE PANEL SHOWS THE ANCUD AND CORCOVADO GULFS BETWEEN CHILOÉ ISLAND AND THE MAINLAND (41-45°S). THE RED ARROW SHOWS THE CHACAO CHANNEL, WHERE THE CHILOÉ'S INTERIOR SEA CONNECTS WITH THE PACIFIC. THE LOCATION OF PETROHUÉ (41.13°S), PUELO (41.60°S), YELCHO (42.98°S), PALENA (43.82°S) AND CISNES (44.75°S) RIVERS IS SHOWN AS THE REGION'S MAIN TRIBUTARY RIVERS. AYSÉN (45.4°S) IS SLIGHTLY FURTHER SOUTH. THE LEFT PANEL SHOWS THE RELONCAVÍ ESTUARY. THE RED RHOMBUSES INDICATE PUELO AND PETROHUÉ RIVERS GAUGING STATIONS, AND THE BLUE ARROW INDICATES THE COCHAMÓ RIVER (41.51°S), WHOSE FLUX IS NOT MEASURED (CASTRO, 2010; AGUAYO ET AL., 2021).

Therefore, river inputs dominate in the subsection between 44°-46°S, with the main being the Palena (43.82°S), Cisnes (44.75°S) and Aysén Rivers (45.41°S; Aguayo et al., 2021; Figure 3.7 and 3.8). Meanwhile, glacial meltwater dominates 52°-53°S. These rivers have averaged

low NO_3^- and PO_4^{-2} concentrations (1.5 and 0.5 µM) with low seasonal differences, while SiO_4^{-2} varies from 40 to 150 µM (Castro, 2010; De La Torre, 2016). The rivers fed by glaciers increase the dissolved Si slightly (15 to 50 µM), while dissolved Fe concentration is over 50 nM on average. At the same time, they also have significant concentrations of colloidal material reach in Si and Fe that can be potentially dissolved (Pryer et al., 2020). When the fluxes of these rivers are too high, they tend to reduce the salinity, creating stratification in the coast with a surface 20-30 m layer of water with low density and generally low nutrients except for the SiO_4^{-2}, forming a sort of estuarine system with high nutrient concentration under that layer from AAIW (Landaeta et al., 2011; Aracena et al., 2011; Sievers and Silva, 2008; Figure 3.6). Additionally, the nutrients in deepwater over 75 m depth have a significant concentration from the remineralisation process (Thiel et al., 2007; De la Torre, 2016). The extreme stratification has affected fish populations due to zooplankton's sensitivity to salinity, from 42°S southwards but with a higher frequency in the region 52°-53°S because it also has low SST (Landaeta et al., 2011; Aracena et al., 2011). These layers tend to mix, bringing nutrients to the euphotic layer when the mentioned eddies occur during the spring or summer (Aracena et al., 2011; Strub et al., 2019).

Furthermore, this stratification problem is increased by precipitations that occur mainly during the winter, fjord inputs and river discharges (Marchant et al., 2007). Nevertheless, from 42°S to the South, rainfall episodes are present the whole year due to the SPSA limits (Quintana and Aceituno, 2011; Thiel et al., 2007). El Niño has shown a precipitation reduction in the Zone from 38°-41°S, especially in the following summer, driven by SLP variations in the mid and high latitudes that increase the southerly winds or block the storms from the south (Montecinos and Aceituno, 2003; Strub et al., 2019). El Niño modoki and La Niña provoke the opposite effect (González-Reyes and Muñoz, 2013; DMC, 2018). In any case, the precipitation in this Zone is more influenced by the AAO's negative phase, particularly from December to April (González-Reyes and Muñoz, 2013; Aguayo et al., 2021; Rahn, 2012). Still, due to the AAO positive trend and the big drought, the rainfall has declined in the last decade during these months (Aguayo et al., 2021).

The phytoplankton bloom in this Zone until 45°S occurs in spring-summer with an essential quantity of pelagic fishes, while during the winter, it is mainly populated by microorganisms for the reduced solar radiation (Landaeta et al., 2011; Castro, 2010; De La Torre, 2016; Strub et al., 2019). The top layer's thickness is narrow due to stratification. Thus, phytoplankton does not have much space for dispersion forming patches, which are very common in this Zone, especially during the cold season (Landaeta et al., 2011; Strub et al., 2019). The phytoplankton here tends to vary significantly in terms of space and season. Diatoms are the dominant species due to the extra Si and Fe from the freshwater inputs, which are essential for their development, whereas dinoflagellates and nanoflagellates are present on specific occasions with higher frequency in the summer (De La Torre, 2016; Aracena et al., 2011).

Of all the islands located in the Southern Zone, the Chiloé is the biggest and most important for its productivity, with a significant Chl signal (CONAMA, 2008; Leon-Muñoz et al., 2018; Diaz et al., 2021). Indeed, the interior Sea of Chiloé, located at 41.5°-43°S, has complex geography with micro-basins and geographical barriers that create a semi-closed environment with depths from 50 to 400m (Figures 3.6 and 3.8; Lara et al., 2010; Saldías et al., 2016). This basin is also exposed to the oceanic regime in the west with equatorwards currents in the spring-summer that enters by Corcovado Gulf and discharges freshwater from different rivers where the most important are Petrohue (41.1°S), Colchamó (41.5°S) and Puelo (41.6°S) for the northern Interior Sea while Yelcho is for the central(43.0°S; Figures 3.6, 3.8; Aguayo et al., 2021; Strub et al., 2019). A study in that area showed that Chl patterns are higher in spring-summer with a heterogeneous and compact distribution (30 km patches with an averaged concentration over 4 mg m^{-3} with a range of 1-25 mg m^{-3}). In contrast, Chl had a

lower concentration with a homogenous distribution (50 km patches with an averaged concentration of 1-2 mg m^{-3}) during the autumn-winter. There was an anisotropic effect in Chl in that period, with a predominant East-West direction (Lara et al., 2010; Aracena et al., 2011). This effect was caused by increased ocean stratification from extra river flow typical of the winter and the general northerly winds influence that become southerly in the summer driven by the SPSA motion (Saldías et al., 2016; Strub et al., 2019; Thiel et al., 2007). Phytoplankton behaviour in the further south has not been well documented, but Aracena et al. (2011) showed that they have a lower range than Chiloé (0.1-15 mg m^{-3}). The phytoplankton bloom in North Patagonia (43.5°-46°S) also occurs during spring and summer (Figure 3.6). In contrast, Central Patagonia (46°-51°S) has a lower signal that is slightly higher during the spring. The Southern Patagonian(51°-56°S) continues having a higher response only in the spring, which is higher than Central Patagonia but is still not as significant as the North.

In terms of nutrients, these also have shown differences by season and region with an intensive stratification. For example, the spring averaged surface concentrations of NO_3^-, PO_4^{-2} and SiO_4^{-2} in Chiloé (6.8, 1.0 and 7.9 µM) and North Patagonia (7.4, 0.9 and 15.3 µM) are more significant than the Central (3.6, 0.7 and 4.8 µM) and Southern Patagonia (4.7, 0.7 and 4.4 µM; Figure 3.6; Aracena et al., 2011).

Since the 1980s, the interior sea of Chiloé has been intensively used for economically productive activities such as aquaculture (Lara et al., 2010; Saldías et al., 2016; Leon-Muñoz et al., 2018; Diaz et al., 2021). In recent years this has become the fourth most important economic activity in Chile, specialising in salmon farms with a production of 800,000 tonnes per year, extending further south to 55°S in 2015 (Castillo et al., 2016; Buschmann et al., 2016; Armijo et al., 2020). The extra feeding and faeces produce a significant level of NH_4^+ and PO_4^{-2} through the coastal waters, adding approximately 49 kg N and 8 kg P per tonne of salmon (Armijo et al., 2020). This extra intake of nutrients, especially the NH_4^+, has increased the eutrophication risk in this region, particularly in the fjords where the water is semi-constrained, impacting the oxygenating renewal processes (Buschmann et al., 2016; Armijo et al., 2020; Diaz et al., 2021). The eutrophication produced by salmon farms is very common, creating anoxic conditions. Thus, the companies must constantly monitor the nearby waters (Sernapesca, 2018; Buschmann et al., 2006). Although this industry is the most relevant for the Zone, few studies exist concerning their impacts on the ocean and rivers (Castillo et al., 2016). Moreover, a well-known company with nineteen farm instalments at 53.8°-54.5°S in Magallanes has been fined by the Chilean Superintendency of the Environment (SMA) for several infringements such as: modifying the benthic soils, counterfeiting the quantity of salmon mortality, and managing the solid waste poorly. These bad practices occurred at least from 2013 to 2018 (Molinari, 2021).

Additionally, harmful algal blooms have appeared in the Southern Zone since the 1970s, particularly the specimen called red tides due to their pigment have caused more problems (Leon-Muñoz et al., 2018). However, their frequency and intensity have risen in recent years, stretching to more northern areas than Chiloé Island (Buschmann et al., 2016; Strub et al., 2019). This phenomenon has also been observed in other parts of the world driven by many factors such as climate change, El Niño and the accelerated eutrophication caused by aquaculture (Leon-Muñoz et al., 2018; Diaz et al., 2021; Wells, 1997). Red tides are a proliferation of flagellates and dinoflagellates capable of producing deadly toxins for fish, molluscs or humans who have consumed infected seafood (Yang et al., 2018; Armijo et al., 2020; Leon-Muñoz et al., 2018; Iriarte et al., 2012).

The red tides tend to increase rapidly in environments with high SST and a large quantity of N and P (Wells, 1997; Armijo et al., 2020). For that reason, waters near salmon farms are

susceptible to having a significant number of toxic dinoflagellates (Buschmann et al., 2006). Effectively, these algae metabolise the excess of N generating deadly toxins in OMZ. This process is even faster when NH_4^+ is high. Additionally, some red tide species, like *A Alexandrium catenella,* are mixotrophic, devouring bacteria that grow in anaerobic conditions (Armijo et al., 2020; Iriarte et al., 2012). Although salmon farms tend to accelerate eutrophication conditions, which leads to red tide cases, no study nor model has indicated that farm salmon could cause a massive red tide alone (Armijo et al., 2020).

Two intense red tide blooms occurred in Chiloé from February to May 2016, the same year as an extreme El Niño (Buschmann et al., 2016). The first was *Pseudochattonella verruculosa* bloom, which exterminated 40,000 tonnes of salmon. The second one, *Alexandrium catenella* bloom, was even more extensive and detrimental, reaching 39°S, further north than ever before (Armijo et al., 2020; Leon-Muñoz et al., 2018; Buschmann et al., 2016). This specimen is even more noxious, causing human fatalities in the past in Chile (Buschmann et al., 2016; Armijo et al., 2020; Diaz et al., 2021). This second event attracted the press's attention because the water was tinted red, and an enormous quantity of seabirds and molluscs were found dead on the Chiloé's coasts (Armijo et al., 2020). Consequently, the government banned the extraction of marine products for several weeks. This bloom was right after the disposal of 4700 tonnes of dead salmon near Chiloé Island (Buschmann et al., 2016; Leon-Muñoz et al., 2018; Armijo et al., 2020).

3.2. Data collection.

3.2.1. Introduction.

The data were mainly collected from satellite imagery. Ocean colour sensors provided this data. The best known of this type are the Sea-viewing Wide Field-of-view Sensor (SeaWiFS) and the Moderate Resolution Imaging Spectro-radiometer (MODIS; Franz et al., 2005). Both scanning radiometers offer extensive temporal and spatial coverage with a pixel resolution of 1 km^2 at the nadir. The mission design allows global observation of the Earth's surface twice a day with approximately constant speed. Although these satellites are capable of detecting phytoplankton in the ocean using the chlorophyll-α band (Chl) by the same algorithm (Eq. 3.1), they might offer slightly different values due to their spectral bandwidth differences (Table 3.1; Franz et al., 2005). This algorithm is an empirical relationship between the wavelengths (λ) of blue and green. A particular satellite-like MODIS or SeaWiFS obtain both. SeaWiFS uses 2-4 and 5 bands for producing blue and green, while MODIS-aqua uses 9-10 and 12 (Table 3.1). The α values used in Eq. 3.1 are standardised coefficients that depend on the sensor that provides the information (Table 3.2, NASA, 2018).

$$\text{Log}(Chl - \alpha) = \alpha_0 + \sum_{i=1}^{4} \alpha_i \left(log \left(\frac{R_{rs}(\lambda_{blue})}{R_{rs}(\lambda_{green})} \right) \right)^i \tag{3.1}$$

TABLE 3.1. MODIS AND SEAWIFS SPECTRAL BANDS USE IN OCEAN COLOUR PROCESSING, WHERE NIR MEANS NEAR-INFRARED BAND (FRANZ ET AL., 2005; CAMPBELL, 2002).

MODIS Band	SeaWiFS Band	MODIS Bandwidth (nm)	MODIS Wavelength (nm)	SeaWiFS Bandwidth (nm)	SeaWiFS Wavelength (nm)	Primary use
8	1	405-420	412	402-422	412	Blue; yellow pigment/phytoplankton
9	2	438-448	442	433-453	443	blue; Chl
10	3	483-493	488	480-500	490	blue-green; Chl
11	4	526-536	531	500-520	510	green; chl
12	5	546-556	551	545-565	555	red; yellow pigment/ phytoplankton
13	6	662-672	667	660-680	670	red; Chl
15	7	743-753	748	745-785	765	NIR; land-water contact, atmospheric correction
16	8	862-877	869	845-885	865	NIR; land-water contact, atmospheric correction

MODIS-Aqua is the component of MODIS that focuses on ocean measurements. It has been operational since approximately June 2002, while SeaWiFS was from September 1997 to

December 2010 (Franz et al., 2005). These satellites also can measure other relevant parameters, such as SST.

TABLE 3.2. MODIS AND SEAWIFS DEFAULT ALPHA VALUES USE IN OCEAN COLOUR PROCESSING (NASA, 2018).

Alpha	α_0	α_1	α_2	α_3	α_4
MODIS	0.3272	-2.994	2.7218	-1.2259	-0.5683
SeaWiFS	0.2424	-2.7423	1.8017	0.0015	-1.228

There are many ways to obtain processed ocean-colour data. One of these is the SeaDAS (SeaWiFS Data Analysis System). This program can display data extracted through the Ocean-colour website, where the available information is provided in detail (NASA, 2019). Another possible option is the GES DISC (Goddard Earth Sciences Data and Information Services Center) Interactive Online Visualization and Analysis Infrastructure (GIOVANNI). The web page processes data well. It is more comfortable to access and contain 1981 variables from different sources, including MODIS and SeaWiFS. Even it can deliver means for a specific delimited area or at its maximum resolution. For instance, the first objective aims to define the main parameters affecting production, so extracting high spatial/temporal resolution data was unnecessary. For that reason, a monthly value per parameter for a broader location was considered. While for the other objectives, a full resolution was needed. Thus, GIOVANNI accomplished both requirements.

3.2.2. Defining the Study Area.

a) Zones:

The first step was to consider the references as Thiel et al. (2007) and state the different Zones. Chile is a long country with entirely different climates. Therefore, it was divided into three regions mentioned in section 3.1: Northern Zone (18°-30°S, coded as N), Central Zone (30°-40°S, coded as C) and Southern Zone (40°-53.5°S coded as S; Figures 3.2 and 3.9). The Southern Zone was limited to avoid the Drake Passage in the south, where the AAO is dominant. Both also affect the Southern Zone, but this study's primary focus is on more local impacts, such as the Kelvin waves transferring information southward and the runoff inputs from the mountains along the coast, which are not relevant at the Drake Passage.

b) Subsections:

The Chilean shelf is variable and defines the onshore and offshore subsection delimitation (Figure 3.1; Thiel et al., 2007). Both types of subsections, onshore and offshore, should have different Chl concentrations due to the difference in depth and other mechanisms explained above, like upwelling. However, studying both is important because their behaviour might be related. For that reason, the coastal strip was coded as T, and the ocean was coded as O. Authors like Vergara et al. (2017), Yuras et al. (2005), and Gómez et al. (2017) considered a 100 km offshore distance to define their study area. This value is approximately the maximum Chilean shelf width located in the Southern Zone (Thiel et al., 2007). The maximum ocean depths around 100 km offshore oscillate between 2,600 to 5,500 m (NOAA, 2000; Table 3.3). This is also the typical distance where the surface waters are dragged during the upwelling in the Northern and Central Zones in Chile (Thiel et al., 2007). Therefore, the width per subsection was defined as 1°-1.5°, equivalent to almost 100-150 km. This ensures that the whole shelf is part of each onshore subsection and is consistent with the width used for mentioned authors.

Each Zone was divided into sub-sections to get more information. The main criterion in dividing these zones was based on the complexity of the coastline to study the capes variation, keeping a 100-150 km width along the coastal edge. This decision was made considering that Chile has a roughly straight N-S-oriented coastline (Thiel et al., 2007), particularly in the Northern Zone. As a result, this Zone was divided into three subsections

(Table 3.3 and Figure 3.9). On the other hand, the Central Zone geography has a more pronounced curve area, especially in the region 32.7-35°S, so four subsections were used instead (Figure 3.9). Additionally, 3C and 4C have been highly studied due to their high production (Vergara et al., 2017; Corredor-Acosta et al.,2015). Thus, having more information about this area enables better comparisons with past work. The Southern territory is made up of a fragmented territory (Lara et al., 2010). 1S was selected to focus on Chiloé Island, one of the most studied territories. The 2S-3S division was chosen since the coastal edge has an increasing curve in subsection 45.8°-47°S. However, the area from 47°-50°S is relatively straight, but westerly winds start to dominate from 50° to 53.5°S. The final subsection (50°-53.5°S) presents a width close to 250 km. This is the higher distance between the coastal edge and the limit subsection of the grid. This could be avoided by splitting 3S in two, but the behaviour of the regions created through such a division should be similar, so it was not considered. Also, this sub-subsection is not populated and has not been adequately studied.

TABLE 3.3. SUBSECTIONS CHARACTERISTICS, INCLUDING THEIR DEPTHS IN THE OCEAN, LENGTHS AND WIDTHS, WHERE W MEANS WIDTH, L IS LENGTH, AND D IS DEPTH.

Subsection	Initial Lon.	Initial Lat.	Final Lon.	Final Lat.	W1st corner (km)	W2nd corner (km)	Shortest W (km)	Longest W (km)	L (km)	D1st Corner (m)	D2nd Corner (m)
1NT	71°W	18.3°S	70°W	23°S	76	73	73	102	546	778	5200
1NO	72°W	18.3°S	71°W	23°S	111	111	111	111	546	2600	4500
2NT	71.5°W	23°S	70°W	27°S	109	80	77	122	491	5600	4900
2NO	72.5°W	23°S	71.5°W	27°S	111	111	111	111	491	3900	4000
3NT	72.5°W	27°S	70.5°W	30°S	190	120	110	190	380	4000	5700
3NO	73.5°W	27°S	72.5°W	30°S	111	111	111	111	380	4000	4000
1CT	72.5°W	30°S	71°W	32.7°S	120	111	89	122	351	6000	3500
1CO	73.5°W	30°S	72.5°W	32.7°S	111	111	111	111	351	4500	3700
2CT	73.2°W	32.7°S	71°W	35°S	180	110	110	186	308	4500	2000
2CO	74.2°W	32.7°S	73.2°W	35°S	111	111	111	111	308	4100	4800
3CT	74°W	35°S	71°W	36.4°S	188	120	120	198	193	5000	3000
3CO	75°W	35°S	74°W	36.4°S	111	111	111	111	193	4200	4200
4CT	74.6°W	36.4°S	72°W	40°S	170	98	98	183	510	4800	1800
4CO	75.6°W	36.4°S	74.6°W	40°S	111	111	111	111	510	4200	4000
1ST	75.5°W	40°S	72°W	43.5°S	196	122	122	260	522	4100	3400
1SO	76.5°W	40°S	75.5°W	43.5°S	111	111	111	111	522	4000	3500
2ST	76°W	43.5°S	72°W	45.8°S	130	118	89	207	364	3600	3300
2SO	77°W	43.5°S	76°W	45.8°S	111	111	111	111	364	3500	2800
3ST	77°W	45.8°S	71°W	53.5°S	200	253	150	272	1328	2800	4000
3SO	78°W	45.8°S	77°W	53.5°S	111	111	111	111	1328	3200	2700

Ocean depths at the edge of the offshore and onshore subsection vary between 2,600-5,000 m, except 1NT, which presents a 778 m in its edge subsection. This is the shallowest of the whole grid. This border is at the limit with Peru and presents a curve that increases the shelf width in that area, which is noticeable in Figure 3.1. Overall, it is a small subsection that only is unusual at one end.

TABLE 3.4. MAIN CITIES PER SUBSECTION, INCLUDING THEIR LATITUDES.

Subsection	Initial Lat.	Final Lat.	Main Cities
1N	18.3°S	23°S	Arica (18.5°), Iquique (20.2°)
2N	23°S	27°S	Mejillones (23.1°), Antofagasta (23.6°), Chañaral (26.3°)
3N	27°S	30°S	Caldera (27.0°), Copiapo (27.4°), Huasco (28.5°), Vallenar (28.6°), La Serena (29.9°) , Coquimbo (30.0°)
1C	30°S	32.7°S	Ovalle (30.6°), Illapel (31.6°)
2C	32.7°S	35°S	Ventanas (32.7°), Quintero (32.8°) Valparaiso (33.0°), Santiago (33.4°), San Fernando (34.6°), Curicó (35.0°)
3C	35°S	36.4°S	Talca (35.4°), Linares (35.8°)
4C	36.4°S	40°S	Chillán (36.6°), Concepción(36.8°), Temuco (38.7°), Valdivia (39.8°)
1S	40°S	43.5°S	Osorno (40.6°), Puerto Montt (41.5°), Ancud (41.9°), Castro (42.5°)
2S	43.5°S	45.8°S	Puerto Aysén (45.2°), Coyhaique (45.6°)
3S	45.8°S	53.5°S	Puerto Natales (51.7°), Punta Arenas (53.2°)
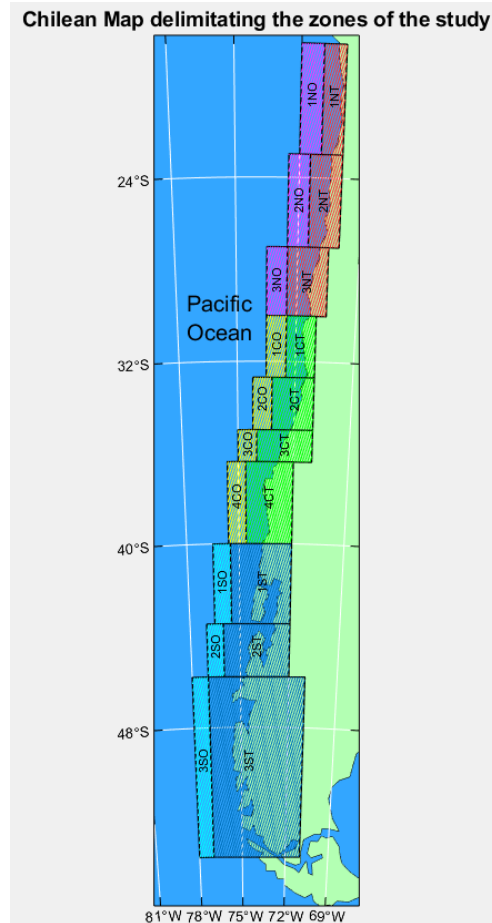
FIGURE 3.9. CHILEAN MAP DELIMITING THE ZONES OF STUDY (RED FOR THE NORTH, GREEN FOR THE CENTRAL AND BLUE FOR THE SOUTH; PURPLE, LIGHT GREEN AND LIGHT BLUE TO SHOW THEIR RESPECTIVE OFFSHORE ZONES) AND ITS SUBSECTIONS (NOAA, 2000).

3.2.3. Variables Selection and Data Collection.

This study aims to understand the Chilean alongshore phytoplankton variation and identify its physical mechanisms. Consequently, phytoplankton is the response variable, which could be detected indirectly by the ocean's Chl concentration (Franz et al., 2005; Falkowski, 1994). The primary physical mechanism that affects phytoplankton is upwelling. This phenomenon is provoked by equatorward coastal winds (Mogollón and Calil, 2017; Vergara et al., 2017). Upwelling also creates a SST decrease (Ancapichun and Garcés, 2015; Yuras et al.,2005). SST could be used to determine the impact that is done by ENSO as well. Considering these, SST and wind speed and directions are vital factors in the investigation.

The precipitation rate (PR) was included as well. The PR is a parameter that has an opposite pattern in the Northern and Southern Zone, while the Central Zone presents an intermediate behaviour (Thiel et al., 2007). This parameter could affect phytoplankton differently, depending on the amount of rain and the season. For example, Thompson et al. (2015) found a positive relationship between both components when rainfall happens during the warm season. Nonetheless, it does not have the same effect during the cold seasons. Even though no studies about the nutrient concentration in the rainfall in the South Pacific were found in this investigation, they can be inferred from South Atlantic data. Baker et al. (2010) showed averaged concentrations of 2.8 nmol m^{-3}, 3.7 nmol m^{-3} and 12.4 pmol m^{-3} for NO_3^-, NH_4^+ and PO_4^{-2} during regular rainfall events, while storms or extreme events could increase their concentration to 3.5 nmol m^{-3}, 6.4 nmol m^{-3} and 14.6 pmol m^{-3}, respectively.

These inputs could be introduced through the ocean directly or indirectly by increasing river flow and discharging into the coastal seas (Dezileau et al., 2004; Thompson et al., 2015). This

is more important in places where the precipitation is occasional but dense, as is the case in the Northern Chilean area. However, a region with a high precipitation level could provoke the opposite effect. These extra inputs might create stratification, reducing the first oceanic layer's thickness owing to the lower salinity (Landaeta et al., 2011). Therefore, the phytoplankton movement is reduced. This stratification reduces the mixing process, affecting the nutrient concentration (Silva et al., 2009). Finally, when this stratification occurs, the area affected becomes more susceptible to ENSO and red tides. This high PR happens in the Southern Zone (Landaeta et al., 2011; Buschmann et al., 2016). Table 3.5 shows the parameters considered in this study to achieve O.1.

The wind vector has two components, as Table 3.5 shows. This is important because only the upwelling is generated by the southerly component (VW) in the case of straight N-S-oriented coastlines, which is the majority of Chilean shores (Thiel et al., 2007). If WV is negative, it will lead to a downwelling, reducing phytoplankton production. The westerly winds (UW) have little influence on phytoplankton. The SLP was used in some circumstances to estimate the SPSA in O.2. In O.3 was used to evaluate SPSA variation and position and understand wind patterns.

The GIOVANNI database comes from many sources. For this research, MODIS-Aqua was used to obtain SST and Chl. TRMM (Tropical Rainfall Measuring Mission) and Merra-2 (Modern-Era Retrospective analysis for Research Application, version 2) were used in the precipitation and wind variables. TRMM is a satellite launched in 1997 to measure rainfall in tropical and subtropical areas (Li et al., 2018). In 2015, the Global Precipitation Measurement program replaced TRMM, using Multi-satellite Precipitation Analysis, which continued giving PR data until 2019 (Tang et al., 2020). Merra-2 is based on an atmospheric reanalysis of NASA's current satellite data, using models and actual observation data from different sources (Gelaro et al., 2017).

The data extracted are the monthly means for each subsection. Chl and SST data are available from July 2002. Precipitation Rate and Wind components are available from January 1998 and January 1980, respectively. Thus, the O.1 study period was defined based on the key parameters Chl and SST because, in this period, all the variables are available. SeaWiFS data is also available in the GIOVANNI library, where it measures Chl and SST from 1997 to 2010. However, it was decided to use MODIS-Aqua data to avoid possible errors using different sensors (Franz et al., 2005; Table 3.1). Therefore, the study Period for O.1 started in July 2002 and extended to June 2018.

O.2 requires an extended time period in order to study climate drivers, while a better spatial and temporal resolution is required for the case studies addressed in O.3. Giovanni had an excellent spatial resolution for Chl and SST, but the wind resolution was deficient. Concerning the time scale, GIOVANNI MODIS-aqua Chl and SST can be weekly, while MERRA2 winds can be hourly and PR from TRMM are daily.

TABLE 3.5. PARAMETERS USED FROM THE GIOVANNI DATABASE (NASA, 2018).

Parameter	Unit	Source	Temp res.	Spatial res.	Date begins	End Date
Chl	mg m^{-3}	MODIS-Aqua	Monthly	0.04° x 0.04°	2002/07/04	Until now
SST 11µm (day)	°C	MODIS-Aqua	Monthly	0.04° x 0.04°	2002/07/04	Until now
Precipitation Rate	mm mth^{-1}	TRMM	Monthly	0.25°x 0.25°	1998/01/01	Until now
Westerly Wind (10m)	m s^{-1}	MERRA-2	Monthly	0.63° x 1.25°	1980/01/01	Until now
Southerly Wind (10m)	m s^{-1}	MERRA-2	Monthly	0.63° x 1.25°	1980/01/01	Until now

An alternative dataset source that accomplishes the requirements for these objectives is ERA5 (ECMWF ReAnalysis) from The European Centre for Medium-Range Weather Forecast (ECMWF). This source contains the physical parameter datasets from 1979 (Table 3.6). ERA5 is the fifth integrated global forecast model system with the assimilation of satellite

observations. This is a consistent dataset for the whole world and is available in Copernicus Climate Change Service (C3S, 2021; Hennermann and Guillory, 2020; Hersbach et al., 2020). The ERA5 spatial resolution is a 0.25°x0.25° grid with 137 vertical levels from the surface to 0.01 hPa, reaching 80 km on an hourly and monthly scale (Hersbach et al., 2020). The datasets are public and available in NetCDF format (C3S, 2021).

TABLE 3.6. PARAMETERS USED FROM O.2 AND O.3 USING GIOVANNI AND C3S AS SOURCES (C3S, 2021).

Parameter	Unit	Source	Temp res O2	Temp res O3	Spatial res.	Date begins	End Date
Chl	mg m^{-3}	MODIS-Aqua	Monthly	Weekly	0.04° x 0.04°	04/07/2002	Until now
SST	K	ERA5	Monthly	Hourly	0.25°x 0.25°	01/01/1979	Until now
Total Precipitation	m	ERA5	Monthly	Hourly	0.25°x 0.25°	01/01/1979	Until now
Westerly Wind (10m)	m s^{-1}	ERA5	Monthly	Hourly	0.25°x 0.25°	01/01/1979	Until now
Southerly Wind (10m)	m s^{-0}	ERA4	Monthly	Hourly	0.25°x 0.25°	31/12/1978	Until now
Sea Level Pressure	Pa	ERA5	Monthly	Hourly	0.25°x 0.25°	01/01/1979	Until now

ERA5 became available in 2016, replacing ERA-interim with a higher spatial and temporal resolution. ERA5 also includes model improvements that give a better global balance of precipitations and more consistent SST and Ice patterns than ERA-interim, MERRA-2 and TRMM (Hennermann and Guillory, 2020; Hersbach et al., 2020; Tang et al., 2020). ERA5 precipitation hourly data accuracy is lower than the monthly due to its lack of capacity for reproducing diurnal cycles, but its precision improves daily. However, it had some trouble with the rainfall quantities in the arid regions (Tang et al., 2020).

Then, all the physical parameters for O.2 were taken from ERA5 on a monthly scale (1979-2018), while the Chl data was still from GIOVANNI (2002-2018). This decision was made because ERA5 data is available for a longer time, allowing studying the climate drivers correctly and maintaining the same source for all variables will help to be more consistent results, especially considering that MERRA-2 has a lower resolution. The Chl data were used from GIOVANI over C3S because it is reanalysed, becoming more accurate. The Chl data was extended using statistical methods explained in chapter 5.

O.3 data source selection was the same as the O.2 data source. The difference is that the time scale here is weekly, and the period considered was the same as O.1. The weekly scale for the physical parameters was calculated using the hourly data from ERA5 (Table 3.6). Concerning SST, while this variable has a better resolution using GIOVANNI, ERA5 was selected to be more consistent with the other variables, and its SST data does not present gaps due to cloudiness. Also, it is essential to highlight that precipitation might not be as accurate in the arid zones (Tang et al., 2020).

4. Trends in Seasonal, Interannual and Spatial Variability for Parameters that affect Phytoplankton Production [O.1].

4.1. Introduction.

This chapter addresses themes associated with O.1 and will identify critical trends and behaviour within the Zones and subsections previously defined in sections 3.2.1 and 3.2.2 from June 2002 to July 2018. The parameters that are used to address O.1 are Chl, SST, PR, UW and VW. These were measured by remote sensing data and models (MODIS-Aqua, TRMM and MERRA-2; cf. Table 3.5 and section 3.2.3). All these data were extracted using GIOVANNI except for subsections 2S and 3S in June of every year. Due to the severe weather conditions during winter in these locations, GIOVANNI could not provide Chl information any year that month. In this analysis, a linear interpolation between May and July was undertaken to derive these missing values.

The analyses presented here and O.2 (chapter 5) will be used to select study cases that will form the basis for O.3 (chapter 6). The methods used in this chapter represent the application of statistical analyses [O.1.1], comparison plots, and correlations [O.1.2] to determine seasonal, interannual, and spatial variability in key parameters that directly affect phytoplankton production. The methodology and results will be discussed in sections 4.2 and 4.3, respectively, while a general analysis will be discussed in section 4.4. This later section will focus on the Zones' behaviour, while the results will focus on the parameters themselves, except when considering potential events selection, which is concentrated in the Zones.

4.2. Methodology.

4.2.1. Parameter behaviour and a zonal overview [O.1.1].

The preliminary analysis studied the Chl general behaviour and how these changes per subsection and Zone, using boxplots (Figure 4.1). A boxplot defines the outliers using the interquartile range multiplied by 1.5 from the first and third quartile, respectively (Freedman, 2007). Von Storch and Zwiers (1999) recommended determining the outliers as the values over two times the standard deviation (SD) from the mean (μ). This will be useful to address the O.3 criteria selection for case studies in chapter 6. After that, each parameter (Chl, SST, PR, UW and VW) will be plotted per subsection, focusing on the seasonal and annual cycle during the whole study period (July 2002 to June 2018). This is the first step to understanding each parameter's particular behaviour in each subsection and how these are related. Furthermore, it is possible to establish relationships among parameters and subsections and define which subsections are the most productive during what time of year. This will also help define the selection of extreme events.

Output plots show the maximum, minimum, mean and SD values reached each month, considering the annual cycle and the whole study period. The difference between the seasonal and interannual study periods is that the data were grouped per month in the first one while the second was collected per year (Figures 4.1-4.3 and A.1.1-A.1.10). The plots in section 4.3.1 and Appendix A.1 were grouped by subsection. This allows it to notice how all parameters behave in one particular subsection. The same Figures contain the coastal and ocean components per subsection. This was useful for noticing the differences between both strips.

4.2.2. Data correlations and Parameter connections [O.1.2].

Based on Chapter 3, the Chl is severely affected by the physical parameters chosen (SST, VW, UW and PR), particularly the SST and the longshore winds, mainly southerly winds (VW), due to particular Chilean geography (Thiel et al., 2007). The last is a sensible factor to study because its behaviour varied considerably across the three zones driven by the SPSA (Aguirre et al., 2021). Finally, the PR is a potentially significant parameter because it brings nutrients into the ocean through the rivers in arid regions such as the Northern Zone (Dezlileau et al., 2004). However, if it is too high, it can cause stratifications, reducing the Chl in rainy regions like the Southern Zone (Lara et al., 2010; Landaeta et al., 2011).

This hypothesis is sustained by the literature review done in chapter 3, but it will be studied in this chapter by correlation analysis to establish which zones, subsections (Figure 3.9) and parameters present possible links to each other. This will be useful to determine which parameters are dominant in which Zone. To choose the best correlation tool is necessary to know whether the data is skewed or not first. Usually, climate data is skewed (Storch and Zwiers, 1999). For each subsection, each parameter's normality was checked using the Kolmogorov-Smirnov test. This test is used when the data contain more than 50 samples. Its purpose is to estimate the difference between the data and an empirical function that has a normal distribution (von Storch and Zwiers, 1999).

a) *Cross-correlation Approach:*

Spearman correlation was selected instead of Pearson because the variable response in each subsection was skewed, not fitting with a normal distribution. When data are not parametric, Spearman is used to avoid assumptions related to the frequency distribution and a possible linear relationship between the two variables analysed (Xiao et al., 2016). This approach does not allow the study of more than two variables at the same time. In a case such as here, where more than two variables are of interest, all the possible interactions must be estimated separately, and then they should be compared to each other (Hauke and Kossorwski, 2011). However, the Spearman correlation produces similar sorts of output to a Pearson correlation, with an R usually called Rho and a P-value related to the statistical significance level (Xiao et al., 2016). The Spearman correlation has a reduced sensitivity to outliers. This is relevant considering the number of outliers detected in the variable response at the selection of extreme events (Figures 4.1-4.3 and A.1.1-A.1.10; Table 4.4).

The correlations were calculated using the monthly anomalies instead of working with the data directly. This helps to avoid an overestimation of the data from the annual cycle. The anomalies were calculated by the difference between observed data and the mean for a given month's data considering the study period (2002-2018). Work with data anomalies is often used in climatology and oceanography. Examples of this type are El Kenawy and McCabe (2016); Thiel et al. (2007); Ancapichun and Garcés (2015). Although a high correlation does not necessarily mean causality, this could imply a link that sustains or denies the initial hypothesis. Therefore, to ensure this, a multiple variable analysis looks for interactions and consistencies, avoiding physically implausible relationships (Trauth, 2021).

Rho and P-values were estimated for each parameter's correlation in each subsection. This was used to define which parameters present a potential statistically significant correlation, depending on the Zone and the subsection. Rho takes values in a range of -1 to 1. The sign indicates if the variables present a negative or positive correlation. Rho also defines relationship strength. In Table 4.1, the generic relationship between the value of Rho and its strength is shown (Xiao et al., 2016). P-value is the most used technique to identify if the relationship is statistically significant. The P-value is the probability (0-1) that the null hypothesis is correct. In this case, the null hypothesis means the tested variables are not related (Patil and Yaligar, 2017). Therefore, a lower P-value means a stronger relationship

and that the null hypothesis is less likely to be true. The typical P-value ranges are shown in Table 4.1 (Xiao et al., 2016).

Rho value	Relationship Strength	P-value	Significance
±1 to ±0.8	Very strong	0 to 0.01	Very significant
±0.8 to ±0.5	Strong	0.01 to 0.05	Significant
±0.5 to ±0.3	Moderate	0.05 to 0.1	Low significant
±0.3 to ±0.1	Weak	0.1 to 1	Not significant
±0.1 to 0	very weak	-	-

The data in each subsection was correlated with that in all others, including itself. Then, the five parameters shown in Table 3.5 were correlated, considering the twenty subsections and all their possible combinations. These generated a matrix with 100x100 correlations or twenty-five matrices of size 20x20. Each of these matrices represents the whole system as seen through two parameters. As a result, ten-thousand correlations were made in total. A matrix example is shown in Table 4.8.

When a subsection is correlated with itself (like Chl1NT~Chl1NT in Table 4.8), this will be referred to as a window. The window's Rho is one if the same parameter evaluates that subsection. However, Rho is not necessary one when different parameters correlate with the window.

b) Dealing with leads, lags and Kelvin waves:

Coastal Kelvin waves propagate poleward from the Equator along the Chilean coast in a time scale of sixty to seventy days (Echevin et al., 2014). To study this aspect, the parameter anomalies were compared against data with one (+1) and two-month lags (+2). This was useful for determining if distant subsections presented a relationship due to the Kelvin wave propagation. Spearman correlations were carried out for this time-shifted data.

As a first approach to this Kelvin wave propagation, only the Chl, SST and PR were analysed, considering only the combinations that physically make sense. The wind components were considered depending on the results. To not extend this work excessively, some correlation parameters were not taken into account for different reasons. Table 4.2 shows the correlations that were made. The number of correlations that were carried out in this part of the study was 6400.

TABLE 4.2. CORRELATIONS USED TO STUDY COASTAL KELVIN WAVE MOVEMENT, WHERE ~ NOTATE THE CORRELATION BETWEEN BOTH VARIABLES.

Parameters	Correlations
Chl	Chl~Chl+1; Chl~Chl+2
SST	SST~SST+1; SST~SST+2
PR	PR~PR+1; PR~PR+2
Chl~SST	Chl+1~SST; Chl+2~SST;
Chl~PR	Chl+1~PR; Chl+2~PR;
PR~SST	PR+1~SST; PR~SST+1; PR+2~SST; PR~SST+2

For all the correlation analyses of the primary system and the Kelvin wave propagation, the P-value was taken to define whether the relationship was significant or not. Rho was selected to measure the relationship strength and determine if it was positive or negative. For better visualisation, the results of each correlation were presented in a scheme that considered the physical aspects of the whole system. This scheme contains twenty boxes that represent all the subsections. They kept the same location to observe the physical links in a simple way. The box colours and size were standardised to represent Rho values and P-values, respectively. All the correlations per parameter combination evaluated are shown in one

Figure (section A.2). Thus, twenty schemes represent the whole system that was evaluated. The six most significant correlation combinations are shown in section 4.3.2 (Figures 4.5-4.10).

4.3. Results.

4.3.1. Parameter Behaviour and a Regional Overview [O.1.1].

The first analysis implemented was to determine the Chl behaviour per subsection using a statistical summary and boxplots (Figure 4.1). This defined which subsection was more productive and gave an initial idea of the Chl distribution. This allowed the selection of possible outliers that might become potential case studies that will be studied in chapter 6 to address O.3. Table 4.3 and Table 4.4 show this statistical summary and the numbers of Chl outliers per subsection.

Figure 4.1 indicates that in terms of Zones, the Southern Zone had the highest productivity, followed by the Central Zone. Although the Northern Zone usually had the lowest Chl coastal levels, the subsection close to Peru (1NT) had slightly higher productivity. In terms of subsections, 2NT to 1CT showed the lowest Chl concentration but with very similar variability. However, 1CT had more outliers than the rest, reaching the highest concentrations among this group. This lower productivity is likely related to extreme aridity associated with the SPSA around this area (Ancapichun and Garcés, 2015; Thiel et al., 2007).

The higher productivity was reached in 3CT to 2ST, whereas that of 2CT was between 1CT and 1NT. This Chl response comes from a more pronounced seasonal cycle due to the SPSA movement allowing periods of precipitation during the winter that increase the nutrient uptake (Quintana and Aceintuno, 2002; Delizileau et al., 2004). This seasonal variation increases southward, delivering more marked Chl variations between the winter and the summer. Consequently, 1ST and 2ST had more extreme values than the rest. Although 2ST showed a slightly lower median than 1ST, its variability was higher, having even the highest Chl concentration. This was unexpected because the SPSA, responsible for upwelling winds, generally does not regularly extend to the Southern Zone (Quintana and Aceituno, 2011; Thiel et al., 2007). This seasonal cycle will be studied in more detail in the next section. Finally, 3ST showed a lower production and variability than this Zone but similar to 1NT.

The ocean strip had lower Chl levels than the coast, with low variability in the whole system. From 1NO to 1CO, the variability was particularly low, while the rest exhibited a slightly higher variability. Effectively, from 3CO towards 3SO, the number of extreme outliers increased intensively. These findings are coherent with Yuras et al. (2005), who reported a lower Chl in the Northern Zone that spread oceanward some 100 km. Meanwhile, the productivity is higher and spreads 200 km oceanward in the Central Zone.

3CO and 2SO were subsections with the highest variability in the ocean strip, which coincidentally had the two highest outliers, which could be compelling case studies (chapter 6). Interestingly enough, their coastal counterparts showed the highest variability, proving a possible correlation. The extreme cases mentioned were the 9.0 mg m^{-3} observed in 3CO during May 2018, which was the highest Chl level on average for this study period (Figures 4.1, 4.3, and A.1.5, panel k and p) and 2SO in November 2014 with (4.23 mg m^{-3}; Figures 4.1, 4.4 and A.1.9 panel k and p). These two events are potential case studies for chapter 6.
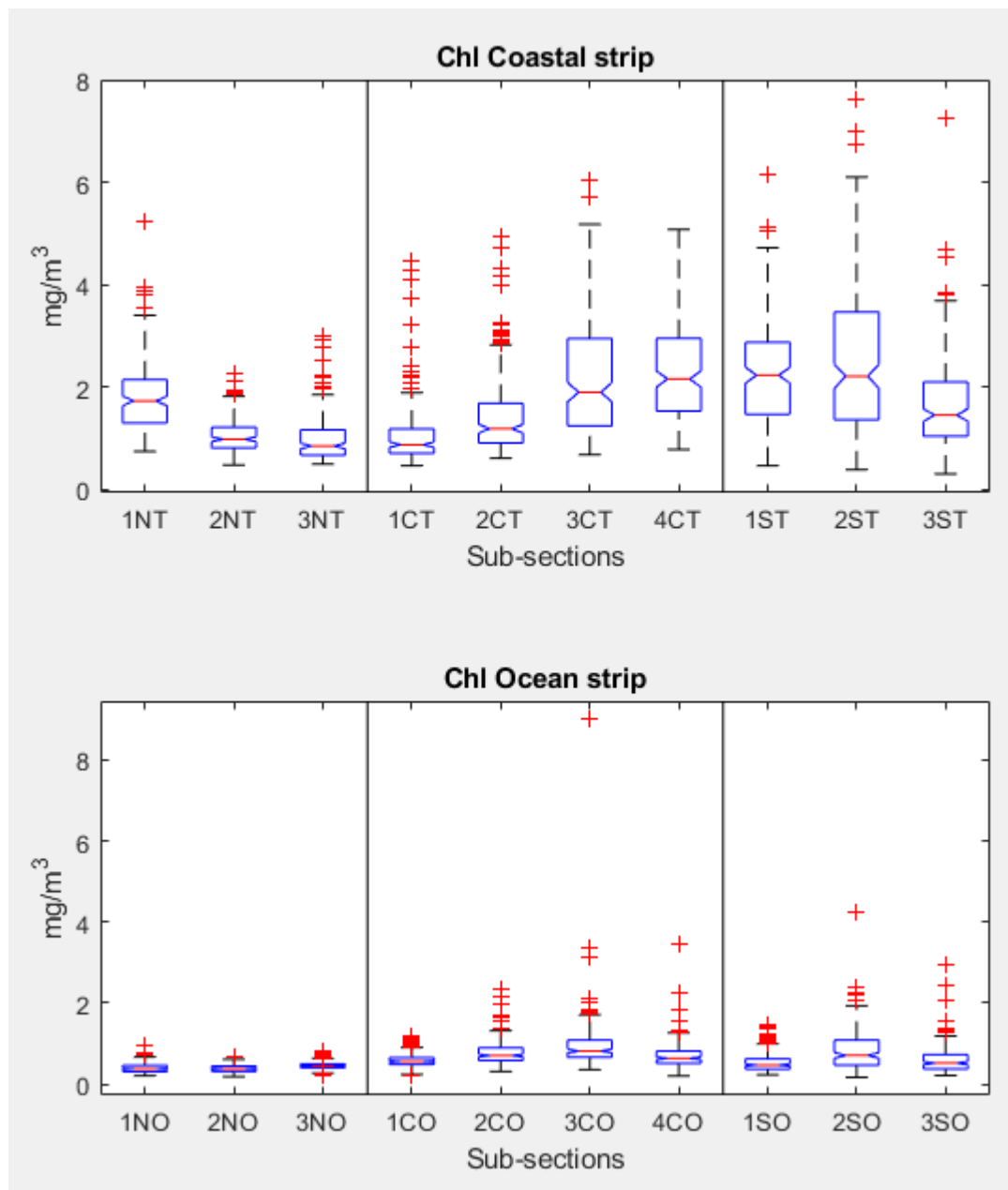
FIGURE 4.1. CHL BOXPLOT FOR EACH SUBSECTION, SEPARATED BY ZONE AND STRIP.

Tables 4.3 and 4.4 present similar results to Figure 4.1 but are expressed in numbers. However, using the SD instead of the quartiles reduced the middle range, increasing the number of outliers. In any case, these outliers will be used from now on. Observing Tables 4.3 and 4.4 and Figure 4.1 showed that the minimum Chl detected was above 0.15 mg m^{-3}, which means a nonzero background level. These minimum values were similar in the ocean and the coastal strips.

TABLE 4.3. STATISTICAL SUMMARY OF THE CHL PER SUBSECTION IN THE COASTAL STRIP, WHERE μ IS THE MEAN AND SD IS THE STANDARD DEVIATION. ALL UNITS ARE MG M^{-3}.

Zones	Northern Zone			Central Zone				Southern Zone		
Subsection	Chl1NT	Chl2NT	Chl3NT	Chl1CT	Chl2CT	Chl3CT	Chl4CT	Chl1ST	Chl2ST	Chl3ST
Max	5.25	2.25	2.99	4.47	4.94	6.06	5.08	6.15	7.64	7.27
μ	1.8	1.04	0.99	1.08	1.45	2.21	2.36	2.28	2.55	1.66
SD	0.68	0.32	0.45	0.64	0.8	1.17	1.04	1.03	1.46	0.9
Min	0.75	0.48	0.5	0.46	0.61	0.68	0.78	0.46	0.39	0.34
μ+2SD	3.16	1.68	1.89	2.35	3.04	4.55	4.43	4.34	5.47	3.45
μ-2SD	0.45	0.4	0.09	0	0	0	0.29	0.22	0	0
Higher Outliers	9	10	8	8	10	9	9	7	7	7
Lower Outliers	0	0	0	0	0	0	0	0	0	0

42

Zones	Northern Zone			Central Zone				Southern Zone		
Subsection	Chl1NO	Chl2NO	Chl3NO	Chl1CO	Chl2CO	Chl3CO	Chl4CO	Chl1SO	Chl2SO	Chl3SO
Max	0.96	0.67	0.81	1.17	2.34	9.01	3.44	1.45	4.23	2.96
μ	0.39	0.38	0.46	0.59	0.77	0.96	0.7	0.54	0.81	0.59
SD	0.12	0.09	0.1	0.17	0.31	0.72	0.34	0.24	0.5	0.35
Min	0.21	0.18	0.21	0.23	0.31	0.36	0.2	0.23	0.17	0.21
μ+2SD	0.63	0.56	0.67	0.94	1.38	2.39	1.38	1.02	1.81	1.29
μ-2SD	0.15	0.19	0.26	0.24	0.16	0	0.02	0.06	0	0
Higher Outliers	7	4	8	10	6	3	4	10	8	7
Lower Outliers	0	3	2	2	0	0	0	0	0	0

Northern Zone outliers comprised fifty-one events over forty different dates. Hence, they do not usually occur at the same time. The Central Zone had sixty-one events over forty dates. Finally, forty-six extreme episodes in thirty-one dates were found for the Southern Zone. Only seven of all these outliers were for low values of Chl. These low outliers were in ocean strips between 2N and 1C, demonstrating that the minimum Chl levels were relatively stable. However, the 2SD value was limited to a physically sensible minimum of zero in eight subsections.

For the Northern and Central Zone, extreme events in ocean strips were lower than for coastal strips (37%). In contrast, in the Southern Zone, 54% of its total episodes were offshore. The extreme ocean events showed some relation with the extreme coastal events. However, the ocean did not show much variability, giving a low SD. Therefore, the ocean subsection outliers were not as extreme as the coastal values. The exceptions were extreme events detected in the Central Zone and Southern Zone ocean strips and the highest value detected in each ocean subsection mentioned before. This will be studied in greater detail in chapter 6.
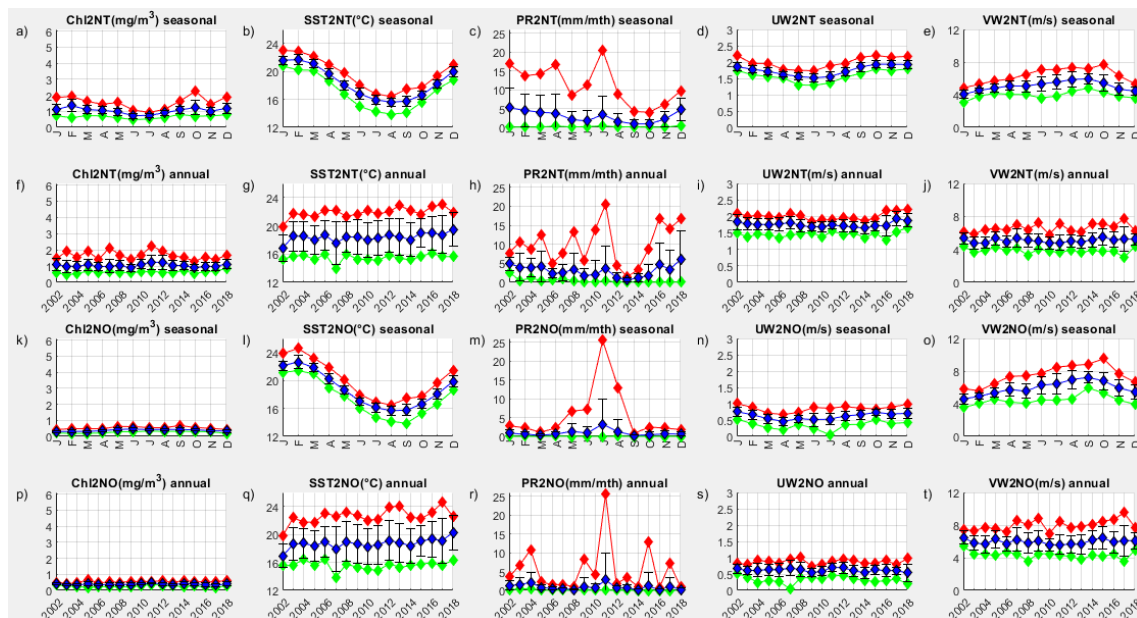
FIGURE 4.2. 2NT (A-E) AND 2NO(K-O) SEASONAL MEANS FROM 2002-2018 AND ANNUAL MEANS (F-J AND P-T) OVER THE WHOLE STUDY PERIOD FOR ALL THE PARAMETERS STUDIED IN O.1. THE RED LINE IS THE MAXIMUM, THE GREEN IS THE MINIMUM, AND THE BLUE IS THE MEAN.
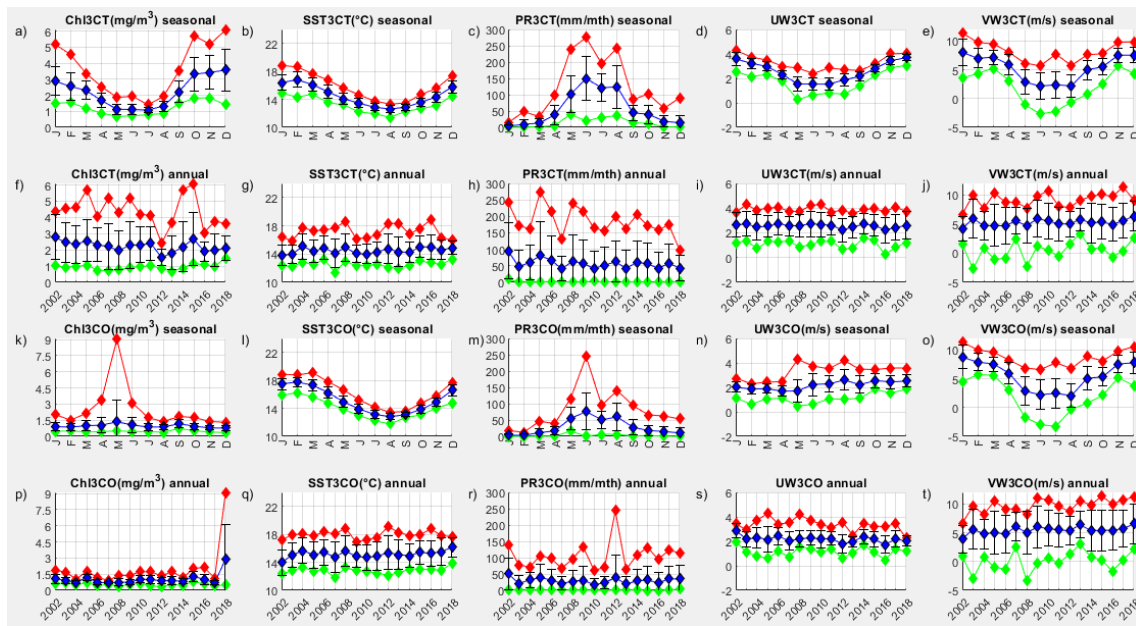
FIGURE 4.3. 3CT(A-E) AND 3CO(K-O) SEASONAL MEANS FROM 2002-2018 AND ANNUAL MEANS (F-J AND P-T) OVER THE WHOLE STUDY PERIOD FOR ALL THE PARAMETERS STUDIED IN O.1. THE COMPLETE LEGEND IS IN FIGURE 4.2.
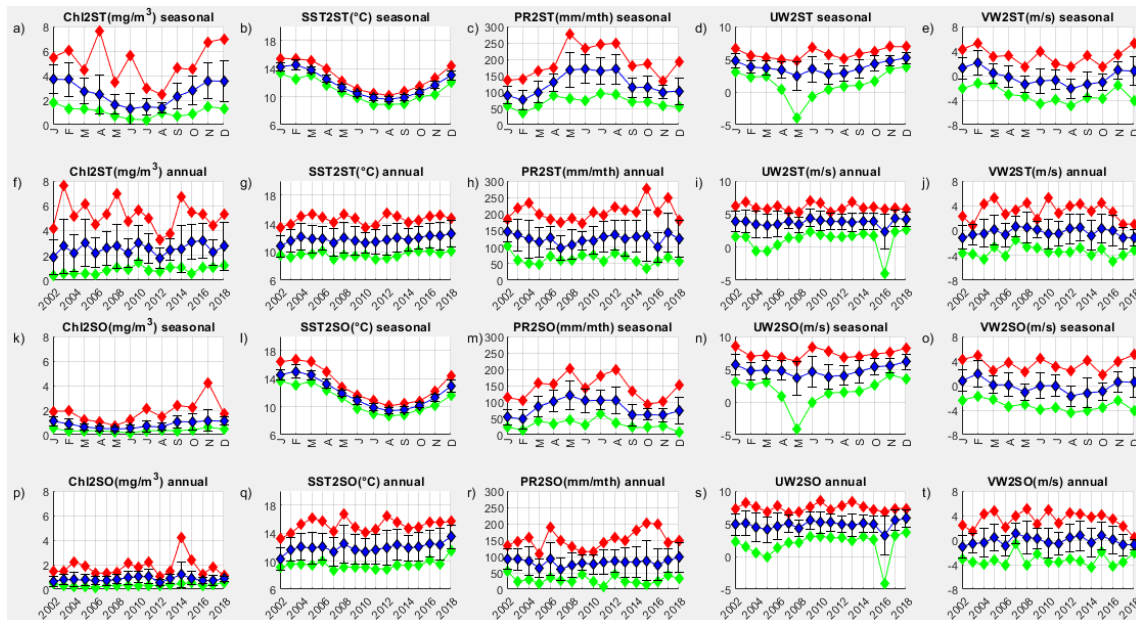
FIGURE 4.4. 2ST (A-E) AND 2SO (K-O) SEASONAL MEANS FROM 2002-2018 AND ANNUAL MEANS (F-J AND P-T) OVER THE WHOLE STUDY PERIOD FOR ALL THE PARAMETERS STUDIED IN O.1. THE COMPLETE LEGEND IS IN FIGURE 4.2.

Once the Chl was studied, the next step was to include the physical variables and compare them with the Chl. Figures 4.2-4.4 show the seasonal cycle and annual means over the whole study period (2002-2018) for the middle subsection for each of the three Zones. All the plots for each subsection along the Chilean coast can be found in Appendix A.1. Studying these plots of each variable in each subsection allowed the formulation of the following general overview per parameter, which in section 4.4 will be analysed per Zone.

a) Chl:

As expected, the means showed the influence of the radiative seasons, having low productivity in June and July and high productivity from September to April, with peaks in September, October and February. This was because sunlight is necessary for phytoplankton bloom. Also, summer presents favourable conditions for upwelling, at least for the Central Zone and partly the 1S-2S subsections, while in the Northern Zone, the winds were present

44

and were weaker the whole year. Thus, this pattern got more marked moving southward. However, the plots showed some interesting variations. 1NT showed a slight increment in September and February, while 2NT was flat (Figures A.1.1-A.1.2 panel a). 3NT to 2CT showed an increment from September to October, which was less noticeable in 3NT and more pronounced in 2CT (Figures A.1.3-A.1.5 panel a). From 4CT to 2ST, the pattern is as it was described at the beginning (Figures A.1.7-A.1.9 panel a). Lastly, in 3S, as for 3N, its mean Chl was flat but with higher productivity (Figure A.1.10 panel a).

The maxima line, coloured red in the plots, exacerbated the average behaviour, marking the difference between the cold and warm seasons. Thus, 2NT to 3NT showed an increment in September-October, plus in February in 3NT (Figures A.1.2 to A.1.3 panel a). In 1CT and 2CT, the peaks were in October, November and February, while in 3CT and 4CT, there were additional peaks in December and January. 1NT could also be in this last group, but the difference here was that the maxima line was significantly higher than the average, indicating these were infrequent (Figures A.1.4-A.1.7 and A.1.1 panel a). The Southern Zone maxima line was less clear, with some extremes higher than the rest. These events were due to particular situations that will be investigated through case studies (chapter 6). 3S displayed extreme events the whole year (Figures A.1.8-A.1.10 panel a).

The seasonal cycle in the ocean in the Northern subsection 1-2NO presented a slight Chl increment in the cold season but with low productivity (Figures A.1.1 and A.1.2, panel k), while the Central Zone did not follow a clear behaviour (Figures A.1.4-A.1.7 panel k). This may be because their values often did not change very much. However, 1S and 3S showed an influence of the coast, with the coastal pattern being similar to offshore but with more limited periods of extreme values (Figures A.1.8 and A.1.10, panel k).

The annual cycle helped determine which years had a more significant production per subsection, shown in Table 4.5. This, along with Figures A.1.1 to A.1.10 panel f, reveal that the Chl levels in 2NT were the flattest with no significant increments. It also showed that 2004-2005 was a particularly high year with significant concentrations in the coastal strip of 1N, 1C-2S. On the other hand, 2012 presented the lowest maximum values in the majority of the subsections. Oddly enough, the SPSA[1] was below 0.2 in 2004-2005, driven by a weak El Niño and La Niña, respectively. Meanwhile, 2012 showed no ENSO effect and a slightly higher SPSA (0.5) but still low.

TABLE 4.5. FIVE HIGHEST MAXIMUM CHL YEARS IN EACH COASTAL SUBSECTION IN DECREASING ORDER.

Subsection	years with high Max.	Range (mg m⁻³)	Averaged Max (mg m⁻³)
1NT	2003, 2004, 2017, 2005, 2011	3.1-5.2	2.8
2NT	2011, 2007, 2005, 2003, 2012	1.9-2.3	1.7
3NT	2011, 2009, 2017, 2013, 2002	3.0-2.2	2.0
1CT	2004, 2002, 2003, 2010, 2005	2.7-4.5	2.4
2CT	2007, 2004, 2005, 2009, 2011	3.3-5.0	3.0
3CT	2015, 2014, 2005, 2009, 2007	4.9-6.1	4.4
4CT	2007, 2009, 2013, 2005, 2016	4.6-5.1	4.1
1ST	2005, 2003, 2007, 2013, 2016	4.3-6.2	4.0
2ST	2003, 2008, 2014, 2005, 2010	5.7-7.7	5.3
3ST	2015, 2004, 2014, 2007, 2002	3.8-7.3	3.4

The higher concentrations in 1N and the Central Zone were found more frequently from 2002 to 2005, especially in 1N, reducing the mean concentration by around 30%. A low concentration was found in the Northern Zone in 2015 and part of the Central Zone (1C-3C) in 2016. Meanwhile, the Chl increased in 3C and 3S through 2015 and 4C-2S in 2016. In 2015

---

[1] The SPSA index was obtained by Vicencio (2021), whereas the ENSO index by NOAA (2019) both indices are normalised. This will be discussed more fully in 5.2.2.1.

there was an extreme El Niño, followed by an extremely high SPSA in 2016, showing a different effect per Zone. In Contrast, the La Niña extreme in 2007 was also associated with a Chl increase from 1C to 1S. Besides these episodes, the Chl signal went down from 2012 onwards from 2N to 2C, while 3C to 2S rose again.

b) SST:

SST was the only parameter that presented a similar seasonal behaviour across the whole system, with a poleward decrease of 0.5°-1°C per subsection, except for subsections 2S to 3S, where there was a difference of -2°C, probably because 3S had a more extensive latitudinal range (section 3.2.2 for more details). The highest value was reached in February (January in 1N) and the lowest value in August (Figures A.1.1-A.1.10 panel b). The average difference between these months varied from 5.2°C (for 1N) to 6°C (for 2N) for 1N to 2C. This range was smaller in the rest (3C-3S), moving from 4.2 (3C) to 4.9 (1S and 2S). The seasonal SST variability was very low, except for the warmest months. These high variations during the summer were more evident at the coast. In general, SST was driven by the annual cycle in the whole climate system with minor variations. The ocean strip, in general, had a SST of 0.3°-0.7°C higher than the corresponding coastal strip, as a result of the coastal upwelling, except 3S. Here, the coastal area was 0.5°C warmer than the Ocean subsection (Figures A.1.-A.1.10 panel l).

Although the SST had a low variation per year in general, some tendencies were observed (Figures A.1.1-A.1.10 panel g). 2015-2017 was the period with the highest SST in the whole territory owing to El Niño. 2004-2005 also had a significant SST increase from 3C to 4C. Another interesting pattern was the increase in the maxima line in 2003-2005 and 2008-2015 in the Northern and Central Zone, which was more marked in 3N-2C. On average, the lowest SSTs were in 2003 and 2007-2011 in the whole territory. However, this drop was more significant in 3C-4C in 2009 and 2011. This behaviour was coherent with the extreme La Niña episodes in 2007-2008 and 2010-2011. Furthermore, the La Niña effect was also reflected in the minima line, reaching the lowest SST in 2007 in the three Zones excluding 3S. The minima line showed the lowest variation of all the lines. The exceptions to that were in subsections 1N and 3S. Both seem to be more influenced by ENSO, with lower values in 2007, 2010 and 2011 and higher from 2015 to 2017.

c) PR:

The overall PR trended to increase poleward, as expected from large-scale climate considerations (Table 4.6). Therefore, the further south the subsection was located, the more rainfall there was, except that 2S was higher than 3S. The ocean strip PR showed similar values to the coastal strip, but the latter was slightly lower, except for 3S, where its ocean strip had higher PR (Figures A.1.1-A.1.10, panels c and m).

Table 4.6. COASTAL SUBSECTIONS' PR ANNUAL AVERAGE (MM MTH^{-1}), THE SECOND AND THIRD ROWS SHOWED THE LOWEST AND THE HIGHEST AVERAGED YEAR.

Subsection	Annual aver	lowest year	highest year
1NT	2.34	1.0 (2013)	4.0 (2004)
2NT	2.73	0.7 (2013)	4.6 (2016)
3NT	3.47	1.4 (2007)	10.4 (2017)
1CT	11.18	4.9 (2007)	21.9 (2017)
2CT	32.61	18.9 (2007)	44.7 (2005)
3CT	55.58	40.8 (2007)	80.9 (2005)
4CT	85.91	69.3 (2007)	106.6 (2006)
1ST	107.53	81.6 (2007)	122.6 (2017)
2ST	123.68	98.4 (2007)	143.8 (2017)
3ST	84.24	65.4 (2016)	94.3 (2017)

The PR events were scarce in the Northern Zone with an average line below 5 mm mth^{-1}, but with a few extreme episodes. Effectively, 3N showed intense extreme events where the most

significant were in May 2017 (79.5 mm mth^{-1}), June 2011 (37 mm mth^{-1}) and July 2004 (30 mm mth^{-1}; Figure A.1.3, panel c and h). The first event was in one day, provoking a massive flood in the cities located there (Sernageomin, 2017). Subsections 1N-2N presented higher values during summer, while 3N's events were in the winter, with the extreme events more concentrated from May to July (Figures A.1.1-A.1.3, panel c).

The PR increased significantly from 1C to 2S (Table 4.6 and Figures A.1.4-A.1.9, panel c). This increase was primarily during the winter. Moreover, the rainfalls in that season were more pronounced from 2C onwards, where the minima PR was not zero. However, the Southern Zone PR's events were also present in the rest of the year but with a lower intensity. Indeed, in this Zone, the minima line was never zero. 3S's PR did not grow as much during the winter, so they were lower than 1S and 2S (Figures A.1.8-A.1.10, panel c).

Table 4.6 reveals that 2007 was the driest year from 3N to 3S associated with the La Niña episode. At the same time, 2016 was also very dry from 4C to 3S, while the Northern Zone was wetter than usual, which might be associated with the extreme El Niño episode in 2015 and strong SPSA in 2016. In contrast, 2017 and 2005 also were very rainy in the whole territory, which was unexpected because a weak La Niña modulated both years. The annual plots show that Northern Zone's extreme episodes occurred at particular times (Figures A.1.1-A.1.3 panel m). 1N's episodes stopped in 2008, whereas 3N showed a few events with a significant magnitude, as mentioned before. 2N events were more constant, especially in recent years (2016-2018). Still, from 2012 to 2015, no significant event was registered in 2N. These plots also show that the big drought, mentioned in the literature by Garreaud et al. (2020) and Aguayo et al. (2021), was more notorious in the Central Zone, with low average PR from most years from 2009 to 2016. The Meteorological Directorate of Chile (DMC, 2018) reported that the PR events had been reduced significantly in the Central and Southern Zone in recent years. Though, the data were insufficient to affirm or deny this observation.

d) Winds:

VW presented a southerly wind dominance with a seasonal behaviour such that this variable's values reached a maximum in summer and decreased during winter from 1C to 2S. This seasonality increased polewards with 4C reaching the higher range. The Southern Zone exhibited the opposite effect decreasing the seasonal difference further south (Figures A.1.4-A.1.9 panel e). The wind direction in the Northern and Central Zone was unchanged over the year, but this was not always the case in the Southern Zone. Moreover, 4C and 1S northerly winds were more dominant during the winter, while 3C exhibited northerly winds in that season in a few years, such as 2003 and 2008. The 3S general trend was to have northerly winds the whole year, whereas 2S's southerly winds were more frequent in the summer, particularly in February (Table 4.7 and Figures A.1.4-A.1.10 panels e and j).

TABLE 4.7. COASTAL SUBSECTIONS' VW AND VW ANNUAL AVERAGE (M S^{-1}), THE SECOND AND THIRD ROWS SHOWED EACH VARIABLE'S LOWEST AND HIGHEST AVERAGED YEAR.

Subsection	VW			UW		
	Annual aver	lowest year	highest year	Annual aver	lowest year	highest year
1NT	3.9	3.8 (2003)	4.1 (2007)	1.6	1.5 (2016)	1.7 (2003)
2NT	5.0	4.7 (2003)	5.5 (2015)	1.7	1.6 (2014)	1.9 (2017)
3NT	6.5	6.1 (2012)	7.0 (2009)	2.0	1.8 (2013)	2.1 (2017)
1CT	7.0	6.3 (2016)	8.0 (2003)	1.6	1.5 (2012)	1.7 (2005)
2CT	5.4	4.8 (2008)	6.6 (2003)	2.4	2.1 (2016)	2.5 (2009)
3CT	5.3	4.7 (2006)	6.0 (2003)	2.6	2.2 (2016)	2.7 (2006)
4CT	3.3	2.7 (2006)	4.2 (2013)	2.0	1.2 (2016)	2.3 (2017)
1ST	0.6	-0.2 (2017)	1.4 (2013)	2.5	1.4 (2016)	2.9 (2017)
2ST	-0.2	-1.2 (2017)	0.7 (2007)	3.7	2.3 (2016)	4.4 (2009)
3ST	-1.7	-2.9 (2010)	-0.5 (2015)	5.2	4.1 (2005)	6.2 (2009)

The Northern Zone showed a slight VW variation, with a low increment during the winter, reaching its maximum value in September, where 1N and 2N exhibited winds with a maximum speed below 4.5 and 6 m s^{-1}, respectively (Figures 4.1 and A.1.1-A.1.3 panel e). This low maximum speed range was like 1S and 2S, varying from 0.8 to 5.6 m s^{-1}. Despite the 3S northerly winds trend, a few southerly winds can be seen throughout every year (except 2011), with slightly more frequency in the winter, but these were below 4 m s^{-1}. The maximum speed winds, on average, were in 3N-1C, reaching velocities over 9.0 and 9.5 m s^{-1} almost every summer. However, 1C showed a higher variation than 3N. 3C also experienced intense southerly winds through the summer, but these showed a more extensive range, varying from 7.5 to 11 m s^{-1}, while 2C and 4C were slightly lower with a range between 6.5 and 10 m s^{-1}. All these observations are related to the SPSA influence and movement.

Table 4.7 and Figures A.1.1-A.1.10 panel j demonstrate that the wind variations were marked from 3C to 3S with the strongest southerly winds in 2013, 2007, 2009 and 2015. Except for 2007, the SPSA was below 0.7, while ENSO's behaviour was completely different in the three years. In contrast, 2017, 2010, 2006 and 2011 had the weakest winds. Excluding 2006, in these years the SPSA was more intense, or La Niña was present. From 3N to 2C, the winds were more intense in 2003 and 2009 and the weakest in 2016, 2012 and 2008. Surprisingly, the SPSA was below 0.3 in 2003 and 2009, while in 2012 and 2008, the index was close to 0.48. On the other hand, 2016 was one of the highest SPSA years. Thus, the climate driver influence on the intensity of the southerly wind was not as evident.

The UW component showed westerly winds dominance with weak values and a low variation in 1N-1C, while this component was more significant in 2S-3S (Table 4.7 and Figures A.1.1-A.1.10. panel d and i). The rest of the subsections had intermediate UW values. The behaviour of this component showed weak values during the winter and strong during the summer over 2C and 3C (Figures A.1.5 and A.1.6 panel d). From 4C to 3S, UW's seasonal trend was not influenced by the seasons, but it had a significant variation. This was more marked in 2S and 3S, where westerly winds reached magnitudes over 7 m s^{-1} in the winter and 5 m s^{-1} in the rest of the year. Furthermore, this variable's variability was only significant in 4C to 3S, reaching easterly winds in 2004, 2005 and 2016. Meanwhile, 2017 and 2009 exhibited the highest westerly winds. 2016-2017 were strong SPSA years, whereas it was weak, and negative AAO was more present in 2004, 2005 and 2009. Thus, the intensity was not straightforward for these climate drivers, as with the VW.

The VW component represented more than 80% of the wind magnitude in the subsections 1N to 2C. From 3C to 1S, the UW values were more significant than VW on some occasions, especially during the winter. However, this mixture was more similar in 1S than in 3C. In contrast, the UW component was the dominant component in 2S-3S. Here, UW was higher than VW in many months. These values were more significant than VW on some occasions, with more frequency during winter. The SPSA movement that was described in chapter 3 matches perfectly with these behaviours.

4.3.2. Data Correlations and Parameter Connections [O.2.2].

The data correlations were made per parameter combination based on the data anomalies relative to the monthly means. The number of correlations required to evaluate one parameter combination (Chl~Chl) across the whole system leads to a matrix of 20x20. An example of this is shown in Table 4.8. Twenty-five matrices are required to evaluate the five parameters; eighteen extra matrices were made to study the Kelvin wave propagation. A summary figure was created for each parameter combination to simplify the presentation of the results from these correlations. A description of the structure is given in section 4.2.2. Here, examples for Chl~Chl, SST~Chl, PR~Chl, VW~Chl, UW~Chl and VW~SST are shown in

Figures 4.5 to 4.10. All the correlation Figures can be found in Appendix A.2. Studying these figures allowed the identification of the links among the parameters and subsections.

In these Figures, the cyan to blue scale was used to represent positive relationships (0 to 1), while a gold to red scale, using an orange variation in the middle, was used to represent negative relationships (-1 to 0). When a colour presented a darker shade, it meant the relationship was more robust. The Rho scale was built with a 0.2 step. The significance was standardised in four sizes using P-value (Table 4.1.): very significant (P-value < 0.01) with a full-size block; significant (0.01 < P-value < 0.05) with a block 80% of its full size; low significant (0.05 <P-value <0.1) with a 40% block; Not significance with a 20% block (Figures 4.5-4.10 and A.2.). Rhos between 0.15 to 0.18 were significant, while Rhos over 0.19 were very significant. This occurred owing to the quantity of data correlated, which was one hundred ninety-two dates (July 2002 to June 2018).

a) Chl~Chl:
Chl~Chl, Chl~Chl+1 and Chl~Chl+2 relationships are analysed here (Figures A.2.1-A.2.3, Chl~Chl is shown in Table 4.8 and Figure 4.5). The relationships were mainly positive, with a substantial similarity between subsection neighbours. This link was present for Chl+1 but weaker. Chl+2 had fewer clear bonds, with some negative relationships.

1NT, 1NO and 2NT did not correlate well with the other subsections. 1NO presented a stronger correlation with 1CT and 2CT (Figure 4.5 or A.2.1). These correlations were seen in Chl+1 and Chl+2 as well (Figures A.2.2 and A.2.3). 3NT had a better correlation with 1CT than 2NT. This correlation was only observed in Chl+1, not in Chl+2. From 2NO to 1SO, a similar and strong correlation was visible. This was so for all windows in these subsections. The Rho in the ocean strip was higher than it was along the coast. This behaviour was also seen in Chl+1, where it was stronger in some cases (2NO). Chl+1 presented a weaker coastal strip correlation than it was when Chl was evaluated. Some remains of the ocean strip relationship can be seen when Chl+2 was evaluated, but they were weaker. This could reflect Kelvin wave movement to the south or a lack of variability.

The Central Zone presented a higher correlation range compared with the Southern and Northern Zone. At the same time, this Zone showed a better link with the North. However, 4C to 2S presented an excellent correlation. Subsection 3S did not show any relationship beyond 1S. Thus, extreme areas presented a lower link than the rest. This makes sense because they were influenced by other factors that the core Chilean coastline is not.

TABLE 4.8. RHO RESULT FOR THE WHOLE SYSTEM EVALUATED CHL~CHL.

Chl	1NT	1NO	2NT	2NO	3NT	3NO	1CT	1CO	2CT	2CO	3CT	3CO	4CT	4CO	1ST	1SO	2ST	2SO	3ST	3SO
1NT	1.0	0.5	0.2	0.1	0.1	0.0	0.1	0.1	0.1	0.0	0.1	-0.1	-0.1	-0.2	0.0	-0.1	0.0	0.0	0.1	0.0
1NO	0.5	1.0	0.2	0.1	0.0	0.0	0.2	0.1	0.1	0.1	0.1	0.0	0.0	0.0	-0.1	0.1	0.0	0.0	0.0	0.1
2NT	0.2	0.2	1.0	0.4	0.1	0.0	0.2	0.1	0.0	0.0	0.0	0.1	-0.1	0.1	0.0	0.1	0.0	0.1	-0.1	0.0
2NO	0.1	0.1	0.4	1.0	0.2	0.3	0.2	0.4	0.1	0.2	0.2	0.2	-0.1	0.1	0.0	0.2	0.1	0.1	0.0	0.0
3NT	0.1	0.0	0.1	0.2	1.0	0.3	0.5	0.2	0.2	0.0	0.0	0.0	0.0	-0.1	0.1	0.1	0.1	0.1	0.1	0.1
3NO	0.0	0.0	0.0	0.3	0.3	1.0	0.3	0.6	0.3	0.2	0.2	0.1	0.1	0.3	0.0	0.1	0.0	0.1	0.0	-0.1
1CT	0.1	0.2	0.2	0.2	0.5	0.3	1.0	0.5	0.5	0.2	0.4	0.1	0.1	0.0	0.1	0.1	0.2	0.1	0.0	0.0
1CO	0.1	0.1	0.1	0.4	0.2	0.6	0.5	1.0	0.5	0.5	0.3	0.2	0.1	0.2	0.1	0.2	0.1	0.1	0.0	0.0
2CT	0.1	0.1	0.0	0.1	0.2	0.3	0.5	0.5	1.0	0.5	0.5	0.3	0.2	0.0	0.1	0.1	0.1	0.0	0.1	0.0
2CO	0.0	0.1	0.0	0.2	0.0	0.2	0.2	0.5	0.5	1.0	0.5	0.6	0.2	0.2	0.2	0.2	0.2	0.0	0.1	0.0
3CT	0.1	0.1	0.0	0.2	0.0	0.2	0.4	0.3	0.5	0.5	1.0	0.4	0.4	0.1	0.1	0.2	0.1	0.0	0.0	0.0
3CO	-0.1	0.0	0.1	0.2	0.0	0.1	0.1	0.2	0.3	0.6	0.4	1.0	0.3	0.3	0.1	0.2	0.1	0.0	0.1	0.1
4CT	-0.1	0.0	-0.1	-0.1	0.0	0.1	0.1	0.1	0.2	0.2	0.4	0.3	1.0	0.3	0.4	0.2	0.3	0.2	0.0	0.1
4CO	-0.2	0.0	0.1	0.1	-0.1	0.3	0.0	0.2	0.0	0.2	0.1	0.3	0.3	1.0	0.3	0.4	0.2	0.2	0.1	0.1
1ST	0.0	-0.1	0.0	0.0	0.1	0.0	0.1	0.1	0.1	0.2	0.1	0.1	0.4	0.3	1.0	0.3	0.5	0.2	0.1	0.1
1SO	-0.1	0.1	0.1	0.2	0.1	0.1	0.1	0.2	0.1	0.2	0.2	0.2	0.2	0.4	0.3	1.0	0.4	0.5	0.2	0.2
2ST	0.0	0.0	0.0	0.1	0.1	0.0	0.2	0.1	0.1	0.2	0.1	0.1	0.3	0.2	0.5	0.4	1.0	0.4	0.5	0.3
2SO	0.0	0.0	0.1	0.1	0.1	0.1	0.1	0.1	0.0	0.0	0.0	0.0	0.2	0.2	0.2	0.5	0.4	1.0	0.3	0.3
3ST	0.1	0.0	-0.1	0.0	0.1	0.0	0.0	0.0	0.1	0.1	0.0	0.1	0.0	0.1	0.1	0.2	0.5	0.3	1.0	0.6
3SO	0.0	0.1	0.0	0.0	0.1	-0.1	0.0	0.0	0.0	0.0	0.0	0.1	0.1	0.1	0.1	0.2	0.3	0.3	0.6	1.0
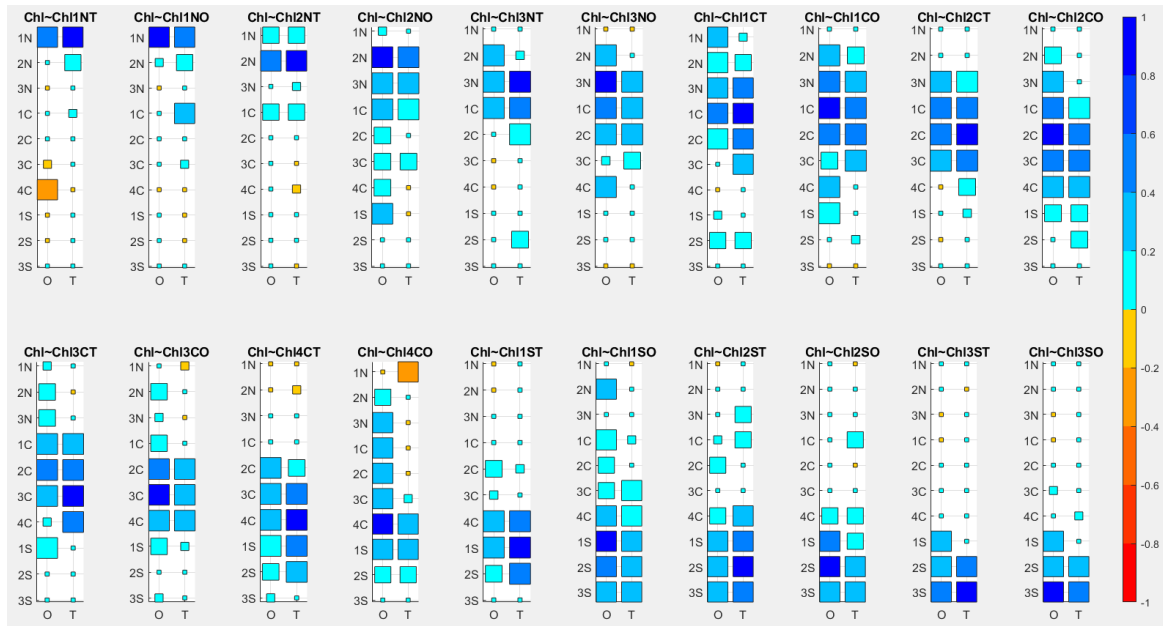
FIGURE 4.5. CHL~CHL CORRELATION IN THE WHOLE SYSTEM, WHICH SHOWS IN TABLE 4.3 VISUALLY. THE CYAN TO BLUE SHADES REPRESENTS POSITIVE RELATIONSHIPS (0 TO 1), WHILE A GOLD TO RED SCALE REPRESENTS NEGATIVE RELATIONSHIPS (0 TO -1). A FULL-SIZE BLOCK MEANS THAT IT IS VERY SIGNIFICANT (<0.01); A SIGNIFICANT (0.01-0.05) IS REPRESENTED WITH A BLOCK 80% OF ITS FULL SIZE; LOW SIGNIFICANT (0.05-0.1) WITH A 40% BLOCK; NOT SIGNIFICANT WITH A 20% BLOCK.

Overall, Chl correlations from 3N to 2S were positive, with values over 0.3 against a surrounding range of 3 subsections in the coastal strip. The ocean strip presented a constant strong correlation from 2NO to 1SO. When Chl+1 and Chl+2 were evaluated against Chl, these correlations were weaker. Only a few subsections Rho overpass the Rho's that were detected in Chl~Chl (Figures A.2.1-A.2.3.).

b) SST~SST:
SST~SST, SST~SST+1 and SST~SST+2 relationships are analysed here (Figures A.2.4-A.2.6). SST presented robust correlations, with almost the whole system being well connected. This was predictable based on its seasonal and interannual behaviour, which was studied in the previous section. Even the furthest north subsection 1NT, when it was correlated with the furthest south subsections of 3ST and 3SO, showed a statistically significant correlation, but it was a lower correlation value when compared with the rest. This decline in correlation makes sense due to the long distance between the subsections, combined with the CHC's influence in 3S.

The SST~SST+1 relationship was slightly weaker than SST~SST, but the correlation was still high in strength and statistically significant. Their linking patterns remained the same as SST~SST. SST~SST+2 Rhos' were still statistically significant. However, the Central Zone presented less connection with the rest, especially 1CT and 2CT. On the other hand, the correlation between 1NT and 3ST was higher than the relationships that were found in SST~SST and SST~SST+1. SST was very similar across the whole system; thus, the correlations were very high even when SST+1 and SST+2 were evaluated. This is likely related to the low variation and consistency that the SST had in the whole territory.

c) PR~PR:
In this section, PR~PR, PR~PR+1 and PR~PR+2 are analysed (Figures A.2.7-A.2.9). These correlations are essentially seeking evidence of auto-correlation or persistence in similar rainfall. There is little persistence apart from one month to the next then any PR influence will be short-lived. PR's correlations were mainly positive, with a good connection between subsection adjacents. The three Zones presented a good correlation with their subsections.

50

For instance, 2N was strongly correlated with 1N and 3N, 1C with 4C and 1S with 3S. This demonstrated that one of the main differentiating factors between zones was PR. The Central Zone showed a better link with the South. This was likely owing to the North's dryness. Furthermore, the Northern Zone presented more rainfall in the summer instead of winter compared to the Central and Southern Zone case.

When PR was correlated with PR+1, it showed a weaker relationship than PR~PR. It also showed a mix of negative and positive relationships. PR+1 had some areas of similar correlations, as was detected with PR~PR, such as 1N-3N and 2S-3S, but the correlations were less statistically significant. The exception was when the window was in 2NO. Here, the strength was weaker than PR~PR (1N-1CO), but the ocean strip correlation was slightly higher (1NO-2CO). The Central Zone in PR+1 did not show any relevant relationships. PR~PR+2 showed mostly insignificant relationships with some exceptions. PR3NO to PR2CO showed statistically significant but low (0.2) negative correlations with PR+2 (2NT, 3NT). PR1NT had statistically significant correlations with PR+2 (1NT, 2NT). Their Rhos were 0.4 and 0.25, respectively.

Overall, the PR~PR showed strong positive correlations over 0.4 with the surrounding area. This area range depended on the Zone. The Northern Zone range was 2-3 subsections, while in the Central and the Southern Zone, this extended over 4-6 subsections. The PR+1 and PR+2 did not show these patterns, and their correlations were quite weak, with some exceptions.

   d) VW~VW and UW~UW and their relationships:
In this section, both wind components were analysed when they were evaluated by themselves and with each other. VW~VW (Figure A.2.17) presented a good correlation with nearby subsections. 3N-3C presented a strong correlation that was highly connected across the band. This area also had stronger winds and a similar seasonal variability. In general terms, the Central Zone presented a higher link with the Northern Zone (Except 1NT). This is coherent with VW's statistically significant influence over the Central and Northern Zone. 1S-2S showed a negative relationship with the subsection range 3N-3C, while 3S showed a statistically significant negative correlation with 3C only, while with the rest of the subsection set, the correlations were not statistically significant. 1N presented a lower correlation with other subsections. 1NT did not show a statistically significant relationship with 3N, 2CO, 3C, or 2S-3S, whereas 1C was negative. These inverse relationships could be an expression of the SPSA movement.

UW~UW showed a regular strong correlation from 2C to 2S (Figure A.2.18). This was because UW did not become statistically significant until 2C. The Southern Zone correlations were even stronger. This Zone had a good correlation with all its components. The North did not show a constant correlation with the rest. Some interesting relationships were seen, such as 2NO and 3NO presented a negative correlation with the Central and Southern Zone. 3NT presents a robust negative relationship with 1NO (-0.4).

VW~UW presented a negative relationship in the area near the window when it was evaluated (Figure A.2.19). This was usually surrounded by a section with an insignificant or positive relationship. This behaviour is consistent because both components presented the opposite behaviour. An example of this was when VW was evaluated in UW1NO; all the Northern Zone was negative, 2C-3C was positive, and the rest was insignificant. When UW1CT was assessed, the Central Zone correlations were entirely negative, and 1N-2N was positive. This expresses the critical difference that exists between each Zone. This makes sense because UW was weak in the Northern and robust in the Southern Zone, while VW had the opposite behaviour. The exception to this was 1NT, where both components were weak. However, each pattern's limits seem to be not so clear because the relationships change

drastically when the window moves. Therefore, the variations were not evident when a particular subsection was compared with a subsection next to it, but it was statistically significant when compared with a distant subsection. This also could be expressing the SPSA movement.

VW~W with UW~W were compared with W~W (Figures A.2.20-A.2.2), where W is the magnitude of the wind vector ($\sqrt{VW^2 + UW^2}$). This showed that VW had a more evident dominion in the Northern Zone. There, the UW almost had no presence. Except for 1NT, where neither VW~W nor UW~W had statistically significant correlations. Effectively, the winds in this subsection were low. The UW had a significant role in the Southern Zone, with a lower magnitude for VW. Both were present in the Central Zone case, but VW had a bigger prominence over the UW from 1C-3C, while 4C was more similar to UW.

In general, wind behaviour could be split into four sections. In the first (1N-2N), the wind was weak. Next is the 3N-3C subsections, where VW was the dominant component. Then, 4C-1S, where both components were present. The final section comprises the southern subsections 2S-3S, where UW was the dominant component. These results were like those of the previous section.

e) SST~Chl:

SST~Chl and SST~Chl+1 correlations are analysed here (Figures A.2.10-A.2.11). Of these, SST~Chl showed the more evident correlations, while SST~Chl+1 did not show any statistically significant correlation that was important.

SST~Chl showed no statistically significant relationships from 1N to 2NT. Negative correlations were detected from 2NO-1S, while those from 2S to 3S were all positive (Figure 4.6). In general terms, lower SST is linked to more nutrients from upwelling. However, the Southern Zone usually has cold waters, but they are not produced by upwelling here. The Southern Zone SST reduction could be seasonal or due to another event, such as glacier melting in 3S and the increase of river fluxes in 2S that affect phytoplankton development (chapter 3). These positive correlations detected in the Southern Zone were also observed when Chl~SST+1 was evaluated. Indeed, in subsection 3S, there was a more statistically significant Rho than for Chl~SST.
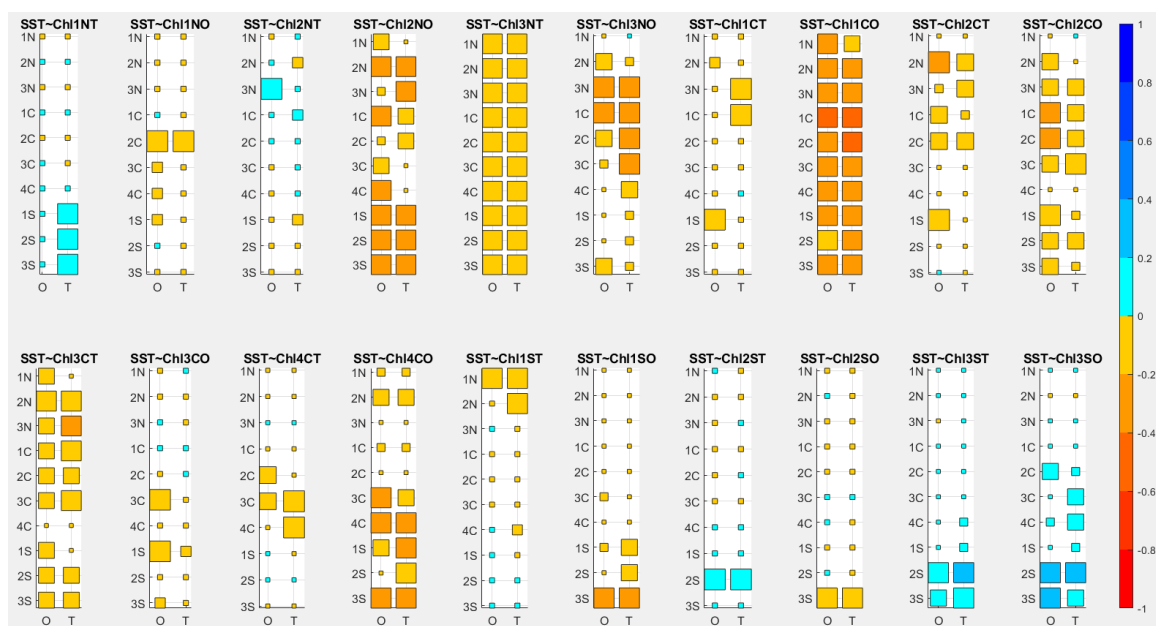
FIGURE 4.6. SST~CHL CORRELATION IN THE WHOLE SYSTEM. SECTION 4.2.2 AND FIGURE 4.5 FOR A FULL LEGEND EXPLANATION.

SST showed higher correlations in the offshore section between 2NO-4CO along the central zone, with some lower values. The 1CO subsection presented the highest Rho of 0.48. These highest values may be related to the higher winds located in 3N-1C. The Offshore subsection also had a high correlation when SST+1 was evaluated. This pattern was similar to the arrangement observed in the Chl~Chl diagram (Figure 4.5). This could show the influence of SST on Chl.

Overall, the Central Zone presented higher SST~Chl correlations, especially in 1C. Except for the ocean strip between 2N to 3N, the Northern Zone did not present any statistically significant correlation between these two parameters. The Southern Zone showed a weak but positive correlation from 2S to 3S.

f) PR~Chl:

PR~Chl and PR~Chl+1 correlations were made (Figures A.2.12-A.2.13). Of these three, only PR~Chl showed statistically significant correlations, while the rest were insignificant. PR~Chl correlations were mainly negative, except for subsections 1N and 2N. This was probably because these two subsections had deficient levels of rainfall. In this case, precipitation inputs could increase the number of nutrients through run-off. In contrast, increased rainfall could produce stratification in a region with high precipitation levels, decreasing phytoplankton production (chapter 3).

The highest PR~Chl correlations were observed between 2C-2S (Figure 4.7). These correlations kept constant while the window was moving from 4C to 2S. Furthermore, higher correlations were found in the coastal strips. The maximum Rho (-0.39) was detected in 1ST. This implies that the PR on the coast was more related to reducing stratification in this section. In conclusion, the Southern Zone, plus subsection 4C, showed a higher correlation between these two parameters.
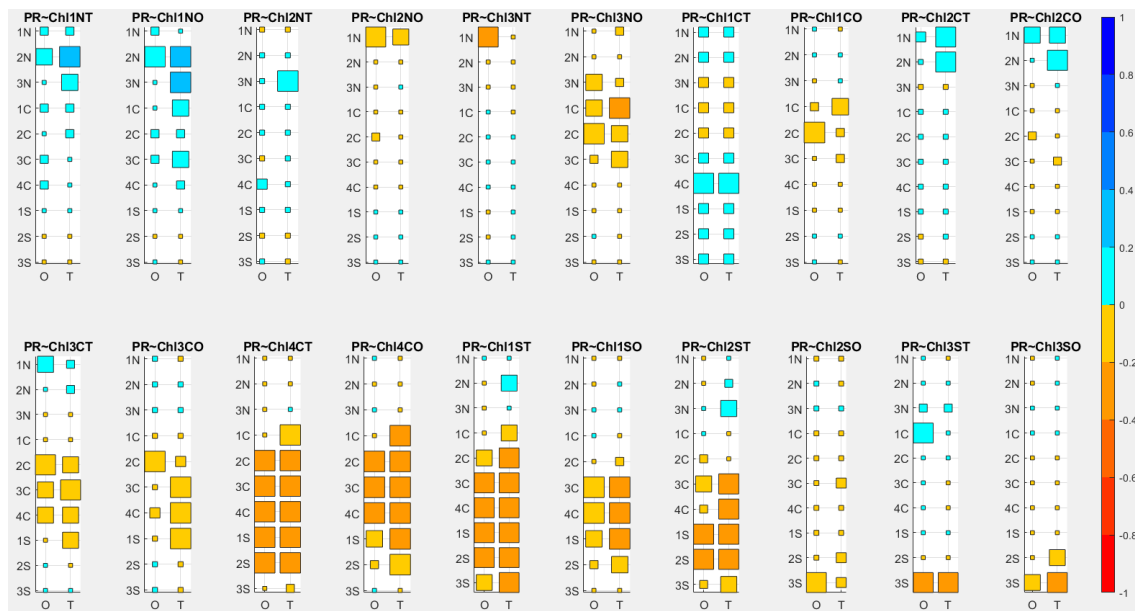
FIGURE 4.7. PR~CHL CORRELATION IN THE WHOLE SYSTEM. SECTION 4.2.2 AND FIGURE 4.5 FOR A FULL LEGEND EXPLANATION.

g) VW~Chl and UW~Chl:

This section analyses VW~Chl and UW~Chl correlations (Figures 4.8 and 4.9). In general, VW showed positive correlations with Chl in the subsections surrounding the window that was evaluated, while subsections that were far from it were primarily negative. UW did not have any statistically significant correlations until 4C. From there to the southern subsection, all the correlations were negative.

VW~Chl showed statistically significant positive correlations in 2NO-1CO (Figure 4.8), along with the coastal strips from 3C to 3S. Its highest Rhos were detected when Chl1ST was evaluated with VW1ST and VW1SO, reaching Rhos of 0.45 and 0.42, respectively. These correlations imply a connection between the offshore and onshore wind regiments, and the VW influenced the 1ST's Chl concentration.
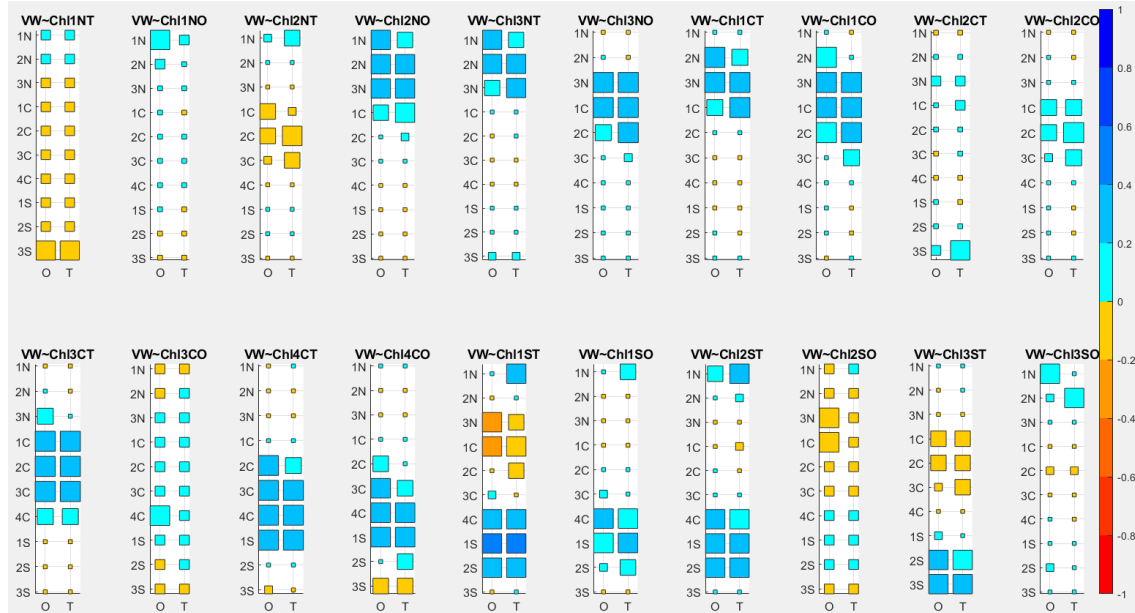
FIGURE 4.8. VW~CHL CORRELATION IN THE WHOLE SYSTEM. SECTION 4.2.2 AND FIGURE 4.5 FOR A FULL LEGEND EXPLANATION.

UW~Chl had strong negative correlations in the region from 4C to 3S (Figure 4.9), where 1ST showed the highest Rho values, as was also found with VW. However, in this case, the UW subsections from 2C to 2S had statistically significant correlations with Chl located in 1ST. Moreover, 4C to 1S were the highest correlations with Rhos over -0.4. Another section that gave a correlation over -0.4 was Chl3ST with UW2S.
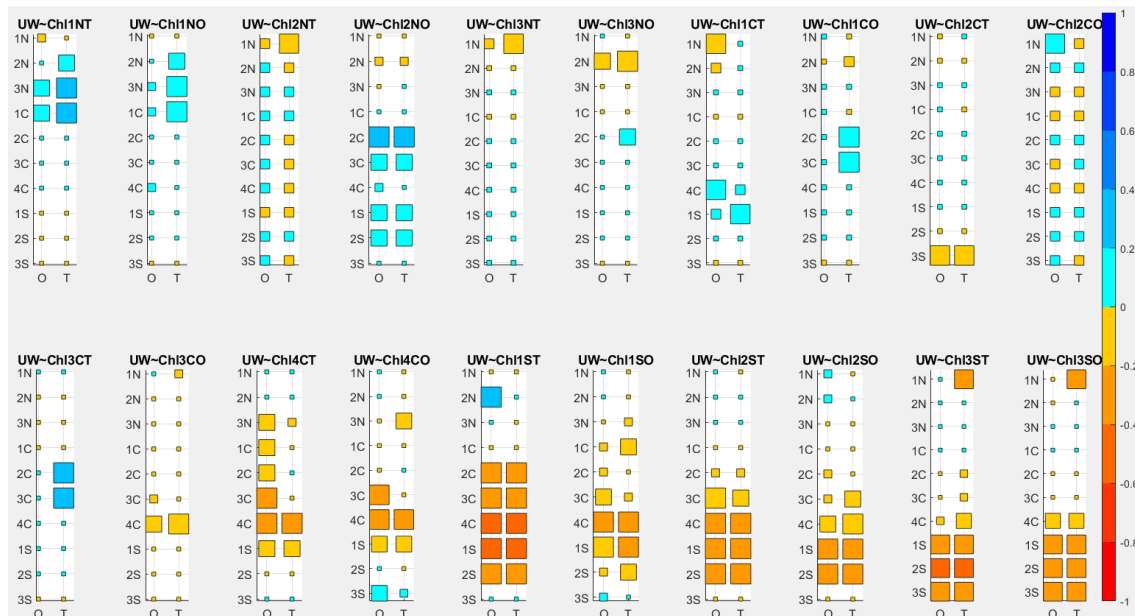
FIGURE 4.9. UW~CHL CORRELATION IN THE WHOLE SYSTEM. SECTION 4.2.2 AND FIGURE 4.5 FOR A FULL LEGEND EXPLANATION.

1N did not show any correlation with either of the wind components. Thus, its high production must be related to other parameters that were possibly more connected with

those of Peru. These correlations could imply that UW had a negative influence on phytoplankton, but it probably only means that if the UW component is strong, the VW component will be weak and that the latter had a statistically significant influence on phytoplankton.

h) PR~SST:

PR~SST, PR~SST+1 and PR+1~SST correlations were made (Figures A.2.14-A.2.16). Of these, PR~SST and PR~SST+1 presented similar patterns. Here the correlations were low with some exceptions, while PR+1~SST presented no statistically significant correlations. In subsections 1C and 2C, PR positively correlated with SST with a Rho around 0.2-0.23, which was slightly stronger when PR~SST+1 was evaluated (0.23-0.26). This could be related to this region having the strongest winds. Despite this, there was no other significant correlation between these two parameters.

i) VW~SST and UW~SST:

This section analyses wind component correlations with SST (Figures 4.10, A.2.25 and A.2.26). Both components presented negative correlations, excluding UW1N with SST1N, which was expected because the winds increase led to upwelling. Consequently, the SST was reduced. VW showed a statistically significant negative correlation only with the Northern and Central Zone. These correlations were over -0.4 in subsections 3NT, 1CT and 3CT (Figure 4.10). This could be related to 3NT and 1CT having the highest mean winds in the study area.
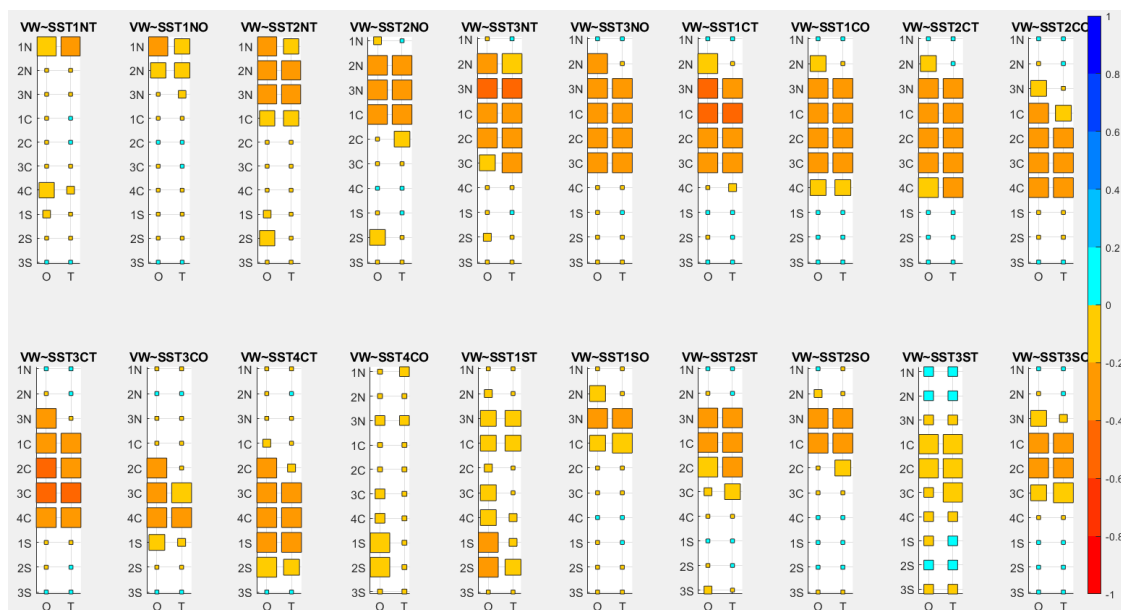
FIGURE 4.10. VW~SST CORRELATION IN THE WHOLE SYSTEM. SECTION 4.2.2 AND FIGURE 4.5 FOR A FULL LEGEND EXPLANATION.

UW~SST presented negative correlations from 2S-3S, 3CT and 2CT. These correlations did not cross the 0.3 boundaries and were weaker when compared with the VW~SST Rhos. Although UW did not generally have a statistically significant correlation with the Northern zone, UW1NT with 1NT and 1NO's SST were the exception. However, its Rho was below 0.2. In conclusion, VW had more influence over the SST than UW. These correlations were exceptionally high in subsections with stronger winds.

j) VW~PR and UW~PR:

In this section, VW~PR and UW~PR are analysed (Figures A.2.27 and A.2.28). VW~PR correlations were primarily negative in the study area, except for 1N-2N, where rain was barely seen. The correlations were stronger from 2CT to the Southern subsections, reaching Rho values from -0.36 to -0.6. PR correlations in 1ST and 2ST reached even higher Rhos,

which were over -0.60 to -0.67. Nevertheless, these Rhos were obtained with the VW located in 4CT and 1ST instead of 1ST and 2ST, respectively. These correlations reflect the SPSA movement to the north during the winter, allowing fronts in the Central Zone.

UW~PR had positive correlations across the whole study area, but they were spread with limited physical connections between each other. However, this tendency changes from subsection 3CT to the end. This subsection sets presented a more consistent connection and statistically significant correlations, where 1ST and 2ST PR presented the highest Rho (0.6) against the UW4CO. This was quite similar to the pattern detected with VW~PR. The other Zones presented some statistically significant correlations that are worth mentioning. Although 1NT and 1NO have low PR levels, the subsections positively correlated with UW. This could make sense because the precipitation in this area comes from the Andes or fronts with low pressure. Another interesting pattern was that PR2CT showed statistically significant correlations with UW ocean strips from 3N to 3C.

Overall, VW and UW showed strong correlations in the Southern Zone, affecting the PR negatively and positively. Subsections 4C and 1ST presented the highest correlations for both components. This is consistent, considering that high PR and westerly winds are associated with low-pressure systems, while high-pressure systems drive southerly winds.

4.4. Analysis per Zone.

The results showed that the three Zones have different Chl concentrations. The Southern, closely followed by the Central Zone, had the highest concentration, while the Northern Zone had the lowest Chl levels. The diverse interactions among the parameters produced these differences. These connections were studied by correlation analysis, which was explained in section 4.3.3. However, the Chl correlations with the physical parameters are the most relevant for this analysis, which are shown in Table 4.9.

TABLE 4.9. CHL REGRESSION WITH THE PHYSICAL PARAMETERS PER SUBSECTION IN THE COASTAL STRIP, THE STATISTICALLY SIGNIFICANT CORRELATIONS ARE UNDERLINED ($0.01 < $P-VALUES$ < 0.05$), AND THE STATISTICALLY VERY SIGNIFICANT ARE IN BOLD (P-VALUES$ < 0.01$).

Rho	Chl~SST	Chl~PR	Chl~VW	Chl~UW
1NT	-0.10	0.14	0.07	-0.12
2NT	-0.13	0.05	0.09	-0.03
3NT	-0.12	-0.08	**0.21**	0.10
1CT	_-0.16_	-0.07	**0.20**	-0.03
2CT	_-0.15_	0.04	0.08	0.06
3CT	-0.19	-0.20	0.27	**0.20**
4CT	-0.20	-0.33	0.38	-0.27
1ST	-0.06	-0.39	0.45	-0.41
2ST	_0.15_	-0.24	0.26	-0.29
3ST	0.20	-0.20	0.23	-0.32

4.4.1. The Northern Zone.

The mean coastal Chl concentration in the Northern Zone was around 0.8 to 1.5 mg m^{-3} in 2NT and 3NT. 1NT presented a higher output with a mean of approximately 1.4 to 2.6 mg m^{-3}. 1NT showed a slight increase in September and February, 2NT and 3NT showed an increase from September to October, but 2NT was more constant. These conditions are driven by the SPSA's core, which is centred in 3N-1C. 1N to 2N showed statistically significant positive correlations (0.45) with their ocean contra part, and 3NT presented a Rho of 0.47 with 1CT, but the correlation with 3NO was only 0.28.

The PR in the Zone was below 5 mm mth^{-1}. The three subsections presented different PR seasonal cycles, where 1NT and 2NT showed higher precipitation in the summer, while 3NT was in the winter. 3NT experienced higher rainfall events, including a flood event with 80 mm mth^{-1} in May 2017 (Sernageomin, 2017). 1N and 2N also exhibited extreme events, but these

were less intense and common. Effectively, 1N extremes stopped in 2008, while 2N's were more frequent in recent years. PR~Chl correlations were not statistically significant (below 0.15), where the most significant was 1NT with 0.14, with a P-value of 0.06 (Table 4.9). This is coherent because 1NT highest production was 2002-2005, 2011 and 2017, while the highest PR events were 2002-2008, 2015 and 2017. SST mean range in 1NT was from 17.4° to 22.6°C. This range decreased by approximately 1.3 °C per subsection southwards. The maxima were reached in February for the three, while the minima were in August. SST~Chl presented an insignificant negative correlation (Table 4.9).

The VW component was dominant in this Zone but weak, increasing southwards. 1NT showed the lowest and most constant winds (3.8-4.7 m s^{-1}), followed by 2N (4.5-5.5 m s^{-1}), while 3N had one of the strongest southerly winds (6-7 m s^{-1}). Also, 2NT showed a minor increase during the winter, reaching the maximum value in September. In contrast, 3NT exhibited slightly higher southerly winds during the warm season. As the VW was more intense in 3NT, this showed a statistically significant correlation with the Chl (0.21), while the rest were insignificant. SST and VW also showed statistically significant negative correlations with a range of -0.2 to -0.44, with the highest peak in 3NT (-0.44). On the other hand, the UW was irrelevant in this Zone.

The North ocean strip showed a Chl concentration that was similar among the three subsections. Here, Chl reached concentrations around 0.3 to 0.5 mg m^{-3}. However, 3NO showed slightly higher values (0.6 mg m^{-3}). Simultaneously, 1NO and 2NO Chl showed a slight trend to increase during the winter, while 3NO's seasonal cycle was flat. Chl from 2NO to 4CO showed a statistically significant positive correlation among the subsections, with a Rho around 0.4-0.6. These correlations were still present when Chl+1 and Chl+2 were evaluated but weaker.

SSTs in the ocean were generally 0.6°C warmer than the SST at the coast. They showed a statistically significant negative correlation of 0.25-0.27 to the Chl concentration in 2NO and 3NO. These two subsections presented similar Rhos values but positive correlations when the VW was evaluated against Chl concentration. The VW component in the northern ocean strip was 1 m s^{-1} faster than the coastal strip winds, with similar seasonal behaviour. PR in the ocean was lower than was detected in the coastal strip. The mean range was around 0.3 to 7.3 mm mth^{-1}. PR's correlations with Chl were insignificant, and their seasonal cycle was less variable. However, 2NO and 3NO presented high episodic events over 30 mm mth^{-1} related to flood events (Sernageomin, 2017).

4.4.2. The Central Zone.
The Chl concentration in the coastal Central Zone showed a mean of around 0.8 to 2.0 mg m^{-3} in the first two subsections, with lower productivity in 1CT. Meanwhile, 3CT and 4CT presented a higher production with a mean around 1.5 to 2.9 mg m^{-3}, where 4CT showed a slightly higher concentration, but 3CT showed a higher variability. Their seasonal Chl cycle was higher than the cycle observed in the Northern Zone due to its production increment during the warm period. These seasonal differences were more pronounced in 3CT to 4CT, related to the SPSA movement. Chl~Chl correlations in 1CT and 2CT were statistically significant with their surroundings from 3N to 3C with a Rho between 0.3 to 0.5. When 3CT and 4CT correlations were evaluated, this range moved from 1C to 4C and 3C to 2S, respectively, with a lower correlation.

1CT and 2CT showed a PR average range of 4.9 to 45 mm mth^{-1}, while 3CT and 4CT were 40 to 107 mm mth^{-1}. The four subsections presented a seasonal cycle where the precipitations were higher during the winter, especially in 3CT and 4CT. PR~Chl correlations were insignificant and negative in 1C and 2C, while in 3C and 4C were statistically significant with -

0.2 and -0.34, respectively (Table 4.9). The SST mean range in 1CT was from 13.7° to 19.3°C. The remaining Central Zone subsections had a reduction of 0.8°C per subsection. SST~Chl correlations were slightly higher than the Northern Zone but statistically significant. The most significant were in 3C to 4C with -0.19 and -0.20.

The VW was also dominant in this Zone, reaching higher averaged speeds in 1C (6.2-8 m s^{-1}), followed by 2C-3C (4.8-6.5 m s^{-1}), while those in 4C were even lower (2.7-4.2 m s^{-1}). The VW showed a cycle with lower values in the winter and higher in the summer. This cycle was more marked moving southwards. Hence, 1C was barely noticeable, while 3C and 4C were prominent. Furthermore, VW reached negative values during the winter in 3CT and 4CT. This was linked to the SPSA moving northwards during the winter. Additionally, 1CT showed the strongest winds because the VW showed less variability. However, 3CT showed the maximum wind (11.37 m s^{-1}). The VW showed statistically significant positive correlations against Chl, with Rho values over 0.2 in the whole Zone, except in 2CT, where its correlation was insignificant (0.08). The highest VW~Chl correlation was found in 4CT with a Rho of 0.38 (Table 4.9). SST~VW showed statistically significant negative correlations with a Rho range of 0.2-0.4. Two correlation peaks of 0.44 were found in SST1CT and SST3CT with VW1C and VW3C, respectively.

UW was more relevant in this Zone than in the Northern, exhibiting a similar VW behaviour but reduced in magnitude. Then, UW in 1C was relatively flat, while 3C displayed a similar pattern to VW but smoother. 4C's UW seasonal wind did not show a tendency but was almost flat but with a high variation, especially in the winter. Although the UW winds were similar in the Central Zone, the correlations showed statistical significance for the Chl in 4C (-0.27) and 3C (0.2; Table 4.9). This is coherent because Southerly winds were weaker here. Moreover, 3CT showed slightly stronger UW winds on average (2.2-2.7 m s^{-1}), while 4CT had a higher variation (1.2-2.3 m s^{-1}).

The Chl in the ocean strip in the Central Zone presented a similar range among the subsections from 2CO to 4CO. Their concentrations were around 0.5 to 1.3 mg m^{-3}. The 1CO range was slightly lower (0.4-0.8 mg m^{-3}). Their seasonal production cycle in the Central ocean strip was relatively flat, but it showed some particular, extreme events discussed in section 4.3.3. As the previous section mentioned, the correlations between 2NO to 4CO were statistically significant, with Rhos around (0.4-0.6).

SSTs in the ocean were 0.5°C warmer in comparison to the coast. They showed a statistically significant correlation with the Chl in the whole ocean strip in the Central Zone. The minimum of these correlations was found in 3CO with -0.17, while the maximum was in 1CO with a Rho of -0.48. The VW component was 0.25 m s^{-1} faster than the coastal strip, while the UW in the ocean was 0.1 m s^{-1} slower than the coastal strip showing a minor difference between both. The VW annual cycle was very similar to the coastal strip but with less frequent northerly winds during the winter. The UW component showed an annual cycle flatter compared to the coastal strip. VW~Chl correlations were positive. Only 1CO and 4CO presented a statistically significant Rho over 0.2, reaching 0.25 and 0.38, respectively. Although PR was lower here than the PR detected in the coastal strip, they had the same seasonal behaviour. Only Chl in 4CO showed a statistically significant correlation (-0.32) with PR.

4.4.3. The Southern Zone.

The Chl concentration in 1S and 2S showed similar behaviour to 4C and 3C, respectively (Figure 4.1), which might be linked to the SPSA. Although the Chl concentration mean range was almost identical in 1ST and 2ST (1.6-3.2 mg m^{-3}), 2ST had a higher variation reaching higher values. Despite this, 1ST had the major stability with the highest mean and median.

3ST had a slightly lower concentration (1.2-2.1 mg m^{-3}). The typical Chl seasonal cycle behaviour of higher values in the summer was present in 1ST and 2ST, while for 3ST was flat. This was because the SPSA is seldom present in the final subsection. Extreme events were observed throughout the whole year in 2ST and 3ST. The entire coastal strip showed strong positive correlations close to 0.5 with the neighbouring coastal subsections. Their Rhos with their ocean part were 0.3, 0.38 and 0.6, respectively, showing a very statistically significant relationship compared to the other Zones. This is likely related to the strong stratification that this Zone has, spreading the Chl offshore.

The PR range in the Southern Zone varied from 65 to 143 mm mth^{-1}, which was present the whole year. 2ST showed the highest precipitation and 3ST the weakest due to 1S and 2S showing higher events during the winter, while 3S did not exhibit significant differences throughout the year. The PR~Chl showed statistically significant correlations; 2ST and 3ST presented Rhos of -0.24 and -0.2, while 1ST's correlation was -0.39. SST decreased by 1°C between 1ST and 2ST, with a further decrease of around 2°C in 3ST. This could be related to the extended length of 3S (section 3.2.2 for more details). SST~Chl correlations were statistically significant and positive in 2ST and 3ST, reaching 0.15 and 0.2, while 1ST was negative and insignificant (Table 4.9).

UW showed a more significant role in this Zone rather than VW. The westerly winds increased further South, while VW showed the opposite behaviour. The 1ST's UW mean was around 1.4-2.9 m s^{-1}, while 3ST's was 4.1-6.2 m s^{-1}. A weak seasonal cycle was observed in UW, owing to consistently strong winds with relatively low variation throughout the year. Nonetheless, from 4C to 2S, the variations were more significant in May, while in 3S, these occurred over the whole winter. 1ST's VW means range was -0.2 to 1.4 m s^{-1}, while 3ST had mainly northerly winds from -2.9 to -0.5 m s^{-1}. Despite the 3S northerly wind trend, a few periods of southerly winds could be seen throughout every year (except 2011), with slightly more frequency in the winter, but the strength were below 4 m s^{-1}. In general, 3ST was not affected by the seasons, while 1ST and 2ST experienced Southerly winds mainly during the warm season. The VW~Chl correlations were statistically significant; the highest correlation was found in 1ST with a Rho of 0.45, while the other two subsections were close to 0.24. The UW~Chl in 1ST and 2ST were similar to VW but negative (-0.41 and -0.29), while the strength was greater in 3ST (-0.32; Table 4.9), demonstrating the immense influence that UW had in the Southern Zone.

SST~VW showed no statistically significant correlations. However, SST~UW showed some negative correlations with Rhos close to -0.25 for 2ST and 3ST. Both wind components showed high correlations with PR; VW showed negative correlations, while UW's were positive. In both cases, the correlations were over 0.45 in the coastal strip, but with winds located in a southern location. For example, PR1ST had the highest correlation with UW (0.60) and VW (-0.65), both situated in 4CT. The strong PR and UW correlations were consistent, as both are associated with the cold fronts. Nevertheless, the SST correlations with VW and Chl were unexpected because these first were low, while the others were positive (Table 4.10). This could be related to very low SST and PR events increasing it in the extreme south. This will be investigated in chapter 6 through case studies.

The Chl in the Southern Zone ocean strip showed a similar range in 1SO and 3SO. The means were around 0.4 to 0.8 mg m^{-3}, while 2SO presented a slightly higher range with mean values around 0.4 to 1.15 mg m^{-3}. This Zone also showed no seasonal cycle in the ocean. Here, the Chl showed high statistically significant correlations (above 0.3) with the Chl detected in the surrounding subsections. 3SO showed lower correlations with the rest, while 1SO showed significant correlations with 4CO, 1CO and 2NO. Those were the remains of the correlation connection seen in the Northern and Central Zone in the ocean strip.

SSTs in the ocean strip behaved differently compared to the coastal strip of this Zone. 1ST presented a difference of 0.61°C with 1SO, while 2ST and 2SO SSTs were very similar. Finally, the 3S ocean subsection was 0.5°C colder than the coast. 3SO had the only statistically significant correlation between SST and Chl, with a Rho of 0.25. The PR in 2SO and 3SO had a similar range (50-120 mm mth^{-1}), while 1SO's level was a little lower. Regarding its seasonal cycle, 1SO and 2SO showed a similar cycle to their coastal strip counterpart, while 3SO was not affected by the seasons. The PR in the ocean strip did not show any statistically significant correlation with Chl. However, PR3ST showed a significant negative correlation with the Chl3SO, with a Rho of 0.22. The ocean UW component across the Zone averaged 1 m s^{-1} faster than in the coastal strip, while the VW presented a different range to that found in the coastal strip but was still smaller than the UW component. UW~Chl correlations were statistically significant, with Rhos close to -0.2. For VW~Chl, only Chl 1SO presented a correlation of 0.2 with VW in the same subsections of 1S. SST did not correlate with VW, while SST~UW showed statistically significant correlations with a Rho range from 0.2 to 0.3.

4.5. Discussion.

Overall, the SPSA is the main climate driver that creates southerly winds that produce favourable upwelling conditions (Thiel et al., 2007; Rahn, 2012). This was observed in the results by a high negative correlation between VW with SST in subsections from 1NT to 1ST. This driver is particularly dominant in the Central Zone (Figure 4.10), in which 3CT-4CT is the most productive region except for 1ST and 2ST in the Southern Zone. The SPSA moves to the south during the summer and the north during the winter (CONAMA, 2008). This provokes a reduction in Chl during the winter in the Central Zone and 1ST (Rahn, 2012; Ancapichun and Garcés, 2015). It also allows the intrusion of rain fronts and northerly winds when SPSA is not present. Nonetheless, some southerly winds were present in particular situations in 2ST and 3ST.

Although climate drivers play a significant role in the forcing of the Chl, the annual plots showed confusing results that are hard to interpret. The only exception was anomalies during El Niño 2015-2016, which revealed different impacts on VW, PR and SST and consequently the Chl across the three Zones. In contrast, La Niña 2007 clearly increased the VW and reduced the SST and PR in the Central and Southern Zone, resulting in a Chl raise that year in these Zones. Therefore, climate drivers will be investigated in-depth in the next chapter.

Another part of this study focused on establishing relationships among the parameters and studying coastal Kelvin waves' possible propagation effect. This was based on finding possible correlations with one and two months of time lag, consistent with likely coastal Kelvin wave speeds. This study showed that the Kelvin waves do not produce a strong mean relationship in the long term.

Except for 1NT, the Northern Zone presented a low phytoplankton production with small seasonal variability. This pattern is due to weak winds (not in 3NT), lack of precipitation and relatively stable weather conditions (Yuras et al., 2005). This happens because of the SPSA movement to the north during the winter (Thiel et al., 2007). 1NT presented a higher Chl concentration, but it was almost constant, with a slight rise in September and February. Thus, its concentration is likely related to the increased production from neighbouring Peruvian waters that are brought by ESSW (Echevin et al., 2014; Thiel et al., 2007). This was mentioned in more detail in section 3.1.1. Chl in 3NT showed a weak seasonal cycle with a maximum value in September that seems to be partly triggered by the high southerly winds in that subsection (0.21). The Chl~PR showed insignificant but positive correlations in this Zone due

to PR scarcity but with occasional extreme events. Although PR events might positively impact the Chl by alleviating the Fe through runoff (Thiel et al., 2007; Dezileau et al., 2004), extreme events could produce the opposite effect. Indeed, 1NT had the highest correlation with the Chl (0.14 and P-value of 0.058) with a more constant PR. However, 1NT highest production (2002-2005, 2011 and 2017) loosely matches the high PR years (2002-2008, 2015 and 2017).

The Central Zone presented a seasonally varying production, with a high Chl concentration during the summer and low winter. This was derived from the SPSA movement and the sunlight reduction during the winter (Thiel et al., 2007). This seasonal difference was more pronounced in 3C and 4C, leading to higher PR and lower VW during the winter, while 1C and 2C exhibited more significant longshore winds. As a result, 1CT and 2CT exhibited a low production while 3CT and 4CT showed a more significant concentration, where 4CT showed a slightly higher concentration, but 3CT showed a higher variability. Therefore, this sustains the hypothesis that PR might have a significant role in increasing nutrient intake. Effectively, 3C's and 4C's Chl exhibited statistically significant correlations with all the parameters (Table 4.9). However, a further study must be done to estimate the potential nutrient load by precipitation and rivers compared to those from upwelling. It also should include other factors, such as shelf width (chapter 7).

The Southern Zone has similar characteristics to the Central Zone but with extra complexity. This complexity is associated with the AAO effect, especially in 3ST that is not affected by the SPSA, while its effect is weak in the other subsections (Ancapichun and Garcés, 2015). The SPSA dominantly produces southerly winds along the Chilean margin, while the AAO is linked to storm production and predominantly westerly winds that might affect the whole Southern Zone. Both wind components had strong correlations with the Chl concentration in 1S, being influenced by VW positively and UW negatively (0.45, -0.41). UW had a major impact on the Chl in 3S (-0.32) than VW (0.23), and both influenced 2S's Chl but in a minor way (VW 0.26, UW -0.29). Hence, 1ST and 2ST Chl concentrations showed a seasonal cycle with a high production analogous to 4CT and 3CT but with a slightly lower signal during the winter, respectively, while 3ST production had almost no variation but with still some Chl concentration. The rainfall amount, along with river and glacier flow, leads to ocean stratification, reducing phytoplankton production (Lara et al., 2010; Landaeta et al., 2011). Thus, Chl~PR in this Zone showed a statistically significant negative relationship, particularly in 1ST (-0.39). At the same time, both wind components showed a statistically significant correlation with the PR, showing a negative influence with VW and a positive one with UW. The ENSO impacted this Zone differently from the Central Zone, which must be studied in the following chapters.

4.6. Conclusion.

In principle, the SST is a sensible component to predict the Chl concentration (Schollaert Uz et al., 2017). The SST decrease is generally related to upwelling, resulting in a greater nutrient supply and higher Chl levels (Thiel et al., 2007). This hypothesis is true, at least in the Northern and Central Zone. Nevertheless, their correlations were weakly negative in the Northern Zone (-0.13 to -0.1), mainly because it does not have a high variation in SST and Chl (Yuras et al., 2005). As predicted from the above argument, the relationships were statistically significant in the Central Zone (-0.20 to -0.15). However, in the Southern Zone, the correlations were similar but positive (0.15 to 0.20), except for 1ST (-0.06). This region intrinsically has cold waters because of its latitude. Still, SST was not affected much by VW, linked to the upwelling.

The PR is the parameter with a higher variation across the Zones, varying from scarcity in the Northern Zone and high intensity in the Southern Zone (Thiel et al., 2007). The hypothesis that involves the PR significance on the Chl is based on the fact that positive PR anomalies in the Northern Zone might produce a Chl rise due to a possible elevation of low nutrient levels through runoff (Dezileau et al., 2004). Meanwhile, the Southern Zone Chl concentration might fall with increased precipitation due to the elevation of ocean stratification (Lara et al., 2010; Landaeta et al., 2011). The Central Zone could experience either aspect, leading to PR can cause changes to the ocean that are different in different Zones. The correlations between the Chl and PR were statistically significant beyond 3C, where the PR increased significantly. The strongest correlations were in 4CT (-0.33) and 1ST (-0.39), but they are negative. These results are consistent with a hypothesised physical behaviour because the Chl~PR correlations are positive in the Northern Zone, coinciding with the Chl bloom in the summer as well as the PR, while in the Central and Southern Zone, the PR is in the winter when the Chl signal is weak. Also, the PR is driven by fronts associated with low pressure and weak longshore winds. Nevertheless, more investigation is needed to determine PR's real impact on the Chl.

VW is the most critical factor in producing upwelling along the coast, driven by the SPSA (Aguirre et al., 2021). Thus, the initial hypothesis states that VW triggers the Chl. These were reflected in the correlations obtained in this chapter with the Chl. The majority were about 0.2 to 0.3, which are statistically significant. 1NT, 2NT, and 2CT were below 0.1, likely related to the weak winds in the Northern Zone and low Chl activity in 2C. At the same time, the most productive subsections 4CT and 1ST had the most significant correlation with 0.38 and 0.45. The UW component was insignificant in its impact on Chl from 1NT to 2CT. Further south, the correlations were statistically significant but negative, being more than -0.2 to -0.3, except in 1S and 3S with -0.41 and -0.32. Nonetheless, 3NT and 1CT had the highest VW, but the Chl was low, implying that the PR might also have a relevant role in the mix. Also, these winds are over 6 m s^{-1} which might produce turbulent upwelling spreading the nutrients and phytoplankton (Thiel et al., 2007).

Overall, the correlation analysis supported the hypothesis that the main parameter affecting the Chl concentration across all zones is the southerly winds, followed closely by the PR. On the other hand, these parameters are linked to opposite conditions associated with high- and low-pressure systems driven by the SPSA and AAO. These reach an equilibrium in 3CT to 1ST, having the highest Chl signal. However, 1NT, 3ST, and 2ST presented higher Chl levels that were not necessarily related to wind patterns nor PR. Additionally, the ENSO extreme cases significantly impacted the Chl, but the effect varied substantially in the Central and Southern Zone. Thus, these subsections and climate drivers will be studied in detail in the following chapters.

These correlations will be used as a guide for the physical parameter' possible effect on the Chl in the climate drivers analysis in chapter 5. The Chl extreme cases mentioned will be considered possible case studies for chapter 6.

5. Understanding how Climate Drivers Contribute to Phytoplankton Production [O.2].

5.1. Introduction.

In chapter 4, the main physical parameters were analysed in order to understand their general trends and behaviour per Zone for the period 2003 to 2018. These parameters are forced by known climate drivers (ENSO, SPSA, PDO, and AAO), which have characteristic cycles. It is clear that these climate drivers will affect the main parameters at different time and space scales (section 2.3; Ancapichun and Garcés, 2015; Vergara et al., 2017). These effects were loosely observed in the parameters annual cycle (section 4.3.1.). However, their impact was not straightforward. Therefore, this chapter aims to understand how these climate drivers contribute to phytoplankton production. To accomplish this, it is necessary to characterise the extent to which these fundamental climate drivers contribute to the observed patterns in PR, SST, UW, and VW in space/time and generate a baseline understanding of phytoplankton status within the study region.

As chapter 2 mentioned, the climate drivers cycles vary from decades to months depending on what driver is studied (Rahn et al., 2012; Ancapichun and Garcés, 2015). Therefore, the parameters must have a long extension in time. The physical parameters were available from 1979 onwards in ERA5, but the Chl data is only available from 2003. Thus, the first sub-objective is to reconstruct the Chl time-series [O.2.1]. This will be done by Canonical Correlations Analysis (CCA), which can extend a partially known variable in time and space as the Chl, using a fully known parameter with a good relationship with the Chl such as PR, SST or winds components. Then, Chl is predicted in the unknown period based on the other variable behaviour at that time using the correlations that both variables had in the known period. This technique is often used with deconstructed parameters by Empirical Orthogonal Function (EOF), which help maximise the correlations between both parameters (Taylor et al., 2013; Schollaert Uz et al., 2017). The mathematical details of how these methods work will be discussed in section 5.2.1.

Once all variables are known for the whole new period (1979-2018), the next step is defining each variable's response during every climate driver's positive and negative phases. This is done by generating climate composites [O.2.2] to facilitate data analysis. The composite map is used to determine each variable's average behaviour using the years when that climate driver was more intense (von Storch and Zwiers, 1999). Each climate driver intensity is obtained by an index, which well-known institutions measure. As all the climate drivers overlap and do not have the same impact on Chile, the most relevant will be studied.

5.2. Methods and Workflow.

Here a range of standard indices is used to help quantify the impact of each climate driver. These indices include data obtained from NOAA (Table 5.1). The SPSA index was the only exception, which was obtained by Vicencio (2021), but it was calculated by the Meteorological Directorate of Chile (DMC) based on Quintana and Aceituno's (2011) methodology. Linear regressions were used to understand how these indices influenced each other and had a significant role in Chile. The climate drivers' influence on the different parameters (Chl, SST, VW, UW and PR) is obtained by Composite Analysis [O.2.2]. This contrasts the typical parameter behaviour under one particular climate driver in either its positive or negative phase (von Storch and Zwiers, 1999). Then, the parameter anomalies are averaged using the years where the climate drivers were either strongly positive or negative

set by the climate driver index. As a result, each map will represent a typical monthly parameter variation in a year where that climate driver is dominant. Then, the study period must be extended beyond 2002, so the composite will have enough years. For that reason, another source was used to obtain these data over an extended period.

As mentioned in chapter 3, the physical parameter came from ERA5 because the data was available from 1979 onwards, and it has a better spatial resolution with 0.25°x0.25° (C3S, 2021). The Chl parameter was obtained from GIOVANNI using the MODIS version of the data (2003-2018), keeping the same data source used in O.1. The extreme southern part of Chile presented relatively few satellite images owing to its excessive cloudiness, particularly during Austral winter, approximately 24% (Gómez et al., 2017). These data gaps were filled up using Data Interpolating Empirical Orthogonal Functions (DINEOF; section 5.2.1.2; Echevin et al., 2014).

The Chl dataset from the long pre-MODIS period of 1979 to 2002 was reconstructed using CCA [O.2.1]. In this technique, another parameter is used to forecast the Chl. The variables tested were UW, VW and SST, all of which had a high correlation with Chl according to O.1 results. Although the error associated will be considerable, it will be enough to establish a general Chl pattern that this objective seeks. The CCA is an innovative approach to environmental data reconstruction, and recently successful Chl prediction using this approach has been carried out by Taylor et al. (2013) and Schollaert Uz et al. (2017), where instead of using the variables directly, the EOF of each parameter is used. The statistical methods of EOF and DINEOF are functions extracted from the Sinkr R package (Taylor, 2017). At the same time, the CCA code was written by Taylor (2012). The following section will explain the indices calculation and the procedure needed to calculate the Chl.

The Composite maps grid was built over the following coordinates 10° to 65°S and 85°W to 65°S both coordinates having a 0.25° step giving 17901 grid-points. The area of interest was expanded to facilitate analysis of higher latitude zones to incorporate possible patterns connecting the Chilean coast with the open ocean, Peru and the Drake Passage.

5.2.1. Chlorophyll Time-Series Reconstruction [O.2.1].

Characterising and understanding the spatial and temporal variability in biological parameters such as Chl are challenging due to complex relationships with a wide range of variables. However, CCA has been shown to be a reliable and flexible analysis tool for these data (Schollaert Uz et al., 2017). The CCA determines the number of relationships between two or three sets of variables called *predictors* and *predictands* and projects them in a new coordinate system. This is achieved by using the optimum correlation between variables via EOF analysis (Schollaert Uz et al., 2017; Barnett and Preisendorfer, 1987). When the predictand and the predictor have comparable/matching space-time layout enough to establish a significant correlation, CCA can forecast the predictand to a time gap based on the predictor behaviour using the best correlation possible (Wilks, 2011).

CCA can be used with the variable directly as well, but Taylor et al. (2013) and Schollaert Uz et al. (2017) have recommended the EOF approach. The advantage of using Spatial EOFs instead of the original data is that only the relevant information remains, and the algebraic calculations are more straightforward (von Storch and Zwiers, 1999).

Thus, CCA was used to determine the Chl, during the extension period (1979-2002). This prediction is made following the maximised relationships that Chl had with the predictor variable post-2002. Therefore, the predictors must be available for the whole period (1979-2018; von Storch, 1995; Schollaert Uz et al., 2017; Wilks, 2011). SeaWiFS's data (1997-2010) was not used to extend the Chl time scale. This decision was made because the moment this

chapter was done, the Chl data that fused both scales was unavailable due to maintenance. Fusing both scales by hand will increase the associated error considerably due to a spatial and temporal resolution presented gaps hard to fix with no experience. Also, their spectral bandwidth has significant differences (Table 3.1; Franz et al., 2005).

Prior to carrying out the CCA itself, some preparation is needed. The first step is to identify possible variables that could have a good relationship with the Chl and their availability in the forecast period (von Storch and Zwiers, 1999). Based on O.1 results, Chl has been shown to correlate well with VW, SST and UW (Table 4.9). However, these correlations varied per subsection.

Then the EOFs of each variable is estimated after normalisation and divided by its monthly gridpoint SD (Schollaert Uz et al., 2017). The predictors' candidates should be separately tested because if they are intercorrelated, the results will not be independent (Barnett and Preisendorfer, 1987; Taylor et al., 2013). The variables studied present a high intercorrelation. Therefore, it is sensible not to use more than one variable in the formal CCA if they are related. Nonetheless, due to the spatial gaps in the Chl data, it is not possible to apply EOF techniques directly. Thus, DINEOF is used first. The following section will explain the basic maths of EOF, DINEOF and CCA. As DINEOF fundamentals are related to EOFs, the EOF technique will be explained first.

5.2.1.1. Empirical Orthogonal Function (EOF).

EOF is a multivariate statistical technique widely used in several fields. EOF is the name used in climate sciences. It is also known as Principal Component Analysis, which is the name given in other areas such as genetics, chemistry, and ecology, among others, where they work with discrete datasets rather than spatial grids (Beckers and Rixen, 2003; Hess and Hess, 2018).

EOF analysis helps determine patterns in datasets with many variables and observations. The main principle of this method is to create new variables called principal components or spatial EOF that try to explain the significant variability in the dataset using minimal data (Hess and Hess, 2018; Wilks, 2011). These components are linear combinations of the original data in a new orthogonal coordinate system where the original data is projected. In this way, it will be possible to explain the data patterns in a lower dimension, analysing only the leading spatial EOFs (Hess and Hess, 2018; Wilks, 2011).

Let X be a matrix representing a previously normalised dataset (von Storch and Zwiers, 1999). X also contains the intrinsic error associated with each value, such as the instrumental error, which can be seen as noise (Becker and Rixen, 2003). Each element is defined as $(X)_{ij}$ where i is the time component with a length of m, and j is the spatial index with a range of n. Therefore, this can be seen as n column vectors with m rows (Eq. 5.1). These column vectors are time-series samples from which the EOF patterns are derived (Taylor et al., 2013; Björsson and Venegas, 1997). However, the position could be a single value such as the ENSO index or a two-dimension location referred to as a coordinate system (Beckers and Rixen, 2003).

$$X_{(m \times n)} = (x_1, x_2, \dots x_n) \tag{5.1}$$

There are many ways to estimate the EOFs, where the most common techniques are by Covariance decomposition or Singular Value Decomposition (SVD; Beckers and Rixen, 2003; Wilks, 2011; Taylor et al., 2013). Both approaches have similarities with an eigenvalue problem. An eigenvalue problem is expressed in Eq.5.2. A is a square matrix, p is a non-zero vector, and λ is a scalar. In Eq. 5.2 p and λ are the eigenvector and eigenvalue of A, respectively (Björsson and Venegas, 1997).

$$Ap = \lambda p \qquad (5.2)$$

An eigenvector is a vector that is not affected by the linear transformation represented by matrix A. The eigenvalue is a scalar that multiplies the eigenvector after the linear transformation embodied in A has occurred (Björsson and Venegas, 1997). The SVD approach decomposes X directly into three matrices, as Eq. 5.3 shows (Beckers and Rixen, 2003). This technique was used in this work because the covariance matrix that is needed in the eigenvalue decomposition is hard to compute when X presents a high dimensionality (Wilks, 2011).

$$X_{(m \times n)} = U_{(m \times n)} D_{(n \times n)} V_{(n \times n)}{'} \qquad x_{ij} = \sum_{k=1}^{q} u_{i,k} \rho_k v_{k,j} \qquad (5.3)$$

In eq. 5.3 D is the identity matrix that had the singular values ρ_i in its diagonal, q are non-zero values (q=min(m, n); Taylor et al., 2013; Beckers and Rixen, 2003). Therefore, D and V' are retained to dimension q. The squared singular values are the same as the eigenvalues (Taylor et al., 2013). U and V are matrices that contain spatial and temporal EOFs in their columns, respectively. U is time and V space averaged and unitary matrices; thus, rescaling is not necessary. U*D is the spatial scaled EOF (Taylor et al., 2013). The whole set is sorted in decreasing order of ρ_i (Beckers and Rixen, 2003; Wilks, 2011). The temporal EOF elements are called loadings and determine the weights from X to develop the Spatial EOF, while spatial EOF elements are called scores or coefficients (Wilks, 2011; von Storch, 1995).

From the Eq. 5.3 decomposition only the first p EOFs are required to give an acceptable approximation of X on average where p<q. The percentage of the explained variance of the p EOF is calculated as follows (Beckers and Rixen, 2003):

$$f_i = \sum_{i=1}^{p} \rho_i^2 * 100 / \sum_{i=1}^{q} \rho_i^2 \qquad (5.4)$$

The main idea of using p instead of q is separating X from noise. Noise in this context means anything that is not relevant to the question under consideration. The EOFs that show well-defined extended patterns should be considered, while the EOFs that do not show a dominant direction are noise, which is determined by its variability (von Storch, 1995). Thus, using previous equations, X can be reconstructed in X_p as Eq. 5.3, where only the most relevant EOFs are retained. As a result of this, X reduces their dimensionality (Taylor et al., 2013).

$$X_{(m \times n)} \approx X_{p(m \times n)} = U_{(m \times p)} D_{(p \times p)} V_{(n \times p)}{'} \qquad (5.5)$$

There are many truncation approaches; the three more used are Rule-N (Normalisation); Define a particular value to cut, which usually is 95%; and the North's Rule-of-Thumb (von Storch, 1995). Of these three, cut at 95% is seldom used, while Rule-N is the most common. This method truncates when two consecutive eigenvalues reach the same value, meaning that the rest will not contribute to the variability (Wilks, 2016). The North's Rule-of-Thumb defines a tolerance level per eigenvalue and EOFs, as is shown in Eqs. 5.6 and 5.7 (explained below; von Storch, 1995). The North's Rule-of-Thumb was chosen because it retains only a small number of EOFs. Thus, North's is considered the most honest approach (von Storch, 1995; Wilks,2016).

$$\Delta \rho_i \approx \sqrt{\frac{2}{l}} \rho_i \qquad (5.6)$$

$$\Delta u_i \sim \frac{\Delta \rho_i}{\rho_j - \rho_i} u_j \qquad (5.7)$$

In these equations ρ_i and u_i represent their eigenvalue and EOFs selected, respectively; l is the number of independent samples in the original data, while j is the u_j that is closer to u_i. Therefore, the EOF sequence is truncated if successive eigenvalues differ by less than a factor of (1+sqrt(2/n)) (von Storch,1995).

As was mentioned, the EOF approach was used to identify the main patterns of Chl, SST, UW and VW. These patterns were then correlated using the CCA. This previous step increases the prediction quality (Taylor et al., 2013; Barnett and Preisendorfer, 1987). Many authors employ this methodology alone to define Chl patterns in Chile. Corredor-Acosta et al. (2015) and Gómez et al. (2017) used the EOF method to describe Chl and SST patterns using only two EOFs. Ancapichun and Garcés (2015) used EOFs to establish SST patterns originating from AAO, ENSO and PDO.

5.2.1.2.   Data Interpolation using Empirical Orthogonal Function (DINEOF).

Most datasets have missing data for one reason or another, which is particularly true of the Chl data. However, EOF requires a completely known matrix X. Missing data can be filled in with different interpolation techniques. The most used method is the DINEOF which is based on the SVD method (Eq. 5.3; Beckers and Rixen, 2003). This technique can simultaneously interpolate in space and time, is parameter-free and permits an infilling of the data gaps without requiring extra information (Gómez et al., 2017; Corredor-Acosta et al., 2015). This technique can reduce the noise intrinsic in MODIS data (Gómez et al., 2017).

DINEOF is an iterative technique that assumes that the missing data points are zero instead of NaNs, which the entire matrix will be called X_0. This implies that these points had no variation; Therefore, this matrix must contain the Chl anomalies, not the absolute values. The First UDV matrix is estimated using the X_0 Matrix as outlined in Eq. 5.3. The matrix (X_1) is then reconstructed using the first N EOFs. X_1 is then compared with X_0, with only the missing values in X_1 being changed. The same procedure is repeated, deconstructing the new matrix (X_{01}), with the condition that N must be the same for the whole process. N represents the number of EOFs used per iteration. The iteration will be continuous until the convergence tolerance criteria for the missing data are achieved (Beckers and Rixen, 2003).

The N of EOFs per iteration can be calculated in different ways. The technique used here is cross-validation (Beckers and Rixen, 2003; Corredor-Acosta et al., 2015). This technique has several advantages and is able to provide an assessment of interpolation errors. The procedure uses randomly discarded valid data points from the initial matrix. The volume of data selected depends on the size of the real matrix, but it should be at least 30 points to have a robust statistical estimation or one per cent of the data if the size is large (Beckers and Rixen, 2003).

The cross-validation technique is applied until the DINEOF iterations converge using only the first EOF (N=1). Next, the interpolation error is estimated by the Root Mean Square (RMS). This method compares the distances between the data obtained by the DINEOF iterations with the validation data. The initial matrix with the same data points set aside is interpolated again, but this time, the first two EOFs are considered for convergence. The new error is calculated and compared with the previous iteration (Beckers and Rixen, 2003).

This procedure uses more EOFs each time until the error increases again or when N equals q. However, it is recommended that it continue two or three more attempts if that error is a

local minimum. The number of iterations until convergence will not necessarily be the same each time N changes (Beckers and Rixen, 2003).

Due to the poor weather conditions, many authors have used DINEOF to obtain Chl missing data in the Central-South zone and extreme Southern Chile. For example, Corredor-Acosta et al. (2015) estimated the error using cross-validation with a tolerance of 10%. N fluctuated between three and eight in their case. Gómez et al. (2017) used DINEOF to fill the gaps in Chl and SST data. Nevertheless, no more information was reported. Taylor et al. (2013) compared DINEOF with Recursively Subtracted Empirical Orthogonal Functions (RSEOF) and Least-Squares Empirical Orthogonal Functions (LSEOF), where DINEOF showed the most reliable result, especially with noisy data. However, RSEOF is less computationally demanding and presents acceptable results.

5.2.1.3. Canonical Correlation Analysis (CCA) mechanics.

CCA and EOF share an analogue procedure using an eigenproblem structure, so the logic and equations had some similarities. The eigenvalues in the EOF represent the variance, so they are used to identify which are the essential temporal EOFs. These work as a new coordinate system; therefore, they must be uncorrelated to each other (von Storch and Zwiers, 1999; Wilks, 2011). In CCA, the eigenvalues represent the correlations between predictands and predictors (von Storch and Zwiers, 1999; Barnett and Preisendorfer, 1987). The eigenvectors establish new basis vectors called Canonical Vectors that determine the correlation between the predictor and the predictand in space (Wilks, 2011).

The spatial EOFs (U), called B and A of the predictor Y and the predictand X, are computed using the SVD technique explained in Eq. 5.3. The number of EOFs, q and p, respectively, were selected using North's Rule-of-thumb (Wilks, 2011; Barnett and Preisendorfer, 1987). Both spatial EOFs are comparable because both have unit variance (Wilks, 2011; Barnett and Preisendorfer, 1987). Then, the maximised relationships existing among the covariance of A (C_{AA}) and B (C_{BB}) and the cross-covariance (C_{AB}) are computed by eigendecomposition (Wilks, 2011; Barnett and Preisendorfer, 1987; Friederichs and Hense, 2003). This can be done in many ways, but SVD was used in the code provided by Taylor (2012).

$$C_{AA\ (p \times p)}^{-1/2} C_{AB\ (p \times q)} C_{BB(q \times q)}^{-1/2} = E_{(p \times q)} Rc_{(q \times q)} F_{(q \times q)}{}' \qquad (5.8)$$

This is only true if p is higher than q. In the opposite case, the A and B covariances order will be inverse, while transpose cross-covariance will be used instead (Wilks, 2011). Rc diagonal has the canonical correlations between X and Y, represented in E and F. Rc expresses how good the correlation is (Barnett and Preisendorfer, 1987; Friederichs and Hense, 2003). The set is arranged in decreasing order of Rc elements (μ) (Wilks, 2011; Friederichs and Hense, 2003). E and F eigenvectors are used to maximise the correlation forming the Canonical Vectors that set the linear combinations with their respective covariances, then Eq. 5.9 appears (Barnett and Preisendorfer, 1987; Wilks, 2011; Friederichs and Hense, 2003).

$$\mathrm{H}_{(p \times q)} = C_{AA\ (p \times p)}^{-1/2} E_{(p \times q)} \qquad (5.9)$$
$$G_{(q \times q)} = C_{BB\ (q \times q)}^{-1/2} F_{(q \times q)}$$

H and G are the Canonical Vectors in Eq. 5.9, also known as canonical maps. These are the basis change vectors of E and F to the original coordinate system. H and G are easy to interpret because they are not unit vectors nor orthogonal to each other (Barnett and Preisendorfer, 1987). H and G are related by the canonical correlation computed in Eq. 5.8. Assuming that p is higher than q, they are q pairs of H and G column vectors. The Canonical

Vectors are the weights necessary to transform X and Y in new variables, as Eq. 5.10 shows (Wilks, 2011).

$$V_{(m_1 \times q)} = X_{p\,(m_1 \times p)} H_{(p \times q)} \qquad v_{ij} = \sum_{k=1}^{q} x_{i,k} h_{k,j} \qquad (5.10)$$
$$W_{(m_2 \times q)} = Y_{p\,(m_2 \times q)} G_{(q \times q)} \qquad w_{ij} = \sum_{k=1}^{q} y_{i,k} g_{k,j}$$

$$X_{p\,(m_1 \times p)} = V_{(m1 \times q)} H_{(p \times q)}{}' \qquad (5.10a)$$
$$Y_{p\,(m_2 \times q)} = W_{(m2 \times q)} G_{(q \times q)}{}'$$

In these equations, V and W are the Canonical Variates, the same as Spatial EOF (A and B), X_p and Y_p are the variables reconstructed using EOF (Eq. 5.5). The dimensions m_1 and m_2 represent the time that both variables had. Consequently, m_2 is higher than m_1 (Wilks, 2011; Barnett and Preisendorfer, 1987). X_p and Y_p can be reconstructed by transferring H and G to the other side of Eq. in 5.10, giving Eq. 5.10a (Barnett and Preisendorfer, 1987). Y_p is used to reconstruct and forecast the X_p from m_1 to m_2 by replacing V with W and the associated canonical correlation (Eq. 5.8). Resulting in Eq. 5.11 (Barnett and Preisendorfer, 1987; Schollaert Uz et al., 2017; Wilks, 2011).

$$X_{pred(m_2 \times p)} = W_{(m_2 \times q\prime)} Rc_{(q\prime \times q\prime)} H_{(p \times q\prime)}{}' \qquad x_{pred\,ij} = \sum_{k=1}^{q\prime} w_{i,k} \mu_k h_{k,j} \qquad (5.11)$$

In Eq. 5.11, q' is less than q and represents the number of CCA components (modes) that were used to reconstruct X (Barnett and Preisendorfer, 1987; Schollaert Uz et al., 2017; Wilks, 2011). Therefore, the number of modes is closely related to the number of EOFs. The number of modes can be computed in different ways, but here, the Pillai–Bartlett trace was used (Friederichs and Hense, 2003; Taylor, 2012). This test criterion establishes a null hypothesis that μ_k is 0. Eq. 5.12 used a significance of $p < 0.05$ to reject the test (Friederichs and Hense, 2003).

$$\frac{\text{trace}(Rc)}{p - \text{trace}(Rc)} \geq \frac{p}{m - p - 1} F_{(p, m_1 - p - 1)} \qquad (5.12)$$

In Eq. 5.12, F is the F cumulative distribution function, and m is the period both variables had in common (m_1). This equation is only valid if $p > q$. In contrast, all the p will be q instead. Although this test is more robust than others, it is more conservative (Friederichs and Hense, 2003). This method allowed the extension of the Chl data, which helped create Chl composites based on climate drivers' extreme years. Eqs. 5.10-5.11 can be used to obtain the EOF of X. In this case, the Canonical Variates are calculated using A and B instead of X_p and Y_p, respectively (Wilks, 2011).

5.2.2. Generation of Climate Driver Composites [O.2.2].
In this section, climate drivers will be selected to create composites. These composites will be useful for understanding how the parameters studied in chapter 4 are affected by the climate drivers' negative and positive cycles. The general behaviour of the indices over 1979-2018 was studied on a monthly and annual scale (Figure 5.1), and the five indices were compared in a monthly and yearly range by regression analysis.

5.2.2.1. Selection of Climate Drivers and Indices.
Due to ENSO's complexity, many indices are used to measure it. These indices are estimated using atmospheric and oceanic data. The El Niño index is the most used, calculated by SST anomalies averaged relative to a base period of thirty years in the central Pacific (Vicente-Serrano et al., 2016). These anomalies are measured in different regions (Figure 5.1). Each section gives a different response to ENSO (NOAA, 2019). El Niño 1+2 was the first Zone discovered that is affected by ENSO, and it tends to have the most substantial variation

compared to the rest. El Niño 3 was the most studied Zone, but the investigators noticed that the area mainly affected by atmospheric-oceanic interactions was El Niño 3.4. El Niño 4 is the index that has the lowest variance with South American conditions. This index represents the SST variation in the Central Equatorial Pacific (Trenberth, 2020). El Niño 3.4 is considered the region that best represents the SST anomalies that affect South America, which is the main interest of this project (Trenberth, 2020). The positive anomalies in El Niño 3.4 index mean an El Niño year, while the negative represents a La Niña (NOAA, 2019).
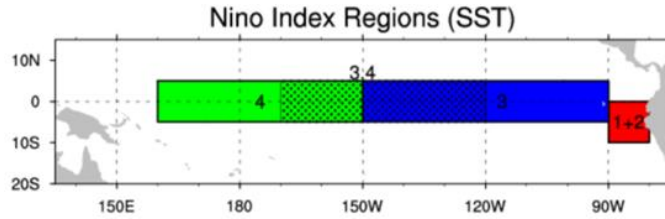
FIGURE 5.1. OUTLINE OF REGIONS USED FOR DIFFERENT EL NIÑO INDICES (TRENBERTH, 2020). THE STIPPLED AREA SHOWS THE COMBINED NIÑO 3.4 REGION.

The SOI measures the atmospheric variation in the Pacific. As mentioned in section 2.3.3, the SOI is based on the standard SLP differences between the stations located in Tahiti, French Polynesia and Darwin, Australia. The SOI is computed following Eq. 5.14, while the SLP standardisation process is shown in 5.15, where N is the number of months considered, generally thirty years (Colling, 2001; NOAA, 2019). Negative SOI means Tahiti SLP is below average and high in Darwin, while the positive phase represents the opposite behaviour (NOAA, 2019).

$$SOI = \frac{Standardised\ SLP\ in\ Tahiti - Standardised\ SLP\ in\ Darwin}{\sqrt{\frac{\sum(Standardised\ SLP\ in\ Tahiti - Standardised\ SLP\ in\ Darwin)^2}{N}}} \tag{5.14}$$

$$Standardised\ SLP\ in\ X = \frac{Actual\ SLP\ in\ X - Mean\ SLP\ in\ X}{\sqrt{\frac{\sum(actual\ SLP\ in\ X - Mean\ SLP\ in\ X)^2}{N}}} \tag{5.15}$$

The PDO index quantifies the SST anomalies in the whole North Pacific Ocean Basin from 20°N northwards; then, the first EOF (EOF1) is used to determine the index (Deser and Trenberth, 2016; Ancapichun and Garcés, 2015). Hence, PDO positive values represent positive SST anomalies in the North and South Pacific, while the negative shows the opposite effect (Linsley et al., 2015).

The AAO index is linked to the 700 millibars height anomalies detected from 20°S to the South Pole (Silvestri and Vera, 2003). As with the PDO, the data is condensed using only the projection onto EOF1 to produce the index. The AAO's greatest impact is from 45° to 90°S (NOAA, 2019; Stammerjohn et al., 2008). Positive values in AAO's index mean a drop and an increase in SLP anomalies around Antarctica and the midlatitudes, respectively. Meanwhile, negative values in AAO's index reflect a swap in this behaviour (Quintana and Aceituno, 2011; Ancapichun and Garcés, 2015; Garreund et al., 2020).

TABLE 5.1. INDICES SOURCE USED IN THIS WORK.

Index	Period	Link
El Niño 3.4	1950-2019	https://origin.cpc.ncep.noaa.gov/products/analysis_monitoring/ENSOstuff/ONI_change.shtml
SOI	1951-2019	https://www.ncdc.noaa.gov/teleconnections/ENSO/indicators/soi/
PDO	1854-2019	https://www.ncdc.noaa.gov/teleconnections/pdo/
AAO	1979-2019	https://www.cpc.ncep.noaa.gov/products/precip/CWlink/daily_ao_index/aao/aao.shtml

All indices used here were taken from NOAA data sources with a temporal resolution of a month. Table 5.1 gives the URLs from which the data and metadata were taken. The

Composites were created using the data from 1979 to 2018, as 1979 is the longest time where all the parameters' data and indices are available, except the Chl.

The SPSA index is calculated using monthly SLP anomalies normalised from eight meteorological stations between the Northern and Central Zone (Table 5.2). The SPSA has a higher presence in these stations, including two Chilean islands, to measure the SPSA border (Quintana and Aceituno, 2011). Similarly to AAO and PDO, the normalised SLP is compressed to one metric, using the first EOF to create the SPSA index. Quintana and Aceituno (2011) introduced the methodology, and DMC computes it on a monthly scale. The index results were obtained by Vicencio (2021). Therefore, positive values in the SPSA index mean an SLP intensification over the normality in the Northern and Central Zone, while the opposite is seen when the index has negative values (Rahn, 2012; Ancapichun and Garcés, 2015; Aguirre et al., 2021).

TABLE 5.2. METEOROLOGICAL STATIONS AND THEIR LOCATIONS USED TO ESTIMATE THE SPSA INDEX (QUINTANA AND ACEITUNO, 2011).

Station	lat (°S)	long (°W)
Arica	18.5	70.25
Iquique	20.25	70.25
Antofagasta	23.5	70.5
La Serena	30	71.25
Santiago	33.5	70.75
Concepción	37	73
Juan Fernández	33.75	79
Easter Island	27.25	109.5

5.2.2.2. General Patterns among Climate Drivers.

ENSO: The El Niño index shows a variable 2-5-year periodicity, but with some major exceptions. The yearly means over 1.0 SD were in 2015, 1987 and 1997 (Figure 5.2). Also, 1982 was only slightly lower (0.99). The fifth highest value, detected in 2002, was considerably lower (0.66). Five of these six years presented their peak in December or November, while for 1987 was in September. The years 2015 and 1987 did not give any months with values below 0, while 1997 presented negative values from January to March. 1982 and 2002 only had one negative value in February and January, respectively. Considering the pattern discussed above, 2015 and 1987 are peaks within the main El Niño phase, while the other three years show peaks during an opening El Niño phase. This cycle will be studied in detail in section 5.3.1.3. The strongest La Niña was in 1999-2000, with an annual average value below -1.22 and -0.85. The following stronger La Niña years were 2011, 1988 and 2008, reaching an average of -0.84, -0.81 and -0.76, respectively. The annual minimum for 1999 and 1988 was in December and October, respectively. For the years 2000, 2011 and 2008, this was in January. That means that 1999 and 1988 were more representative of La Niña's opening stage. Meanwhile, the other extreme years were La Niña's main stage.

SOI: **It showed a relatively constant cycle that looks opposite to the ENSO cycle**. This cycle usually takes two to three years with an annual positive mean, followed by two or three years with an annual negative mean (Figure 5.2). The exceptions to this were the prolonged negative period from 1990 to 1995 and the prolonged positive period from 2006 to 2013. The latter included two extreme years with an average that exceeded 1 (2008 and 2011).

PDO: **the PDO index is more stable due to its decadal nature**. In general, it presented extensive periods on a negative scale with small positive periods (Figure 5.2). This is particularly notable from 1997 to 2013 when only 2003 was positive. The minimum values were reached in 1999, 2008, and 2011-2012. In the period from 1979 to 1998, the PDO presented a more positive tendency. However, it was not as large or as stable as was seen in its negative phase. Then only 1983, 1987 and 1997 means exceeded 1.

SPSA: This index presented higher monthly variation and higher positive values than the other indices due to its seasonal cycle. However, its annual cycle duration seems to be two to four years (Figure 5.2). Also, its annual cycle presented a marked periodic tendency; with a more negative trend in the mid-1980s and 1990s first half, a more neutral behaviour from 2000 to 2005 and a positive from 2006 onwards. In that order, the positive years that had values higher than 0.9 were 2010, 2017, 2018 and 2006. The negative years below -0.9 were 1992 and 1987. The SPSA intensification in recent years was reported by Salvetteci et al. (2017), Aguirre et al. (2021) and Garreaud and Muñoz. (2005).

AAO: This index showed more positive annual values rather than negative, **with an increasing tendency over time.** Nine years had annual means that exceeded an average of 0.5, while four were below -0.5 (Figure 5.2). Note that five of the six highest AAO' years are from 1999 to 2018, and for the last four years (2015-2018), there were only positive values. The monthly data did not show a particular cycle that could be followed because the data presented a high variability per month. Worth noting that the positive annual values reflect the strong positive trend in the austral summer, which have been reported by Cai et al. (2003), González-Reyes and Muñoz (2013), Hendon (2007), Cordero et al. (2019), Aguayo et al. (2021) and DMC (2018).
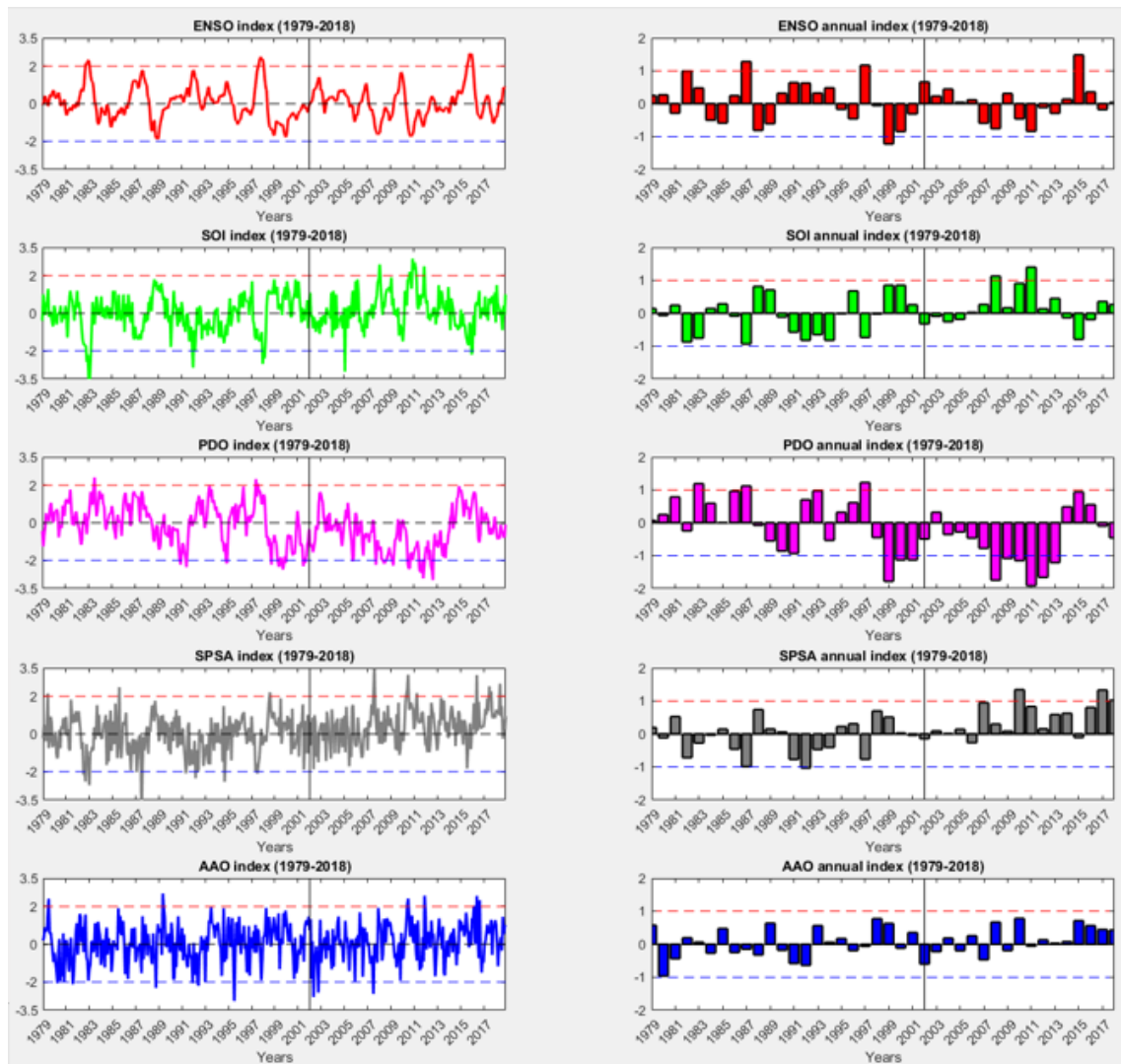
FIGURE 5.2. ENSO, SOI, PDO, SPSA, AND AAO INDICES ON A MONTHLY AND ANNUAL SCALE. A VERTICAL LINE SHOWS THE BEGINNING OF THE STUDY PERIOD OF OBJECTIVE 1. THE SCALE IS NORMALISED TO 1.0 SD.

5.2.2.3. Relationships among Climate Drivers.

The relationships among the climate drivers were studied with Pearson correlation because the distribution of each index was normal. This was checked with histograms. In Table 5.3, the Pearson correlation is shown. In general terms, Table 5.3 showed that the annual correlation was higher than the monthly data. Nonetheless, the annual P-values tend to be less significant due to their lower dimensionality.

TABLE 5.3. CLIMATE DRIVERS REGRESSION RESULTS FOR MONTHLY (M) AND ANNUAL (A) SCALE. R AND P-VALUES WERE ESTIMATED USING PEARSON REGRESSION.

R Monthly	ENSOm	SOIm	PDOm	SPSAm	AAOm	P Monthly	ENSOm	SOIm	PDOm	SPSAm	AAOm
ENSOm	1	-0.72	0.43	-0.39	-0.13	ENSOm	0.000	0.000	0.000	0.000	0.005
SOIm	-0.72	1	-0.40	0.50	0.14	SOIm	0.000	0.000	0.000	0.000	0.002
PDOm	0.43	-0.40	1	-0.19	-0.05	PDOm	0.000	0.000	0.000	0.000	0.292
SPSAm	-0.39	0.50	-0.19	1	0.24	SPSAm	0.000	0.000	0.000	0.000	0.000
AAOm	-0.13	0.14	-0.05	0.24	1	AAOm	0.005	0.002	0.292	0.000	0.000
R Annual	ENSOa	SOIa	PDOa	SPSAa	AAOa	P Annual	ENSOa	SOIa	PDOa	SPSAa	AAOa
ENSOa	1	-0.90	0.55	-0.63	-0.15	ENSOa	0.000	0.000	0.000	0.000	0.343
SOIa	-0.90	1	-0.62	0.70	0.21	SOIa	0.000	0.000	0.000	0.000	0.202
PDOa	0.55	-0.62	1	-0.38	-0.18	PDOa	0.000	0.000	0.000	0.015	0.278
SPSAa	-0.63	0.70	-0.38	1	0.35	SPSAa	0.000	0.000	0.015	0.000	0.026
AAOa	-0.15	0.21	-0.18	0.35	1	AAOa	0.343	0.202	0.278	0.026	0.000

As expected, ENSO showed the strongest negative correlation with SOI due to the inverse nature of the two indices. However, the correlation for the yearly data was considerably higher (-0.72m, -0.90a). ENSO also showed a significant negative correlation with SPSA in the yearly cycle (-0.63a), while with PDO, it showed a moderate positive correlation (0.40m,0.50a). These relationships are consistent with SPSA dependency on ENSO and PDO mentioned in section 2.2.

AAO presented weak correlations with most of the climate drivers, especially in its annual cycle, where the p-values were mainly not significant. The exception to this is the correlation that AAO showed with SPSA (0.24m and 0.35a). This indicated that AAO might have been related to the SPSA. These results make sense because SPSA represents the midlatitude high-pressure centre that is part of the AAO influence area. SPSA is the index that is more linked to the other climate drivers, showing its higher correlation with SOI (0.50m and 0.7a) because both are linked to the SLP variation in the Pacific. Additionally, SPSA shows a low monthly correlation with PDO (-0.19) but was more significant on the annual scale (0.38).

5.2.2.4. Climate Driver Selection and Composite Creation.

As shown above, ENSO is closely related to all climate drivers except AAO, and it is similar to SOI for both to provide any measure of independent forcing. ENSO and SOI explain the same climate phenomenon, but the ENSO index is more used and mentioned in the papers compared to the SOI (Echevin et al., 2014, Vergara. 2017, Gómez et al., 2017). Hence ENSO is selected over SOI for this analysis. AAO is shown above to be an orthogonal driver, with high contrast to ENSO, and it is known for its effect in the Southern Zone. Thus, AAO was selected as an important driver as well.

The PDO and SPSA were also discarded for fuller analysis because PDO had a strong correlation with ENSO, and owing to its decadal behaviour, it will be challenging to represent in a composite selected by the strongest years from a limited number of decades. SPSA, on the other hand, was the only signal that showed a statistically significant correlation with all the indices, including AAO and ENSO. Authors like Vergara et al. (2017), Ancapichun and Garcés (2015), Montecinos and Aceituno (2003), and Aguirre et al. (2021) have reported that AAO and ENSO have a significant impact on the SPSA and this is the most significant climate driver in Chile. Effectively, these drivers represent the tropical and polar drivers that

converge in Chile, modulating the SPSA significantly. Therefore, the SPSA relationship is likely to overlap with the other two indices previously selected, plus the SPSA index did not show a clear pattern due to its high monthly variation. Thus, representing it correctly through a composite will be difficult.
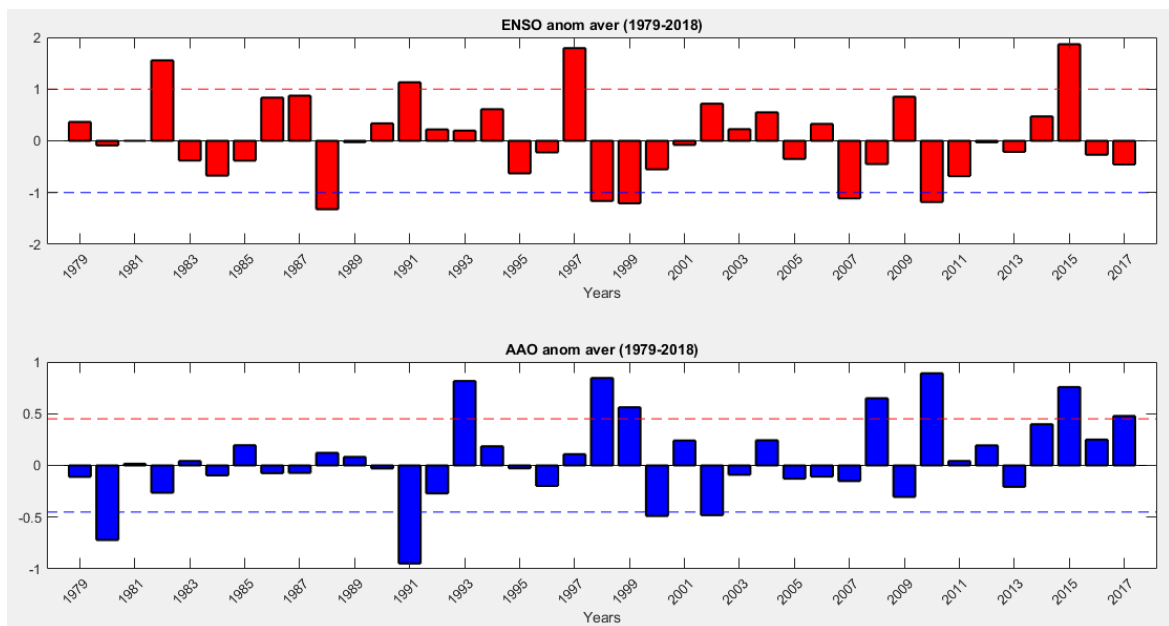
FIGURE 5.3. ENSO AND AAO ANNUAL INDICES (JUNE TO MAY), WHERE THE DASHED LINES REPRESENT THE LIMITS THAT WERE SET TO CREATE THE COMPOSITES.

A more in-depth annual behaviour study was made to construct ENSO and AAO composites. ENSO generally showed a relatively stable cycle but reached high positive and negative values. Strong El Niño generally started a significant rise in September (Figure 5.4). The peak of this rise was reached from November to January. The following months' indices tend to decrease until March or April, when the SST anomalies are close to 0. Therefore, the starting month of an ENSO composite must be in June, so in that way, the highest point in the cycle is centred, and the composite does not cut the year ENSO cycle. The AAO cycle did not show an apparent annual behaviour owing to its short cycle. This erratic behaviour can be seen in Figure 5.4; a 3-month period seems to appear in some years. However, some trends were found. The highest value per year was found in December and July, nine times each. In its negative peaks, five times were in November. Hence, to simplify the comparison with ENSO, June was chosen as the starting month for the AAO index composite as well. As a result of changing the starting point to June, the annual average was calculated again for AAO and ENSO, given in Figure 5.3.

The criteria to create the Composite was to have between four and seven outliers per cycle, while at the same time keeping similar limits for both indices and ideally obtaining the same quantity of values for the negative and positive Composite for each one. These limits should be the same for the positive and the negative phases as well. However, Figure 5.3 shows a significant difference between ENSO and AAO. The limit selected for ENSO was ±1, which means four positive (2015, 1997, 1981 and 1991) and five negative outliers (1988, 1999, 2010, 1998, and 2007).
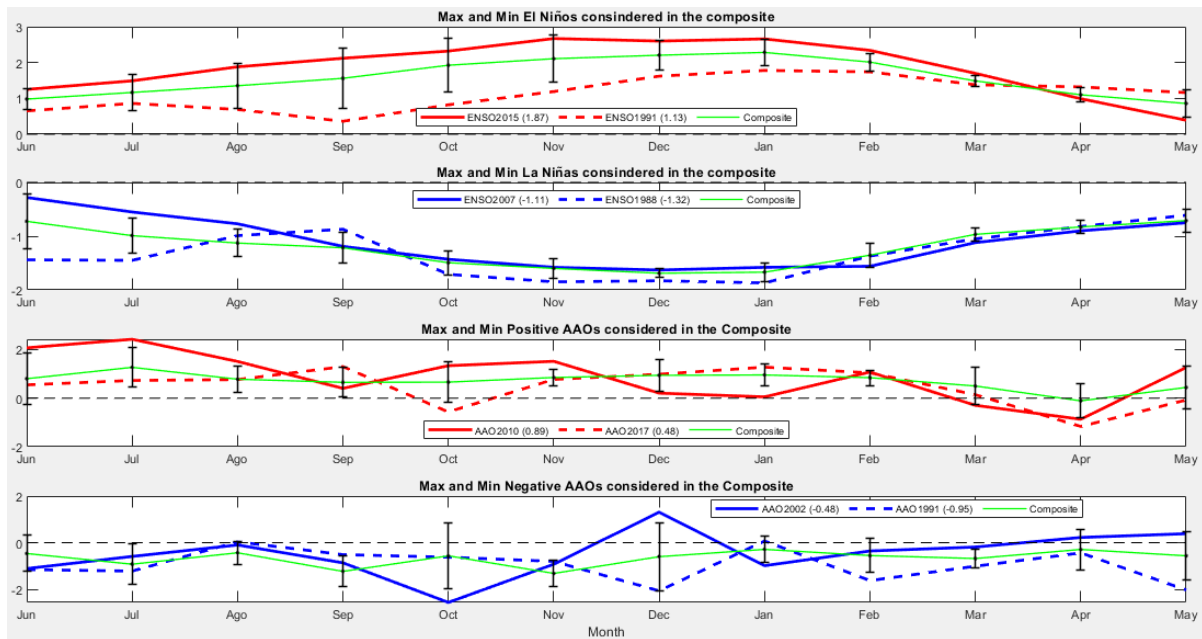
FIGURE 5.4. MAXIMUM (CONTINUOUS LINE) AND MINIMUM (DASHED LINE) FOR THE POSITIVE (RED) AND NEGATIVE (BLUE) ENSO AND AAO INDICES. THE GREEN LINE REPRESENTS THE MEAN OF THE YEARS CONSIDERED TO CREATE THE COMPOSITE, AND THE BARS SHOW THE SD.

In the AAO case, it was more challenging to define peak limits owing to the differences found in the negative AAO (-AAO) cycle where, apart from 1991 and 1980, the series did not show high outliers, while the positive AAO (+AAO) showed a noticeable difference between the highest values and the rest. The criterion selected was to use the same value for both positive and negative excursion, which gives us a similar number of outliers that ENSO produced per level; the resulting value was ±0.48. These limits give us seven +AAO (2010, 1998, 1993, 2015, 2008, 1999, and 2017) and four -AAO outliers (1991, 1980, 2000 and 2002). Figure 5.4 shows the largest and the smallest annual cycles selected and the composite mean annual cycles for ENSO and AAO. It is worth mentioning that AAO+ had one year that belonged to an El Niño composite (2015) and three from La Niña composite years (1999, 2010 and 1998), while -AAO had one El Niño year (1991).

The ENSO curves had relatively similar shapes with smooth variations in relation to the composite mean value, especially La Niña, where the Composite is very similar to the individual contributing years. La Niña (El Niño) presented positive (negative) values, indicating a high consistency. El Niño showed a significant difference from August to December, while La Niña showed some variation during June and July. However, overall, the Composite is a good representation of the annual cycle in both cases, with Root Mean Square Error (RMSE) ranges of 0.64-0.23 for El Niño and 0.15-0.29 for La Niña. RMSE is the difference between the data obtained by the composite with the real driver index divided by the number of samples (Beckers and Rixen, 2003; Taylor et al., 2013).

AAO showed more variability in its annual cycle and was less well represented by the Composite. These differences were more evident in the -AAO, where December showed the same value for both events but with the opposite sign. This difference is likely related to the AAO short cycle mentioned in chapter 2. Nonetheless, October and December were the only months with significant variation in terms of SD, while +AAO's composite shows relatively low variability. Therefore, the AAO composite lines fit with an RMSE range of 0.86-0.38 for the positive Composite and 0.93-0.57 for the negative one.

5.3. Results.

5.3.1. Chlorophyll Reconstruction [O.2.1].

In this section, Chl was reconstructed by CCA to extend the data from 2003-2018 to 1979-2018 to create Chl composites. CCA is based on correlations obtained between the Chl EOF and another EOF variable. The variables tested were SST, VW and UW. The data were normalised and divided by their monthly gridpoint SD. Before this, gaps in the Chl data had been filled using the DINEOF. The results discussed here are divided into three subsections. Section 5.3.1.1 explains the DINEOF and EOF results, while the CCA results are shown in section 5.3.1.2. Finally, an overall analysis appears in section 5.3.1.3.

5.3.1.1. Canonical Correlation Analysis Settlement.

Due to adverse weather conditions, around 24% of the Chl data were missing (553,891 points). The subsections affected by this were largely 2S, towards the Drake Passage from April to August. The DINEOF technique was used to fill these gaps. The error was calculated using cross-validation, so 1% of the remaining data (17,002 points) were discarded randomly. As a result, the final N was 22 after 169 iterations, while the RMS stabilised at 0.829. This is acceptable, considering the range of Chl anomalies was -3.3 to 3.6, which means a tolerance error of around 12%. Then, the EOF analysis was performed for the four variables; Figure 5.5 shows the truncation and the cumulative explained variance. The selection was made according to North's Rule-of-Thumb (section 5.2.1.1.).
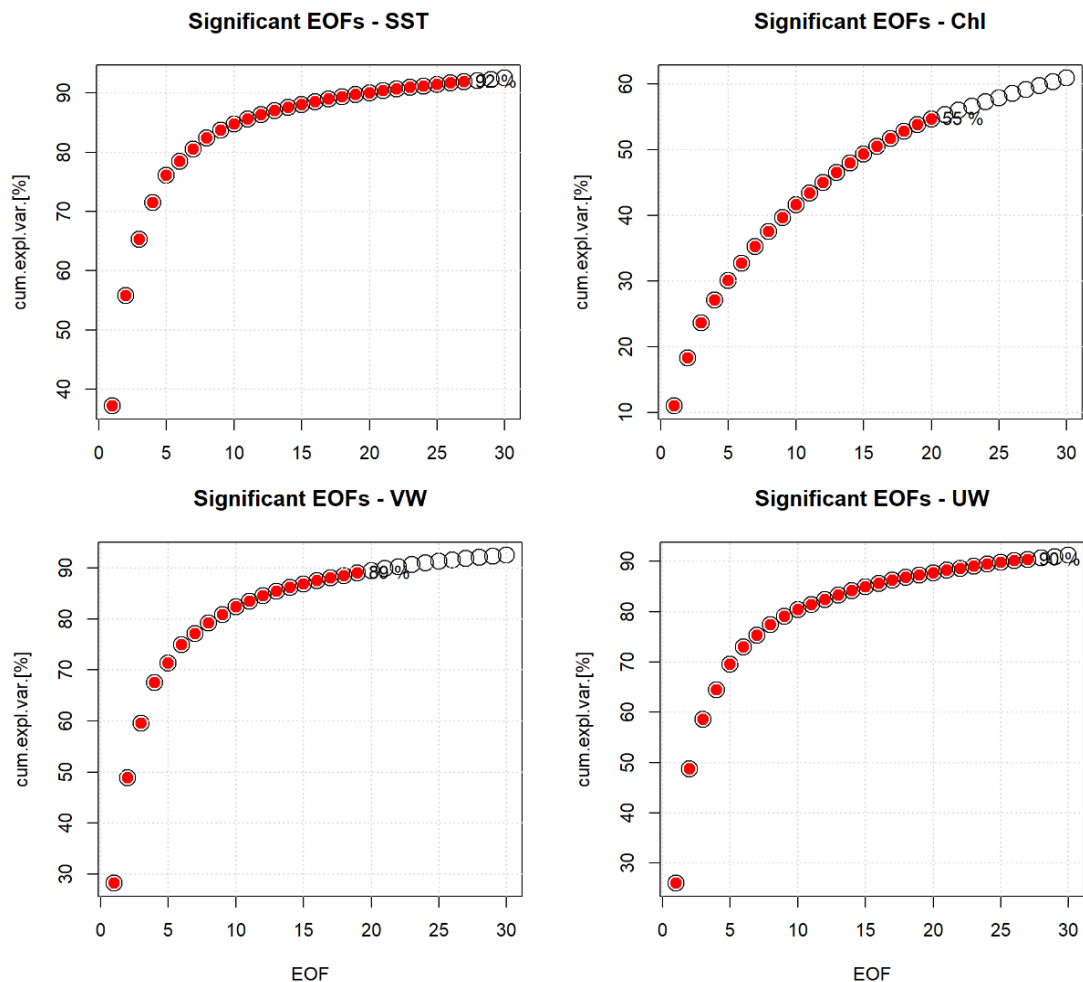
FIGURE 5.5. THE CUMULATIVE SUM OF THE VARIANCE IN THE PERCENTAGE OF SST, CHL, VW AND VW. THE RED POINTS SHOWED THE TEMPORAL EOF SELECTED IN THE CONSTRUCTION.

Figure 5.5 shows that SST possessed the sharpest curve, followed by UW and VW. This means that SST had more well-defined patterns, so fewer EOFs were needed to obtain a good approximation. On the other hand, the Chl curve was very shallow, which means the Chl was less well represented by its EOFs because it possessed fewer distinct patterns than the rest.

Despite this, the North's Rule-of-Thumb criteria were fulfilled first by Chl needing only twenty EOFs. However, only 55% of the variance is kept. Twenty-seven EOFs were needed for SST and UW and nineteen for VW, explaining 92%, 90% and 89%, respectively. The sensitivity of the Chl pattern was tested by examining less (fifteen) and more (thirty) EOFs being retained, leading to 50% and 61% of the variance being explained, respectively, showing no significant differences to the Chl prediction.

5.3.1.2.   Canonical Correlation Analysis Final Results.

CCA maximised the correlation between the covariance of the predictor and the predictand's EOF, which is made by an SVD decomposition (For a full explanation, section 5.2.1.3). This result shows Canonical Vectors and their respective correlation (Canonical Correlation Rc). The Canonical Vectors represent the weight needed to transform the predictor and predictand that were previously reconstructed by EOF in the Canonical Variates (Eq. 5.10). Thus, the predictor and the predictand can be obtained by rearranging eq. 5.10, where the variables are equal to the Canonical Variate multiplied by its respective Canonical Vector (Eq. 5.10a). Finally, the predictand Variate is replaced by the predictor Variate multiplied by the associated Rc (Eq. 5.11). This allows extension of the predictand in time using the predictor. The number of correlations used to predict the variable is called the mode, and it is the same or lower than the number of EOFs used to reconstruct the variable in the EOF technique.

The prediction error was estimated in different ways. First, the prediction was correlated with the Chl data that were previously interpolated, showing the R per location in a map (Figure 5.6). The R means in absolute value were estimated as well as a reference. At the same time, the Mean Absolute Error (MAE) was calculated using Eq. 5.13, where m1 is the number of pairs that were compared (Taylor et al., 2013). MAE is enough, considering that data were previously normalised (Taylor et al., 2013).

$$MAE = \frac{1}{m1}\sum_{k}^{m1}\left|x_{pred\,k} - x_k\right| \tag{5.13}$$

However, this procedure was not accurate because all the data were used in the prediction (Full-Mode). Therefore, a Training-Mode was tested; this consisted of performing CCA over a shorter period where part of the Chl was not considered (Taylor et al., 2013; Schollaert Uz et al., 2017). For the Training-Mode period, the prediction was constructed using data from 2003 to 2013, while the predicted period was from 2003 to 2018. The Chl prediction regression using SST, UW and VW versus the Chl is shown in Figure 5.6, while Figure 5.7 shows only the predicted period.
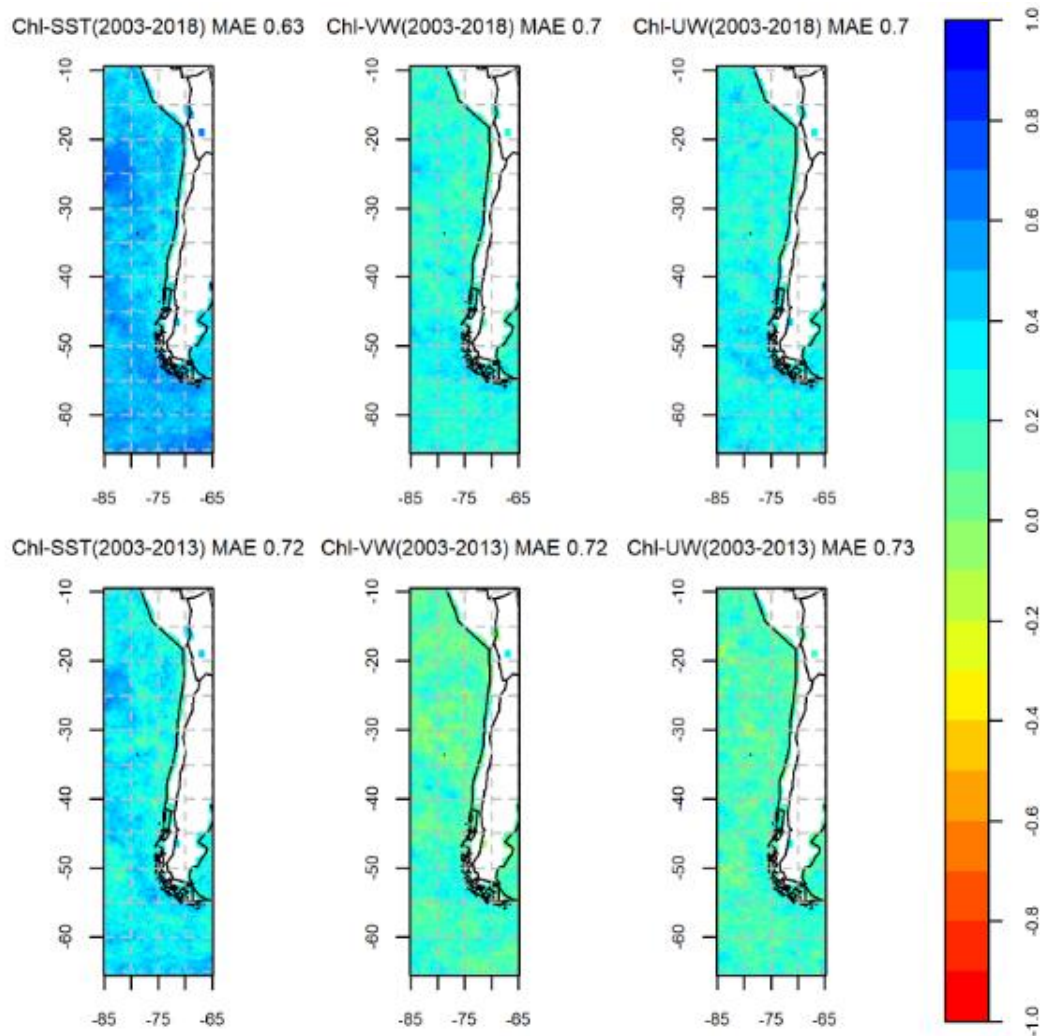
FIGURE 5.6. CORRELATION OF THE CHL VS THE CHL PREDICTED FIELDS USING SST, VW AND UW (RIGHT, CENTRE AND LEFT, RESPECTIVELY). THE FIRST ROW SHOWS THE CCA PREDICTION USING FULL CHL DATA. THE BOTTOM ROW SHOWS THE TRAINING-MODE (2003-2013) CORRELATED WITH THE CHL DATA (2003-2018).

Figure 5.6 exhibits that the best Full-Mode Chl prediction was made using SST (Chl-SST) with R=0.45 on average and MAE=0.63, producing an error of 9.7%, while VW and UW showed R on average of 0.21 and 0.23 respectively. Chl-SST was also the best at the Training-Mode, but the R fell to 0.33 with an MAE of 0.72, increasing the error to 10.7%. However, the R dropped to 0.19, with an MAE of 0.85, when only the predicted time (2014-2018) was considered, raising the error to 12.7% (Figure 5.7). The VW and UW showed a lower MAE, but their R on average was lower than SST (0.14 and 0.12, respectively). It is worth noting that Chl-VW showed a better correlation in the Southern Zone coast, indicating that the southerly winds heavily influence the Chl concentration there when they are present.

Although the relationships are weak where real data was not present, the error was relatively homogeneous because the CCA method is based on patterns. The number of modes used to construct the SST and Chl Variates was fourteen of twenty, with Rc ranging from 0.89 to 0.45 during Full-Mode. The Training-Mode required sixteen Modes of twenty, with Rc ranging from 0.93 to 0.46 (Table 5.4). The Training-Mode presented higher correlations owing to its shorter period. The criteria used to define the number of modes used the Pillai–Bartlett trace, as explained at the end of subsection 5.2.1.3.
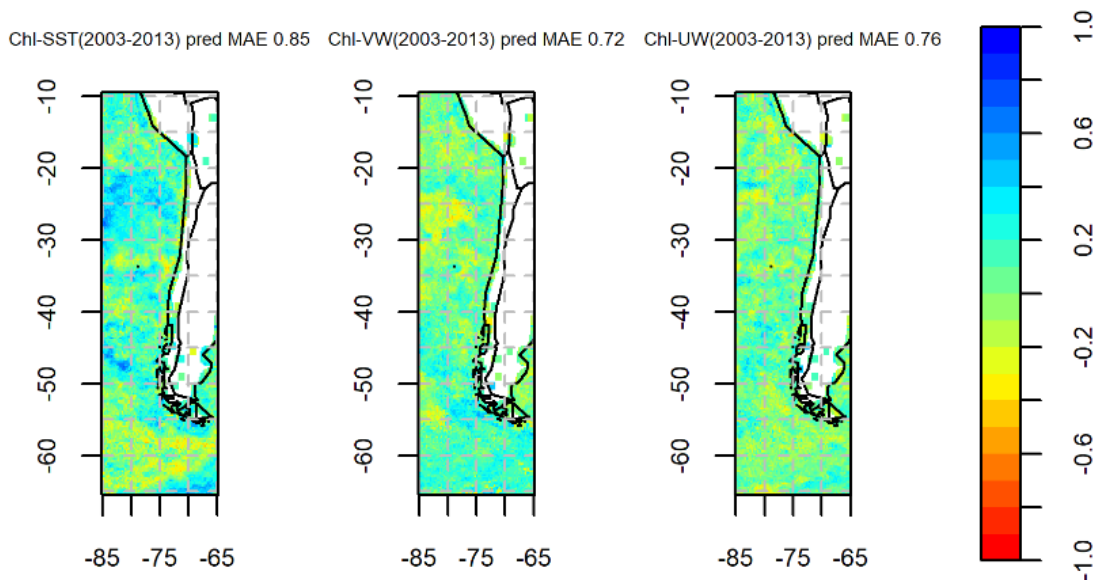
FIGURE 5.7. CORRELATION OF THE CHL VS THE CHL PREDICTED FIELDS USING SST, VW AND UW (RIGHT, CENTRE AND LEFT, RESPECTIVELY). THE MAPS SHOW THE TRAINING-MODE (2003-2013) PREDICTION CORRELATED WITH THE CHL DATA (2014-2018).

TABLE 5.4. RC FOR THE MODES USING CHL-SST IN THE FULL-MODE AND TRAINING-MODE, THE UNDERLINED VALUE INDICATES WHEN IT WAS TRUNCATED.

Mode	Full-Mode	Training-Mode
1	0.89	0.93
2	0.87	0.91
3	0.84	0.9
4	0.82	0.89
5	0.79	0.85
6	0.76	0.81
7	0.73	0.75
8	0.69	0.73
9	0.67	0.74
10	0.62	0.69
11	0.57	0.67
12	0.51	0.64
13	0.49	0.57
14	<u>0.45</u>	0.53
15	0.42	0.51
16	0.36	<u>0.46</u>
17	0.30	0.43
18	0.26	0.37
19	0.19	0.34
20	0.13	0.20

Figures 5.8 and 5.9 show how Variates SST and Chl in CCA Full-Mode mode 1 (CCA 1) are correlated using the whole Chl data and during the CCA Training-Mode mode (training CCA 1). The Variate is obtained by Eq. 5.10, where q=1, so only the first temporal EOF (V) is used. Chl monthly anomalies patterns from the full CCA 1 and training CCA 1 are almost identical but with the opposite sign, while the SST anomalies showed a slightly different pattern (Figures 5.8 and 5.9). The Chl pattern showed a noticeable variation in the Northern Zone in the open ocean, while the coastal strip did not show large spatial variability, except for particular zones at 20°S, 40°S and the Southern Zone (50° to 60°S). This Zone generally presents more variation due to its geomorphological complexity and possibly the AAO impact.

79
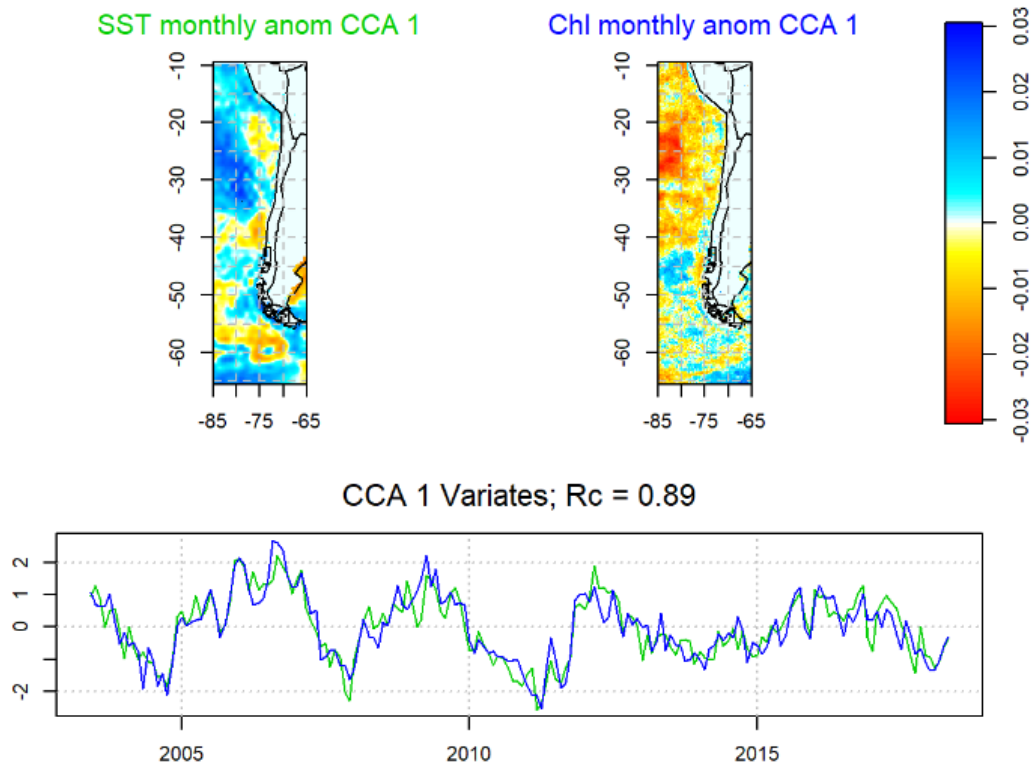
FIGURE 5.8. FIRST CCA FULL MODE OF CHL AND SST (2003-2018) MONTHLY ANOMALIES, THE BOTTOM SHOWS THE VARIATES OF CHL AND SST BELONGING TO THE FIRST CCA WITH THEIR CORRELATION RC.

The Variates created using the Chl and SST data from 2003 to 2018 (bottom Figure 5.8) presented a three-year parabolic cycle that repeated twice from 2005 to 2011. From 2011 onwards, it tends to have a flatter behaviour. The Variates in the Training-Mode (bottom Figure 5.9) exhibited a lower variability with a parabolic cycle with a frequency that varies from four to two years.

The Chl's spatial EOFs (A) can be recreated using the CCA code based on the SST spatial EOF (B). These were done by replacing X_p and Y_p in Eqs. 5.10 and 5.11 with their spatial EOFs. Finally, A_{pred} was multiplied by D_a to add the units back. The first ten of twenty Chl EOFs for the predicted data and Training-Mode data are shown in Figures 5.10 to 5.13.

The first three Chl EOFs were reproduced with good accuracy by Chl-SST prediction at the Full-Mode (Figures 5.10 and 5.11); this was especially the case for EOFs 2 and 3. The EOFs 7 and 14 also were well correlated, with an R over 0.7. In the case of the other EOFs, their general tendency is matched with an R above 0.5, apart from EOF 12 (R=0.48). The main differences in these were that the Predicted EOF curves had smoother behaviour than the originals, which presented a high variability. In the case of the Training-Mode (Figures 5.12 and 5.13), the first three EOFs were also well reproduced, specifically EOF 3. However, the predicted EOFs did not follow the original EOF curves correctly over the period in which the data were not used (2014-2018). This reduced the correlation. Only EOFs 1-3, 9 and 11 had an R above 0.5. The EOFs 4, 10, 13, 15 and 16 were loosely followed, with R below 0.4.
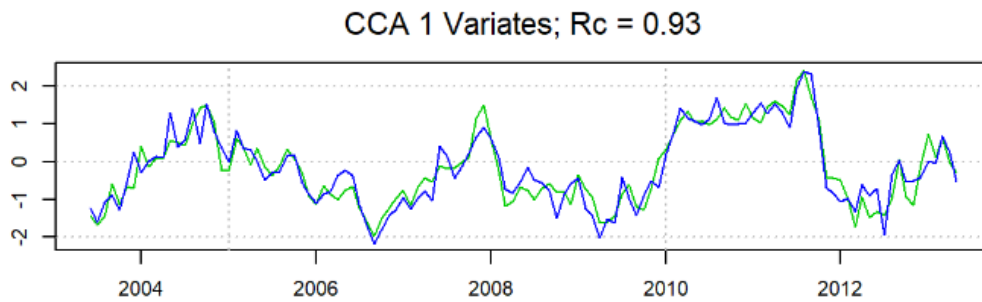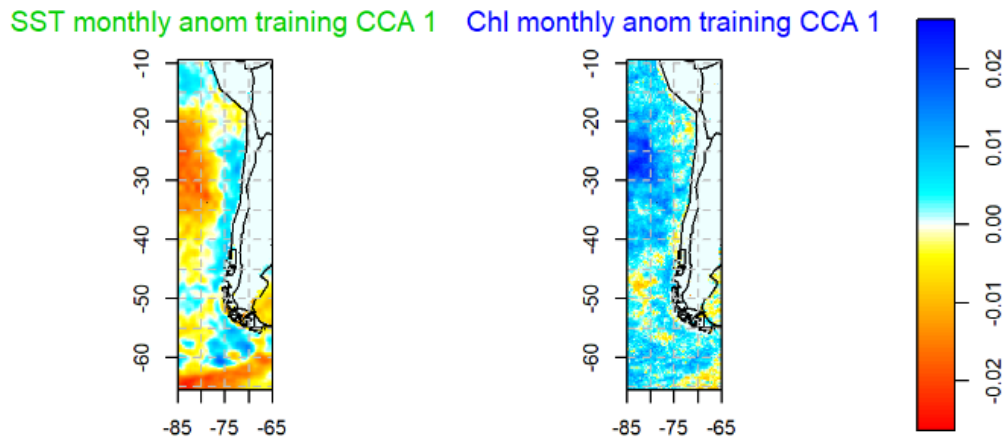
FIGURE 5.9. FIRST CCA TRAINING MODE OF CHL AND SST (2003-2013) MONTHLY ANOMALIES, THE BOTTOM SHOWS THE VARIATES OF CHL AND SST BELONGING TO THE FIRST CCA WITH THEIR CORRELATION RC.
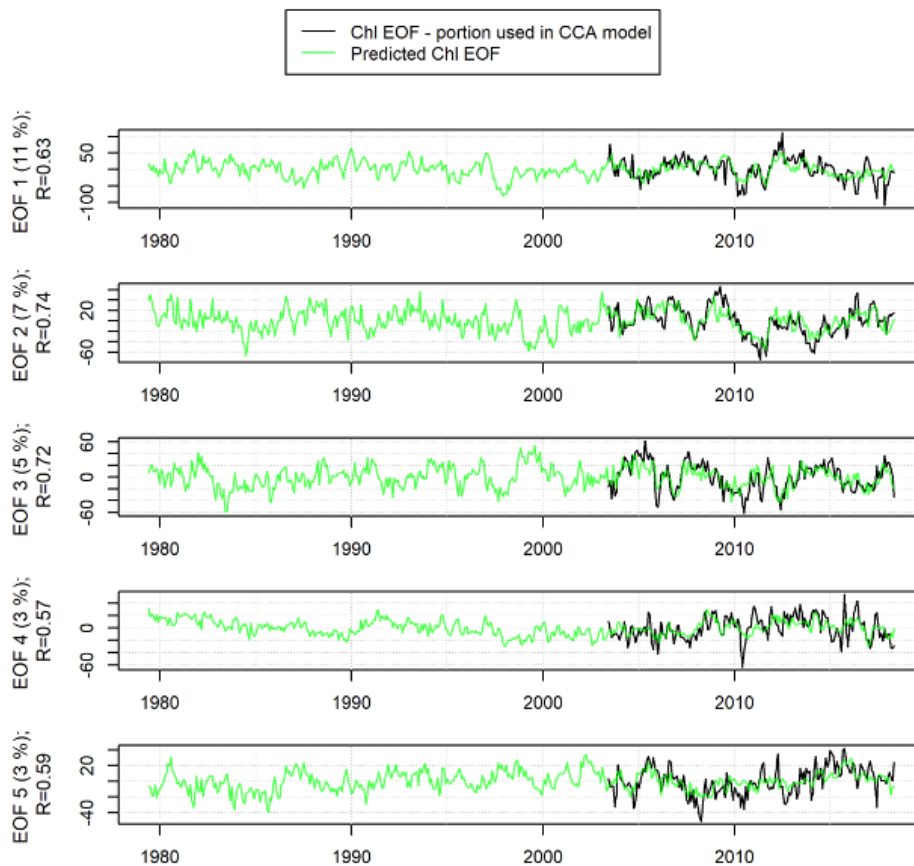
FIGURE 5.10. CCA CHL-EOF 1-5 PREDICTION (1979-2018) USING CHL-SST FULL-MODE (2003-2018), R INDICATES THE CORRELATION BETWEEN THE PREDICTION AND EACH REAL CHL EOF.
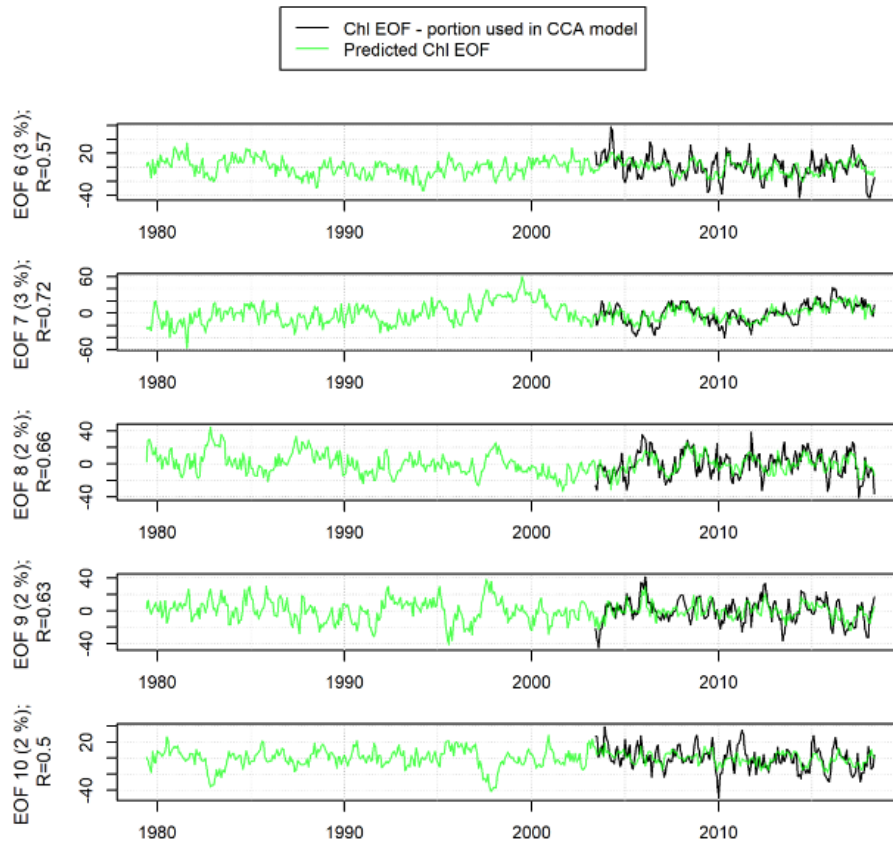
FIGURE 5.11. CCA Chl-EOF 6-10 prediction (1979-2018) using Chl-SST Full-Mode (2003-2018). R indicates the correlation between the prediction and each real Chl EOF.
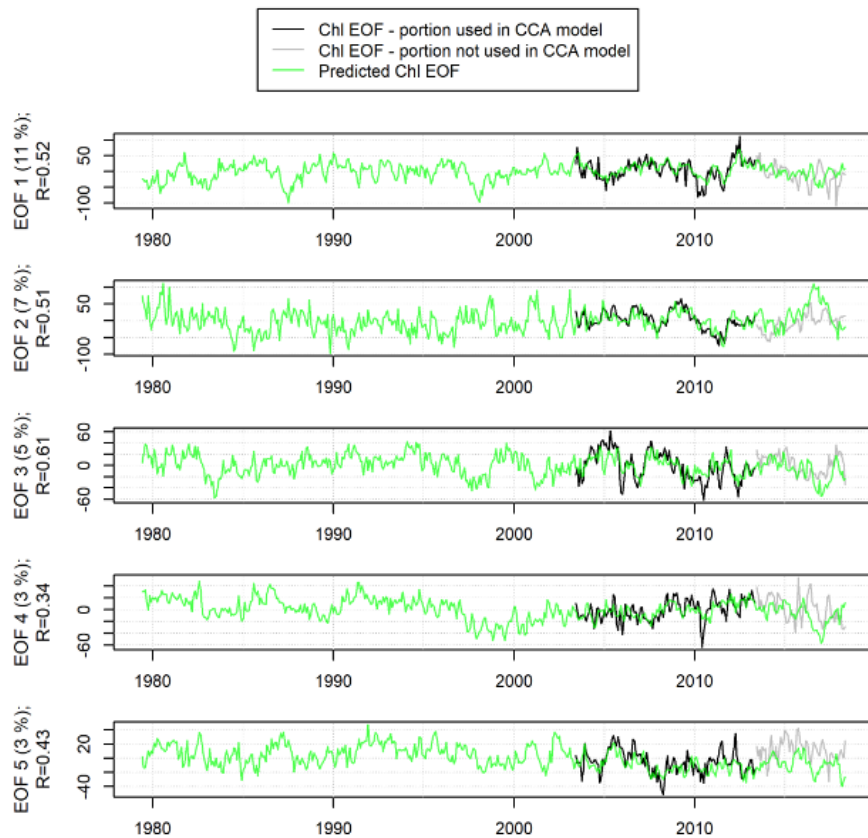
FIGURE 5.12. CCA Chl EOF 1-5 prediction (1979-2018) using Chl-SST Training-Mode (2003-2013). R indicates the correlation between the prediction and each real Chl EOF.
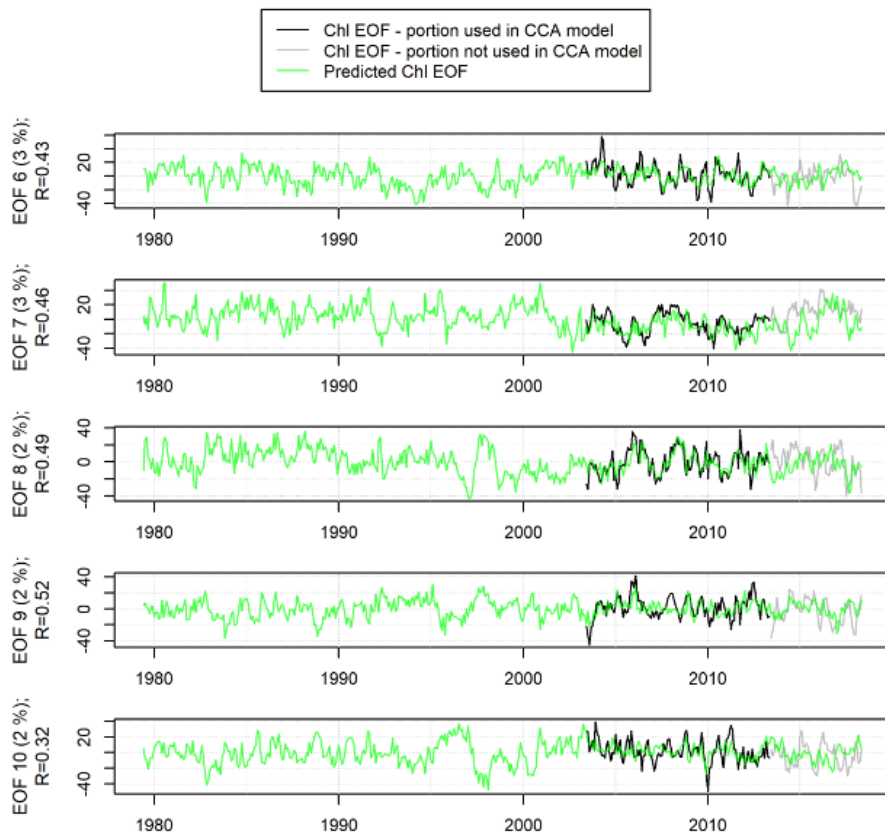
FIGURE 5.13. CCA CHL EOF 6-10 PREDICTION (1979-2018) USING CHL-SST TRAINING-MODE (2003-2013). R INDICATES THE CORRELATION BETWEEN THE PREDICTION AND EACH REAL CHL EOF.

The fourteen modes (Table 5.4) used in the Full-Mode Chl-SST could explain the Chl EOFs patterns responsible for 33% of the variance with an R over 0.6, while 13% of the variance was followed with an R over 0.5. This represents 46% of the 55% Chl variance that could be represented. In the case of the Training Mode, 27% of the Chl total variance was reproduced with an R over 0.5. The Full-Mode reconstruction was used for the subsequent analysis, but the error is likely more like the Training Mode.

5.3.1.3. Overview.

Overall, the SST variable was the best of the three parameters considered to predict Chl. Although Chl-SST prediction showed a 0.45 mean R using Full-Mode (Figure 5.6) and 0.19, taking into account only the Chl section that was not used in the forecast at Training-Mode, the MAE was acceptable in both cases. This occurs because the CCA predicts the general patterns rather than the data itself. This prediction was an outstanding achievement representing 46% of the variance with an R above 0.5 in each Chl EOF (Figures 5.10-5.11), bearing in mind that Chl showed high variability, needing twenty EOFs to explain only 55% of the variance. Also, this 55% was reached using the DINEOF to fill the gaps. Thus, only 9% of the variance could not be explained adequately through the CCA. This data quality is enough to establish reasonable Chl patterns that will determine how the climate drivers impact the Chl through the composites. Thus, Chl-SST Full-Mode data was used from 1979 to 2003, while the remaining analysis used the Chl data interpolated directly.

5.3.2. Climate Driver Composites [O.2.2].
5.3.2.1. Physical Composites.

This section shows and discusses the SST, W and PR anomalies associated with positive and negative ENSO and AAO composites. These anomalies were divided by SD to normalise them. The wind was seen as a unique parameter with arrows and a colour scale to represent its direction and intensity. However, this information was complemented with UW and VW

maps; these are not shown. In addition to this, difference maps between the positive and negative parts of the respective cycles were considered. The exception was the winds because the difference would create an arrow in a direction that physically does not make sense. The construction of the ENSO and AAO composition is explained in section 5.2.2.4. In this section, the anomalies higher than ±1 were considered significant. Also, the discussion will be mainly focused on the coastal strip, with some exceptions.
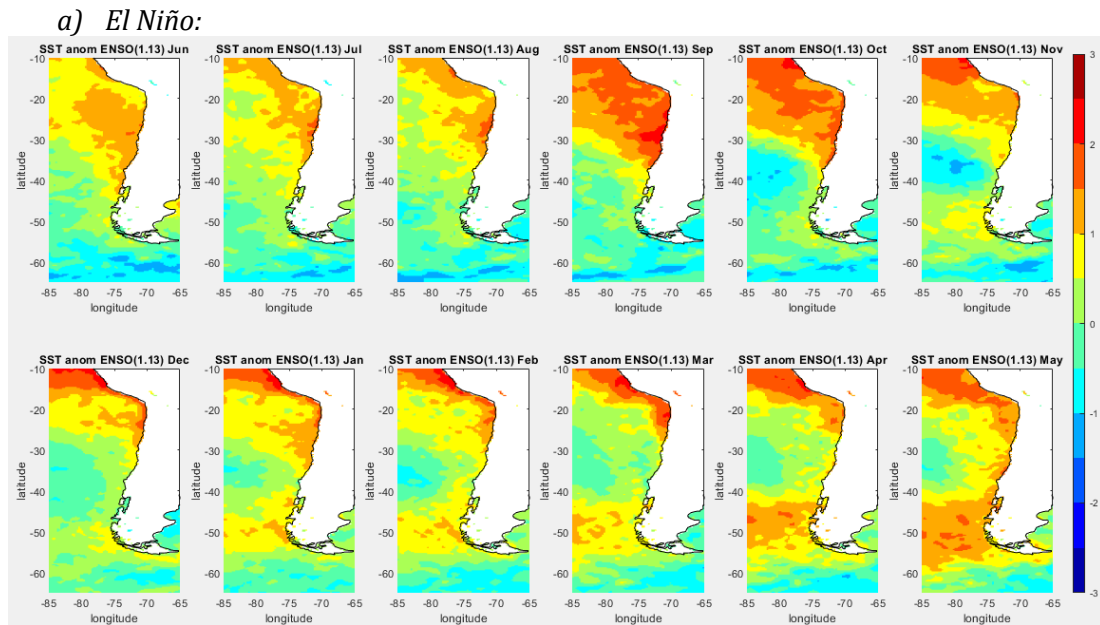
a) El Niño:

FIGURE 5.14. ANNUAL SST CYCLE ANOMALY NORMALISED COMPOSITE FOR EL NIÑO.
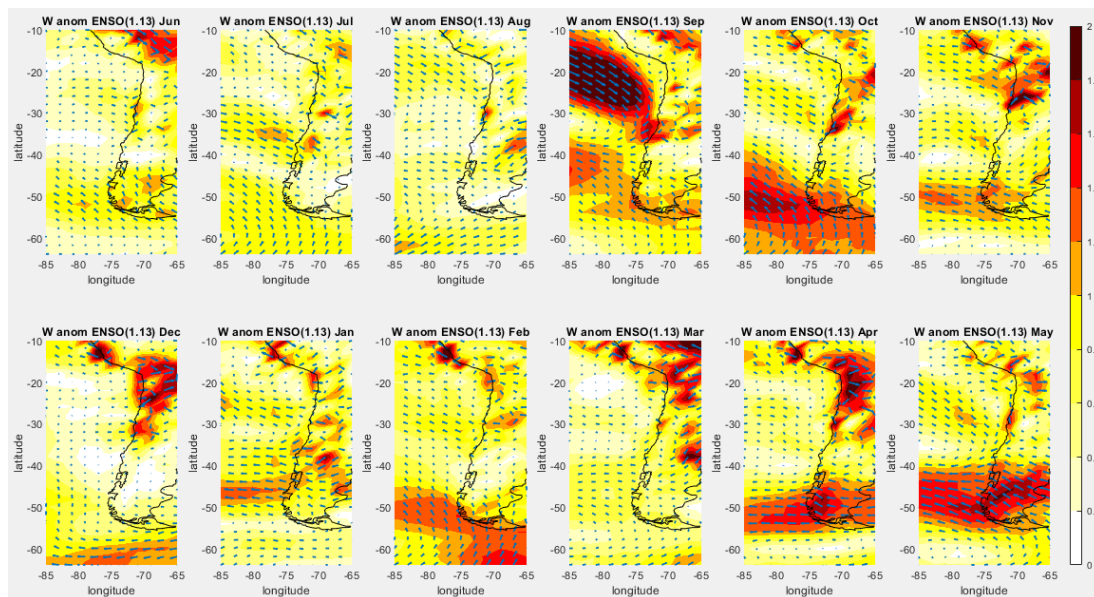
FIGURE 5.15. ANNUAL WIND CYCLE ANOMALY NORMALISED COMPOSITE FOR EL NIÑO.

The El Niño SST (Figure 5.14) showed a significant positive anomaly coming from the Equator and moving poleward along the Chilean coast. This anomaly was present the whole year, but it covered an extensive area in September-October where the SST was highest and raised in the entire Northern and parts of the Central Zone. Then, this warm anomaly slowly retreated, covering only from the Equator to 2N by April. From July to October, the most affected subsections were 3N-1C (section 3.2.2 to know how the subsections were created). Meanwhile, the Equator exhibited a very significant positive anomaly for September to March. The Southern Zone presented a slight positive anomaly during this time. However,

84

this Zone suffered a significant SST increase from January to May that spread and moved westward, particularly in the 40° to 60°S strip. In May, this rise moved equatorward, meaning that the whole Chilean coast experienced a considerable SST rise.
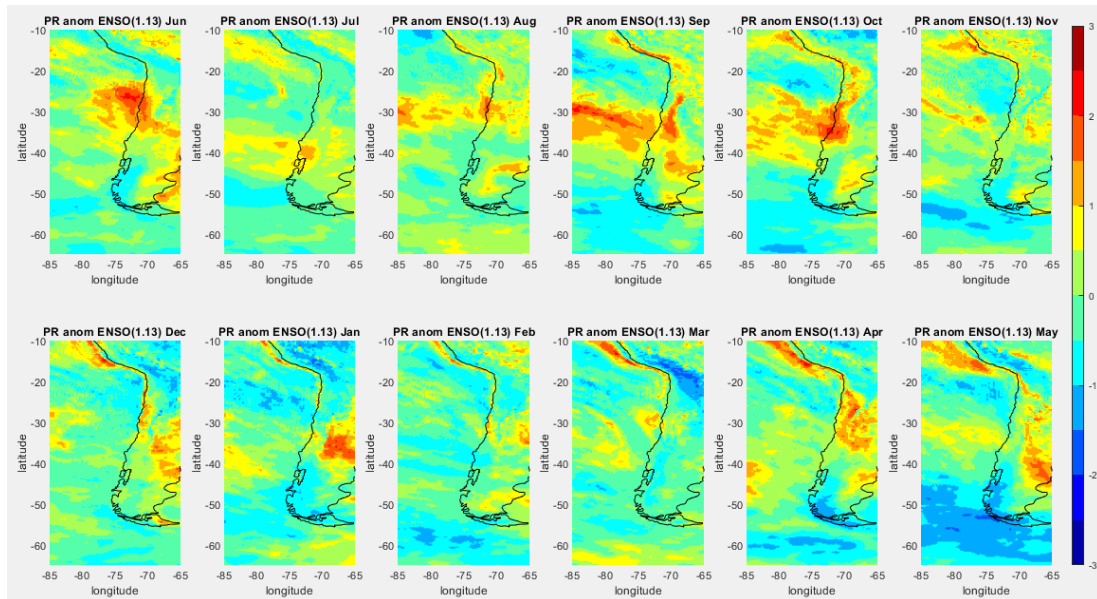
FIGURE 5.16. ANNUAL PR CYCLE ANOMALY NORMALISED COMPOSITE FOR EL NIÑO.

The El Niño Wind composite (Figure 5.15) showed how the anomalies change the wind direction, which might reduce the coastal upwelling in subsections 3N to 3C in October, December, and March, with a peak in September. 3N also exhibited westerly wind anomalies in June and July that could affect its regular upwelling. However, 3N, with 2N, showed southerly wind anomalies that increased the upwelling in November. Subsection 1N showed winds increasing that may raise the upwelling in December, February and April. The 3S presented high anomalies adjusting the wind speed and changing with a significant southerly component from September, October, February, and May. This is relevant because this Zone does not present upwelling winds under normal circumstances.

The El Niño PR (Figure 5.16) showed a positive PR anomaly in the Central Zone and 3N, while the Southern Zone was mainly negative. 3N-1C were the most affected subsections reaching significantly higher PR anomalies in June, August, October, December and April. Subsections 2C-4C also experienced a PR increment in September-October, which extend the regular rainfall season from winter to spring. A slight PR increase was found in 1S in July. The other southern subsections exhibited a slight drop in their anomalies throughout the year, with a more significant reduction in April-May. The Peruvian Zone presented an increment in their PR anomalies almost the entire year, except for June and July.

Overall, El Niño was characterised by SST and PR increment anomalies that mainly affected the Central Zone. Positive SST anomalies were present the whole year in the Northern Zone, whereas in the Central Zone, this was not the case in most of the Austral summer and autumn. The wind variations were less clear and sporadic. The changes experienced in the Southern Zone were sporadic. 3S was the most affected by episodic southerly winds and SST anomalies rising from January to May.

Based on chapter 4 correlations, summarised in Table 4.9 and reproduced in Table 5.5, the SST increase might decrease the Chl concentration in the Northern and Central Zone. The Southern Zone showed elevated SST anomalies in the autumn with a weak correlation with the Chl. This is consistent with the lack of southerly winds, leading to low upwelling in this Zone. The PR in the Northern Zone is positively correlated with Chl, while in the Central and

Southern Zone was negative. Nevertheless, only from 3C to 3S the correlations were strong with Chl. The southerly winds were positively correlated with Chl, but these were not significant in subsections 1N, 2N and 2C.

TABLE 5.5. CHL REGRESSION WITH THE PHYSICAL PARAMETERS PER SUBSECTION IN THE COASTAL STRIP. THE STATISTICALLY SIGNIFICANT CORRELATIONS ARE UNDERLINED (0.01<P-VALUES<0.05), WHILE THE STATISTICALLY VERY SIGNIFICANT ARE IN BOLD (P-VALUES<0.01).

Rho	Chl~SST	Chl~PR	Chl~VW	Chl~UW
1NT	-0.10	0.14	0.07	-0.12
2NT	-0.13	0.05	0.09	-0.03
3NT	-0.12	-0.08	**0.21**	0.10
1CT	<u>-0.16</u>	-0.07	**0.20**	-0.03
2CT	<u>-0.15</u>	0.04	0.08	0.06
3CT	**-0.19**	**-0.20**	**0.27**	**0.20**
4CT	**-0.20**	**-0.33**	**0.38**	**-0.27**
1ST	-0.06	**-0.39**	**0.45**	**-0.41**
2ST	<u>0.15</u>	**-0.24**	**0.26**	**-0.29**
3ST	**0.20**	**-0.20**	**0.23**	**-0.32**

Considering all of these, the Northern Zone should be affected negatively in their Chl concentration during El Niño. Though subsections 2N and 3N might experiment with Chl rise in June and November. The first was due to a very significant PR anomaly, while in November, the rise would be related to southerly winds. Nevertheless, In June, the SST anomalies increased that reducing the Chl. Therefore, June is less likely to have a Chl increment. The 1C and 2C might suffer a Chl reduction due to PR and SST increments from June to October, plus January and May for SST increments only, affecting 3C and 4C. 3S exhibited Southerly winds in September, October, February and May. Also, this subsection and 2S suffered a SST increase and PR reduction anomalies in April that might increase the Chl.

b) La Niña:

The La Niña composite (Figure 5.17) showed only a slight drop in the SST anomalies along the Chilean coast from June to January, except for the Drake Passage, where there was a mild SST anomaly increase from June-July. The SST anomaly tended to disappear during February and March; subsections 2N, 2C-3C and 2S normalised slightly faster than the rest. However, they cooled down again in April and May. The Central Zone was the most affected by this SST variation, reaching significant negative anomalies during August (3N, 2C-3C), December (1N, 4C) and April (1C-2C). Finally, 1N also showed a significant SST drop near the Peruvian coast in October.
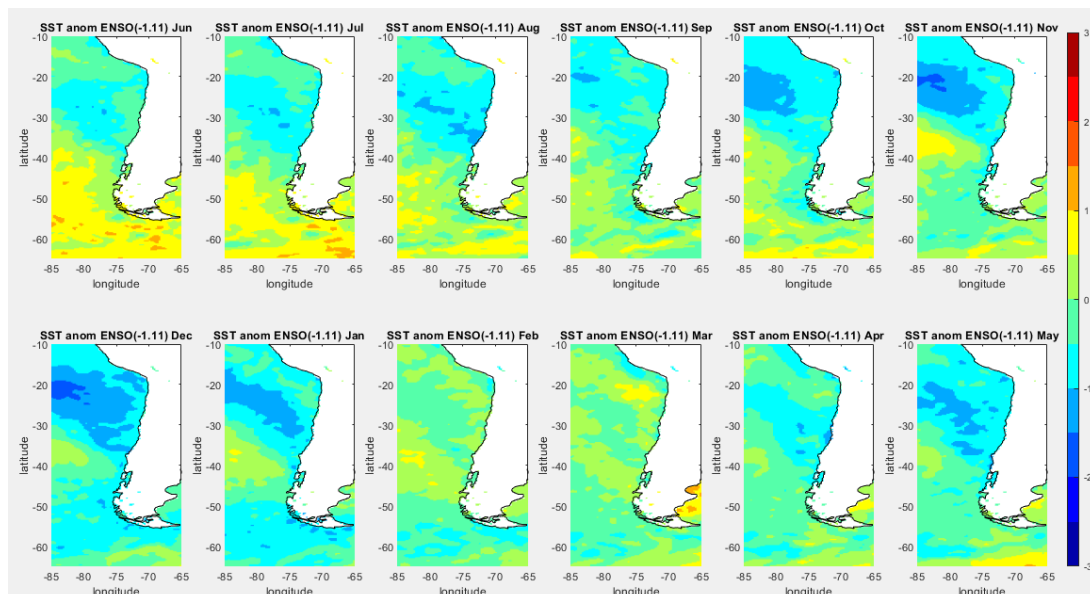
FIGURE 5.17. ANNUAL SST CYCLE ANOMALY NORMALISED COMPOSITE FOR LA NIÑA.

The wind direction was not altered during La Niña, with some exceptions (Figure 5.18). The Northern Zone showed southerly winds increment in July and March, which may produce more upwelling in subsections 1N-2N. Although the southerly winds here are not weak these months, the Chl is low due to the lack of radiation (chapter 4), so it will not necessarily produce a Chl increment. 3N and 1C also showed variations in July, but these were westerly winds anomalies. These westerly anomalies appeared in May in 2N with low intensity. In the Central Zone, 4C showed a significant rise in their southerly winds anomalies during April, whereas 1C exhibited westerly winds increment in August. 3S typically had westerly winds that do not produce upwelling, but parts of it exhibited significant northerly winds anomalies that might provide an additional downwelling in June, while in December and April, an increment in the easterly winds anomalies appeared.
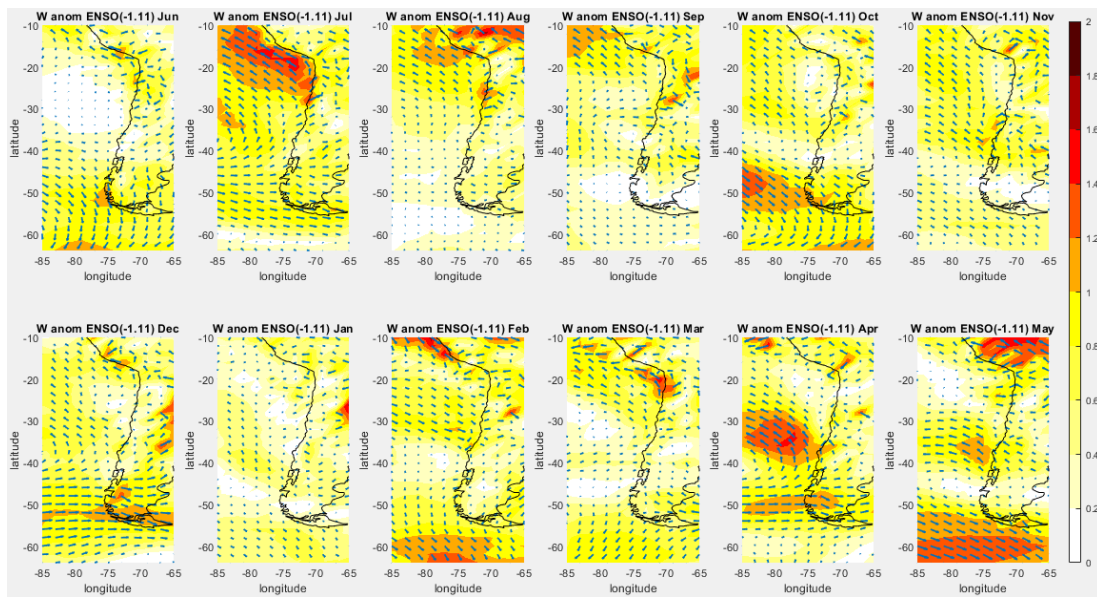
FIGURE 5.18. ANNUAL WIND CYCLE ANOMALY NORMALISED COMPOSITES FOR LA NIÑA.
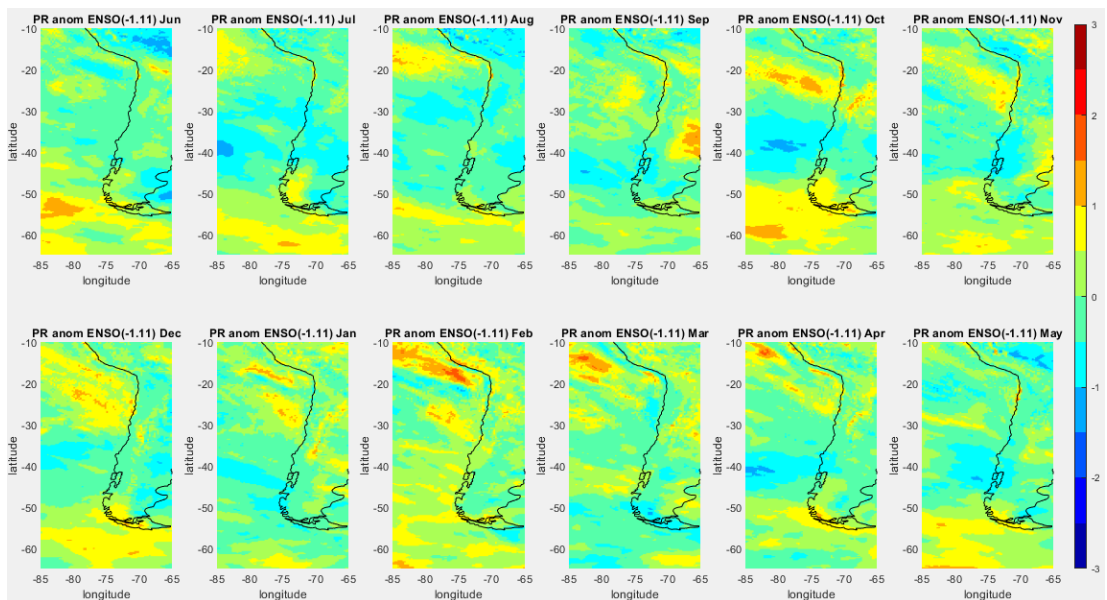
FIGURE 5.19. ANNUAL PR CYCLE ANOMALY NORMALISED COMPOSITE FOR LA NIÑA.

La Niña had a weaker impact on PR than El Niño (Figure 5.19). The Northern Zone showed a slight rise in typical PR values from October to December. The 1N increase in October was the only significant anomaly on PR that happened in La Niña near the Chilean coast. Along the Peruvian coast, significant PR anomalies were observed from February to April. Subsections

1C-3C suffered a slight drop in July. A similar decline was detected in 4C-1S in October, November (plus 2S), April and May (plus 2S). Subsection 3S suffered a minor rise in a region close to the Drake Passage. This happened in July, April and May. This increment on 3S covered a higher extension In October and December, which included the open ocean strip, but these were not significant.

In general, La Niña showed some episodic significant SST reduction anomalies in the Central Zone, mainly a few southerly winds anomaly events in the Northern Zone. Considering chapter 4 relationships, 1N might increase the Chl in July, October, December and March owing to wind, SST and PR variations. 2N might show an increase in July due to wind variation. 3C might exhibit a Chl increase in August (with 2C), November, December and April (along with the rest of the central Zone) due to SST anomalies reduction. Finally, 3S might have a Chl drop in June based on the northerly wind anomaly increment.

c) ENSO comparison:

The difference in SST between El Niño and La Niña is shown in Figure 5.20. This demonstrates that the Northern and Central Zone (especially 2C-3C) were the subsections with the most significant contrast between these phases. The highest difference was in September. 1S presented different responses the entire year as well, but at a lower intensity. 2S-3S differences started in October, increasing slowly until January. They then slightly retreated in February-March to grow again in April. This analysis pointed out that El Niño and La Niña share similarities in their SST patterns. However, the Northern Zone (September-October, March-May) and the Southern Zone (March-May) were more affected by El Niño. On the other hand, La Niña affected 4C more in August. December showed a significant impact from La Niña covering 1N and 4C.
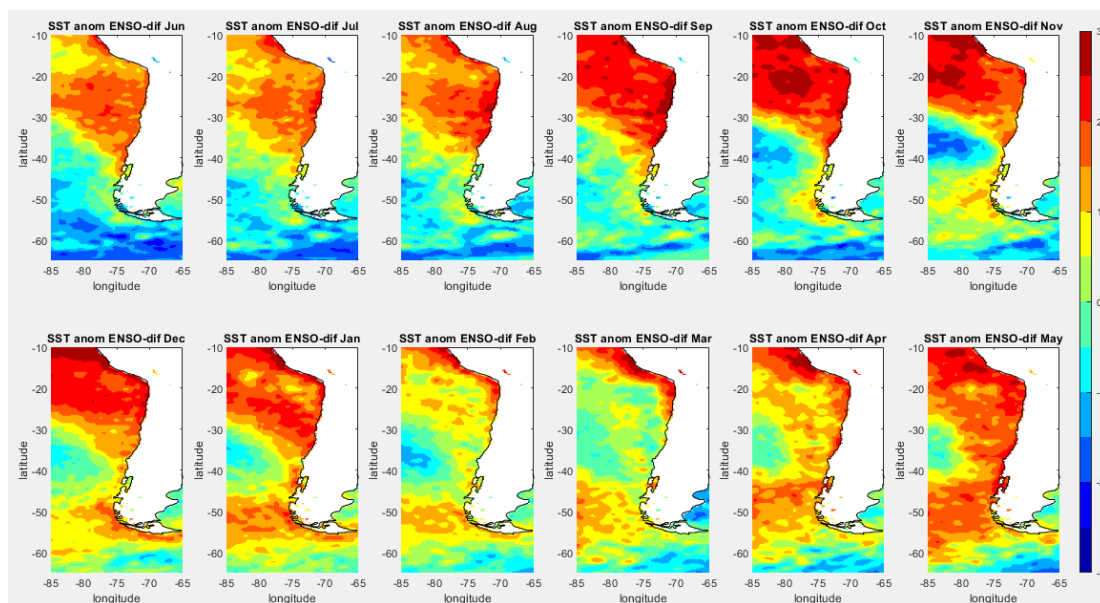
FIGURE 5.20. ANNUAL SST CYCLE ANOMALY DIFFERENCE BETWEEN THE POSITIVE AND NEGATIVE ENSO PHASE COMPOSITES.

The PR variations were more intense in the Central and Southern Zone during ENSO (Figure 5.21). During El Niño, 3N-1C was the most affected subsection reaching the highest PR anomaly in June, while 2S-3S was the most affected negatively, getting the lowest value in May. La Niña showed an opposite pattern, but the differences were less clear, especially in the Central Zone. Although in the Southern region, the PR anomalies rise were present in seven of twelve months. The Northern Zone showed some small PR increment during the Austral spring.
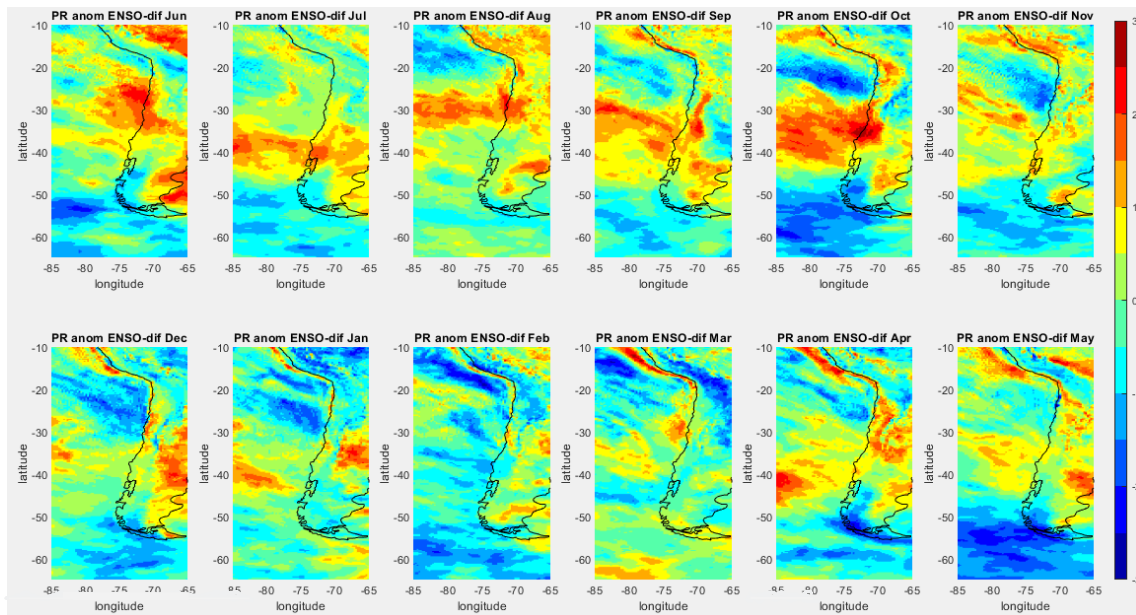
FIGURE 5.21. ANNUAL PR CYCLE ANOMALY DIFFERENCE BETWEEN THE POSITIVE AND NEGATIVE ENSO PHASE COMPOSITES.

d) Positive AAO (+AAO):

The SST +AAO composite (Figure 5.22) had a fairly general drop in the SST but was not significant. This tendency for negative SST anomalies started in 2N in June and slowly spread to the Northern and Southern Zone covering the whole Chilean coast in December. However, September and November showed local anomaly increments in 2C-3C. 3S was the only subsection that suffered a slight SST increase during June and July, while the rest of the year exhibited a negative anomaly. The 3S variation propagated from the Drake Passage directly. Here, a significant drop in the SST was found in the Austral summer and May.
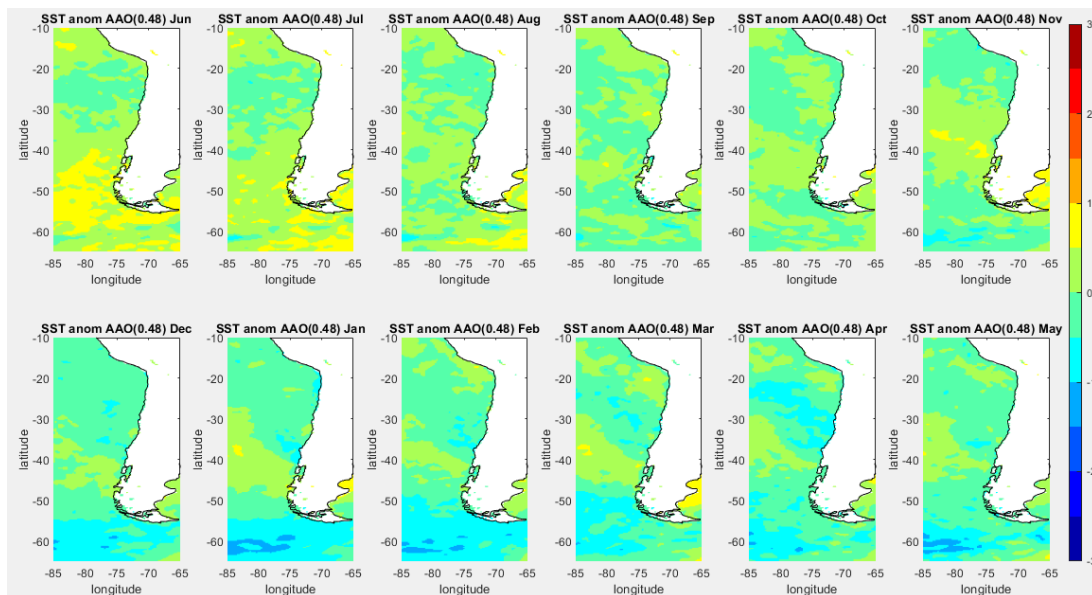
FIGURE 5.22. ANNUAL SST CYCLE ANOMALY NORMALISED COMPOSITE FOR +AAO.

Figure 5.23 shows the wind behaviour anomalies during a +AAO phase, indicating minor variations. The great exception was in July, when the wind patterns were significantly more intense. This was particularly true in Subsection 2N, having higher southerly winds anomalies but with a westerly component, while 3S exhibited northerly winds increment. The central Zone remains in its typical conditions. The rest were minor occasional wind anomalies that were not significant, such as a slight increase in southerly winds detected in 1S during September and January, while February and March exhibited little northerly winds in 1S and

89

3S. Finally, minor variations in the southerly winds were also detected in 2N in October and 4C in March.
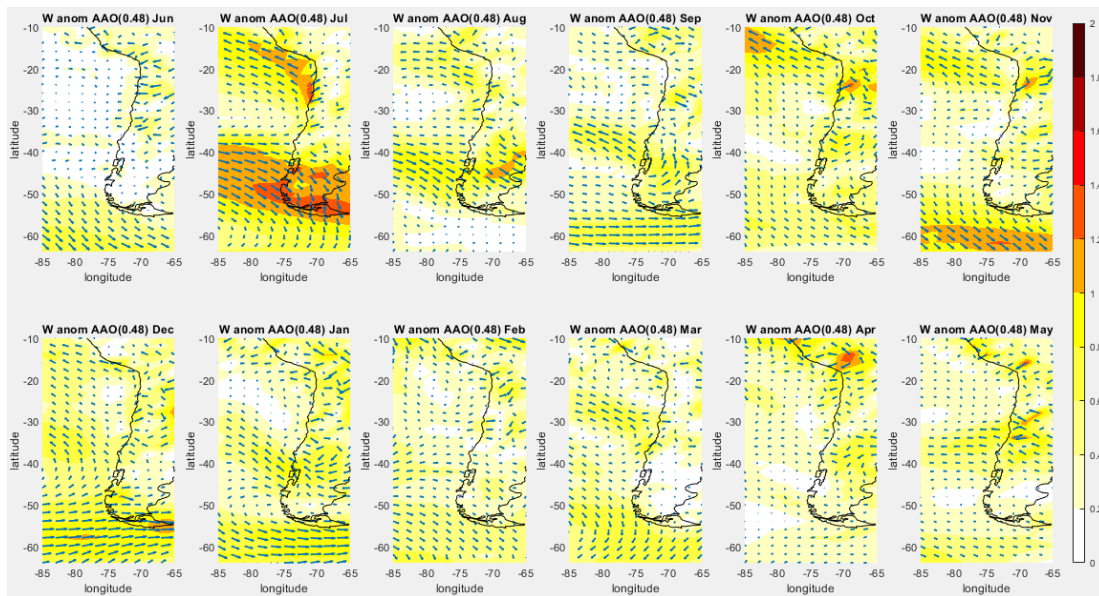
FIGURE 5.23. ANNUAL WIND CYCLE ANOMALY NORMALISED COMPOSITE FOR +AAO.

The +AAO had a modest effect on PR (Figure 5.24). The only significant PR anomalies along the coast were found in subsections 2S-3S during July and August, which were positive. Besides that, 1S-2S showed a monthly cycle variation intercalating from slightly negative to slightly positive in January-February. There were also minor negative anomalies in September and May. In May, the Central Zone showed a slight drop as well. The Northern Zone showed a slight PR rise in October and November. Despite a significant positive PR anomaly near 1N and 3S in August, these were in the ocean strip.
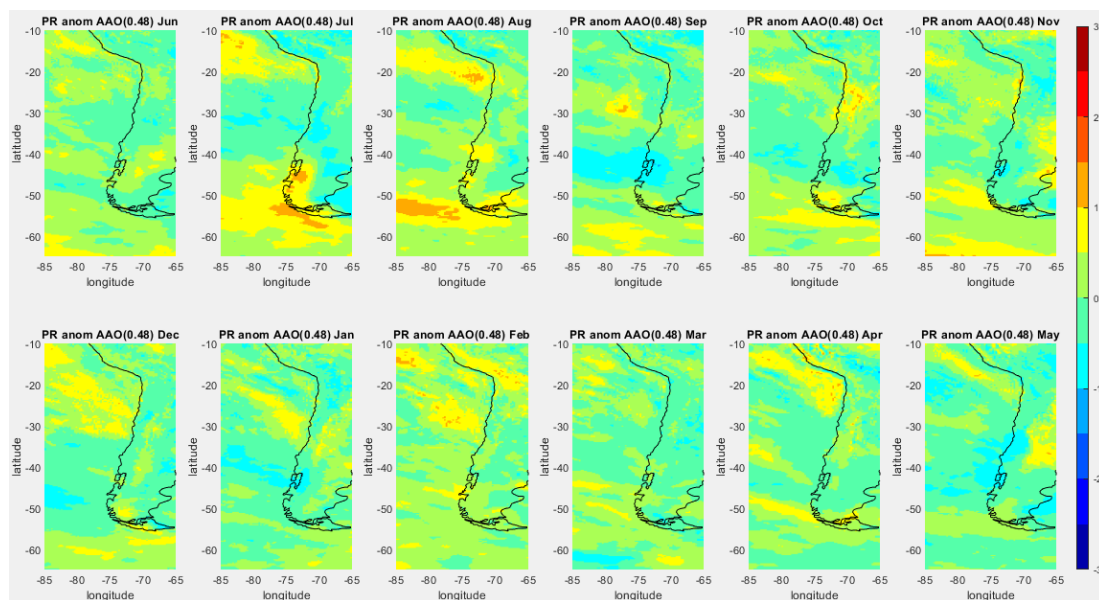
FIGURE 5.24. ANNUAL PR CYCLE ANOMALY NORMALISED COMPOSITE FOR +AAO.

The +AAO did not show significant anomalies that could produce a Chl variation. The exception to this was a PR anomaly increase with northerly winds in July that was found in subsections 2S and 3S. Also, in that month, a southerly wind anomaly was detected in 2N, which increased the upwelling. During August, there was an increase in PR in 3S and 1N, but both were in the ocean strip. 1S and 2S showed a slight PR reduction in September, January and May. Based on chapter 4 correlations and these results, it is concluded that +AAO does

not have a major impact on the Chl, except in July when there is a Chl anomaly reduction in the Southern Zone and a possible increase in 2N. 1N may also show an increase in August due to the extra rainfall. It is essential to mention that these months generally had the lowest Chl concentration due to low radiation, meaning that low differences might produce high anomalies. Meanwhile, 1S to 2S could have an increase for the slight PR reduction in January and September.

e) Negative AAO (-AAO):

The -AAO Composite showed mixed results for SST (Figure 5.25), with slightly positive and negative anomalies in different Zones. The Southern Zone had mostly negative anomalies from June to December. After that, SST anomalies started to rise slowly until April in 3S; SST anomalies fell slightly in May in 4C-1S. 2N-2C exhibited raised anomalies from June to October. Then, the anomalies were negative in the Northern and Central Zone from November to January and April-May. 3N-1C experienced negative anomalies in February. However, the only significant anomalies were detected in 2N and 1C-2C. The first was a drop in November, while 1C-2C showed an occasional rise in April. Also, a significant reduction was seen in the Drake Passage in the Austral winter.
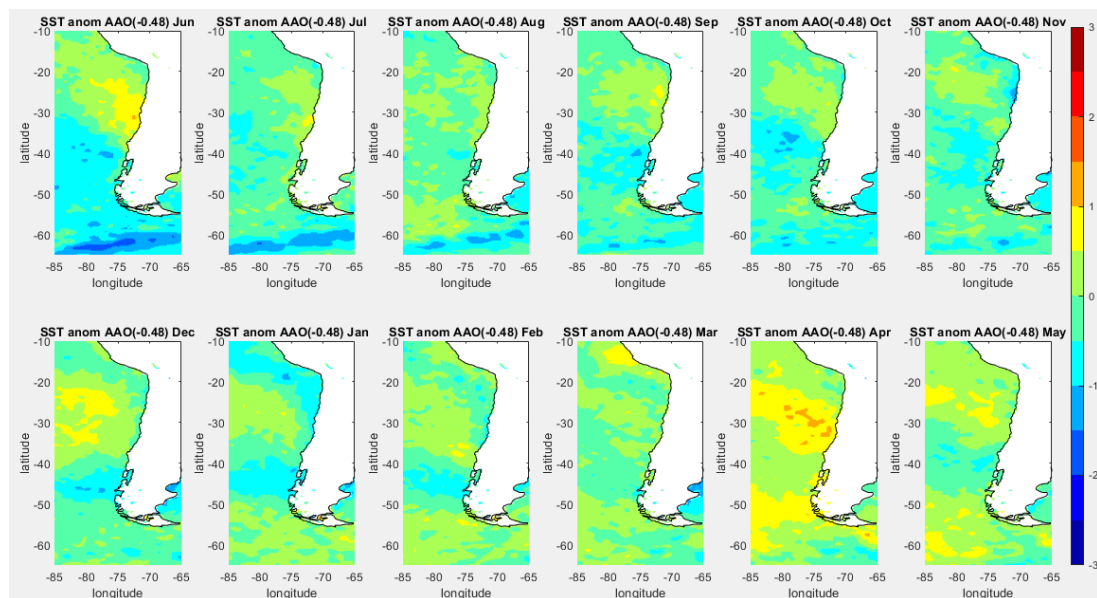
FIGURE 5.25. ANNUAL SST CYCLE ANOMALY NORMALISED COMPOSITE FOR -AAO.

The -AAO revealed that the wind variations (Figure 5.26) were primarily located in the Southern and part of the Central Zone. The Southern Zone showed significant north-westerly winds anomalies in February. 3S experienced a major southerly wind increase in June and March, with the first covering a more extensive area. This is interesting because this Zone generally has northerly winds, meaning the appearance of southerly or weaker northerly winds there. A westerly wind increase was found in September in this subsection as well. Subsections 2N-3N exhibited northerly winds in September and December, while in April, the contrary winds were seen but covering a more extended section of 2N to 3C. However, only 1N and 2N showed a significant variation. 3C-4C presented a similar cycle in February-March, starting with southerly winds. These rapid variations are related to the variability in the AAO cycle (Figure 5.4).
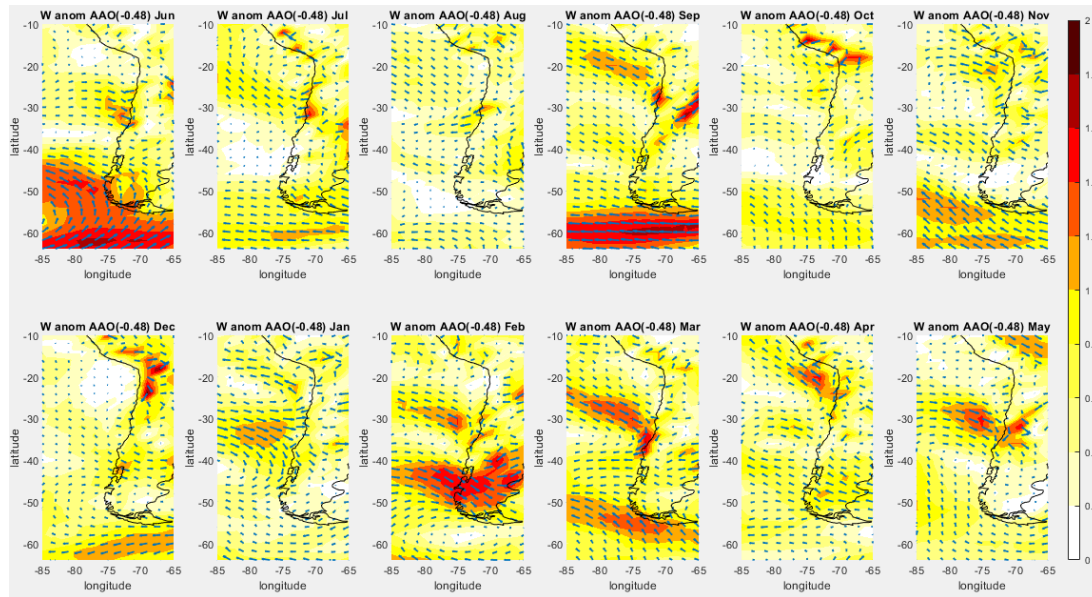
FIGURE 5.26. ANNUAL WIND CYCLE ANOMALY NORMALISED COMPOSITE FOR -AAO.
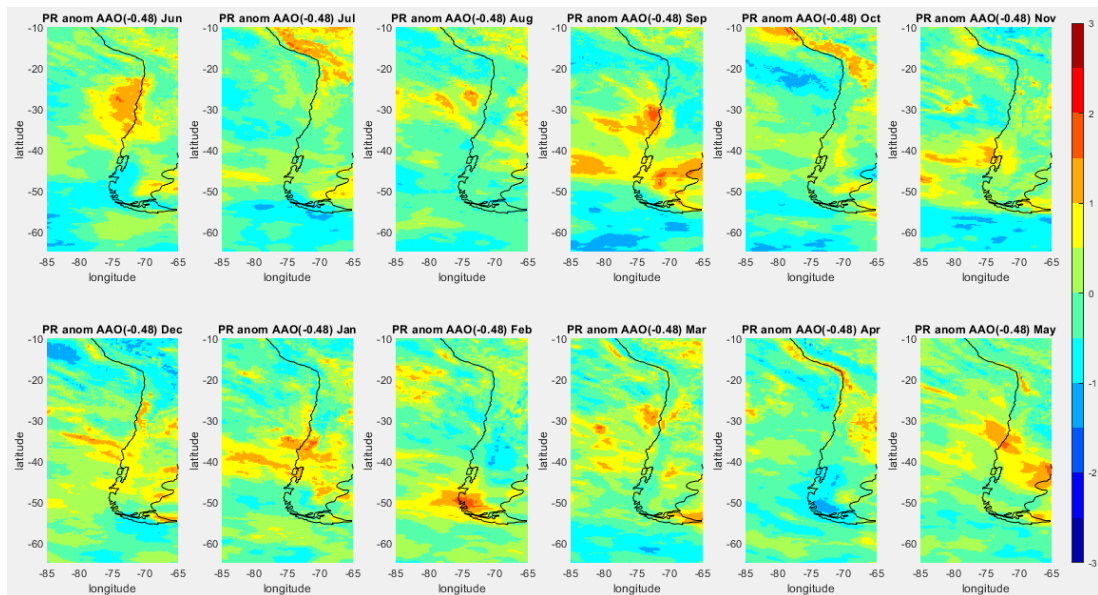
FIGURE 5.27. ANNUAL PR CYCLE ANOMALY NORMALISED COMPOSITE FOR -AAO.

The -AAO showed a more significant role in PR than its positive phase or even in ENSO. The anomalies were more positive and affected the three Zones (Figure 5.27). The Northern Zone showed a rise in March (3N-1C), April, June (2N-3N), and December. 1N also exhibited a significant PR enhancement near the Andes in July, October and May that could increase the Chl anomalies indirectly due to fertilisation from runoff, which will be studied in chapter 6. The Peruvian coast also showed a significant PR anomaly increase in July, October, March and April. Subsections 1C-3C showed a more significant increase in June and September, while in January and May, 3C-4C experienced a PR increase, the last included 2C. Subsection 1S showed a substantial increase in November and January. In general, 3S exhibited small decreases in the PR anomalies. The exceptions to this were February and April, during which both suffered significant positive and negative anomalies, respectively.

PR increases dominated the physical anomalies during -AAO. These were mainly over regions 2N to 3C in June, September and the Austral autumn. Also, northerly wind anomalies, with a westerly component, appeared occasionally in the same region. Based on chapter 4 results, the consequences of these variations may lead to a Chl anomaly reduction in the Central

92

Zone and possibly an increase in the Northern Zone. Therefore, the Central Zone (1C-3C) might have a Chl drop in June, August, September, March and May. Subsections 2N and 3N might show a rise in June, December and April (including 1N), while August may have an increase for PR in 3N. 3S might have a Chl increase in June due to upwelling winds, while 1S might show a Chl decrease in November, January and February based on PR and northerly winds increase.

f) AAO Comparison:

The differences in SST between the positive and negative AAO phases are shown in Figure 5.28. This Figure shows that both phases had similar low variations but with opposite signs. The exception is in the Drake Passage, which showed more differences between the AAO phases. The most contrasting months were June and April. Then the positive (negative) AAO's SST anomalies were rising (falling) in the Southern Zone, while the Central Zone showed the opposite behaviour during June. However, the Central and the Southern Zones anomalies fell and rose in April, except in 4C, whose SST anomaly did not change. The AAO phases produced slight SST changes in particular year periods and specific subsections. The Southern Zone was the most affected, with mainly minor negative anomalies, except in June and July when the anomalies were in the positive phase. Therefore, the Chl concentration might not be affected so much by the AAO, considering only the SST parameter.
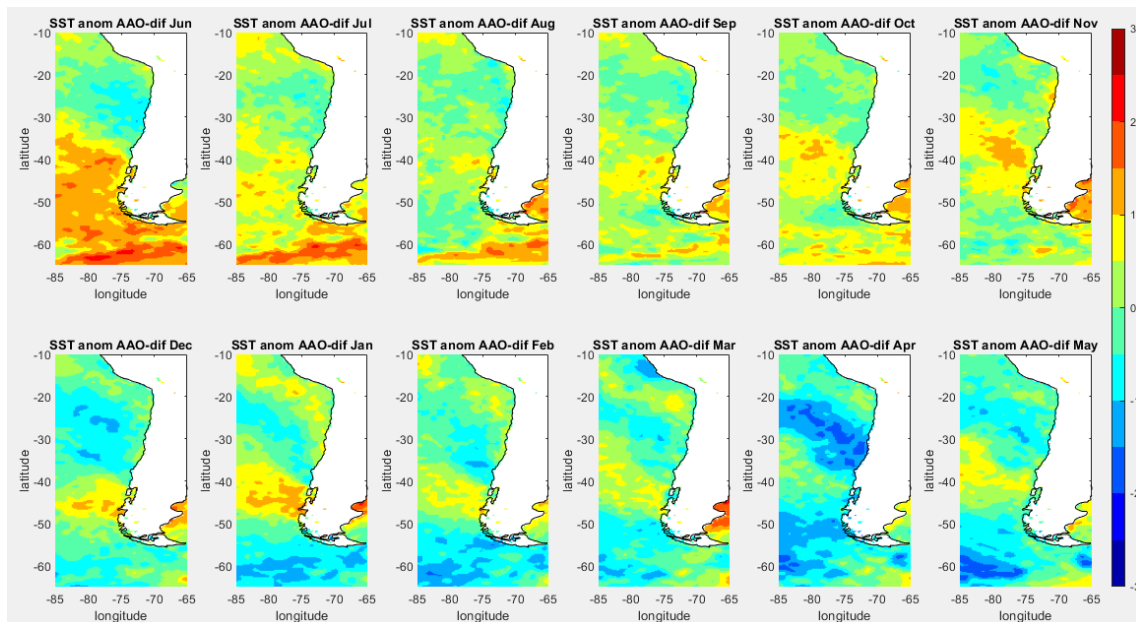
FIGURE 5.28. ANNUAL SST CYCLE ANOMALY DIFFERENCE BETWEEN POSITIVE AND NEGATIVE AAO PHASES.

In the PR variable's case, the Southern and Central Zone was affected (Figure 5.29). This makes sense because the Northern Zone usually does not have precipitation. However, this Zone was also affected, though to a lesser extent than the other two, and its impact on Chl may be more dramatic. Despite the lower significant impact of the positive phase over the negative phase, the patterns showed a resemblance but with the opposite sign and different intensities. Both phases affect the same subsections in similar periods of the year. An example of this was seen in September and January, where both phases showed a similar PR anomaly pattern over 1S-2S.
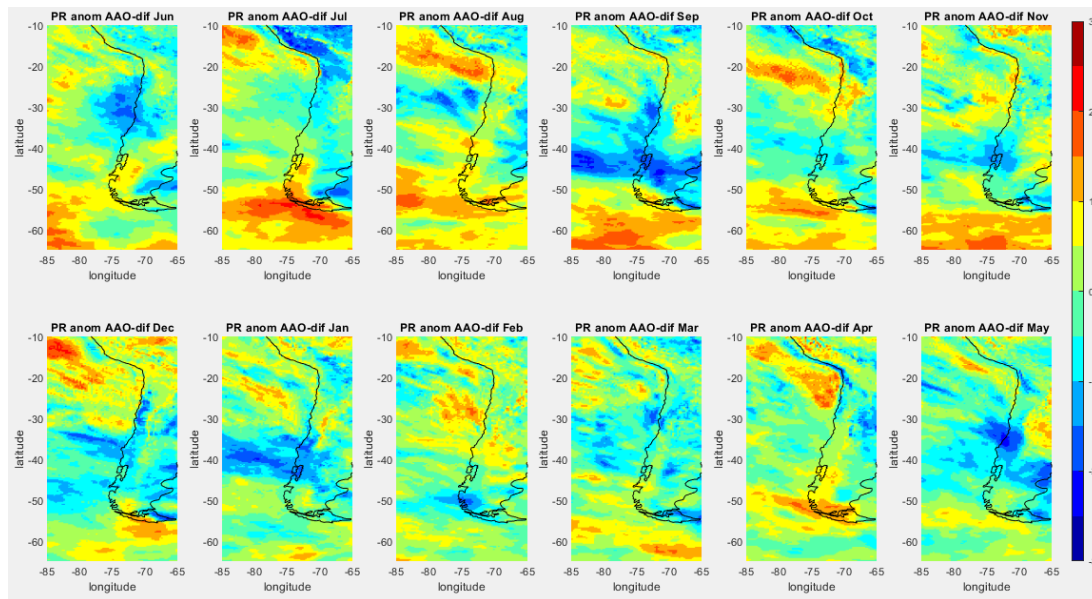
FIGURE 5.29. ANNUAL PR CYCLE ANOMALY DIFFERENCE BETWEEN POSITIVE AND NEGATIVE AAO PHASES.

5.3.2.2. Chlorophyll Composites.

The positive and negative ENSO and AAO Chl anomaly composites are shown and discussed in this section. These anomalies were divided by the SD to normalise them as well. As in the previous section, difference maps between the respective cycles were made. The Chl data from 1979 to 2003 was constructed using CCA based on SST (section 5.3.1), while data from 2003 to 2018 was obtained from observed Chl measured by MODIS-aqua but using DINEOF to fill the gaps. El Niño and La Niña composites were made with 25% and 40% of actual data, respectively. The AAO was more extreme, having 57% actual data for its positive phase, while only reconstructed data was used for its negative phase. Chl composite maps (not shown) were created using only the real interpolated data as a reference. A Chl composite with latitudinal means was made in each subsection due to the lack of detail on the coast and its high variation. This was summarised in one map per climate driver, taking the value nearest to the coast(El Niño and La Niña in Figures 5.31 and 5.34, positive and negative AAO in Figures 5.39 and 5.42 ENSO and AAO comparison Figures 5.37 and 5.45). All these maps will be discussed, focusing on the coastal strip, except for particular cases. Significant anomalies were detected on the coast on rare occasions, so the analysis will include anomalies over ±0.5. Finally, the expected Chl variation will be discussed in light of the parameter variations shown in the previous section. These are represented as a schematic combining the chlorophyll maps and the physical variables per climate driver (El Niño and La Niña in Figures 5.32 and 5.35, positive and negative AAO in Figures 5.40 and 5.43).

a) El Niño:

The El Niño Chl composite (Figure 5.30) showed positive Chl anomalies starting in September that continued until May, with a peak from September to December. The most affected Zone was the Southern, especially 2S and 3S. This Chl rise was from the coast out into the open ocean sections. This was also connected with a Chl change from September to May in the Drake Passage. Another focus of significant Chl increments was seen in the 1N-2N subsections from October to November. In the same period, a Chl drop was also seen in the Peruvian Zone. The Central Zone (1C-3C) showed no significant changes, except for a reduction between January and April. However, 2C and 3C showed a slight increase in Chl anomalies during the last month of that period. El Niño 2015, the only positive composite year with MODIS-aqua data instead of reconstructed data, showed Chl in 1S-3S starting with the lowest values during August and September but with a significant increase from March to

May. The Northern and Central Zone showed a substantial increment as well from June to August. The anomalies mentioned here were above one.
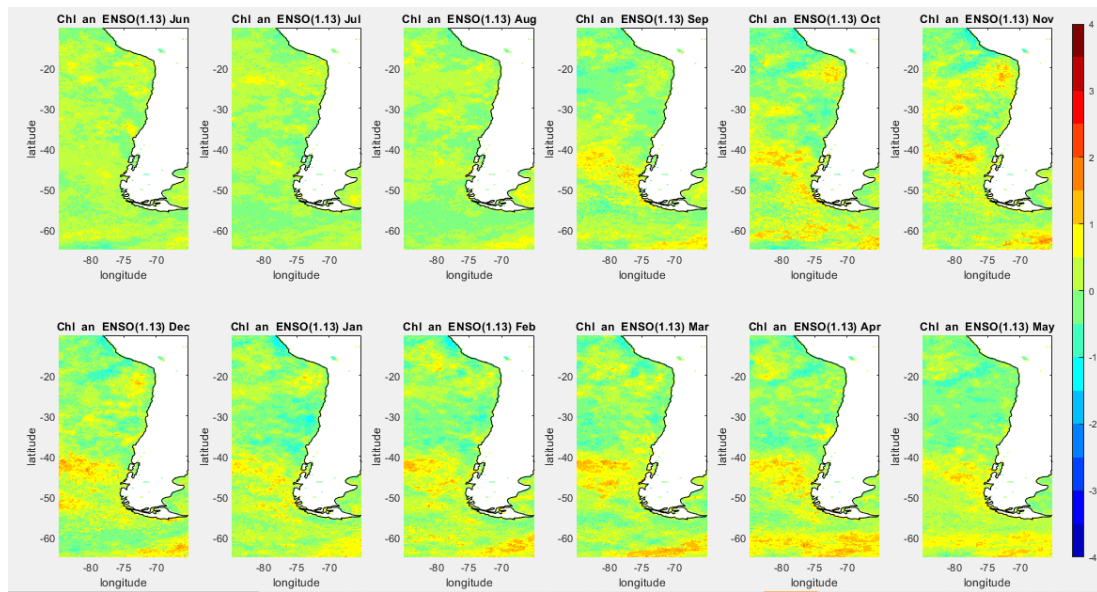
FIGURE 5.30. ANNUAL CHL ANOMALY NORMALISED COMPOSITE FOR EL NIÑO.
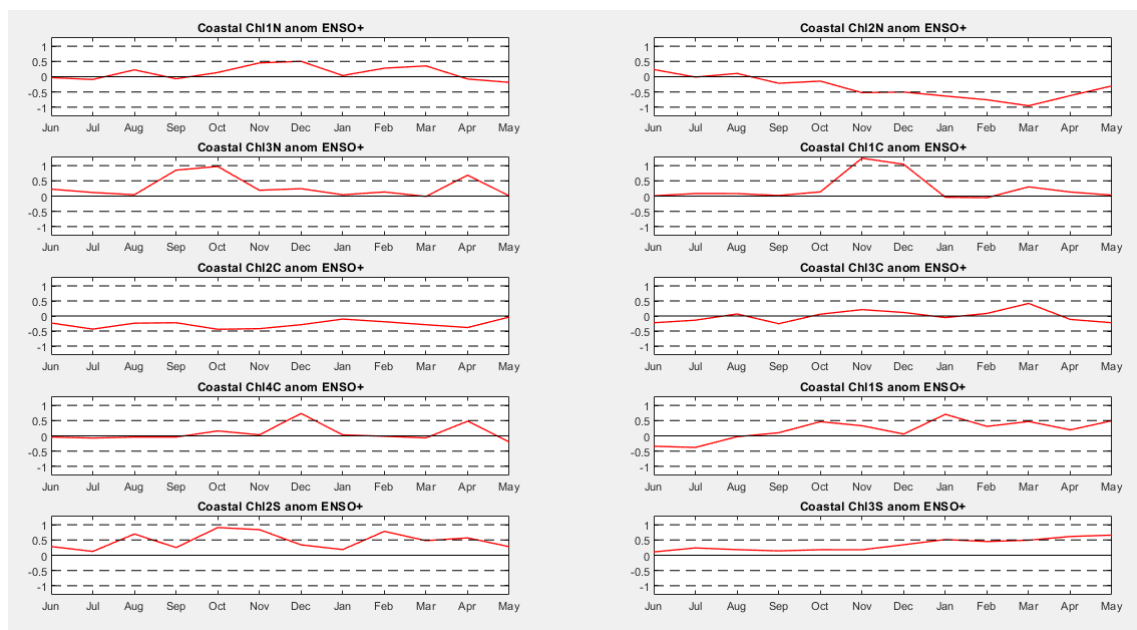
FIGURE 5.31. ANNUAL CHL CYCLE ANOMALY NORMALISED COMPOSITE FOR EL NIÑO LOCATED AT THE COAST IN THE MIDDLE OF EACH SUBSECTION.

Figure 5.31 shows the Chl anomalies in the coastal midpoint of each subsection during El Niño annual cycle composite. These results were slightly different from Figure 5.30. Here, the highest anomalies were often detected during the warm season (September to December plus a few events in April) in the Northern and Central Zone. Subsections 1N, 3C and 4C showed a more stable Chl variation with some particular increments. 3N, 1C and 2S exhibited this regular pattern as well, but these showed exceptionally high normalised values over 0.8 during the warm season. In contrast, 2N presented a drop in Chl to below -0.5 from November to April. 2C also had that negative tendency but without reaching -0.5. Finally, the 1S and 3S showed a slight constant rise from June to May, which means that the warm season did not influence them.

Comparing Figures 5.30 and 5.31, the Chl showed a slight increase in the coastal waters, particularly from September to May. However, these increases were not as high as the Chl anomalies detected a bit further from the coast in the ocean. The strongest were across the whole Southern Zone in the summer. At the coast, 2N and 2C experienced declines in Chl during ENSO, whereas 3N, 1C and 2S showed a more significant increase during the spring. The contrast observed in 2N is the most significant, caused by a drop in the middle section.
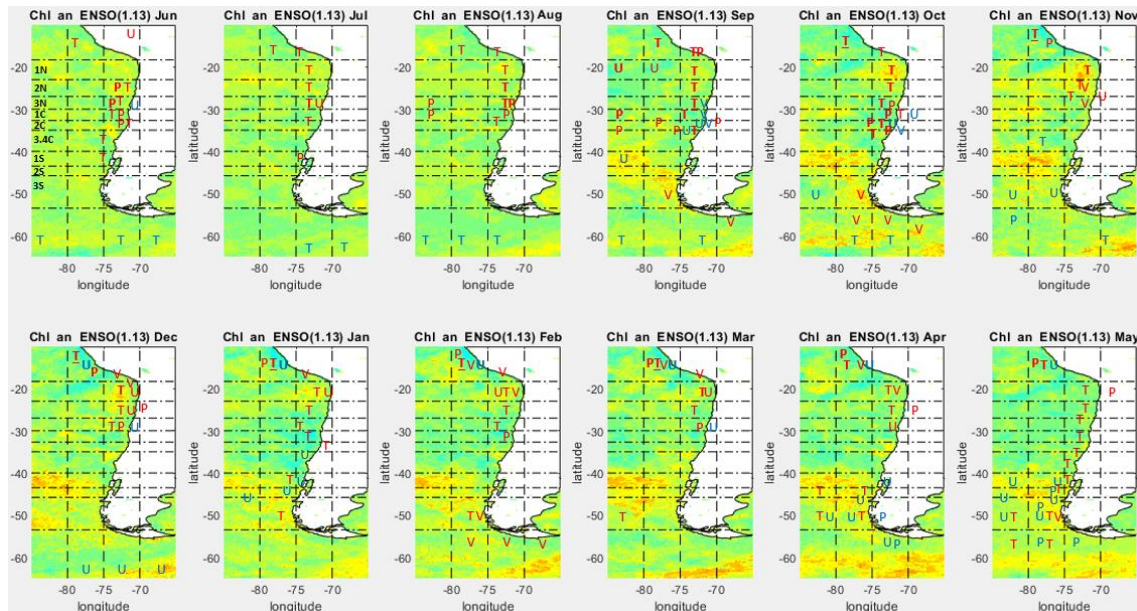
FIGURE 5.32. SCHEMATIC SHOWING THE SIGNIFICANT PHYSICAL ANOMALIES DURING EL NIÑO. WHERE P IS PR; T IS SST; U AND V ARE THE WIND COMPONENTS. COLOUR RED MEANS POSITIVE, AND BLUE IS NEGATIVE ANOMALIES NORMALISED OVER 1. THE BOLD TERMS ARE BETWEEN 1 AND 1.5, AND THE BOLD UNDERLINED ARE BEYOND 1.5. THE DASHED VERTICAL LINES INDICATE THE SUBSECTION LIMITS, BUT 3C AND 4C WERE MERGED (3.4C) TO AVOID EXTRA LINES IN A SMALL REGION. THESE WERE LABELLED ONLY IN THE FIRST PANEL.

The significant physical parameter anomalies during El Niño are shown in Figure 5.32, with the Chl composite as the background. As it was mentioned before, subsections 3S and 2S were more anomalous from September to May. These anomalies can clearly be explained by the significant southerly wind increase in September, October, February and May, along with a SST anomaly rise in January and April. Interestingly enough, the Chl anomalies were not as high in the remaining months. The significant Chl increments observed in 1N-2N from October to November are not compatible with significant SST anomalies observed there. However, significant southerly winds appeared in 2N and 3N in November, which should have enhanced the Chl anomalies observed. These winds were also present in the previous month but were not as high. The 1N's Chl rise was present until April with less intensity, despite the unfavourable SST conditions experienced over the whole time, but with some upwelling-inducing winds. This suggests that shallower upwelled water, but will only affect Chl if nutrients are limited. Chl drops were also seen in the Peruvian Zone in the same months. These were consistent with the SST anomaly increase in that section. From January through the rest of the seasonal cycle, the Central and part of the Northern Zone exhibited a general Chl anomaly decrease, which is compatible with the rise of SST and easterly wind anomalies appearing there.

Overall, physical parameters could explain most of the Chl anomalies variation, where the Southern Zone was the most sensitive to these changes. On the other hand, the Northern Zone Chl anomalies were positive despite being subject to positive SST anomalies. This was particularly marked in 1N. Nonetheless, the Chl in 1NT showed insignificant correlations with the SST (chapter 4 for more details and Table 5.5).

b) La Niña:

La Niña (Figure 5.33) did not reveal positive Chl anomalies as significant as El Niño. In fact, it seems the trend was more towards negative anomalies here, with no anomalies over ±1 along the coast, which is unexpected. The Northern and Central Zone experienced a drop in the Chl concentration from June to October during La Niña. A slightly increasing trend was shown in the same area for the rest of the cycle. 1S presented a positive anomaly for almost the whole year, reaching the whole section in July-August. 2S-3S showed a slight reduction from December to May. La Niña's Chl composite used the years based on actual data, only two of five (2010 and 2007), pointing out a general low anomaly with limited local rises. The most relevant was in 3S in July and August and 3N-1C in February, which is not in the composite shown here.
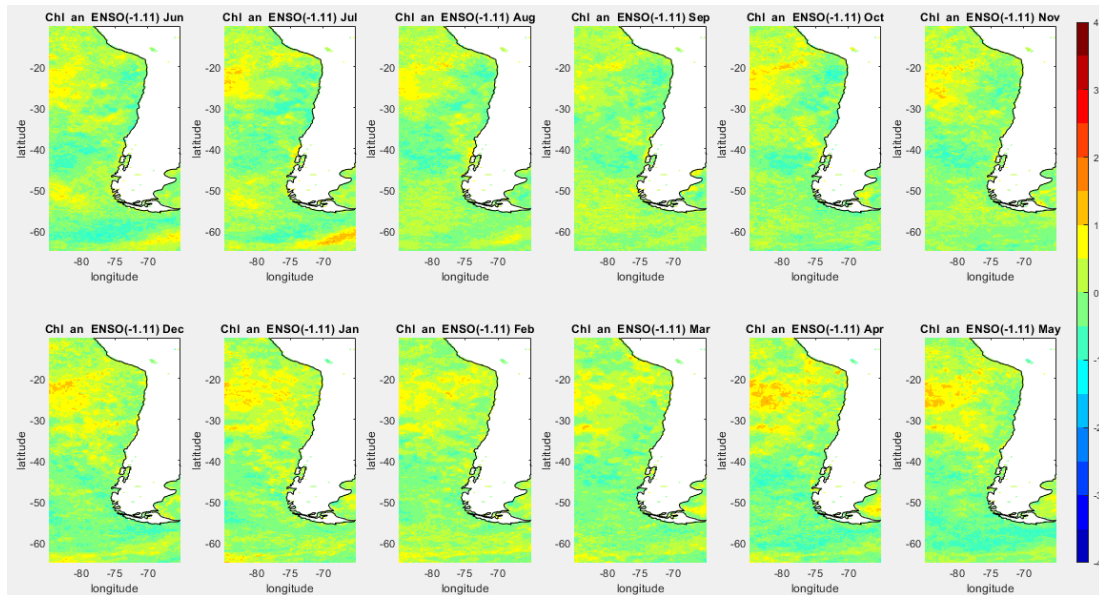
FIGURE 5.33. ANNUAL CHL CYCLE ANOMALY NORMALISED COMPOSITE FOR LA NIÑA.
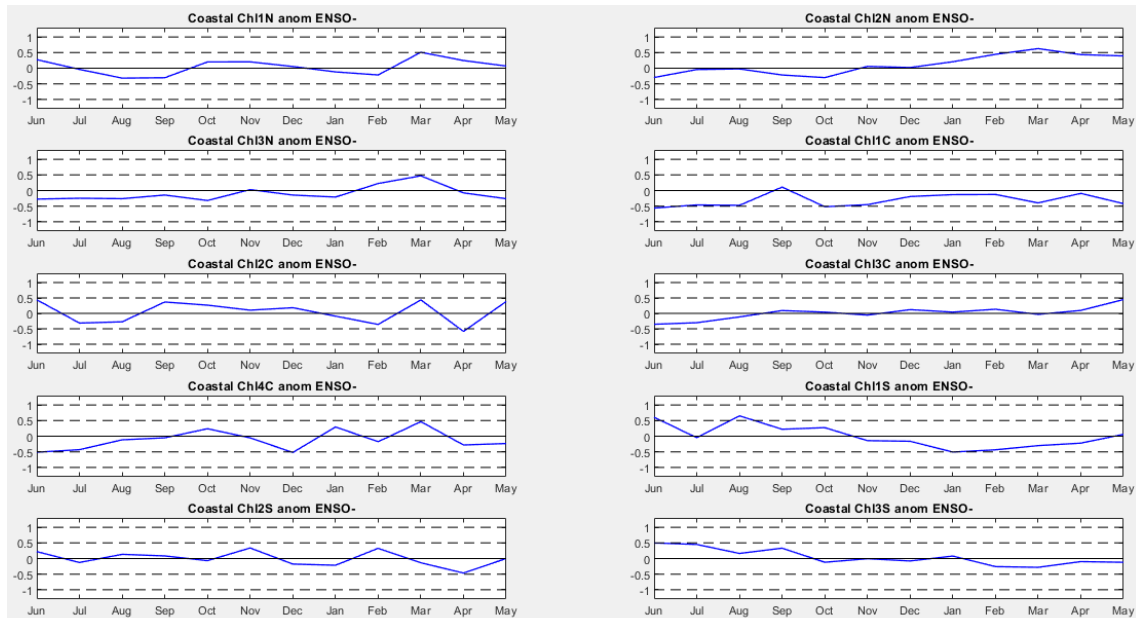
FIGURE 5.34. ANNUAL CHL CYCLE ANOMALY NORMALISED COMPOSITE FOR LA NIÑA LOCATED AT THE COAST IN THE MIDDLE OF EACH SUBSECTION.

Figure 5.34 shows the coastal Chl anomalies during the composite La Niña annual cycle. In general, each subsection had both negative and positive anomalies, but these were significant (±0.5) only on a few occasions. The negative anomalies were more often observed

97

from July to December, whereas the rest were positive in the Northern and Central Zone. The Southern Zone showed the opposite pattern. This pattern was evident in 1S and 3S. 3S showed a slight but sustained downward trend from June to May, which is the opposite behaviour observed during El Niño. 2S presented a flatter trend with a few small increases and decreases. The Northern Zone subsections showed a more similar behaviour this time, with their maximum anomaly increase in March over 0.45. 1C showed a more negative tendency with anomalies lower than -0.45 from May to November (without September). 3C had the most steady anomalies with almost no variation. 2C did not follow completely the pattern mentioned at the beginning, reaching more negative anomalies in April and February and their maximum in June and March.

A negative tendency was seen from June to December, but an increasing trend was seen for the rest of the cycle in both the Chl map and the coastal Chl plot in Figures 5.33 and 5.34, respectively. However, the coastal anomaly showed a slightly more positive trend than the Chl map. The Southern Zone presented different patterns compared to the other Zones using both approaches. The coastal anomalies showed lower variations with a positive tendency in 3S and negative in 1S, from January to March than the Chl composite maps result.
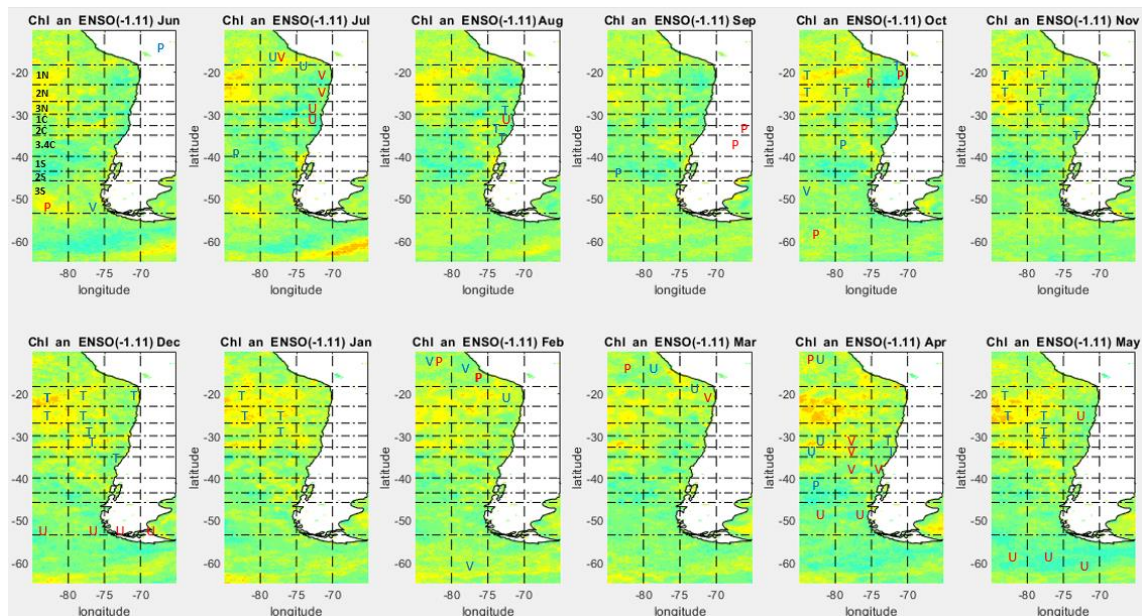
FIGURE 5.35. SCHEMATIC SHOWING THE SIGNIFICANT PHYSICAL ANOMALIES DURING LA NIÑA. FULL DESCRIPTION IN FIGURE 5.32.

The physical parameters during La Niña are shown in Figure 5.35 with the Chl composite in the background. Based on this, La Niña did not offer as many significant physical anomalies as El Niño. Still, these might produce some local Chl increases, owing to the majority being favourable conditions for productivity enhancement. The 1N and 2N experienced a drop in the Chl concentration from June to October. These results were not compatible with the Southerly winds detected in July in both subsections and the SST drop and precipitation rise in October in 1N. On the other hand, the SST dropped and southerly wind anomalies in December and March, respectively, coinciding with a Chl increment observed in 1N. The westerly wind detected in 2N in May was consistent with the Chl drop there. The decrease experienced in 3N and 1C in July and August matches with westerly winds there. A slight Chl rise in 3C in August, November, December and April were related to a SST drop experienced in that area, except for April, which was provoked by a southerly wind anomaly. That same month, a slight Chl rise in 1C and 2C is consistent with the decrease in the SST anomalies. In the Southern Zone, the 1S behaviour cannot be attributed to any significant physical parameter anomaly, but minor southerly winds anomalies were observed there in some months. In contrast, unfavourable wind conditions can explain the 2S-3S slight reduction

from December to May. Nonetheless, these conditions were present in December, April and March, when the Chl reductions were higher.

Overall, La Niña drove Chl drops in the three Zones. Although the physical parameters could explain many of them, 1S was not related to any significant climatological event. Furthermore, as in the El Niño case, the Northern Zone physical parameters opposed the Chl response. Additionally, the Chl response in the Northern Zone was inconsistent with the physical variables anomalies. Although this response is contradictory, it is consistent with the low Chl and VW variations observed in chapter 4 and, consequently, low Chl correlations in the Northern Zone.

c) *ENSO comparison:*
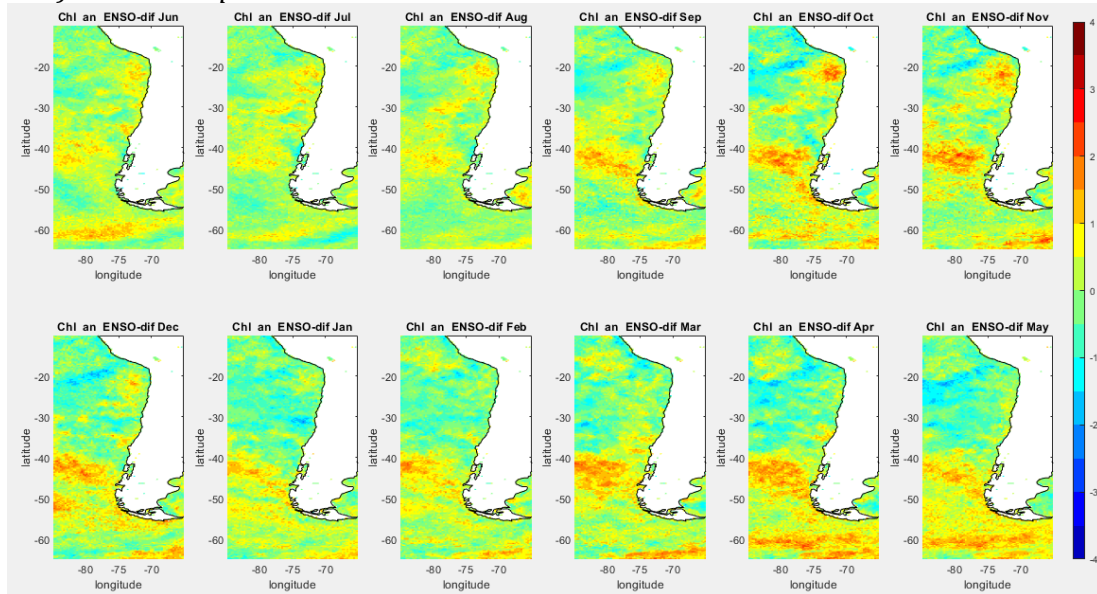
FIGURE 5.36. ANNUAL CHL CYCLE OF ANOMALY DIFFERENCE BETWEEN THE POSITIVE AND NEGATIVE ENSO PHASES.
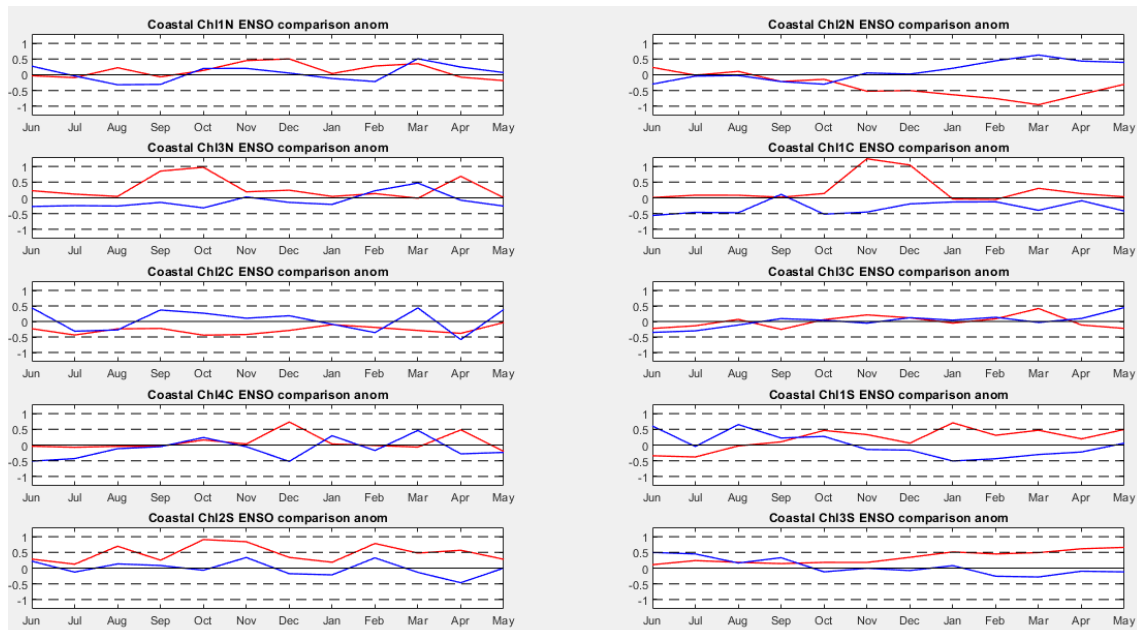
FIGURE 5.37. ANNUAL CHL CYCLE ANOMALY NORMALISED FOR THE POSITIVE (RED) AND NEGATIVE (BLUE) ENSO PHASES LOCATED AT THE COAST IN THE MIDDLE OF EACH SUBSECTION.

Figure 5.36 reveals that the subsections that had the highest difference in impact on Chl concentrations between ENSO phases were 1S-2S. This was across the whole year, with a

peak in November. This high anomaly difference moved poleward to 3S from February to May, reaching another peak in April. Elsewhere, the Northern Zone was most different from June to November, with a peak in October. These variations mainly came from the El Niño part of the cycle because of a Chl anomaly rise. In the Central Zone, 1C exhibited the lowest difference in January. This particular subsection was more affected during La Niña when the difference calculated using actual Chl data showed a high impact across the whole region during the Austral winter.

Figure 5.37 indicates that El Niño has a more positive impact on coastal Chl than la Niña, except in regions 2N and 2C, where the reverse case is found. Nevertheless, 2N and 3S were the only subsections that presented the opposite behaviour during ENSO phases, although 4C and 1S showed elements of this pattern. 2S showed a very similar pattern in both phases, with higher anomalies in El Niño. In 3C and 1N, both phases had similar values, with the difference that 3C exhibited no significant changes in Chl anomalies. Finally, 3N and 1C showed the highest anomalies during El Niño, which were not reflected during La Niña. Overall, the difference detected in the large-scale maps did not fit the coastal behaviour, demonstrating the importance of examining the coastal strip in detail.

d) Positive AAO (+AAO):
Figures 5.38 and 5.41 show that neither AAO phase has as significant an impact on Chl concentration as ENSO. However, some minor anomalies were seen. For the +AAO (Figure 5.38), a slight negative anomaly was observed from June to September with a more homogeneous Chl drop in August in the Northern and Central Zone, while 2S and 3S showed a small anomaly gain (Figures 5.38 and 5.39). Subsection 1C seemed to be the most consistently affected in these months. 1N exhibited a slight Chl rise from November to March. A noticeable Chl increase in 3S was observed in the ocean strip during November and January, but this was only weakly manifested along the 3S coast. +AAO's Chl composite using the years that were based on actual data (2010, 2008, 2015 and 2017) showed some small local increases in the Chl anomalies in subsections 2N-3C from June to August, which is opposite to what was seen in this Composite.
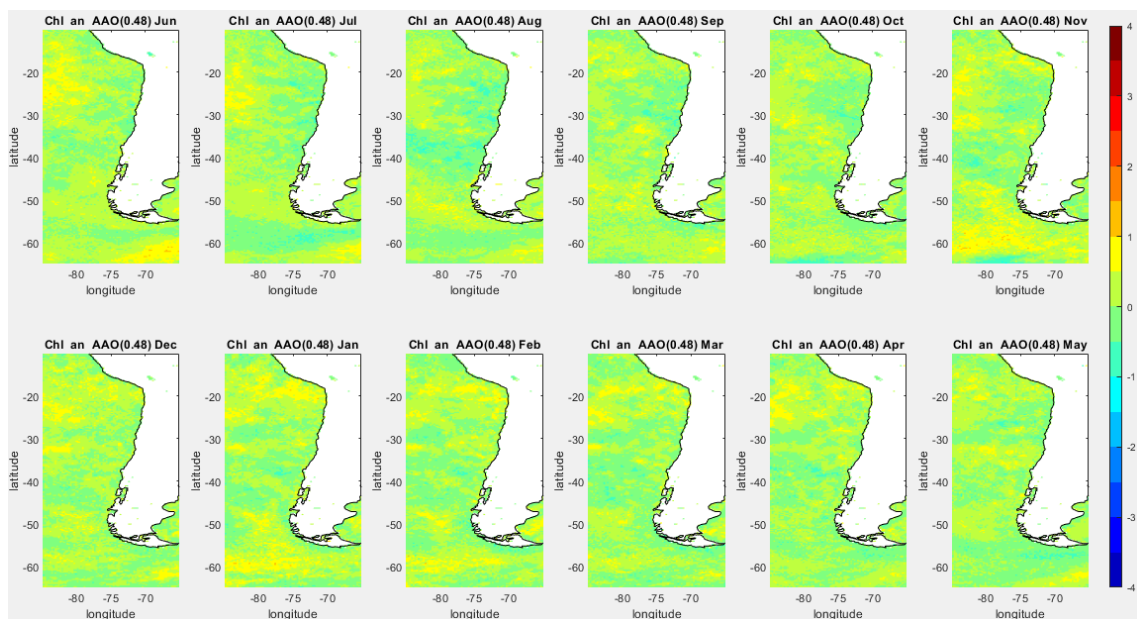
FIGURE 5.38. ANNUAL CHL CYCLE ANOMALY NORMALISED COMPOSITE FOR +AAO.

Figure 5.39 also shows minor variations in the Chl anomalies, where the majority of the subsections had a flat curve with sporadic rises or drops. 2S and 3C showed in August and February, respectively, the only two occasions these anomalies were over 0.5. The Southern

Zone showed a higher variation with more anomalies over ±0.3. The three subsections showed positive behaviour in the first six months of the cycle, followed by three months with a negative trend in the 3S case, while the other two presented minor variations. The other subsections did not show particular patterns owing to their flat trend. Except for 2C, which exhibited the most negative tendency, this still was very flat. Overall the coastal Chl plot and the Chl map showed similar results. For example, the negative Chl anomalies were seen in almost all subsections in August.
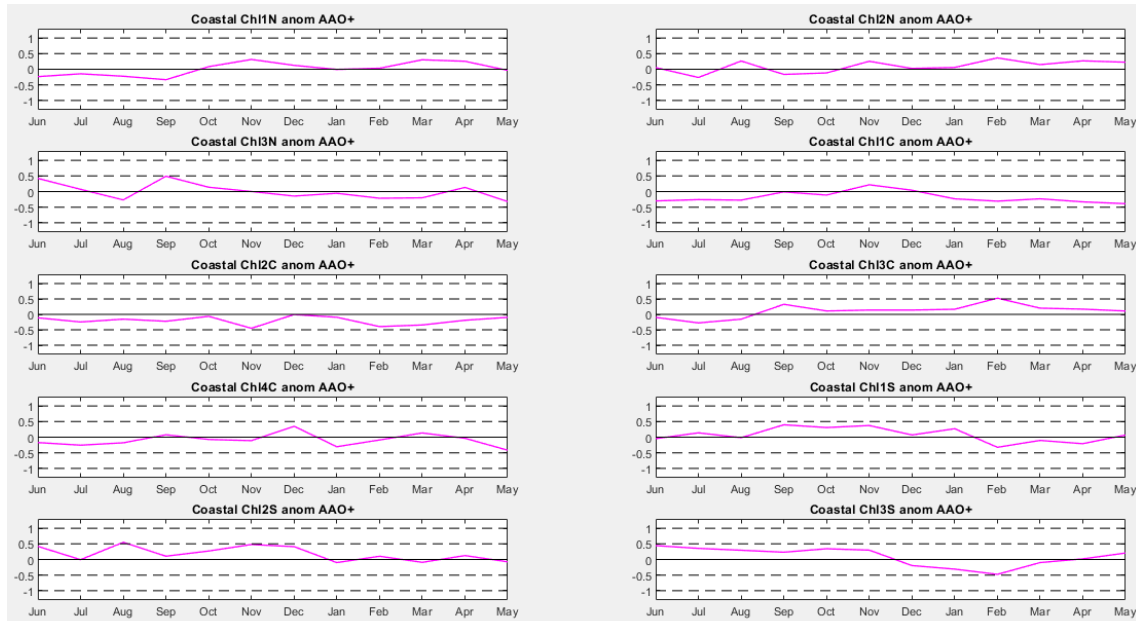
FIGURE 5.39. ANNUAL CHL CYCLE ANOMALY NORMALISED COMPOSITE FOR +AAO LOCATED AT THE COAST IN THE MIDDLE OF EACH SUBSECTION.
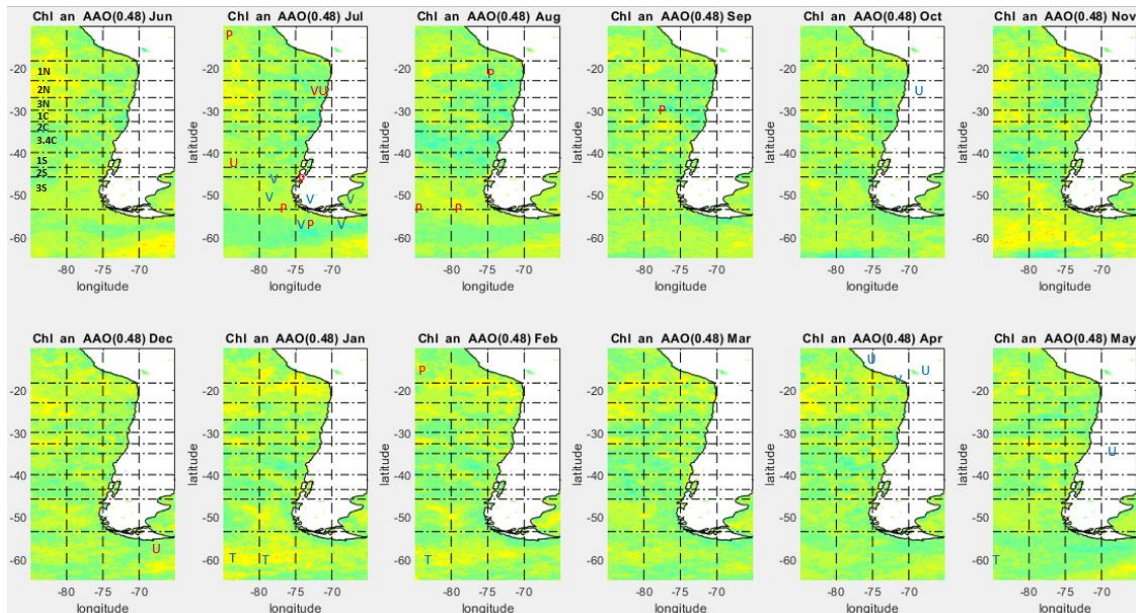
FIGURE 5.40. SCHEMATIC SHOWING THE SIGNIFICANT PHYSICAL ANOMALIES DURING +AAO. FULL DESCRIPTION IN FIGURE 5.32.

A few significant physical anomalies occurred in the +AAO. These were in 2N, 2S and 3S during July, where distinct wind anomalies in each subsection were seen, and to a lesser extent, precipitation anomalies in the Southern Zone during July and August (Figure 5.40). Therefore, the physical variable anomalies were not consistent with either the Chl drop in the Northern or the small gain in the Southern Zone.

101

e) Negative AAO (-AAO):

For -AAO (Figure 5.41), small Chl increases were seen in 1C-3C from June to August and November. Also, in August, a slight Chl increase was seen in 3N. 4C exhibited a slight rise as well in March and May. The 3S section near the Drake Passage showed a boost in Chl from December to April and June. Also, a slight Chl drop was seen near the coast in February. A sharp Chl concentration drop was seen in 2N from December to May in the open ocean. This decrease affected the on-shore Chl concentration mentioned in the last three months (Figure 5.42). All these Chl variations were not significant.
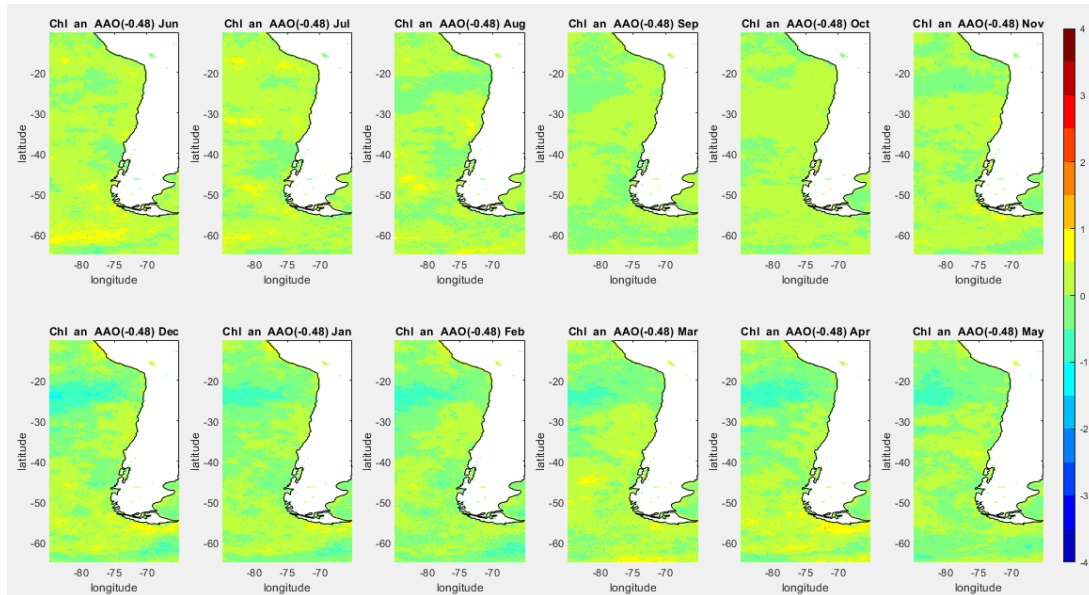
FIGURE 5.41. ANNUAL CHL CYCLE ANOMALY NORMALISED COMPOSITE FOR -AAO.

The coastal Chl anomalies during -AAO are seen in Figure 5.42. These results show weak variations with no significant anomalies, where the vast majority of regions showed essentially normal Chl conditions throughout the year. Subsection 2C exhibited anomalies in June-August and April-May, where the first three were positive, and the others were negative. 1C had the highest variation, where for the entire cycle, the anomalies were positive, with a peak of 0.46 in November. However, the anomalies were over 0.3 in three months only.
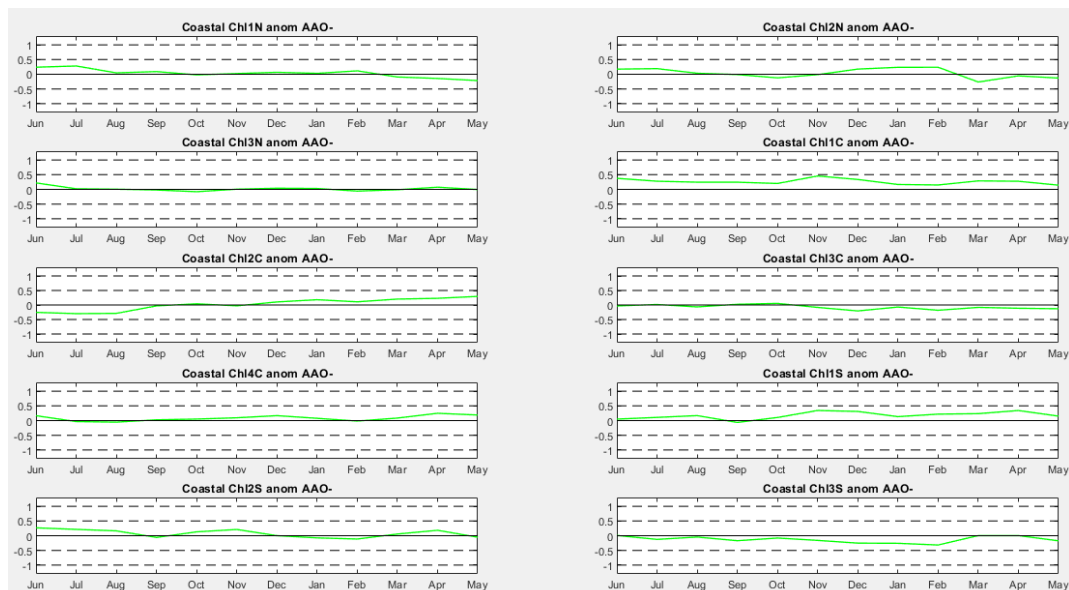
FIGURE 5.42. ANNUAL CHL CYCLE ANOMALY NORMALISED COMPOSITE FOR -AAO LOCATED AT THE COAST IN THE MIDDLE OF EACH SUBSECTION.

102
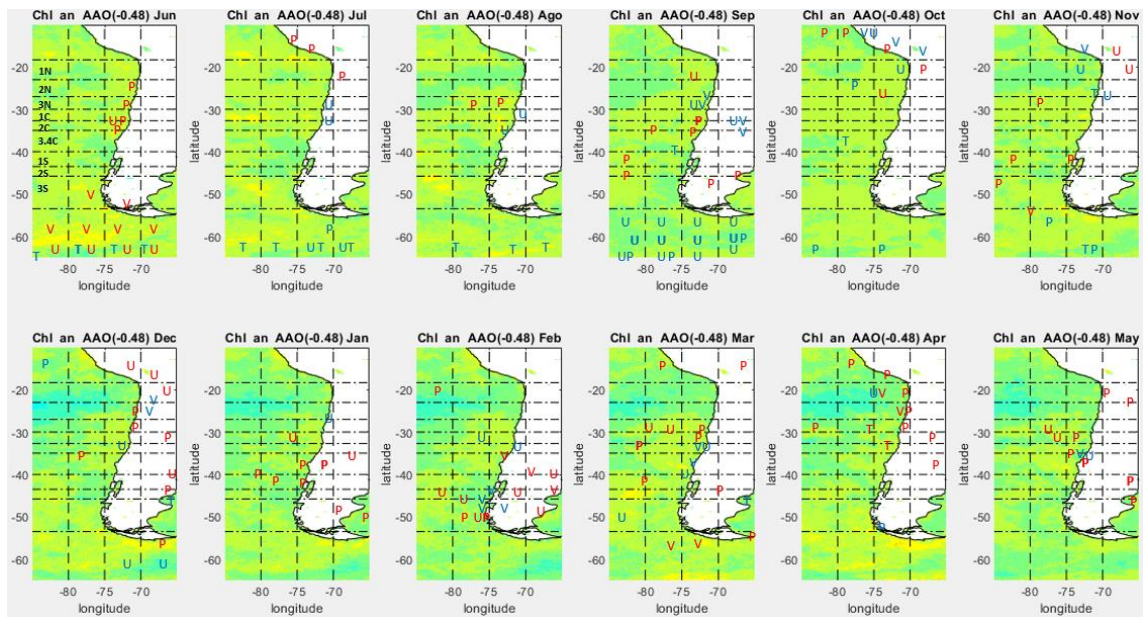
FIGURE 5.43. SCHEMATIC SHOWING THE SIGNIFICANT PHYSICAL ANOMALIES DURING -AAO. FULL DESCRIPTION IN FIGURE 5.32.

The Chl physical parameters (Figure 5.43) showed high PR anomalies with some wind variations. Subsections 1C-3C presented high PR anomalies along with downwelling wind conditions from June to September. The same conditions applied for 4C. These are not consistent with the slight Chl positive anomaly seen in these subsections. However, the 3N's Chl rise in August is compatible with a PR argument if the latter was linked to high runoff and consequent offshore nutrient delivery. The Chl rise experienced in the Drake Passage in March and April can be explained by favourable wind conditions coinciding with a drop in PR. 3S's coast experienced a slight decline in February, which is consistent with downwelling winds.

Overall, the minor Chl anomalies observed are not consistent with the PR and UW anomalies in the three Zones associated with -AAO. This lack of correlation might be related to its Chl composite being made with reconstructed Chl data exclusively based on SST patterns.

f) AAO Comparison:

Figure 5.44 shows that, in general, the Northern and Central Zone, along with 3S, were the most different between both phases of AAO. Chl is enhanced during the AAO's negative phase in these regions from June to November. In the following six months, 1N-3N presented a positive tendency in its ocean strip, primarily due to the AAO's positive rise and a drop in the negative phase. Also, negative Chl differences were found in 3S simultaneously as 1N-3N. Nevertheless, both phases presented limited Chl variations.

103
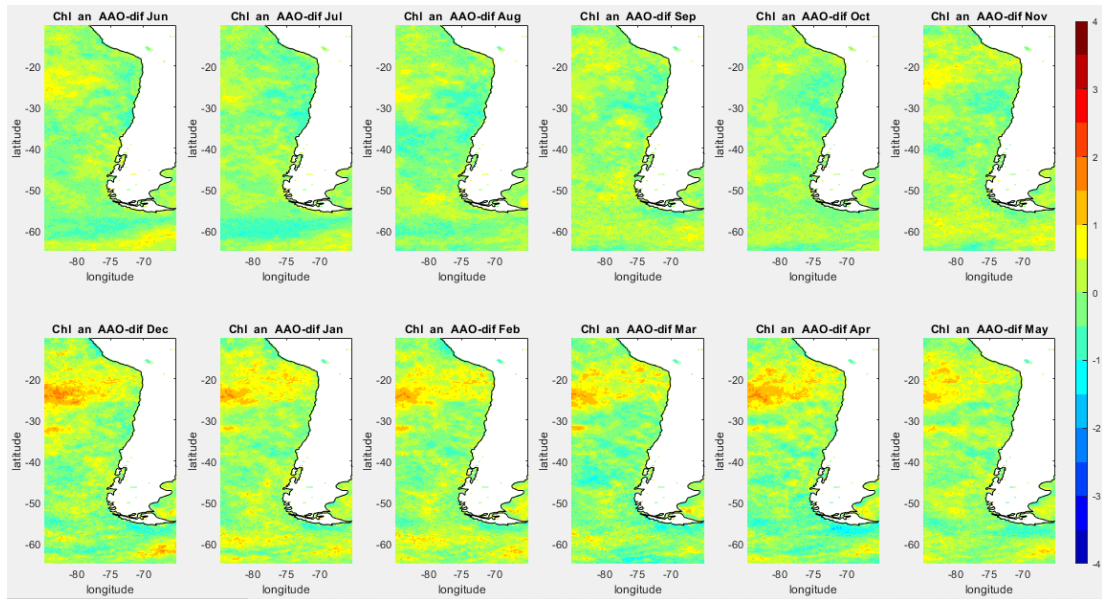
FIGURE 5.44. ANNUAL CHL CYCLE ANOMALY DIFFERENCE BETWEEN THE POSITIVE AND NEGATIVE AAO PHASES.

Figure 5.45 demonstrates that although -AAO was associated with a significant rainfall increment in the Northern and Central Zone, +AAO showed generally higher Chl anomalies. Subsections 1C, 2C and 4C were the only ones where the negative phase had higher Chl anomalies. Furthermore, 1C was the unique subsection that showed a similar pattern between both phases, namely positive Chl anomalies. The other two subsections (2C and 4C) showed a more neutral anomaly variation, while +AAO was associated with more negative Chl anomalies.

Overall, the small effect that AAO has on Chl was seen in the Chl prediction maps, the coastal Chl anomaly plots and the Chl assumption based on the physical parameter composites, with some exceptions. These exceptions are related to the difficulty of predicting not significant Chl anomalies. Additionally, as mentioned in sections 5.2.2.4 and Figure 5.4, the AAO has a high variation that is hard to be represented by an annual composite. Also, the -AAO Chl composite was made with constructed data exclusively.
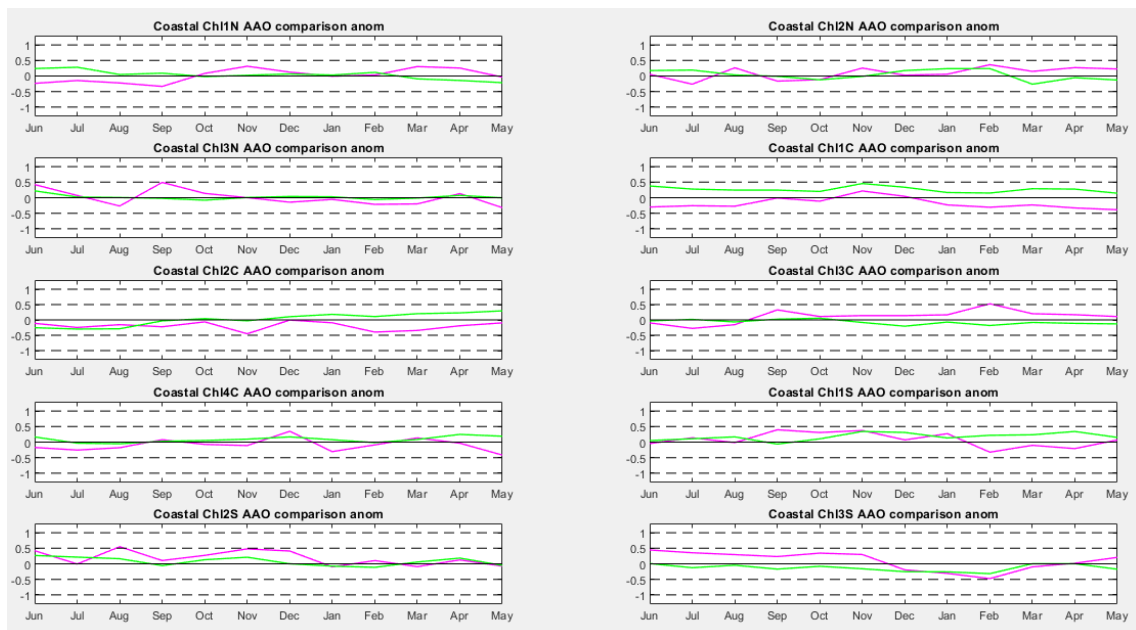
FIGURE 5.45. ANNUAL CHL CYCLE ANOMALY NORMALISED FOR THE POSITIVE (MAGENTA) AND NEGATIVE (GREEN) AAO PHASES LOCATED AT THE COAST IN THE MIDDLE OF EACH SUBSECTION.

5.4. Discussion.

Chl is a complex parameter to predict due to its high variability and dependence on many factors (sections 5.2.1 and 5.3.1; Schollaert Uz et al., 2017). Although the VW showed better correlations with the Chl in the previous chapter, the best predictor of Chl patterns was obtained using SST (Table 5.5). Of course, using only one predictor variable might produce uncertainties in the results with MAE from 0.63 to 0.85. Also, Figure 5.7 (section 5.3.1.2) illustrates that Chl-SST showed more uncertainties in specific places along the coast and in the Drake Passage. Nevertheless, the CCA was able to make an adequate prediction to establish general tendencies in the missing period (1979-2002; Schollaert Uz et al., 2017).

In any case, this procedure can be improved using the SeaWiFS data and adding a second variable that is not dependent on SST. Schollaert Uz et al. (2017) used the SST and the sea surface height. These improvements were not made in this work because the SeaWiFS data fuse with MODIS-Aqua was unavailable when this chapter was written, while the CCA code used here required several modifications to add another variable to the mix.

ENSO and AAO were climate drivers with higher independence from each other. Nonetheless, both significantly impacted the SPSA and, consequently, the Chilean coast. This is supported by Ancapichun and Garcés (2015), DMC (2018), Garreaud et al. (2021) and Aguirre et al. (2021). ENSO can be easily represented on an annual scale, whereas AAO showed a high monthly and yearly variability (section 5.2.2.4 and Figure 5.4). Thus, AAO is less well represented by an annual composite, meaning the results could be less accurate.

El Niño was the climate driver with a significant number of physical anomalies, which can be summarised in positive SST anomalies present the whole year in the Northern Zone, whereas in the Central Zone were in the winter, spring and part of the summer. Also, a PR increase was observed here during the winter. Meanwhile, 3S experienced increased SST and southerly winds with a PR reduction from January to May. These results are consistent with the Regional Summary in section 3.1, the only difference being that the PR should be reduced in the Northern Zone (Garreaud, 2009). La Niña, in particular, showed minor anomalies mostly related to southerly winds increment in the Northern Zone in July and sporadic SST negative anomalies in the Central Zone. These results are a bit lower than those observed in section 3.1. Significantly a PR increase in the Northern Zone during the Summer and an increment of the southerly winds in the Central Zone (Garreaud, 2009; Gomez et al., 2017).

El Niño showed significant Chl anomaly rises that were more noticeable in the Northern and Southern Zone, while the Central was more negative (section 5.3.2.2 and Figure 5.30). La Niña showed a more negative trend with significant Chl anomalies in the ocean strip (Section 5.3.2.2 with Figure 5.33). These results differ from the literature in the Northern Zone, where reports mention a reduction in the Chl by 11 to 48% during El Niño (Iriarte et al., 2000; DMC, 2018), while in La Niña, the Chl concentration should have increased (Thiel et al., 2007).

Only ENSO's Chl variations could be explained by substantial changes in physical parameters (section 5.3.2.1-5.3.2.2 with Figures 5.32 and 5.35). However, Chl anomalies in the subsections 1NT and 2NT were not consistent with the physical variations observed there and in the literature (section 3.1.1), while 2ST and 3ST showed high sensitivity to these variations. This is consistent with the correlations found in chapter 4 and Table 5.5. Furthermore, the poor correlations between the Chl and the physical parameters in the Northern Zone are related to the low variation that Chl had in that Zone product of being an HNLC Zone (Yuras et al., 2005). Thus, this Zone may require particular conditions to have a

Chl enhancement that are more complex. Meanwhile, most physical parameters showed statistically significant correlations with the Chl from 3CT to 3ST.

AAO did not show as many significant physical changes as ENSO, except for the PR rate in its negative phase. These results are consistent with PR increments reported in 1S from December to April during this phase (González-Reyes and Muñoz, 2013; Aguayo et al., 2021; Rahn, 2012). However, the PR had weak relationships with the Chl, except in the Southern Zone. Therefore, AAOs showed a low Chl variation (sections 5.3.2.2 with Figures 5.38 and 5.41). Despite that, the local significant physical anomalies observed did not match with the Chl patterns. This might mean that the physical variables need to have a higher presence in a particular subsection to impact the Chl.

Another possibility is that the composite did not adequately represent the AAO's phases due to its high monthly variation. Also, negative AAO's years were all before 2003, which means that its Chl composite was only made with predicted data, potentially leading to a significant error on that composite. This is relevant because the Chl anomalies that were considered significant were over ±0.5, while the MAE was 0.85. Nevertheless, El Niño only had one year during, 2002-2018, and the results were reasonable.

5.5. Conclusions.

CCA gave a reasonable reconstructed Chl series and pattern despite its high variation. SST produced the best Chl prediction, although the Chl showed a better correlation with VW in the previous chapter. Nonetheless, the SST correlated more consistently along the Chilean coast, reaching slightly higher correlations in the Northern Zone but still insignificant, while VW was extremely weak in 1NT, 2NT and 2CT (Table 5.5). Schollaert Uz et al. (2017) also used the SST and sea surface height to reconstruct the Chl data with adequate results. However, they used Chl data from SeaWiFS and MODIS-aqua.

ENSO and AAO showed a statistically significant correlation with SPSA, having a critical influence on the Chilean coast (Vergara et al., 2017; Ancapichun and Garcés, 2015; DMC, 2018, Garreaud et al., 2021; Aguirre et al., 2021). The ENSO Chl Composites were consistent with the physical parameter composites, except for the Northern Zone implying the Chl reconstruction was accurate enough, despite using a significant amount of reconstructed Chl data (75%). Still, the AAO composites were less accurate due to the high variation of this climate driver, producing minor or negligible Chl variation. This was particularly more significant for the negative AAO, which was made entirely with reconstructed Chl data.

El Niño showed a high Chl variation with a positive trend in the Southern Zone during the warm season driven by southerly winds increment, while the Central Zone exhibited drops (Montecinos and Aceituno, 2003). The Northern Zone did not show significant changes despite a consistent SST rise and a few southerly winds increases, especially 1NT. In contrast, La Niña experienced a Chl drop in the Northern and Central Zone from June to October. Nevertheless, the conditions in the Northern Zone were inconsistent with the favourable variations of the physical variables and the Chl response found in the literature. These unexpected results are likely related to its low concentration and the uncertainties associated with the CCA method, which increases its error with a low Chl variation. The Southern Zone also had a Chl reduction driven by westerly winds anomalies from December to May.

For the positive AAO, the Chl suffered a slight decline in the Northern and Central Zone from June to September, while 2ST and 3ST exhibited a minor increase. 1ST showed a Chl

increment, but this was for September to December, which might be associated with the slight PR reduction observed (5.24; Rahn et al., 2012). These Chl minor variations were inconsistent with the few northerly winds and PR increment observed in July and August in the Southern Zone. Meanwhile, although negative AAO increased the PR patterns significantly in the three Zones with a slightly higher impact in the Central and Southern Zones, these changes did not influence the Chl. However, these results are uncertain.

Most of the significant physical parameters anomalies were synchronous, showing a high dependency on each other, such as VW with SST or UW with PR. Most of the Chl variation observed in ENSO can be explained by the significant climate changes, particularly during El Niño. 2ST and 3ST proved to be more sensitive to these physical parameter changes. On the other hand, 1NT and 2NT did not respond to these climate parameters. These match the correlations obtained in chapter 4. Additionally, the 2NT to 2CT had a low Chl concentration and variation, which is hard to analyse with this technique.

Subsections 1NT and 3ST should be investigated to understand why 1NT was not affected by the physical changes, whereas 3ST is very sensitive to them. 1ST also should be studied because its increase during La Niña was unrelated to significant physical changes. Another aspect that needs to be studied is the effect of El Niño along the three Zones, but especially in the Southern Zone. These conclusions lead to some of the case study choices that will be seen in the next chapter, also focusing on the climate drivers' effect on them.

6. Mechanisms Identification for an Increase of Phytoplankton in Case Study Events [O.3].

6.1. Introduction.

This research's primary focus is to determine drivers that affect phytoplankton behaviour and causes of spatial variability in its productivity along the Chilean coast. O.1 focused on the Chl relationships with physical parameters and how they vary depending on the study's different Zones (Northern, Central and Southern Zone; Figure 3.9). O.2 focused on a macroscale impact established by climate drives, such as ENSO and AAO.

The next step is a microscale analysis which is addressed in this chapter. O.3 aims to study cases more deeply to understand how the climate drivers influence the physical parameters and the phytoplankton in each subsection at a particular moment and derive general relationships. This is significant considering O.1 findings that all Zones exhibited distinct behaviour that warranted further investigation. Thus, the case study selection [O.3.1] was based on Chl outlier events per Zone from 2002 to 2018 using the subsections addressed in chapter 3. Three cases were chosen per Zone using criteria selection that will be explained in section 6.2. Additionally, two case studies were added based on the literature review, giving eleven cases.

Then, the case study analysis [O.3.2] on a case-by-case basis was done, considering all the physical parameters on a weekly scale to give a feasible explanation. This analysis was complemented based on O.1. relationships and findings (chapter 4). These parameters were correlated with Chl through the coast to identify their impact. Also, the two main climate drivers studied in O.2 (chapter 5) were considered a factor. This analysis was complemented by meteorological reports and rivers flow to observe the land-ocean interaction. Finally, all the mechanisms observed in each case were brought together at the end of the chapter.

6.2. Case Study Selection [O.3.1].

The first step was to study the list of Chl outliers developed in chapter 4. The outliers per subsection were delineated by two times the SD from Chl monthly mean (Table 4.3 and 4.4). However, this list was too extensive, so the anomalies divided by SD were used instead. This technique was recommended by von Storch and Zwiers (1999). From here, the term outlier refers to the Chl anomalies over ±2 SD.

Using anomalies instead of the absolute values reduced the outlier numbers but still were a considerable quantity per Zone. As the main idea is to select study cases that have a prolonged impact on time or space, the outliers were grouped to form an event. These events were defined by contemplating these aspects: Criteria 1, extreme Chl anomalies coincided on the same date. Criteria 2, if a particular subsection presented an outlier that extends over more than a month or another subsection presented an extreme anomaly in the following month, it was also considered one event. Criteria 3, either the highest Chl concentration or anomaly per subsection, were considered outliers or an event. Criteria 4, the negative outliers were considered as events independently as well. This was done because only five negative outliers were found. All these conditions were applied per Zone (e.g., Northern, Central and Southern Zone). Criteria 5, extreme terrestrial and ocean events found in the literature, were added to study external factors. These were a dust storm in the Northern Zone and the worst red tide case in the Southern Zone. Both events were particularly intense and unusual.

6.2.1. Northern Zone Case Study Selection.

The outliers that satisfied the ±2 anomaly criteria were forty-five positives and one negative spread over thirty-three dates, having 2.8 outliers per year. These mostly did not happen simultaneously, except for 1NT and 1NO. They did not, therefore, seem to be closely related. Nevertheless, there were distinctly more episodes in 2011 with seven, followed by 2018 and 2005 with six, while 2008 was the only year with no outliers. There was not a clear tendency for months, but March, September and December exhibited six outliers each, while July and January were the months with fewer cases, with two each. The average number of outliers per subsection was 7.7. The coastal subsections showed a similar quantity of outliers, with eight for 2N and 3N, while 1N had ten. Their ocean counterparts were more varied, with nine cases for 1N, seven for 3N and four for 2N, one of them being the only negative outlier.

Twelve events were found to fulfil criteria 1-4 that considered twenty-one dates (Table 6.1). An extra case was added from the literature: the dust event mentioned in chapter 3 that happened from June to July 2016 (section 3.1.1). The additional event did not show any significant Chl anomalies; Still, many subsections showed minor negative anomalies.

From these twelve events, 1N showed the most extensive number of outliers, with only four events, 1N was not over ±1.5. This is likely related to the higher Chl concentration this subsection has and its link with Peru. Six events had a two-month duration, only two had a three-month length, while the rest was one month. Two of these one-month cases showed more than one outlier. The rest of the one-month cases were composed of a maximum Chl anomaly or concentration or the only negative anomaly detected.

TABLE 6.1. EXTREME EVENTS OF CHL ANOMALIES IN SD THAT FULFIL THE CRITERIA IN THE NORTHERN ZONE. THE GREEN VALUES ARE THE ANOMALIES IN SD ABOVE 2, WHILE THE RED ARE BELOW -2. THE ANOMALIES MARKED IN BOLD ARE THE MAXIMUM ANOMALY PER SUBSECTION, WHILE THE ANOMALIES UNDERLINED REPRESENT THE MAXIMUM CONCENTRATION REACHED IN THAT SUBSECTION. THE FINAL ROW SHOWS THE NUMBER OF OUTLIERS PER SUBSECTION.

Event	North	1NT	1NO	2NT	2NO	3NT	3NO
1	1 Feb 2003	2.7	2.64	-0.2	0.23	1.51	1.77
	1 Mar 2003	2.26	2.58	0.24	0.3	0.01	-0.15
2	1 Jun 2003	0.1	-0.75	-1.54	-2.09	0.42	0.8
3	1 May 2005	2.29	2.49	0.15	0.06	-0.16	0.1
4	1 Aug 2005	2.27	1.39	0.48	1.3	-0.57	-0.57
	1 Sep 2005	2.02	2.05	1.12	2.86	-0.84	-0.71
5	1 Sep 2009	-1.34	-0.42	0.41	-0.08	1.91	2.75
6	1 Mar 2011	-0.05	-0.03	0.7	2.53	1.65	-0.26
	1 Apr 2011	0.08	0.52	0.99	1.02	1.53	2.59
7	1 Aug 2011	1.49	-0.51	0.66	1.76	3.59	2.55
	1 Sep 2011	0.02	-0.47	1.06	0.61	1.99	0.67
	1 Oct 2011	2.28	0.8	2.04	1.74	-0.72	1.36
8	1 Dec 2011	0.11	0.56	0.22	0.84	-0.46	2
	1 Jan 2012	0.8	2.49	2.37	1.24	1.6	0.5
9	1 May 2014	-0.56	1.71	2.37	1.76	1.86	0.07
10	1 Jul 2016	0.89	-0.78	-0.76	-0.91	-0.44	-1.57
	1 Aug 2016	-0.51	-1.47	1.41	-0.92	0.52	-0.08
11	1 Apr 2017	2.13	-0.69	1.61	-0.64	2.72	-0.29
12	1 Jun 2018	0.95	3	0.79	2	0.71	1.66
	1 Jul 2018	-0.34	2.68	0.35	1.67	0.26	-0.08
13	1 Oct 2018	1.68	1.55	1.38	-0.25	2.11	-1.18
	1 Nov 2018	3.04	1.07	2.09	0.76	-1.28	-1.64
	1 Dec 2018	2.66	0.52	1.79	1.71	0.6	0.31
	N° of Outliers	9	7	4	3	4	4

The events highlighted in yellow in Table 6.1 are the case studies selected for the Northern Zone. Despite event 10 does not show any outlier was selected for being the dust event selected by Criteria 5. The case study criteria selection prioritised events in the coastal strip (NT) rather than the open ocean (NO). Also, the events with at least two-month length were

prioritised to select the other three cases. Consequently, events 2, 3, 5, 9, and 11 were discharged from Table 6.1. At the same time, events 6 and 12 were thrown out because the outliers were only part of the ocean strip.

For the remaining, the main focus was to keep extreme cases of each coastal subsection ideally. Also, the selection criteria concentrate slightly more on 1N due to higher Chl variation and less sensitivity to the other physical variables (section 5.5). Therefore, events 1, 7 and 13 were chosen over 4 and 8. Event 1 was selected for containing the highest Chl concentration on 1NT (2.7 SD 5.25 mg m^{-3}). Event 7 was the second Case chosen because it has the highest Chl concentration in 2NT and 3NT, plus the highest anomaly for 3NT. Finally, event 13 was selected for containing outliers in the three subsections on the coastal strip and the highest 1NT anomaly (3.04 SD 3.89 mg m^{-3}). Besides, events 7 and 13 had a length of three months.

6.2.2. Central Zone Case Study Selection.

The number of outliers in this Zone was fifty-nine positive and three negatives spread over forty-two dates, having 3.5 events per year. These numbers indicate that more outliers occurred on the same dates than in the Northern Zone. This was expected considering that the Central Zone has four subsections instead of three, which increases the number of outliers and the probability of having more cases in the same month; Also, 3C-4C have a considerably higher variation than the Northern Zone. Indeed, the Central Zone almost had the same amount of outliers as the previous one per subsection, 7.8 per subsection.

TABLE 6.2. EXTREME EVENTS OF CHL ANOMALIES IN SD THAT FULFIL THE CRITERIA IN THE CENTRAL ZONE. TABLE 6.1 FOR THE FULL LEGEND.

Event	Central	1CT	1CO	2CT	2CO	3CT	3CO	4CT	4CO
1	1 Feb 2003	0.16	0.13	0.94	1.58	2.26	-0.53	0.88	-0.65
	1 Mar 2003	-0.07	0.05	-0.03	2.13	1.82	1.49	0.52	1.09
2	1 Apr 2004	0.22	-0.72	1.20	-0.68	-0.19	-0.66	-2.35	-1.42
	1 May 2004	0.95	0.76	2.21	-0.08	0.60	-0.23	0.48	0.63
3	1 Oct 2004	2.17	1.88	1.76	0.26	-0.02	-1.49	-1.24	-1.42
	1 Nov 2004	3.21	1.27	1.98	0.81	1.13	-0.06	0.44	-1.40
4	1 Mar 2005	0.78	1.04	3.32	0.34	-0.40	-0.12	0.44	-0.98
	1 Apr 2005	-0.01	1.03	1.82	0.36	1.92	0.35	2.36	1.76
5	1 Sep 2005	0.15	1.13	2.66	2.47	1.10	1.69	0.09	-0.11
	1 Oct 2005	0.64	1.05	1.63	1.54	2.26	0.30	0.91	-0.27
6	1 Nov 2007	0.14	0.89	2.17	0.71	1.59	-0.30	0.90	0.33
	1 Dec 2007	0.85	1.74	1.41	-0.01	0.19	-0.01	1.77	0.11
7	1 Aug 2008	-0.83	-0.81	-0.72	-1.97	-1.15	-2.03	-1.49	-1.79
8	1 Nov 2008	0.14	1.02	0.48	2.34	0.82	2.82	0.19	1.65
9	1< Sep 2009	2.26	1.85	0.02	0.67	-1.08	0.56	0.63	3.01
	1 Oct 2009	-0.25	1.43	1.46	1.39	1.28	-0.51	2.17	0.60
10	1 Aug 2010	-0.04	1.82	0.48	2.79	0.34	0.20	-0.08	0.49
	1 Sep 2010	0.28	-0.20	-0.48	0.21	1.78	1.50	2.01	0.80
	1 Oct 2010	-0.62	-1.15	-0.93	-0.76	-0.20	0.13	0.95	2.50
11	1 Dec 2012	-0.66	-0.66	-0.38	-0.60	-1.70	-1.76	-2.32	-1.13
12	1 Feb 2014	3.36	3.18	-0.37	-0.97	-0.62	-1.16	-0.40	3.08
	1 Mar 2014	2.62	1.62	0.11	-0.13	-0.68	-0.67	-0.54	1.08
13	1 Jan 2015	-0.60	0.22	1.02	2.99	2.60	3.27	0.10	0.84
	1 Feb 2015	-0.30	0.23	1.06	2.44	1.70	2.19	-0.56	-0.60
14	1 Nov 2015	0.71	1.63	0.23	0.55	-0.16	0.05	-0.30	-0.14
	1 Dec 2015	1.00	1.38	1.67	0.27	1.92	2.35	0.74	1.65
15	1 Mar 2016	-0.34	-0.91	-0.17	0.88	1.30	2.37	2.26	2.22
	1 Apr 2016	-0.37	0.83	2.28	1.20	1.47	0.76	0.63	-0.58
16	1 Apr 2018	-1.75	-1.21	-0.95	2.92	-0.35	3.23	0.05	-0.43
	1 May 2018	-0.75	-0.54	0.42	3.46	2.23	3.71	-0.34	1.79
	1 Jun 2018	-0.31	1.66	-0.17	2.08	2.77	3.00	0.83	2.51
	N° of Outliers	5	1	5	9	5	9	6	5

2018 presented nine outliers, becoming the year with more, which all belong to the same event from April to June (Table 6.2). 2015 had seven outliers, of which three happened in 3CO, followed by 2005 and 2016 with six. 2012 and 2002 did not present outliers. These

110

outliers happened more frequently during the Austral summer-autumn, with seven cases from February to June, except for April with five. In contrast, July showed only two cases, while December and January had three. Although the outliers were estimated, eliminating the seasonal behaviour using the anomalies divided by SD, they were found more frequently during the warmer season.

The number of outliers per subsection was more dissimilar than in the Northern Zone. In the coastal strip, ten cases were in 4C, eight for 1C and 2C, while 3C only had five. Two of the ten cases in 4C were negative. The ocean strip showed several outliers in 2C and 3C with eleven cases each, seven for 4C and only two for 1C.

Concerning the extreme events that fulfilled criteria 1-4 (Table 6.2), sixteen events were found where ten months simultaneously presented more than two subsections with extreme episodes. Five of these had more than two subsections affected in the same month. This suggests a stronger link between each subsection, but it is also related that this Zone has eight subsections. The majority of the events were two months long, and only three were one month. As in the Northern Zone case, two events whose duration was more than two months in a row were detected. As mentioned before, 2CO and 3CO showed the highest number of outliers, three of which were part of event 16. On the other hand, 1CO showed a single outlier, and the other subsection had five or six.

The events selected for the Central Zone are highlighted in yellow in Table 6.2. In the Northern Zone, the primary selection criteria for the three cases were that they were concentrated more on the coastal strip, and the events were two or more months in duration. Hence, single month events such as 7, 8 and 11 were thrown away (Table 6.2). However, event 16 was the exception due to the very high and unusual concentration on 3CO found in the preliminary analysis in section 4.3.1, which is the highest Chl concentration detected per subsection. Furthermore, this event has the maximum anomaly and concentration in 2CO and 3CT. Despite event 10 also having a length of three months, it was eliminated because the outliers' location had a similar distribution (2CO, 4CT and 4CO) to event 16 (2CO, 3CT, 3CO and 4CO). The same happens with event 13 (2CO, 3CT and 3CO), and the idea covers different scenarios.

Event 4 was chosen because it contains the highest anomaly in 2CT and 4CT plus the highest concentration in 1ST, which is event 3 from the Southern Zone (Table 6.3). Neither of the two events chosen has a 1CT outlier, so the final Case was selected under that condition. The options were events 3, 9 and 12. Event 12 was selected over the other two because it has four outliers, while events 3 and 9 have two and three, respectively. Furthermore, event 12 has the maximum anomalies for 1CT, 1CO and 4CO.

6.2.3. Southern Zone Case Study Selection.

The Southern Zone had one negative and fifty-one positive outliers, spread out over thirty-two dates, having three outliers per year on average. This Zone concentrated its outliers in fewer dates, which means that more extremes happen simultaneously, even more than the Central Zone. This could be related to the fact that this Zone has the highest quantity of outliers per subsection with 8.7, increasing the probability of having more than one outlier on the same date.

In this region, the annual outlier distribution was diverse. 2012 was again a year with no extremes, but 2002, 2006, 2013 and 2018 only have one outlier, concentrating the cases on a few dates. On the other hand, 2014 had more outliers with eight. This is a significant difference from the five outliers found in 2004, the second year that most outliers have. Six years have four, and the rest varies between three and two. These extreme Chl values

happen more often in the second half of the year. November and December have six outliers each, while from July to September and April have five. March showed four, whereas the other months exhibited three outliers. This shows that although this Zone, especially 3S, does not have a pronounced seasonal cycle, and the outliers were calculated using Chl anomalies, a tendency here was more evident than in other Zones.

The number of outliers per subsection was more homogeneous than the other Zones. 2S had eight outliers in both strips. 1SO and 3ST shared the same amount with nine. 3SO had the highest quantity with eleven, while 1ST had seven, including one negative outlier. These match with O.2 findings,.which were that 3S have an extreme sensitivity to climate drivers, especially in the open ocean, while 1S in the coastal strip was the opposite (section 5.5).

TABLE 6.3. EXTREME EVENTS OF CHL ANOMALIES IN SD THAT FULFIL THE CRITERIA IN THE SOUTHERN ZONE. TABLE 6.1 FOR THE FULL LEGEND.

N°	South	1ST	1SO	2ST	2SO	3ST	3SO
1	1 Mar 2003	2.08	2.21	1.71	0.28	1.05	0.47
	1 Apr 2003	1.96	1.05	3.30	2.51	0.85	1.09
2	1 Aug 2004	1.28	1.46	2.66	2.82	2.49	1.21
3	1 Apr 2005	2.73	0.59	0.74	-0.87	-0.04	-0.28
4	1 Sep 2006	1.27	2.41	0.34	-0.12	-0.18	-0.54
5	1 Dec 2008	1.54	0.07	2.18	0.53	2.74	3.35
6	1 Jun 2009	2.76	2.60	-0.37			
	1 Jul 2009	0.19	0.54	2.32	3.07	0.04	1.57
7	1 Mar 2010	-1.60	0.64	0.94	2.43	1.71	2.95
8	1 Jun 2010	-0.11	-0.15	3.39	-0.47		
9	1 Dec 2010	-0.14	2.35	-0.60	-0.37	-0.44	-0.53
	1 Jan 2011	0.24	2.37	1.07	2.14	0.56	0.49
	1 Feb 2011	0.35	3.07	0.18	-0.17	-0.03	-0.78
10	1 Jul 2014	-0.72	-0.85	1.05	-0.48	2.84	2.33
11	1 Oct 2014	-0.42	1.49	0.09	-0.05	1.05	2.29
	1 Nov 2014	-0.27	2.21	2.26	3.72	0.52	3.66
12	1 Sep 2015	0.27	-0.26	1.46	2.74	3.19	3.46
	1 Oct 2015	0.97	1.42	1.52	-0.26	0.88	2.12
13	1 Feb 2016	0.65	-0.91	0.44	-0.74	-0.55	1.26
	1 Mar 2016	1.97	0.20	1.47	0.05	0.39	-0.16
	1 Apr 2016	-0.16	0.66	-0.06	0.58	1.15	2.60
	1 May 2016	1.24	1.25	1.00	1.56	2.37	1.41
14	1 Aug 2016	-0.89	-0.94	-0.98	-0.77	-0.02	2.44
	1 Sep 2016	0.89	-0.81	2.20	-0.68	0.54	0.51
15	1 Jan 2017	-2.06	-1.11	-1.60	0.16	-1.12	0.08
	N° of Outliers	4	7	7	7	5	9

Considering the events grouped by criteria 1-4 (Table 6.3), fifteen events were found, gathering twenty-one dates. As the Northern Zone, an extra event was added based on chapter 3 as an external factor following criteria 5. This event was an intense red tide produced by a powerful El Niño and pollution from salmon farming in 1S between February to May 2016 (Buschmann et al., 2016; section 3.1.3). It has Chl extreme anomalies, but these were in 3S. Chl measured by MODIS-aqua can read red tide cases, but the algorithm could struggle a bit near the shore where they usually develop (Yang et al., 2018), and it does not differentiate a typical Chl signal over a red tide episode (Armijo et al.,2020).

Excluding the extra event, eleven months had more than two subsections with extreme episodes simultaneously on twenty-one dates, with four having more than three subsections (Table 6.3). This suggests an excellent oceanographic linkage among the subsections or a large scale atmospheric drivers in this Zone. In contrast, there were eight cases in a single month, which was more than in the other Zones. Note also that five events were found of two months duration and just one event of three months. As mentioned before, the subsection had a relatively similar number of outliers, except for 3SO with nine and 1ST that had only four, followed by 3ST with five; the rest had seven outliers each.

Similarly to the other Zones, the events selected are highlighted in yellow in Table 6.3 using the same approach. It prioritised coastal strip subsections, especially 1S and 3S, due to chapter 5 findings and selected events with longer durations. Events 2-5, 7, 8, 10, and 15 were dismissed. In any case, event 3, which has the highest Chl concentration in 1ST, will be studied as part of a selected event in the Central Zone, related to event 4 in Table 6.2.

Event 13 was the first case selected because it is the red tide episode mentioned in section 3.1.3. Event 11 was the next selected because 2SO in November 2014 was so high that it was detected in chapter 4 statistical analysis (section 4.3.1). Besides that, this is the event with more outliers. Two of the five are the highest Chl concentrations, and anomalies detected there.

O.2 conclusions (section 5.5) mentioned that 1S and 3S should be studied in more detail. For that reason, the selection for the other two case studies was concentrated on them. For 3ST, event 12 was chosen because it contains four outliers, where one of them is the highest anomaly and concentration in 3ST during an extreme El Niño. Therefore, this case study will help to reinforce the O.2 findings. Events 1 and 6 were the possible options for a 1ST study case. Both have similar behaviours with high Chl concentration in 1S strips followed by high variation in 2S strips the next month. The pivotal difference between the two was that event 1 has 2ST's highest Chl concentration, while event 6 has the maximum anomaly in 1ST. Since a 1ST event was also considered in the Central Zone case, event 1 was selected to prioritise 2ST.

6.3. Case Studies Analysis [O.3.2].

In this section, the eleven cases were discussed split by Zone. Each case was studied using PR, SST, VW, UW, SLP and Chl monthly and weekly maps. These are the same variables studied before, but SLP was added to observe the SPSA effect better. Table 6.4 shows a summary indicating why they were selected. Table 6.4 relabel the events into cases. Therefore, the selected Northern Zone events 1, 7, 10 and 13 now are Cases 1 to 4, while Central Zone events 4, 12 and 16 are Cases 5 to 7, and Southern Zone events 1, 11-13 are Cases 8 to 11, keeping the chronological order per Zone.

As O.2 in chapter 5, both Chl time series data were extracted using Giovanni, whereas Copernicus was used for the physical parameters. However, the weekly scale was calculated using hourly data. Chl has a higher resolution with 0.04° in both directions, while the physical parameters' resolution is 0.25°.

The monthly maps were displayed using the anomalies from 2002 to 2018. Nonetheless, absolute values were used for weekly maps due to the complexity of calculating the anomalies on that scale. These maps were built to focus on each Zone. In this way, it was easier to understand what was happening in each case study and their surroundings and then compare them per Zone. Therefore, the Northern Zone case maps show from the Peruvian Zone to 1C (Figure 6.2); the Central Zone maps show the territory between 3N and 1S (Figure 6.16), while the Southern Zone maps are from 3C to the Drake Passage (Figure 6.29). Each case was extended at the beginning and the end by a month, giving a temporal context.

The map analysis per case study was based on O.1 variable relationships and findings (Table 4.9 or 5.5 and section 4.6). Also, the two primary climate drivers studied in O.2 of ENSO and AAO were considered (section 5.5). Using Spearman in their weekly scale, all the physical parameters were correlated with the Chl using only the case's core dates to contrast the map

analysis. The correlated coastal cross-sections are constructed from 0.25° to 2.0° wide with a 0.25°step oceanwards. As the Chl has missing values but better resolution, their available values were averaged to fit the 0.25° interval. The correlations used for these case studies were 0°-0.5° from the coastline, except for the cases focused on the ocean strip (0.75°-2°). Finally, when the data was available, this analysis was supplemented with extra information to investigate the terrestrial-ocean interactions affecting Chl, such as outflow from rivers. The outflow data was extracted from Central Climate Resilience Research (CR2, 2018), and measured by the General Directorate of Water Management (DGA). Also, monthly meteorological reports were consulted to contrast the climate driver's effect on the territory and determine how accurate the physical parameters are. These reports were developed by Universidad de Chile researchers Aceituno et al. (1995-2014) and the Meteorological Directorate of Chile (DMC; 2013- onwards).

TABLE 6.4. CASE STUDIES SUMMARY INDICATES THE ZONE, SUBSECTIONS AFFECTED, PERIOD, ENSO AND AAO ANNUAL INDEX (A), MONTHLY VARIATION, AND THE REASONS FOR SELECTION. THE ANOMALIES ARE IN SD UNITS.

Zone	Case	Subsections	Start	End	ENSOa	ENSOm	AAOa	AAOm	Comments
N	1	1NTO	Feb-03	Mar-03	2002 0.72	F(0.7) M(0.5)	2002 -0.48	F(-0.4) M(-0.2)	Highest [Chl] [5.3 mg m^{-3}] in 1NT; moderate El Niño (0.72)
	2	1-3NT, 3NO	Aug-11	Oct-11	2011 -0.68	A(-0.7) S(-0.9) O(-1.1)	2011 0.04	A(-1.2) S(-1.3) O(0.4)	Highest [Chl] [3.0 mg m^{-3}] & anom (3.6) in 3NT; highest anom 2NT (2.0); moderate La Niña (-0.68), strong -AAO these months
	3	1-2NT	Jul-16	Aug-16	2016 -0.27	J(-0.4) A(-0.6)	2016 0.25	J(0.4) A(-0.7)	Dust storm case w/t negative anomalies in the whole Zone; weak La Niña (-0.27)
	4	1-3NT	Oct-18	Dec-18	2018 0.55	O(0.9) N(0.9) D(0.8)	2018 0.46	O(0.5) N(1) D(0.9)	Highest anom in 1NT (3.0); weak El Niño (0.55), strong +AAO these months
C	5	2,4CT, 1ST	Mar-05	Apr-05	2004 0.55	M(0.5) A(0.4)	2004 0.24	M(0.2) A(0.4)	Highest anom in 2CT (3.3) & 4CT (2.4); highest [Chl] 1ST [6.2 mg m^{-3}]; weak El Niño (0.55) and +AAO (0.24)
	6	1C, 4CO	Feb-14	Mar-14	2013 -0.21	F(-0.5) M(-0.2)	2013 -0.21	F(0.3) M(0.5)	Highest anom in 1CT (3.4), 1CO (3.2) & 4CO (3.1); weak La Niña and -AAO (-0.21,-0.21)
	7	2-4CO, 3CT	Apr-18	Jun-18	2017 -0.46	A(-0.4) M(-0.1) J(0.1)	2017 0.48	A(-1.2) M(-0.1) J(0)	2-3CO highest [Chl] [2.3, 9 mg m^{-3}] & anom (3.5, 3.7); highest anom 3CT (2.8); weak La Niña (-0.46), 1mth with strong -AAO.
S	8	1-2STO	Mar-03	Apr-03	2002 0.72	M(0.5) A(-0.1)	2002 -0.48	M(-0.2) A(0.2)	2ST highest [Chl] [7.6 mg m^{-3}] & anom (3.3); moderate El Niño (0.72), weak -AAO (-0.48).
	9	1-3SO, 2ST	Oct-14	Nov-14	2014 0.47	O(0.4) N(0.7)	2014 0.40	O(0) N(-0.5)	2-3SO highest [Chl] [4.2, 3 mg m^{-3}] & anom (3.7, 3.7); weak El Niño (0.47), 1mth moderate -AAO.
	10	2SO, 3STO	Sep-15	Oct-15	2015 1.87	S(2.1) O(2.3)	2015 0.76	S(0.5) O(-0.2)	Highest [Chl] [7.3 mg m^{-3}] & anom (3.2) in 3ST; very strong El Niño (1.87), moderate +AAO (0.76).
	11	1STO	Feb-16	May-16	2015 1.87	F(2.3) M(1.7) A(1) M(0.4)	2015 0.76	F(1.1) M(2) A(0.1) M(0)	The worst red tide episode in Chile; extreme El Niño (1.87) and +AAO (0.76).

6.3.1. Northern Zone.

The Northern cases are three Chl anomalies (Case 1, 2 and 4) plus a dust storm event (Case 3). 1NT was affected in three cases, despite having a low variation but high concentration (Table 4.3), indicating that it is the most productive subsection. Case 1 exhibited the highest Chl concentration over 1NT. Case 2 had the highest Chl concentration in 2NT and 3NT, plus the highest anomaly for 3NT. Finally, Case 4 was selected as it included significant anomalies across three subsections on the coastal strip, including the highest anomaly detected in 1NT.

6.3.1.1. Case 1:

This case showed the highest Chl concentration in 1NT, which was 5.25 mg m^{-3}, or 2.69 over SD, as an average for the whole subsection. The event started in February 2003 and continued for two more months but with a decline in the monthly Chl mean (3.79 and 3.09

mg m^{-3}). Also, a moderate El Niño (0.72) marked this year, with a peak between November to December 2002 (1.2 and 1.4 ENSO index anomalies). Thus, El Niño was entering its final stage during the months this case happened (Table 6.5).

This event is linked to a fairly sudden cessation of the preceding El Niño, with the return of strong alongshore winds through January-March leading to significant upwelling and so enhanced Chl concentration. This can be seen through the local SST reduction consistent with the Chl pattern (Figure 6.2), which is also coherent with Chl~SST negative correlations observed off Peru and in 1N (Figure A.3.1). Although the climate variables were relatively stable in April, displaying a slightly higher SPSA (0.59) with its core closer to the north, which could have produced a second wave, the Chl increment was not as strong as during the first peak, dissipating rapidly in the third week of April (Figure 6.1).

TABLE 6.5. CASE STUDY 1 SUMMARY INDICATING THE SUBSECTIONS AFFECTED THEIR CHL ANOMALIES IN SD, ENSO, AAO AND SPSA MONTHLY VARIATION, AND ADDITIONAL COMMENTS.

Subsections	Date	Chl (anom)	ENSOm	AAOm	SPSAm	Comments
1NT, 1NO	Feb-03	2.7, 2.6	0.74	-0.36	0.50	Highest [Chl] [5.3 mg m^{-3}] in 1NT (Feb); moderate El Niño
1NT, 1NO	Mar-03	2.3, 2.6	0.45	-0.19	-0.38	(0.72) weak -AAO (-0.48) & a low SPSA (0.07).
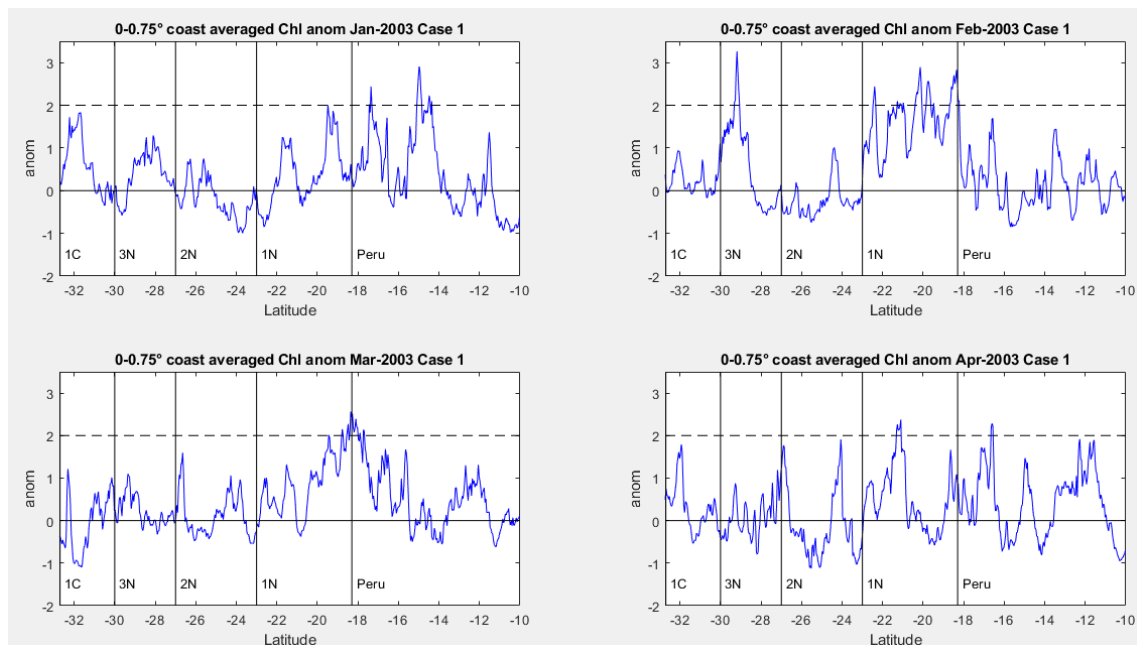
FIGURE 6.1. CASE 1 MONTHLY CHL CROSS-SECTIONS FROM THE COAST TO 0.75° OCEANWARD USING THE ANOMALIES DIVIDED BY SD ON THE PERUVIAN, NORTHERN ZONE AND 1C. THE DASHED LINE DRAWS ATTENTION TO THE SECTIONS WITH SIGNIFICANT CHL ANOMALIES, SUCH AS IN THE MIDDLE OF PERU IN JANUARY, THE HIGH ANOMALY IN 1N WITH A PEAK IN 3N DURING FEBRUARY, AND THE HIGH CHL ANOMALY IN THE BORDER OF PERU-1N IN MARCH.

As seen in Figure 6.1, January showed a high Chl signal off Peru, with two peaks in 1N at 21.5°S and 19°S latitude. This is consistent with the weekly maps of each variable, where a narrow Chl concentration appeared at the 1N coast during the second half of January, along with high-speed southerly winds further north in Peru. In February, the Chl presented a substantial anomaly in 1N, covering the whole coast and part of the ocean strip (Figure 6.1), while 3N showed a particular peak near 29°S latitude.

The weekly scale maps of Figures 6.2 and 6.3 showed how the Chl signal increased during the first week of February at the start of this case. The following week the Chl peaked, focusing on the middle of 1NT (Figure 6.2). It continued at a similar strength for another week but moved towards the Peruvian frontier (Figure 6.3). Also, a high Chl concentration appeared in 3N that week, along with a significant signal in Peru, as shown in Figure 6.1.

The VW showed a slight increase in 1N with 4 m s^{-1} onshore in the first week of February. During the second week, 1N retained the VW conditions for the previous week, while in the third, it showed speeds above 6 m s^{-1} in the 1N middle section, which might enhance the Chl in 1N. A high VW was also observed near the Chl rise in 3NT. O.2. findings determine that 1N is not as sensitive to ENSO as other subsections (section 5.5), and O.1 correlations indicate that 1-2NT were the sections with a lower sensibility to the VW component (section 4.5). However, VW is considered the main trigger for this case, even though their direct correlations with Chl were not high. One reason for such a weak relationship is that the Chl signal described these weeks were northwards of the high VW position (Figure 6.2 and 6.3). Interestingly, these winds were not part of SPSA.
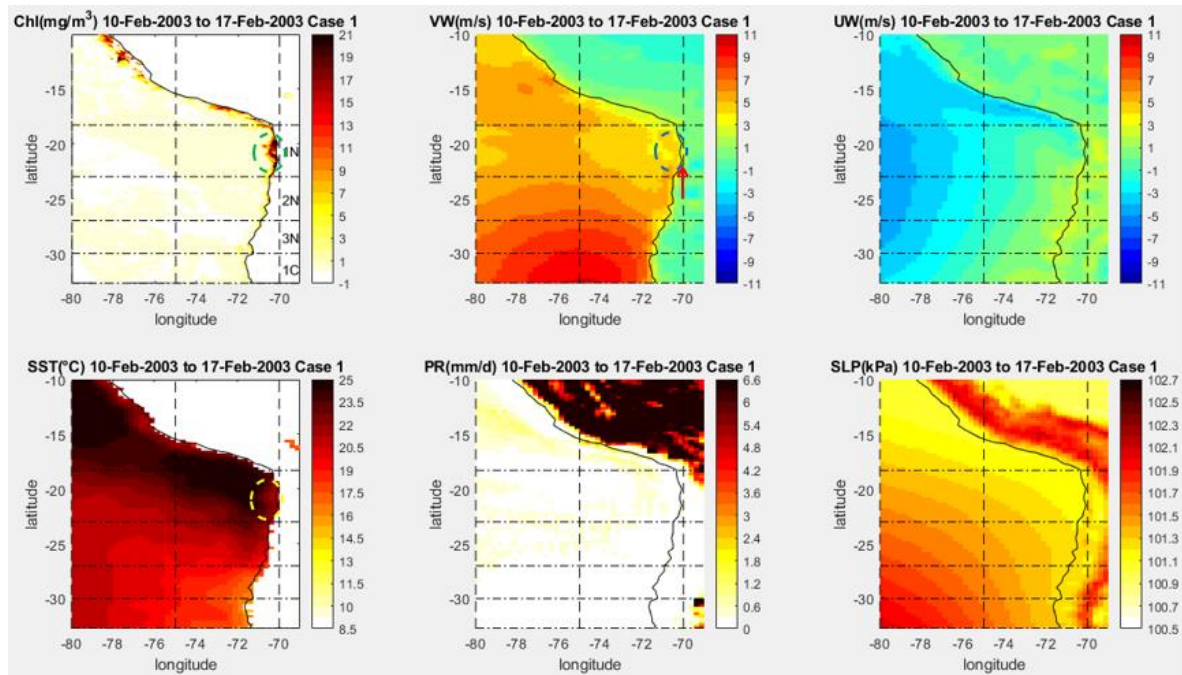
FIGURE 6.2. CASE 1 CHL, VW, UW, SST, PR AND SLP WEEKLY VALUES ON THE NORTHERN AND PERUVIAN ZONE FOR CASE 1 PEAK FIRST WEEK BETWEEN 10TH-17TH FEBRUARY 2003. THE DASHED CIRCLES HIGHLIGHT THE CHL INCREMENT LOCATION IN THE CHL, SST AND VW PANELS. THIS HELPS TO IDENTIFY THAT THE SST DROP HAS THE SAME SHAPE AS THE CHL INCREMENT, WHILE THE STRONGER SOUTHERLY WINDS, HIGHLIGHTED WITH A RED ARROW, ARE LOCATED BELOW THE CHL. THE SLP PANEL SHOWS THAT THE SPSA'S CORE IS LOCATED AT 30°S WITH A WEAK EFFECT ON THE WINDS IN 1N.

The February SST anomalies estimated in this research were a bit higher in 1NT, while the meteorological reports mentioned that their anomalies were 2°C lower than for a typical year in the Northern Zone (Aceituno et al., 2015). However, the weekly maps showed a 3°C reduction in the section where Chl rose in the second week (Figure 6.2). Thus, the drop in the SST was likely associated with the upwelling that produced the Chl rise.

Finally, a spread-out drizzle appeared in the open ocean in 1NT over the whole of February. Nonetheless, meteorological reports pointed out that El Niño 2002-2003 significantly reduced the PR on the altiplano region in the 1-2N subsections from January to April, while the coastal strip also experienced a lack of PR as it typically does (Aceituno et al., 2015). Therefore, this likely is an error within ERA5, which has some trouble with rainfall quantities in arid regions (Tang et al., 2020).

The next month, Chl anomalies were only in the section surrounding 1N and Peru and along the ocean offshore of Peru (Figure 6.1). The significant southerly wind anomalies were weaker than in the last month and were in similar areas to the Chl anomalies, likely related to the SPSA drop (-0.39). Due to the ending of El Niño (0.45), SST showed more Chl-favourable conditions in 1N, but SST was even lower in 2N and 3N with a big SST difference with its

116

ocean strip. Thus, the physical variables were weaker this month, reducing the Chl influence area to the 1N top section. Although SST anomalies were more favourable than the previous month, the VW was weaker, which might produce a Chl decrease ceasing the upwelling. This extension will depend on nutrient exhaustion or depredation by zooplankton.
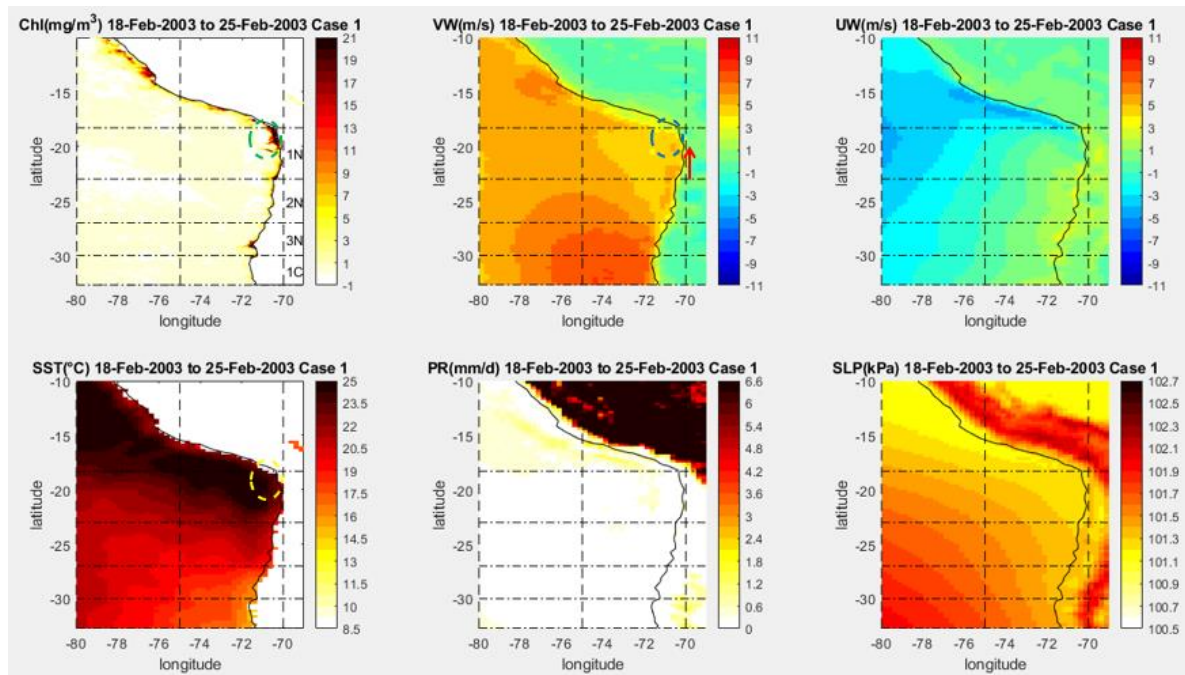
FIGURE 6.3. CASE 1 CHL, VW, UW, SST, PR AND SLP WEEKLY VALUES ON THE NORTHERN AND PERUVIAN ZONE, SHOWING CASE 1 PEAK SECOND WEEK BETWEEN 18TH-25TH FEBRUARY 2003. THE DASHED CIRCLES HIGHLIGHT THE CHL INCREMENT LOCATION IN THE CHL, SST AND VW PANELS. HERE THE CHL SIGNAL MOVED NORTHWARD. THE SST DROP SHARES PART OF THE CHL INCREMENT LOCATION, WHILE THE STRONGER SOUTHERLY WINDS, HIGHLIGHTED WITH A RED ARROW, ARE LOCATED SOUTH OF THE CHL AS IN THE PREVIOUS WEEK. THE SLP PANEL SHOWS THAT THE SPSA CONTINUED WITH A WEAK EFFECT ON THE WINDS 1N.

The Chl signal anomalies were weaker in April (Figure 6.1), moving to the centre of 1N and spreading to the ocean strip, while the Chl patch anomalies near Peru that were there from January started to fade away. The other variables showed lower anomalies than in previous months (maps not shown). The exception was the VW component that continued with significant anomalies around Peru, but it was low in 1N. In contrast, the UW had large values near the 1-2N zone limits. On the other hand, the SLP anomalies were particularly elevated in this subsection, as the SPSA (0.59) drifted to the north, as it does at this time of year (Aceituno et al., 2015).

The UW increment is consistent with meteorological reports that mention a dust movement that happened in the first week of April as the product of a low-level jet stream from the Andes toward the coast from 22.5 to 23.5°S (Aceituno et al., 2015; Garreaud and Muñoz, 2005). This event may help to increase the phytoplankton, explicitly considering that 1N and 2N are HNLC regions. This is consistent with O.1 findings where UW and PR were the variables more relevant to 1NT's Chl variation. Nevertheless, they seem not to be the main trigger, especially considering that higher PR and dust movements occurred this month, and 1N did not exhibit a Chl increment. Thus, a persistent dust event is needed to impact the phytoplankton.

In conclusion, the Chl increment resulted from a rapid increase of the southerly winds due to a sudden return to normality after a moderate El Niño, causing the highest Chl concentration in 1N. These conditions were from January to March, but only February experienced a high Chl concentration that continued into the first weeks of March. Peru also exhibited a significant Chl signal that could enhance the Chl in 1NT.

Despite VW being the main trigger, the VW~Chl correlation was not significant (Figure A.3.1). This was because the locations of anomalies in both variables were not identical, as mentioned in Figures 6.2 and 6.3. One possible explanation could be an error of working with different scale resolutions that produce this mismatch, but it could also mean that it takes a little time for changes to force conditions to impact the Chl field in the prevailing current. Although the easterly winds produced some dust inputs through the ocean, this did not have any apparent influence on the Chl signal. Therefore, prolonged and more intense dust inputs are likely to be needed to have an impact on phytoplankton production. This will be studied in more detail in Case 3 (section 6.3.1.3).

6.3.1.2. Case 2:

This case contains significant Chl anomalies in the three Northern subsections. This event initiated in August 2011 with 3NT's highest Chl anomaly followed by its highest concentration the following month, which were 3.6 times SD (1.77 mg m^{-3}) and 3.00 mg m^{-3}(1.99 times SD), respectively. In addition, 2NT exhibited its highest concentration of 2.3 mg m^{-3} (2.0 times SD) in October, while 1N had a significant anomaly of 2.3 times the SD the same month (Table 6.6). A rapid La Niña increase mainly drove these anomalies from August to December 2011.

TABLE 6.6. CASE STUDY 2 SUMMARY INDICATING THE SUBSECTIONS AFFECTED THEIR CHL ANOMALIES IN SD, ENSO, SPSA AND AAO MONTHLY VARIATION, AND ADDITIONAL COMMENTS.

Subsections	Date	Chl (anom)	ENSOm	AAOm	SPSAm	Comments
3NT, 3NO	Aug-11	3.6, 2.6	-0.70	-1.20	0.59	Highest [Chl] [3.0 mg m^{-3}] (Sep) & anom (3.6) in 3NT and
3NT	Sep-11	[3.0 mg m^{-3}]	-0.88	-1.25	1.13	2NT [2.3 mg m^{-3}] (Oct) & (2.0); moderate La Niña (-0.68);
1NT 2NT	Oct-11	2.3, 2.0	-1.09	0.39	1.19	strong -AAO these months.
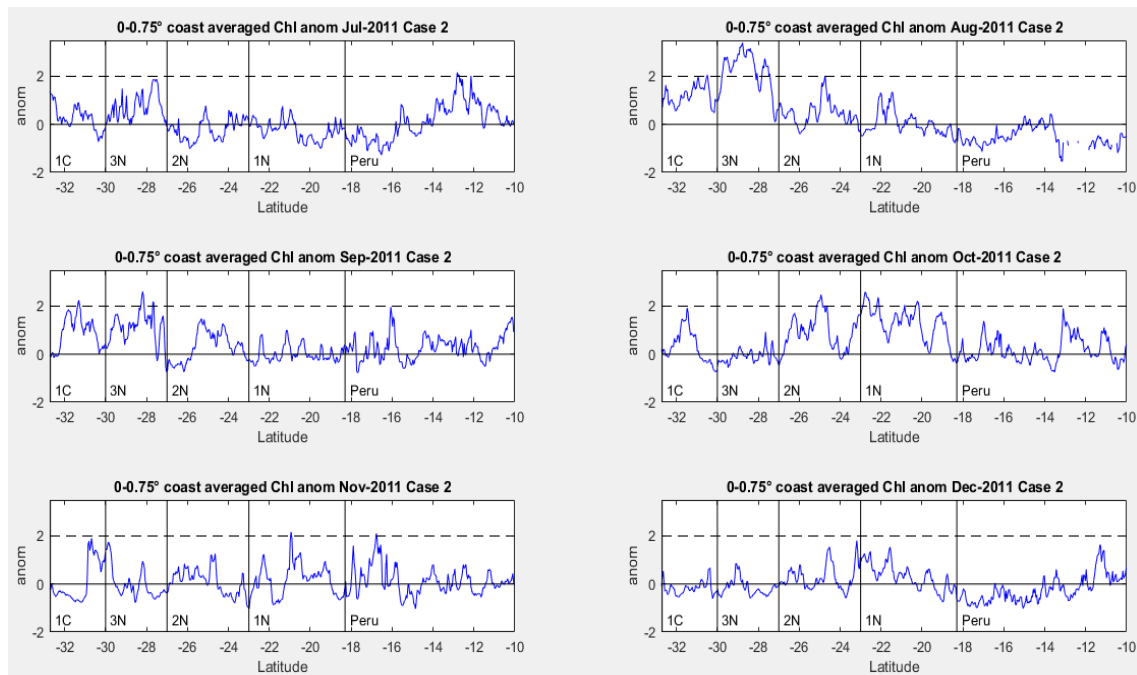
FIGURE 6.4. CASE 2 MONTHLY CHL CROSS-SECTIONS FROM THE COAST TO 0.75° OCEANWARD USING THE ANOMALIES DIVIDED BY SD ON THE PERUVIAN, NORTHERN ZONE AND 1C. THE DASHED LINE DRAWS ATTENTION TO THE SECTIONS WITH THE MOST SIGNIFICANT CHL ANOMALIES, SUCH AS 3NT IN AUGUST AND SEPTEMBER, AND MORE LOCALISED ANOMALIES IN 2N AND 1N IN OCTOBER.

Similarly to Case 1 (section 6.3.1.1), this event was linked to an ENSO change, namely, relatively fast La Niña intensification, increasing the SPSA and consequently the alongshore winds and raising the coast's thermocline through August-November, leading to significant upwelling and enhanced Chl concentration. Also, the AAO was associated with some intense PR in June in the Northern Zone that could help to increase the nutrients. However, the combination of La Niña and AAO produced a critical PR deficit in the study area during the

rest of the time, except for particular opportunities (Aceituno et al., 2015). Therefore, local SST reductions and intensive Southerly winds are consistent with these Chl increments (Figures 6.5-6.7). This hypothesis is consistent with negative correlations with SST observed off 3N and part of 1C, and positive correlations with VW (Figure A.3.2). Still, the latter was not as significant as with the SST.

Figure 6.4 shows a relatively high Chl anomaly in 3N in July, along with a reasonably high Chl anomaly in the Peruvian section near 12° to 14°S latitude. This Chl variation appeared on weekly maps with a slight Chl rise in the last two weeks of July. This was triggered by suddenly southerly alongshore winds in both regions linked to a slight SPSA intensification (0.68), reducing the SST. In general, La Niña produces negative anomalies in PR, but the negative AAO allowed the appearance of cut-off lows, which produced a local SLP drop associated with heavy rains (Aceituno et al., 2015). This produced locally heavy rains in the Northern and Central Zone in June and July. Indeed, some cities experienced floods in 3N in June due to these heavy rains (Sernageomin, 2017). Still, climate drivers sometimes modulated the cut-off lows, such as El Niño 2015 (Barrett et al., 2016). In any case, both PR episodes were not close to the Chl signal increase, so they are unrelated.
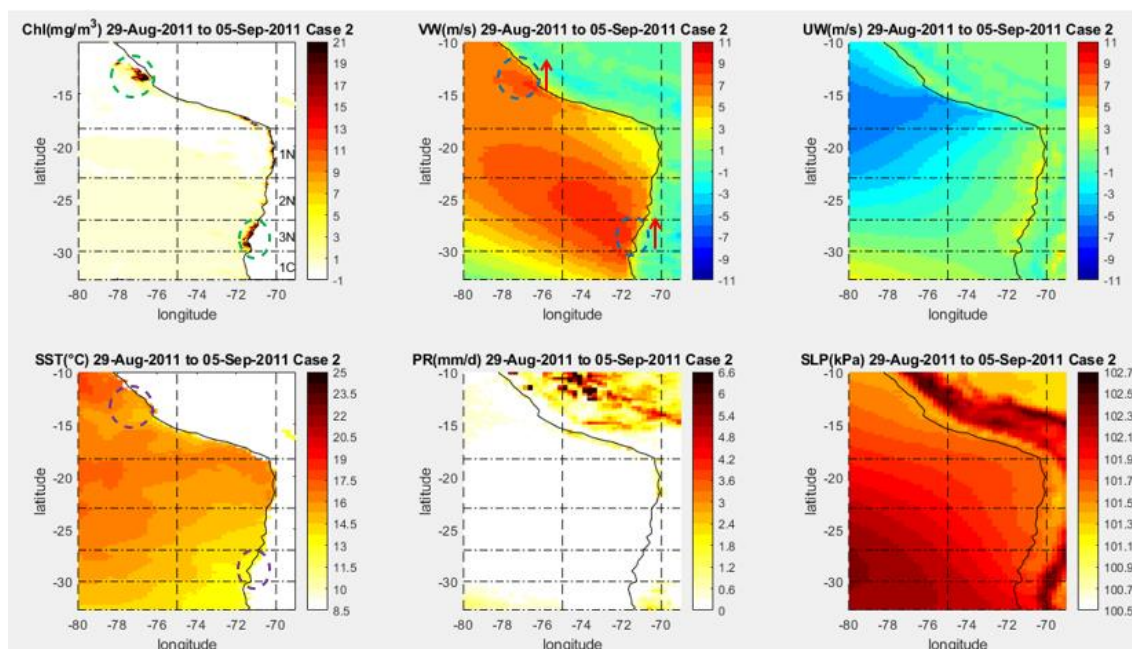
FIGURE 6.5. CASE 2 CHL, VW, UW, SST, PR AND SLP WEEKLY VALUES ON THE NORTHERN AND PERUVIAN ZONE, SHOWING 3N AND PERU PEAK BETWEEN 29TH AUGUST TO 5TH SEPTEMBER 2011. THE DASHED CIRCLES HIGHLIGHT THE CHL INCREMENT LOCATIONS IN THE CHL, SST AND VW PANELS. THE CHL SIGNAL MATCHED PERFECTLY WITH TWO REGIONS WHERE THE SST DROPPED, AND SOUTHERLY WINDS WERE MORE INTENSE, WHICH MATCHED WITH A REINFORCED SPSA LOCATED IN THE NORTH. 1N ALSO SHOWED AN INCREMENT, BUT THE VW AND SST COMPONENTS WERE NOT SIGNIFICANT. THE UW PANEL SHOWS STRONG EASTERLY WINDS IN THE 15°S LATITUDE AS A PRODUCT OF LA NIÑA THAT INCREASED THE SPSA.

Although VW and SST conditions persisted, the Chl was low again in the first week of August. From the middle of August, Chl in 3N went up again slowly until the end of the month, when it peaked (Figure 6.5). The Chl kept a relatively similar strength, except in the third week of August when VW was very low, but the Chl continued growing. Other regions that had a Chl increment were part of Peru and 1N. These could be linked again with the VW and SST variations that matched the Chl peak driven by the reinforced SPSA located in the north (1.19; Figure 6.5). The negative AAO (-1.23) was still associated with PR anomalies this month, but now, it was focused from 2C to 1S, while the rest of the coastal zones had a deficit due to La Niña (-0.88), which increased the SPSA significantly (Aceituno et al., 2015).

The physical parameter patterns observed in Figure 6.5 were even stronger the following week (the first week of September). Still, the Chl lost intensity. The southerly winds showed a considerable reduction for the rest of September, reducing the Chl values in 3N. However, the strong southerly winds appeared again the last week of the month, but this time was located at 1C, leading to a slight Chl increment there and in the remaining Northern Zones subsections.
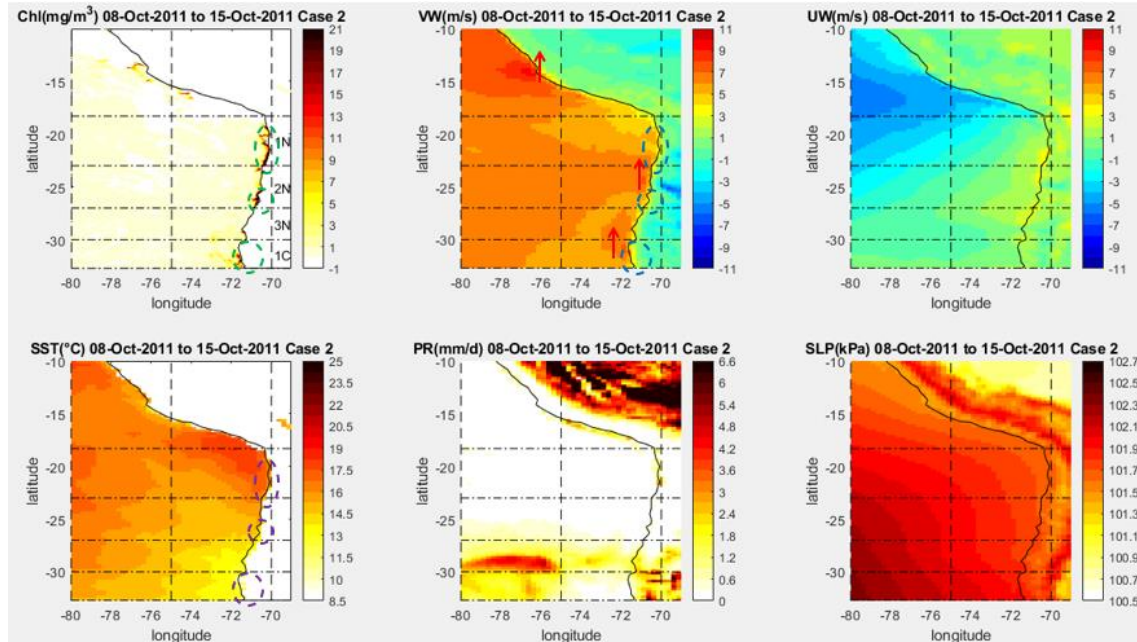
FIGURE 6.6. CASE 2 CHL, VW, UW, SST, PR AND SLP WEEKLY VALUES ON THE NORTHERN AND PERUVIAN ZONE, SHOWING 1-2N AND 1C BETWEEN 8TH-15TH OCTOBER 2011. THE DASHED CIRCLES HIGHLIGHT THE CHL INCREMENT LOCATIONS IN THE CHL, SST AND VW PANELS. THE CHL SIGNAL SHOWED SIMILARITIES WITH SOUTHERLY WINDS IN 1N AND 1C, WHILE SST REDUCTIONS SHOWED SIMILARITIES WITH THE CHL. THE SLP PANEL REVEALS THAT SLP ROSE RELATED TO THE SPSA (1.19), WHICH PRODUCED THESE LONGSHORE WINDS. FINALLY, THE PR IN 3N THAT WEEK HAD A MAXIMUM OF 14 MM D^{-1} ON 14TH OCTOBER.
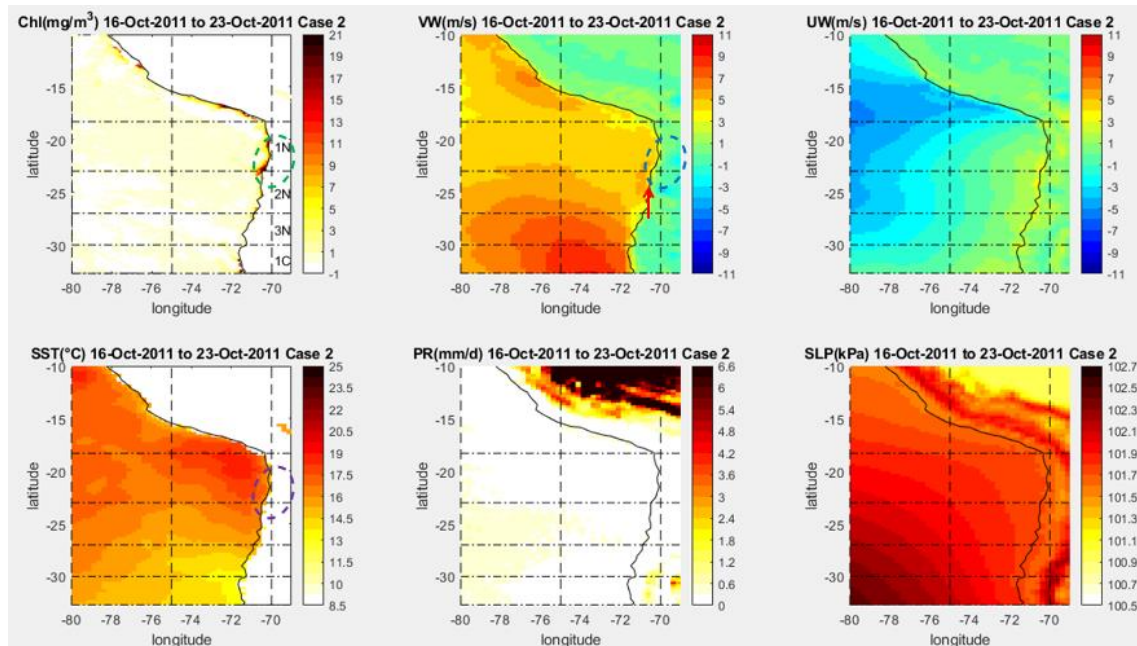
FIGURE 6.7. CASE 2 CHL, VW, UW, SST, PR AND SLP WEEKLY VALUES ON THE NORTHERN AND PERUVIAN ZONE, SHOWING THE 1N PEAK BETWEEN 16TH-23RD OCTOBER 2011. THE DASHED CIRCLES HIGHLIGHT THE CHL INCREMENT LOCATION IN THE CHL, SST AND VW PANELS. THE CHL SIGNAL MATCHES WITH SST, WHILE THE SPSA, AND CONSEQUENTLY THE SOUTHERLY WINDS, MOVED SOUTHWARD, SIMILAR TO CASE 1. THE RED ARROW INDICATES THE SOUTHERLY WIND LOCATION.

October continued with the Chl anomalies that showed at the end of September remaining and becoming intensified; this is clearly seen in Figure 6.4. The weekly maps showed these Chl signal increments reaching their peak in the second week of this month. 1N's Chl was even higher in the subsequent week, while it faded utterly along the rest of the coast (Figures 6.6 and 6.7). However, these Chl patterns with VW and SST patterns did not fit as well as the patterns observed in Figure 6.5. The Chl levels seen in October were a product of La Niña (-1.09) intensification that continued enforcing the SPSA (1.19) and reducing the SST along the Northern and part of the Central Zone, while an uncommon PR anomaly occurred in the second week of October in the 3N-1C subsections, associated with the switch of AAO to its positive phase (0.39; Aceituno et al., 2015). The SST reduction was more significant in 1N and 1C, and a rise of southerly winds in 1N was observed in the monthly anomaly maps used in this study.

November showed some particular high anomalies near the 1C border with 3N and some peaks in the 1N middle section and Peruvian southern section, but neither of them was above 2SD (Figure 6.4). The weekly maps demonstrated that the 1C Chl increase occurred in the second week of November (not shown), while in 1N's was at the end of this month. Although the La Niña index rose slightly (-1.23), the SPSA went down (0.51). Hence, VW and SST anomalies were less favourable for the Chl concentration compared to the previous month. December did not show any particular high anomaly owing to La Niña reduction.

In conclusion, the Chl increment resulted from a rapid increase of the southerly winds due to a rapid La Niña onset that enforced the SPSA located in the north, similar to Case 1 in section 6.3.1.1. These conditions persisted from August to November, with high Chl signals during the first three months but in different coastal locations. These specific locations seem to be related to their orientation. The Chl increase in these particular coastal places did not endure for more than two-three weeks due to its direct dependency on the intensity of the southerly wind, which alternated in speed and position.

VW~Chl correlation was more significant and consistent than in Case 1 (section 6.3.1.1), but only in 3N and 1C; in the other subsections, the correlations were low. SST~Chl was even higher and more steady than VW but again only in 3N and 1C, which experienced a very low SST (Figure A.3.2). Similarly to Case 1, the wind pattern and Chl did occur in the same position (Figures 6.6 and 6.7).

3N did not show a high Chl in October (Figure 6.6) due to the high PR from the second week. This conclusion is consistent with PR~Chl results, which were noisier and less precise than the Chl~VW and Chl~SST (Figure A.3.2). Nonetheless, the 3N middle section showed a significant negative correlation with PR, compatible with a rainwater lens suppressing upwelling and production.

6.3.1.3.   Case 3:

This case was selected for being one of the heaviest dust storms in the period studied (Figure 6.8). This event occurred on 8th July 2016, affecting 1N and 2N. A small dust event with a dense rain event happened there a week earlier. However, Chl did not show any significant anomalies around this episode at first glance. These dust events were during a transition stage between a strong El Niño's cessation and La Niña's initiation and a sudden transition in the AAO from being remarkably strong in June to considerably weaker the next month (Table 6.7), but the key factor in the event was the SPSA's atypical behaviour.

TABLE 6.7. CASE STUDY 3 SUMMARY INDICATING THE SUBSECTIONS AFFECTED THEIR CHL ANOMALIES IN SD, ENSO, SPSA AND AAO MONTHLY VARIATION, AND ADDITIONAL COMMENTS.

Subsections	Date	Chl (anom)	ENSOm	AAOm	SPSAm	Comments
1NT, 2NT	Jun-16	-0.8, 0.22	0.05	2.57	3.12	Dust storm case w/t negative anom in the North; transition b/w
1NT, 2NT	Jul-16	0.89,-0.76	-0.44	0.41	0.17	a strong El Niño (1.87) & a weak La Niña (-0.27), strong positive &
1NT, 2NT	Aug-16	-0.51, 1.41	-0.63	-0.74	1.71	by a moderately strong negative AAO, extreme SPSA (1.01).

The SPSA remained in its southern location during May and June instead of shifting northward, as it usually would do at this time. This abnormal behaviour produced a PR reduction toward the Central and Southern Zone (DMC, 2018). At the end of June, the Northern region experienced SLP drops driven by cut-off lows in 1N and 2N near the Andes. These cut-off lows created heavy rains and snow formation in the Altiplano with low jet streams at speeds around 10 to 25 m s^{-1}, moving dust from the Andes towards the ocean on 8th July for a few hours (DMC, 2018; Sutherland, 2016). The dense dust plume covered from 18° to 20°S while the secondary plume was from 21° to 23.5°S latitudes affecting 1N and a thin section of 2N. Prior to this, the 2N coastal strip showed heavy rains with dust clouds through the coast on 24th June due to the same conditions. Additionally, the SPSA returned to its Northern position in the first two weeks of June with high intensity (3.12), increasing the longshore winds drastically in 2N (Figure 6.10). However, this event's exact reasons are unclear (Reyers et al., 2019).
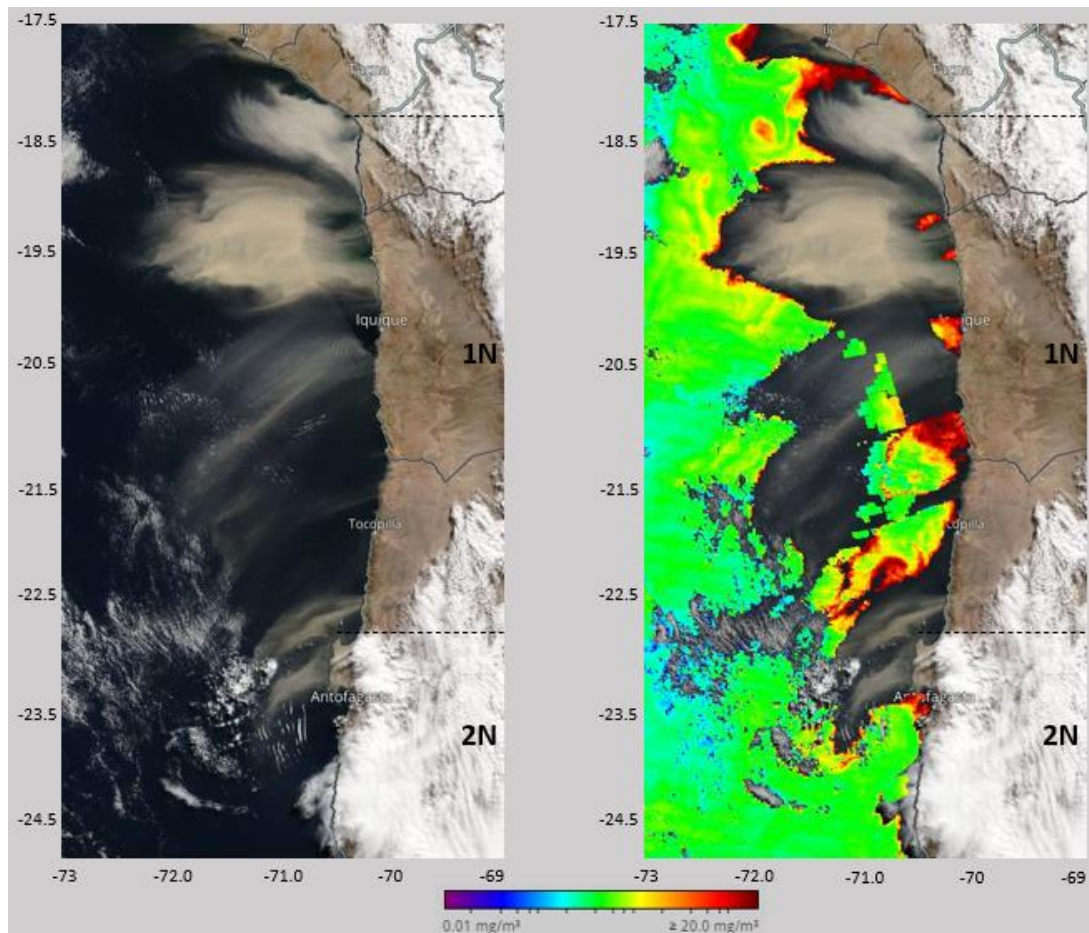
FIGURE 6.8: MODIS-AQUA SATELLITE VIEW OF CYCLONE EVENT WITH CHL CONCENTRATION TAKEN 8TH JULY 2016, SHOWING THE DUST STORM INTENSITY IN 1N AND 2N.
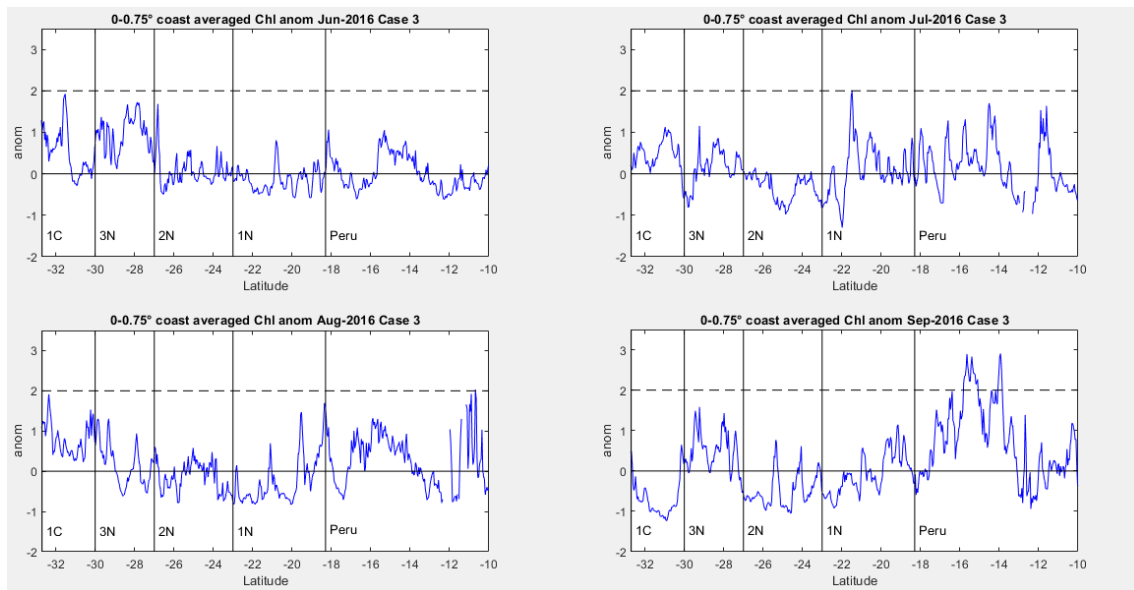
FIGURE 6.9. CASE 3 MONTHLY CHL CROSS-SECTIONS FROM THE COAST TO 0.75° OCEANWARD USING THE ANOMALIES DIVIDED BY SD ON THE PERUVIAN, NORTHERN ZONE AND 1C. THE MAIN AREA AFFECTED BY THE DUST STORM WAS 1N AND 2N IN JULY, WHERE THE CHL PROFILE SHOWED STEADY ANOMALIES CLOSE TO ZERO OR BELOW. THE EXCEPTION TO THIS WAS THE SECTION BETWEEN 21.5° TO 20°S IN 1N, WHERE THE CHL ANOMALIES WERE RELATIVELY HIGH.

1N and 2N showed low Chl anomalies with some negative values along the coast during June (Figure 6.9). 1N showed positive SST anomalies and northerly winds, reducing the Chl, while 2N exhibited easterly winds related to the dust event. Also, the weekly maps showed a slight Chl rise the week after the dust event happened. This is consistent with the SPSA's more southern location during this time. Figure 6.9 shows low negative Chl anomalies in 2N and part of 1N during July, reaching a negative peak at 22°S but with a positive peak at 21°S followed by a minor increment at 20°S. The rest of 1N showed a slightly positive trend. The other physical variables were consistent with the meteorological report in its monthly scale, showing negative SLP anomalies and predominance of easterly winds in 1N and 2N, but the weekly maps did not show a UW increment when the dust event occurred due to its short duration (Figure 6.10). The weekly maps showed the Chl rise near 21°-21.5°S starting the first week of the month and continued for two weeks. However, only one spot presented a significant Chl increase, although Chl levels rose slightly in the rest of 1N (Figure 6.10). The SST reduction pattern near 1N resembles the Chl increment pattern, but the spot with a significant Chl increase did not show any additional variation for SST. Although the VW was notably lower in 1N due to the SLP drop in the Zone product of the SPSA first southerly location and later weakening (0.17), VW was relatively high near 21°S when the dust event happened. This continued for one more week reaching the maxima VW, which later weakened and moved southwards when the Chl reached its climax (Figure 6.10).

The following month, the Chl anomalies stayed low in 2N, while those in the 1N considerably decreased towards the 2N border, keeping roughly its shape, including the anomaly spot at 21.5°S. The 1N section near Peru showed a reasonable increase but below two times SD (Figure 6.9). The weekly maps showed a flat Chl signal in 1N and 2N until the last weeks of August, when southerly winds appeared, raising the Chl again but with no significant anomalies. The winds returned to their regular patterns due to the SPSA reinforcement (1.71; DMC, 2016). Thus, this Chl behaviour is not related to the dust storm.

To conclude, the SPSA's more southern position seemed to be related to the strong El Niño in the previous year combined with an exceptionally high positive AAO that produced an unusual SLP drop in the Northern Zone, resulting in rain and dust movements linked to strong easterly winds. This case study demonstrated how SPSA could be modulated by ENSO and

123

AAO but also shows how dust events are not necessarily linked to ocean fertilisation in this region, at least in the long term. This is likely related to the low occurrence of these events. Nevertheless, these events have been more common in the last period. Therefore, more studies must be done in relation to this topic.
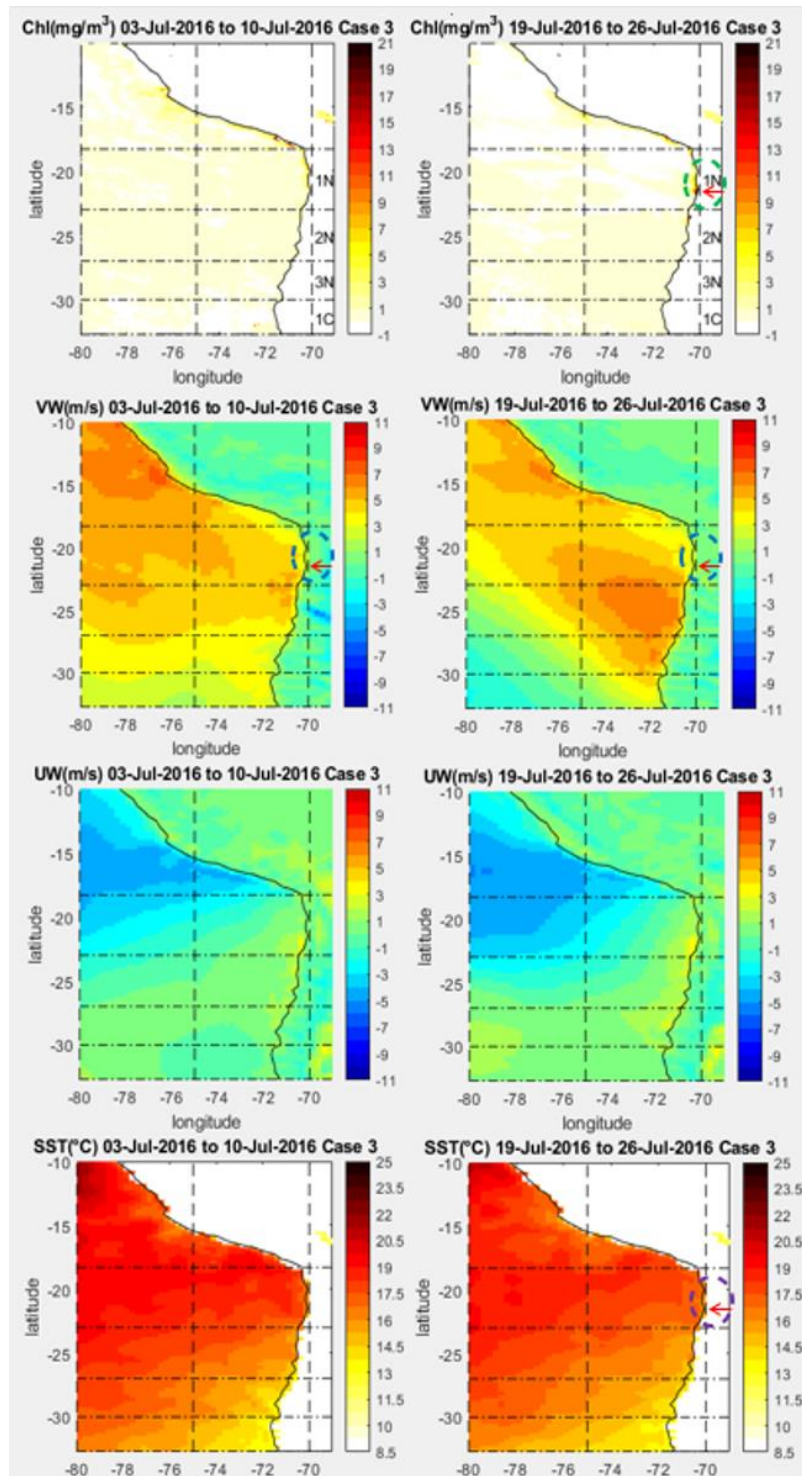
FIGURE 6.10. CASE 3 CHL, VW, UW AND SST WEEKLY VALUES ON THE NORTHERN AND PERUVIAN ZONE. THE LEFT SIDE SHOWS THE WEEK 3RD-10TH JULY 2016, WHEN THE DUST STORM OCCURRED. THE UW FOR THIS WEEK DID NOT SHOW ANY SIGNIFICANT EASTERLY WINDS IN 1N OR 2N. THE RIGHT SIDE SHOWS TWO WEEKS LATER, WHERE THE CHL SIGNAL REACHED ITS PEAK IN 1N. THE DASHED CIRCLES HIGHLIGHT THIS INCREMENT IN THE CHL, SST AND VW PANELS, WHILE THE RED ARROW INDICATES THE EXACT SPOT WHERE THE CHL INCREASED MORE. THE CHL SIGNAL MATCHES WITH SST, BUT THIS WAS NOT PARTICULARLY LOW AT THE RED ARROW, WHILE SOUTHERLY WINDS WERE LOW, SHOWING NO EFFECT ON THE CHL INCREMENT ON THE RIGHT SIDE, BUT IT WAS CLOSE ON THE LEFT. THESE WIND DIFFERENCES ARE LINKED TO THE SPSA'S CORE MOVING TO 23°S ON THE LEFT, WHILE IT WAS ALREADY SETTLED ON THE RIGHT, BUT IT WAS VERY LOW.

The PR and the dust inputs into the ocean should positively impact the Chl signal, but this did not have the expected influence producing mainly a slight general Chl rise, especially considering that PR and UW have a slightly stronger influence on the Chl in 1N than do SST and VW (section 4.5). The reason for this is that a strong El Niño had already diminished the Chl in 1N and 2N. Therefore, the Chl rise from the dust event was not significant. Also, the climate conditions that produce the dust events happen when the SPSA is weaker, reducing one of the primary triggers for a Chl increment, namely the southerly winds. So the Chl increase, in this case, was short-lived. However, there is a possibility that the Chl response was more significant but was covered. On the other hand, Ridame et al. (2014) report that only the wet dust movement leads to significant Chl response in places without nutrients because dry dust deposits do not contain enough NO_3^- (Ridame et al., 2014).

6.3.1.4.   Case 4:

This case was selected for having significant Chl anomalies in the three coastal subsections, similar to Case 2 (section 6.3.1.2). This event started in October 2018 with a significant Chl anomaly in 3N, followed by 1N's highest Chl anomaly the next month (3.04 SD). 2N showed a significant Chl anomaly that month as well. Finally, 1N continued showing a high anomaly in December (Table 6.8). This case occurred during a weak El Niño initial stage and a positive AAO. Both presented rapid fluctuations before this event, varying from 0.4 and 1.5 to 0.9 and 0.5 in September-October, respectively. Nonetheless, these drivers had a low impact on the Northern Zone. The critical factor was the SPSA absence from the Northern Zone, producing unstable winds. Additionally, 2018 was affected by a scorching spring-summer, with heat waves at the end of November and December (DMC, 2018).

This event was driven by the reappearance of alongshore winds in 3N and part of 2N in October-December, after a lower than average SLP in September due to the SPSA's southern orientation (DMC, 2018). This can be appreciated through the local SST reduction and VW higher speed around 3N, matching with the Chl signal (Figure 6.12). This was consistent with high Chl~SLP and Chl~VW correlations in 3N (Figure A.3.4). These climate conditions were variable in the second half of both November and December due to heatwaves and cyclonic conditions in the Zone, alternating with strong and weak southerly winds, disrupting the Chl signal. However, some local winds appeared sporadically, sustaining a weakened Chl concentration in 1N in the last month of the case.

TABLE 6.8. CASE STUDY 4 SUMMARY INDICATING THE SUBSECTIONS AFFECTED THEIR CHL ANOMALIES IN SD, ENSO, SPSA AND AAO MONTHLY VARIATION, AND ADDITIONAL COMMENTS.

Subsections	Date	Chl (anom)	ENSOm	AAOm	SPSAm	Comments
3NT	Oct-18	2.1	0.86	0.53	0.77	Highest anom in 1NT (3.0); weak El Niño (0.55), +AAO(0.46) & strong SPSA (0.84) and strong +AAO these months.
1NT, 2NT	Nov-18	3.0, 2.1	0.86	0.99	0.23	
1NT	Dec-18	2.7	0.84	0.93	0.94	

Figure 6.11 shows relatively high Chl anomalies in 1N in the section near Peru without being significant during September, while the rest of the Northern Zone mainly showed negative anomalies. The Chl increment in 1N is barely seen on the weekly maps but occurred in the last week of September, which could be linked to a slight increase in the southerly winds during the previous week. This low productivity is driven by a weak SPSA (-0.25; DMC, 2018; Thiel et al., 2007). Therefore, the SLP anomalies were lower than usual, and the westerly winds were predominant. Thus, two frontal systems were able to enter, despite the positive AAO (1.46), producing unusual snow and PR events in the Central Zone and further south, but this did not influence the study region. Furthermore, the Northern Zone did not experience much PR this month. In fact, it presented slightly higher atmospheric temperatures than a typical year (DMC, 2018).
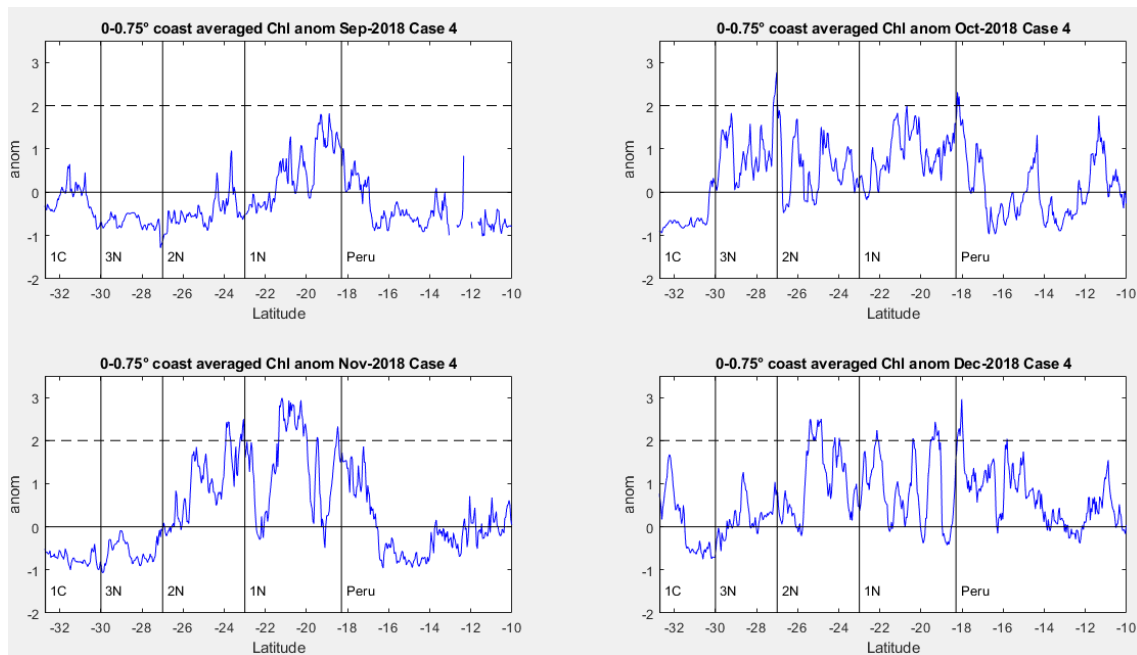
FIGURE 6.11. CASE 4 MONTHLY CHL CROSS-SECTIONS FROM THE COAST TO 0.75° OCEANWARD USING THE ANOMALIES DIVIDED BY SD ON THE PERUVIAN, NORTHERN ZONE AND 1C. THE DASHED LINE DRAWS ATTENTION TO THE SECTIONS WITH THE MOST SIGNIFICANT CHL ANOMALIES, SUCH AS THE 2N-3N LIMIT IN OCTOBER, 1N AND SMALL SECTIONS OF 2N IN NOVEMBER, AND MORE LOCALISED ANOMALIES IN 2N AND 1N IN DECEMBER.

The Chl anomalies increased considerably in October, showing a generally positive trend through the Northern Zone. 3N reached its peak at the border with 2N (Figure 6.11). This is consistent with the increased southerly winds anomalies due to a slight increment in the SLP anomalies linked to a more normal SPSA (0.77), but westerly winds were still present. The weekly maps show a persistent enhancement of the Chl through the whole northern Zone from the first to the third week of this month (Figure 6.12). 3N was the subsection with a higher Chl because it also experienced the highest southerly winds, which achieved their maximum speed the previous week. This is consistent with a SST drop in that subsection (Figure 6.12). Although 1N exhibited Chl favourable conditions as well, these were weaker than in previous years. Meteorological reports indicate that SLPs were typical at this time. However, this summer was hot (DMC, 2018). Even though the southerly winds strengthened in 3N during the last week, the Chl continued to be anomalously high only in 1N.

The following month, the chl anomalies persisted and were enhanced in 1N, while 2N's Chl was enhanced near 1N. 3N showed negative anomalies (Figure 6.11). The weekly maps confirm that the Chl signal in 1N continued from October, reaching its peak in the second week of November, including a slight Chl rise in 2N. The 2N Chl increase was linked to a local southerly wind intensification coming from 3N. A heatwave spread across the Northern Zone in the second half of this month, increasing SST drastically and weakening the southerly winds, and the SLP, especially in 1N (DMC, 2018). Despite these unfavourable conditions, a weaker Chl signal remained in 1N, assisted by local southerly winds that sporadically appeared (Figure 6.13).

126
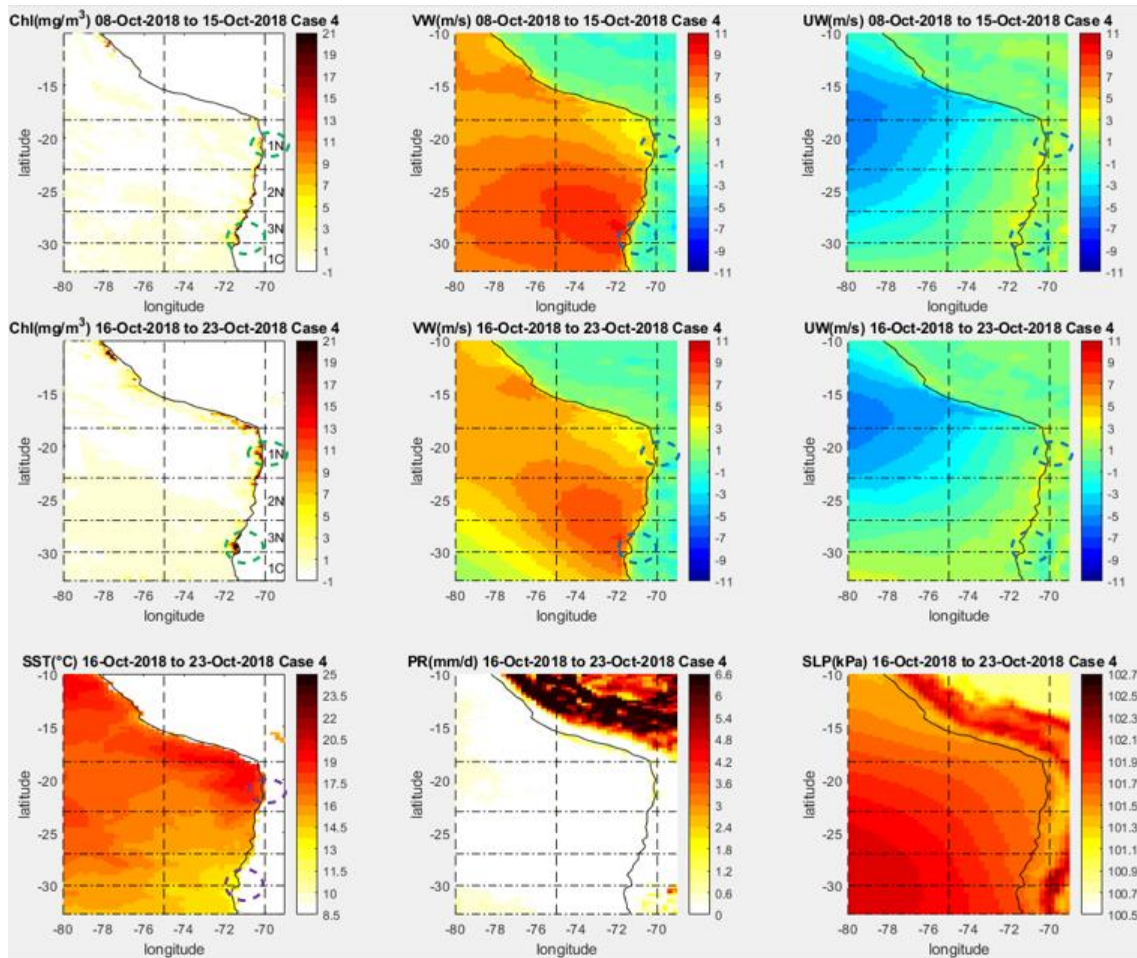
FIGURE 6.12. Case 4 Chl, VW, UW, SST, PR and SLP weekly values on the Northern and Peruvian Zone. The top panels show data from 8ᵀᴴ-15ᵀᴴ October 2018, when the VW and SLP peaked; only Chl, VW and UW are shown. The other two rows show all the variables data from 16ᵀᴴ -23ᴿᴰ October 2018, where the Chl signal reached its peak in 3N. The dashed circles highlight the Chl's peak locations in the Chl, SST, VW and UW panels. The Chl signal matches with SST reduction and VW increments. However, the VW in 3N matched a bit better with a higher wind speed. UW panels match the Chl's peak limits in both weeks, but UW is lower in the Chl's peak week.

The high atmospheric temperatures observed were slightly weakened during the first three weeks of December, especially in 2N (DMC, 2018). This marked the return of normal conditions with the appearance of southerly winds, boosting the Chl in 1N and 2N, while 3N's Chl continued low (Figure 6.11). The weekly maps confirm that Chl growth peaked in the second week (Figure 6.14). These can be linked to the VW return that appeared the previous week on 2N and part of 1N. The Chl faded away because the southerly winds weakened during the last week of December. This was driven by a heatwave reinforcement, which was exceptionally high in 3N due to coastal lows, producing warm easterly winds coming from the coast (DMC, 2018; Garreaud et al., 2002). These extreme weather conditions continue for the rest of the summer, eliminating the Chl signal (DMC, 2018).

Overall, the Chl increments in 3N and 1N were caused by strong southerly winds in the first half of both October and November, the same period observed in Case 2 (section 6.3.1.2). However, variable winds decreased owing to the SPSA moving southwards, and extreme atmospheric temperatures significantly reduced the Chl signal in the region for the rest of November and the final part of December. Still, local southerly winds were enough to maintain the Chl anomaly in 1N.

127
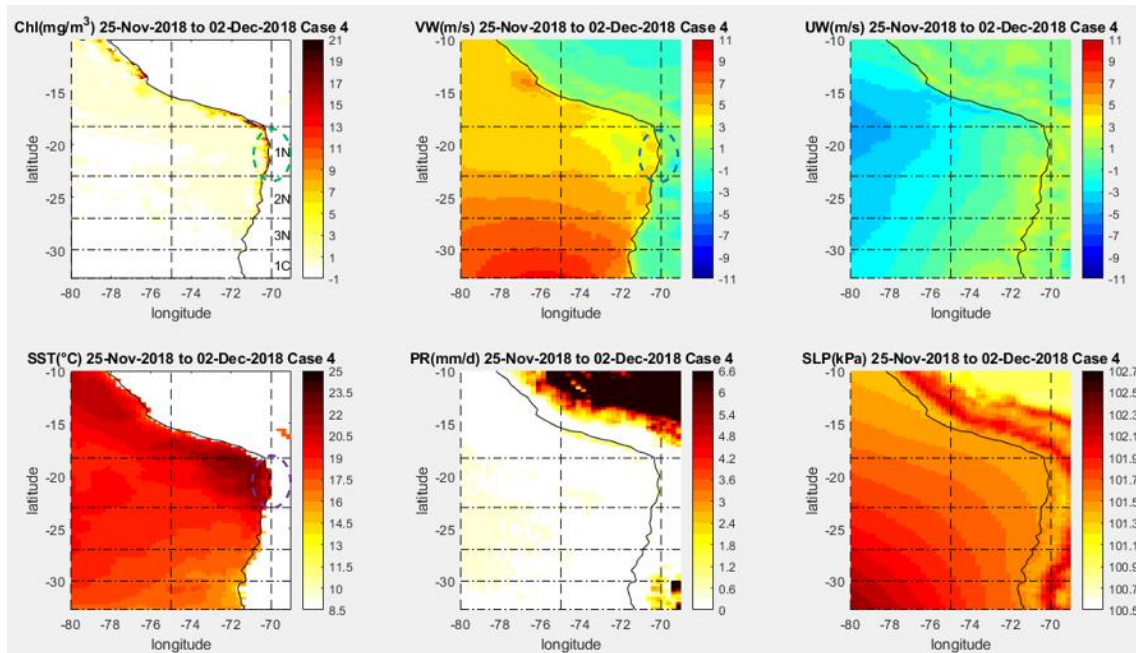
FIGURE 6.13. Case 4 Chl, VW, UW, SST, PR and SLP weekly values on the Northern and Peruvian Zone, showing 1N Chl persistence, despite the extreme SST in the week 25th November to 2nd December. The dashed circles highlight the Chl increment locations in the Chl, SST and VW panels. The Chl signal matches with the local southerly wind and the SST.
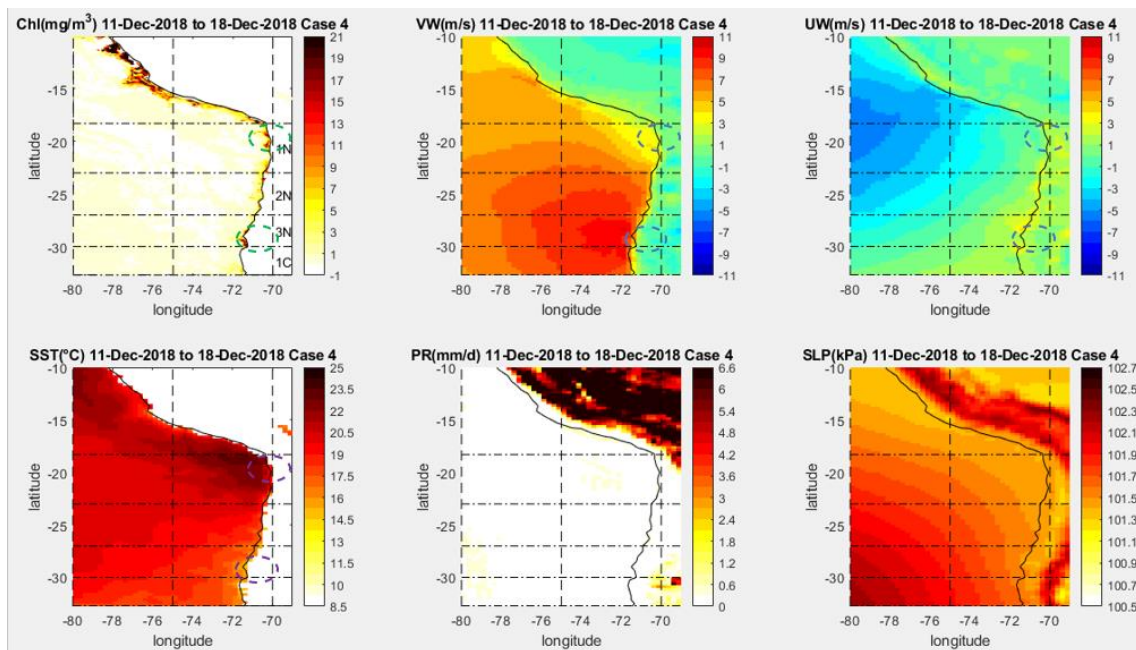
FIGURE 6.14. Case 4 Chl, VW, UW, SST, PR and SLP weekly values on the Northern and Peruvian Zone showing its peak between 11th-18th December 2018. The dashed circles highlight the Chl's peak locations in the Chl, SST, VW and UW panels. The Chl signal matches with SST reduction and VW increments. However, the VW in 1N only partially matches at the bottom. The UW panel matches the Chl's peak limits in 3N, while UW is not present in 1N. The SLP panel showed lower SLP values than the previous Figure, but the winds are higher here.

Similarly to the previous cases, the VW~Chl correlations for this case were not significant in 1N, but they were in 3N. This is because 1N presented a high VW variation alternating between low and high speed. Also, the Chl signal remained for a week more when the southerly winds were weak again (Figure 6.12). Something similar happened with SST~Chl, where the 3N region showed significant negative correlations while 1N's signal was less clear. That is because 1N had a higher SST while 3N's SST was typically lower. On the other hand, the 3N and 1C generally have the highest southerly winds, so the correlations are direct (Figure A.3.4). Interestingly, 1N usually has a higher Chl concentration than 3N and 2N

128

because it is close to Peru. The link is associated with a poleward ESSW from northern Peru delivering nutrients from this Zone, which has a constant Ekman transport that allows a constant nutrient supply in the central region of Peru (Thiel et al., 2007; Echevin et al., 2014).

1N being the highest Chl concentration in the Northern Zone might be related to different factors. Firstly, its proximity to Peru, which generally had an even higher Chl concentration. Indeed, the Peruvian coast had a significant Chl signal in this case and the previous ones (sections 6.3.1.1 and 6.3.1.2). Secondly, its location is slightly oriented SE-NW; thus, the westerly winds could produce upwelling in some sections, adding dust inputs from the land on some occasions. Finally, 1N has shown in these case studies that southerly wind is a crucial factor in its Chl increment, but the big difference with the other two subsections is that 1N is capable of maintaining the Chl anomaly for a couple of weeks without favourable winds (Cases 1 and 2). Anthropic activities also could be a factor because 2N and 3N are more polluted by tailings, but 1N has had more fisheries since the 1960s (Camus, Hajek, 1998), meaning that its primary production has not been affected.

6.3.2. Central Zone.

In the Central Zone, three cases were selected (Cases 5 to 7), all related to Chl anomalies. Case 5 showed the highest anomalies in 2CT and 4CT and the highest concentration in 1ST, which is the only cross-Zone case. Case 6 contained the highest 1C anomaly in the coastal and ocean strip. Finally, Case 7 is the most remarkable event because it is the highest Chl concentration detected in this study and is located in the ocean strip. Also, river fluxes become more significant in the Central and Southern Zone. Hence, they will be added to this analysis.

6.3.2.1. Case 5:

This case showed the highest Chl anomalies in two Central Zone subsections and the highest concentration in 1ST, which is also the second highest Chl anomaly, becoming the only cross-Zone case study. This event began in March 2005 with the highest Chl anomaly in 2CT. The following month 4CT and 1ST showed significant anomalies, which essentially disappeared in the following month. AAO and ENSO were particularly weak during this case development (Table 6.8 and Figure 6.15). However, the AAO index was 1.24 earlier in February, which was associated with a significant PR reduction in the Southern Zone, becoming the starting point for this case.

TABLE 6.9. CASE STUDY 5 SUMMARY INDICATING THE SUBSECTIONS AFFECTED THEIR CHL ANOMALIES IN SD, ENSO, SPSA AND AAO MONTHLY VARIATION, AND ADDITIONAL COMMENTS.

Subsections	Date	Chl (anom)	ENSOm	AAOm	SPSAm	Comments
2CT	Mar-05	3.3	0.53	0.16	1.44	Highest anom in 2CT (3.3), 4CT (2.4), [Chl] [6.2 mg m^{-3}] 1ST;
4CT, 1ST	Apr-05	2.4, 2.7	0.35	0.36	0.47	weak El Niño (0.55) & +AAO (0.24), normal SPSA (0.12).

This case consisted of two separate events. The first was linked to coastal winds in the Central Zone driven by the SPSA (1.44), leading to a constant Chl signal in 2C during March (Figures 6.15 and 6.16). This is consistent with the high positive correlation between the Chl and VW in 2C (Figure 6.17). The second event was linked to retreating cyclonic conditions in 1S towards the extreme Southern Zone at the end of March, producing a significant drought, which reduced the stratification and consequently increased the Chl in 1S's interior sea in April (Figure 6.15). This is consistent with significant positive correlations observed between the Chl with SLP and VW in 1S's interior sea and the significant inverse correlations with SST and PR (Figure 6.17).
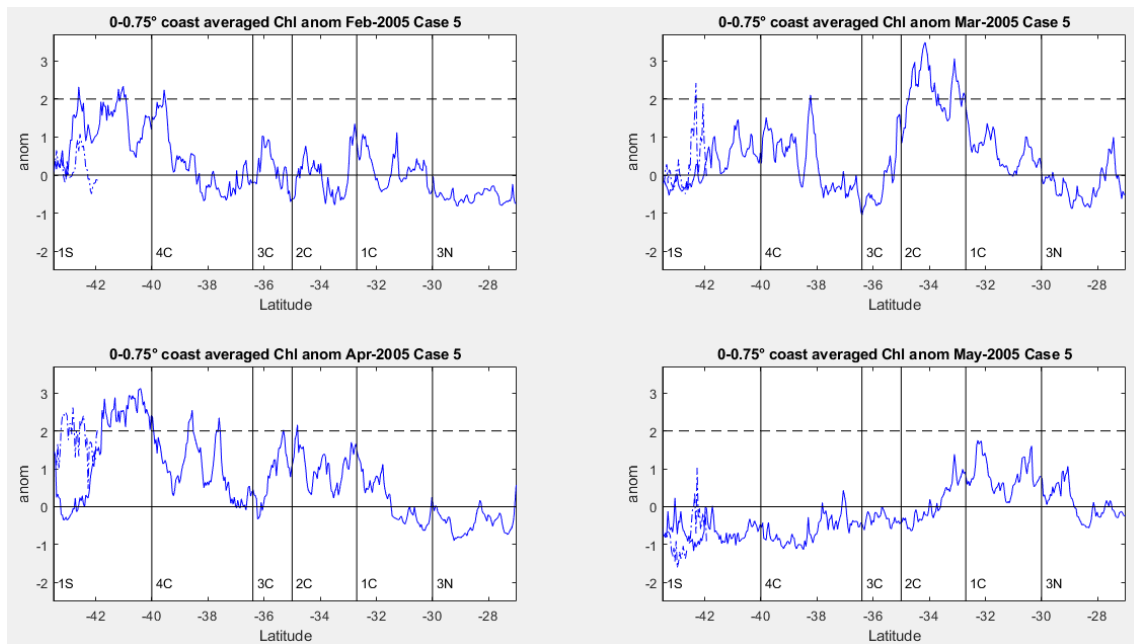
FIGURE 6.15. CASE 5 MONTHLY CHL CROSS-SECTIONS FROM THE COAST TO 0.75° OCEANWARD USING THE ANOMALIES DIVIDED BY SD ON THE 3N, THE CENTRAL ZONE AND 1S. THE DASHED BLUE LINE IN 1S REPRESENTS THE CHL ANOMALY ACROSS THE ANCUD AND CORCOVADO GULFS BETWEEN CHILOÉ ISLAND AND THE MAINLAND (41.9°-43.25°S), WHILE THE CONTINUOUS LINE IS THE CHL ANOMALY ACROSS THE CHILOÉ COASTLINE AND THE PACIFIC BASIN. THE BLACK DASHED LINE DRAWS ATTENTION TO THE SECTIONS WITH THE MOST SIGNIFICANT CHL ANOMALIES, SUCH AS 2C IN MARCH, 1S FIRST PART AND THE WHOLE OF CHILOÉ'S INTERIOR SEA.

The central Zone showed low Chl anomalies associated with a low SPSA (-0.97) in February, except for the 4C subsection at 39.6°S across the 1S Pacific coast at 42.6°S (Figure 6.15). The weekly maps showed this anomaly peaked the first week of February, decreasing slowly until the end of the month, except for slight growth in the 39.6°S section during the third week. This Chl increment was driven by southerly winds, which were more intense during the first week, showing a significant relation (Figure 6.17). This atypical wind-linked pattern was related to anticyclonic conditions in the Southern Zone formed by a positive AAO (1.24), which was associated with regular cold fronts moving polewards. This high SLP also delivered a 40-80% PR reduction for this month (Aceituno et al., 2015). Vergara et al. (2017) and Masotti et al. (2018) reported that the Itata (36.47°S) and Biobio Rivers (36.84°S), both located in 4C (Figures 3.4 and 3.5), influence the phytoplankton's bloom. Itata River showed a 39%[2] increment in its flow, while Biobio did not have any significant variation. 2C and 3C also have rivers that boost the phytoplankton (Masotti et al., 2018). These are Maipo (33.72°S), Mataquito (34.98°S) and Maule Rivers (35.41°S), where the last is located in 3C and the other two in 2C (Figure 3.4). Only the two rivers in 2C showed a flux reduction of 35 to 55% this month.

The Chl anomalies were higher in March, but they were spread across different locations. 2C exhibited its highest Chl anomaly. Also, 4C's mid-section and 1S's interior sea showed some significant Chl variation (Figure 6.15). The weekly maps showed a remaining Chl concentration from the previous month in the 4C middle part. Nevertheless, this had disappeared utterly by the next week. A relatively steady Chl signal appeared in 2C from the second to the final week of March, weakening in the following week. This is consistent with high southerly winds concentrated in 1-2C during March's second week, which were even more intense and expanded slowly to the whole Central Zone until April's third week (Figure 6.16). The behaviour of this wind pattern was associated with an SLP rise there due to the

---

[2]These percentages were estimated dividing the flows with their respectively averaged flow (2003-2017) for each month.

SPSA rise (1.44). PR was exceptionally high this month in 1-2S due to cold fronts, while the 2C and 4C exhibited some heavy rains at the beginning of March due to an SLP drop associated with cut-off lows (Aceituno et al., 2015). The Itata and Biobio Rivers showed the same increases found in the previous month, while 2C's rivers showed their typical flux, but the Maule increased 30% (Figure 3.4).
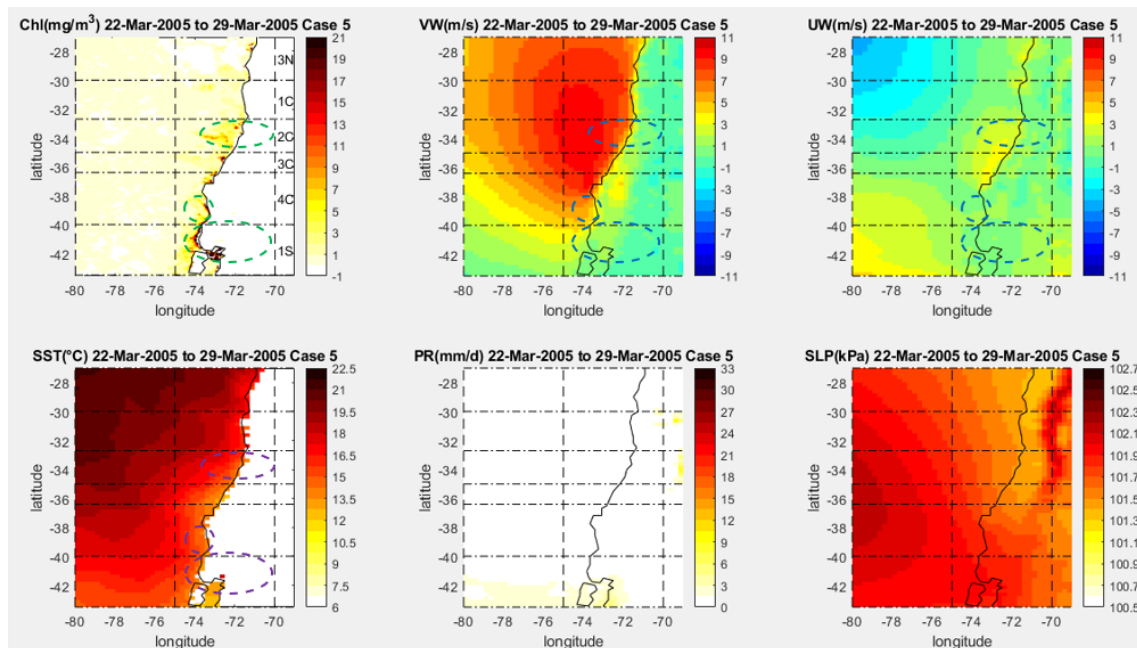
FIGURE 6.16. CASE 5 CHL, VW, UW, SST, PR AND SLP WEEKLY VALUES ON THE 3N, THE CENTRAL ZONE AND 1S SECTIONS, SHOWING THE LAST WEEK OF MARCH 2005. THE DASHED CIRCLES HIGHLIGHT THE CHL INCREMENT LOCATION IN THE CHL, SST, VW AND UW PANELS. THIS HELPS TO IDENTIFY THAT THE SST DROP HAS THE SAME SHAPE AS THE CHL INCREMENT, WHILE THE HIGH SOUTHERLY WINDS WERE ASSOCIATED WITH THE CHL INCREMENT IN 2C, BUT NOT WITH 4C-1S. ON THE OTHER HAND, THE SLP ANOMALIES WERE SIGNIFICANT IN 4C AND 1S. THE UW WAS WEAK IN BOTH CASES AS WELL.

An even stronger Chl signal appeared from 38°S in 4C to 1S's inner sea in the last week of March (Figure 6.16). This Chl anomaly was present during April, achieving two peaks in the first and final week of that month. This signal is clearly seen in Figure 6.15, including some peaks in 4C. This is 1S's highest Chl concentration and second-highest anomaly. The weekly maps showed that the SST were lower in the 4C and 1S north inner sea, which experienced the high Chl concentration. Although the SPSA was slightly weak (0.44), the southerly winds were powerful during the first three weeks of April, explaining the Chl increment in 4C. However, these did not come close to the 1S's coastline. Instead, a strong westerly wind appeared in the first two weeks of April, which fitted with the 1S's Chl peak. An easterly wind emerged there the last week of that month, matching with the last significant 1S's Chl week. The PR anomalies were lower than for a typical year but still present the whole month as a drizzle, except in the first week of April and May, decreasing Itata and Biobio River fluxes by 20 to 25% and Mataquito by 50% in April (Figures 3.4 and 3.5). These PR anomalies matched with Chl reductions, particularly in May, when the Chl signal disappeared. This is consistent with meteorological reports indicating that SST and PR drops resulted from cold high-pressure sections moving northwards from the Southern Zone (Aceituno et al., 2015).

According to the O.1. findings (section 4.5), 1S's Chl typically had a statistically significant correlation with VW (0.45) and a negative correlation with UW(-0.41) and PR (-0.39), while the SST correlation was insignificant. In contrast, the coastal correlations using only the data for this case showed that the Chl in Chiloé's interior sea had significant positive correlations with SLP and VW in that order while also having significant negative correlations with PR and SST. On the other hand, UW~Chl did not significantly correlate in 1S's interior sea (Figure 6.17 and A.3.5). The Chl bloom occurs during the spring-summer because solar radiation is the

critical component for its development (Castro 2010; De La Torre, 2016; Landaeta et al., 2011). Certainly, the stratification is lower during spring and higher during autumn due to PR's seasonal variations (Castillo et al., 2016). The westerly winds help feed the Chiloé's interior sea with Pacific waters, renewing its nutrients and elevating the Chl. This occurred with higher frequency during the summer; for that reason, the exterior and interior seas tend to have similar Chl concentrations (De La Torre, 2016). Therefore, a lower PR and a westerly wind slight increase lead to the Chl increment.
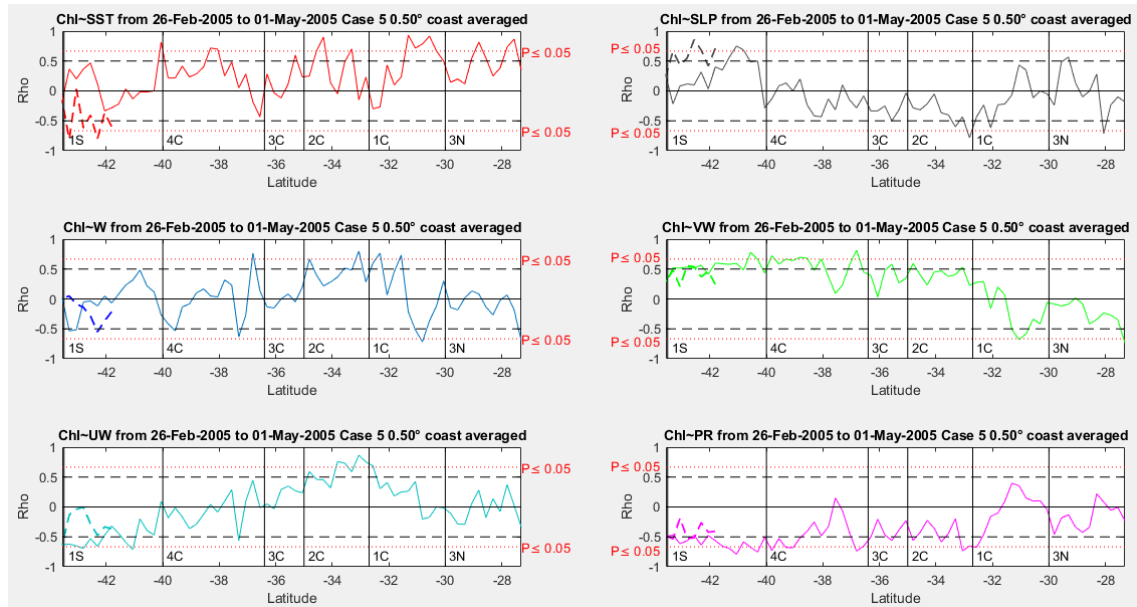
FIGURE 6.17. CASE 5 COASTAL AVERAGED FROM 0 TO 0.5° CHL CORRELATIONS WITH ALL PHYSICAL VARIABLES USING ONLY THE CORE PERIOD.

However, there are Chl concentration differences between both 1S regions because the interior sea has additional river discharge providing nutrients and fresh water (De La Torre, 2016; Castillo et al., 2016). The Reloncaví Estuary mainly feeds the Northern Chiloé's interior sea (Figure 6.18), whose main tributary rivers are Puelo, Petrohué and Cochamó. Puelo is the largest in volume and is likely to have a bigger impact on Chl's behaviour (Castillo et al., 2016; Castro, 2010). De La Torre (2016) reported that when the Puelo flow is over 1,000 m^3 s^{-1}. The Chl anomaly in the Ancud Gulf decreases regardless of whether it is a warm or cold season. In contrast, when the flow is under 360 m^3 s^{-1}, the Chl anomalies could be positively affected due to less stratification, but this is less clear. Figure 6.19 shows these rivers' fluxes; the Puelo flux was lower than 360 m^3 s^{-1} in February and April 2005 (293.1 and 309.8 m^3 s^{-1}), which was a 20% drop compared to its usual flux in both cases. Thus, they can be linked with the Chl increase. Other significant rivers are the Yelcho for the central interior sea region, while the Palena (43.82°S), Cisnes (44.75°S) and Aysén (45.41°S) are more significant for the Southern section located in 2S (Aguayo et al., 2021; Figure 6.18).
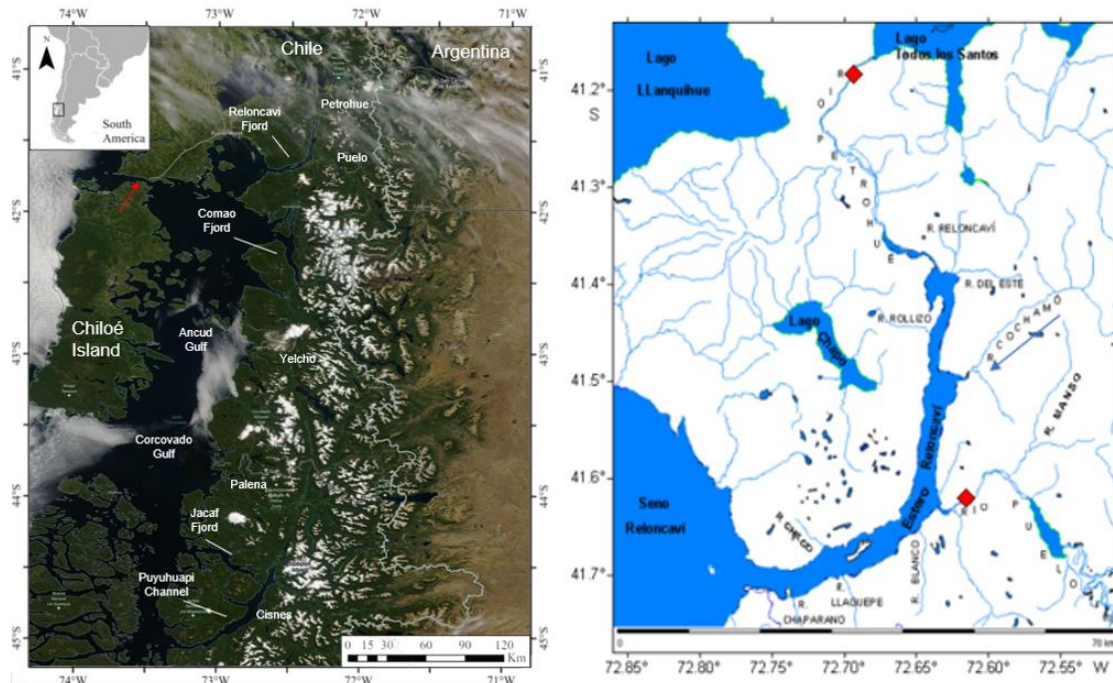
FIGURE 6.18. THE LEFT PANEL SHOWS THE ANCUD AND CORCOVADO GULFS BETWEEN CHILOÉ ISLAND AND THE MAINLAND (41-45°S), AND THE RED ARROW SHOWS THE CHACAO CHANNEL, WHERE THE CHILOÉ'S INTERIOR SEA CONNECTS WITH THE PACIFIC. THE LOCATION OF PETROHUÉ (41.13°S), PUELO (41.60°S), YELCHO (42.98°S), PALENA (43.82°S) AND CISNES (44.75°S) RIVERS IS SHOWN AS THE REGION'S MAIN TRIBUTARY RIVERS. AYSÉN (45.4°S) IS SLIGHTLY FURTHER SOUTH. THE RIGHT PANEL SHOWS THE RELONCAVÍ ESTUARY. THE RED RHOMBUSES INDICATE PUELO AND PETROHUÉ RIVERS GAUGING STATIONS, AND THE BLUE ARROW INDICATES THE COCHAMÓ RIVER (41.51°S), WHOSE FLUX IS NOT MEASURED (CASTRO, 2010; AGUAYO ET AL., 2021).
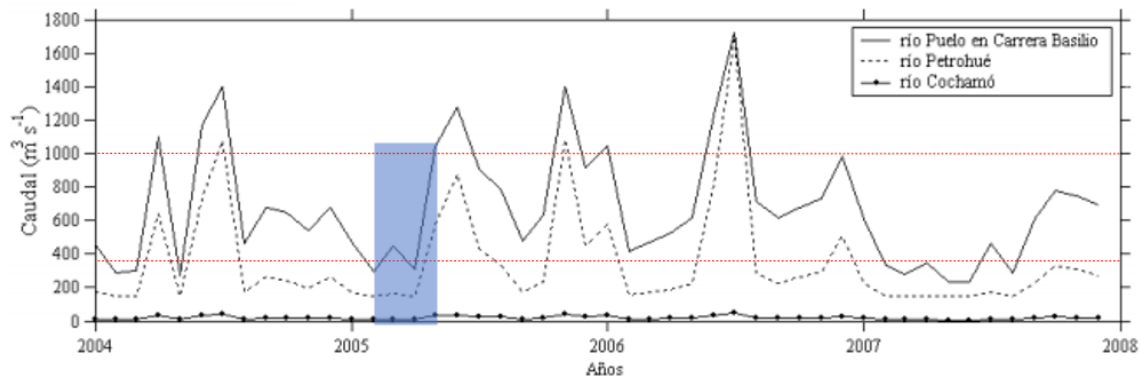
FIGURE 6.19. HYDROGRAPH OF THE PUELO, PETROHUÉ AND COCHAMÓ RIVERS; COCHAMÓ WAS ESTIMATED. THE BLUE SHADED AREA HIGHLIGHTS THE MONTHS STUDIED (FEBRUARY-MAY 2005), AND THE RED DOTTED LINES (1,000 AND 360 m^3 s^{-1}) INDICATE THE FLOWS THAT AFFECT THE CHL IN THE ANCUD GULF (DE LA TORRE, 2016; CASTRO, 2010).

As mentioned above, the Chl anomalies were low in May, especially in the 1S-4C subsections, when they were negative (Figure 6.15). The weekly maps show the Chl was very weak the whole month (not shown). In the 4C-1S section, the Chl abruptly decreased during the first week. This is linked to heavy PR, occurring over the whole month, and intense NW-SE winds in May's second and final week. The meteorological reports indicated that these conditions were caused by a cold front in the Southern Zone during the second and third week of May, associated with negative AAO (-0.30) that reduced the SPSA even more (0.25; Aceituno et al., 2015). Furthermore, all the rivers mentioned displayed increments of over 20%. Indeed, the Itata, Biobio and Mataquito exhibited 50 to 70% stronger flow than usual; Biobio, in particular, exceeded 1,000 m^3 s^{-1}. Meanwhile, the Puelo River showed an 85% increase, with a flow of 1,045 m^3 $s^{-1,}$ likely caused by the PR events (Figures 6.19 and 3.5).

To conclude, the Chiloé's interior sea's Chl increments had more complex reasons than was found for 2C. However, both events were driven by SLP variations. The Central Zone

133

experienced strong anticyclonic conditions that enhanced the Chl, while the 1S region exhibited more neutral conditions, which generally are cyclonic. These neutral conditions reduced the PR, and consequently, the river flux that feeds the Chiloé's interior sea, preventing a high stratification. Therefore, the Puelo River had a bigger role in the stratification process than the other rivers, owing to the semi-constrained Chiloé's north interior sea.

Other significant factors that influenced the Chl in Chiloé's interior sea were that this event occurred close to the time of phytoplankton typical bloom, which means there was higher solar radiation, especially considering the lack of PR in the region. Finally, sporadic westerly winds allowed Pacific waters to introduce more nutrients. Nonetheless, if the 4C-1S basin coast does not have a high Chl, the westerly winds will not lead to a Chl increase in the interior sea. For that reason, May westerly winds did not positively affect the Chl.

Although UW was a critical factor in enhancing the Chl in the 1S interior sea, UW~Chl did not show significant correlations (Figure 6.17). This might be because they were made with the coastal values, and the westerly winds are more relevant in the Pacific basin. In fact, the correlations in the pacific were significant but negative (Figure 6.17 continues line).

6.3.2.2. Case 6:

This two-month event started in March 2014, with the highest Chl anomalies detected in 1CT, 1CO and 4CO. The Chl was reduced the following month considerably but still showed high anomalies in 1CT to fade away the subsequent month (Table 6.10 and Figure 6.20). Similarly to Case 5 (section 6.3.2.1), AAO and ENSO were very weak in this period. However, La Niña peaked in February, whereas AAO was slightly more intense before and after the Case 6 core months, reaching -0.68 and 0.6 in January and April. The critical factor was the sudden SPSA intensification from January (-0.19) to February (0.52), which continued until April (1.50; DMC, 2018; Aceituno et al., 2015). Finally, the Central and Southern Zone experienced a significant drought in the previous spring-summer that continued through this case (Aceituno et al., 2015).

TABLE 6.10. CASE STUDY 6 SUMMARY INDICATING THE SUBSECTIONS AFFECTED THEIR CHL ANOMALIES IN SD, ENSO, SPSA AND AAO MONTHLY VARIATION, AND ADDITIONAL COMMENTS.

Subsections	Date	Chl (anom)	ENSOm	AAOm	SPSAm	Comments
1CT, 1CO, 4CO	**Feb-14**	**3.4, 3.2, 3.1**	-0.51	0.32	0.52	Highest anom in 1CT (3.4), 1CO (3.2) & 4CO (3.1); normal
1CT	**Mar-14**	**2.6**	-0.19	0.47	1.17	year ENSO (-0.21), & AAO (-0.21), but strong SPSA (0.79).

This event was linked to the SPSA increment that produced positive SLP anomalies in the Central Zone and 1S in February-March. This reduced cloudiness increased the atmospheric temperatures and decreased PR, except for isolated events related to cold fronts in 1S (DMC, 2018). Moreover, these SLP increments led to southerly winds matching 1C's, 4C's and 1S's Chl increments. These winds had a higher effect on 1S because they were intermittently seen in this period (Figures 6.21 and 6.22). This is consistent with the high positive correlations between 1S's Chl with VW and SLP in the northern limit surrounding the island of Chiloé (Figure A.3.6).

The Chl anomalies were relatively low in the Central Zone during January. However, 1C with 3N showed some sections where the Chl was higher than 2 SD (Figure 6.20). According to the weekly maps, these anomalies are linked to weak Chl increments in those subsections during January's first and final week. 3C through 1S's interior sea showed a weak Chl signal in January's first two and last weeks as well. Nevertheless, Chl was relatively intense the second week. The Chl behaviour was led by a high-pressure region that led southerly winds across 3N to 4C the first and final week. In the second week, the pressure region moved southwards, producing longshore winds to be present in 3C to 1S's interior sea. The SLP was

very low during the third week, associated with a weaker Chl signal. This low productivity was because the SPSA was weak this month (-0.39), consequently producing weaker winds (DMC, 2018). Despite this, the high-pressure system was enough to reduce cloudiness between 3N and 4C, raising the atmospheric temperatures and reducing the PR in these subsections. Since the previous year, this drought had been present in the Central and Southern Zone, with a 40 to 70% deficit, reducing the main river fluxes in the Central Zone (Maipo, Mataquito and Maule) between 40 and 90%. The exception was heavy rain associated with a cold front in 1S to 4C during the third week when the SLP was low, causing the Biobio stream to increase inflow by 90%, whereas the Puelo's flux had a 15% reduction. The Itata River was not measured during this case (Figure 3.5; DMC, 2018; Aceituno et al., 2015).
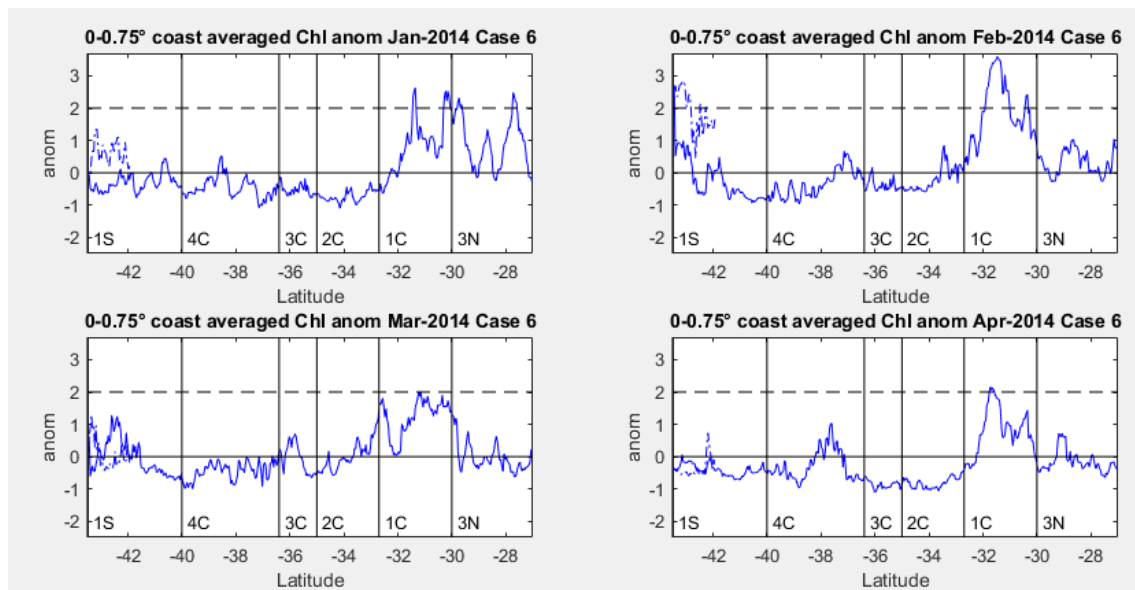

FIGURE 6.20. CASE 6 MONTHLY CHL CROSS-SECTIONS FROM THE COAST TO 0.75° OCEANWARD USING THE ANOMALIES DIVIDED BY SD ON THE 3N, THE CENTRAL ZONE AND 1S. THE DASHED BLUE LINE IN 1S REPRESENTS THE CHL ANOMALY ACROSS THE ANCUD AND CORCOVADO GULFS BETWEEN CHILOÉ ISLAND AND THE MAINLAND (41.9°-43.25°S), WHILE THE CONTINUOUS LINE IS THE CHL ANOMALY ACROSS THE CHILOÉ COASTLINE AND THE PACIFIC BASIN. THE BLACK DASHED LINE DRAWS ATTENTION TO THE SECTIONS WITH THE MOST SIGNIFICANT CHL ANOMALIES, SUCH AS 1C AND 1S'S INTERIOR SEA IN FEBRUARY. IN THE OTHER MONTHS, 1C SHOWED A SLIGHTLY HIGH ANOMALY, ALMOST REACHING 2SD.

Figure 6.20 shows high Chl anomalies in 1C and 1S's interior sea during February, whereas the other subsections had insignificant Chl anomalies. Both Chl variations appeared on the weekly maps, where 1C showed a high Chl only in the first week (Figure 6.21), while the Chl was seen the whole month in 1S's interior sea, with a particularly intense signal in the second and third week (Figure 6.22). During these two weeks, the Chl was also present through 3-4C's coasts. These subsections had a weaker Chl signal in the last week as well. Like the previous month, the Chl signal was driven by positive SLP anomalies in the Central and Southern Zone, owing to SPSA reinforcement (0.52), leading to strong alongshore winds in 3N-1C during the first week, whereas they shifted to 4C-1S during the second and third weeks. In the final week of February, slightly lower southerly winds spread over 3N to 4C.

The SPSA in February was enough to maintain the high atmospheric temperatures and low PR observed in the previous months. An exceptional case was a low-pressure front in 1S in the first week, provoking westerly winds and a PR episode (DMC, 2018). This was the starting point of the Chl rise in 1S's interior sea (sea Figure 6.21). As was mentioned in Case 5 (section 6.3.2.1), this section has a lower stratification when the Puelo River streamflow is below 360 $m^3 s^{-1}$ (De la Torre, 2016). Although its flow was 402.5 $m^3 s^{-1}$ this month, which is 7% higher than its typical flux, its daily flux was under the 360 limit from February's second week until the last week of March, except on 16th and 17th March. On the other hand, the Biobio

streamflow was 662 m³ s⁻¹, doubling its typical flux (Figure 3.5). The 2C's and 3C's rivers had the same flux reduction observed in January.
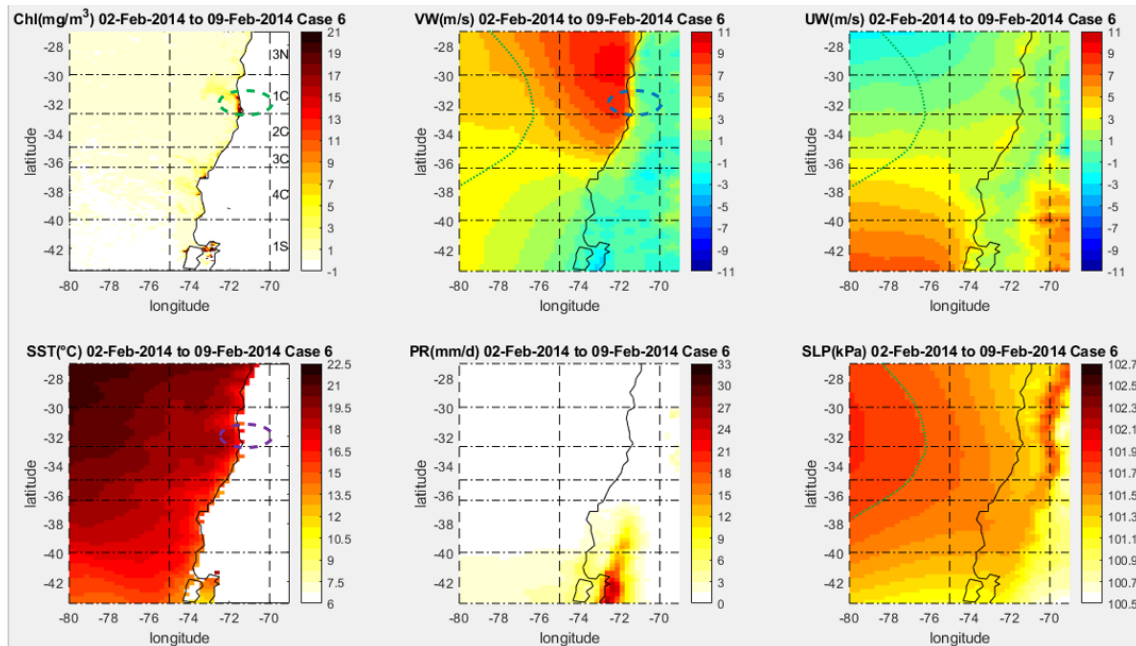
FIGURE 6.21. CASE 6 CHL, VW, UW, SST, PR AND SLP WEEKLY VALUES ON THE 3N, THE CENTRAL ZONE AND 1S SECTIONS, SHOWING THE FIRST WEEK OF FEBRUARY 2014. THE DASHED CIRCLES HIGHLIGHT THE CHL INCREMENT LOCATION IN THE CHL, SST, VW AND UW PANELS. THIS HELPS TO IDENTIFY THAT THE SST DROP HAS THE SAME SHAPE AS THE CHL INCREMENT, WHILE THE HIGH SOUTHERLY WINDS WERE ASSOCIATED WITH THE CHL INCREMENT IN 1C. THE DOTTED LINES SHOWED HOW THE SLP IMPACTS SOUTHERLY AND WESTERLY WIND PATTERNS. THE SLP PANEL ALSO INDICATES THAT THE SLP WAS LOWER THAN USUAL. THE PR PANEL SHOWS THE EPISODIC RAIN THAT MONTH IN 1S, WHICH LIKELY REDUCED THE CHL IN THAT SECTION, WHILE THE WESTERLY WINDS ADDED NUTRIENTS AND SALTWATER INTO THE CHILOÉ'S INTERIOR SEA.
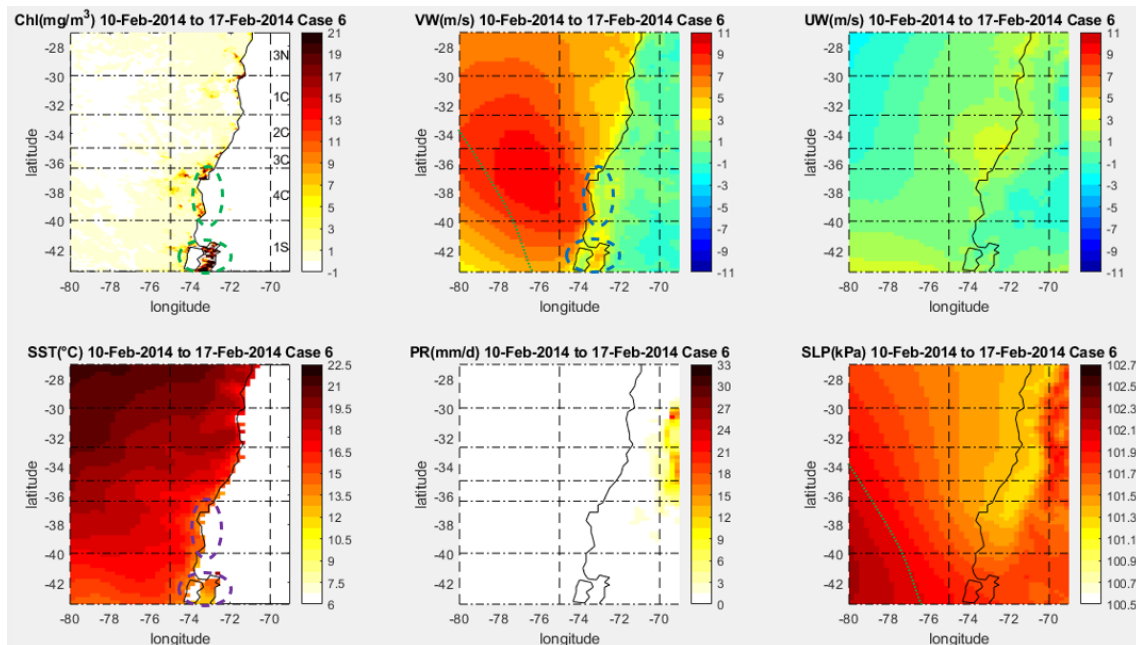
FIGURE 6.22. CASE 6 CHL, VW, UW, SST, PR AND SLP WEEKLY VALUES ON THE 3N, THE CENTRAL ZONE AND 1S SECTIONS, SHOWING THE SECOND WEEK OF FEBRUARY 2014. THE DASHED CIRCLES HIGHLIGHT THE CHL INCREMENT LOCATION IN THE CHL, SST, VW AND UW PANELS. THIS HELPS TO IDENTIFY THAT THE SST DROP HAS THE SAME SHAPE AS THE CHL INCREMENT, WHILE THE HIGH SOUTHERLY WINDS WERE ASSOCIATED WITH THE CHL PEAK IN 1S'S INTERIOR SEA AND THE SLIGHT RISE IN 4C. THE DOTTED LINES SHOWED A MORE INTENSE SPSA MOVED SOUTHWARDS, DEVELOPING SOUTHERLY WINDS IN 4C AND 1S SUBSECTIONS. THE PR PANEL SHOWED NO PR THAT WEEK, ACTING TO REDUCE PUELO'S STREAMFLOW AND RESULTING STRATIFICATION.

In March, the Chl anomalies were considerably down in 1S's interior sea; while 1C's anomalies were reduced, they still were near 2 SD (Figure 6.20). Effectively, the weekly maps

136

did not show such high Chl concentrations as the previous month. A low Chl signal appeared in 1C the whole month. Even in its maximum Chl productivity during the third week, 1C did not exhibit significant peaks, but the Chl covered a higher area oceanwards. The 1S interior sea only experienced higher Chl concentrations in the Ancud Gulf (Figure 6.18) into March's first days. A significant Chl signal occurred in Chiloé's northern site in March's final days as well. As in the February case, the Chl patterns were linked to the southerly winds, focusing on 3N-3C in the first three weeks, with a lower strength in the third. In the fourth week, even lower longshore winds shift to 4C and 1S. The SPSA was stronger than in February (1.17), but SLPs were more concentrated in the Northern and partially the Central Zone, allowing more steady and slightly stronger southerly winds in 1C. As the SLP anomalies were more concentrated in these Zones, 1S experienced PR episodes from the second to the final week of March. All of them were low, except for heavy rains registered on the last days of the month (Aceituno et al., 2015). Although the Puelo flow was even lower than in February, with a 20% reduction, the Chl dropped in 1S's interior sea due to the limited southerly winds and high PR.

The following month, the Chl showed generally negative anomalies, except in 1C, where some of its sections were approaching anomalies of 2SD (Figure 6.20). Nonetheless, 1C's anomalies were barely visible in the weekly maps. The only clear Chl signal was located in 1S, showing a weak remnant of the previous month in the Chiloé's northern Pacific during the first week and an intense signal restricted to a small area in the north of Ancud Gulf during the rest of the month. The SPSA was even stronger this month (1.50), but it moved further north as it typically does. Thus, the strong winds were present in the majority of the Central Zone, but they were absent from 1S, except for weak winds during the first week. Therefore, the drought continued in the Northern and Central Zone this month. 1S measured low PR episodes the whole month except in the last week, where a severe PR event occurred due to a cold front driven by AAO changing to its negative phase (DMC, 2018; Aceituno et al., 2015). Hence, the Puelo River exhibited an averaged flux, while the Biobio reached 1,107 m^3 s^{-1}, almost three times its typical flux (Figure 3.5). On the other hand, the Maipo and Mataquito streams had half of their typical value.

Overall, 1C's Chl anomalies were related to the rapid SPSA intensification from January to February, leading to strong and constant southerly winds. These more extreme anticyclonic conditions were also present in 1S during February, increasing the Chl in that section. Although 1C's Chl anomalies were higher than 1S's, the weekly maps showed that 1S had a more pronounced concentration. This was because 1C had a generally lower Chl concentration, presumably because of a lower nutrient supply.

Even though the SPSA was higher in March and April, 1C's Chl anomalies were more significant in February due to the rapid intensification of the southerly winds. The following month, the southerly winds were stronger at 1C, producing a steady Chl signal that spread over the whole section. Finally, the SPSA was moved to the north in April, increasing the winds even more to 1C, but the Chl went down probably because of reduced sunlight at the beginning of autumn.

Although the Puelo's flow was lower in March and April, the Chl concentration in 1S's interior sea was higher in February because that month had prominent southerly winds and higher sunlight. Furthermore, March and April exhibited a significant amount of PR, increasing the stratification and reducing the sunlight. On the other hand, the Biobio, Maipo and Mataquito River variations did not affect 2C's and 4C's Chl response compared to the longshore winds.

These findings are consistent with the Chl~VW and Chl~SLP positive correlations observed in both the interior and Pacific borders of Chiloé island (Figure A.3.6). On the other hand, the 1C

Chl concentration did not significantly correlate with the physical variables because the Chl signal was relatively weak.

6.3.2.3. Case 7:

This is the first of two cases selected specifically because of the Chl anomaly in the ocean strip owing to the very high and unusual concentration in sub-region 3CO (Table 6.11 and Figure 6.23). This case started in April 2018 with a high anomaly in 2CO and 3CO, followed by concentrations three times bigger detected in these subsections in the next month. Additionally, 3CT also showed a significant anomaly that month. In the last month of the case, 2CO and 3CO's Chl dropped but still retained significant anomalies, while 3CT and 4CO increased, reaching significant anomalies. During this case, the SPSA was located in the Central Zone, while a weak La Niña was in its final stage, shifting to El Niño. The AAO was weak, except in April (-1.2). Thus, the affected region was surrounded by high- and low-pressure that significantly impacted this case.

TABLE 6.11. CASE STUDY 7 SUMMARY INDICATING THE SUBSECTIONS AFFECTED THEIR CHL ANOMALIES IN SD, ENSO, SPSA AND AAO MONTHLY VARIATION, AND ADDITIONAL COMMENTS.

Subsections	Date	Chl (anom)	ENSOm	AAOm	SPSAm	Comments
2CO, 3CO	Apr-18	2.9, 3.2	-0.41	-1.17	1.24	2-3CO highest [Chl] [2.3, 9 mg m^{-3}] & anom (3.5,
2CO, 3CT, 3CO	May-18	3.5, 2.2, 3.7	-0.11	-0.08	1.00	3.7) in May; highest anom 3CT (2.8); weak La Niña
2CO, 3CT, 3CO, 4CO	Jun-18	2, 2.8, 3, 2.5	0.12	0.01	2.67	(-0.46), extreme SPSA (1.34),& +AAO (0.48), but with a strong -AAO (-1.2) in April.

Climate drivers played a crucial role in this case. The SPSA was centred in the Central Zone at 36°S, modulated by a weak La Niña. An extended but weak Chl sign occurred in 4C, which slowly moved oceanward. This signal was later concentrated by a subtropical cyclone driven by the interaction of the SPSA's core with a low-pressure system coming from the Southern Zone, leading to a sudden negative AAO. Although the cyclone weakened the Chl ocean signal, it persisted and was reinforced by the later appearance of intense southerly winds. Cyclones have been reported in the Southern Zone, but this event was utterly unusual for the Central Zone (NOAA, 2019).
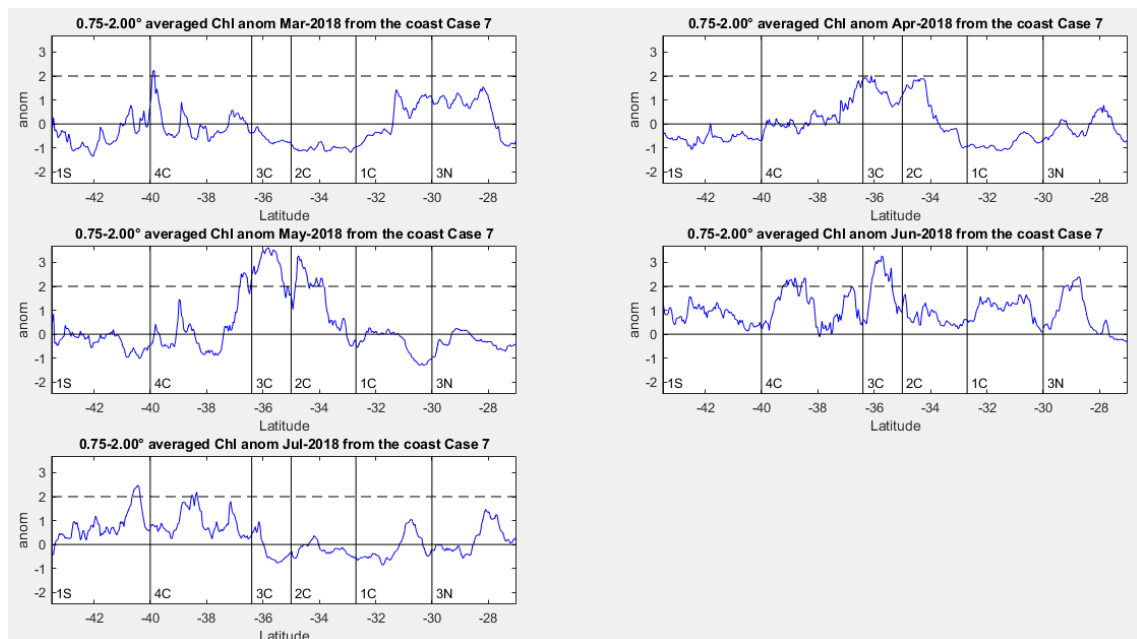
FIGURE 6.23. CASE 7 MONTHLY CHL CROSS-SECTIONS IN THE OCEAN STRIP PARALLEL TO THE COAST FROM 0.75° TO 2.0° OCEANWARD USING THE ANOMALIES DIVIDED BY SD FOR THE 3N, THE CENTRAL ZONE AND 1S. THE BLACK DASHED LINE DRAWS ATTENTION TO THE SECTIONS WITH THE MOST SIGNIFICANT CHL ANOMALIES, SUCH AS 3C FROM APRIL TO JUNE, 2C IN APRIL AND MAY, WHILE 4C SHOWS SMALL SECTIONS OVER 2 SD FROM MAY TO JULY WITH MORE CONSISTENT ELEVATION IN JUNE.

Figure 6.23 showed low Chl anomalies in the ocean strip in the Central Zone and 1S in March. These were also relatively low in the coastal strip that month, except in the area near 36-38°S at 4C. This anomaly is visible in the weekly maps, and it started spreading oceanwards in the last week of March, forming an extensive patch with a low concentration (Figure 6.24). This particular phenomenon seems related to the SPSA centred at 35°S (1.13) as it typically is in March, leading to alongshore winds in this section. 1S exhibited a minor SST increment in Chiloé's exterior sea during the first half of March. A SST elevation in this region tends to produce red tide episodes owing to a significant presence of salmon farms here, which contribute to a sustained NH_4^+ and PO_4^{-2} increment through the coastal waters (Buschmann et al., 2016; Armijo et al., 2020; Wells, 1997). Effectively, red tide incidents were seen in January and February related to that SST elevation, killing 4,800 tonnes of salmon. However, this year the situation was less severe than usual events seen in recent years (Sernapesca, 2018). At the end of March, an extratropical cyclone covered the Southern Zone, the indicator of an incipient negative AAO (-1.17 in April), generating high PR, westerly winds and lowering the SST. Indeed, the Puelo River exhibited a flow of 450 m^3 s^{-1}, 40% higher than usual. The Maule River also increased by 20%, while the Maipo, Biobio and Mataquito experienced a 40 to 60% reduction (Figure 3.5).

The Chl patch observed in March continued through April, concentrating in the 3C and 2C ocean strip at the end of April (Figures 6.23 and 6.25). The weekly maps showed that the Chl signal in the ocean continued increasing during May, concentrating more in the 3C ocean and coastal strips with an oval shape and a slightly weaker signal in 2CO during the first week. The Chl signal diminished the following week to reach its peak in the third week of that month, exceeding 20 mg m^{-3} in some sections (Figure 6.25).
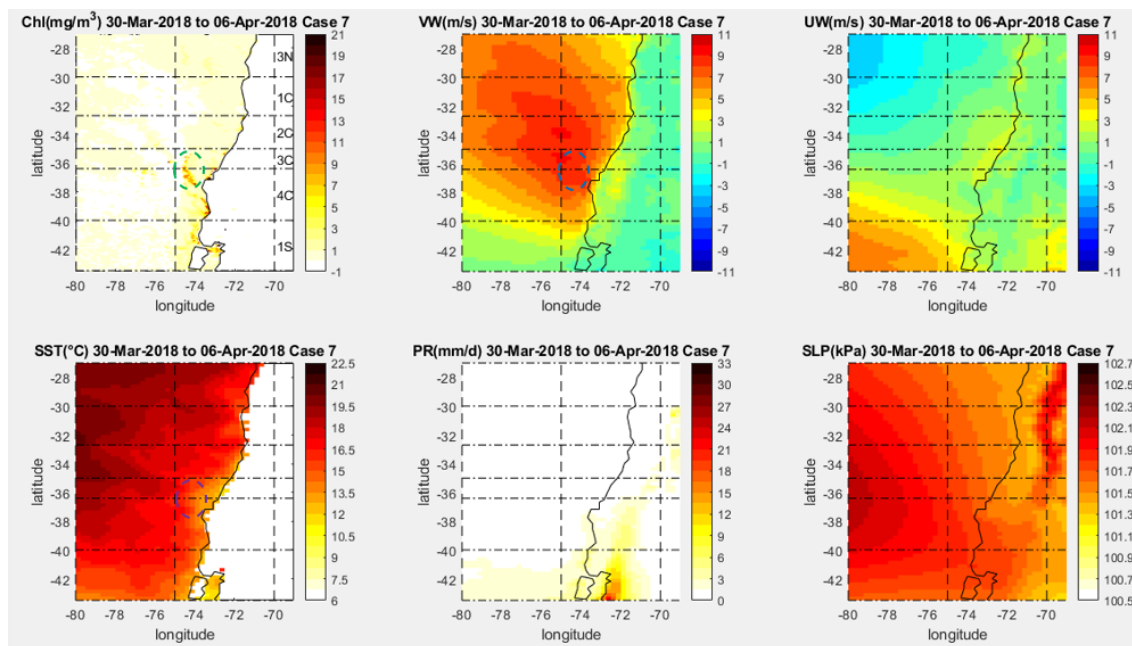
FIGURE 6.24. CASE 7 CHL, VW, UW, SST, PR AND SLP WEEKLY VALUES ON THE 3N, THE CENTRAL ZONE AND 1S SECTIONS, SHOWING THE FIRST WEEK OF APRIL 2018. THE DASHED CIRCLES HIGHLIGHT THE CHL INCREMENT LOCATION IN THE CHL, SST AND VW PANELS. THIS HELPS TO IDENTIFY THAT THE SST DROP EXTENDED WHERE THE CHL IS, WHILE THE HIGH SOUTHERLY WINDS WERE ASSOCIATED WITH THE CHL SEGMENT IN THE OCEAN NEAR 3C. THE PR PANEL SHOWS THE HIGH PR THAT WEEK IN 1S DUE TO THE CYCLONE. THE SLP PANEL SHOWS THAT THE SPSA'S CORE IS AT 36°S, LEADING TO STRONG WINDS AT 3C AND 4C.

A subtropical cyclone appeared near 3C from 5th to 10th May. This cyclone was quasi-stationary because the Andes acted as a barrier (DMC, 2018). As a result, SST rose, and widespread northeasterly winds surrounded the Chl signal, weakening and concentrating it in 3C (Figure 6.26). The cyclone drove only a few weak thunderstorms because its core SSTs were not warm enough to produce high convective activity (NOAA, 2019). After the cyclone,

cold fronts dominated the Southern Zone during the next and the fourth week, not allowing the return of the southerly winds to the 3C-4C subsections (DMC, 2018). However, in the third week, a high-pressure system was driven by the SPSA re-formation (1.0), leading to intense southerly winds in the Chl signal area (Figure 6.27).
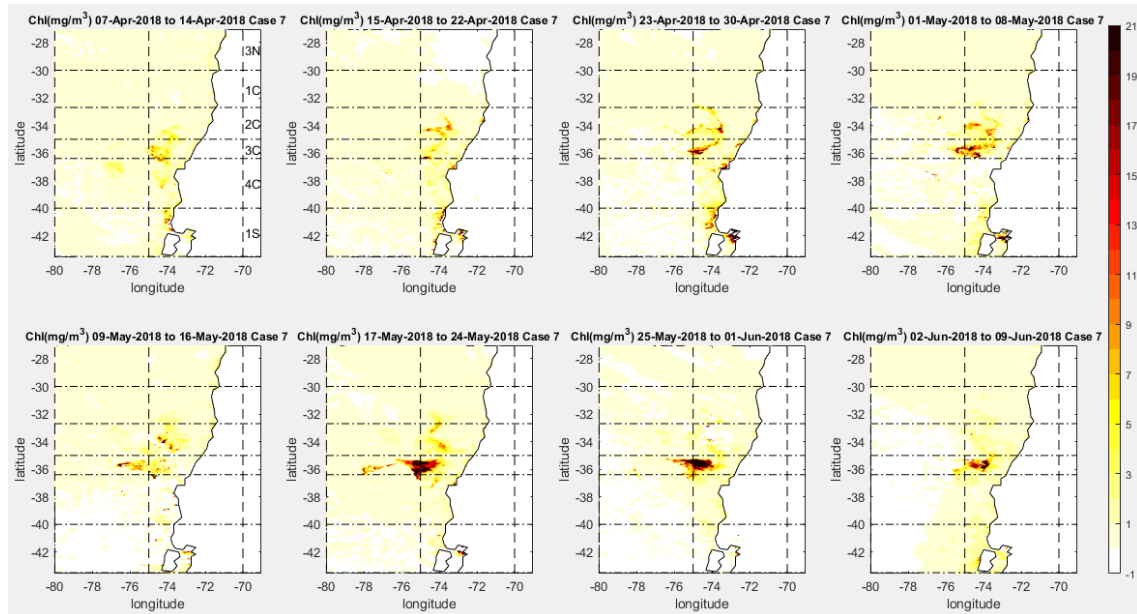
FIGURE 6.25. CHL WEEKLY EVOLUTION IN THE CRITICAL WEEKS FOR CASE 7 DEVELOPMENT. THIS FIGURE SHOWS HOW THE CHL SIGNAL SPREAD IN RESPONSE TO THE CYCLONE BUT WEAKENED IN THE FIRST WEEKS OF MAY AND HOW IT REACHED THE MAXIMUM CHL CONCENTRATION IN THE LAST WEEKS OF MAY, WITH SOME SECTIONS WHERE THE CHL EXCEEDED 20 MG M^{-3}.
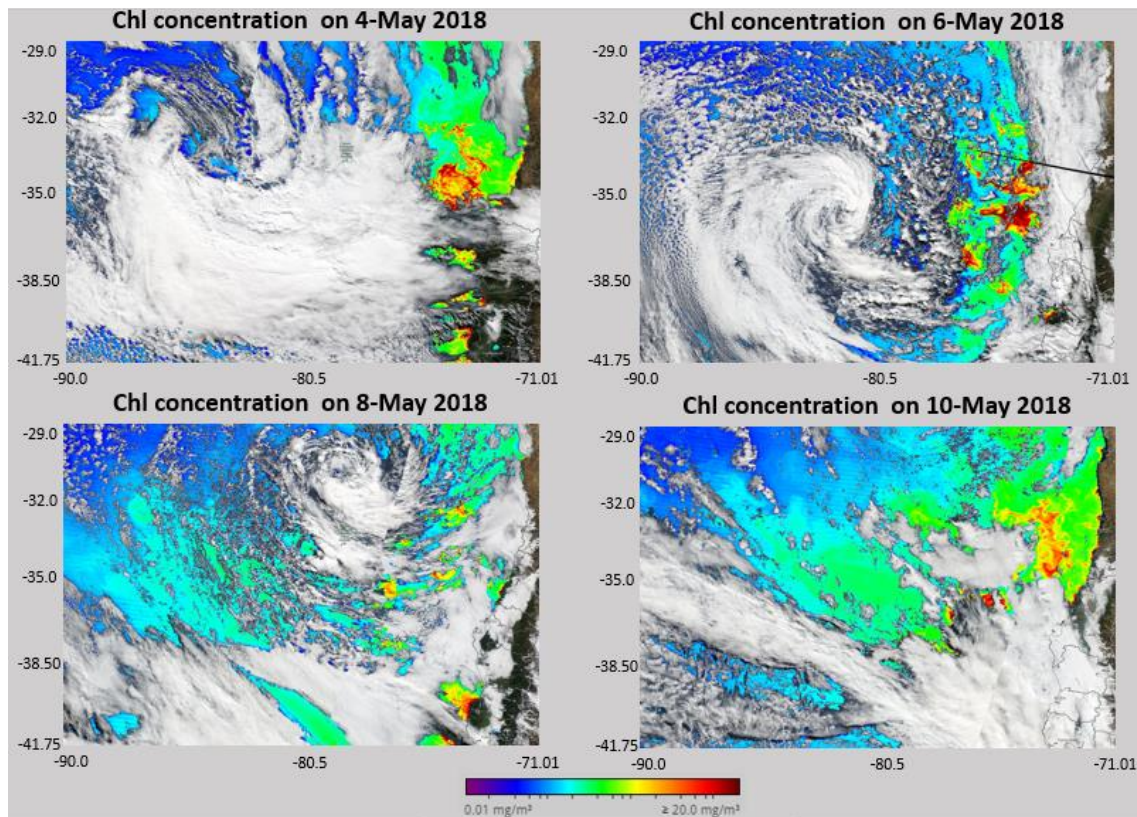
FIGURE 6.26. MODIS-AQUA SATELLITE VIEW OF CYCLONE EVENT WITH CHL CONCENTRATION TAKEN BETWEEN 4TH–10TH MAY 2018. THIS FIGURE SHOWS HOW THE CYCLONE SHAPED THE CHL SIGNAL, WHICH REACHED OVER 20 MG M^{-3} ON 6TH MAY.

3CO showed weaker but still significant, Chl monthly anomalies in June, indicating the final stage of this case (Figure 6.23). Certainly, the June weekly maps demonstrated that the Chl

signal was strong only in the first week (Figure 6.25). Remnants of the Chl signal could be seen in the following week, but it completely faded away for the rest of the month. Although the southerly winds were consistent during the first three weeks, they were more located in the north due to the SPSA centre moving to 30°S as it typically does in this period (2.64). Finally, the SPSA was weakened at the end of June and the beginning of July (0.94), linked to a Kelvin wave that arrived in the west Pacific, increasing the SST on the coast. This was considered a transition between La Niña's final stage and an incipient El Niño (0.16; DMC, 2018).

In July, the Chl anomalies were average in the ocean and coastal strip (Figure 6.23). The weekly maps did not show any significant Chl concentration in the Central Zone during this month. The winds were weak until 11th June from 1C to 3S. For the rest of the month, the southerly winds dominated conditions from 1C to 3C. However, 4C experienced southerly winds the last week, but they were relatively weak. These conditions were driven by the SPSA's northern location, weakening the winds. Additionally, a frontal system from the Southern Ocean arrived at the Central Zone in the first week (DMC, 2018).
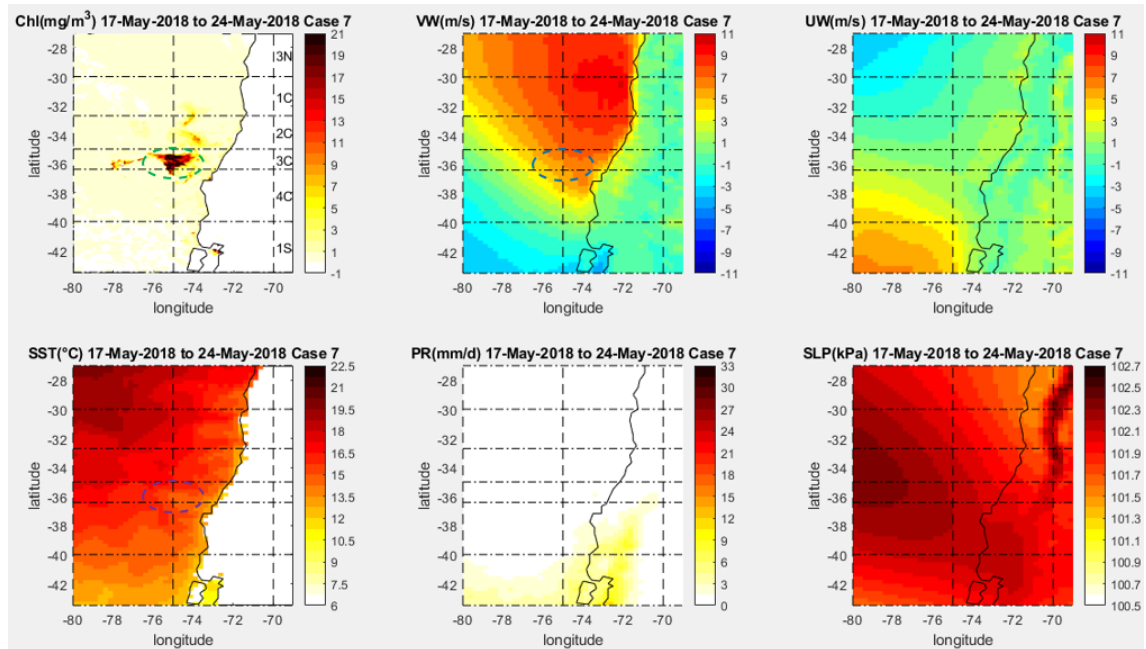

FIGURE 6.27. Chl, VW, UW, SST, PR AND SLP WEEKLY VALUES ON THE 3N, THE CENTRAL ZONE AND 1S FOR CASE 7 PEAK BETWEEN 17TH-24TH MAY 2018. THE DASHED CIRCLES HIGHLIGHT THE CHL INCREMENT LOCATION IN THE CHL, SST AND VW PANELS. THIS HELPS TO IDENTIFY THAT THE SST DROP EXTENDED WHERE THE CHL WAS, WHILE INTENSIVE SOUTHERLY WINDS DROVE THE CHL INCREMENTS. THE SLP PANEL SHOWS THAT THE SPSA CENTRE IS MOVING NORTHWARDS.

In conclusion, this case resulted from particular synoptic conditions driven by the interaction between extreme pressure systems. The case began when rapid wind variation appeared in 4C, driven by the SPSA centred in the Central Zone, which La Niña enforced, drastically reducing the PR and the Maipo and Biobio River fluxes. Then this high-pressure interacted with a low-pressure system from the south, linked to negative AAO, forming a cyclone. This cyclone's winds led to an expansion and concentration of the Chl signal, which later was increased through the impact of strong southerly winds that generate upwelling, dragging nutrients offshore by the Ekman transport. Finally, the case halted because the SPSA moved northwards, weakening the southerly winds in the area.

Although the origin of this case is relatively straightforward, it is not necessarily clear why the Chl signal was so high, reaching concentrations that exceed 20 mg m^{-3} in the ocean strip while the coastal strip showed only average concentrations. One possible explanation is that the red tide's nutrient transport could produce that particular response, considering that MODIS-

aqua cannot differentiate these events (Yang et al., 2018). Another option is fishing vessels that dump dead fish through the ocean, increasing the nutrient levels rapidly and then increasing phytoplankton. Though no records have shown that companies had done that for this event, they did it during the 2016 red tide (Case 11 section 6.3.3.4). Moreover, a well-known company was fined for doing this practice in 3S, at least from 2013 to 2018 (Molinari, 2021).

Due to the high variability of meteorological conditions responsible for this case, the correlations among the Chl and the physical parameters in 3CO were not significant, except for the SST showing a positive response, which might be associated with SST rise during the cyclone phenomenon (Figure A.3.7).

6.3.3. Southern Zone.

Similarly to the Northern Zone, the Southern cases are three Chl anomalies (Case 8, 9 and 10) plus a red tide event linked to El Niño 2015 (Case 11). Case 8 showed the highest concentration and anomaly in 2ST. Like Case 7, Case 9 experienced a high concentration at the ocean strip for the entire Southern Zone. Lastly, Case 10 contained the highest anomaly and concentration in 3S. As with the Central Zone, the most significant rivers will be mentioned for these cases.

6.3.3.1. Case 8:

This case started in February 2003 with an ephemeral Chl event in 1S (1.5 SD), which was not noticeable in the monthly average anomalies. This anomaly increased significantly to 2.1 SD in March (Table 6.12). Although the Chl concentration in 1ST slightly rose the following month (from 4.37 to 5.1.4 mg m^{-3}), it went down in terms of the anomaly (from 2.1 to 1.9 SD). Meanwhile, the 2ST subsection exhibited its highest Chl concentration and anomaly with 7.6 mg m^{-3} or 3.3 SD that month. Additionally, this case occurred in a transitional stage from El Niño to normal conditions and the AAO's from a negative to a positive phase. This led to meteorological conditions marked by a PR deficit that affected the Central and Southern Zone, which helped reduce the stratification and boost the Chl. Finally, Case 8 happened at a similar time as Case 1 (section 6.3.1.1).

TABLE 6.12. CASE STUDY 8 SUMMARY INDICATING THE SUBSECTIONS AFFECTED, THEIR CHL ANOMALIES IN SD, ENSO AND AAO MONTHLY VARIATION, AND ADDITIONAL COMMENTS.

Subsections	Date	Chl (anom)	ENSOm	AAOm	SPSAm	Comments
1ST, 1SO	Mar-03	2.1, 2.2	0.45	-0.19	-0.38	Highest [Chl][7.6 mg m^{-3}] & anom (3.3) in 2ST; moderate El
2ST, 2SO	Apr-03	3.3, 2.5	-0.05	0.22	0.59	Niño (0.72), weak -AAO (-0.48).

Case 8 is linked to pressure disturbance driven by a positive AAO and El Niño, shifting the SPSA to an unusual, southerly position. Due to this, the Southern Zone experienced a significant drought and southerly winds that provoked a rapid Chl signal response. This can be observed through the local rivers' flux deficit and the SLP rise that were coincident with the Chl patterns (Figures 6.29 and 6.30). Furthermore, 2S's Chl showed significant positive correlations with SLP and VW and a negative correlation with PR (Figure A.3.8).

In February, the Chl anomalies were significant in parts of 2S, 4C and specifically 1S's interior sea (Figure 6.28). The weekly maps displayed a significant Chl concentration from 3C to 2S in the second week, with a higher concentration in the aforementioned subsections (Figure 6.29). However, the Chl was relatively low for the rest of the month, except in the northern part of zone 4C. This response was consistent with the SPSA reinforcement (0.5) in February's second week, where its core reached 40°S, leading to strong southerly winds from the Central Zone to the 2S border with 1S. These conditions persisted for the upcoming weeks but at a lower level. As a result of these anticyclonic conditions and El Niño (0.74), PR was

down in the Southern Zone (1S and 2S). 3S' PR episodes were slightly higher owing to cold front interventions associated with the negative AAO (-044; Aceituno et al., 2015).
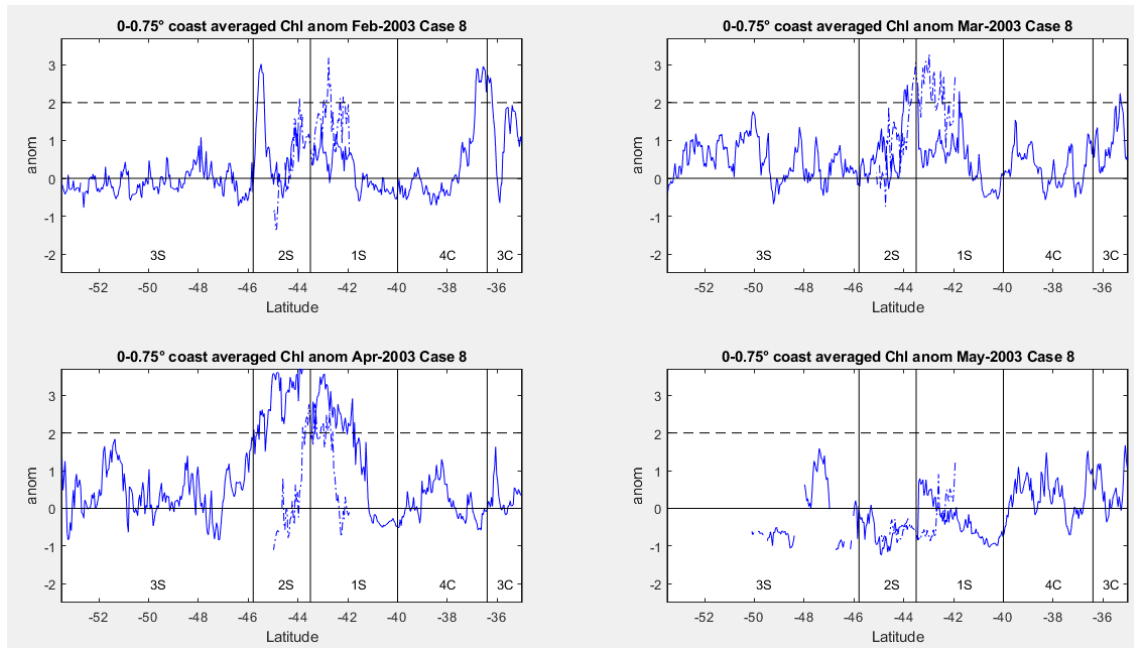
FIGURE 6.28. CASE 8 MONTHLY CHL FROM THE COAST TO 0.75° OCEANWARD USING THE ANOMALIES DIVIDED BY SD ON THE 3C, 4C AND THE SOUTHERN ZONE. THE DASHED BLUE LINE IN 1-2S REPRESENTS THE CHL ANOMALY ACROSS THE ANCUD AND CORCOVADO GULFS BETWEEN CHILOÉ ISLAND AND THE MAINLAND (41.9°-45°S), WHILE THE CONTINUOUS LINE IS THE CHL ANOMALY ACROSS THE CHILOÉ COASTLINE AND THE PACIFIC BASIN. THE BLACK DASHED LINE DRAWS ATTENTION TO THE SECTIONS WITH THE MOST SIGNIFICANT CHL ANOMALIES, SUCH AS 1S CHILOÉ'S INTERIOR SEA IN MARCH, AND 1-2S PACIFIC BASIN, WHICH IS OVER 3 SD IN 2S. ALSO, 3C, 2S AND 1S'S INTERIOR SEA SHOW SMALL SECTIONS OVER 2 SD IN FEBRUARY.
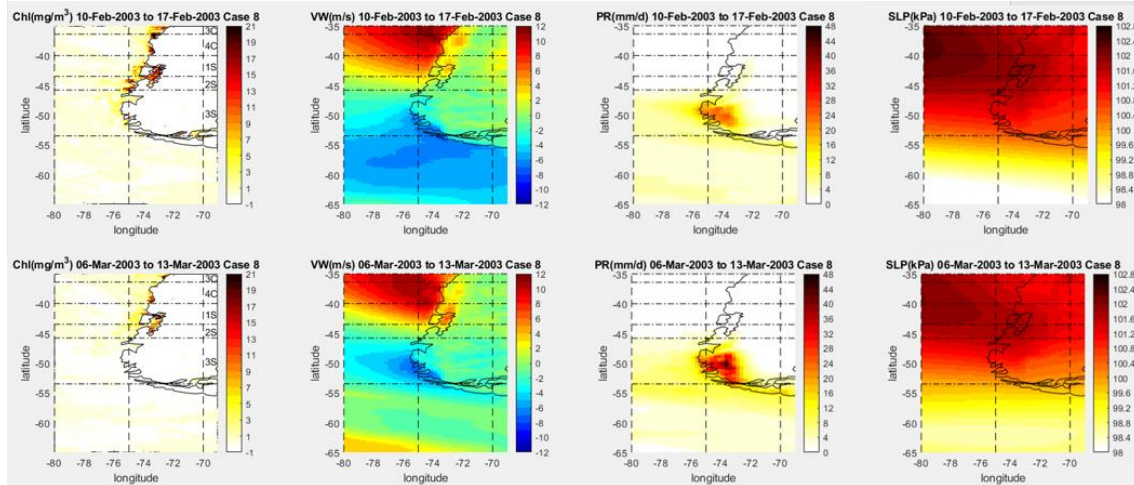

FIGURE 6.29. CASE 8 CHL, VW, UW, PR AND SLP WEEKLY VALUES ON THE 3C, 4C, AND THE SOUTHERN ZONE FOR THE PEAK WEEKS FOR FEBRUARY AND MARCH 2003. THE SLP PANEL SHOWS THAT BOTH DATES EXHIBITED HIGH-PRESSURE SYSTEMS MAINLY AFFECTING 4C -2S SECTIONS, WITH A HIGHER INTENSITY IN FEBRUARY. THE VW PANEL DEMONSTRATES THAT THE SLP INCREMENTS LED TO SOUTHERLY WINDS IN 4C TO 2S IN FEBRUARY AND 4C TO 1S IN MARCH. THEREFORE, THE CHL WAS HIGHER IN FEBRUARY THAN IN MARCH. AS A RESULT OF THE SLP DIFFERENCES, THE PR EVENTS IN 3S WERE MORE INTENSE IN MARCH THAN THOSE IN FEBRUARY.

The following month, the Chiloé's interior sea showed a significant Chl signal reaching anomalies above 3 SD in the 43°-43.5°S band (Figure 6.28). March's weekly maps indicated that this anomaly appeared in the second week (Figure 6.29). Nonetheless, it was not as high as the last month. The Chl persisted in the next two weeks but declined and rose again. The SLP patterns, described in February, continued with a lower strength but gradually spread into the Southern Zone, reaching 3S in March's last week, with a slight weakening in the third week linked to a rapid cold front passing by. This provoked southerly winds with high intensity in 4C-1S during the second week (Figure 6.29). In the subsequent week, these winds

143

vanished from 1S, reappearing in the Southern Zone in the last week, but with lower intensity. This SLP behaviour is typically observed in the Southern Zone during the summer when El Niño occurs (Montecinos and Aceituno, 2003). Also, it diminished the SPSA effect in the Northern Zone during this month (-0.38), which can be seen in Case 1 (section 6.3.1.1).

Due to these anticyclonic conditions associated with El Niño, the PR dropped drastically in 1S and 2S, whereas 3S exhibited high PR episodes in the first two weeks of March associated with negative AAO (-0.2), which was displaced by the high-pressure system in the last week. Furthermore, significant positive atmospheric temperature anomalies dominated 1S in the second and final week and negative in the third (Aceituno et al., 2015). Therefore, the Chl signal in the interior Chiloé sea was driven by southerly winds and the PR reduction that presumably reduced the Puelo's flux. Although the latter's outflow was not measured during this month, the Palena and Cisnes Rivers were 25% lower (Figure 3.7). These are the main tributary rivers for the Southern interior sea (43.82°-45°S), feeding the Corcovado Gulf and Puyuhuapi Channel, respectively (Figure 6.18) 1S and part of the 2S subsection. On the other hand, Aysén River (45.41°S) located in 2S, was normal this month.

In April, the Chl anomalies declined in the Chiloé interior sea, but the 43°-43.5°S band's Chl continued over 2 SD. In contrast, a sharp Chl increment was seen across the Chiloé's Pacific basin and 2S, with sections that exceeded 3 SD (42°-45°S; Figure 6.28). The weekly maps showed that outside the third week, an intensive Chl signal was present the whole month (Figure 6.30). The Chl signal was concentrated in the Chiloé's interior sea in the first week, with a slight presence in its Pacific border. The next week a high Chl concentration appeared along Chiloé's Pacific coast, spreading oceanward, while the interior sea could not be monitored due to heavy cloudiness. During the third week, the Chl was only significant in the 1S' interior sea border; however, the signal in 2S was unavailable that week. Finally, the Chl signal was significantly intense in 2S with a slight concentration in the Chiloé Island surroundings in the last week (Figure 6.30).

April was marked by an incipient La Niña (-0.05) reinforcing SPSA (0.5), whose core oscillated between 35° and 45°S (Figure 6.30), while the AAO was positive (0.22). These conditions led to southerly winds that triggered the Chl patterns (Figure 6.30). Although these were lower than those observed in February and March, they were more consistent and extended further south. Consequently, only three low PR episodes were registered in the Southern Zone, where the highest was in the third week associated with a frontal system (Aceituno et al., 2015). The lack of rain reduced the Puelo streamflow by 50% (206 m^3 s^{-1}), whereas the Palena, Cisnes and Aysén Rivers exhibited a flow deficit over 55% (Figure 3.7).

In May, the Chl plummeted with negative anomalies in Chiloé's interior sea from 42.6S° to the end of 2S (Figure 6.28). Indeed, this month the weekly maps exhibited only a Chl concentration during the first and third week in the northern interior sea coast, near Reloncaví Fjord and 4C's middle section (Figure 6.18). This reduction was related to cyclonic conditions in the Southern Zone during the first and fourth weeks, leading to intensive northerly winds and PR events. Even though anticyclonic conditions returned to the Southern Zone in the second and part of the third week, generating southerly winds and no PR events, these winds were not as high as the April conditions. After this, the Southern Zone was dominated by low-pressure systems, regularising the PR events. Still, this Zone exhibited negative PR anomalies in May (Aceituno et al., 2015). Continuing with the previous month's trend, the Puelo was substantially affected by the drought, reducing its flow (252 m^3 s^{-1}) by 60%. Meanwhile, the Palena, Cisnes and Aysén showed a deficit of 31%, 15% and 38%, respectively, owing to a higher PR event further south 42°S (Figure 3.7).
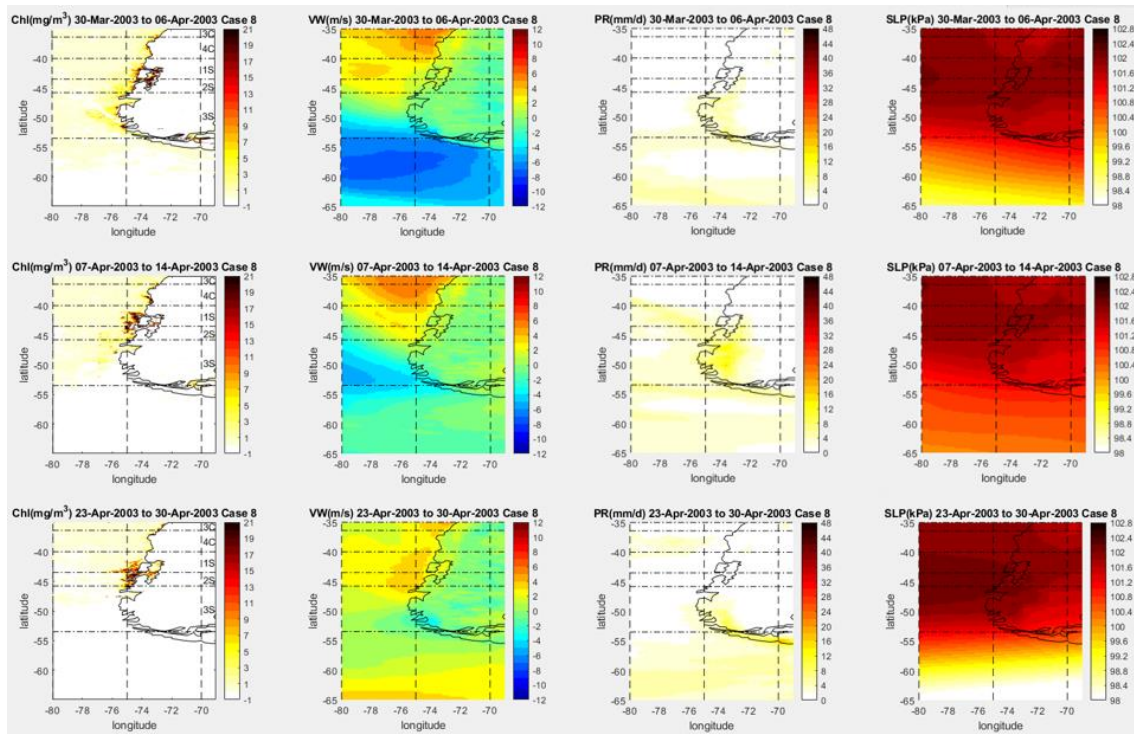
FIGURE 6.30. CASE 8 CHL, VW, UW, PR AND SLP WEEKLY VALUES ON THE 3C, 4C, AND THE SOUTHERN ZONE DURING THE FIRST, SECOND AND LAST WEEK OF APRIL 2003. THE SLP PANEL SHOWS HOW THE CORE WAS BOUNCING AROUND 40°, 35° AND 45°S, RESPECTIVELY, WITH A HIGHER PRESSURE IN THE FIRST WEEK FOLLOWED BY THE LAST. THESE SLP PATTERNS MATCH WITH THE LONGSHORE WINDS AND THE CHL INCREMENTS. ALTHOUGH THE SOUTHERLY COASTAL WINDS IN CHILOÉ WERE SLIGHTLY MORE INTENSE IN THE SECOND WEEK, THE FIRST WEEK SHOWED A HIGHER CHL CONCENTRATION IN THE INTERIOR SEA. THIS WAS LIKELY BECAUSE OF THE PR EVENT OBSERVED IN THE SECOND WEEK INCREASING STRATIFICATION.

In conclusion, the Chl increment resulted from the southerly winds and the lack of PR events in the Southern Zone due to the SPSA's more southerly position. The SPSA shift was triggered by El Niño and a positive AAO. A similar situation was observed in Case 3 (section 6.3.1.3) but with a Northern Zone perspective. Also, this case is the continuation of Case 1 (section 6.3.1.1), where the SLP decreased at the end of March as a result of the SPSA moving southwards. Montecinos and Aceituno (2003) reported that typically the Southern Zone experiences arid summers after important El Niño events, consistent with this conclusion.

The Chl coastal values in 2S exhibited significant positive correlations with SLP and VW and negative with PR and SST near its limit with 3S (Figure A.3.8), which are consistent with the conclusion. On the other hand, the Chl's coastal correlations with the physical variables in 1S's Pacific border and Chiloé's interior sea were less clear. The positive Chl~SST in the interior sea was the exception, which might be associated with the lack of PR, lower river flow, and higher atmospheric temperatures due to the cloudiness reduction.

6.3.3.2. Case 9:

This is the last case selected for the Chl anomaly in the ocean strip in subsection 3SO (Table 6.13 and Figure 6.31). However, it was not as extreme as Case 7 (section 6.3.2.3), and the Chl signal was also present in the coastal strip. Case 9 started in October 2014 with a high anomaly in 3SO (2.9 SD), followed by the case's peak with anomalies of 3.7 SD in 2SO and 3SO in the next month. 1SO and 2ST also exhibited significant Chl anomalies that month. During this case, an incipient weak El Niño and moderate negative AAO deflected the SPSA to the west. In addition, this year, the same as Case 6 (section 6.3.2.2), was characterised by arid conditions over the entire territory, which extended a PR deficit from the previous year and continued through this case (DMC, 2018).

145

TABLE 6.13. CASE STUDY 9 SUMMARISES THE SUBSECTIONS AFFECTED, THEIR CHL ANOMALIES IN SD, ENSO, AAO AND SPSA MONTHLY VARIATION, AND ADDITIONAL COMMENTS.

| Subsections	Date	Chl (anom)	ENSOm	AAOm	SPSAm	Comments
3SO	Oct-14	2.9	0.40	-0.04	-0.04	2-3SO highest [Chl] [4.2, 3 mg m^{-3}] & anom (3.7, 3.7); weak El Niño (0.47), moderate -AAO nov (-0.52) & extreme SPSA (1.21).
1SO, 2ST, 2SO, 3SO	Nov-14	2.2, 2.3, 3.7, 3.7	0.71	-0.52	1.21	
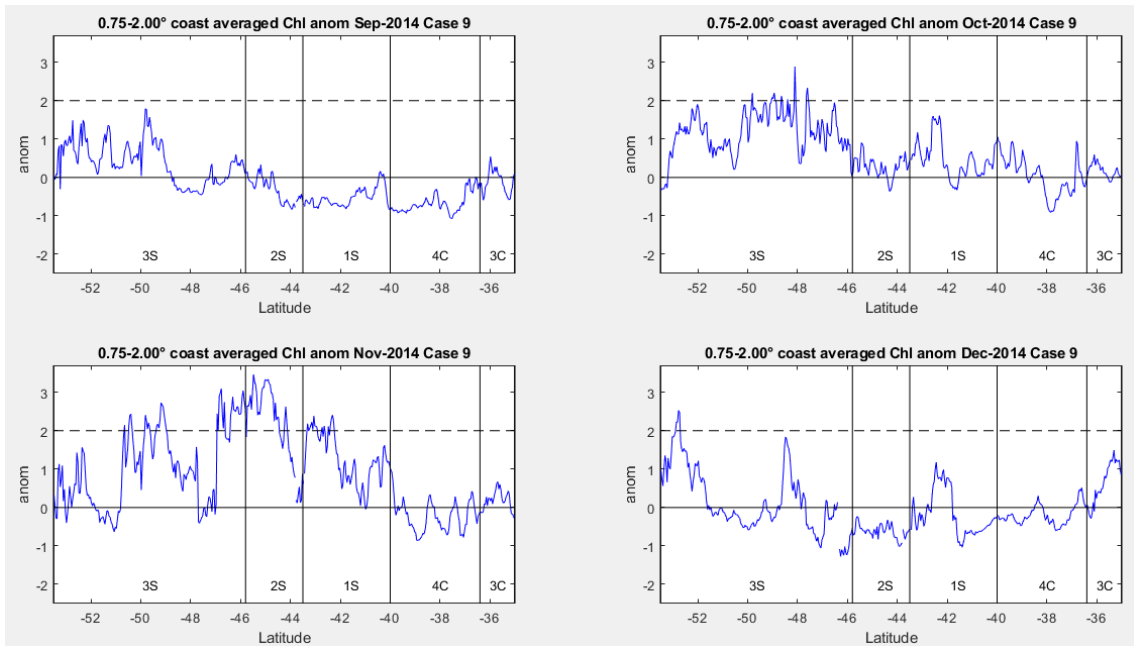
FIGURE 6.31. CASE 9 MONTHLY CHL CROSS-SECTIONS IN THE OCEAN STRIP PARALLEL TO THE COAST FROM 0.75° TO 2.0° OCEANWARD USING THE ANOMALIES DIVIDED BY SD FOR THE 3C, 4C SECTIONS AND THE SOUTHERN ZONE. THE BLACK DASHED LINE DRAWS ATTENTION TO THE SECTIONS WITH THE MOST SIGNIFICANT CHL ANOMALIES, SUCH AS 3S IN OCTOBER AND THE 1S-3S IN NOVEMBER, WHERE THE MORE SIGNIFICANT INCREMENT WAS IN 2S.
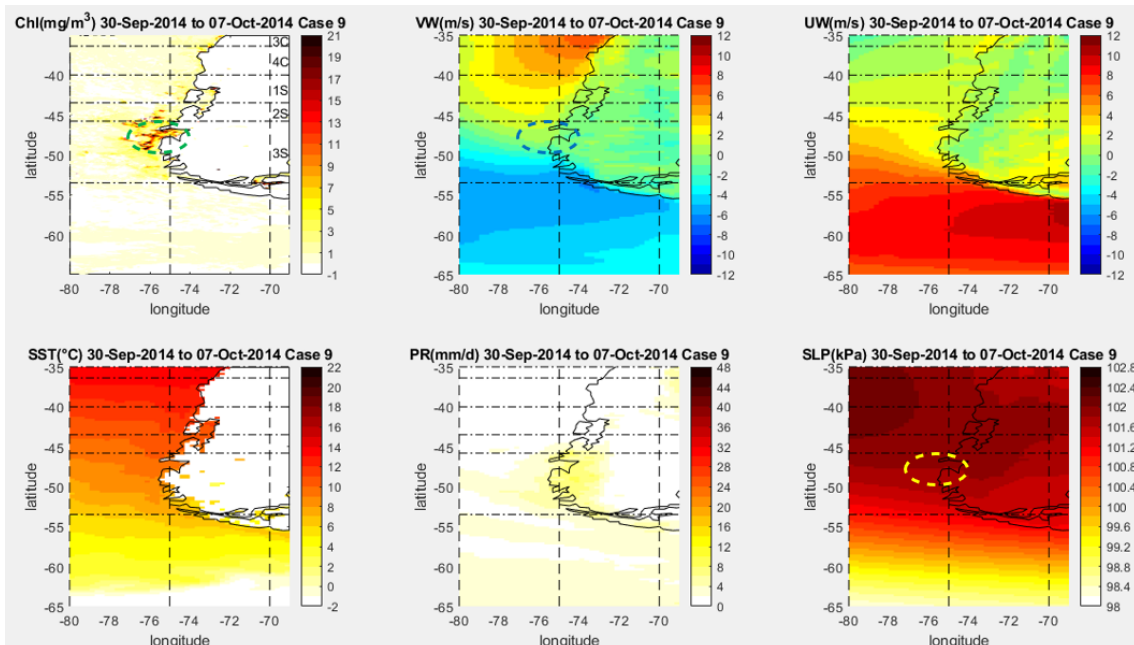

FIGURE 6.32. CASE 9 CHL, VW, UW, SST, PR AND SLP WEEKLY VALUES ON THE 3C, 4C AND THE SOUTHERN ZONE SECTIONS, SHOWING THE FIRST WEEK OF SEPTEMBER 2014. THE DASHED CIRCLES HIGHLIGHT THE CHL INCREMENT LOCATION IN THE CHL, SLP AND VW PANELS. THIS HELPS TO IDENTIFY THAT THE SLP INCREASE MATCHES THE SOUTHERLY WIND AND THE CHL SEGMENT. THE PR PANEL SHOWS THE LACK OF PR THAT WEEK DUE TO THE ANTICYCLONE CONDITIONS. THE SST IN THE 3S SECTION EXPERIENCED POSITIVE ANOMALIES DRIVEN BY THE SOUTHERLY WINDS.

Similarly to Case 8 (section 6.3.3.1), Case 9 was linked to negative SLP anomalies in Antarctica and anticyclonic conditions in the Southern Zone, driven by El Niño, with the anticyclonic

conditions later enhanced by the SPSA (DMC, 2018; Figure 6.33). This reduced the PR events in an arid year and increased the southerly winds, boosting the Chl. This is consistent with positive Chl correlations with SLP, VW and negative with the PR in the coastal strip in 3S (Figure A.3.9). Still, PR events were seen during the case, leading to extensive cloudiness in 2S and 3S that reduced the availability of Chl data in the weekly maps. As a result, MODIS-Aqua daily data were used as a complement to determine the Chl evolution correctly (Figure 6.35).

In September, the Chl anomalies were low in the ocean (Figure 6.31) and coastal strips, which was confirmed by the weekly maps that did not show any significant Chl signal this month. This is consistent with the SLP negative anomalies in this month associated with incipient El Niño (0.21) but most importantly, a strong negative AAO (-1.12) weakening the SPSA (-0.19), which moved oceanwards (DMC, 2018). Consequently, the Southern Zone showed intense westerly winds the whole month. The weakened SPSA allowed the penetration of five frontal systems and one cut-off low through the Northern and Central Zone this month, leading to an intense but short rain episode in 2C-3C and 1S and 2S in the second week. However, this PR event was insufficient to cancel the deficit from the past year (DMC, 2018).

The coastal strip continued without significant Chl anomalies the following month, except for a section at 44.5°S in 2S's interior sea and 3S in the 47-48°S band. The last was also visible in the ocean strip (Figure 6.31). According to October's weekly maps, the 3S event occurred in the first week (Figure 6.32), showing a Chl signal extending from the 3S's coast through the ocean with patches over 20 mg m^{-3}. The following week the signal retreated to the coast.
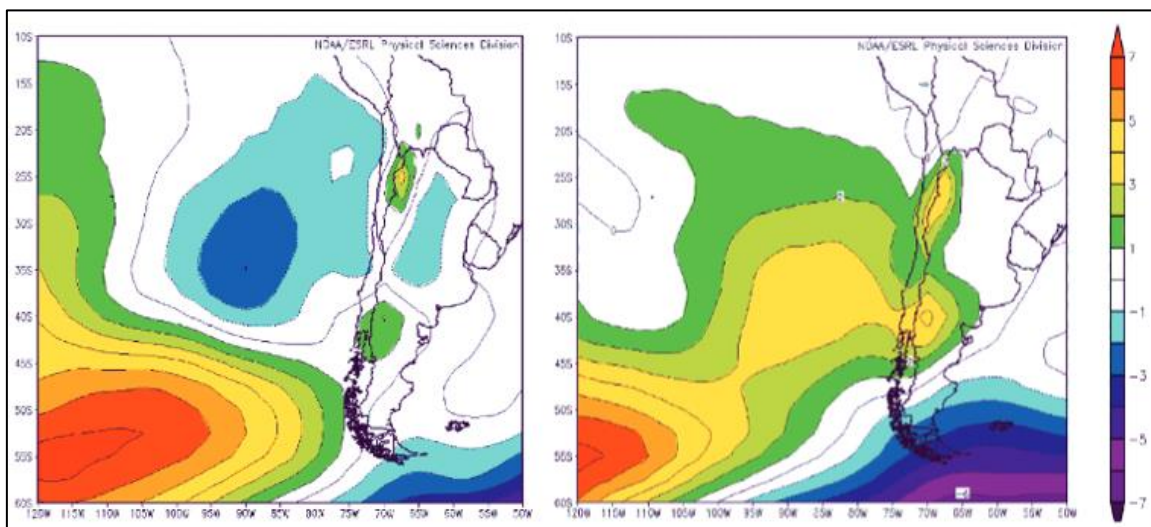

FIGURE 6.33. CASE 9 SLP ANOMALIES IN OCTOBER (LEFT) AND NOVEMBER (RIGHT) 2014, INDICATING THAT POSITIVE SLP ANOMALIES IN OCTOBER WERE ONLY IN THE SOUTHERN ZONE, WHILE THE SPSA REINFORCEMENT LED TO POSITIVE SLP ANOMALIES IN NORTHERN CENTRAL AND PART OF THE SOUTHERN ZONE IN NOVEMBER, BUT WITH NEGATIVE ANOMALIES FURTHER SOUTH (DMC,2018).

The SPSA was stronger this month than the previous one (-0.04) but maintained negative SLP anomalies in the Northern and Central Zone. These were linked to the SPSA's withdrawal to the west, associated with a starting moderate El Niño (0.4; Aceituno et al., 2015; DMC, 2018). The Southern Zone experienced anticyclonic conditions coming from the west (Figure 6.33; DMC, 2018). Indeed, the weekly maps revealed positive SLP anomalies in the Southern Zone, excluding the third week. As a result, southerly winds were present in 3S in the first two weeks of October (Figure 6.32). In the fourth week, higher southerly winds spread through 2S driven by the reappearance of the SPSA at 35°S (Figure 6.34; DMC,2018). As expected, the PR was low during the anticyclonic conditions but significant in the third week.

This case peaked in November, with significant Chl anomalies along the coast from 45°S to 47°S, belonging to the 2S-3S border region. However, these anomalies were even higher in the ocean strip, reaching a more extensive area (Figure 6.31 and Table 6.13). The weekly maps illustrated a significant Chl concentration in 2S that spread out into the ocean during the first week of this month (Figure 6.34). This signal was not seen in the next week due to heavy cloudiness. Nevertheless, a big Chl patch was observed in the ocean strip in 3S that week (Figure 6.34). For the upcoming two weeks, the clouds hid these subsections, not allowing a view of the signals' evolution.

Daily satellite images were used as the weekly maps hid critical information to establish if both events were linked. Although MODIS-Aqua images had excessive cloudiness as well, they were helpful in defining that 2S's and 3S's Chl signals appeared on 1st November with segments having concentrations over 20 mg m^{-3}. These signals weakened in the subsequent days, fading away on 10th and 19th November, respectively (Figure 6.35). Additionally, the satellite images captured a similar Chl pattern in 2S on 22nd October, but it was not present on the 30th day of the same month.
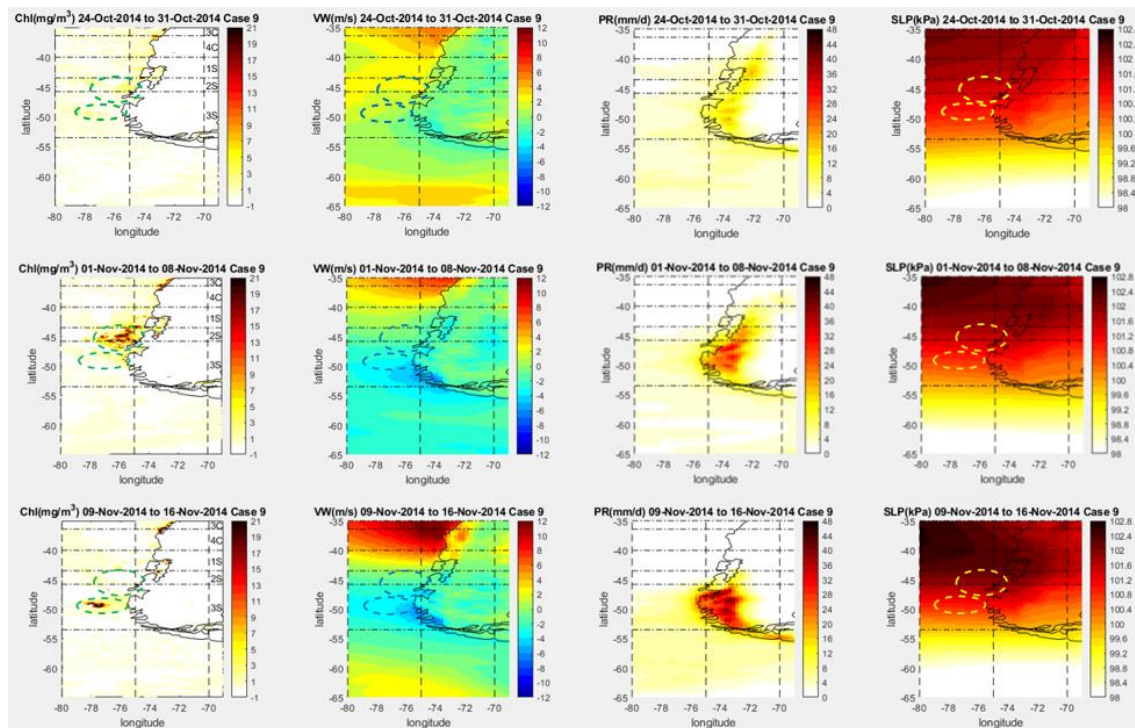

FIGURE 6.34. CASE 9 CHL, VW, UW, PR AND SLP WEEKLY VALUES OVER THE 3C, 4C, AND THE SOUTHERN ZONE FROM THE LAST WEEK OF OCTOBER TO THE SECOND WEEK OF NOVEMBER 2014. THE DASHED CIRCLES HIGHLIGHT THE CHL INCREMENT LOCATION IN THE CHL, VW AND SLP PANELS. THE SLP PANEL SHOWS THAT ALL DATES EXHIBITED HIGH-PRESSURE SYSTEMS MAINLY AFFECTING THE 4C -2S SECTIONS, WITH A HIGHER INTENSITY IN THE SECOND WEEK OF NOVEMBER. THE VW PANEL INDICATES THAT THE SOUTHERLY WINDS WERE HIGH IN HIGH CHL LOCATIONS AT THE END OF OCTOBER, BUT THEY WERE LOW IN THE FIRST WEEK OF NOVEMBER, WHILE THEY WERE IN THE OPPOSITE DIRECTION IN THE SECOND WEEK OF THAT MONTH. HOWEVER, THE CHL WAS HIGH IN NOVEMBER. ALSO, 3S'S CHL SIGNAL WAS UNAVAILABLE THE FIRST WEEK, THE 2S'S SIGNAL WAS NOT AVAILABLE IN THE SECOND WEEK, AND A SIGNIFICANT PART OF BOTH HIGHLIGHTED AREAS WAS ABSENT IN THE LAST WEEK OF OCTOBER.

Despite the negative AAO (-0.52) and a strengthening El Niño (0.71), the SPSA increased this month (1.21) as it typically does in this period (DMC, 2018). Figure 6.33 showed positive SLP anomalies from 1C to 2S, whereas the cyclonic conditions driven by the AAO were south of 50°S (DMC, 2018). This is consistent with the SLP maps in Figure 6.34. Still, the southerly winds in 2S and 3S were weak or retreated to the north during the first half of November, not coinciding with the Chl signals' peak. Meteorological reports pointed out that the PR events in the Southern Zone were in the first and fourth week of this month, where the first showed a higher intensity (Aceituno et al., 2015). This is not consistent with the weekly maps that

indicated high PR events the whole month, with a more intense episode in the second week (Figure 6.34).

The coastal Chl anomalies in the Southern Zone did not experience any significant anomaly in December, while 3S exhibited a significant anomaly around 52.7°S in the ocean strip (Figure 6.31). Nevertheless, this anomaly is not visible in December's weekly maps. In fact, 2S and 3S were mainly covered by clouds. The SPSA and El Niño decreased this month but were still significant (1.21 and 0.66, respectively), while the AAO switched to its positive phase (1.32). For these reasons, the Southern Zone exhibited weaker but still positive SLP anomalies (DMC, 2018). This is consistent with the weekly maps that showed a high-pressure system present as far north as 1S (43.5°S), except in the second week, where it reached 46°S. Hence, aside from the second week, the southerly winds in the Southern Zone were not significant. Three PR episodes occurred in the Southern Zone in the first, third and fourth week. However, only the third-week episode showed a significant intensity, specifically in 1S and 2S (Aceituno et al., 2015). From the 2S's rivers, only Palena and Aysén Rivers were available for this case. Palena's flow did not show significant changes from September to November, although it dropped 25% in December, whereas the Aysén had flow increases above 45% in October and November.
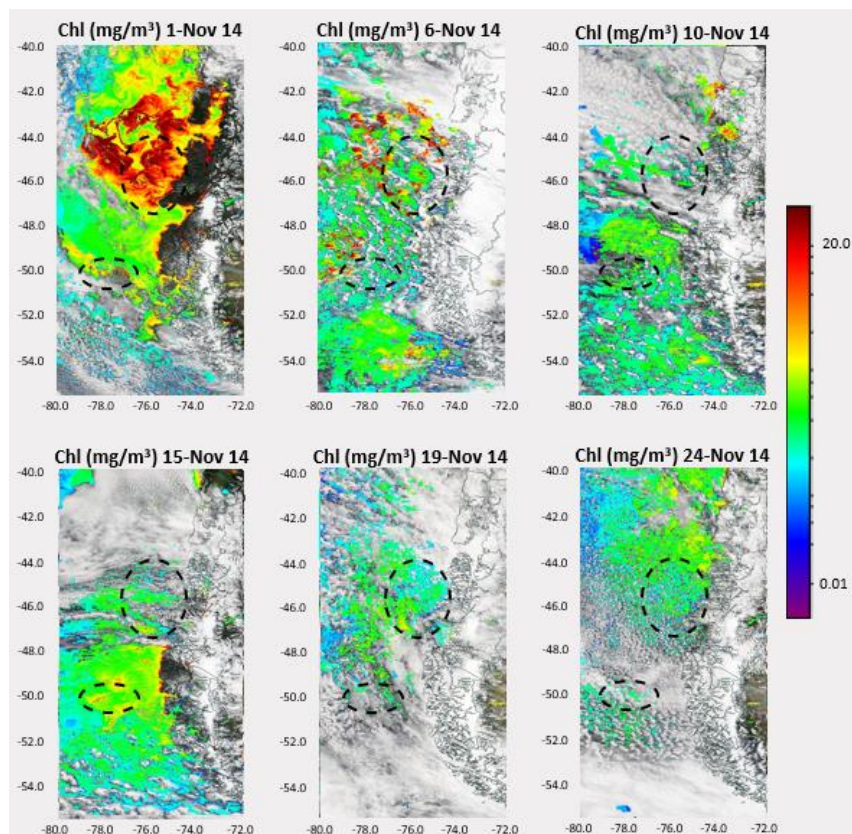

FIGURE 6.35. CHL CONCENTRATION FROM MODIS-AQUA SATELLITE IMAGES TAKEN BETWEEN 1ST AND 24TH NOV 2014. THE BLACK DASHED LINES INDICATE THE CHL CONCENTRATION LOCATIONS SEEN IN FIGURE 6.34. THIS FIGURE SHOWS HOW BOTH EVENTS STARTED ON 1ST NOV. 2S'S CHL SIGNAL WAS VISIBLE UNTIL 6TH NOVEMBER. MEANWHILE, 3S'S CHL SIGNAL WAS VISIBLE UNTIL 15TH NOVEMBER.

To conclude, this case was triggered by a SLP increment in the Southern Zone linked to negative SLP anomalies in the Southern Ocean and the SPSA, the last associated with El Niño. This reduced the PR events in an arid year and increased the southerly winds, boosting the Chl. However, a few PR events were still seen during the peak of the case (Figure 6.34), reducing the information captured by the Satellite images. In any case, the excessive cloudiness is typical for 2S and 3S. As a result, this case was more challenging to evaluate.

Although the southerly winds were the primary trigger for this case, the Chl's peak in November occurred when weak southerly winds were present. Nonetheless, these were significant in that region in the previous week (Figure 6.34). As the Chl data is incomplete, the observed signal is likely higher or presumed to have started earlier. This is consistent with the significant positive correlations of 3S's Chl coastal values with SLP and VW, and negative correlations with PR and UW (Figure A.3.9). The Chl in the ocean strip at the same latitude only exhibited a significant positive correlation with the SLP (Figure A.3.10).

Disposals from salmon farming or red tide cases are possible external factors that could have raised the Chl. Nevertheless, no information was found to confirm or deny these possible mechanisms in this case.

6.3.3.3.   Case 10:

This case was chosen for having the highest Chl anomaly and concentration in 3ST (3.2 SD and 7.3 mg m^{-3}; Table 6.14). This occurred in September 2015, registering significant anomalies in the ocean strip near this subsection. The following month the Chl dropped substantially, keeping a significant anomaly in 3SO only. Undoubtedly, the most significant factor for this case was the extreme El Niño (1.86) that year, which peaked from September to February, weakening the SPSA for the majority of those months (DMC, 2018). This led to anticyclonic conditions in the Southern Zone.

TABLE 6.14. CASE STUDY 10 SUMMARISES THE SUBSECTIONS AFFECTED, THEIR CHL ANOMALIES IN SD, ENSO, AAO AND SPSA MONTHLY VARIATION, AND ADDITIONAL COMMENTS.

| Subsections	Date	Chl (anom)	ENSOm	AAOm	SPSAm	Comments
2SO, 3ST, 3SO	Sep-15	2.7, 3.2, 3.5	2.12	0.54	-0.83	Highest [Chl] [7.3 mg m^{-3}] & anom (3.2) in 3ST;
3SO	Oct-15	2.1	2.32	-0.17	-0.16	very strong El Niño (1.86), moderate +AAO (0.76).
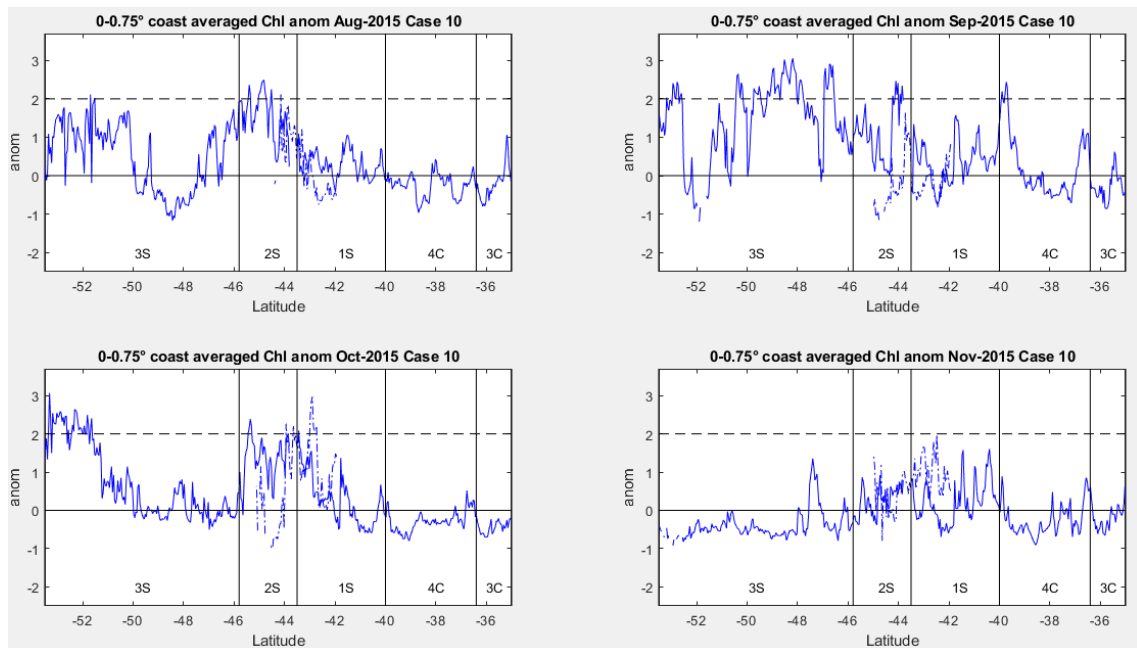
FIGURE 6.36. CASE 10 MONTHLY CHL FROM THE COAST TO 0.75° OCEANWARD USING THE ANOMALIES DIVIDED BY SD ON THE 3C, 4C AND THE SOUTHERN ZONE. THE DASHED BLUE LINE IN 1-2S REPRESENTS THE CHL ANOMALY ACROSS THE ANCUD AND CORCOVADO GULFS BETWEEN CHILOÉ ISLAND AND THE MAINLAND (41.9°-45°S), WHILE THE CONTINUOUS LINE IS THE CHL ANOMALY ACROSS THE CHILOÉ COASTLINE AND THE PACIFIC BASIN. THE BLACK DASHED LINE DRAWS ATTENTION TO THE SECTIONS WITH THE MOST SIGNIFICANT CHL ANOMALIES, SUCH AS 2S IN AUGUST TO OCTOBER, WHILE 3S IN SEPTEMBER AND OCTOBER IN 51°S.

Following the same pattern as the two previous cases (sections 6.3.3.1 and 6.3.3.2), Case 10 was linked to anticyclonic conditions in the Southern Zone, driven by a primarily positive AAO and extreme El Niño that forced the SPSA south. As a result, the SLP increment reduced the PR event and the river's fluxes, while the southerly winds were enhanced in specific periods

that roughly matched the Chl signal boost. This is consistent with positive Chl correlations with SLP, VW, and SST, and negative with the PR and UW in the coastal strip in 3S near its border with 2S (Figure A.3.11).

In August, the Chl anomalies were average in the Central Zone. The Southern Zone showed significant anomalies in 2S, while 3S experienced a slight increment 50°S southwards (Figure 6.36). The weekly maps only revealed a weak Chl concentration in 2S and 3S in the second and fourth weeks, respectively. However, the Chl was incomplete owing to excessive cloudiness. This low productivity was linked to the El Niño enhancement (1.88), drastically reducing the SPSA (-1.83, the lowest value since May 2002). Thus, the negative SLP anomalies dominate the whole territory, including the Southern Zone, despite positive AAO (1.06; DMC, 2018). Due to this, significant PR events were registered in the three Zones, with a higher impact in the 1C-2S subsections. This was also seen in the increased flux of The Puelo, Palena and Cisnes Rivers (Figure 3.7). The Southern Zone winds were intense with a significant westerly component, except in the second week when weak southerly winds reached the 1S and 2S coasts.

The Chl anomalies rose drastically in 3S and 2S's 43.5°-44.2°S band in the following month (Figure 6.36). These anomalies were seen in September's third and fourth weeks, spreading oceanward (Figures 6.37 and 6.38). These locations were hidden in the previous week so that the Chl signal could have started earlier. Although the SPSA increased and moved southwards, as it typically does in this period, its index continued to be negative (-0.83) driven by a still strengthening El Niño (2.12; DMC, 2018). This, combined with a positive AAO (0.54), raised the Southern Zone's SLP anomalies slowly in the first three weeks of September (Figure 6.37). Intense southerly winds reached the Southern Zone during these weeks, covering as far south as 2S in the first week and the whole southern coast in the second and third week (Figure 6.37). However, northerly winds dominated this region in the last week of the month (Figure 6.38). Despite that, the high Chl persistence this week is likely related to the winds' intensity during the previous weeks. Additionally, several PR events were observed in the midlatitudes this month, whereas in the high latitudes declined, particularly in the third week when the Chl peaked. Indeed, the Puelo and Aysén River's flow slightly increased while the Palena's and Cisnes' was reduced by 20 to 40% (Figure 3.7).
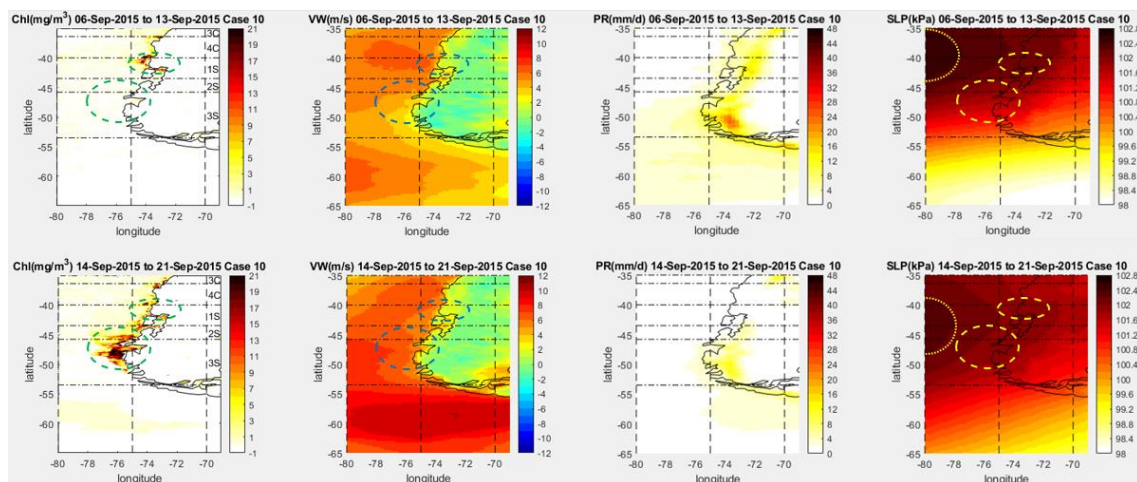

FIGURE 6.37. CASE 10 CHL, VW, UW, PR AND SLP WEEKLY VALUES OVER THE 3C, 4C, AND THE SOUTHERN ZONE FOR THE SECOND AND THIRD WEEK OF SEPTEMBER 2015. THE DASHED CIRCLES HIGHLIGHT THE CHL INCREMENT LOCATION IN THE CHL, VW AND SLP PANELS. THE SLP PANEL SHOWS THAT THE HIGHEST PRESSURE AREA (DOTTED LINE) COINCIDES WITH SOUTHERLY WINDS AND HIGH CHL AREAS. THIS PATTERN ALSO MATCHES THE LIGHTER PR IN THE SECOND AND THIRD WEEKS. ALTHOUGH 3S'S CHL SIGNAL WAS UNAVAILABLE IN THE SECOND WEEK, IT CAN BE INFERRED THAT IT WAS NOT AS HIGH AS IN THE THIRD WEEK BECAUSE THE WINDS WERE LOW.
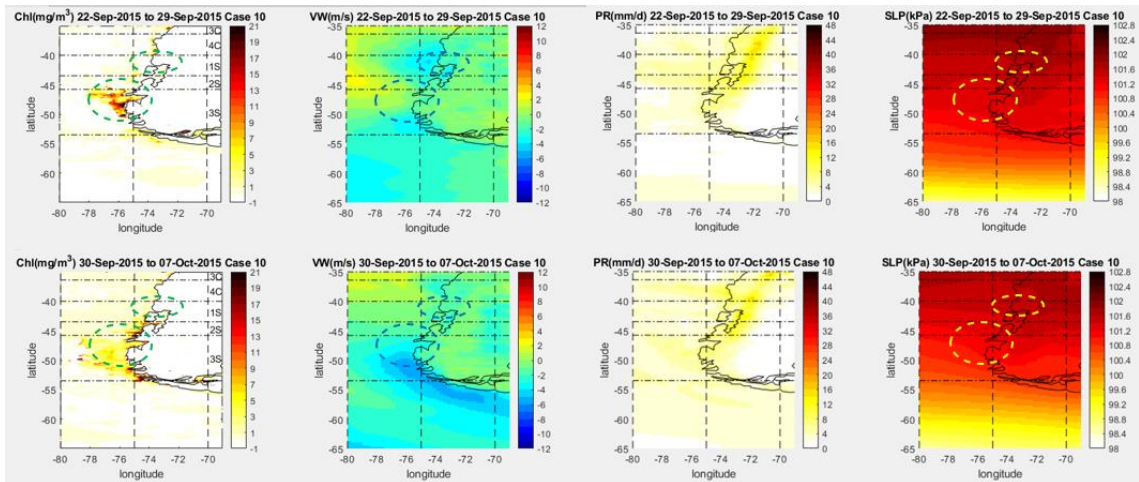
FIGURE 6.38. CASE 10 CHL, VW, UW, PR AND SLP WEEKLY VALUES OVER THE 3C, 4C, AND THE SOUTHERN ZONE FOR THE LAST SEPTEMBER WEEK AND THE FIRST WEEK OF OCTOBER 2015. THE DASHED CIRCLES HIGHLIGHT THE CHL INCREMENT LOCATION FOR FIGURE 6.37 IN THE CHL, VW AND SLP PANELS. THE SLP PANEL SHOWS HOW THE SLP DROPPED THESE WEEKS COMPARED TO THE PREVIOUS WEEKS. VW PANEL REVEALS WEAK NORTHERLY WINDS IN THE DASHED AREAS. THE CHL PANEL DEMONSTRATES THAT CHL IN 3S SHARED A ROUGHLY SIMILAR LOCATION TO THE PREVIOUS WEEKS.
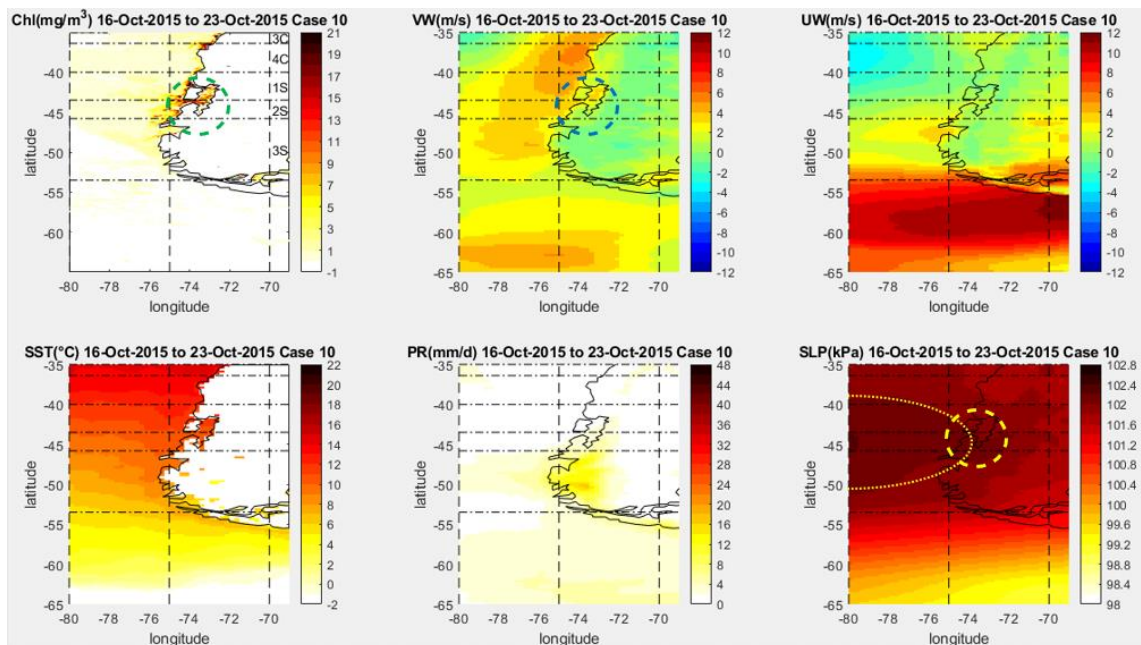

FIGURE 6.39. CASE 10 CHL, VW, UW, SST, PR AND SLP WEEKLY VALUES ON THE 3C, 4C AND THE SOUTHERN ZONE SECTIONS, SHOWING THE THIRD WEEK OF OCTOBER 2015. THE DASHED CIRCLES HIGHLIGHT THE CHL INCREMENT LOCATION IN THE CHL, SLP AND VW PANELS. THIS HELPS TO IDENTIFY THAT THE SLP INCREASE MATCHES THE SOUTHERLY WIND AND THE CHL SEGMENT. THE PR PANEL SHOWS A SLIGHT PR REDUCTION THAT WEEK DUE TO THE ANTICYCLONE CONDITIONS.

In October, the Chl anomalies dropped, but significant anomalies were still shown in 1S's interior sea, 2S and 3S's 51.5°-53.5°S band (Figure 6.36). These Chl variations appeared on the weekly maps in the first and third weeks. The first-week event had the Chl of 3S and 2S remaining similar to the Chl concentration from the previous month but spreading oceanwards (Figure 6.38), while the third week exhibited a concentration in 1S and 2S (Figure 6.39). The Chl behaviour was consistent with an SLP drop in the first week and a later slow rise in the Southern Zone until the third week. This was triggered by an almost recovered SPSA (-0.16) that kept its southern location modulated by an even higher El Niño (2.32), combined with a slightly negative AAO (-0.17; DMC, 2018). Consequently, strong southerly winds moved southwards, reaching 3S in the third week (Figure 6.39) but retreating to the Central Zone in the fourth week. Due to SLP negative anomalies in the Central Zone, the PR

events were concentrated in 2C-3C and diminished in 4C and the Southern Zone (DMC, 2018). This decreased the Puelo, Palena and Cisnes River's fluxes by 35 to 60% (Figure 3.7).

Figure 6.36 shows relatively flat Chl anomalies in November, except for 1S's interior. According to the weekly maps, this was during the first week, while the Southern Zone still had anticyclone conditions, which led to alongshore winds. In the fourth week, a lower Chl signal resurged in 1S's interior sea and 2S coast. The SLP anomalies were slightly negative in the second and third weeks due to a reinforced SPSA (0.5) moving northwards as it usually does in this period (DMC, 2018). Meanwhile, in the fourth week, these anomalies were positive again associated with a slight SPSA withdrawal. The PR anomalies in the Southern Zone were slightly negative, driven by a positive AAO (0.7) that suppressed the frontal system access to the region, reducing the river average fluxes by 25%. Another factor that could harm the phytoplankton bloom was expansion in the Ozone Hole northwards until 1S, leading to higher UV radiation, which generally affects further south than 53°S only (DMC, 2018).

Overall, Case 10 showed the exact mechanisms observed in the other Southern Zone cases, reinforcing the conclusion of the importance of El Niño combined with a positive AAO being capable of modulating the SPSA moving southwards. Like the previous cases, this diminished the PR and raised the southerly winds, enhancing the Chl. Although the typical cloudiness in 2S and 3S remained for this case, it was not as relevant to determine the Chl evolution.

The 3S Chl's peak was in the third week of September but continued for two weeks despite the northerly winds in those weeks (Figures 6.37 and 6.38). However, these winds significantly reduced the intensity of the signal, proving that the high Chl can continue for a short time with cyclonic conditions.

3S's Chl signal in the northern band (45.8°-46.5°S) displayed a significant positive correlation with SLP, VW and SST and negative with PR and UW (Figure A.3.11), while 2S showed the exact significant correlations in 44.5°S interior sea, except the SST, which was negative. On the other hand, in 3S's Chl southern band (52.75°-53.25°S), the correlations were precisely the opposite, demonstrating that the anticyclonic conditions did not arrive there for enough time.

Finally, the Southern Zone cases tended to expand more oceanwards (Cases 7 to 9 in sections 6.3.2.3 to 6.3.3.2) than the Northern and Central Zone, likely because the Southern region contains more nutrients in the deeper layer accessible by the upwelling. These extra nutrients come from the numerous rivers in this Zone, while 3S nutrients proceed from the CHC and AAIW (Thiel et al., 2007; Mongollón and Calil, 2017; Corredor-Acosta et al., 2015). Another factor is the stratification that reduces the euphotic layer thickness extending the Chl signal even more. This was briefly discussed in section 3.2.3.

6.3.3.4.   Case 11:
This case, introduced in section 3.1.3, was selected for being one of the most significant red tide episodes in recent years in Chile, provoking an environmental crisis with significant social and economic impacts (Armijo et al., 2020). This case initiated in January 2016 in 2S and part of 1S, where shellfish were found contaminated with *Alexandrium catenella*. This algal concentration continued until the first weeks of April, especially in the interior sea (Buschmann et al., 2016). At the same time, an enormous *Pseudochattonella verruculosa* bloom killed 40,000 tonnes of salmon from forty-five fish farms located across the Chiloé interior sea in February (Buschmann et al., 2016; Armijo et al., 2020). This bloom was linked to a strong El Niño, which started in 2015 (Table 6.15), leading to low PR that reduced the

local river fluxes, limiting the addition of refreshed waters. Consequently, the waters had lower oxygen and higher SST (Leon-Muñoz et al., 2018; Armijo et al., 2020).

TABLE 6.15. CASE STUDY 11 SUMMARISES THE SUBSECTIONS AFFECTED, THEIR CHL ANOMALIES IN SD, ENSO, AAO AND SPSA MONTHLY VARIATION, AND ADDITIONAL COMMENTS.

Subsections	Date	Chl (anom)	ENSOm	AAOm	SPSAm	Comments
4CT, 1ST	Feb-16	1.9, 0.7	2.34	1.09	0.26	The worst red tide episode in 1ST; extreme El Niño (1.86) & +AAO (0.76); The most extended case studied.
4CT, 1ST, 2ST	Mar-16	2.3, 2.0, 1.5	1.70	2.04	1.64	
1ST, 2ST, 3SO	Apr-16	-0.2, - 0.1, 2.6	0.99	0.10	0.73	
1ST, 2ST, 3ST	May-16	1.2, 1.3, 2.4	0.39	0.01	-0.03	

As the landfills could not process everything, the government permitted the disposal of 9,000 tonnes of rotting salmon 139 km oceanwards from Chiloé (41.77°S, 75.72°W). This was done over trips between 11th-26th March, dumping 4,700 tonnes (Figures 6.40 and 6.42; Buschmann et al., 2016; Armijo et al., 2020). Although the Navy supervised the dumps, 2,000 tonnes were disposed of between the 14th-17th March, where 300 tonnes were disposed of slightly closer to the coast (Armijo et al., 2020). This is relevant because the salmon produced sulfuric acid in their decomposition process and were dumped with unknown chemicals, and illegal disposals were suspected but not corroborated. Additionally, the companies kept the dead salmon in cages for weeks, increasing the eutrophication risk in Chiloé's northern interior sea (Armijo et al., 2020).

FIGURE 6.40. A) VESSELS THAT DISPOSED OF SALMON. B) THE PUMP USED FOR THE DISPOSAL. C) THE SURFACE CONTAMINANT AFTER THE SALMON DISPOSAL. D) DEAD CLAMS ON CUCAO ON 26TH APRIL. E) DEAD SEABIRDS FOUND IN ANCUD (41.87°S, 73.82°W) DURING MID-APRIL. F) PROTEST AGAINST SALMON FARMS AND GOVERNMENT ACTIONS (ARMIJO ET AL., 2020).

The second phase of the *Alexandrium catenella* bloom started right after the first phase, on 8th April of the Chiloé's Pacific coast, specifically at Cucao beach (42.6°S, 74.1°W). Here, the first mollusc was detected with a high toxin level (280 µg STXeq/100 g when the accepted is 80 µg STXeq/100 g). The red tide started to propagate rapidly, reaching Chacao Channel on 13th April (41.8°S 74°W; Figure 6.18; Armijo et al., 2020; Buschmann et al., 2016). This continued expanding to the interior sea and northwards in the next two weeks, covering an area between 39.4°S and 43.5°S. This was the first time a red tide appeared in the Northern interior sea and beyond the Chiloé island (Armijo et al., 2020). Furthermore, many seabirds and molluscs were found dead on the Chiloé's coasts between the second half of April and May; the most dramatic episode was the discovery of 850 tonnes of dead clams at Cucao on 26th April (Figure 6.40). These deaths were unprecedented. The red tide lost intensity during

the first week of May, reducing the algae concentration in the Pacific but not in the interior sea, which persisted for a couple of weeks more (Armijo et al., 2020).
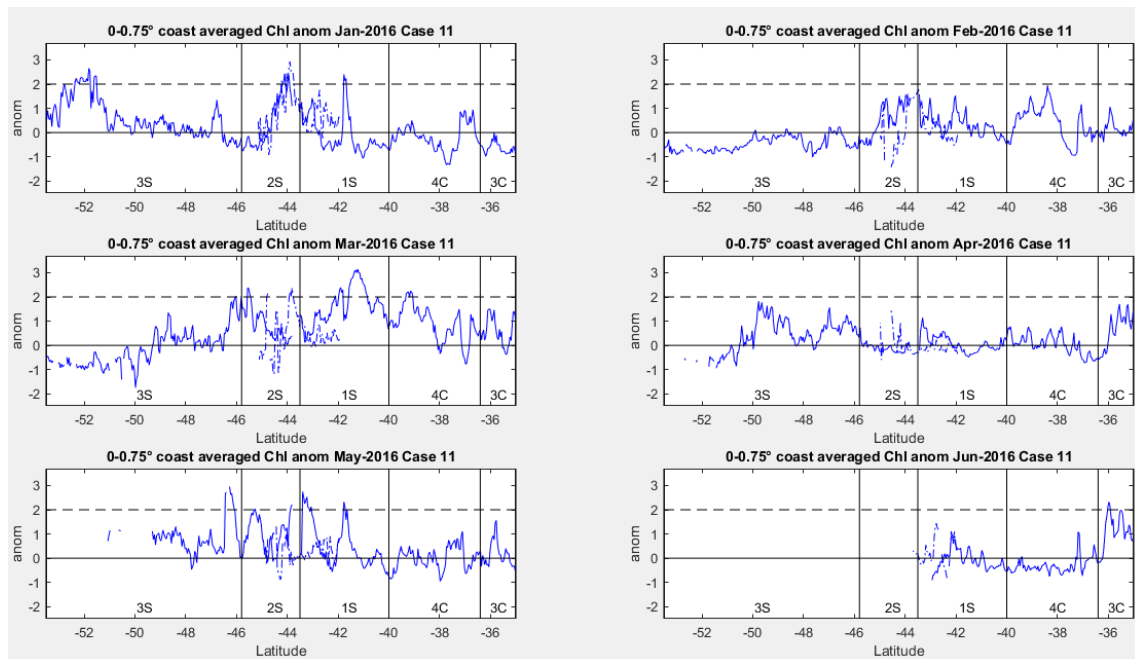
FIGURE 6.41. CASE 11 MONTHLY CHL FROM THE COAST TO 0.75° OCEANWARD USING THE ANOMALIES DIVIDED BY SD ON THE 3C, 4C AND THE SOUTHERN ZONE. THE DASHED BLUE LINE IN 1-2S REPRESENTS THE CHL ANOMALY ACROSS THE ANCUD AND CORCOVADO GULFS BETWEEN CHILOÉ ISLAND AND THE MAINLAND (41.9°-45°S), WHILE THE CONTINUOUS LINE IS THE CHL ANOMALY ACROSS THE CHILOÉ COASTLINE AND THE PACIFIC BASIN. THE BLACK DASHED LINE DRAWS ATTENTION TO THE SECTIONS WITH THE MOST SIGNIFICANT CHL ANOMALIES, SUCH AS 1S AND 2S IN JANUARY, MARCH AND MAY OCTOBER, WHILE 3S IN MAY IN THE 46.5°S.

As the region affected by the red tide was from 4C to 2S, this study will concentrate only there, omitting the 3S anomalies observed in Table 6.15 and Figure 6.41 because they are irrelevant to this case.

In January, the Chl anomalies were significant in parts of 2S and 1S (Figure 6.41). Effectively the weekly maps revealed a Chl bloom from 3C to part of 2S during the whole month driven by slightly weak southern SPSA (0.24) modulated by strong El Niño (2.66) and positive AAO (1.39). This increased the longshore winds along with the SST, while the PR declined considerably compared to previous years. Hence, the Puelo, Palena and Cisnes streams were down by 40%, while the Aysén River showed an average flux (Figure 3.7). This is consistent with the findings of Leon-Muñoz et al. (2018).

The Chl anomalies went down the following month but still showed some regions with higher anomalies (Figure 6.41). The Chl maps showed a high concentration in the first week, while the values tended to go down in the rest of the month. This was linked to the SPSA moving slightly to the north (0.26), withdrawing the southerly winds to 4C. Although the PR slightly increased, it continued with negative anomalies, especially in 1S, owing to a positive AAO (1.09). Consequently, the SST anomalies remained positive, and river fluxes showed a 30% drop. These climatic conditions, plus the pollution by salmon companies in an area in partial confinement, were ideal for *Pseudochattonella verruculosa* proliferation across the Chiloé interior sea (Armijo et al., 2020).
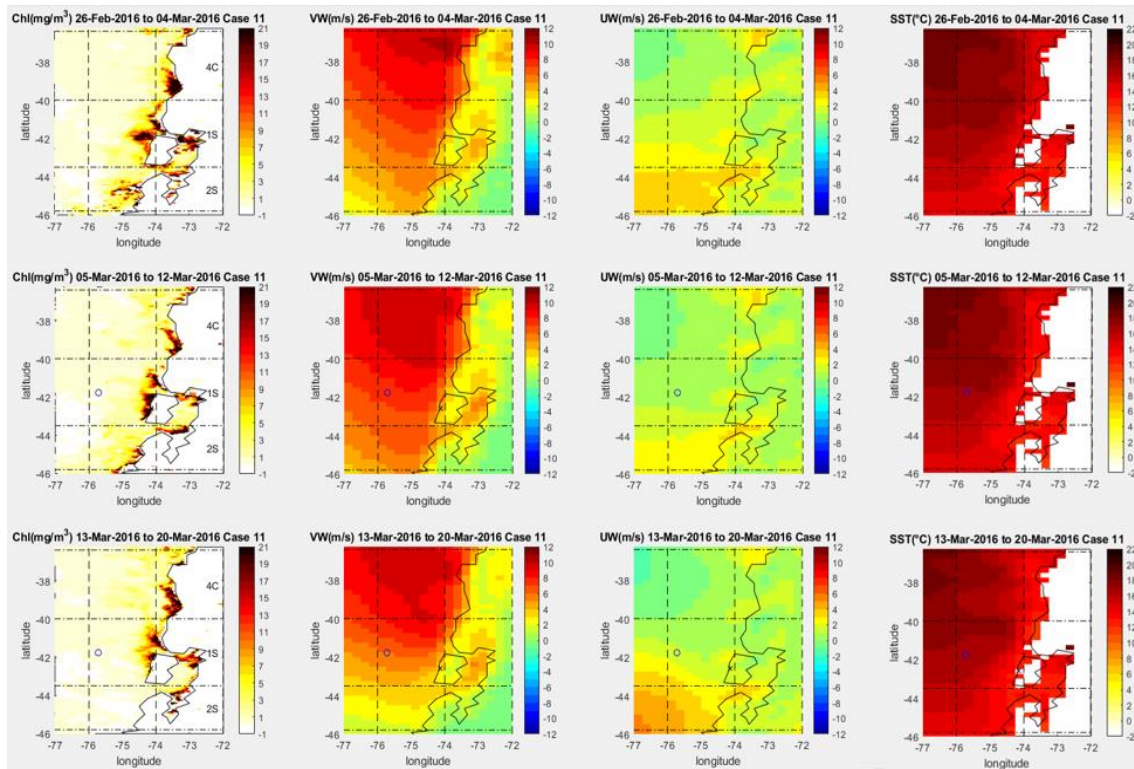
FIGURE 6.42. CASE 11 CHL, VW, UW, AND SST WEEKLY VALUES OVER THE 4C TO 2S SUBSECTIONS FROM THE FIRST THREE WEEKS OF MARCH 2016. THE BLUE CIRCLE INDICATES THE SITE WHERE THE SALMON WERE DISPOSED BETWEEN 11TH-26TH MARCH, AND THE X MARKS THE CUCAO BEACH, THE MOST AFFECTED SITE. THE CHL PANEL SHOWS A SIGNIFICANT SIGNAL ALONG THE CHILOÉ COAST AND NORTH INTERIOR SEA. THESE MATCH WITH STRONG ALONGSHORE WINDS AND THE SST DECLINE IN THESE REGIONS.

In March, the Chl anomalies were significant in 1S (Figure 6.41). Indeed, the weekly maps showed a significant concentration along the Chiloé coast and north interior sea during the first three weeks (Figure 6.42). This is consistent with the persistent southerly winds in the summer and March, boosting the Chl. The upwelling along the coast is consistent with the local SST drop due to the southern SPSA reinforcement (1.64). As expected, the PR was completely absent these weeks in 1S, reducing the river fluxes by 40% associated with an extreme AAO (2.04) and slightly lower El Niño (1.70).

The Chl signal started weakening the last week of March, showing a weak concentration until the third week of April. However, some Chl activity was seen near Cucao during the first week of April related to the red tide, which rose in the following weeks peaking at the end of April. Finally, some significant concentrations were observed close to the disposal region and the coast in the last week of April (Figure 6.43).

The winds constantly switched due to cyclonic conditions linked to the SPSA slightly dropping (0.9), exhibiting a SW-NE tendency in the first three weeks of April, with a significant westerly component in the third week that matched the Chl increment in Cucao (Figure 6.43). These wind alternations are more evident on a daily scale, showing strong north-westerly winds (Figure 6.44). Armijo et al. (2020) modelled these winds to determine the currents, reporting that the winds led to a cyclonic gyre near the disposal site for the salmon in the first two weeks of the month, which could have transported part of the pollution towards the coast (Figure 6.45). The rest of the time, the gyre was still present but at a lower speed. The SST maps showed a SST rise on the coast during the first week of April associated with downwelling (Armijo et al., 2020). These conditions increase the stratification, which raises the red tide formation (Buschmann et al., 2016).

156
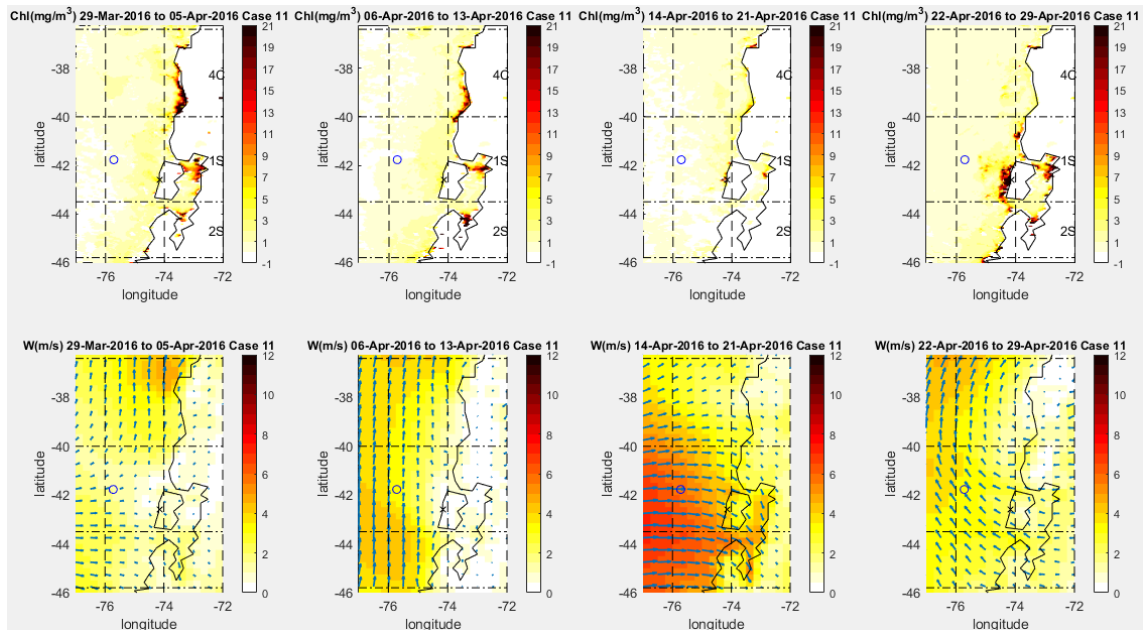
FIGURE 6.43. CASE 11 CHL, W WEEKLY VALUES OVER THE 4C TO 2S SUBSECTIONS FROM APRIL 2016. THE BLUE CIRCLE INDICATES THE SITE WHERE THE SALMON WERE DISPOSED BETWEEN 11TH-26TH MARCH, AND THE X MARKS THE CUCAO BEACH, THE MOST AFFECTED SITE. THE CHL PANEL SHOWS A WEAK THE FIRST TWO WEEKS, WITH A SLIGHT SIGNAL IN THE CUCAO. THIS CONCENTRATION ROSE IN THE THIRD WEEK AND EVEN MORE IN THE FOURTH, MATCHING WITH STRONG WESTERLY WINDS.
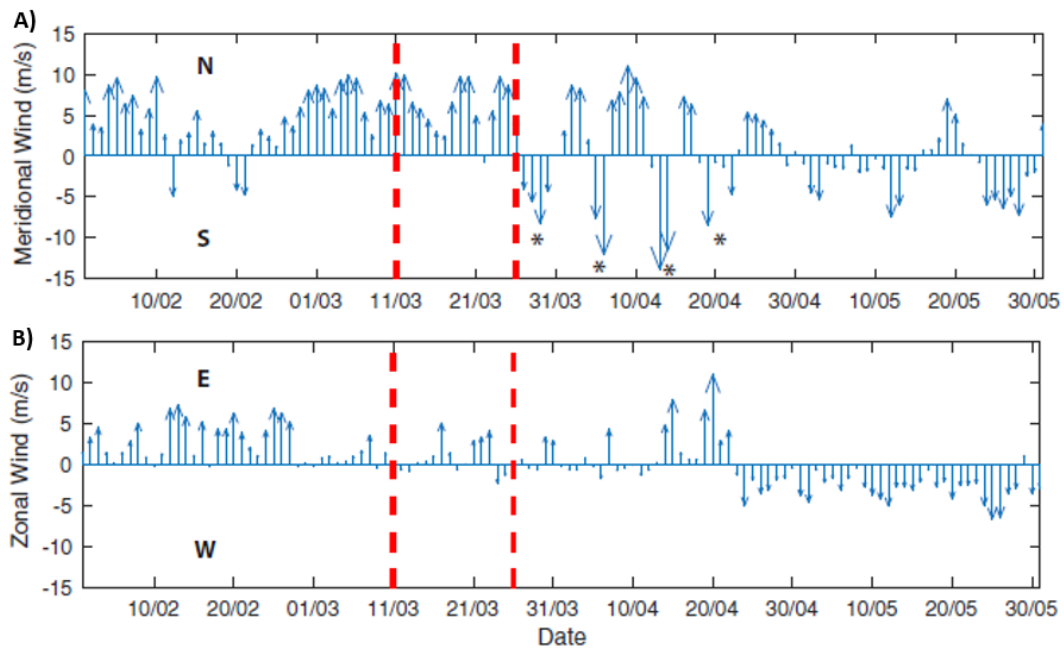

FIGURE 6.44. A) VW DAILY WINDS AROUND THE DUMPING SITE FROM FEBRUARY TO MAY 2016, B) UW DAILY WINDS IN THE DUMPING SITE. THE RED DASHED LINES SHOW THE DISPOSAL DATES. IN LATE MARCH AND APRIL, THE ASTERISKS HIGHLIGHT THE NORTHERLY WINDS WITH A SIGNIFICANT WESTERLY COMPONENT THAT COULD TRANSPORT THE POLLUTION TOWARDS THE COAST (ARMIJO ET AL., 2020).

Armijo et al. (2020) modelled the pollution motion through the currents, showing that most went northwards. The contaminants dumped in the last week of March might have reached onshore linked to the gyre mentioned before. Moreover, the model reveals that the pollution could have been advected to the Chacao Channel on 15th April, when the red tide reached its peak (Figure 6.46). This is consistent with the significant NH_4^+ patches found in surface waters around the disposal area and the Chiloé coast by Buschmann et al. (2016) at the end of May. This is sensible because red tides tend to proliferate over other species producing even more toxins when the NH_4^+ is in high quantities (Armijo et al., 2020). For that reason, waters close to salmon farms tend to have a proliferation of toxic dinoflagellates (Buschmann et al., 2006).
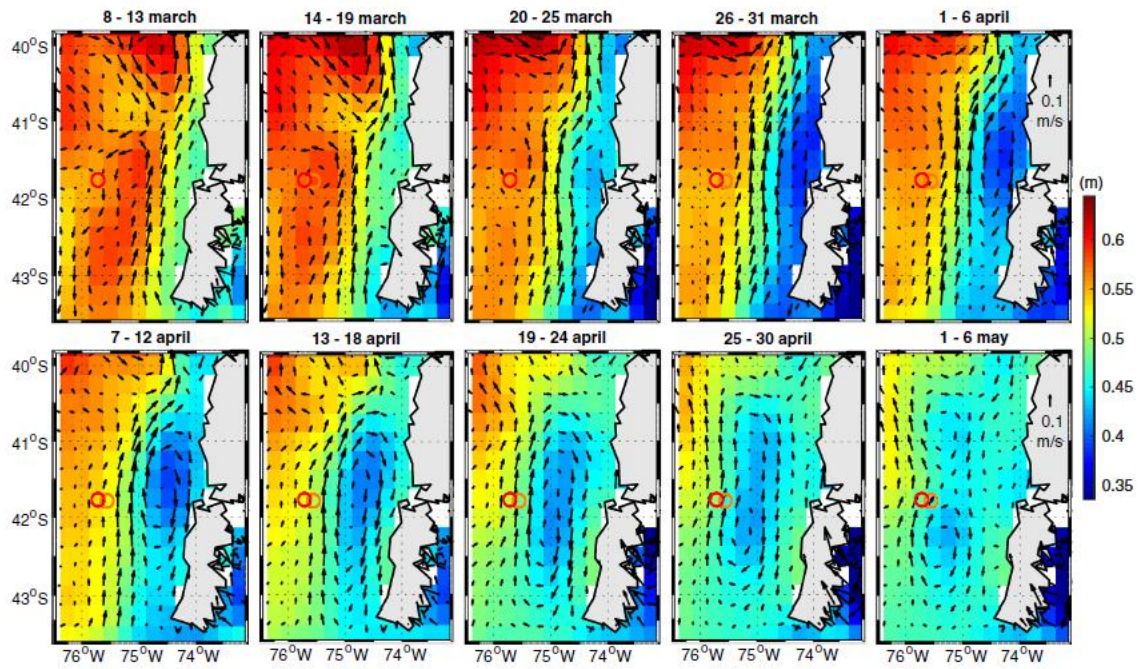
FIGURE 6.45. GEOSTROPHIC CURRENTS MODELLED WITH NEMO USING WIND DATA WITH A RESOLUTION OF 0.25°. THE RED AND ORANGE CIRCLES SHOW THE DUMPING SITE. THE GYRE WAS CLEARLY FORMED DURING THE FIRST TWO WEEKS OF APRIL, WHILE IT LOST STRENGTH FOR THE REST OF THE MONTH (ARMIJO ET AL., 2020).
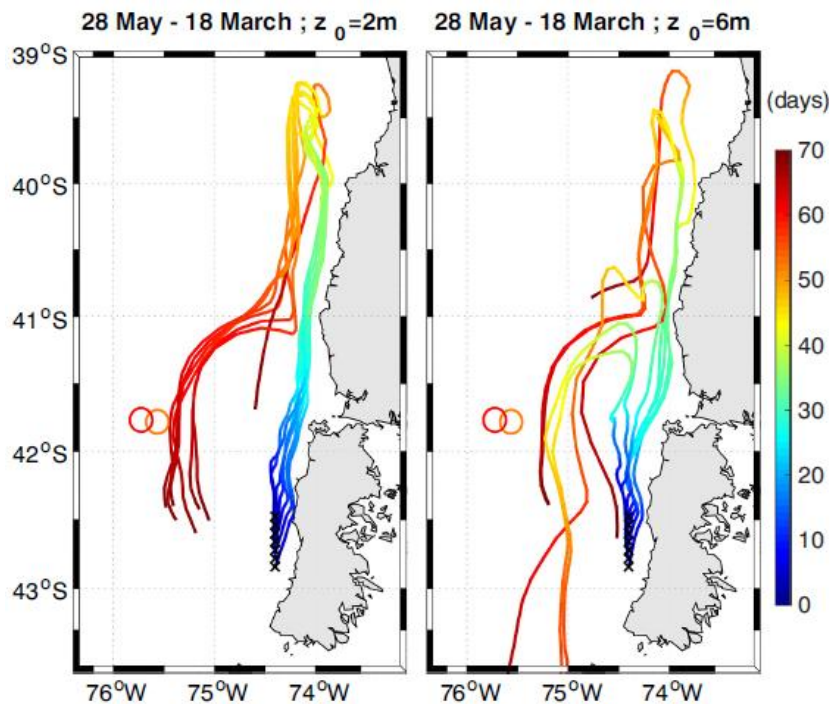

FIGURE 6.46. BACKWARDS TRANSPORT SIMULATION FROM THE NH_4^+ PATCHES FOUND ON 28TH MAY (X) TO THE SALMON DISPOSAL LOCATION (RED AND ORANGE CIRCLES) ON 18TH MARCH. Z_0 IS THE WATER'S DEPTH, GIVING SLIGHTLY DIFFERENT RESULTS. THIS WAS MODELLED WITH ARIANE BASED ON THE CURRENTS SHOWN IN FIGURE 6.45 (ARMIJO ET AL., 2020).

To conclude, this case was one of Chile's most outstanding recent environmental disasters with significant economic and social impacts. Many studies agree that the first red tide bloom was related to climatic conditions, while for the second phase, there is more disagreement. The scientific commission (Buschmann et al., 2016) attributed the second red tide to climate conditions and pointed out that the salmon disposals were not significant due to the winds having spread the pollution northwards, despite the NH_4^+ patches found in the discharge location and near the coast. In contrast, Armijo et al. (2020) analysed the daily winds stating

that the winds moved the contaminants towards the coast. This statement was supported by a Lagrangian model used to establish the trajectory. However, the true causes are unlikely to be uncovered due to the lack of in-situ data (Leon-Muñoz et al., 2018; Armijo et al., 2020).

This event could have been avoided if the government had developed a study to estimate the possible consequences of discharging that quantity of rotting salmon into the ocean or the companies had contingency plans or better monitoring. After this crisis, Sernapesca (2018) monitors the companies and takes samples when El Niño occurs. Despite the severity of this case, the Chl anomalies were not as high as in other cases studied previously. Therefore, more variables are needed to define a red tide.

6.4. Discussion.

These cases have shown how significant alongshore winds are for the Chl increment being the main trigger in most of them. These winds are driven by the SPSA (Aguirre et al., 2021; Thiel et al., 2007). Interestingly, the subsections where the SPSA's core moves through (2NT to 2CT) had the lowest Chl response, while 3CT to 2ST showed the highest. Indeed 3CT to 4CT had the fastest longshore winds in the summer. The Southern Zone is typically not affected by the SPSA. However, as Cases 1-3, 8-10 demonstrated, the SPSA moved southwards when El Niño occurred, even in the year after (Montecinos and Aceituno, 2003). This is even more extreme when a positive AAO blocks the entrance of cold fronts from the Southern Ocean (DMC, 2018; Aguayo et al., 2021). On the other hand, 1NT has a low influence by the SPSA, with weak but constant winds the whole year. Despite this, 1NT cases were driven by local longshore wind increments (Yuras et al., 2005). Nevertheless, these exhibited slight divergence in location and space from 1NT's Chl blooms (Cases 1, 2 and 4 in sections 6.3.1.1, 6.3.1.2 and 6.3.1.4).

The Northern Cases mechanics are linked to rapid longshore wind increments associated with the SPSA returning to normality after weak or moderate El Niño episodes (Case 1 and 4 in sections 6.3.1.1 and 6.3.1.4) or reinforcement by La Niña (Case 2 section 6.3.1.1; Garreaud, 2009). Also, the AAO showed some influence on the Northern Zone, generating cut-off lows (Garreaud, 2009; Aceituno et al., 2015; DMC, 2018), which create heavy rains that help fertilise the ocean with nutrients. In any case, the Northern Zone showed low productivity, except for 1NT (Yuras et al., 2005).

1NT's Chl response might be related to its proximity to Peru, which generally had an even higher Chl concentration (Echevin et al., 2014; Cases 1, 2 and 4). Secondly, 1NT could maintain the Chl anomaly for a couple of weeks without favourable winds. Effectively, 1NT Chl activity was present in the three cases, which means that its response is determined by 2NT, 3NT and Peru Chl activity. Also, 1NT's location is slightly oriented SE-NW; thus, the westerly winds could produce upwelling in some sections. There are also dust inputs from the land in small quantities. Also, 1NT has shown in these case studies that southerly winds are crucial to its Chl increment despite being weakly influenced by the SPSA. However, these local winds seem to arise with a higher frequency when the SPSA is located in the north (September-November), and the mentioned mechanisms with ENSO occurred, leading to winds speeds over 4 m s^{-1} when 1NT average speed was 3.8-4.1 m s^{-1} (Table 4.7). For that reason, 1NT's Chl response was present in three cases. Finally, Anthropogenic activities also could be a factor because 2NT and 3NT are more polluted by mining tailings, but 1NT has had more fisheries since the 1960s (Camus, Hajek, 1998; Thiel et al., 2007; Jara et al., 2014).

Cases 3 and 1 (sections 6.3.1.3 and 6.3.1.1) indicated that dust storms do not produce a phytoplankton response. These episodes do not occur very often, and when they do happen,

the sunlight and the longshore winds are diminished, which are key ingredients for a Chl bloom. Nonetheless, a short-lived response was expected, at least in 1NT, which had significant activity. A possible reason for Case 3 is the dust event that occurred in the winter when a low Chl stock was typically seen, or excessive cloudiness covered its response. In contrast, the dust movement observed in Case 1 was minimal, so the response was negligible. Dust storms increased the phytoplankton activity in zones without nutrients, such as the Mediterranean Sea, for at least a week when these storms were wet instead of dry (Ridame et al., 2014).

The Central Zone mechanics observed in Cases 5 and 6 (sections 6.3.2.1-6.3.2.2) were practically the same, which consisted of a rapid SPSA intensification without the participation of significant anomalies in ENSO or AAO. Additionally, both cases were in the summer, when the radiation peaked, and the SPSA's core was in the Central Zone. Case 7 (section 6.3.2.3) displayed particular meteorological conditions that expanded high Chl oceanwards from 4C to 3C and 2C (DMC, 2018). However, these conditions do not explain why the concentration was so high. A possible explanation is a red tide that occurred prior to this, killing 4,800 tonnes of salmon, or a company dropped some of them illegally. A company was fined in 2021 for such practices (Molinari, 2021).

The Southern Zone exhibited higher phytoplankton blooms along with 3CT and 4CT. This is likely related to the water's background nutrient levels, arising from deep waters as the AAIW (Thiel et al., 2007; Mongollón and Calil, 2017; Corredor-Acosta et al., 2015; Masotti et al., 2018). Nonetheless, these nutrients are located in deeper layers due to the stratification that are adequately mixed with the upwelling product of alongshore winds (Thiel et al., 2007; Lara et al., 2010; Landaeta et al., 2011; section 3.1.3). For that reason, 3ST presented a low Chl concentration when there was a lack of southerly winds. The mechanics observed in the three cases were southerly winds increases driven by the SPSA southern location after El Niño events and low PR due to positive AAO reducing the stratification (Montecinos and Aceituno, 2003). Finally, the Southern Zone cases tended to expand more oceanwards than the other Zones, likely because it contains more nutrients and a higher stratification that reduces the euphotic layer thickness extending the Chl signal even more (Landaeta et al., 2011).

Even though the subsections with more rivers are the most productive (3CT-2ST) due to the addition of NO_3^- and PO_4^{-2} (Masotti et al., 2018), the case studies have shown that when their flux is too high, the Chl activity is severely reduced. The most significant case is the Puelo River in the interior Chiloé Sea', where its flux renewed the waters, adding nutrients slightly but increasing the local stratification and potentially flushing out the plankton and causing it to disperse in the coastal ocean (Cases 5, 6, 8 and 9 in sections 6.3.2.1-6.3.2.2 and 6.3.3.1-6.3.3.2; De la Torre, 2016). Thus, this reduces the red tide bloom risk and the phytoplankton growth in general. However, the Puelo River has shown lower fluxes since the big drought (2010-2018) and a positive AAO tendency in recent years (DMC, 2018; Aguayo et al., 2021; Garreaud et al., 2020). Consequently, more blooms have been seen there, as well as red tides (Armijo et al., 2020; Sernapesca, 2018). On the other hand, the Biobio and Itata Rivers showed a lower impact on 4CT's Chl behaviour compared to the southerly winds' effect (Vergara et al., 2017), whereas the Maipo, Mataquito and Maule Rivers were even less influenced but severely affected by the big drought.

Although the Chl measurement by satellite images captures the red tides, it is impossible to differentiate them from a typical phytoplankton bloom, even considering other physical variables and climate drivers to complement the information. This was demonstrated in Case 11 (section 6.3.3.4), where the Chl anomalies were not as high, despite the red tide's magnitude. Thus, the only possible way to prevent them is to take samples constantly,

particularly in salmon farms, to avoid eutrophication areas that may trigger red tides (Armijo et al., 2020; Sernapesca, 2018). Nonetheless, an algorithm adjustment, increasing the red band, might help differentiate the red tide from a typical Chl bloom. This was not done because it was not the primary purpose of this work, but it is an interesting investigation line.

6.5. Conclusion.

The results confirmed that the southerly winds are the main trigger for these cases. Although the SPSA drives these, the AAO and especially ENSO heavily influenced the SPSA and, consequently, the phytoplankton productivity. Other significant variables are the PR and the river inflows, which introduce the nutrients required by the phytoplankton. However, the case studies have demonstrated that either their excess or shortage harmed phytoplankton production.

The mechanics for all the cases involve an intensification in the southerly winds driven by SPSA enhancement. This SPSA variation was caused by different factors. These included its annual cycle movement, returning to normality after an El Niño event, and, finally, a starting La Niña, which boosted the SPSA.

This mechanism was straightforward in the Central Zone, while in the other Zones was less evident. For instance, the Chl blooms and the wind patterns showed slight divergence in location and space in 1NT because this subsection generally had low wind variations. Furthermore, these wind variations were more influenced by ENSO than by the other Cases. The Southern Zone cases occurred when the southerly winds were dominant, and the PR was low simultaneously. These conditions were driven when the SPSA was moved southwards by El Niño, and the positive AAO blocked the fronts coming from the Southern Ocean, demonstrating that AAO and ENSO modulate the SPSA significantly.

Due to the big drought that started in 2010 and the positive AAO tendency in recent years, the river's fluxes have reduced, while the Chl in the Southern Zone has increased, as well as the number of red tide events. The latter has been even more boosted by the enormous number of fisheries located in the Southern Zone.

The red tide events cannot be differentiated from a typical Chl bloom. Effectively, Case 11 showed lower Chl anomalies (section 6.3.3.4). Therefore, more variables are needed to define a red tide, which must be taken in situ, such as phytoplankton samples, and oxygen levels (Leon-Muñoz et al., 2018; Armijo et al., 2020; Sernapesca, 2018). However, an algorithm adjustment, increasing the red band, might help differentiate the red tide from a typical Chl bloom, but this will need further analysis.

Unexpectedly, the dust storm in the Northern Zone did not produce a clear Chl response (section 6.3.1.3). Nevertheless, the excessive cloudiness could have covered its response. Although these events have led to a Chl rapid response in HNLC zones, the response was direct when the places did not have enough nutrients, and the dust deposits were dry (Ridame et al., 2014). In any case, more studies must be done, especially considering that local newspapers have reported more low-intensity cases between June to September 2015, 2016, and 2018-2020 (24-Horas 2015; Chilevision, 2018; Araya, 2020).

7. Discussion.

7.1. Introduction.

This research's primary focus was to determine climate drivers that affect phytoplankton response and causes of spatial variability in phytoplankton productivity along the Chilean coast. O.1 focused on the Chl relationships with physical parameters and how they vary depending on the study's different Zones (Northern, Central and Southern Zone). O.2 focused on a macroscale impact established by climate drives, such as El Niño, La Niña and AAO. Finally, O.3. was to analyse case studies where the Chl concentration was extreme to understand their particularities and link to the mechanisms observed in the previous objectives. In this chapter, each object will be summarised to produce later an overview highlighting the main findings and conclusions but complemented with oceanic features discussed in chapters 2 and 3. Then an extra analysis will be made to complement the information. Finally, further investigation lines and limitations will also be discussed.

O.1's correlations and all the case studies in O.3 have shown the crucial role of southerly winds in phytoplankton production, which the SPSA drives. O.3 also showed how ENSO and AAO influence the SPSA. Although O.2. analysed ENSO and AAO changes on the physical parameters, the SPSA was not studied itself. Thus, the SPSA behaviour will be studied in this chapter by comparing the SPSA average composite using the SLP and the wind vectors against the ENSO and AAO positive and negative phases. It is worth reminding the reader that the study area was split into three, with the Northern (N), Central (C) and Southern Zones (S), having three subsections each, except the Central Zone, which had four (e.g., 1N, 2N, 1C, 1S). At the same time, each subsection was divided into coastal (T) and ocean strips (O, e.g., 1NT, 2CO; Figure 3.9 and section 3.2.2).

7.2. Objectives Overview.

This study analysed the spatial and temporal variability of phytoplankton behaviour along the Chilean coast, considering the influence of climate drivers by the following objectives:

Determination of the trends in seasonal, interannual and spatial variability for parameters that affect phytoplankton production [O.1]. Thus, O.1 estimated which parameters were more relevant to phytoplankton per subsection and Zone.

Understanding how large-scale climate drivers contribute to phytoplankton production [O.2]. Hence, O.2 defined the impact of the most significant climate drivers in Chile by investigating their influence on the physical parameters and, consequently, the phytoplankton.

Determine specific mechanisms for an increase of phytoplankton in case study events [O.3]. This objective helped to understand what triggered the Chl extreme events in each Zone, studying the physical parameters and the climate drivers as well as external factors such as river inflows, dust storms and red tides.

7.2.1. Trends in Seasonal, Interannual and Spatial Variability for Parameters that affect Phytoplankton Production [O.1].

The monthly averaged Chl and physical parameters (SST, PR, VW and UW) were studied in each subsection from 2002 to 2018. These were measured by remote sensing data and models (MODIS-Aqua, TRMM and MERRA-2; cf. Table 3.5 and section 3.2.3). All these data were extracted using GIOVANNI. These parameters were analysed by observing its annual

and seasonal cycle per subsection [O.1.1]. Also, the anomalies of each parameter were correlated to estimate which parameter is more significant in each subsection [O.1.2].

The results revealed that the Northern Zone had a low phytoplankton concentration with small seasonal variability, except in 1NT. This pattern is due to weak winds (1NT-2NT), lack of precipitation, rivers and relatively stable weather conditions driven by the SPSA that become this Zone in a HNLC region (Yuras et al., 2005; section 4.4.1). 1NT presented a higher Chl concentration but was almost constant, with a slight rise in September and February. Thus, its concentration is likely related to the increased production from neighbouring Peruvian waters, which has a constant Ekman transport that allows a constant nutrient supply. Furthermore, these nutrients are transported through Chile by poleward ESSW from northern Peru (Thiel et al., 2007; Echevin et al., 2014; section 3.1.1). Even though 2NT has filaments in Mejillones and Antofagasta associated with capes, these were not productive, likely related to anthropic activities there, effectively these were more productive 20 years ago (Thiel et al., 2007; Camus and Hajek, 1998).

The Chl in 3NT showed a weak seasonal cycle with a maximum value in September that seems to be partly triggered by its high VW, having a more statistically significant correlation (P-value <0.01, Rho=0.21). The Chl~PR [3]was low and positive due to PR scarcity in this Zone but with occasionally extreme events, which were more significant in 3NT. Although PR events might positively impact the Chl by increasing the Fe supply through runoff, extreme events would produce the opposite effect (Thiel et al., 2007; Dezileau et al., 2004). Indeed, 1NT had the highest correlation with the Chl with a more constant PR. However, this correlation was not significant. This Zone generally had a low Chl variation with no significant correlation with the physical parameters, except for VW in 3NT.

Overall, the constant but low southerly winds and scarce PR in this Zone, driven by the SPSA, lead to a low nutrient renovation process in the euphotic layer, which is even more limited by a shelf lower than 10 km wide, not allowing a correct remineralisation process (Thiel et al., 2007; Marchant et al., 2007). The only exception is 1NT, which has nutrients from Peru and a slightly broader shelf within the Peruvian limits. Antofagasta and Mejillones capes before had a higher Chl signal diminished in recent years.

The Central Zone presented a seasonally varying production, with a high Chl concentration during the summer and spring (Corredor-Acosta et al., 2015; Gómez et al., 2017; section 4.4.2). This is linked to the SPSA movement and the sunlight reduction during the winter (Figure 7.1). The SPSA in the warm season forms a strong eddy that enhances the upwelling from 30°S to 38°S (Thiel et al., 2007; section 3.1.2). The seasonal difference was more pronounced in 3CT-4CT, leading to higher PR with more well-spaced rivers and lower southerly winds with a westerly component during the winter, while 1CT-2CT exhibited more significant longshore winds the whole year. However, the southerly winds have similar values in the whole Central Zone during the summer (Table 7.1).

Therefore, Chl~VW were statistically significant in the whole Zone, excluding 2CT, while UW was statistically significant in 3CT-4CT. Indeed, the Chl~VW were higher there (0.27, 0.38) but also UW (-0.2, -0.27). As a result, 1CT and 2CT exhibited a low Chl signal, whereas the other two subsections had a significant concentration. Specifically, 4CT had a slightly higher concentration, but 3CT exhibited a higher variability. Hence, the VW is a key factor, but it must be in equilibrium with the PR, which also adds nutrients; despite the Chl~PR being

---

[3] This notation means correlation.

negative in these subsections, they were statistically significant in the last two (3CT=-0.2, 4CT=-0.34).

Thompson et al. (2015) stated that the PR increase has only a positive effect in the Chl when this occurs during the warm season, while the opposite effect is seen during the cold season. Effectively, although the PR increases considerably during the cold season in 3CT-4CT, it also increases during the warm season (Table 7.1), but the Chl~PR continued to be negative even when they were split by season (Table 7.2). Additionally, Extreme ENSO years had shown some variation in the Chl concentration in this Zone (Gómez et al., 2017; Ancapichun and Garcés, 2015; Corredor-Acosta et al., 2015). Another factor influencing these differences in these two groups is the shelf configuration, which is lower than 10 km wide in 1CT and 2CT, while the average width for the 3CT and 4CT is 40 to 70 km, except for the middle section in 4CT, where it shelf is 12 km wide. Also, 4CT has a mark filament due to its cape (Thiel et al., 2007; Marchant et al., 2007).

Therefore, this Zone can be split into two: 1CT-2CT with higher winds and lower PR in the summer, leading to a low Chl concentration and 3CT-4CT, with a marked season difference increasing the PR the whole year and reducing the averaged winds but still high during the summer, leading to a high Chl concentration. Finally, the differences in the Chl signal in these two groups are evidently related to the width of their shelves.

TABLE 7.1. SEASONAL AVERAGE CHL CONCENTRATION (MG M^{-3}), PR (MM SEASON^{-1}) AND VW (M S^{-1}) FOR THE STUDY PERIOD (2002-2018).

Chl	1NT	2NT	3NT	1CT	2CT	3CT	4CT	1ST	2ST	3ST
Summer	2.15	1.18	1.00	0.96	1.38	2.58	2.98	2.72	3.37	1.60
Autumn	1.72	0.91	0.74	0.74	0.95	1.30	1.50	1.81	1.82	1.51
Winter	1.60	0.91	0.96	0.90	1.15	1.54	1.78	1.84	1.72	1.75
Spring	1.73	1.14	1.25	1.72	2.31	3.43	3.18	2.76	3.30	1.79
PR	1NT	2NT	3NT	1CT	2CT	3CT	4CT	1ST	2ST	3ST
Summer	14.76	13.68	3.55	3.49	8.71	26.34	83.50	183.61	264.04	205.91
Autumn	3.45	7.50	19.86	66.68	175.59	288.16	409.48	449.42	466.27	307.69
Winter	4.43	5.85	16.56	56.64	179.08	289.56	393.37	436.89	445.70	263.63
Spring	6.51	7.75	2.99	9.70	32.88	73.06	163.56	232.96	317.57	235.59
VW	1NT	2NT	3NT	1CT	2CT	3CT	4CT	1ST	2ST	3ST
Summer	3.93	4.46	5.69	6.65	6.35	7.39	6.30	2.69	1.24	-1.97
Autumn	4.04	5.16	6.12	6.30	4.35	3.64	1.42	-0.53	-0.83	-1.47
Winter	3.96	5.78	7.20	6.99	4.22	3.19	0.78	-1.00	-1.43	-1.95
Spring	3.78	4.85	7.05	8.14	6.88	6.85	4.49	1.14	0.17	-1.77

The Southern Zone is at the limits of the SPSA effect (Figure 7.1). Thus, weak longshore winds are often seen in 1S and 2S during the warm season, whereas they occasionally appear during the winter in 3S. Instead, storms with prominent westerly winds coming from the South Pacific arrived frequently, driven by the AAO and SPSA (González-Reyes and Muñoz, 2013; Aguayo et al., 2021; section 4.4.3).

Due to interactions with the intricate submarine geography, these longshore winds in 1S and 2S produce upwelling events enhanced by sporadic anticyclonic eddies during the summer. Moreover, this effect is even more boosted by shelf width over 70 km (Strub et al., 2019; Marchant et al., 2007; Aracena et al., 2011). Hence, 1ST and 2ST Chl concentrations showed a seasonal cycle with a high production analogous to 4CT and 3CT, respectively. However, their production was lower during the winter. Meanwhile, 3ST's Chl was almost constant throughout the year but with still fair Chl concentration, despite the relatively constant northerly winds and few moments of southerly winds in the winter, with significant westerly winds that were more intense in the winter. Thus, the nutrients are delivered by AAIW in the channels and fjords. Meanwhile, the CHC and AAIW do it for the coastal values, which likely brings nutrients from HCS (Aracena et al., 2011).

Both wind components strongly impacted the Chl concentration in 1ST (VW=0.45, UW=-0.41), UW influenced more 3ST's Chl (VW=0.23, UW=-0.32), and 2ST's Chl was affected by both but in a minor way (VW=0.26, UW=-0.29). Along with river and glacier flow, the PR amount leads to ocean stratification, reducing phytoplankton production (Marchant et al., 2007; Landaeta et al., 2011). Thus, Chl~PR in this Zone showed a significant negative relationship, especially in 1ST (-0.39), while 2ST and 3ST were slightly lower (-0.24, -0.2), with higher values during spring and summer, except for 1S (Table 7.2). The ENSO also impacted this Zone, increasing its production during intense El Niño episodes (Montecinos and Aceituno, 2003). Therefore, despite the low SPSA effect in the Southern Zone, the Chl concentration was higher than expected, driven by upwelling events associated with marked winds and anticyclonic eddies related to the mentioned currents' interaction with the topography. Moreover, lower PR and river inputs allow the AAIW to be on the surface, which is rich in nutrients (Sievers and Silva, 2008; Aracena et al.,2011).

TABLE 7.2: CHL REGRESSION WITH THE PHYSICAL PARAMETERS PER SUBSECTION IN THE COASTAL STRIP SPLIT BY SEASON.

Rho	Season	Chl~SST	Chl~PR	Chl~VW	Chl~UW
1NT	Sum	-0.13	0.15	0.11	-0.04
	Aut	-0.41	0.32	0.06	-0.13
	Win	0.20	0.18	-0.24	-0.10
	Spr	0.06	-0.08	0.31	-0.26
2NT	Sum	-0.18	0.08	0.08	0.00
	Aut	-0.20	0.21	0.00	-0.06
	Win	-0.16	0.06	0.11	0.01
	Spr	0.05	-0.06	0.06	-0.03
3NT	Sum	-0.09	0.07	0.23	-0.01
	Aut	-0.02	0.20	0.04	-0.16
	Win	-0.19	-0.32	0.17	0.02
	Spr	-0.15	-0.01	0.33	0.46
1CT	Sum	-0.15	-0.15	0.27	-0.11
	Aut	-0.26	0.03	0.20	-0.12
	Win	0.15	-0.01	0.10	0.14
	Spr	-0.33	-0.13	0.31	-0.10
2CT	Sum	-0.40	-0.02	0.26	0.23
	Aut	-0.06	0.21	-0.14	-0.26
	Win	0.33	0.06	-0.07	-0.02
	Spr	-0.26	-0.05	0.23	0.20
3CT	Sum	-0.46	-0.33	0.41	0.22
	Aut	0.01	-0.16	0.30	0.06
	Win	0.20	-0.05	0.02	0.11
	Spr	-0.31	-0.37	0.38	0.40
4CT	Sum	-0.30	-0.23	0.31	-0.11
	Aut	-0.11	-0.42	0.34	-0.35
	Win	-0.18	-0.47	0.58	-0.39
	Spr	-0.19	-0.35	0.40	-0.29
1ST	Sum	-0.14	-0.33	0.38	-0.30
	Aut	-0.13	-0.57	0.41	-0.33
	Win	-0.13	-0.27	0.60	-0.60
	Spr	0.10	-0.42	0.39	-0.38
2ST	Sum	-0.12	-0.30	0.16	-0.24
	Aut	0.33	-0.12	0.08	0.05
	Win	-0.04	-0.27	0.62	-0.52
	Spr	0.35	-0.41	0.30	-0.50
3ST	Sum	0.09	-0.20	0.10	-0.56
	Aut	0.24	-0.22	-0.08	-0.26
	Win	0.03	-0.18	0.44	-0.32
	Spr	0.44	-0.20	0.34	-0.28

Overall, the SPSA is the main climate driver that creates southerly winds that produce favourable upwelling conditions in a relatively straight coastline, increasing the Chl. Although its influence is from 1NT to 1ST (Figure 7.1), only 3CT to 2ST had significant production, followed by 1NT and 3ST. The initial hypothesis identified PR as a second mechanism for obtaining nutrients for its increments during the summer, but a seasonal correlation analysis

showed that the Chl~PR were higher but still negative (Table 7.2). A more significant variable is the shelf size, which increases from 3CT to 3ST. Another factor that possibly explains the higher Chl activity for 1NT is its proximity to the more productive Peruvian shelf and a rich ESSW. Meanwhile, 2ST and 3ST nutrients are more accessible due to the lower inputs of the rain, rivers and glaciers driven by the big drought (2010-2018) and the positive AAO tendency in the later years, reducing the stratification. However, these subsections need a deeper analysis.
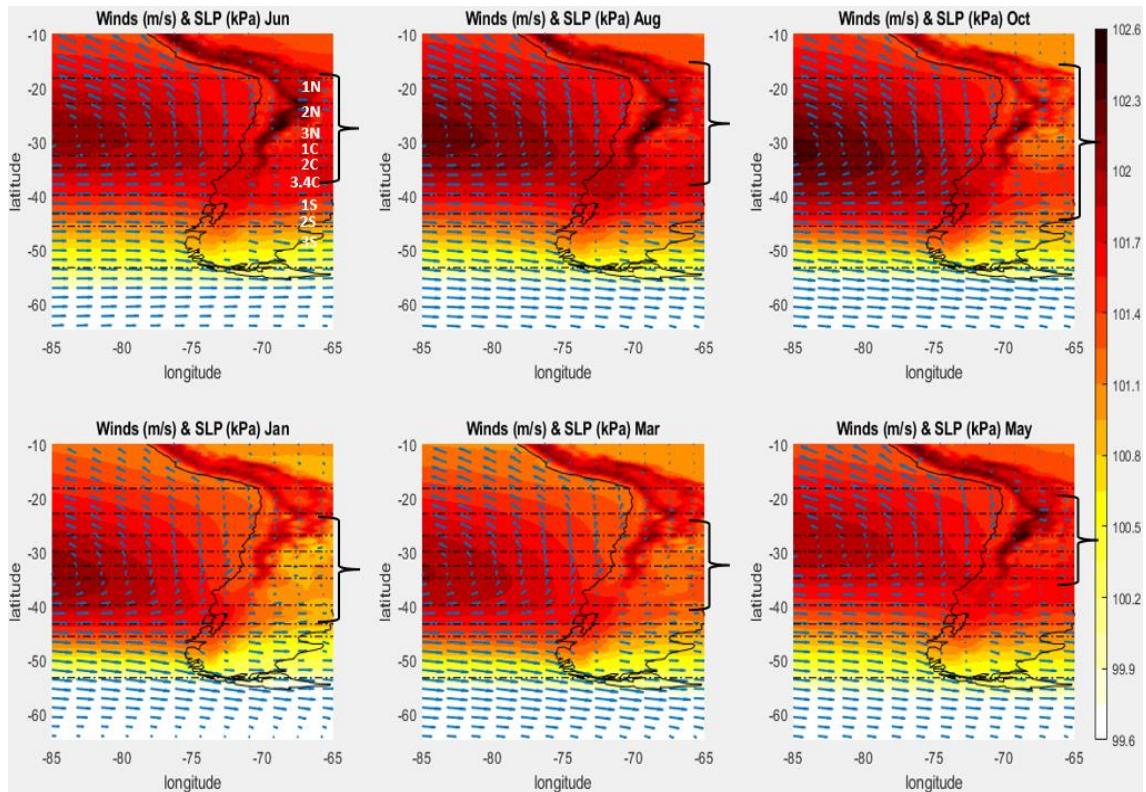
FIGURE 7.1. MONTHLY AVERAGED SLP AND WINDS FROM 1979 TO 2018, USING THE ERA5 DATASET, WHERE THE HORIZONTAL LINES DEFINE EACH SUBSECTION LIMIT AND THE BLACK CURLY BRACKETS SHOW THE SPSA'S CORE RANGE OVER 101.7 KPA. THIS HELPS TO IDENTIFY THE SPSA MOVEMENTS AND INTENSITY. THE SPSA HAD ITS MAXIMUM INTENSITY FROM AUGUST TO OCTOBER, WHILE THE MINIMUM WAS IN MAY. THE SPSA'S CORE WAS MORE CONCENTRATED IN 2NT TO 1ST FROM JANUARY TO MARCH AND 1NT TO 2CT FROM JUNE TO AUGUST. THEREFORE, THE NORTHERN ZONE'S WINDS WERE STRONGER IN THE WINTER, WHEREAS 1ST ONLY HAD SOUTHERLY WINDS IN THE SUMMER. ON THE OTHER HAND, 3CT TO 1ST HAD HIGHER PR IN THE WINTER.

7.2.2. Understanding how Climate Drivers Contribute to Phytoplankton [O.2].

Climate driver indices (ENSO, SPSA, AAO, SOI, PDO and AAO), obtained mainly by NOAA, were studied using correlations. ENSO and AAO were the most independent, significantly impacting the SPSA and, consequently, the Chilean coast. Each parameter's (Chl, SST, VW, UW and PR) behaviour was defined utilising composite maps for ENSO and AAO positive and negative phases. These composites were made using the most extreme years of both climate drivers. The study period was extended to 1979-2018 to obtain more extreme years for each. The physical parameters, available from 1979 onwards, were obtained from ERA5.

The Chl time-series had to be reconstructed [O.2.1] because it was only available from 2003 onwards. CCA was used to extend the Chl based on its EOFs higher correlations with a fully known parameter's EOFs (section 5.2.1). SST, VW and UW were tested, showing the best result with the first with R of 0.45 on average and MAE of 0.63 for available data, while these were 0.19 and 0.85 for unknown data (section 5.3.1). This significant error, linked to Chl excessive variation, was considered acceptable because only Chl anomalies over ±0.5 SD were considered in this composite analysis.

The physical variable composites were compared to the Chl composites per climate driver phase [O.2.2], using the correlations obtained in O.1 (section 5.3.2, Table 5.5). The El Niño composite showed positive Chl variation in the Southern Zone during the warm season, driven by southerly wind increases and PR reductions, whereas the Central Zone exhibited Chl drops (Montecinos and Aceituno, 2003; Figure 7.2), confirming O.1 findings. The Northern Zone did not show significant Chl changes despite a persistent SST rise and a few southerly wind increases. 1NT, in particular, was less sensitive to these changes, which also was found in O.1. Effectively, Figure 7.2 shows that although the SPSA's core had lower intensity during an El Niño warm season, it expanded through the south, increasing the SLP slightly in the Southern Zone. Thus, the westerly winds and PR events decreased considerably during the warm season, whereas the southerly winds increased in September, October and February.
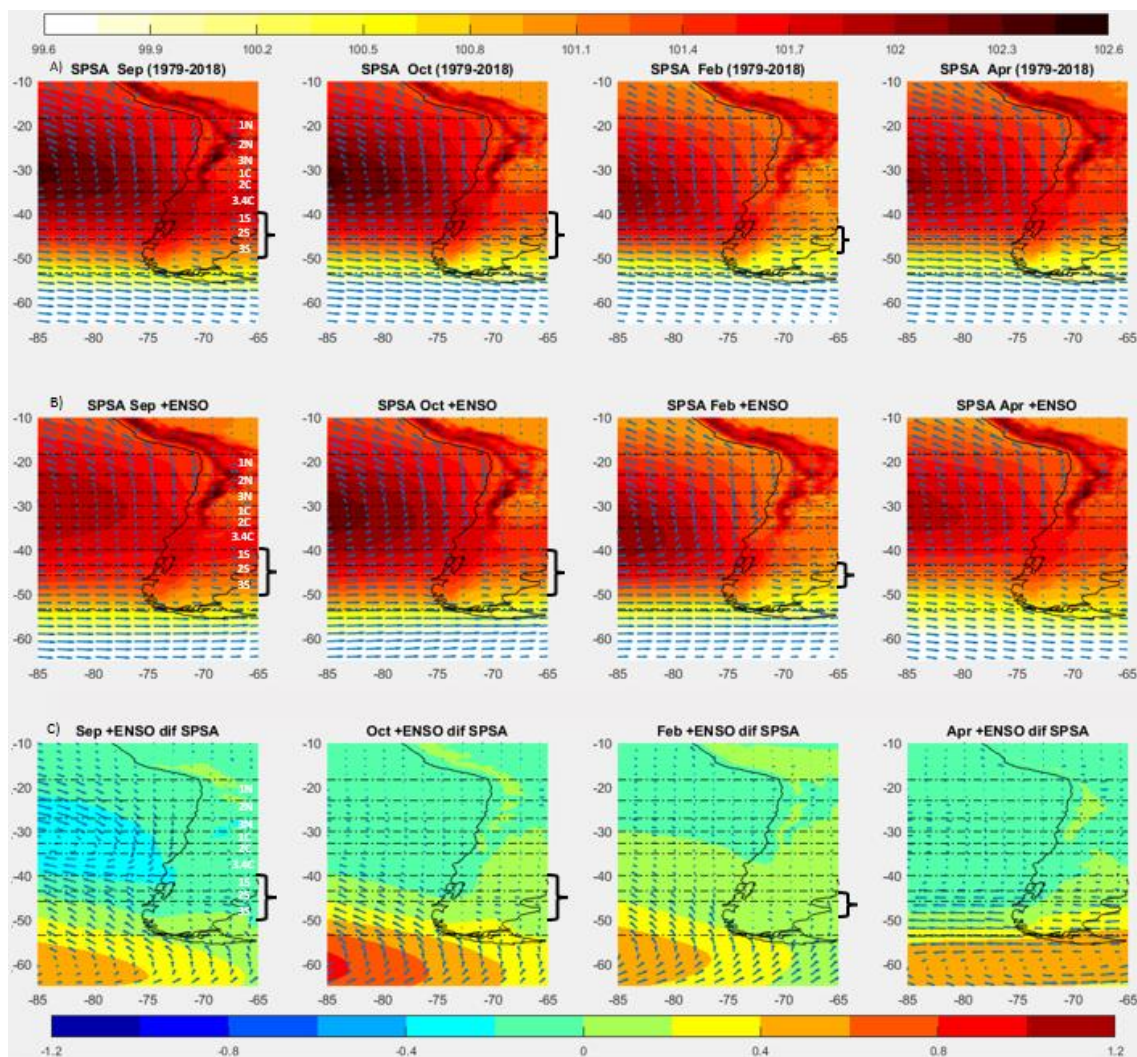
FIGURE 7.2. A) SPSA AVERAGED BEHAVIOUR FOR SEPTEMBER, OCTOBER, FEBRUARY AND APRIL, WHERE THE HORIZONTAL LINES DEFINE EACH SUBSECTION LIMIT (TOP COLOUR BAR). B) SPSA AVERAGED BEHAVIOUR IN EL NIÑO YEARS (2015, 1997, 1981 AND 1991) FOR THE SAME MONTHS (TOP COLOUR BAR). C) EL NIÑO SPSA DIFFERENCE FROM THE REGULAR SPSA (BOTTOM COLOUR BAR). THE CURLY BRACKETS INDICATE THE SECTIONS WHERE THE SOUTHERLY WINDS ARE MORE SIGNIFICANT THAN IN A REGULAR SPSA YEAR. THE C SECTION SHOWED HOW THE SLP WAS HIGHER IN THE EXTREME SOUTH. IT ALSO EXHIBITED HOW THE WESTERLY WINDS WERE WEAKER DURING AN EL NIÑO YEAR.

La Niña experienced a slight Chl drop in the Northern and Central Zone from June to October, while the rest of the cycle was slightly positive. Nevertheless, the conditions in the Northern Zone were inconsistent with the favourable variations of the physical variables. The Southern Zone also had a Chl reduction driven by westerly winds anomalies from December to May. Indeed, Figure 7.3 reveals a SPSA reinforcement during La Niña, leading to more southerly winds in the Central Zone and part of the Northern and more intense westerly winds in the

Southern Zone. The only exception was February, where the SLP was lower, reducing the typical southerly winds in 1ST. In contrast, Gómez et al. (2012) report strong upwelling in 3CT and 4CT during the spring, increasing the Chl.
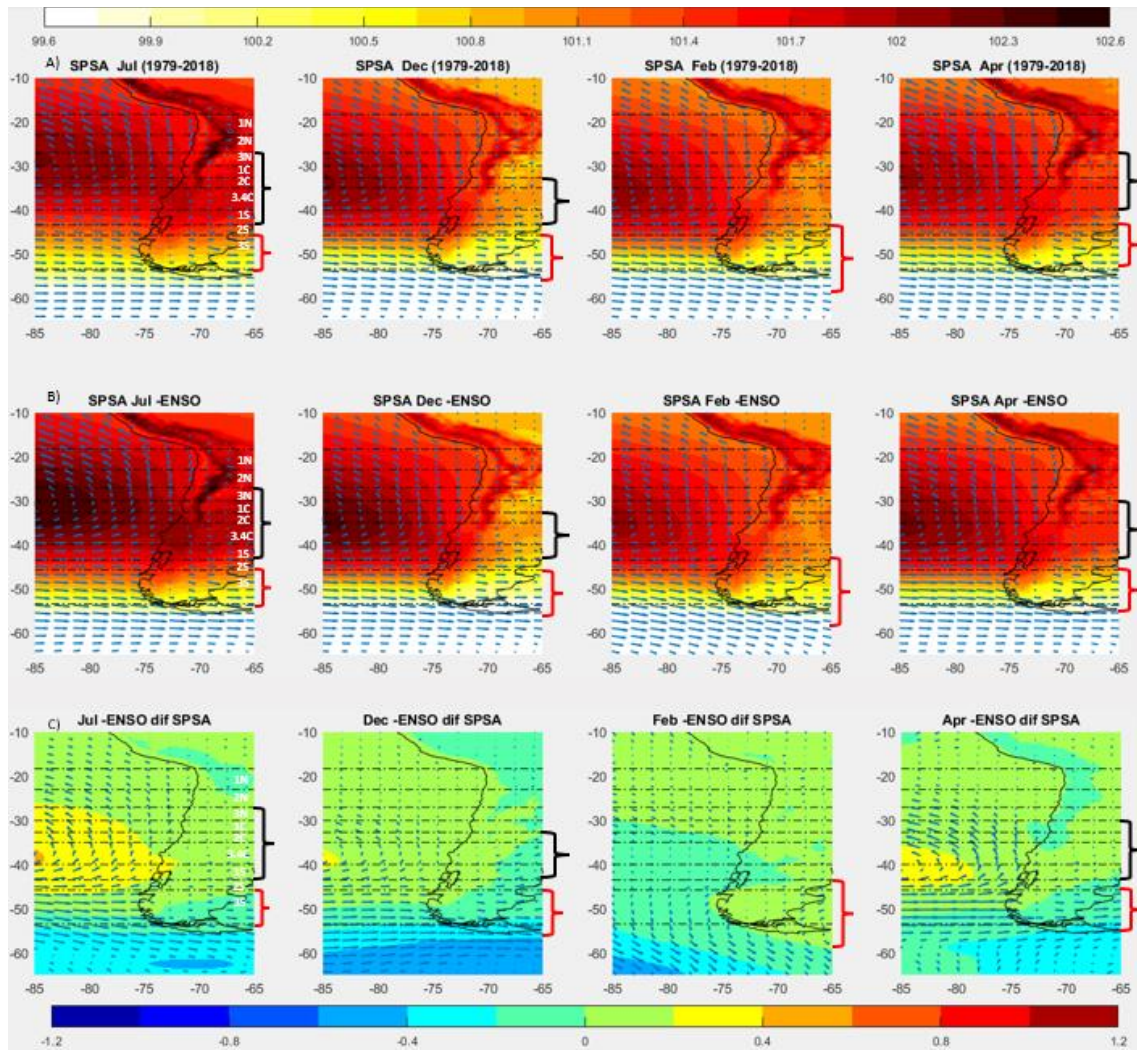

FIGURE 7.3. A) SPSA AVERAGED BEHAVIOUR FOR JULY, DECEMBER, FEBRUARY AND APRIL, WHERE THE HORIZONTAL LINES DEFINE EACH SUBSECTION LIMIT (TOP COLOUR BAR). B) SPSA AVERAGED BEHAVIOUR IN LA NIÑA YEARS (1988, 1999, 2010, 1998 AND 2007) FOR THE SAME MONTHS. (TOP COLOUR BAR) C) LA NIÑA SPSA DIFFERENCE FROM THE REGULAR SPSA (BOTTOM COLOUR BAR). THE BLACK CURLY BRACKETS INDICATE THE SECTIONS WHERE THE SOUTHERLY WINDS ARE MORE SIGNIFICANT THAN A REGULAR SPSA YEAR, WHILE THE RED BRACKETS POINT OUT WHEN THEY ARE LOWER. THE C SECTION SHOWED HOW THE SLP WAS HIGHER IN THE CENTRAL ZONE, BUT IT DID NOT SIGNIFICANTLY INCREASE THE SOUTHERLY WINDS. THE EXTREME SOUTH DISPLAYED LOWER SLP, LEADING TO DOWNWELLING WINDS.

For the positive AAO, the Chl suffered a slight decline in the Northern and Central Zone from June to September, while 2ST and 3ST exhibited a minor increase. 1ST showed a Chl increment as well, but this was for September to December (Figure 5.38). These Chl minor variations were inconsistent with the few northerly winds and PR increases observed in July and August in the Southern Zone, but 1ST-2ST was coherent with a slight PR reduction in January, May, and September (Figures 5.23 and 5.24). These findings were also seen in Figure 7.4, demonstrating that the positive AAO increased the SLP differences between the SPSA's core and the Drake Passage but with minor changes. Rahn et al. (2012), González-Reyes and Muñoz (2013) and DMC (2018) reported dried conditions in the Southern Zone from December to April during positive AAO. These results are not similar to this research, but they are not contradictory either. The negative AAO did not show any significant Chl variation. However, considerable PR and westerly wind increases were seen in the three Zones, with a higher impact on the Central Zone throughout the year. Figure 7.4 reveals a

slight SLP decrease in the Central Zone linked to the PR increase and a SLP rise in the Drake Passage.
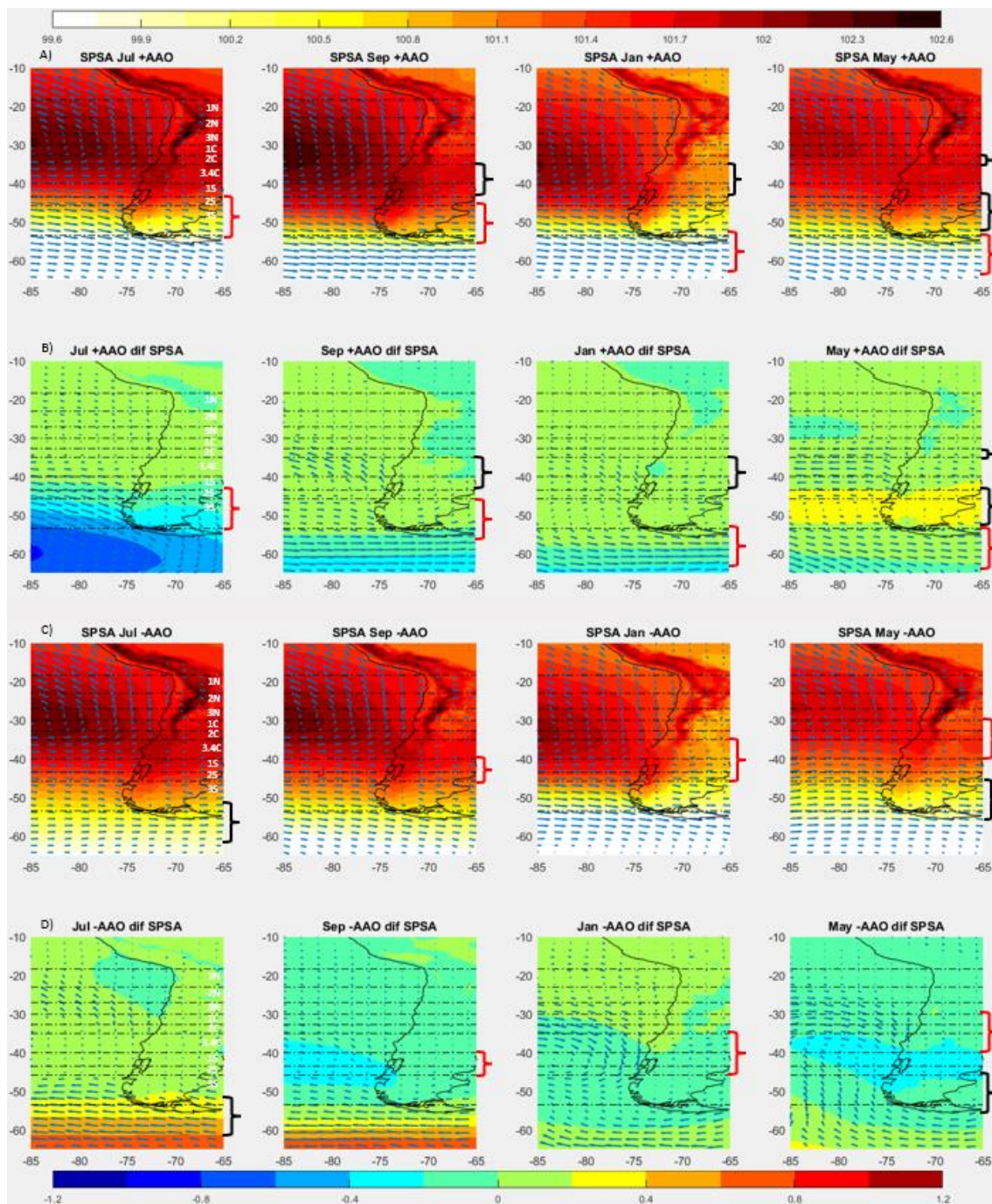
FIGURE 7.4. A) SPSA AVERAGED BEHAVIOUR IN +AAO YEARS (1993, 1998, 1999, 2008, 2010, 2015 AND 2017) FOR JULY, SEPTEMBER, JANUARY AND MAY, WHERE THE HORIZONTAL LINES DEFINE EACH SUBSECTION LIMIT (TOP COLOUR BAR). B) +AAO SPSA DIFFERENCE FROM THE REGULAR SPSA DURING THE SAME MONTHS (BOTTOM COLOUR BAR). C) SPSA AVERAGED BEHAVIOUR IN -AAO YEARS (1980, 1991, 1999, 2000 AND 2002; TOP COLOUR BAR) USING THE SAME MONTHS. D) -AAO SPSA DIFFERENCE FROM THE REGULAR SPSA (BOTTOM COLOUR BAR). THE BLACK CURLY BRACKETS INDICATE THE SECTIONS WHERE THE SOUTHERLY WINDS ARE MORE SIGNIFICANT THAN IN A REGULAR SPSA YEAR, WHILE THE RED BRACKETS SHOW THE SECTIONS WHEN THEY ARE LOWER. B SECTION DISPLAYED HOW THE +AAO SLIGHTLY INCREASED THE SLP IN THE CENTRAL ZONE, BUT WITHOUT AFFECTING THE TYPICAL SOUTHERLY WINDS, EXCEPT IN SEPTEMBER AND MAY, WHERE THESE WERE HIGHER. THE EXTREME SOUTH EXHIBITED LOW SLP, BUT IT DID NOT TOUCH THE LAND EXCEPT IN JULY AND MAY. THE -AAO IN D HAD THE OPPOSITE BEHAVIOUR, DECREASING THE SLP IN THE CENTRAL ZONE AND HIGHER SLP IN THE DRAKE PASSAGE, LEADING TO DOWNWELLING WINDS IN THE CENTRAL AND THE SOUTHERN ZONE.

Overall, the El Niño Chl anomaly composites were consistent with El Niño physical variable anomaly composites. The Chl impact during El Niño was mainly in the Southern Zone during the warm season, which was found by other authors as well. The La Niña was associated with

169

longshore winds intensification in the Central and Northern Zone that did not significantly increase the Chl stock. However, Gómez et al. (2012) found a significant Chl increase in 3C-4CT during La Niña's spring. Although negative AAO increased the PR patterns significantly in the three Zones with a slightly higher impact in the Central Zone, these changes did not influence the Chl, supporting the new hypothesis that the PR itself is not as relevant as other features for adding nutrients. On the other hand, the typically reported reduction in the PR during the positive AAO was not clearly seen in the composites (Figure 5.24), and the Chl response was not clear either. These results are related to the AAO having a substantial monthly variation that was hard to represent in an annual composite. Furthermore, the negative AAO Chl composite was built using only constructed data, increasing the error. Thus, its Chl results are uncertain. Consequently, a seasonal study for this climate driver is required.

7.2.3. Mechanisms Identification for an Increase of Phytoplankton in Case Study Events [O.3].

O.1 focused more on the general behaviour of each Zone, and O.2 studied the climate drivers' impact on a macroscale. Thus, the next step was a microscale analysis identifying how these climate drivers influence the physical parameters and the phytoplankton in each subsection at a particular moment and then observing general trends. This was defined by selecting three case studies per Zone from 2002 to 2018. The Case Study selection criteria [O.3.1] considered different aspects. First, the data was filtered, keeping only the maxima Chl concentration in each subsection and the Chl anomalies over 2SD. Second, prioritise the events with higher duration or spread to different subsections. Finally, all the coastal strip subsections must be represented by the nine cases at least once. A dust storm in the Northern Zone and the worst red tide case in the Southern Zone were added as extra cases to determine their impact on the Chl. These additional cases were particularly intense and unusual. Each Case Study Analysis [O.3.2] examined the Chl, PR, SST, VW, UW and SLP variations on a monthly and weekly scale, using the same data source of O.2. This information was supplemented with ENSO, AAO and SPSA index variations, outflows from the most significant rivers, as well as papers and meteorological reports from Universidad de Chile and DMC.

The Northern Zone cases were driven by rapid longshore wind increases associated with the SPSA moving back to its northern location (Figures 7.5 rows c-e, and 7.1) and returning to normality after El Niño episodes or reinforcement by La Niña (Cases 1, 2 and 4, in sections 6.3.1.1, 6.3.1.2 and 6.3.1.4). The AAO also exhibited some influence in this Zone, generating cut-off lows (Barrett et al., 2016; Aceituno et al., 2015). 1NT higher productivity was present in the three cases, which means the Peruvian coastal Chl activity influenced its response, bringing nutrients by the ESSW (Echevin et al., 2014; Thiel et al., 2007). Moreover, 1NT could continue with a significant Chl anomaly for a few weeks after the longshore winds slight increase (Figure 7.5 rows a and b). Effectively, the Chl and the longshore winds exhibited slight divergences in location and space from 1NT's Chl blooms, explaining the low Chl correlations in 1NT in O.1. The filaments product for the capes in 2N and 3N showed a higher Chl concentration in Cases 2 and 4 (Figure 7.5 rows c and e). Finally, the dust storm did not influence the phytoplankton response for the observed Case (Case 3 in section 6.3.1.3).
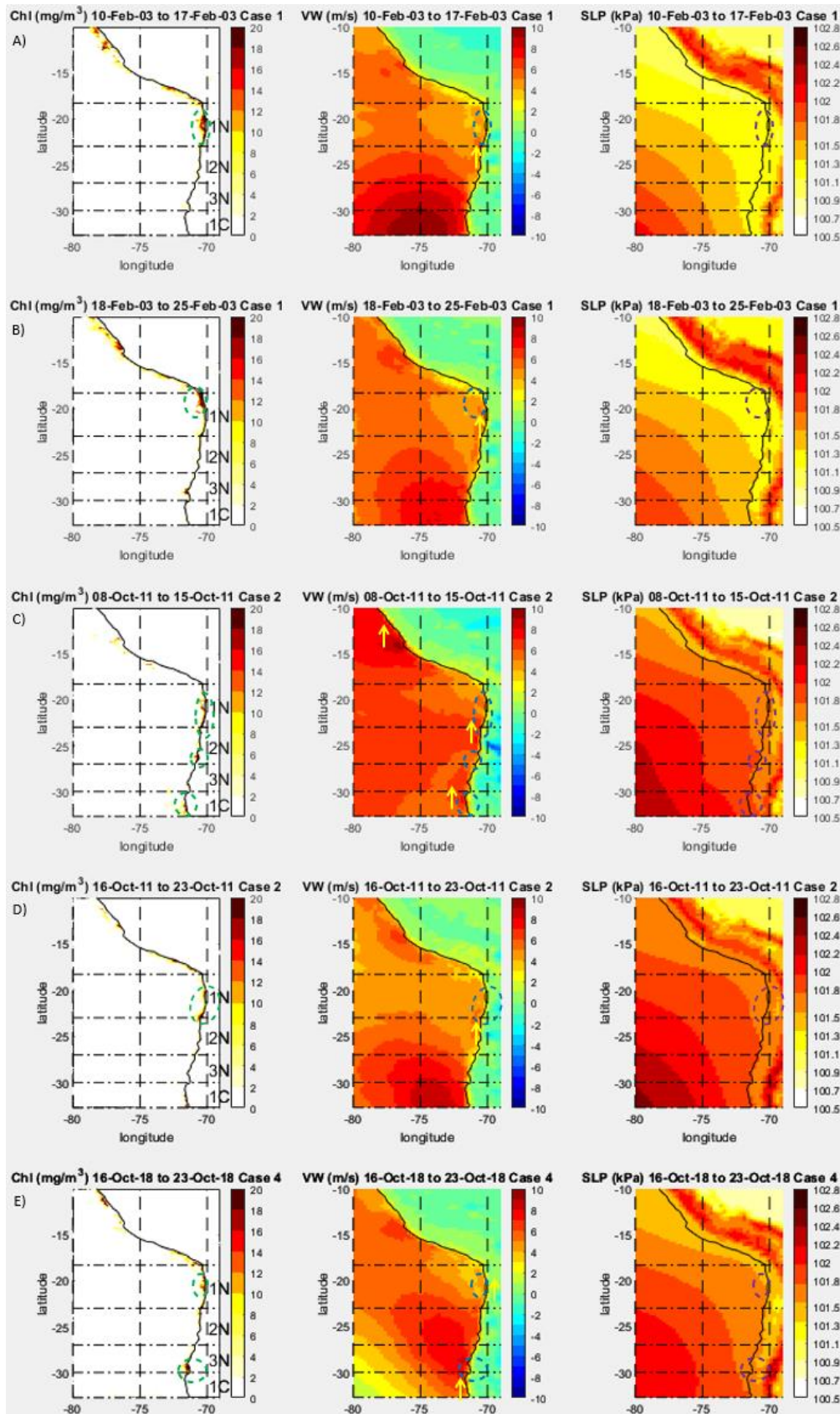
FIGURE 7.5. CASES 1,2, AND 4 CHL, VW, AND SLP PEAK WEEKS. THE DASHED CIRCLES HIGHLIGHT THE CHL INCREMENT LOCATION IN ALL THE VARIABLE PANELS. THIS HELPS TO IDENTIFY THAT VW WAS SLIGHTLY HIGHER. THE STRONGER VW, HIGHLIGHTED WITH A YELLOW ARROW, ARE LOCATED BELOW THE CHL IN ROWS A TO D. HOWEVER, THESE DIVERGENCES BETWEEN THE CHL LOCATION AND VW WERE MORE SIGNIFICANT IN ROWS B AND D, WHICH WERE WEEKS AFTER THE CHL PEAK. CASES 2 AND 4 (ROWS C-E) OCCURRED IN OCT WHEN THE SPSA'S CORE WAS STILL IN THE NORTH, WITH A HIGHER SPSA IN CASE 2. WHEREAS, IN CASE 1 (ROWS A-B), THE SPSA HAD MOVED TO THE CENTRAL ZONE (FIGURE 7.1), LEADING TO A LOWER SLP IN THE 1NT BUT STILL, WV OVER 4 M S-1 WAS SEEN. ALSO, ROWS A AND B SHOW A SIGNIFICANT CHL SIGNAL IN PERU, WHICH COULD HAVE INFLUENCED 1NT'S SIGNAL.
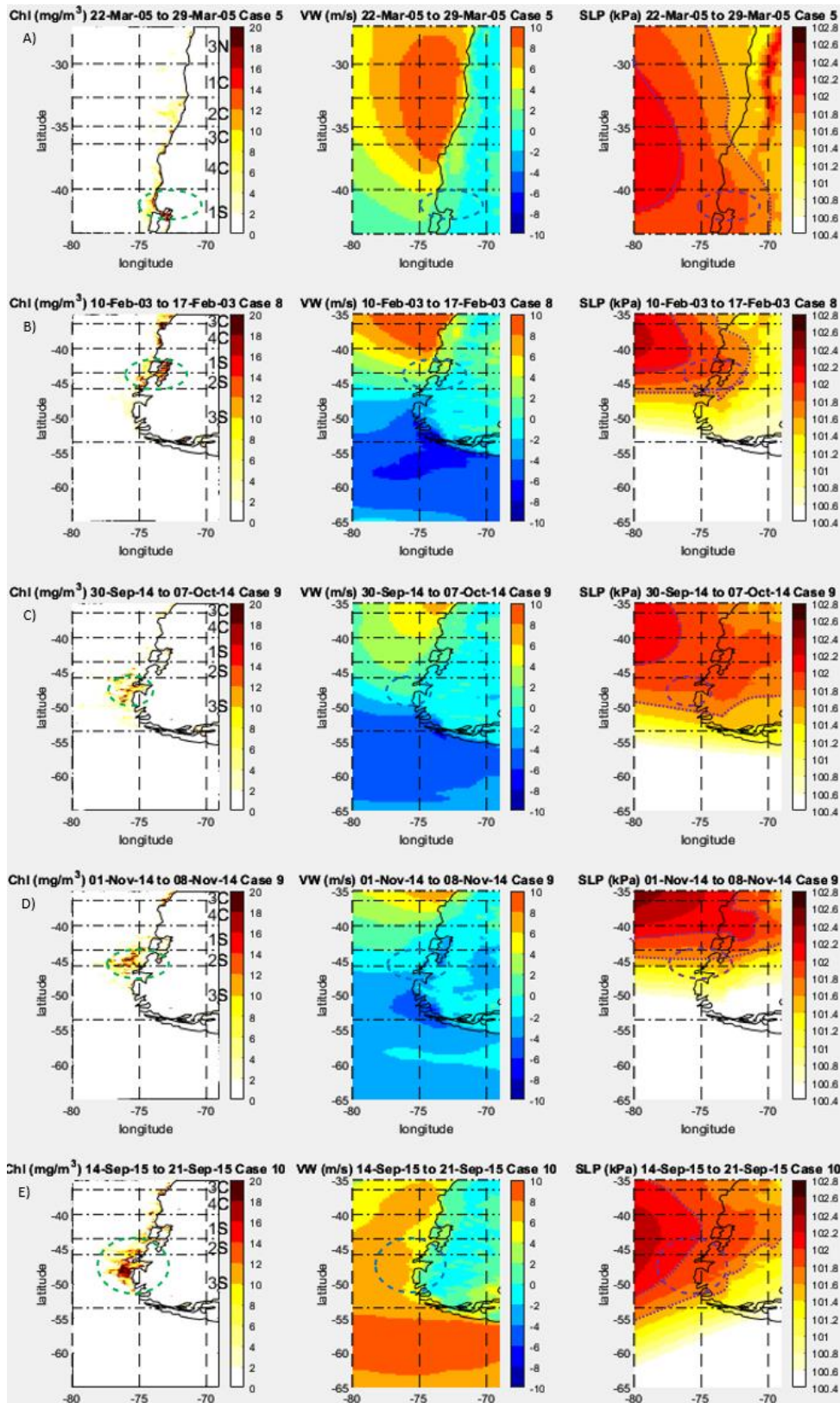
FIGURE 7.6. CASES 5, 8-10 CHL, VW, AND SLP CHL PEAK WEEKS. THE DASHED CIRCLES HIGHLIGHT THE CHL INCREMENT LOCATION IN ALL THE VARIABLE PANELS. THE DOTTED LINES SHOW THE SLP AT 101.6 AND 102 KPA. CASES 5 AND 8 WERE IN FEB WHEN THE SPSA IS IN ITS SOUTHERN LOCATION (FIGURE 7.1), WHICH EL NIÑO ENHANCED (0.45 & 0.74). THUS, THE SPSA WAS PUSHED SOUTHERN, WITH A HIGHER EFFECT IN CASE 8 (ROW B). CASES 9 AND 10 (ROWS C- E) WERE IN SEP-NOV WHEN THE SPSA IS MORE INTENSE AND EXPANDS TO THE SOUTH BUT WITH A PRESENCE IN THE NORTH (FIGURES 7.1 AND 7.5). ROW C SHOWS A WEAK SPSA CORE (-0.04) DRIVEN BY EL NIÑO (0.4), BUT SLP OVER 101.6 KPA REACHED 3S. ROW D SHOWS THE SAME BUT WITH A STRONG SPSA (1.21) AND ENSO (0.71). HERE, THE DOTTED LINE RETREATED TO 1S, LEADING TO WEAK NORTHERLY WINDS IN 2S AND 3S. STILL, A SIGNIFICANT CHL SIGNAL WAS SEEN IN 2ST. ROW E SHOWS A SPSA CORE DISPLACED TO 1ST DRIVEN BY STRONG EL NIÑO (2.32), LEADING TO STRONG SOUTHERLY WINDS AND A SIGNIFICANT CHL CONCENTRATION IN 3ST AND 2ST.

The Central Zone's first two cases (sections 6.3.2.1 and 6.3.2.2) were driven by a rapid SPSA intensification without the influence of ENSO or AAO. Both cases were in the summer when the highest radiation occurred, and the SPSA is located in the Central Zone (Figure 7.1). The last case (Case 7; section 6.3.2.3) was driven by the interaction between extreme pressure systems forming a subtropical cyclone near 3CT (Figure 6.25 and 6.26 in section 6.3.2.3; DMC, 2018). This expanded high Chl oceanwards from 4C to 3C and 2C. However, these conditions do not explain why the concentration was so high. A possible explanation is a red tide that occurred prior to this case near subsection 4CT (Sernapesca, 2018). Finally, these cases also showed a significant link between 4CT and 1ST, which was observed in O.1 Chl~Chl correlations with a rho of 0.45 (Figure 4.5). This link might be related to the split of the HCS bringing part of their nutrients southward by CHC. Also, the shelf from 3C is broader, reaching, on average, 40-70 km wide (Thiel et al., 2007; Marchant et al., 2007).

The Southern Zone cases exhibited a higher Chl signal, which mainly occurred in the warm season when the southerly winds were dominant, the solar radiation was higher, and the PR was low at the same time (Figure 7.6; Cases 5, 8-10 in sections 6.3.2.1, 6.3.3.1-6.3.3.3). These conditions were more marked when the SPSA was moved southwards by El Niño (Montecinos and Aceituno, 2003; Figure 7.2). Effectively, all these cases were in February or September to November, corroborating O.2 findings. However, they occurred with the ENSO index varying from 0.4 to 2.32, which means that even weak El Niño years were enough to produce this change (Figure 7.6). The Chl signal was even more marked when the positive AAO blocked the fronts coming from the Southern Ocean (Cases 5, 8 and 10; Figure 7.4). The low PR in this period has been more frequent in the late years due to AAO's positive tendency and the big drought that occurred from 2010 to 2018 (Aguayo et al., 2021). This drought has affected the river flows, particularly the Puelo River, which is the main tributary for the interior sea located in 1ST (De La Torre, 2016; Castillo et al., 2016; Castro, 2010). Consequently, more blooms have been seen there, as well as red tides. The last has been boosted by the number of fisheries located in the Southern Zone (Armijo et al., 2020; Sernapesca, 2018). Finally, the Southern Zone cases tended to expand more oceanwards than the other Zones and prevailed for several weeks after the longshore winds (Figure 7.6 rows c and d). This is probably because the Southern region contains intricate geography that helps to accumulate nutrients on the coast and produce upwelling eddies during the spring and summer (Thiel et al., 2007; Landaeta et al., 2011; Strub et al., 2019; Aracena et al., 2011). These nutrients, which come from AAIW, are generally trapped in the lower layer due to the fluxes of many rivers and melting glaciers in the Zone, reducing the surface salinity. Nevertheless, when the nutrients are already in the euphotic layer, the Chl signal extends oceanwards (Lara et al., 2010; Landaeta et al., 2011; Sievers and Silva, 2008).

Overall, these results showed that southerly winds are the key factor for these cases driven by the SPSA. Nonetheless, the SPSA location and intensity is heavily influenced by ENSO. Additionally, the AAO significantly influences the PR, especially in the Southern Zone. El Niño's influence in the Southern Zone is consistent with O.2 findings. Still, La Niña enhancing the SPSA for the Northern Zone and the positive AAO tendency to reduce the PR in the Southern Zone was more evident throughout these case studies, demonstrating that the AAO has a significant implication on the PR role and, therefore, the Chl signal. Finally, the subsections with a higher Chl response have a broad shelf and capes that sustain the nutrients in specific locations that correspond with O.1 findings.

7.3. Upwelling Importance.

One of the main conclusions throughout the three objectives is that upwelling is the main trigger to increase the nutrient concentrations and the Chl. However, this quantitive

relevance is unclear compared to other nutrient sources such as PR or rivers. This section tries to probe this, estimating an order of magnitude of upwelling, PR and main river nutrient addition per subsection. WS, ZET and Depth of the layer were computed using Eqs. 2.1 to 2.3 (Table 7.3). As the idea is to establish which variable is more relevant rather than accurate calculations, EP was not considered.

TABLE 7.3. SEASONAL AVERAGE MERIDIONAL WS (KG·M^{-1}·S^{-2}), ZET (M^2·S^{-1}) AND DEPTH OF THE EKMAN LAYER (M) FOR THE STUDY PERIOD (2002-2018).

WS	1NT	2NT	3NT	1CT	2CT	3CT	4CT	1ST	2ST	3ST
Summer	0.03	0.03	0.05	0.07	0.07	0.09	0.06	0.01	0.01	-0.02
Autumn	0.03	0.04	0.06	0.06	0.03	0.02	0.00	0.00	0.00	-0.01
Winter	0.02	0.05	0.08	0.07	0.03	0.02	0.00	0.00	-0.01	-0.01
Spring	0.02	0.04	0.08	0.10	0.08	0.08	0.04	0.01	0.00	-0.02
ZET	1NT	2NT	3NT	1CT	2CT	3CT	4CT	1ST	2ST	3ST
Summer	-0.49	-0.51	-0.72	-0.89	-0.80	-1.03	-0.68	-0.15	-0.07	0.16
Autumn	-0.49	-0.66	-0.82	-0.78	-0.37	-0.25	-0.05	0.02	0.04	0.09
Winter	-0.47	-0.83	-1.13	-0.96	-0.35	-0.20	-0.02	0.03	0.07	0.12
Spring	-0.46	-0.60	-1.10	-1.32	-0.94	-0.90	-0.38	-0.06	-0.01	0.15
Depth	1NT	2NT	3NT	1CT	2CT	3CT	4CT	1ST	2ST	3ST
Summer	7	7	9	10	9	11	8	5	5	7
Autumn	7	8	9	9	6	5	3	3	4	5
Winter	7	9	11	10	6	5	2	3	4	5
Spring	7	8	11	12	10	10	7	4	6	7

ZET negative values indicate upwelling, while positive values indicate downwelling. Considering this, the subsections with higher upwelling in the warm season are 3NT, 1CT and 3CT, but only 3CT has a broad shelf. As expected, the Southern Zone showed a downwelling tendency in the cold season, with 3ST showing downwelling the whole year. The Northern and Central Zones have an average depth of 9 m during the warm season, while this is 5 m in the Southern Zone.

The background nutrient concentrations were obtained from Garcia et al. (2010) in the World Atlas Ocean (2009). Figures 7.7 to 7.9 show the surface, 10 m and 100 m depth concentrations of NO_3^-, PO_4^{-2} and SiO_4^{-2} per season. Although the depth for the Southern Zone is 5 m, the closest depth measurement available is 10 m. Whereas 100 m represents the depth on the coastal edge (Marchant et al., 2007). The first observation about these nutrients is that they are very high in the extreme southern Zone (3ST) in surface and 10 m depths, likely related to how close the Antarctic waters are, with a higher concentration of NO_3^- and PO_4^{-2} during the winter and SiO_4^{-2} in the spring. In contrast, this was low during the summer. Also, the Peruvian Zone has a high nutrient concentration but not as high as 3ST. The nutrient concentrations at 100 m were higher in the Central Zone, followed by Northern Zone, while the Southern Zone was low.

In the summer, NO_3^- and PO_4^{-2} showed higher activity on the surface in the Central Zone. In spring, these were more significant in the Northern Zone. NO_3^- was more significant in 1CT and 4C-1ST. At 10 m of depth, the nutrient concentrations have similar values to the surface but in slightly different locations. For instance, NO_3^- was higher in 3NT-3CT, while PO_4^{-2} was from 2C-3CT during the summer. Meanwhile, NO_3^- was more significant in the Southern Zone in spring. This nutrient was still present in 3NT-3CT but at a lower level. Also, PO_4^{-2} reached a high concentration in 2NT and 3ST that season. For the 100 m depth, NO_3^- was intense from 3NT to 4CT during the warm season. The other two seasons, 1NT, 2CT and 3CT, exhibited higher concentrations. These subsections also exhibited a high PO_4^{-2} concentration during summer, autumn and spring. Winter only showed a high concentration in 1NT.
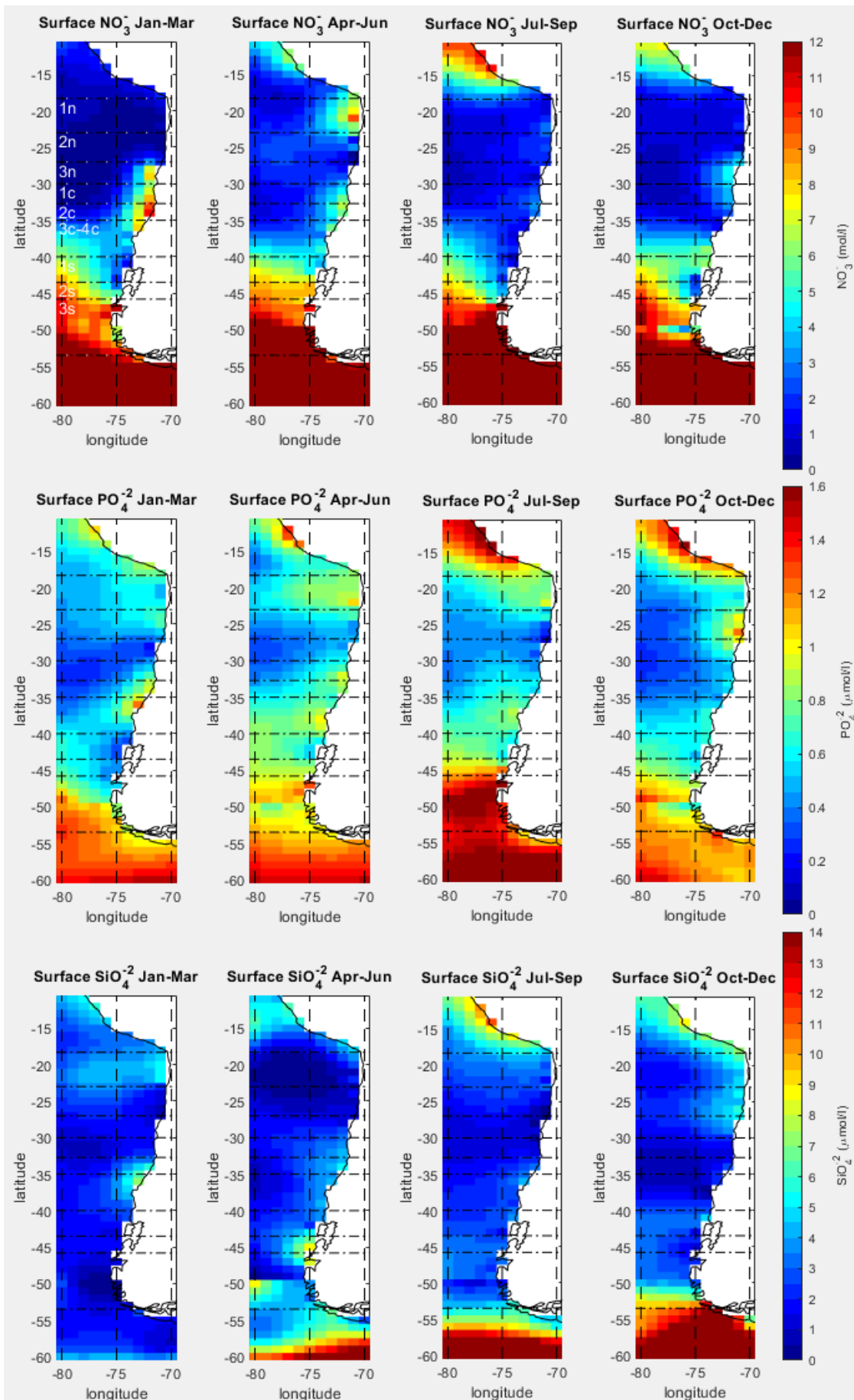
FIGURE 7.7. NO_3^- ($MOL·L^{-1}$), PO_4^{-2} ($\mu MOL·L^{-1}$), AND SiO_4^{-2} ($\mu MOL·L^{-1}$) SURFACE SEASONAL CONCENTRATIONS (GARCIA ET AL., 2010).
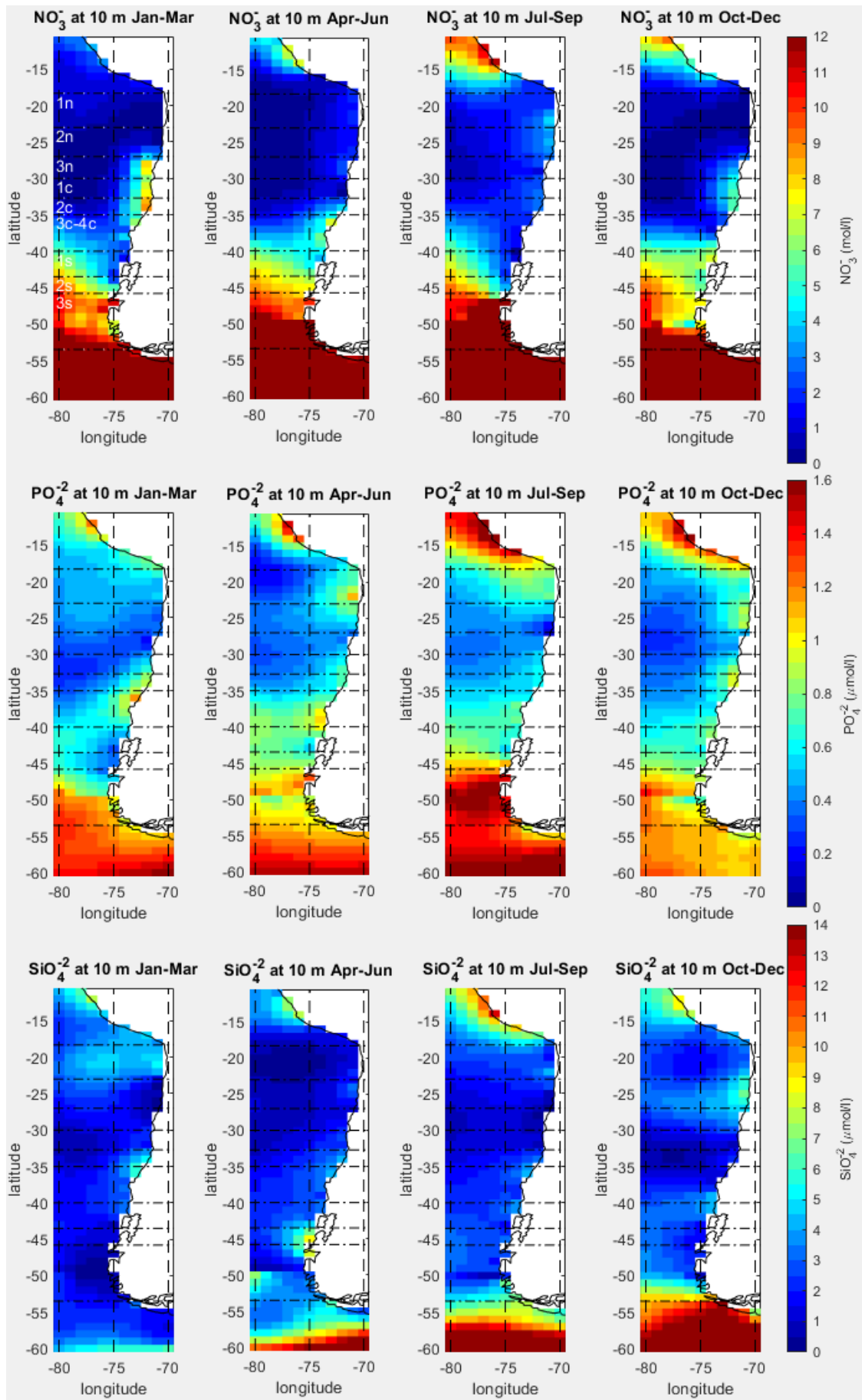
FIGURE 7.8. NO_3^- ($mol \cdot L^{-1}$), PO_4^{-2} ($\mu mol \cdot L^{-1}$), AND SiO_4^{-2} ($\mu mol \cdot L^{-1}$) SEASONAL CONCENTRATIONS AT 10 M OF DEPTH (GARCIA ET AL., 2010).
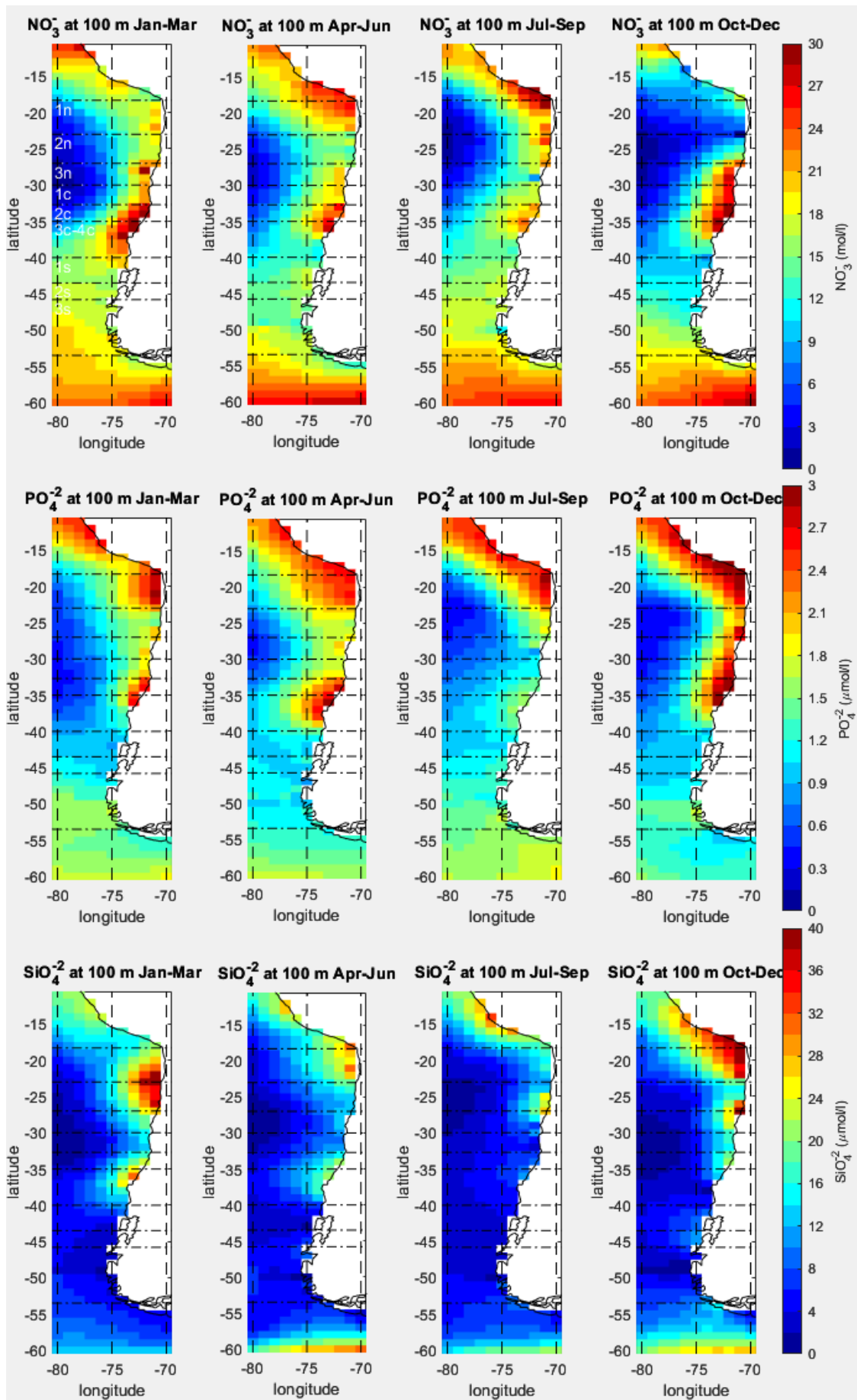
Figure 7.9. NO$_3^-$ (MOL·L^{-1}), PO$_4^{-2}$ (μMOL·L^{-1}), AND SIO$_4^{-2}$ (μMOL·L^{-1}) SEASONAL CONCENTRATIONS AT 100 M OF DEPTH (GARCIA ET AL., 2010).

Finally, surface and 10 m depth showed that SiO_4^{-2} exhibited a more prominent concentration in 1NT and 2CT-3CT during the summer. These similarities between both depths continued in spring, with the difference that SiO_4^{-2} was more significant in the Northern Zone and 1ST. The SiO_4^{-2} showed more consistency in the deeper layer, with a high concentration in the Northern Zone and 2CT-3CT, with a low concentration in the Southern Zone. The only exception was a low SiO_4^{-2} concentration in 2CT-3CT during the winter.

To determine the nutrient mass brought by upwelling in each subsection. The Average ZET was multiplied by coastal length and then by the average concentration of each nutrient (Table 7.4). This depth was chosen over 10 m because Vergara et al. (2017) indicate that 80-100 m is the typical depth of the upwelled water.

TABLE 7.4. THE AVERAGE ANNUAL NUTRIENT MASS FLUX PER SUBSECTION BROUGHT BY THE UPWELLING. FOR SIMPLICITY, ZET WAS MULTIPLIED BY-1. THUS, POSITIVE VALUES MEAN UPWELLING AND NEGATIVE DOWNWELLING.

Subsection	ZET m^2/s	Coast length m	NO_3^- 100m kg/m^3	PO_4^{-2} 100m kg/m^3	SiO_4^{-2} 100m kg/m^3	NO_3^- flux T/yr	PO_4^{-2} flux T/yr	SiO_4^{-2} flux T/yr
1NT	0.47	5.5E+05	1023	2.6E-04	2.5E-03	8.4E+12	2.1E+06	2.0E+07
2NT	0.65	4.9E+05	845	1.6E-04	2.0E-03	8.5E+12	1.6E+06	2.0E+07
3NT	0.94	3.8E+05	1279	1.7E-04	1.6E-03	1.4E+13	1.9E+06	1.8E+07
1CT	0.99	3.5E+05	1256	1.7E-04	1.2E-03	1.4E+13	1.9E+06	1.3E+07
2CT	0.61	3.1E+05	1550	2.4E-04	1.6E-03	9.2E+12	1.4E+06	9.3E+06
3CT	0.60	1.9E+05	1651	2.5E-04	1.6E-03	6.0E+12	9.0E+05	5.7E+06
4CT	0.28	5.1E+05	891	1.5E-04	1.1E-03	4.1E+12	6.9E+05	4.8E+06
1ST	0.04	5.2E+05	984	1.1E-04	4.6E-04	6.4E+11	7.0E+04	3.0E+05
2ST	-0.005	3.6E+05						
3ST	-0.13	1.3E+06						

The PR nutrient addition was computed based on the concentration reported by Baker et al. (2010) in the South Atlantic Ocean, which are approximately 2.8-3.5 nmol m^{-3}, 3.7-6.4 nmol m^{-3} and 12.4-14.6 pmol m^{-3} for NO_3^-, NH_4^+ and PO_4^{-2}, depending on the PR intensity. The NH_4^+ was not used and the SiO_4^{-2} is neglectable in the PR, so only NO_3^- and PO_4^{-2} were considered. These concentrations were multiplied by the annual PR per subsection and by the ocean area considering 100 km of width to obtain the nutrient mass (Table 7.5), which is the same value used to define each subsection (Table 3.3).

TABLE 7.5. THE AVERAGE ANNUAL NUTRIENT MASS FLUX PER SUBSECTION BROUGHT BY THE PR.

Subsection	PR m/yr	Coast length m	PR m^3/yr	NO_3^- flux T/yr	PO_4^{-2} flux T/yr
1NT	0.03	5.5E+05	1.6E+09	2.8E-04	1.9E-06
2NT	0.03	4.9E+05	1.7E+09	3.0E-04	2.0E-06
3NT	0.04	3.8E+05	1.6E+09	2.8E-04	1.9E-06
1CT	0.14	3.5E+05	4.8E+09	8.3E-04	5.6E-06
2CT	0.40	3.1E+05	1.2E+10	2.1E-03	1.4E-05
3CT	0.68	1.9E+05	1.3E+10	2.6E-03	1.7E-05
4CT	1.05	5.1E+05	5.4E+10	1.2E-02	7.4E-05
1ST	1.30	5.2E+05	6.8E+10	1.5E-02	9.4E-05
2ST	1.49	3.6E+05	5.4E+10	1.2E-02	7.5E-05
3ST	1.01	1.3E+06	1.3E+11	2.9E-02	1.9E-04

The rivers in the Central Zone add 0.16-169 and 0.05-10.3·10^6 nmol m^{-3} NO_3^- and PO_4^{-2}, becoming significant (Masotti et al., 2018). The Southern rivers bring low NO_3^- and PO_4^{-2} concentrations on average to the ocean (0.0015 and 0.00011·mol m^{-3}) with low variations per season, while SiO_4^{-2} varies from 40 to 150 10^6 nmol m^{-3} (Castro, 2010; De La Torre, 2016). The nutrient discharge for the main rivers in the Central Zone was studied by Masotti et al. (2018), showing that the highest flux occurs during the winter and the river with a higher nutrient contribution is Biobio (Table 7.6). The nutrients discharged by the main Southern Zone rivers (Table 7.7) were computed based on the averaged fluxed during the study period (CR2,2018). Then, they were multiplied by the typical nutrient concentrations reported by

Castro (2010). Tables 7.6 and 7.7 show the nutrient addition per subsection. As SiO_4^{-2} was not computed by Masotti et al. (2018), it was not calculated by the southern rivers either.

TABLE 7.6. AVERAGE ANNUAL NUTRIENTS ADDED BY THE MAIN RIVERS IN THE CENTRAL ZONE COMPELLED PER SUBSECTION (MASOTTI ET AL., 2018).

Subsection	Rivers	NO_3^- winter T/mnth	NO_3^- rest T/mnth	Total NO_3^- flux T/yr	PO_4^{-2} winter T/mnth	PO_4^{-2} rest T/mnth	Total PO_4^{-2} flux T/yr
2CT	Maipo	160	80	1293	12	4	93
	Mataquito	16	5		4	1	
3CT	Maule	40	16	264	12	4	72
4CT	Itata	120	10	2625	6	2	347
	Biobio	245	160		45	20	

TABLE 7.7. AVERAGE ANNUAL NUTRIENTS ADDED BY THE MAIN RIVERS IN THE SOUTHERN ZONE COMPELLED PER SUBSECTION.

Subsection	Rivers	Flux m^3/s	Flux m^3/yr	NO_3^- T/yr	PO_4^{-2} T/yr	Total NO_3^- T/yr	Total PO_4^{-2} T/yr
1ST	Puelo	615	1.9E+10	1804	203	3129	352
	Yelcho	452	1.4E+10	1326	149		
2ST	Palena	782	2.5E+10	2293	258	4452	500
	Cisnes	214	6.8E+09	628	71		
	Aysén	522	1.7E+10	1531	172		
3ST	Baker	870	2.7E+10	2552	287	4235	476
	Pascua	574	1.8E+10	1683	189		

These results show the small effect rivers and precipitation have in the nutrient addition compared to the upwelling. The upwelling was more significant in the Northern Zone, followed by the Central Zone. Even though 1ST has a low upwelling, this is enough to bring a considerable amount of nutrients to the surface. The other two southern subsections have a downwelling tendency (Table 7.5), so they were not estimated.

The low nutrients added by rivers and precipitation is consistent with Vergara et al. (2017) and Gómez et al. (2017) findings. Furthermore, river flux and precipitation reach their maximum in the Central Zone during winter when the phytoplankton response goes down. Although the nutrient addition by rivers is higher in the Southern Zone (Table 7.7), with a higher flux during the warm season, studies have mentioned that they generate more stratification reducing the phytoplankton response (Landaeta et al., 2011; Aracena et al., 2011; De La Torre, 2016). This is even more evident considering the background nutrient on the surface were significant (Figure 7.7). Effectively Case studies and authors like Aguayo et al. (2020) have reported that the big drought (2010-2018) reduced the PR and river fluxes in the south with a generally positive effect on phytoplankton.

Scatterplots were plotted to go further with this analysis, checking the possible relationship between nutrients and the PR or the upwelling measured by WS. In this section, only NO_3^- are shown (Figures 7.10 and 7.11). PO_4^{-2} and SiO_4^{-2} plots are shown in A.4. These figures showed that NO_3^- and PO_4^{-2} have a higher concentration during the summer and spring when WS is more intense, and the PR, along with river fluxes, are lower due to the SPSA. This tendency was slightly different for SiO_4^{-2}, becoming only clear in 3CT and 4CT. 1NT-2NT and 2ST presented a higher concentration in these components during autumn. Although 3ST did not show a clear tendency in the NO_3^-, it did in PO_4^{-2} with a higher concentration during the winter. 2ST showed a slight positive relationship with the PR with the three nutrients (Figures 7.10, A.4.1 A.4.3), but it is not clear enough. Also, 2NT and 3NT experienced a slightly positive relationship, more marked in 3NT, with PO_4^{-2} and SiO_4^{-2} against WS both higher in Spring (Figure A.4.2, A.4.4).
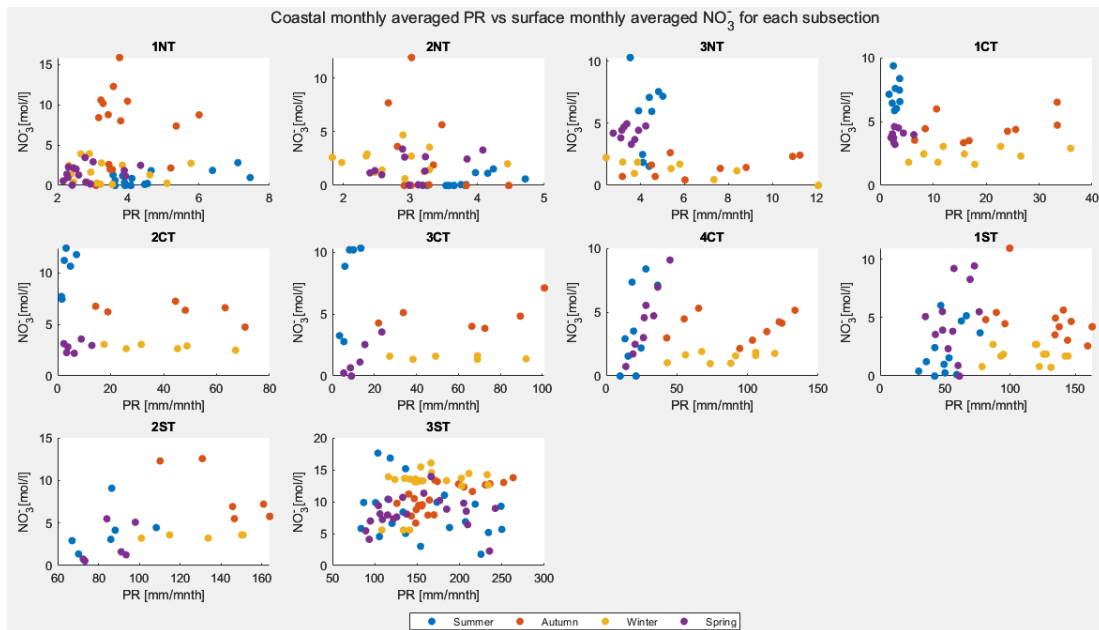
FIGURE 7.10. COASTAL MONTHLY AVERAGED PR VS SURFACE MONTHLY AVERAGED NO₃⁻ FOR EACH SUBSECTION WITH 1° DEGREE RESOLUTION. THE MONTHLY DATA ARE COLOURED BY SEASON.
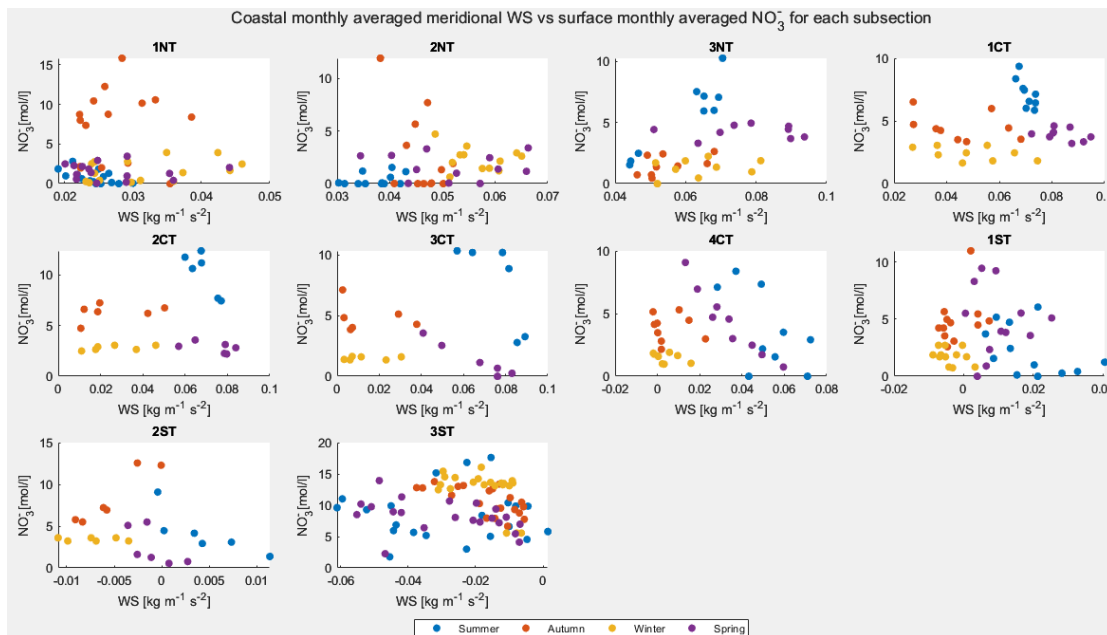
FIGURE 7.11. COASTAL MONTHLY AVERAGED WS VS SURFACE MONTHLY AVERAGED NO₃⁻ FOR EACH SUBSECTION WITH 1° DEGREE RESOLUTION. THE MONTHLY DATA ARE COLOURED BY SEASON.

In conclusion, this analysis contributes to determining that the upwelling in the Central Zone is the predominant factor in obtaining these nutrients in the surface layer. Although the first analysis showed that the upwelling has a significant role in nutrient addition in the Northern Zone, this was not clear in the scatterplots, possibly related to the narrow shelf here. In any case, this helped to reject the initial hypothesis that the PR had a more significant role in adding nutrients in the Northern and Central Zones. Moreover, it can be inferred by the background nutrient maps that the Southern Zone has a high nutrient concentration that does not require upwelling, especially 3ST. Meanwhile, the Peruvian Zone also had a significant nutrient concentration that supports previous arguments. Finally, this study must be done in more detail to include the oceanographic features.

7.4. Final Overview.

The three Objectives confirm the importance of southerly winds for the Chl concentration. These results are complemented with other oceanographic variables not studied in detail in this project, such as the shelf width and the currents driven by HCS but mentioned in chapter 3. The wind is driven by the SPSA presence or absence, creating a high-pressure system in 2NT to 1ST from January to March and 1NT to 2CT from June to August (Figures 7.1 & 7.12). As a result, low-pressure systems arrive in the Southern Zone the whole year and in the Central Zone in the winter, leading to high PR when the low systems are present in these Zones (Ancapichun and Garcés, 2015; Rahn, 2012; Aguirre et al., 2021). Concerning the topography, the shelf presents a significant increment at 3C that continues until the end of Chile (Marchant et al., 2007).

Effectively, O.1 reveals a high Chl signal from 3CT to 1ST, where a bigger shelf and the SPSA are present, leading to a better remineralisation process and more upwelling, respectively (Figure 7.12; Thiel et al., 2007). However, it also showed a significant Chl signal in 2ST, while 3ST and 1NT were slightly lower but significant. This is interesting because 2ST and 3ST had mainly westerly and northerly winds, while 1NT had an average PR lower than 3 mm mth^{-1} and low but constant southerly winds present the whole year with a speed of 3.9 m s^{-1} on average. Also, 1NT had low Chl correlations with all the physical variables, especially with VW (0.07).

The O.2 indicated that ENSO and AAO alter the typical southerly wind and PR patterns. El Niño increased the southerly winds in the Southern Zone in the warm season, leading to a Chl increase (Figure 7.12; Ancapichun and Garcés, 2015; Montecinos and Aceituno, 2003). Meanwhile, the negative AAO increased the PR patterns significantly in the three Zones, with a slightly higher impact in the Central Zone but with uncertain variations in the Chl (DMC, 2018). These results reveal that 2ST and 3ST had southerly winds during significant El Niño episodes increasing their Chl signal rapidly, partially explaining why these subsections had a higher Chl concentration. On the other hand, the climate drivers did not affect the 1NT's Chl signal despite the winds and SST variations. However, this is consistent with O.1 findings.

The case studies in O.3 were helpful in determining the mechanisms that increased the Chl in these subsections that were not clear in the previous objectives. 1NT cases (Figure 7.5 or Cases 1, 2 and 4 in sections 6.3.1.1, 6.3.1.2 and 6.3.1.4) were associated with ephemeral southerly wind speeds over 4 m s^{-1} driven by the SPSA return to normality after El Niño episodes or due to reinforcement by La Niña (Figure 7.11). Furthermore, these cases occurred from September to December and February to March, which are the spring and summer peaks, but also the first period is when the SPSA increases its intensity and is located in the Northern Zone (Figure 7.1 and Figure 7.5 rows c to e). Indeed this Chl increment pattern was observed in the three Northern's subsections. Also, 1NT Chl tended to increase when its surroundings had higher Chl concentration, predominantly northwards, in Peru, which brings nutrients to 1NT by the poleward ESSW (Figure 7.5 rows a to b; Figure 7.11; Thiel et al., 2007). Moreover, 1NT was able to keep a Chl activity for a few weeks after the longshore winds returned to normality or even when southerly winds were in a slightly different place, which explains why the Chl correlations with VW were low in O.1. This is presumably because the nutrient concentration is enough to maintain the phytoplankton activity for a longer time or the predators are not capable of reducing their activity as quickly (Thiel et al., 2007). Previous authors have not reported these findings due to the lack of studies in this Zone.
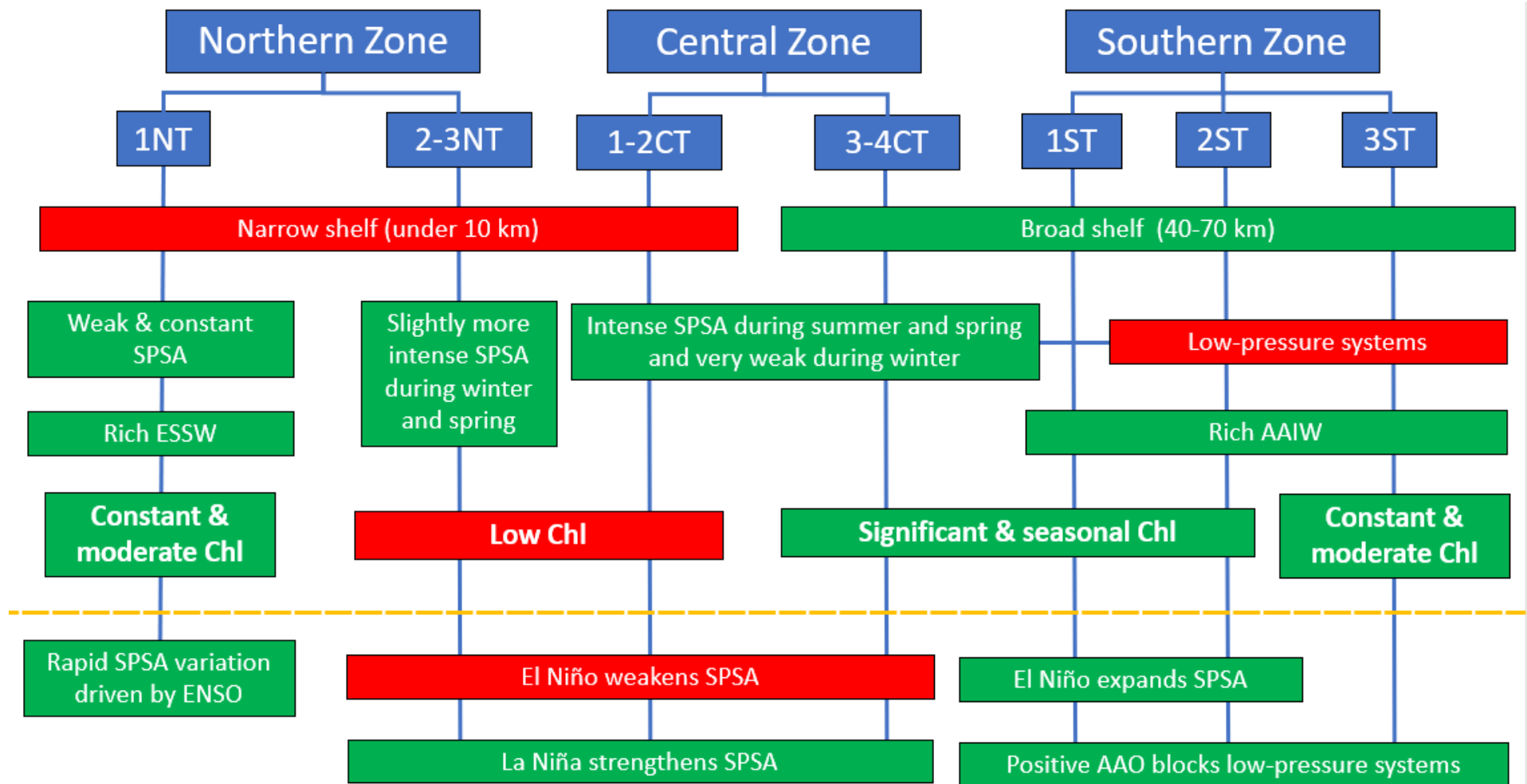
FIGURE 7.12 DIAGRAM WITH THE MAIN FINDINGS THROUGHOUT THIS THESIS, WHERE THE FACTORS THAT ENHANCE THE PHYTOPLANKTON PER SUBSECTION ARE IN GREEN SQUARES WHILE THE RED ONES ARE NEGATIVE. THE DASHED LINE MARKS THE CLIMATE DRIVERS' EFFECTS THAT ARE NOT PRESENT CONSTANTLY. THE UPWELLING IS DRIVEN BY THE SPSA, PROVOKING LONGSHORE WINDS, WHEREAS LOW-PRESSURE SYSTEMS INCREASE THE PR, LEADING TO STRATIFICATION IN THE SOUTHERN ZONE. A BROAD SHELF CONTRIBUTES TO A BETTER MINERALISATION PROCESS, WHILE THE OPPOSITE EFFECT IS SEEN IN NARROW SHELVES.

The Southern Zone cases (Cases 5, 8-10 in sections 6.3.2.1, 6.3.3.1-6.3.3.3) confirmed O.2 findings of the El Niño moving the SPSA to the south in the warm season. Effectively, all the cases were from September to November and February during weak to strong El Niño years (0.4-2.32), with mainly positive AAO blocking the fronts from the Southern Ocean. In all these cases, the Chl signal appeared after positive SLP anomalies in the Southern Zone that increased the southerly winds but also reduced the westerly winds and PR events (Figure 7.6). Although the SLP anomalies were higher than O.2 observations reaching 3ST, they were temporary (Figure 7.6 rows c to e). Thus, the southerly winds did not stay longer, but the Chl signal could prevail for several weeks. Masotti et al. (2018) mentioned the importance of river inflow to the Chl concentration from 3CT to 4CT by adding NO_3^- and PO_4^{-2}, while Vergara et al. (2017) stated this contribution is not significant in comparison to the upwelling. However, section 7.3 showed that rivers do not contribute to a significant nutrient concentration. Additionally, the mentioned cases have shown the lack of rains reduced the river fluxes and consequently the stratification, particularly from the Puelo River, which is the main tributary for the interior sea located in 1ST (Castillo et al., 2016; Castro, 2010; De La Torre, 2016; Landaeta et al., 2011; Lara et al., 2010). Therefore, more blooms have been seen there and red tides (Armijo et al., 2020; Sernapesca, 2018). This Chl relation with lower PR events have also been reported in 2S and 3S, indicating that the nutrients are coming from the AAIW that in the Southern Zone has more nutrients and is at 150 m depth due to its topography (Figures 3.6 and 7.10; Aracena et al., 2011; Sievers and Silva, 2008). Therefore, the phytoplankton signal has been increasing in this Zone owing to the AAO positive tendency and the big drought (2010-2018; Aguayo et al., 2020). This is also consistent with the background nutrients observed in 7.3, which are high in this Zone, particularly in 3ST.

Overall, this thesis has demonstrated the importance of shelf width and southerly winds driven by the presence or absence of the SPSA in ocean fertilisation, increasing the phytoplankton. Thus, the most productive region is from 3CT to 1ST, owing to both variables being present. Although 1ST and 2ST typically exhibited westerly winds and excessive PR that reduced the phytoplankton proliferation, these are significantly reduced when the SPSA is pushed southwards by Niño, leading to higher longshore winds and lower westerly winds and PR events. This is even more marked when the positive AAO blocks cold fronts from the Southern Ocean. On the other hand, 1NT and 3ST also have a significant Chl activity associated with the undercurrent ESSW and AAIW, respectively, which in those subsections have a higher nutrient concentration and upper location. ESSW rapidly comes to the surface when short longshore wind increases, driven by the SPSA return to the north. This is exacerbated when La Niña alters the SPSA. The resulting wind variations elevate the Chl for a few weeks. Meanwhile, AAIW does the same when the PR is reduced and by eddies that occur by submarine constrictions that produce upwelling during the spring. This has been a tendency in late years driven by the more positive AAO and the big drought in the Southern and Central zones. In any case, the background nutrients showed that the surface and 10 m depth waters in 3ST are rich in NO_3^- and PO_4^{-2} (Figures 7.5 and 7.6).

7.5. Limitations and further investigation lines.

7.5.1.   Comparison between selected techniques.

Correlations were used in the first objective because this technique enables an overview of relationships between variables with such an extensive dataset, establishing the strength and direction of relationships that will serve as a good starting point. On the other side, this technique must be used cautiously to avoid false assumptions because it does not prove causation. Therefore, adequate research on the physical implications of these variables is required to determine the correct hypothesis (Trauth, 2021). Due to their simplicity,

correlations have been extensively used in different fields to have a general idea in the early stages of work and are often used in meteorological and oceanographic studies as a first approach (Trauth, 2021). Examples of these are Hauke and Kossorwski (2011), Xiao et al. (2016), Rahn et al. (2012), Linsley et al. (2015) and Montecinos and Aceituno (2003).

The harmonic analysis is also a well-used procedure to study time series such as the wind or the Chl, decomposing it by the Fourier transform. This way, a particular frequency and amplitude can be studied (Trauth, 2021). Even though this technique is a powerful tool for establishing patterns and eliminating noise, correlations were chosen to determine general ideas. Additionally, the composites in objective 2 gave similar results, determining patterns built using EOFs and CCA. The EOF is one of the most used methods in this field (von Storch and Zwiers, 1999), while in all the papers consulted, only Corredor-Acosta et al. (2015) used the wavelet power that shares similarities with harmonic analysis. However, this method is often used in other areas that have data with extensive timelines, such as paleoceanography, which determines the pattern of climate drivers (Truth, 2021).

Effectively, climate drivers are often studied using that type of decomposition, but this objective aimed to study how the Chl is affected by these drivers. The method used to obtain the missing Chl data in a period of time using another variable as reference was the CCA because there are not many techniques capable of doing that. Maximum Covariance Analysis is similar, but the maximum correlation is prioritised over the maximum covariance. Taylor (2012) compared both with similar results but slightly better for CCA.

Although the CCA presented significant uncertainties with a MAE from 0.63 to 0.85 for a variable whose coastal values generally did not exceed ±2, the general tendency of these results was acceptable, considering the complexity and high variation that Chl has onshore. The error was minimised using actual and predicted data in the Chl composite construction, except for the +AAO. Effectively, the patterns obtained by ENSO composites were coherent with the relations observed in the other chapters.

Hence, the CCA result could have been improved by adding a second independent variable and using the SeaWiFS data. Shollaert UZ et al. (2017) worked considering these modifications, having a slightly better prediction. These were not made in this work owing to the fact that both SeaWiFS and MODIS-Aqua data were available only individually. Although they could have been fused by hand, this procedure was complex because they have different time and space scales, requiring a significant effort. Meanwhile, the CCA code could not have more than one predictand without modifications. Furthermore, grid data that contains the depth of the Chilean ocean in great detail is not easy to obtain.

Even though the composite construction showed coherent results to determine general tendencies for the climate drivers, the AAO result has higher uncertainties due to its higher variation, and it was built by predicted Chl data. This could have been partially addressed using seasonal composites, but it was preferred to keep the same construction as the ENSO composite. Thus, they can be comparable in this way.

Overall, studies using methods with Fourier transformation will give extra information that could have been useful. Nonetheless, considering that the timescale was short and the study area was enormous, a more straightforward technique was initially selected to explore the data, which was later complemented with the study cases. The prime objective of the climate drivers analysis was to obtain the missing Chl data, giving only general tendencies. In any case, this method could have been more accurate, using the considerations mentioned before.

7.5.2. Modelling approach and limitations.

The next step for this research is applying models to understand the processes more thoroughly. Especially the ocean mechanics, as the upwelling, the currents directions and the shelf size have been key elements in the discussion. In general, two models are needed: Firstly, a biochemical model to determine the chemical reactions and how this influences the phytoplankton, such as NEMURO (North Pacific Ecosystem Model for Understanding Regional Oceanography), and PISCES (Pelagic Interactive Scheme for Carbon and Ecosystem Studies), used by Gómez et al. (2017) and Vergara et al. (2017). Secondly, there is a need for an oceanic model to understand the current movements and their physical changes. Examples of these are Nucleus for European Modelling of the Ocean (NEMO) used by Armijo et al. (2020) and Simple Ocean Data Assimilation (SODA), Regional Ocean Model System Adaptive Grid Refinement in Fortran (ROMS) by Gómez et al. (2017), Vergara et al. (2017), Echevin et al. (2014) and Mogollón and Calil (2017). The interaction between both models defines how the nutrients spread and, consequently, the phytoplankton change through time and space (Vergara et al., 2017; Gómez et al., 2017).

The application of these models is complex due to the extensive and different geography that Chile has. Thus, they must be used for particular situations similar to the Case Studies. Although Armijo (2020), Gómez et al. (2017) and Vergara et al. (2017) have used these models in Chile, all of them were in 3C to 1S, and only the last two authors used a biochemical model. The reason for that is the scarcity of reliable data to feed this type of model. Effectively, Station 18 (37.5°S), located eighteen nautical miles from the coast near the Itata River in 4C, is the only place where the nutrients are constantly measured (Figure 3.4; Masotti et al., 2018). This data was used by Vergara et al. (2017), Gómez et al. (2017) and Masotti et al. (2018). However, Gómez et al. (2017) complemented this information with data from OFES (Ocean general circulation model For the Earth Simulator), but this model only had data until 2006. Authors such as Iriarte et al. (2012) and Buschmann et al. (2016) have taken a few samples off Chiloé Island, but these were for one campaign. Another factor is the difficulty in estimating the anthropogenic effect because the relevant mining and fishing companies do not characterise their outflows to the ocean, or at least these are not public.

After the phytoplankton modelling, the following step will be to study the predatory interaction that leads to the fish stock movement, including the zooplankton. Gómez et al. (2012) studied initial relationships in Chile between the Chl and the sardine recruitment in the Central Zone. Such a study has been done in the Northern Hemisphere, such as Norway, where the nutrient data has been studied and modelled in great detail, including fisheries pollution. This allowed the application of models that can estimate different species at the trophic level (Hansen et al.,2021). Therefore, this modelling will require even more information that is not available in Chile.

Thus, the modelling process is limited by the lack of information. In fact, Gómez et al. (2017) and Vergara et al. (2017) downplayed the river effect and anthropic activity. They also calculated the nutrients based on Station 18 alone. Furthermore, these data even would have helped the case studies analysis, establishing better the human impact on them and why the Chl activity increased by nutrient analysis. Finally, such models require a significant amount of time to master their features, especially when the expertise in coding languages like Fortran or python is inadequate.

7.5.3. Other investigation lines.

The two extra cases added (Cases 3 and 11 in sections 6.3.1.3 and 6.3.3.4) are possible investigation lines due to their complexity, and both would benefit if nutrient data were available in these locations. Case 11 showed the massive impact that red tide events have

had in the Southern Zone in recent years due to the extensive fisheries industries increasing the nutrients coupled with the global warming that had reduced the PR events (Armijo et al., 2020; DMC, 2018). Thus, further investigation must be done in this area. However, the Chl data does not help identify these particular events, and the lack of samples makes this process difficult (Armijo et al., 2020). Since that incident, Sernapesca (2018) has increased the samples during El Niño summer and the fisheries farms' oxygen levels. Still, companies had altered their outflow data, harming the coast (Molinari, 2021). Therefore, a possible investigation line will be studied to modify the Chl algorithm (Eq. 3.1), giving it a higher weight to the red band (Table 3.1 in section 3.2.1). Algorithm modifications have been tested by different authors, such as Yang et al. (2018), who proposed some modifications to reduce the error in Chl measurements in turbid waters.

Case 3 (section 6.3.1.3) did not show the expected Chl significant increase after its dust storm. Although other studies have mentioned that the Chl response is rapid and short-lived in these events, low Chl activity is seen when the dust deposits are dry and the local ocean does not have enough NO_3^- (Ridame et al., 2014). This could explain the Chl response in 2N and 3N but not in 1N. Also, it is feasible that the Chl reacted but was undetected due to the heavy cloudiness. Therefore, more studies must be done, especially considering that local newspapers reported similar events with lower intensity between June to September in 2015, 2016, 2018, 2019 and 2020 (24-Horas 2015; Chilevision, 2018; Araya, 2020). Similar to the red tide events, in-situ samples will help clarify the nutrient level in the Northern Zone.

Finally, the coastal lows that appeared briefly in Case 4 (section 6.3.1.4) are significant meteorological phenomena in the Northern and Central Zone (section 3.1.2). However, occasionally they lead to rapid southerly coastal low-level jets over 10 m s^{-1} in the Central Zone with more frequency in the spring-summer (Garreaud et al., 2002; Aguirre et al., 2021; Garreaud and Muñoz., 2005). These episodes need further investigation because their frequency has increased in the last decade due to SPSA intensification (Aguirre et al., 2021; Garreaud and Muñoz., 2005), and they could significantly impact the phytoplankton either positively or negatively.

References.

24-Horas. (2015). Impresionante tormenta de arena en Antofagasta. TVN. https://www.24horas.cl/nacional/video-captura-impresionante-tormenta-de-arena-en-antofagasta-1761186

Aceituno, P., Quintana, J., Ramírez, M., & Fuenzalida, H. (2015). Boletines Meteorológicos (2003, 2005, 2011, 2012, 2014). Boletín Climático Departamento de Geofísica de la Universidad de Chile. http://met.dgf.uchile.cl/clima/HTML/BOL_ANT/anterior.htm

Aguayo, R., León-Muñoz, J., Garreaud, R., & Montecinos, A. (2021). Hydrological droughts in the southern Andes (40–45°S) from an ensemble experiment using CMIP5 and CMIP6 models. Sci Rep, 11(1), 5530-5516. https://doi.org/10.1038/s41598-021-84807-4

Aguirre, C., Flores-Aqueveque, V., Vilches, P., Vásquez, A., Rutllant, J. A., & Garreaud, R. (2021). Recent changes in the low-level jet along the subtropical west coast of South America. Atmosphere, 12(4), 465. https://doi.org/10.3390/atmos12040465

Amaya, D. J., & Foltz, G. R. (2014). Impacts of canonical and Modoki El Niño on tropical Atlantic SST. J. Geophys. Res. Oceans, 119(2), 777-789. https://doi.org/10.1002/2013JC009476

Ancapichun, S. (2012). *Variabilidad del Anticiclón del Pacífico sur y su relación con la Oscilación Decadal de Pacífico: Implicancias oceanográficas a lo largo de la costa centro-norte de Chile* [Universidad Austral de Chile].

Ancapichun, S., & Garcés-Vargas, J. (2015). Variability of the Southeast Pacific Subtropical Anticyclone and its impact on sea surface temperature off north-central Chile. Ciencias marinas, 41(1), 1-20. https://doi.org/10.7773/cm.v41i1.2338

Araya, L. (2020). Gran parte de la Región de Antofagasta sufrió estragos por la fuerte tormenta de arena y viento. Diario Antofagasta 6 Junio.2020 https://www.diarioantofagasta.cl/regional/119868/

Aracena, C., Lange, C. B., Luis Iriarte, J., Rebolledo, L., & Pantoja, S. (2011). Latitudinal patterns of export production recorded in surface sediments of the Chilean Patagonian fjords (41–55°S) as a response to water column productivity. *Continental shelf research*, *31*(3), 340-355. https://doi.org/10.1016/j.csr.2010.08.008

Aravena, J. C., & Luckman, B. H. (2009). Spatio-temporal rainfall patterns in Southern South America. *International journal of climatology*, *29*(14), 2106-2120. https://doi.org/10.1002/joc.1761

Armijo, J., Oerder, V., Auger, P.-A., Bravo, A., & Molina, E. (2020). The 2016 red tide crisis in southern Chile: Possible influence of the mass oceanic dumping of dead salmons. Mar Pollut Bull, 150, 110603-110603. https://doi.org/10.1016/j.marpolbul.2019.110603

Ashok, K., Behera, S. K., Rao, S. A., Weng, H., & Yamagata, T. (2007). El Niño Modoki and its possible teleconnection. J. Geophys. Res, 112(C11), C11007-n/a. https://doi.org/10.1029/2006JC003798

Baker, A. R., Lesworth, T., Adams, C., Jickells, T. D., & Ganzeveld, L. (2010). Estimation of atmospheric nutrient inputs to the Atlantic Ocean from 50°N to 50°S based on large-scale

field sampling: Fixed nitrogen and dry deposition of phosphorus. *Global Biogeochem. Cycles*, *24*(3), n/a. https://doi.org/10.1029/2009GB003634.

Barlow, R., Lamont, T., Louw, D., Gibberd, M. J., Airs, R., & van der Plas, A. (2018). Environmental influence on phytoplankton communities in the northern Benguela ecosystem. African journal of marine science, 40(4), 355-370. https://doi.org/10.2989/1814232X.2018.1531785

Barnett, T., & Preisendorfer, R. (1987). Origins and levels of monthly and seasonal forecast skill for United States surface air temperatures determined by canonical correlation analysis. Monthly Weather Review, 115, 1825-1850.

Barreiro, M. (2013). Oceanografía Dinamica. https://www.yumpu.com/es/document/read/6309690/2-movimiento-de-los-oceanos-unidad-de-ciencias-de-la-atmosfera

Barrett, B. S., Campos, D. A., Veloso, J. V., & Rondanelli, R. (2016). Extreme temperature and precipitation events in March 2015 in central and northern Chile. Journal of geophysical research. Atmospheres, 121(9), 4563-4580. https://doi.org/10.1002/2016JD024835

Barrett, B. S., Garreaud, R. D., & Falvey, M. (2009). Effect of the Andes Cordillera on precipitation from a midlatitude cold front. Monthly weather review, 137(9), 3092-3109. https://doi.org/10.1175/2009MWR2881.1

Beckers, J., & Rixen, M. (2003). EOF Calculations and Data Filling from Incomplete Oceanographic Datasets*. Journal of Atmospheric and Oceanic Technology, 20(12), 1839-1856.

Bigg, G. (2003). The Oceans and Climate (Second ed.). Cambridge University Press. https://doi.org/10.1017/cbo9781139165013

Björnsson, H., & Venegas, S. A. (1997). A Manual for EOF and SVD analyses of Climatic Data (Vol. CCGCR Report No. 97-1). McGill University.

Boyd, P., Law, C., Wong, C., & Nojiri, Y. (2004). The decline and fate of an iron-induced subarctic phytoplankton bloom. Nature, 428(6982), 549-553. https://doi.org/10.1038/nature02437

Braun, M. H., Malz, P., Sommer, C., Farías-Barahona, D., Sauter, T., Casassa, G., Soruco, A., Skvarca, P., & Seehaus, T. C. (2019). Constraining glacier elevation and mass changes in South America. Nature Climate Change, 9(2), 130-136. https://doi.org/10.1038/s41558-018-0375-7

Bravo, L., Ramos, M., Astudillo, O., Dewitte, B., & Goubanova, K. (2016). Seasonal variability of the Ekman transport and pumping in the upwelling system off central-northern Chile (~30°S) based on a high-resolution atmospheric regional model (WRF). *Ocean science*, *12*(5), 1049-1065. https://doi.org/10.5194/os-12-1049-2016

Buschmann, A. H., Farías, L., Varela, D., & Vásquez, M. (2016). Informe Final Comisión Marea Roja Universidad de los Lagos. http://www.academiadeciencias.cl/wp-content/uploads/2017/04/InfoFinal_ComisionMareaRoja_21Nov2016.pdf

Buschmann, A. H., Riquelme, V. A., Hernández-González, M. C., Varela, D., Jiménez, J. E., Henríquez, L. A., Vergara, P. A., Guínez, R., & Filún, L. (2006). A review of the impacts of salmonid farming on marine coastal ecosystems in the southeast Pacific. ICES journal of marine science, 63(7), 1338-1345. https://doi.org/10.1016/j.icesjms.2006.04.021

C3S. (2021). ERA5: Fifth Generation of ECMWF Atmospheric Reanalyses of the Global Climate. Copernicus Climate Change Service Climate Data store. https://cds.climate.copernicus.eu/cdsapp

Cai, W., Whetton, P. H., & Karoly, D. J. (2003). The response of the Antarctic Oscillation to increasing and stabilized atmospheric CO2. Journal of climate, 16(10), 1525-1538. https://doi.org/10.1175/1520-0442-16.10.1525

Campbell. (2002). Introduction to remote sensing (3rd ed.). New York : Guilford Press, c1987.

Camus P, & Hajek E. (1998). Historia Ambiental de Chile (first ed.). Vol 1. 226 pp https://www.ecolyma.cl/documentos/hist_amb_chile_v1.pdf

Castillo, M. I., Cifuentes, U., Pizarro, O., Djurfeldt, L., & Caceres, M. (2016). Seasonal hydrography and surface outflow in a fjord with a deep sill: The Reloncaví fjord, Chile. Ocean science, 12(2), 533-534. https://doi.org/10.5194/os-12-533-2016

Castro, J. (2010). Estimación del balance biogeoquímico del nitrógeno y fósforo inorgánico disuelto en el estero Reloncaví en invierno y primavera de 2004, 2005 y 2006. Universidad Católica de Valparaíso.

Chase, Z., Van Geen, A., Kosro, P. M., Marra, J., & Wheeler, P. A. (2002). Iron, nutrient, and phytoplankton distributions in Oregon coastal waters. Journal of Geophysical Research: Oceans, 107(C10), 38-31-38-17. https://doi.org/10.1029/2001JC000987

CHV-noticias. (2018). Nube de polvo: Fenómeno natural alertó habitantes de Arica. https://www.chvnoticias.cl/nacional/nube-de-polvo-fenomeno-natural-alerto-a-los-habitantes-de-arica_20180723/

Colling, A. (2001). Ocean circulation (2nd / prepared by Angela Colling for the Course Team. ed.). Oxford : Butterworth Heinemann, in association with the Open University, 2001.

CONAMA. (2008). Biodiversidad de Chile, Patrimonio y Desafíos (second ed.), Tomo I. https://www.academia.edu/28661207/BIODIVERSIDAD_DE_CHILE_PATRIMONIO_Y_DESAFÍOS_TRADICIONES_CULTURALES_Y_BIODIVERSIDAD

Cordero, R. R., Asencio, V., Feron, S., Damiani, A., Llanillo, P. J., Sepulveda, E., Jorquera, J., Carrasco, J. & Casassa, G. (2019). Dry-Season Snow Cover Losses in the Andes (18°–40°S) driven by Changes in Large-Scale Climate Modes. Sci Rep, 9(1), 16945-16910. https://doi.org/10.1038/s41598-019-53486-7

Corredor-Acosta, A., Morales, C. E., Hormazabal, S., Andrade, I., & Correa-Ramirez, M. A. (2015). Phytoplankton phenology in the coastal upwelling region off central-southern Chile (35°S–38°S): Time-space variability, coupling to environmental factors, and sources of uncertainty in the estimates. Journal of Geophysical Research: Oceans, 120(2), 813-831. https://doi.org/10.1002/2014JC010330

CR2. (2018). Flow data of the rivers of Chile. https://www.cr2.cl/datos-de-caudales/

Dacre, H., Crawford, B., Charlton-Perez, A., Lopez-Saldana, G., Griffiths, G., & Veloso, J. (2018). CHILEAN WILDFIRES Probabilistic Prediction, Emergency Response, and Public Communication. Bull. Amer. Meteorol. Soc., 99(11), 2259-2274. https://doi.org/10.1175/BAMS-D-17-0111.1

Dansie, A. P., Thomas, D. S. G., Wiggs, G. F. S., & Munkittrick, K. R. (2018). Spatial variability of ocean fertilizing nutrients in the dust-emitting ephemeral river catchments of Namibia. Earth Surface Processes and Landforms, 43(3), 563-578. https://doi.org/10.1002/esp.4207

De la Torre, M. (2016). Variabilidad Espacio-Temporal de la Clorofila y Temperatura Satelital en el Mar Interior de Chiloé y su Relación con Procesos Oceanográficos en el Periodo 2003-2014 Universidad de Concepción.

Deser, C., & Trenberth, K. (2016). The Climate Data Guide: Pacific Decadal Oscillation (PDO): Definition and Indices. https://climatedataguide.ucar.edu/climate-data/pacific-decadal-oscillation-pdo-definition-and-indices

Dezileau, L., Ulloa, O., Hebbeln, D., Lamy, F., Reyss, J. L., & Fontugne, M. (2004). Iron control of past productivity in the coastal upwelling system off the Atacama Desert, Chile. Paleoceanography, 19(3), n/a-n/a. https://doi.org/10.1029/2004PA001006

Diaz, P. A., Perez-Santos, I., Alvarez, G., Garreaud, R., Pinilla, E., Diaz, M., Sandoval, A., Araya, M., Alvarez, F., Rengel, J., Montero, P., Pizarro, G., Lopez, L., Iriarte, L., Igor, G., & Reguera, B. (2021). Multiscale physical background to an exceptional harmful algal bloom of Dinophysis acuta in a fjord system. The Science of the total environment, 773. https://doi.org/10.1016/j.scitotenv.2021.145621

DiTullio, G. R., Geesey, M. E., Maucher, J. M., Alm, M. B., Riseman, S. F., & Bruland, K. W. (2005). Influence of Iron on Algal Community Composition and Physiological Status in the Peru Upwelling System. *Limnology and oceanography*, *50*(6), 1887-1907. https://doi.org/10.4319/lo.2005.50.6.1887

DMC. (2018). Boletines Climatológicos Mensuales del 2014, 2015, 2016 y 2018. https://climatologia.meteochile.gob.cl/application/publicaciones/boletinClimatologicoMensual

Dortch, Q. (1990). The interaction between ammonium and nitrate uptake in phytoplankton. Marine ecology progress series. Oldendorf, 61(1-2), 183-201.

Echevin, V., Albert, A., Lévy, M., Graco, M., Aumont, O., Piétri, A., & Garric, G. (2014). Intraseasonal variability of nearshore productivity in the Northern Humboldt Current System: The role of coastal trapped waves. Continental Shelf Research, 73, 14-30. https://doi.org/10.1016/j.csr.2013.11.015

El Kenawy, A. M., & McCabe, M. F. (2016). A multi-decadal assessment of the performance of gauge- and model-based rainfall products over Saudi Arabia: climatology, anomalies and trends. International Journal of Climatology, 36(2), 656-674. https://doi.org/10.1002/joc.4374

Falkowski, P. (1994). The role of phytoplankton photosynthesis in global biogeochemical cycles. Official Journal of the International Society of Photosynthesis Research, 39(3), 235-258. https://doi.org/10.1007/BF00014586

Franz, B. A., Werdell, P. J., Meister, G., Bailey, S. W., Epleejr, R. E., Feldman, G. C., Kwiatkowskaa, E., McClain, C., Patt, F., & Thomas, D. (2005). The continuity of ocean color measurements from SeaWiFS to MODIS. In (Vol. 5882, pp. 58820W-58820W-58813).

Freedman, D. (2007). Statistics (Fourth edition / David Freedman, Robert Pisani, Roger Purves.; International student edition. ed.). New York; London: W.W. Norton & Co., 2007.

Frenger, I., Münnich, M., Gruber, N., & Knutti, R. (2015). Southern Ocean eddy phenomenology. *J. Geophys. Res. Oceans*, *120*(11), 7413-7449. https://doi.org/10.1002/2015JC011047

Friederichs, P., & Hense, A. (2003). Statistical inference in canonical correlation analyses exemplified by the influence of North Atlantic SST on European climate. Journal of Climate, 16(3), 522-534. https://doi.org/10.1175/1520-0442(2003)016<0522:SIICCA>2.0.CO;2

Garcia, H. E., R. A. Locarnini, T. P. Boyer, J. I. Antonov, M. M. Zweng, O. K. Baranova, and D. R. Johnson, (2010). World Ocean Atlas 2009, Volume 4: Nutrients (phosphate, nitrate, silicate). S. Levitus, Ed. NOAA Atlas NESDIS 71, U.S. Government Printing Office, Washington, D.C., 398 pp.

Garreaud, R. D. (2009). The Andes climate and weather. Advances in geosciences, 22(22), 3-11. https://doi.org/10.5194/adgeo-22-3-2009

Garreaud, R. D., Boisier, J. P., Rondanelli, R., Montecinos, A., Sepúlveda, H. H., & Veloso-Aguila, D. (2020). The Central Chile Mega Drought (2010–2018): A climate dynamics perspective. International journal of climatology, 40(1), 421-439. https://doi.org/10.1002/joc.6219

Garreaud, R. D., & Muñoz, R. C. (2005). The low-level jet off the west coast of subtropical South America: Structure and variability. Monthly weather review, 133(8), 2246-2261. https://doi.org/10.1175/MWR2972.1

Garreaud, R. D., Rutllant, J. A., & Fuenzalida, H. (2002). Coastal lows along the subtropical west coast of South America: Mean structure and evolution. Monthly weather review, 130(1), 75-88. https://doi.org/10.1175/1520-0493(2002)130<0075:CLATSW>2.0.CO;2

Gelaro, R., McCarty, W., Suárez, M. J., Todling, R., Molod, A., Takacs, L., Randles, C., Darmenov, A., Bosilovich, M., Reichle, R., Wargan, K., Coy, L., Cullather, R., Draper, C., Lucchesi, R., Merkova, D., Nielsen, J., Partyka, G., Pawson S., Putman, W., Rienecker, M., Schubert, S., Sienkiewicz, M., & Zhao, B. (2017). The modern-era retrospective analysis for research and applications, version 2 (MERRA-2). Journal of Climate, 30(14), 5419-5454. https://doi.org/10.1175/JCLI-D-16-0758.1

Gómez, F., Montecinos, A., Hormazabal, S., Cubillos, L. A., Correa-Ramirez, M., & Chavez, F. P. (2012). Impact of spring upwelling variability off southern-central Chile on common sardine (Strangomera bentincki) recruitment. Fisheries Oceanography, 21(6), 405-414. https://doi.org/10.1111/j.1365-2419.2012.00632.x

Gómez, F. A., Spitz, Y. H., Batchelder, H. P., & Correa-Ramirez, M. A. (2017). Intraseasonal patterns in coastal plankton biomass off central Chile derived from satellite observations and a biochemical model. Journal of Marine Systems, 174(C), 106-118. https://doi.org/10.1016/j.jmarsys.2017.05.003

González-Reyes, Á., & Muñoz, A. A. (2013). Cambios en la precipitación de la ciudad de Valdivia (Chile) durante los últimos 150 años. Precipitation changes of Valdivia city (Chile) during the past 150 years, 34(2), 191-200. https://doi.org/10.4067/S0717-92002013000200008

Hansen, C., Van Der Meeren, G. I., Loeng, H., & Skogen, M. D. (2021). Assessing the state of the Barents Sea using indicators: How, when, and where? *ICES Journal of marine science*, *78*(8), 2983-2998. https://doi.org/10.1093/icesjms/fsab053

Harris, R., Lenz, J., Huntley, M., Wiebe, P., & Rune, H. (2000). ICES Zooplankton Methodology Manual chapter introduction. Academic Press. https://doi.org/10.1016/B978-0-12-327645-2.X5000-2

Hauke, J., & Kossowski, T. (2011). Comparison of values of Pearson's and spearman's correlation coefficients on the same sets of data. Quaestiones Geographicae, 30(2), 87-93. https://doi.org/10.2478/v10117-011-0021-1

Hendon, H., Thompson, D., & Wheeler, M. (2007). Australian Rainfall and Surface Temperature Variations Associated with the Southern Hemisphere Annular Mode. Journal of Climate, 20(11), 2452-2467. https://doi.org/10.1175/JCLI4134.1

Hennermann, K., & Guillory, A. (2020). ERA5: Documentation. https://confluence.ecmwf.int/display/CKB/ERA5%3A+data+documentation

Hersbach, H., Bell, B., Berrisford, P., Hirahara, S., Horányi, A., Muñoz-Sabater, J., Nicolas, J.,Peubey, X., Balsamo, G., Bechtold, P., Biavati, G., Bidlot, J., Bonavita, M., Chiara, G., Dahlgren, P., Dee, D., Diamantakis, M. Dragani, R., Flemming, J., Forbes, R., Fuentes, M., Geer, A., Haimberger, L., Healy, S., Hogan, R., Hólm, E., Janisková, M., Keeley, S., Laloyaux, P., Lopez, P., Lupu, C., Radnoti, G., Rosnay, P., Rozum, I., Vamborg, F., Villaume, S., & Thépaut, J. N. (2020). The ERA5 global reanalysis. Quarterly Journal of the Royal Meteorological Society, 146(730), 1999-2049. https://doi.org/10.1002/qj.3803

Hess, A. S., & Hess, J. R. (2018). Principal component analysis. Transfusion, 58(7), 1580-1582. https://doi.org/10.1111/trf.14639

Ikema, T., Bryant, R. G., & Bigg, G. R. (2013). Environmental controls at multiple scales for the western Pacific: An Okinawan case study. Estuarine, Coastal and Shelf Science, 128(C), 52-63. https://doi.org/10.1016/j.ecss.2013.05.008

Iriarte, J. L., Pantoja, S., González, H. E., Silva, G., Paves, H., Labbé, P., Rebolledo, L., Van Ardelan, M.,.& Häussermann, V. (2012). Assessing the micro-phytoplankton response to nitrate in Comau Fjord (42°S) in Patagonia (Chile), using a microcosms approach. *Environ Monit Assess*, *185*(6), 5055-5070. https://doi.org/10.1007/s10661-012-2925-1

Iriarte, J. L., Pizarro, G., Troncoso, V. A., & Sobarzo, M. (2000). Primary production and biomass of size-fractionated phytoplankton off Antofagasta, Chile (23–24°S) during pre-El Niño and El Niño 1997. Journal of marine systems, 26(1), 37-51. https://doi.org/10.1016/S0924-7963(00)00037-3

Jara, C., Gaete, H., Lobos, G., & Hidalgo, M. E. (2014). Oxidative stress in the mollusk Echinolittorina peruviana (Gasteropoda: Littorinidae, Lamarck, 1822) and trace metals in coastal sectors with mining activity. Ecotoxicology, 23(6), 1099-1108. https://doi.org/10.1007/s10646-014-1253-3

Landaeta, M., Bustos, C., Palacios-Fuentes, P., Rojas, P., & Balbontin, F. (2011). Ichthyoplankton distribution in South Patagonia, Chile: potential effects of ice melting from the Southern Ice Field. Latin American journal of aquatic research (LAJAR), 39(2), 236-249. https://doi.org/10.3856/vol39-issue2-fulltext-5

Lara, C., Miranda, M., Montecino, V., & Iriarte, J. (2010). Chlorophyll-a MODIS mesoscale variability in the Inner Sea of Chiloé, Patagonia, Chile (41-43 degrees S): Patches and Gradients? Rev. Biol. Mar. Oceanogr., 45(2), 217-225.

Lee, M. R., & Correa, J. A. (2005). Effects of copper mine tailings disposal on littoral meiofaunal assemblages in the Atacama region of northern Chile. Mar Environ Res, 59(1), 1-18. https://doi.org/10.1016/j.marenvres.2004.01.002

León-Muñoz, J., Urbina, M. A., Garreaud, R., & Iriarte, J. L. (2018). Hydroclimatic conditions trigger record harmful algal bloom in western Patagonia (summer 2016). Sci Rep, 8(1), 1330-1310. https://doi.org/10.1038/s41598-018-19461-4

Li, D., Christakos, G., Ding, X., & Wu, J. (2018). Adequacy of TRMM satellite rainfall data in driving the SWAT modeling of Tiaoxi catchment (Taihu lake basin, China). Journal of Hydrology, 556, 1139-1152. https://doi.org/10.1016/j.jhydrol.2017.01.006

Liao, X., Zhan, H., & Du, Y. (2016). Potential new production in two upwelling regions of the western Arabian Sea: Estimation and comparison. *Journal of geophysical research. Oceans*, *121*(7), 4487-4502. https://doi.org/10.1002/2016JC011707

Linsley, B. K., Wu, H. C., Dassié, E. P., & Schrag, D. P. (2015). Decadal changes in South Pacific sea surface temperatures and the relationship to the Pacific decadal oscillation and upper ocean heat content. Geophysical Research Letters, 42(7), 2358-2366. https://doi.org/10.1002/2015GL063045

Lo, W., Chung, C., & Shih C. (2004). Seasonal distribution of Copepods in Tapong Bay, Southwestern Taiwan. Zoological Studies 43 (2): 463-474.

Marchant, M., Cecioni, A., Figueroa, S., González, H., Giglio, S., Hebbeln, D., Kaiser, J., Lamy, F., Mohtadi, M., Pineda, V., & Romero, O. (2007). Marine Geology, Oceanography and climate. In T. Moreno & W. Gibbons (Eds.), The Geology of Chile (first ed., pp. 288-293). The Geological Society.

Masotti, I., Aparicio-Rizzo, P., Yevenes, M. A., Garreaud, R., Belmar, L., & Farías, L. (2018). The influence of river discharge on nutrient export and phytoplankton biomass off the Central Chile Coast (33°-37°S): Seasonal cycle and interannual variability. Frontiers in Marine Science, 5. https://doi.org/10.3389/fmars.2018.00423

Ménesguen, A., & Lacroix, G. (2018). Modelling the marine eutrophication: A review. Science of The Total Environment 636:339-354.

Miloslavich, P., Klein, E., Díaz, J. M., Hernández, C. E., Bigatti, G., Campos, L., Artigas, F., Castillo, J., Penchaszadeh, P., Neill, P., Carranza, A. Retana, M., Díaz de Astarloa, J., Lewis, M., Yorio, P., Piriz, M., Rodríguez, D., Yoneshigue-Valentin, Y., Gamboa, L., & Martín, A. (2011). Marine biodiversity in the Atlantic and Pacific coasts of South America: knowledge and gaps. PloS one, 6(1), e14631-e14631. https://doi.org/10.1371/journal.pone.0014631

Mogollón, R., & Calil, P. H. R. (2017). On the effects of ENSO on ocean biogeochemistry in the Northern Humboldt Current System (NHCS): A modeling study. Journal of Marine Systems, 172, 137-159. https://doi.org/10.1016/j.jmarsys.2017.03.011

Molinari, C. (2021). Chile's environmental watchdog fines "serial offender" Nova Austral once again. https://www.seafoodsource.com/news/aquaculture/chiles-environmental-watchdog-fines-serial-offender-nova-austral-once-again

Montecinos, A., & Aceituno, P. (2003). Seasonality of the ENSO-Related Rainfall Variability in Central Chile and Associated Circulation Anomalies. Journal of climate, 16(2), 281-296. https://doi.org/10.1175/1520-0442(2003)016<0281:SOTERR>2.0.CO;2

Nakada, T., & Nozaki, H., (2015). Freshwater Algae of North America (2nd Ed.) Chapter 6: Flagellate Green Algae. Ecology and Classification, Aquatic Ecology: 265-313

NASA. (2018). chlorophyll a. https://oceancolor.gsfc.nasa.gov/atbd/chlor_a/

NASA. (2019). The official NASA (OB.DAAC) Processing software. https://seadas.gsfc.nasa.gov/

NOAA. (2000). Relief Globe slides from the National Geophysical Data Center. https://www.ngdc.noaa.gov/mgg/image/reliefslides.pdf

NOAA. (2019). Teleconnections. https://www.ncdc.noaa.gov/teleconnections/

Patil, N. S., & Yaligar, M. F. (2017). Analysis of linear relation between P-value and co-relational value using R programming. In (Vol. 2017-, pp. 983-987).

Pinet, P. R. (2009). Invitation to oceanography (5th ed.). Sudbury, Mass.: Jones and Bartlett Publishers, 2009.

Preethi, B., Sabin, T. P., Adedoyin, J. A., & Ashok, K. (2016). Erratum: Impacts of the ENSO Modoki and other Tropical Indo-Pacific Climate-Drivers on African Rainfall. Sci Rep, 6(1), 20266-20266. https://doi.org/10.1038/srep20266

Pryer, H. V., Hawkings, J. R., Wadham, J. L., Robinson, L. F., Hendry, K. R, Hatton, J. E., Kellermann, A., Bertrand, S., Gill-Olivas, B., Marshall, M., Brooker, R., Daneri, G., Häussermann, V. (2020). The Influence of Glacial Cover on Riverine Silicon and Iron Exports in Chilean Patagonia. *Global Biogeochem Cycles*, *34*(12), e2020GB006611-n/a. https://doi.org/10.1029/2020GB006611

Quezada, J. (2006). Fenómenos Climáticos Anómalos en el Litoral del Norte de Chile y su Impacto en el Relieve. In (Vol. 2, pp. 133-136). Universidad Católica del Norte: XI Congreso Geológico Chileno.

Quezada, J., Cerda, J. L., & Jensen, A. (2010). Efectos de la tectónica y el clima en la configuración morfológica del relieve costero del norte de Chile. Andean geology, 37(1), 78-109.

Quintana, J. M., & Aceituno, P. (2011). Changes in the rainfall regime along the extratropical west coast of South America (Chile): 30-43° S. Atmosfera, 25(1), 1-22.

Rahn, D. A. (2012). Influence of large scale oscillations on upwelling-favorable coastal wind off central Chile. Journal of Geophysical Research: Atmospheres, 117(D19), n/a-n/a. https://doi.org/10.1029/2012JD018016

Raiswell, R. (2011). Iceberg-hosted nanoparticulate Fe in the Southern Ocean: Mineralogy, origin, dissolution kinetics and source of bioavailable Fe. Deep-Sea Research Part II, 58(11), 1364-1375. https://doi.org/10.1016/j.dsr.2010.11.011

Reyers, M., Hamidi, M., & Shao, Y. (2019). Synoptic analysis and simulation of an unusual dust event over the Atacama Desert. Atmospheric science letters, 20(6), e899-n/a. https://doi.org/10.1002/asl.899

Ridame, C., Dekaezemacker, J., Guieu, C., Bonnet, S., L'Helguen, S., & Malien, F. (2014). Contrasted Saharan dust events in LNLC environments: Impact on nutrient dynamics and primary production. *Biogeosciences*, *11*(17), 4783-4800. https://doi.org/10.5194/bg-11-4783-2014

Saldías, G. S., Largier, J. L., Mendes, R., Pérez-Santos, I., Vargas, C. A., & Sobarzo, M. (2016). Satellite-measured interannual variability of turbid river plumes off central-southern Chile: Spatial patterns and the influence of climate variability. Progress in Oceanography, 146, 212-222. https://doi.org/10.1016/j.pocean.2016.07.007

Salvatteci, R., Field, D., Gutiérrez, D., Baumgartner, T., Ferreira, V., Ortlieb, L., Sifeddine, A., Grados, D., & Bertrand, A. (2018). Multifarious anchovy and sardine regimes in the Humboldt Current System during the last 150 years. Global Change Biology, 24(3), 1055-1068. https://doi.org/10.1111/gcb.13991

Schollaert Uz , S., Busalacchib, A. J., Smith, T. M., Evans, M. N., Brown, C. W., & Hackert, E. C. (2017). Interannual and decadal variability in tropical Pacific chlorophyll from a statistical reconstruction: 1958-2008. Journal of Climate, 30(18), 7293-7315. https://doi.org/10.1175/JCLI-D-16-0202.1

Schulz, N., Boisier, J. P., & Aceituno, P. (2012). Climate change along the arid coast of northern Chile. Int. J. Climatol, 32(12), 1803-1814. https://doi.org/10.1002/joc.2395

Sen Gupta, A., & McNeil, B. (2012). Variability and Change in the Ocean. In Elsevier (Ed.), The Future of World's Climate (Second ed., pp. 141-165).

Sernageomin. (2017). Principales desastres ocurridos desde 1980 en Chile. In: Servicio Nacional de Geología y Minería. http://sitiohistorico.sernageomin.cl/pdf/presentaciones-geo/Primer-Catastro-Nacional-Desastres-Naturales.pdf

Sernapesca. (2018). Informe técnico Situación Ambiental de la Acuicultura en Chile. http://www.sernapesca.cl/sites/default/files/informe_semestral_2018_mayo_vf.pdf

Sievers, H. A., & Silva, N. (2008). Water masses and circulation in austral Chilean channels and fjords. In (Silva,N., Palma, S. ed., pp. 53-58). Progress in the Oceanography Knowledge of Chilean Interior Water, From Puerto Montt to Cape Horn: Comité Oceanográfico Nacional-Ponteficia Universidad Católica de Valparaíso.

Silva, A., Palma, S., Oliveira, P. B., & Moita, M. T. (2009). Composition and interannual variability of phytoplankton in a coastal upwelling region (Lisbon Bay, Portugal). Journal of Sea Research, 62(4), 238-249. https://doi.org/10.1016/j.seares.2009.05.001

Silvestri, G., & Vera, C. (2003). Antarctic Oscillation signal on precipitation anomalies over southeastern South America. Geophysical Research Letters, 30(21). https://doi.org/10.1029/2003GL018277

Soetaert, K., Herman, P. M. J., Middelburg, J. J., Heip, C., Smith, C. L., Tett, P., & Wild-Allen, K. (2001). Numerical modelling of the shelf break ecosystem: reproducing benthic and pelagic measurements. Deep-Sea Research Part II, 48(14), 3141-3177. https://doi.org/10.1016/S0967-0645(01)00035-2

Sospedra, J., Niencheski, L. F. H., Falco, S., Andrade, C. F. F., Attisano, K. K., & Rodilla, M. (2018). Identifying the main sources of silicate in coastal waters of the Southern Gulf of Valencia (Western Mediterranean Sea). *Oceanologia*, *60*(1), 52-64. https://doi.org/10.1016/j.oceano.2017.07.004

Southerland, S. (2016). Weird 'Backward' dust plume flows from the driest place on Earth. https://www.theweathernetwork.com/news/articles/weird-backward-dust-plume-flows-from-driest-place-on-earth/70030

Stammerjohn, S. E., Martinson, D. G., Smith, R. C., Yuan, X., & Rind, D. (2008). Trends in Antarctic annual sea ice retreat and advance and their relation to El Niño–Southern Oscillation and Southern Annular Mode variability. J. Geophys. Res, 113(C3), C03S90-n/a. https://doi.org/10.1029/2007JC004269

Strub, P. T., James, C., Montecino, V., Rutllant, J. A., & Blanco, J. L. (2019). Ocean circulation along the southern Chile transition region (38°–46°S): Mean, seasonal and interannual variability, with a focus on 2014–2016. *Prog Oceanogr*, *172*, 159-198. https://doi.org/10.1016/j.pocean.2019.01.004

Tang, G., Clark, M. P., Papalexiou, S. M., Ma, Z., & Hong, Y. (2020). Have satellite precipitation products improved over the last two decades? A comprehensive comparison of GPM IMERG with nine satellite and reanalysis datasets. Remote sensing of environment, 240, 111697. https://doi.org/10.1016/j.rse.2020.111697

Taylor, M. (2012). Canonical Correlation Analysis for finding patterns in coupled fields. Me nugget. https://menugget.blogspot.com/2012/03/canonical-correlation-analysis-for.html

Taylor, M. (2017). Sinkr: Collection of functions with emphasis in multivariate data analysis. https://github.com/marchtaylor/sinkr

Taylor, M., Losch, M., Wenzel, M., & Schröter, J. (2013). On the Sensitivity of Field Reconstruction and Prediction Using Empirical Orthogonal Functions Derived from Gappy Data. Journal of Climate, 26(22), 9194-9205. https://doi.org/10.1175/JCLI-D-13-00089.1

Thiel, M., Macaya, E., Acuna, E., Arntz, W., Bastias, H., Brokordt, K., Camus, P., Carlos Castilla, J., Castro, L., Cortes, M., Dumont, C., Escribano, R., Fernandez, M., Gajardo, J., Gaymer, C., Gómez, I., Gonzalez, A., González, H., Haye, P., & Alonso Vega, J. (2007). The Humboldt Current System of Northern and Central Chile. In Oceanographic Processes, Ecological Interaction and Socioeconomic Feedback (Vol. 45, pp. 195-344). Oceanography and Marine Biology: An Annual Review.

Thompson, P. A., O'Brien, T. D., Paerl, H. W., Peierls, B. L., Harrison, P., & Robb, M. (2015). Precipitation as a driver of phytoplankton ecology in coastal waters: A climatic perspective. Estuarine, Coastal and Shelf Science, 162, 119-129. https://doi.org/10.1016/j.ecss.2015.04.004

Trauth, M. H. (2021). MATLAB recipes for earth sciences (Fifth ed.). Springer Textbooks in Earth Sciences, Geography and Environment. https://doi.org/10.1007/978-3-030-38441-8

Trenberth, K. (2020). The Climate Data Guide: Nino SST Indices (Nino 1+2, 3, 3.4, 4; ONI and TNI). https://climatedataguide.ucar.edu/climate-data/nino-sst-indices-nino-12-3-34-4-oni-and-tni.

Thorp, J., & Rogers, D. (2016). Thorp and Covich's Freshwater Invertebrates: Keys to Nearctic Fauna (4th ed.). Chapter 2: Protozoa, Academic press. https://doi.org/10.1016/C2010-0-65589-1

Valdes, J. (2012). Heavy metal distribution and enrichment in sediments of Mejillones Bay (23° S), Chile: a spatial and temporal approach. Environ Monit Assess, 184(9), 5283-5294. https://doi.org/10.1007/s10661-011-2339-5

Vergara, O. A., Echevín, V., Sepúlveda, H. H., & Quiñones, R. A. (2017). Controlling factors of the seasonal variability of productivity in the southern Humboldt Current System (30–40°S): A biophysical modeling approach. Continental Shelf Research, 148, 89-103. https://doi.org/10.1016/j.csr.2017.08.013

Vicencio, J. (2021). SPSA index data [mail].

Vicente-Serrano, S., Aguilar, E., Martínez, R., Martín-Hernández, N., Azorin-Molina, C., Sanchez-Lorenzo, A., El Kenawy, A., Tomás-Burguera, M., Moran-Tejeda, E., López-Moreno, J., Revuelto, J., Beguería, S., Nieto, J., Drumond, A., Gimeno, L., & Nieto, R. (2017). The complex influence of ENSO on droughts in Ecuador. Observational, Theoretical and Computational Research on the Climate System, 48(1-2), 405-427. https://doi.org/10.1007/s00382-016-3082-y

Von der Heydt, A. (2016). Rossby and Kelvin waves. In (pp. 18). Institute for Marine and Atmospheric research Utrecht University: Utrecht summer school Physics of the climate system.

Von Storch, H. (1995). Analysis of Climate Variability (N. A., Ed.). Springer. https://doi.org/https://doi.org/10.1007/978-3-662-03167-4_13

Von Storch, H., & Zwiers, F. W. (1999). Statistical Analysis in Climate Research. Cambridge University Press. https://doi.org/10.1017/CBO9780511612336

Wilks, D. S. (2011). Statistical Methods in the Atmosphere Science (Vol. 100). Elsevier Science & Technology. https://doi.org/10.1016/B978-0-12-385022-5.00012-9

Wilks, D. S. (2016). Modified "Rule N" procedure for principal component (EOF) truncation. Journal of Climate, 29(8), 3049-3056. https://doi.org/10.1175/JCLI-D-15-0812.1

Xiao, C., Ye, J., Esteves, R. M., & Rong, C. (2016). Using Spearman's correlation coefficients for exploratory data analysis on big dataset. Concurrency and Computation: Practice and Experience, 28(14), 3866-3878. https://doi.org/10.1002/cpe.3745

Yang, M. M., Ishizaka, J., Goes, J. I., Gomes, H. d. R., Maúre, E. d. R., Hayashi, M., Katano, T., Fujii, N., Saitoh, K., Mine, T., Yamashita, H., & Mizuno, A. (2018). Improved MODIS-Aqua chlorophyll-a retrievals in the turbid semi-enclosed Ariake Bay, Japan. Remote sensing (Basel, Switzerland), 10(9), 1335. https://doi.org/10.3390/rs10091335

Yuras, G., Ulloa, O., & Hormazábal, S. (2005). On the annual cycle of coastal and open ocean satellite chlorophyll off Chile (18°–40°S. Geophysical Research Letters, 32(23), n/a-n/a. https://doi.org/10.1029/2005GL023946

Appendices.

A.1. Seasonal and interannual values per subsection plots.
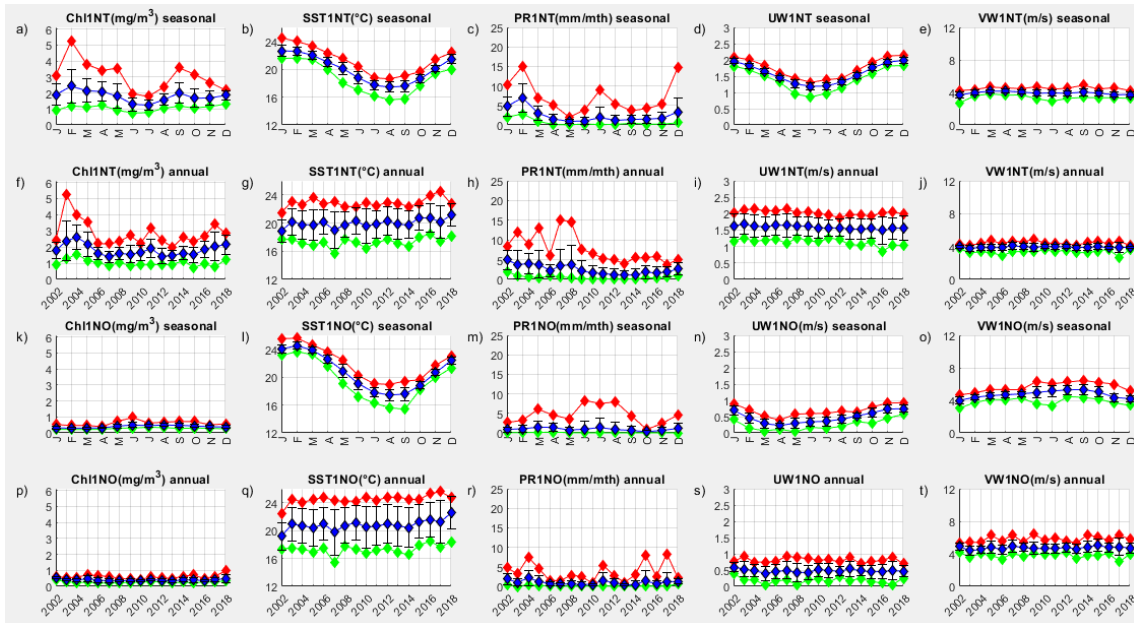
FIGURE A.1.1. 1NT (A-E) AND 1NO(K-O) SEASONAL MEANS FROM 2002-2018 AND ANNUAL MEANS (F-J AND P-T) OVER THE WHOLE STUDY PERIOD FOR ALL THE PARAMETERS STUDIED IN O.1. THE RED LINE IS THE MAXIMUM, THE GREEN IS THE MINIMUM, AND THE BLUE IS THE MEAN.
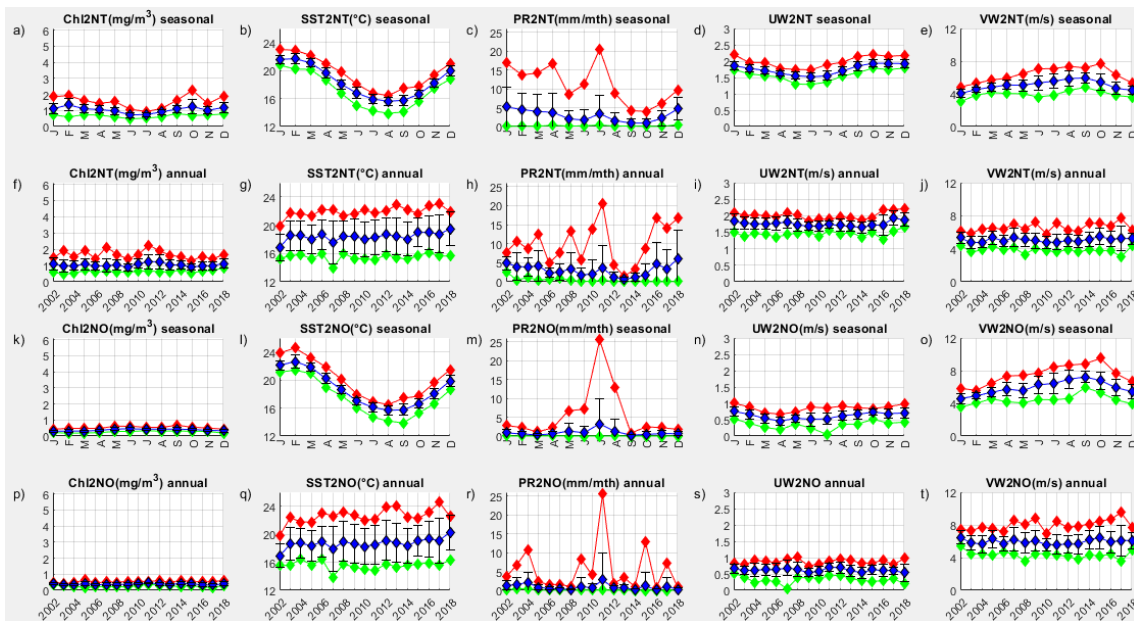
FIGURE A.1.2. 2NT (A-E) AND 2NO(K-O) SEASONAL MEANS FROM 2002-2018 AND ANNUAL MEANS (F-J AND P-T) OVER THE WHOLE STUDY PERIOD FOR ALL THE PARAMETERS STUDIED IN O.1. THE RED LINE IS THE MAXIMUM, THE GREEN IS THE MINIMUM, AND THE BLUE IS THE MEAN.
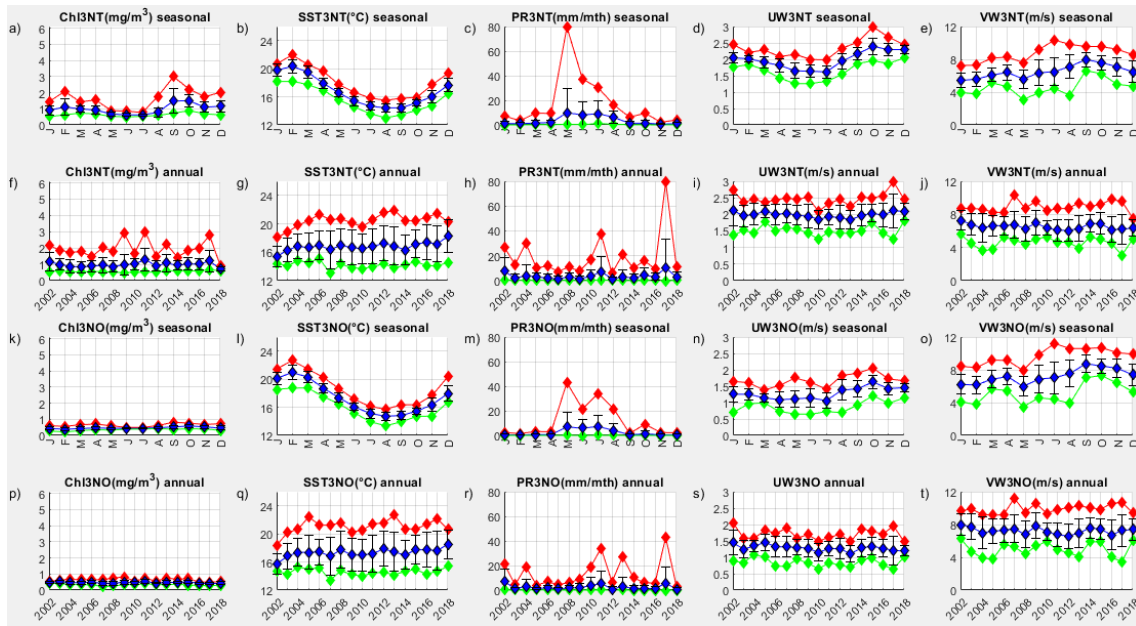
FIGURE A.1.3. 3NT (A-E) AND 3NO(K-O) SEASONAL MEANS FROM 2002-2018 AND ANNUAL MEANS (F-J AND P-T) OVER THE WHOLE STUDY PERIOD FOR ALL THE PARAMETERS STUDIED IN O.1. THE RED LINE IS THE MAXIMUM, THE GREEN IS THE MINIMUM, AND THE BLUE IS THE MEAN.
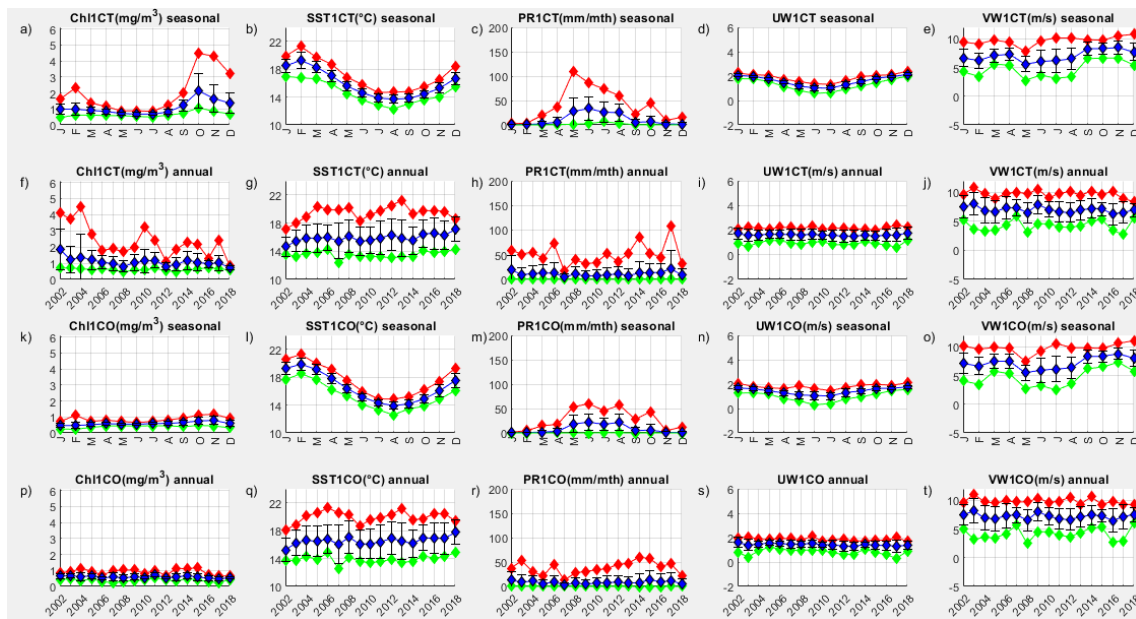
FIGURE A.1.4. 1CT (A-E) AND 1CO(K-O) SEASONAL MEANS FROM 2002-2018 AND ANNUAL MEANS (F-J AND P-T) OVER THE WHOLE STUDY PERIOD FOR ALL THE PARAMETERS STUDIED IN O.1. THE RED LINE IS THE MAXIMUM, THE GREEN IS THE MINIMUM, AND THE BLUE IS THE MEAN.
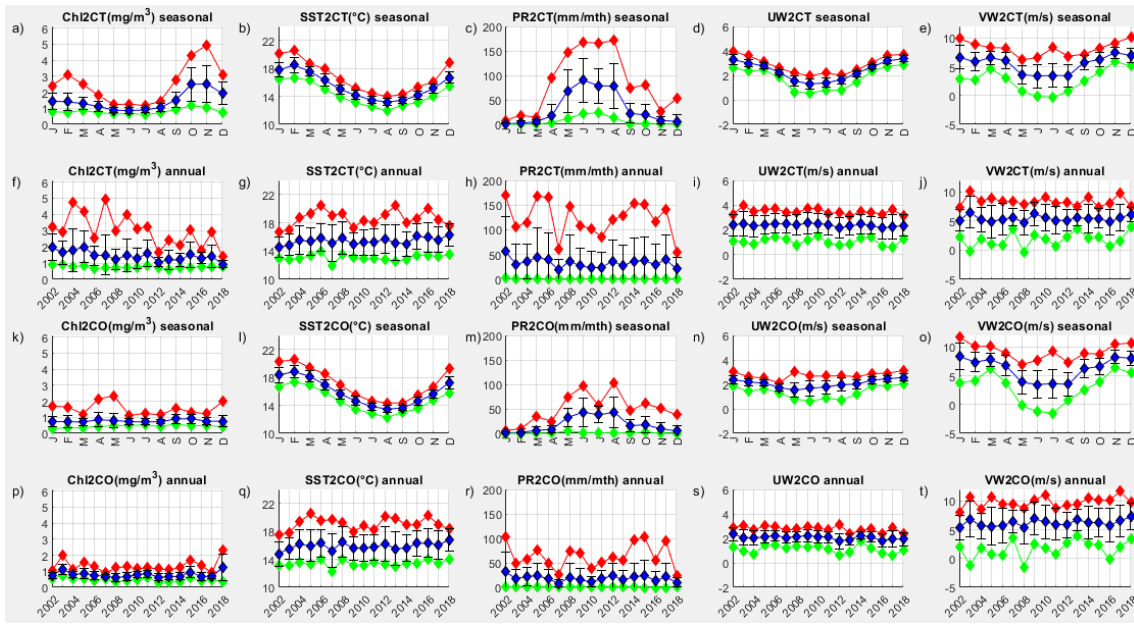
FIGURE A.1.5. 2CT (A-E) AND 2CO(K-O) SEASONAL MEANS FROM 2002-2018 AND ANNUAL MEANS (F-J AND P-T) OVER THE WHOLE STUDY PERIOD FOR ALL THE PARAMETERS STUDIED IN O.1. THE RED LINE IS THE MAXIMUM, THE GREEN IS THE MINIMUM, AND THE BLUE IS THE MEAN.
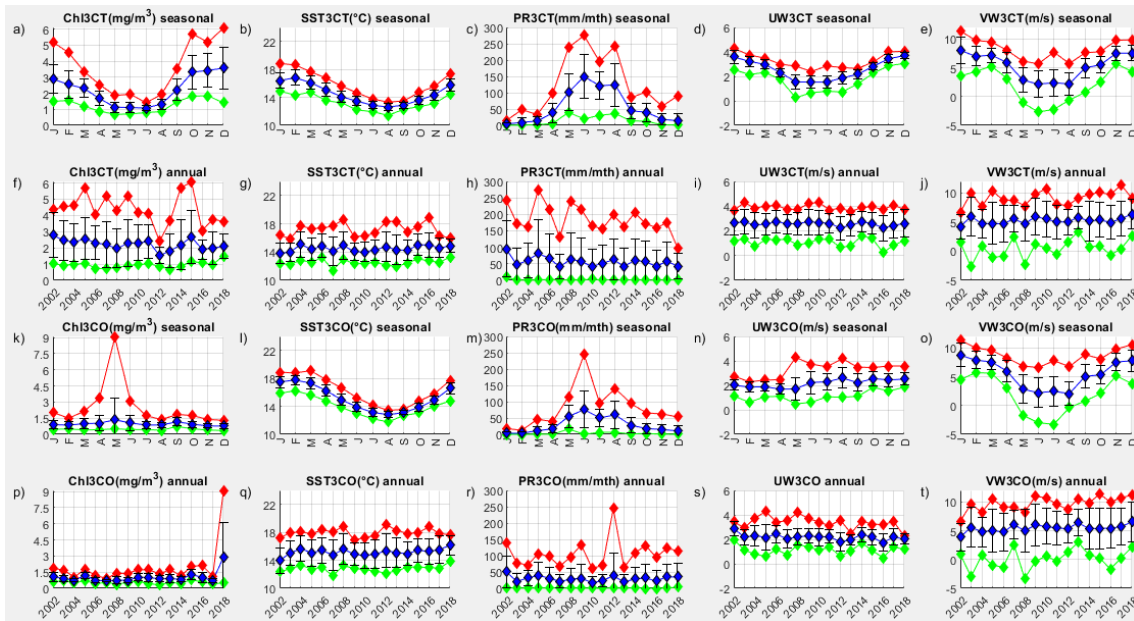
FIGURE A.1.6. 3CT (A-E) AND 3CO(K-O) SEASONAL MEANS FROM 2002-2018 AND ANNUAL MEANS (F-J AND P-T) OVER THE WHOLE STUDY PERIOD FOR ALL THE PARAMETERS STUDIED IN O.1. THE RED LINE IS THE MAXIMUM, THE GREEN IS THE MINIMUM, AND THE BLUE IS THE MEAN.
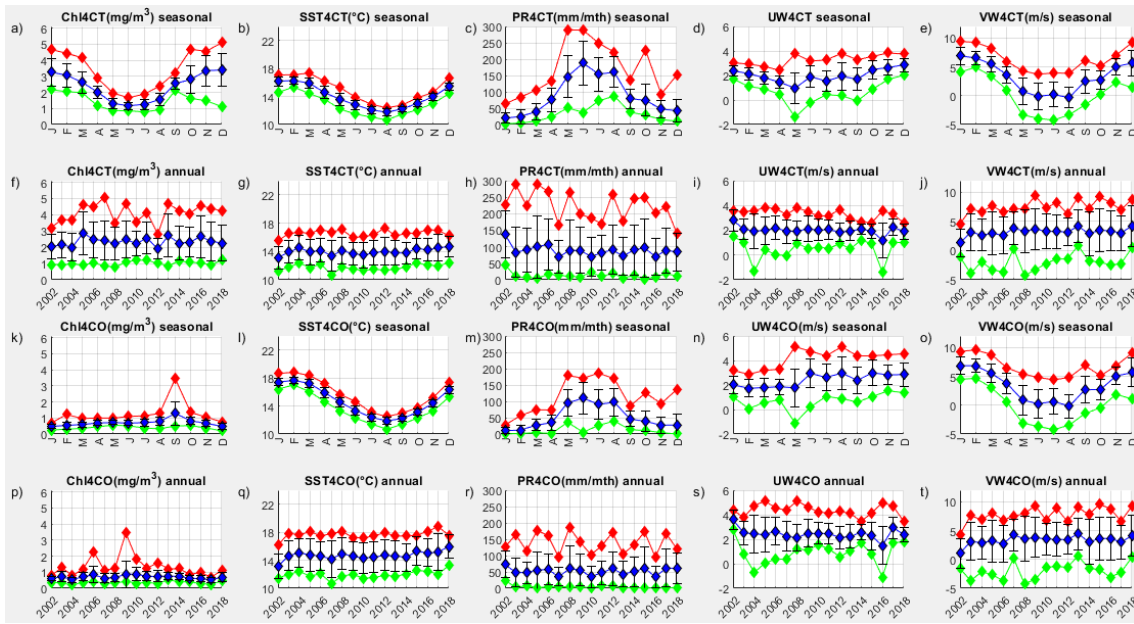
FIGURE A.1.7. 4CT (A-E) AND 4CO(K-O) SEASONAL MEANS FROM 2002-2018 AND ANNUAL MEANS (F-J AND P-T) OVER THE WHOLE STUDY PERIOD FOR ALL THE PARAMETERS STUDIED IN O.1. THE RED LINE IS THE MAXIMUM, THE GREEN IS THE MINIMUM, AND THE BLUE IS THE MEAN.
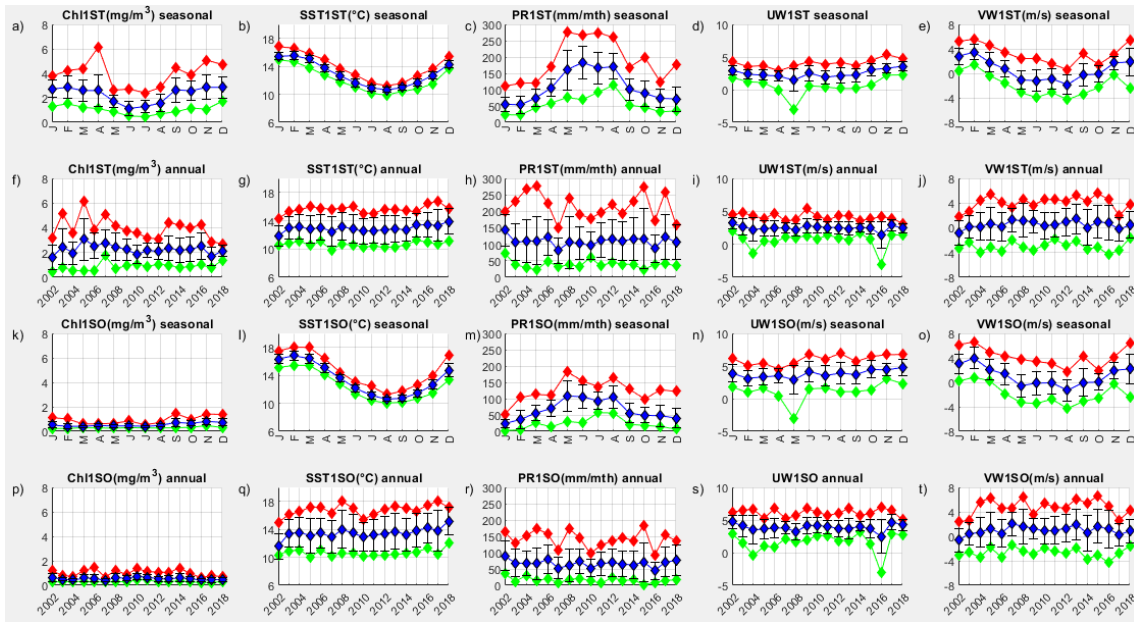
FIGURE A.1.8. 1ST (A-E) AND 1SO(K-O) SEASONAL MEANS FROM 2002-2018 AND ANNUAL MEANS (F-J AND P-T) OVER THE WHOLE STUDY PERIOD FOR ALL THE PARAMETERS STUDIED IN O.1. THE RED LINE IS THE MAXIMUM, THE GREEN IS THE MINIMUM, AND THE BLUE IS THE MEAN.

201
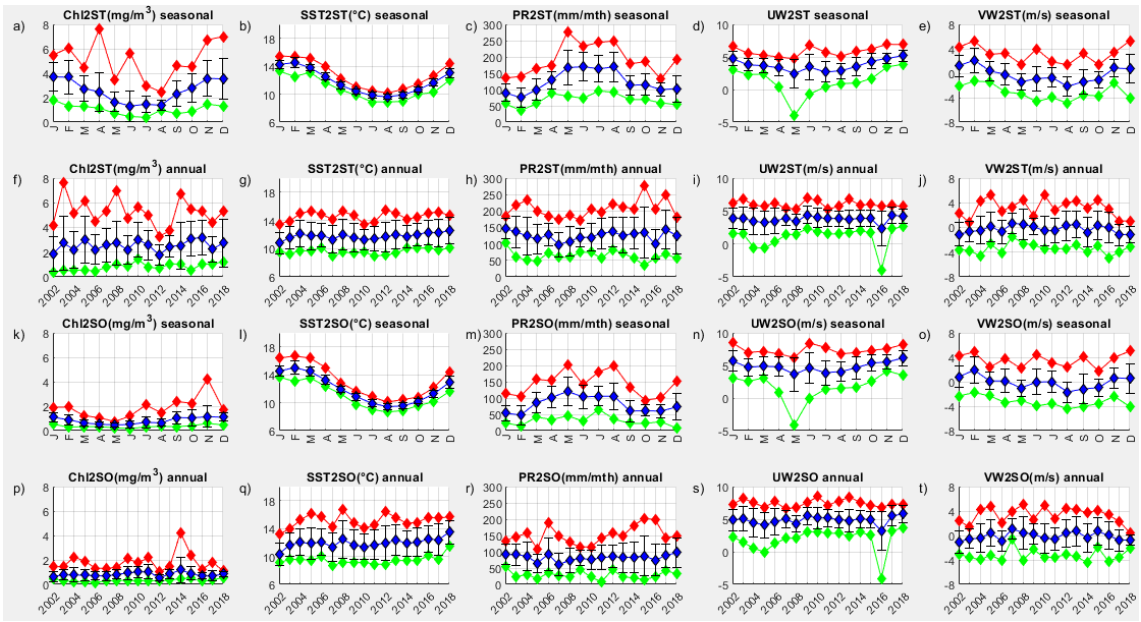
FIGURE A.1.9. 2ST (A-E) AND 2SO(K-O) SEASONAL MEANS FROM 2002-2018 AND ANNUAL MEANS (F-J AND P-T) OVER THE WHOLE STUDY PERIOD FOR ALL THE PARAMETERS STUDIED IN O.1. THE RED LINE IS THE MAXIMUM, THE GREEN IS THE MINIMUM, AND THE BLUE IS THE MEAN.
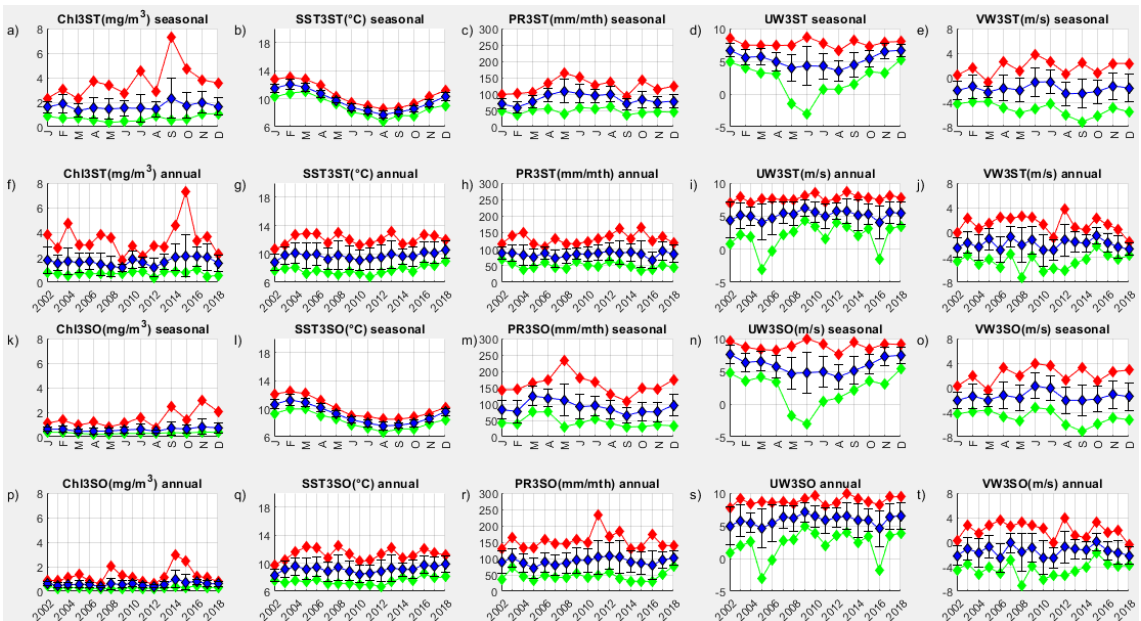
FIGURE A.1.10. 3ST (A-E) AND 3SO(K-O) SEASONAL MEANS FROM 2002-2018 AND ANNUAL MEANS (F-J AND P-T) OVER THE WHOLE STUDY PERIOD FOR ALL THE PARAMETERS STUDIED IN O.1. THE RED LINE IS THE MAXIMUM, THE GREEN IS THE MINIMUM, AND THE BLUE IS THE MEAN.

A.2. All the parameters correlations Figures.
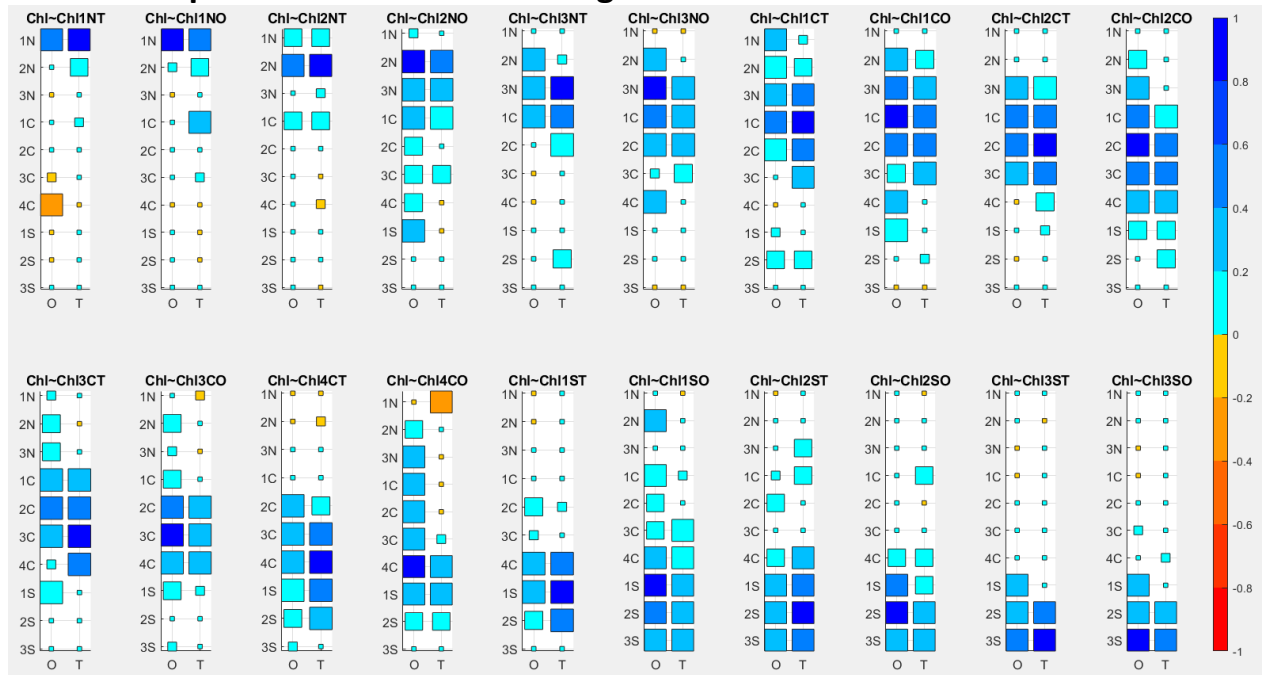
FIGURE A.2.1. CHL~CHL CORRELATION IN THE WHOLE SYSTEM. THE COLOURS CYAN TO BLUE SHADES REPRESENT POSITIVE RELATIONSHIPS (0 TO 1), WHILE A GOLD TO RED SCALE REPRESENTS NEGATIVE RELATIONSHIPS (0 TO -1). A FULL-SIZE BLOCK MEANS THAT IT IS VERY SIGNIFICANT (<0.01); A SIGNIFICANT (0.01-0.05) IS REPRESENTED WITH A BLOCK 80% OF ITS FULL SIZE; LOW SIGNIFICANT (0.05-0.1) WITH A 40% BLOCK; NOT SIGNIFICANT WITH A 20% BLOCK.
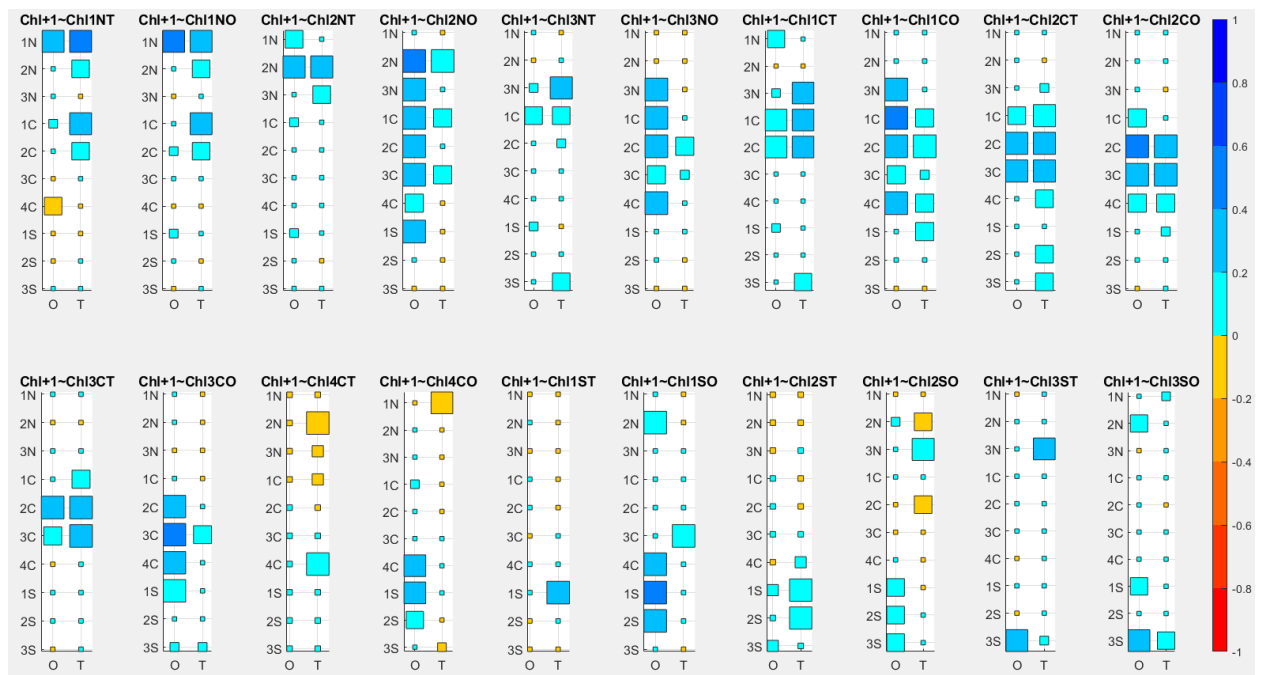
FIGURE A.2.2. CHL+1~CHL CORRELATION IN THE WHOLE SYSTEM. SECTION 4.2.2 AND FIGURE A.2.1 FOR A FULL LEGEND EXPLANATION.
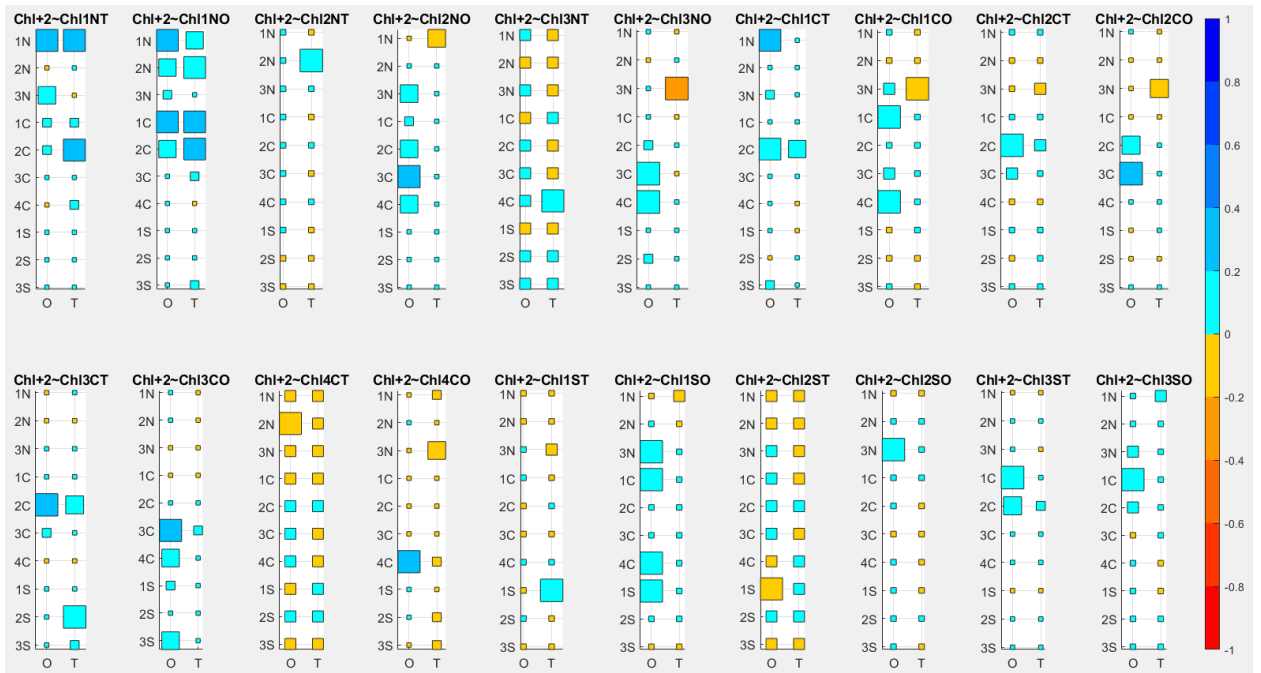
FIGURE A.2.3. CHL+2~CHL CORRELATION IN THE WHOLE SYSTEM. SECTION 4.2.2 AND FIGURE A.2.1 FOR A FULL LEGEND EXPLANATION.
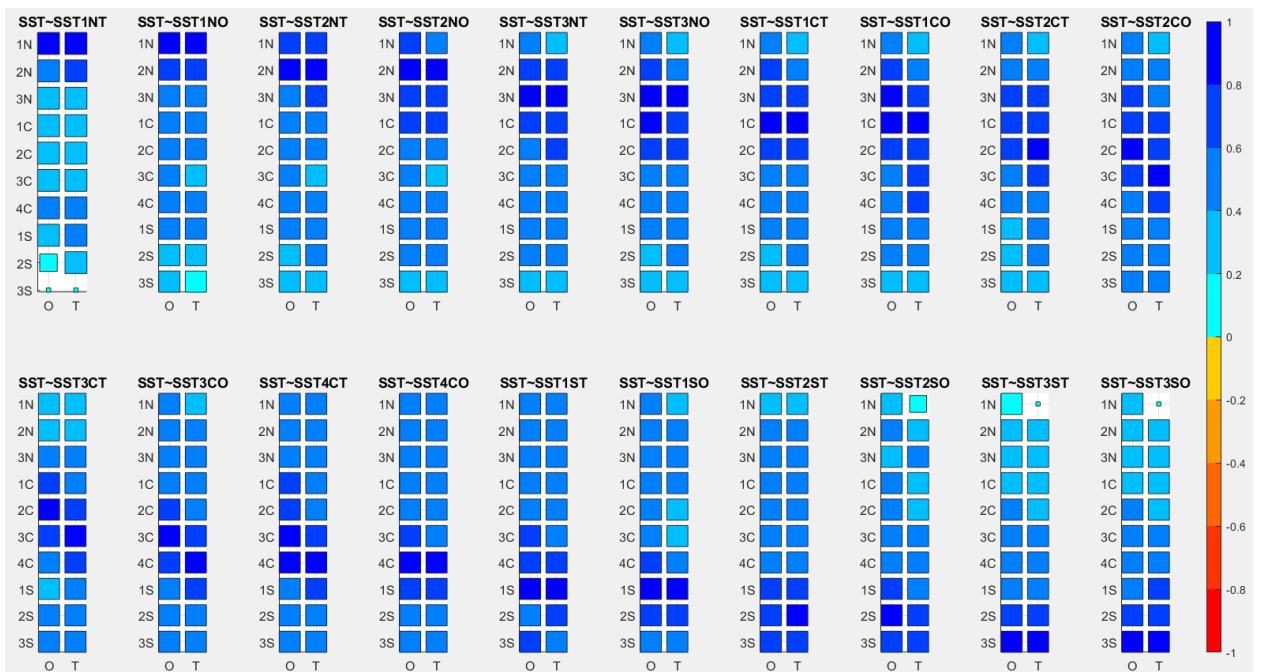
FIGURE A.2.4. SST~SST CORRELATION IN THE WHOLE SYSTEM. SECTION 4.2.2 AND FIGURE A.2.1 FOR A FULL LEGEND EXPLANATION.
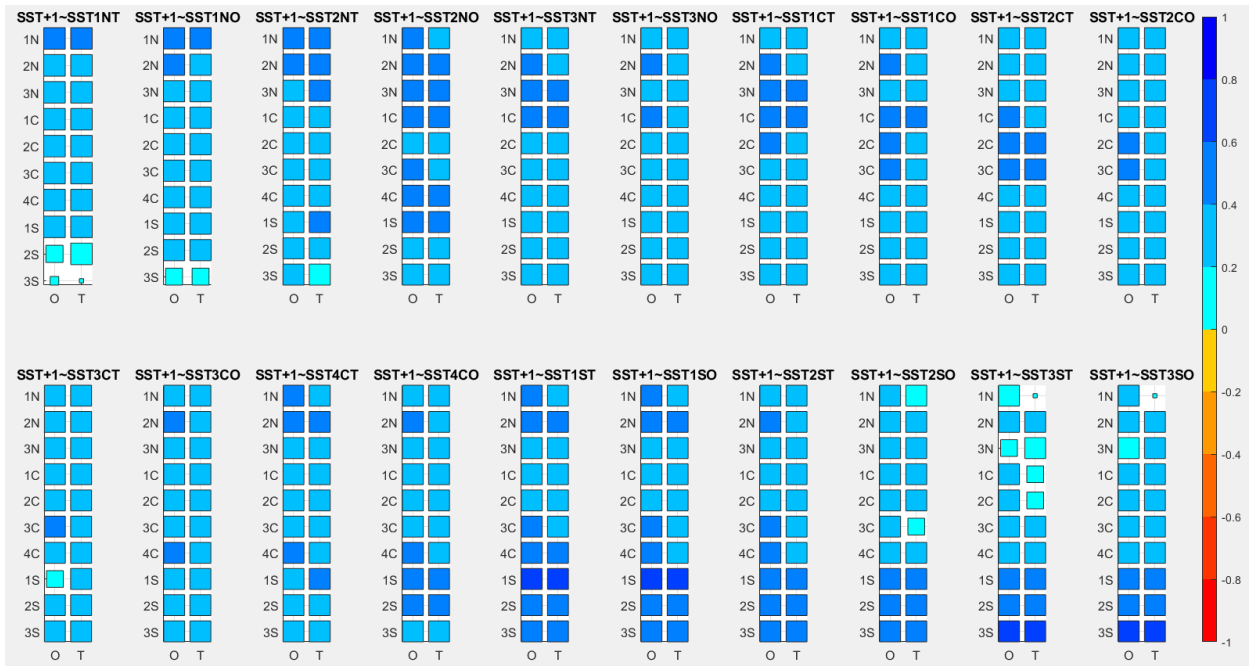
FIGURE A.2.5. SST+1~SST CORRELATION IN THE WHOLE SYSTEM. SECTION 4.2.2 AND FIGURE A.2.1 FOR A FULL LEGEND EXPLANATION.
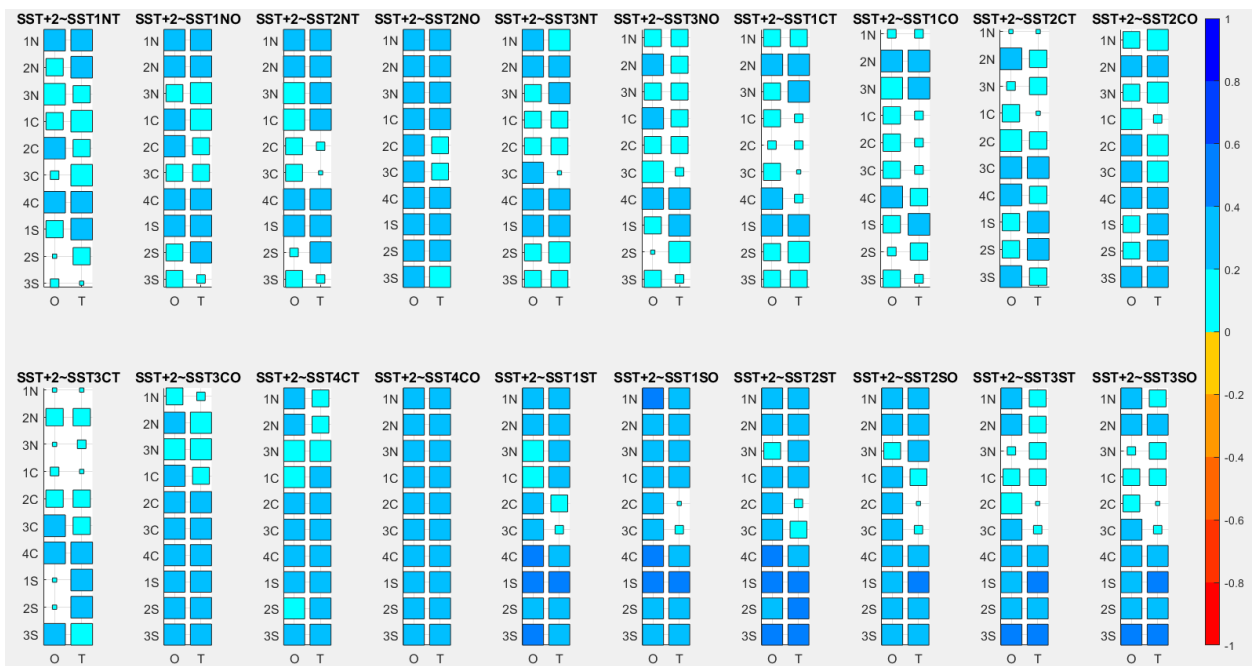
FIGURE A.2.6. SST+2~SST CORRELATION IN THE WHOLE SYSTEM. SECTION 4.2.2 AND FIGURE A.2.1 FOR A FULL LEGEND EXPLANATION.
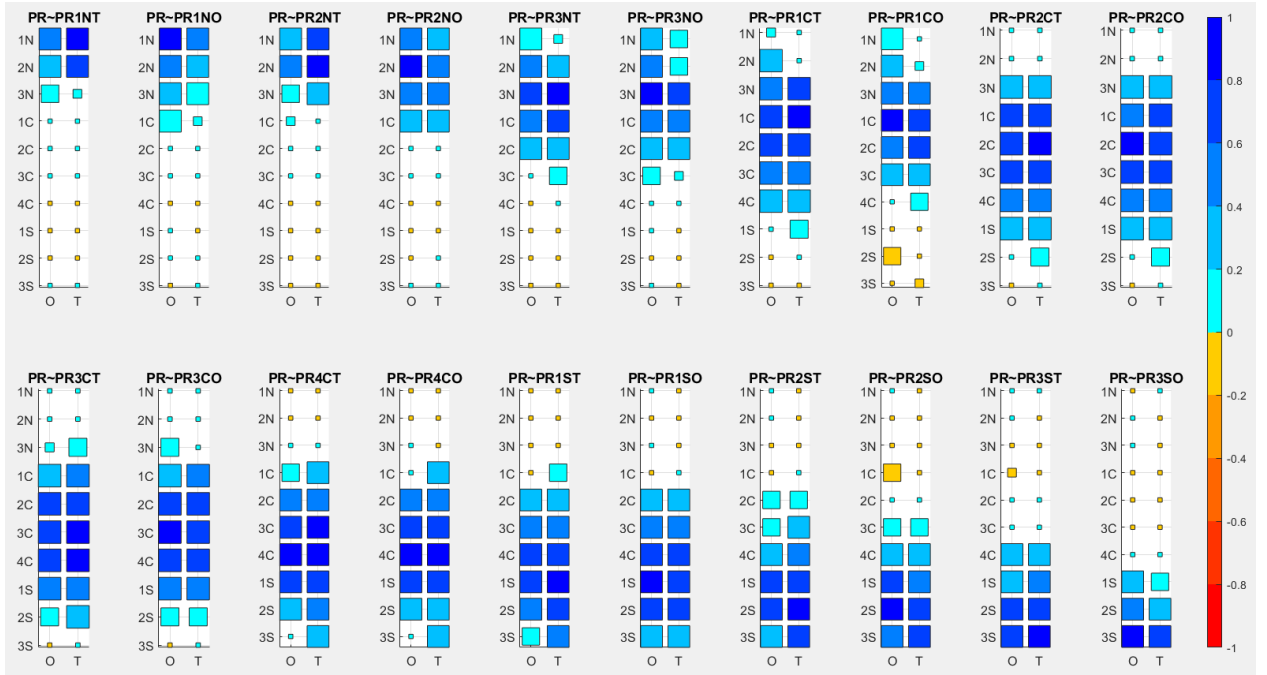
FIGURE A.2.7. PR~PR CORRELATION IN THE WHOLE SYSTEM. SECTION 4.2.2 AND FIGURE A.2.1 FOR A FULL LEGEND EXPLANATION.
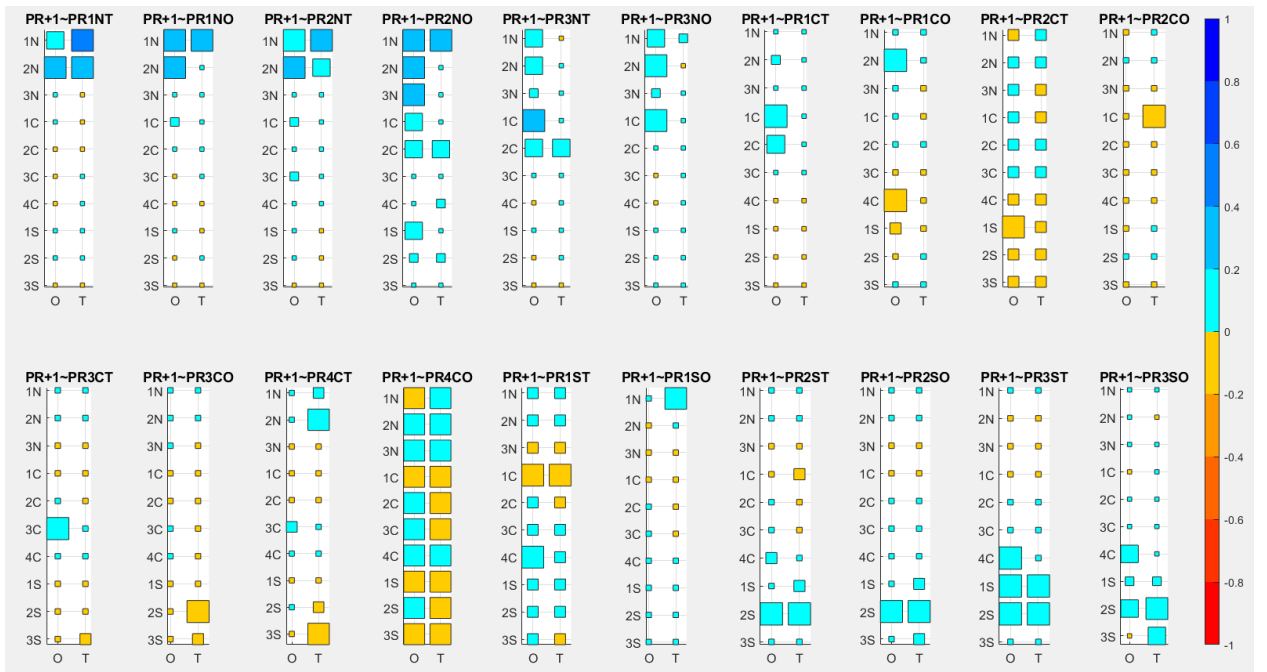
FIGURE A.2.8. PR+1~PR CORRELATION IN THE WHOLE SYSTEM. SECTION 4.2.2 AND FIGURE A.2.1 FOR A FULL LEGEND EXPLANATION.
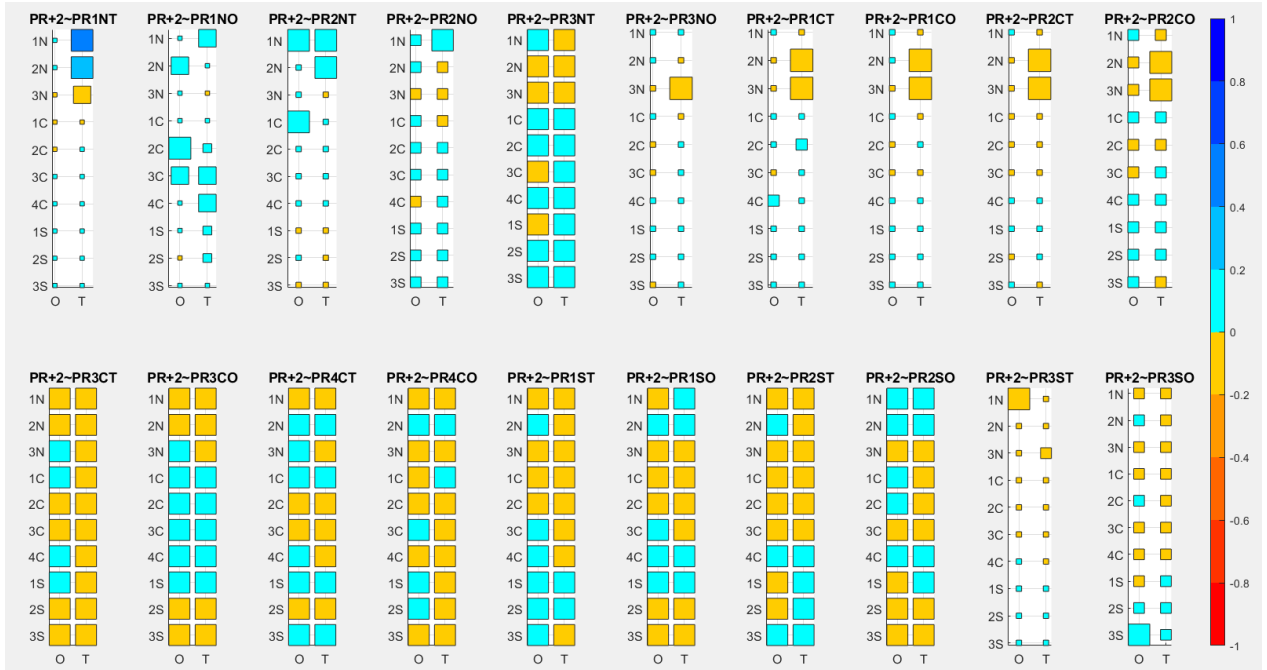
FIGURE A.2.9. PR+2~PR CORRELATION IN THE WHOLE SYSTEM. SECTION 4.2.2 AND FIGURE A.2.1 FOR A FULL LEGEND EXPLANATION.
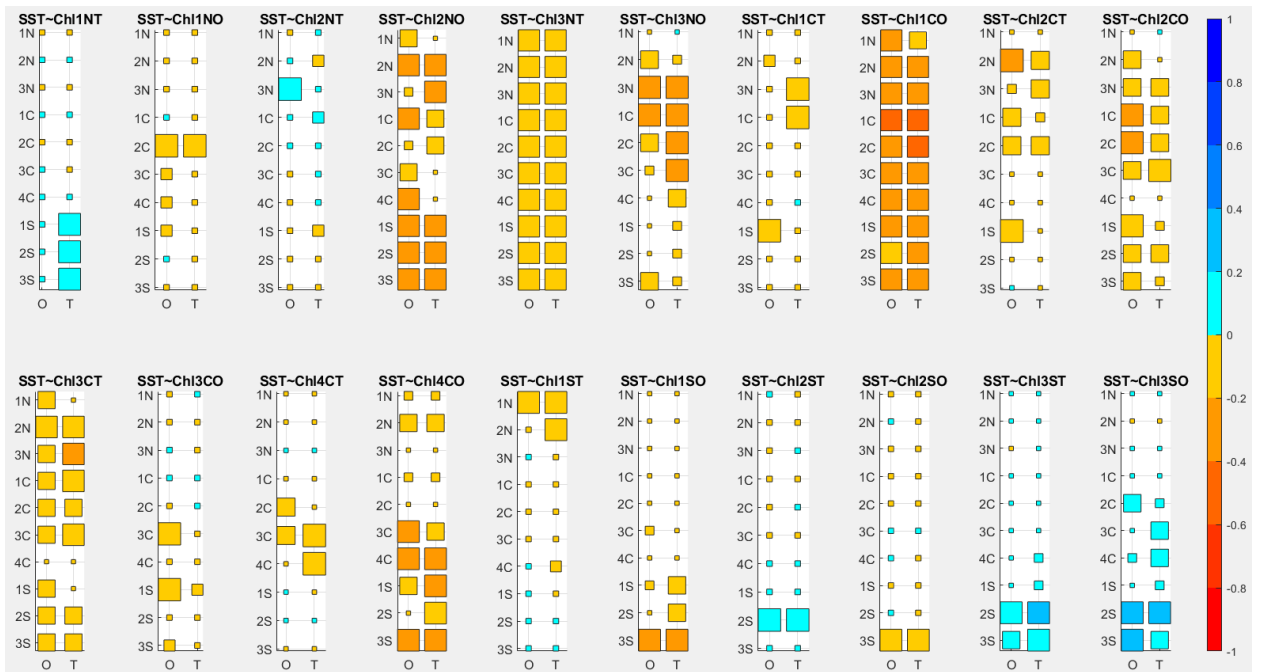
FIGURE A.2.10. SST~CHL CORRELATION IN THE WHOLE SYSTEM. SECTION 4.2.2 AND FIGURE A.2.1 FOR A FULL LEGEND EXPLANATION.
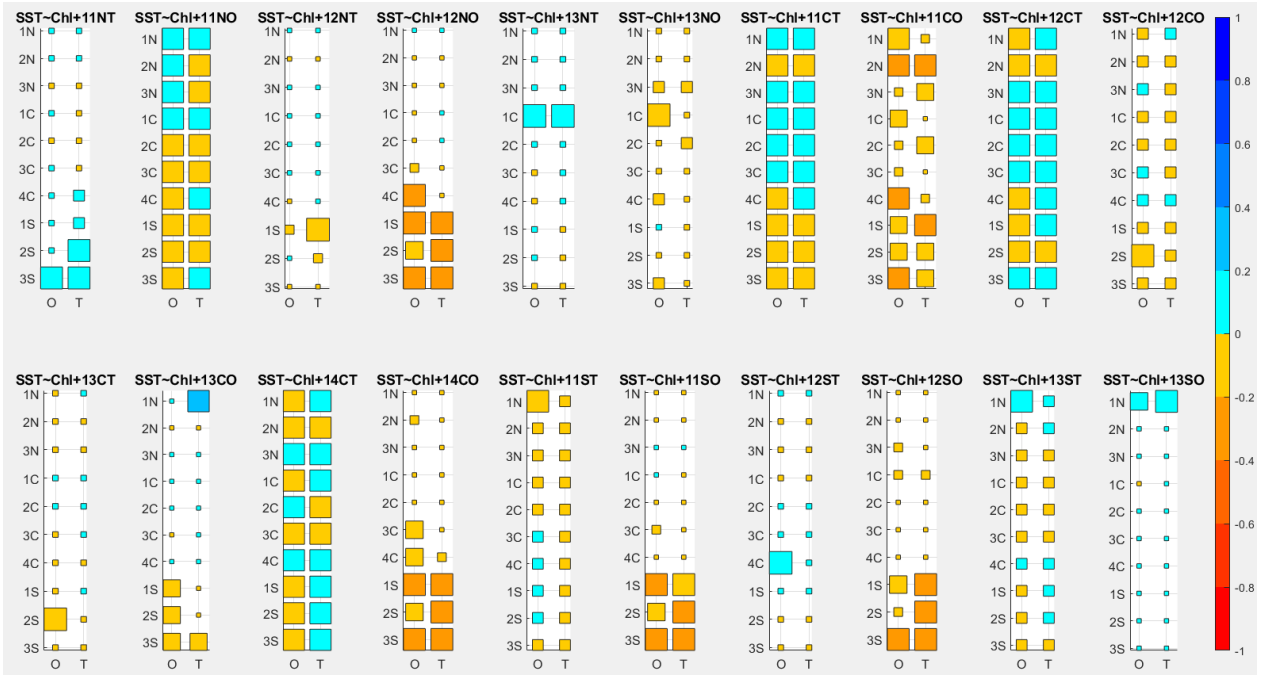
FIGURE A.2.11. SST~CHL+1 CORRELATION IN THE WHOLE SYSTEM. SECTION 4.2.2 AND FIGURE A.2.1 FOR A FULL LEGEND EXPLANATION.
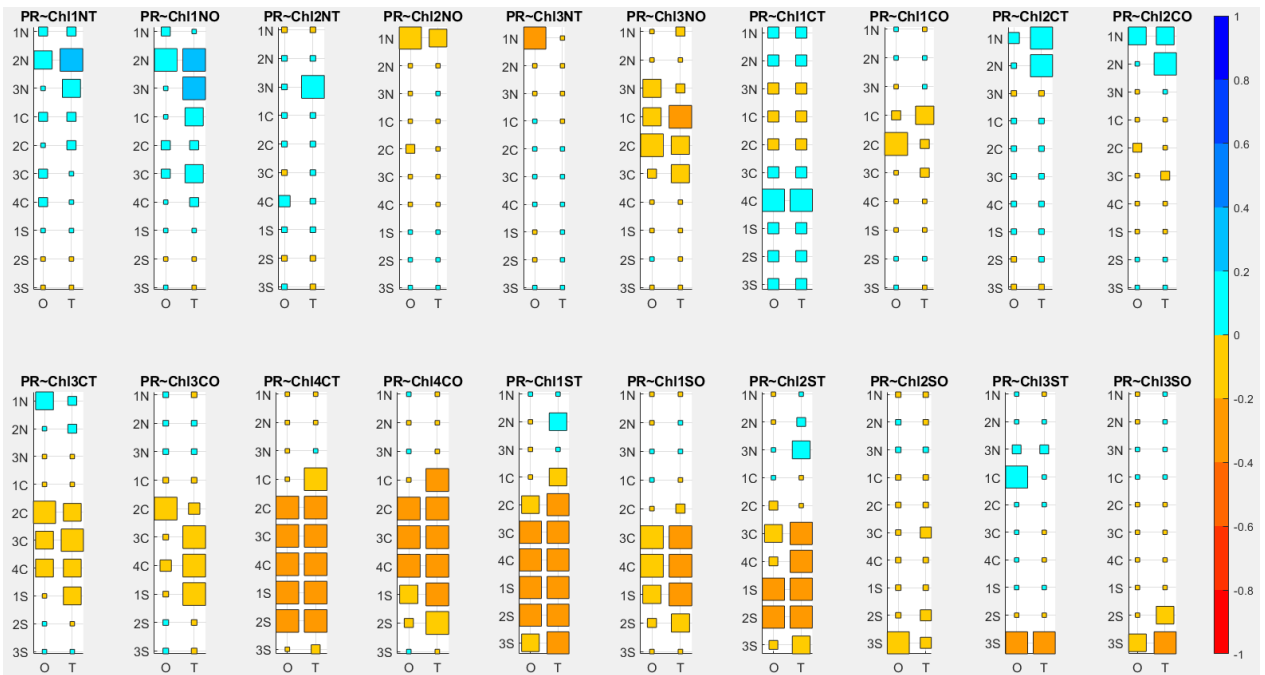
FIGURE A.2.12. PR~CHL CORRELATION IN THE WHOLE SYSTEM. SECTION 4.2.2 AND FIGURE A.2.1 FOR A FULL LEGEND EXPLANATION.
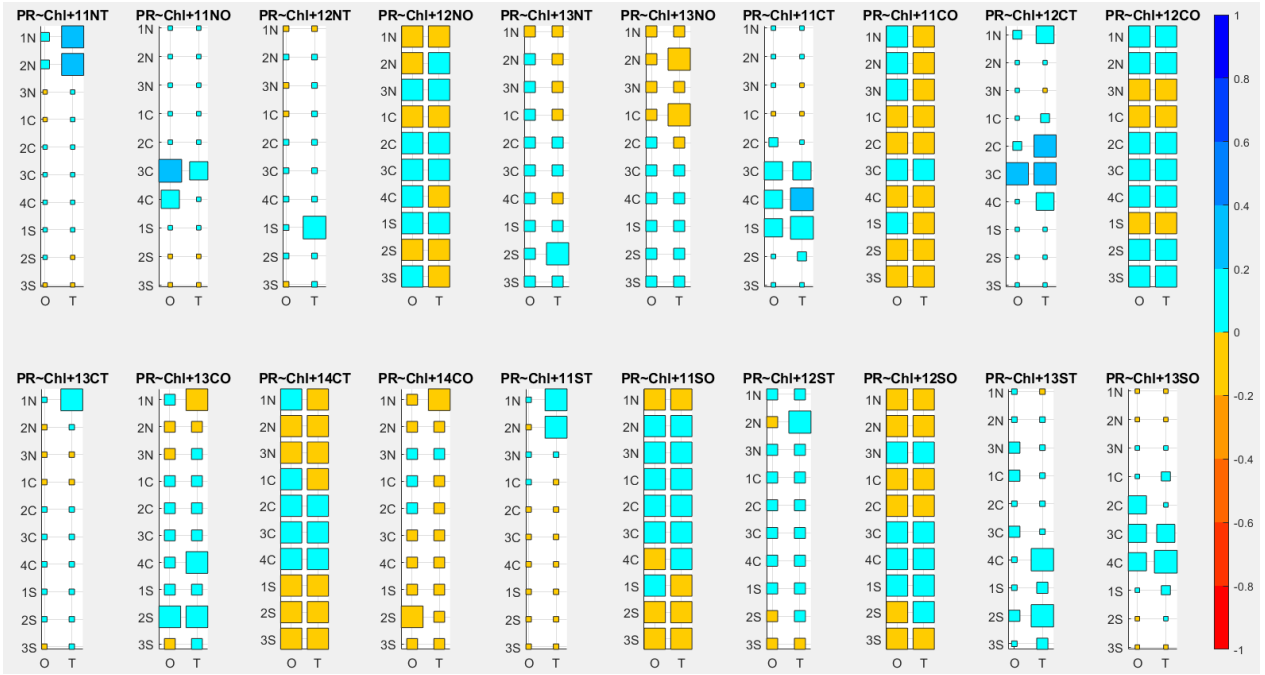
FIGURE A.2.13. PR~CHL+1 CORRELATION IN THE WHOLE SYSTEM. SECTION 4.2.2 AND FIGURE A.2.1 FOR A FULL LEGEND EXPLANATION.
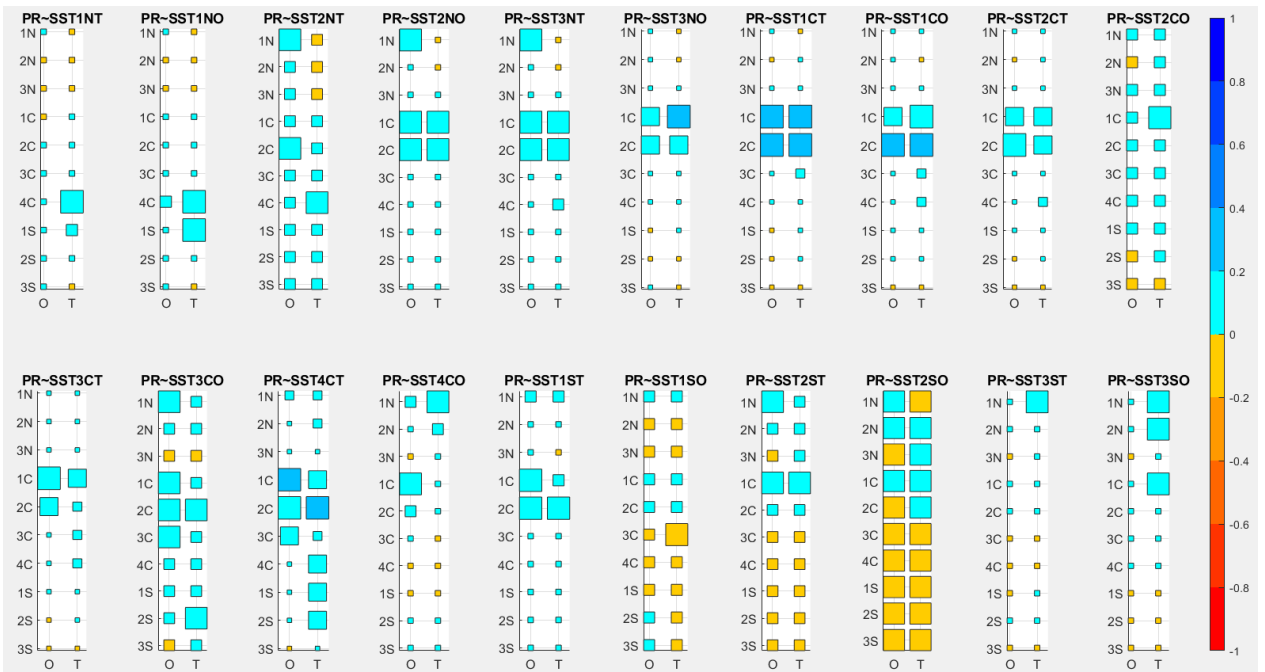
FIGURE A.2.14. PR~SST CORRELATION IN THE WHOLE SYSTEM. SECTION 4.2.2 AND FIGURE A.2.1 FOR A FULL LEGEND EXPLANATION.

209
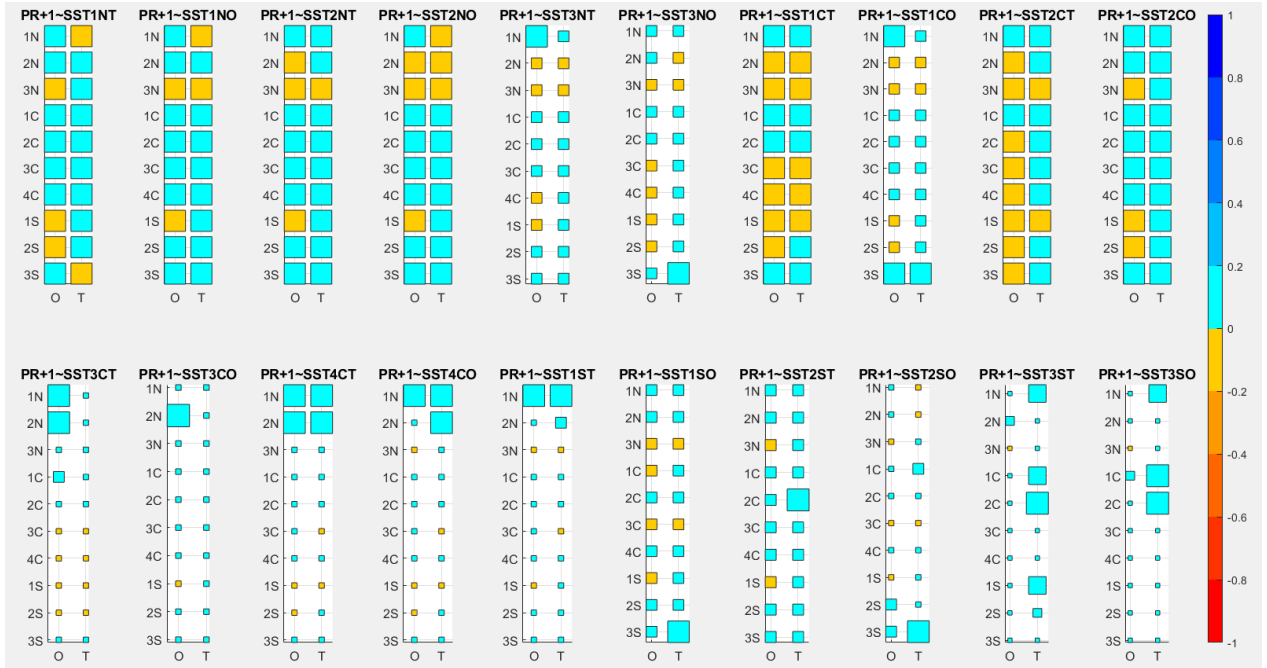
FIGURE A.2.15. PR+1~SST CORRELATION IN THE WHOLE SYSTEM. SECTION 4.2.2 AND FIGURE A.2.1 FOR A FULL LEGEND EXPLANATION.
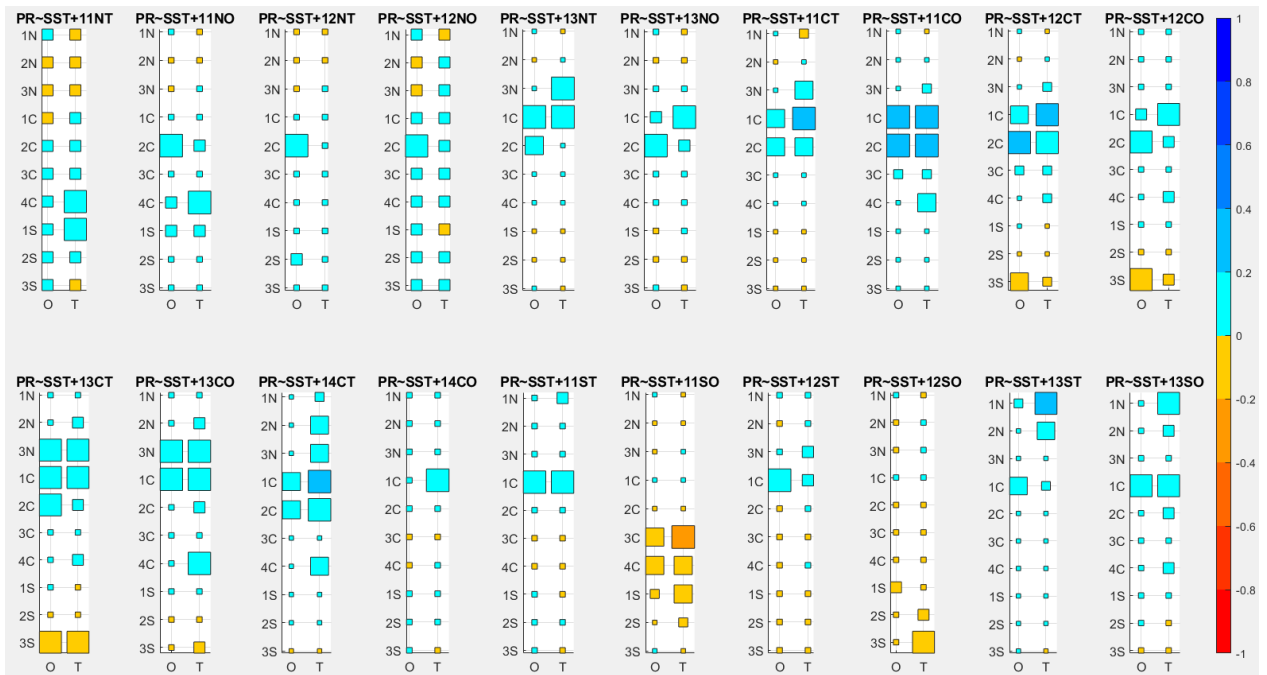
FIGURE A.2.16. PR~SST+1 CORRELATION IN THE WHOLE SYSTEM. SECTION 4.2.2 AND FIGURE A.2.1 FOR A FULL LEGEND EXPLANATION.
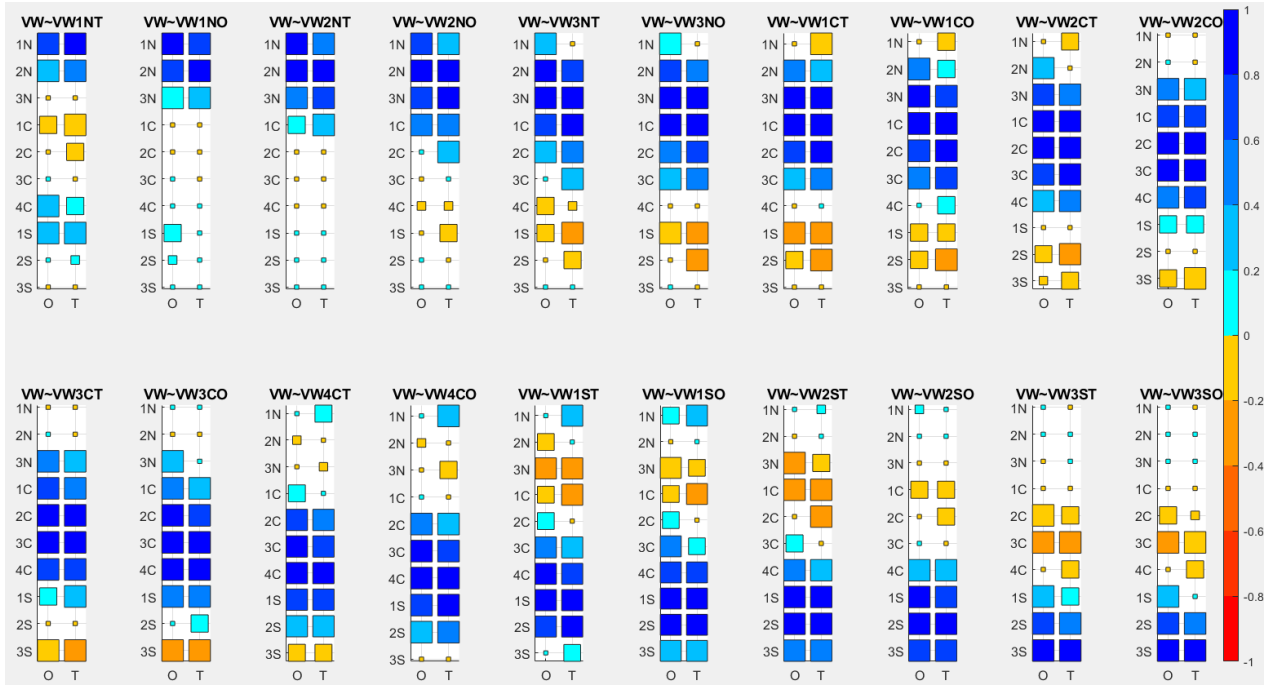
FIGURE A.2.17. VW~VW CORRELATION IN THE WHOLE SYSTEM. SECTION 4.2.2 AND FIGURE A.2.1 FOR A FULL LEGEND EXPLANATION.
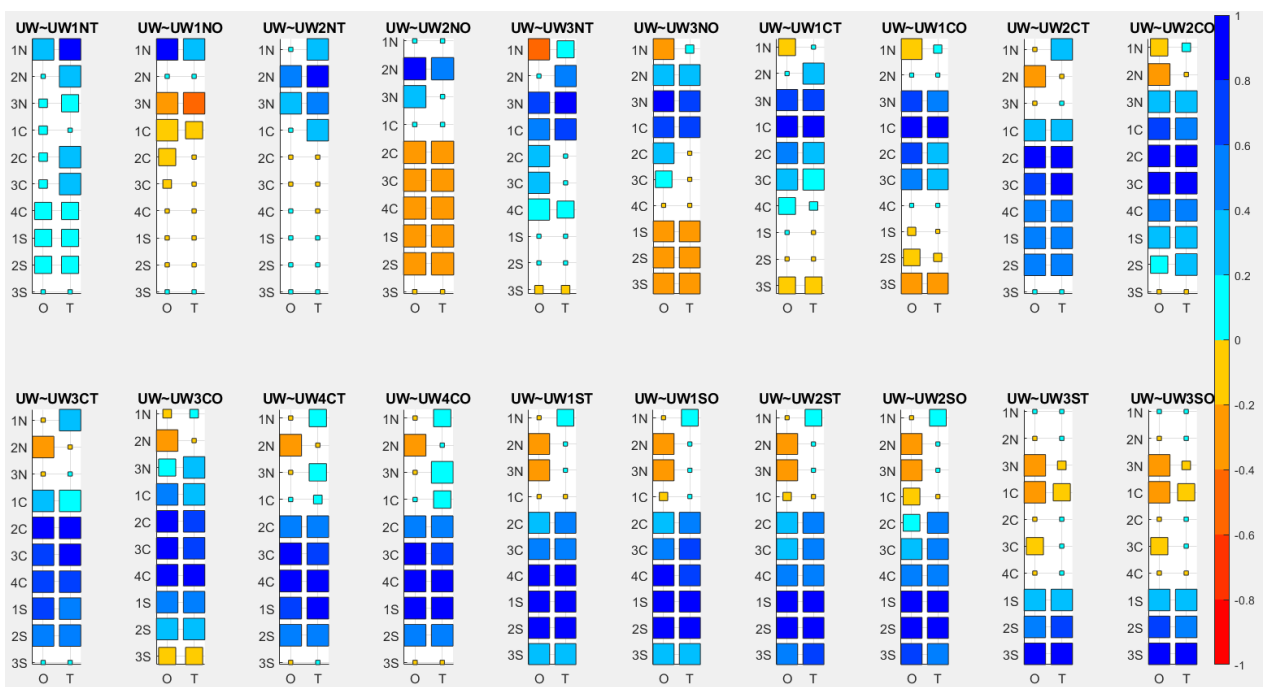
FIGURE A.2.18. UW~UW CORRELATION IN THE WHOLE SYSTEM. SECTION 4.2.2 AND FIGURE A.2.1 FOR A FULL LEGEND EXPLANATION.

211
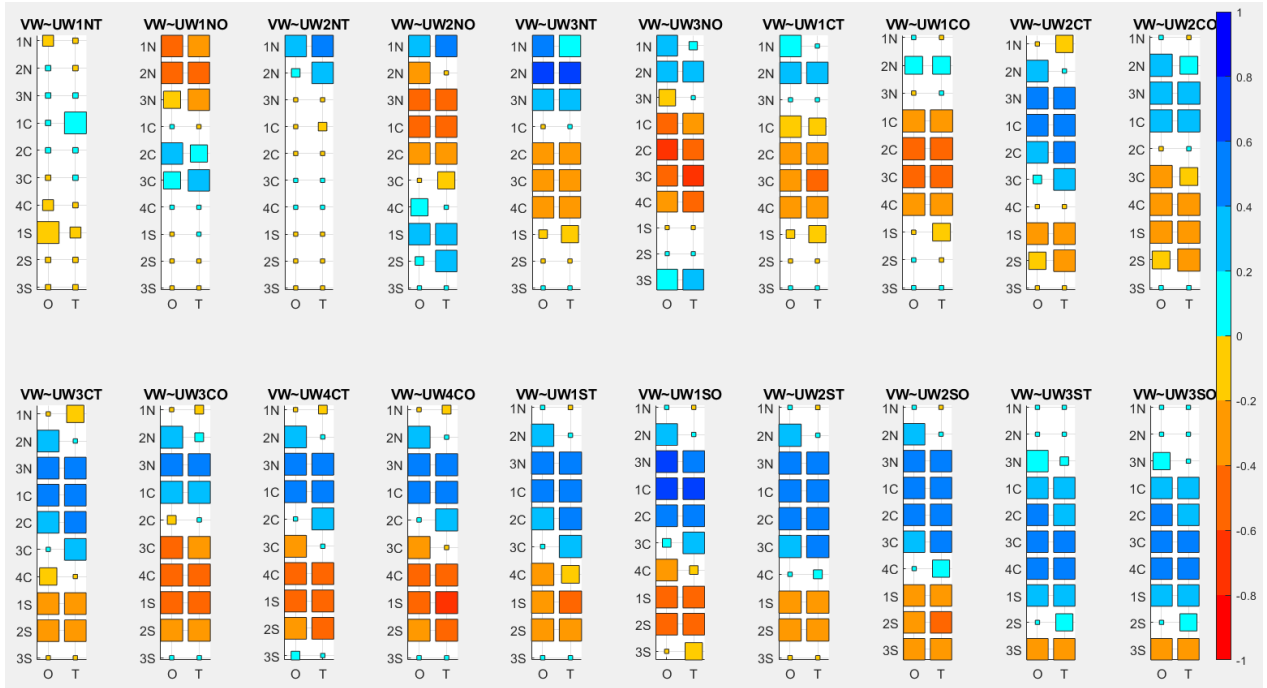
FIGURE A.2.19. VW~UW CORRELATION IN THE WHOLE SYSTEM. SECTION 4.2.2 AND FIGURE A.2.1 FOR A FULL LEGEND EXPLANATION.
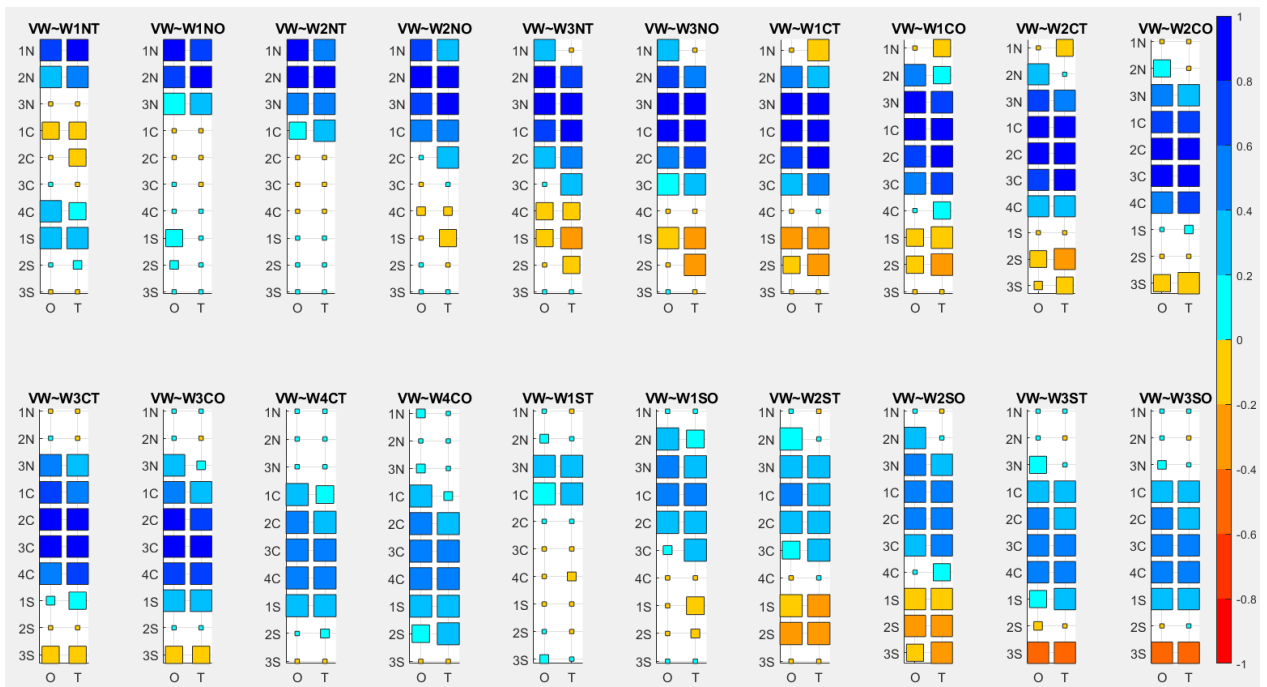
FIGURE A.2.20. VW~W CORRELATION IN THE WHOLE SYSTEM. SECTION 4.2.2 AND FIGURE A.2.1 FOR A FULL LEGEND EXPLANATION
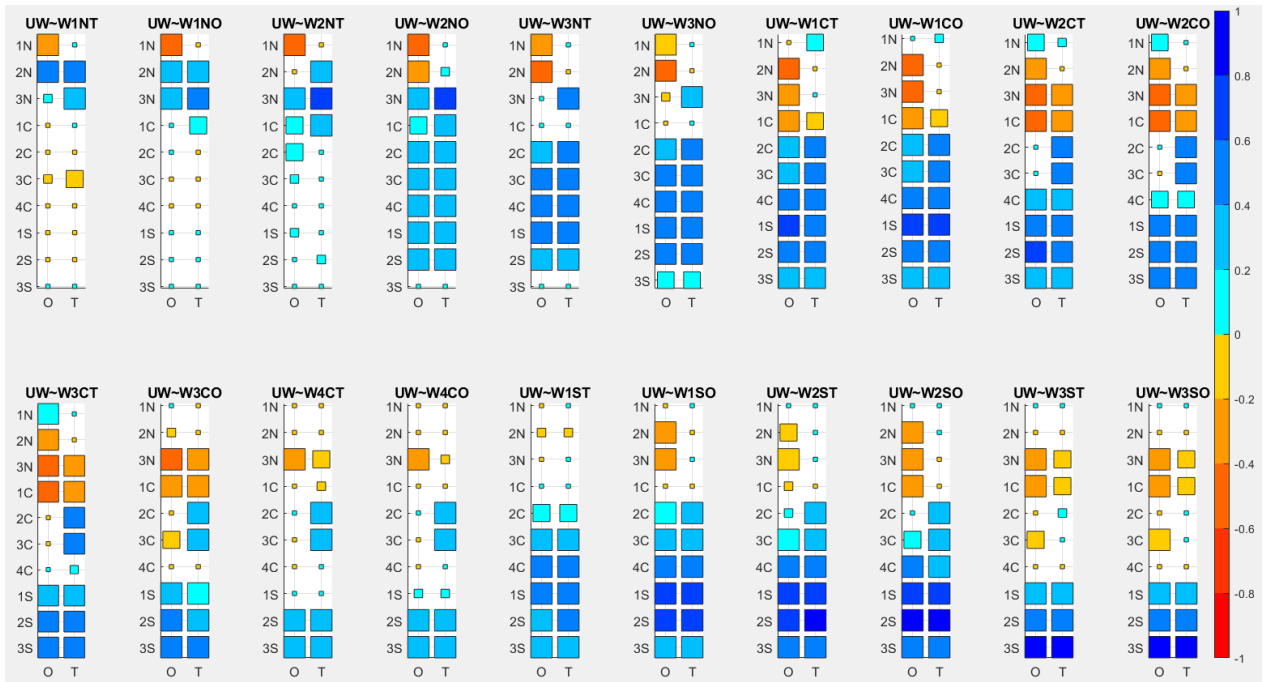
FIGURE A.2.21. UW~W CORRELATION IN THE WHOLE SYSTEM. SECTION 4.2.2 AND FIGURE A.2.1 FOR A FULL LEGEND EXPLANATION.
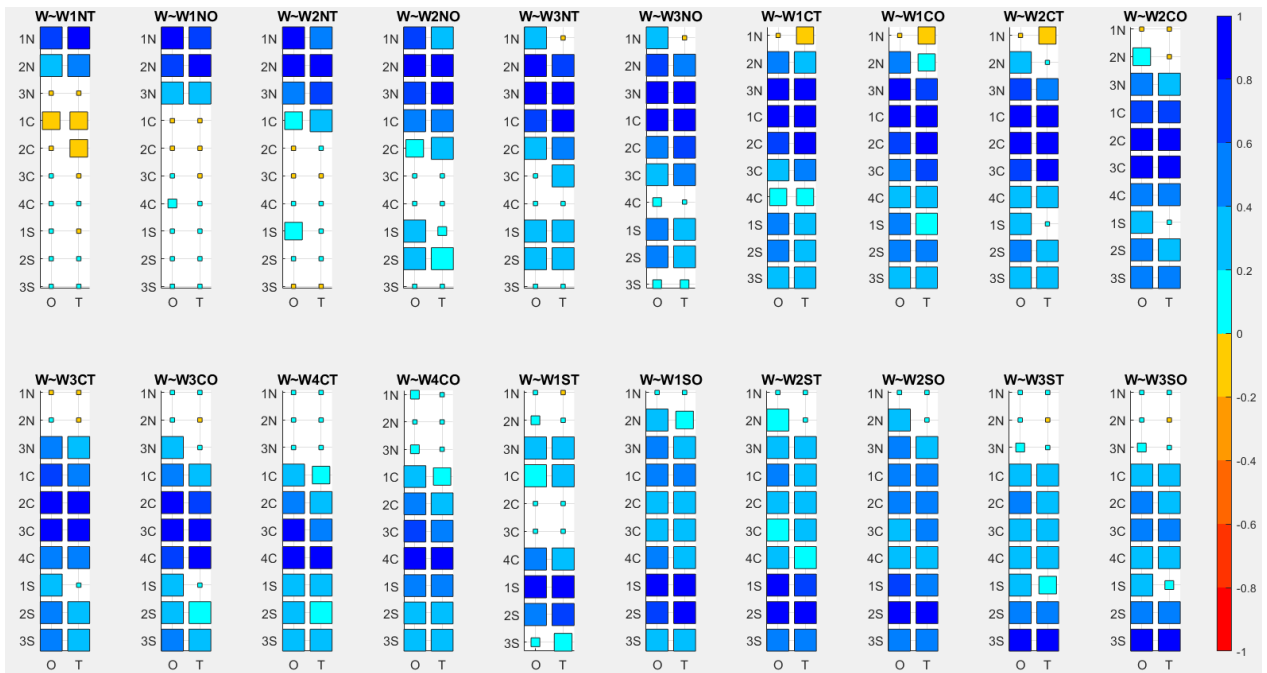
FIGURE A.2.22. W~W CORRELATION IN THE WHOLE SYSTEM. SECTION 4.2.2 AND FIGURE A.2.1 FOR A FULL LEGEND EXPLANATION.

213
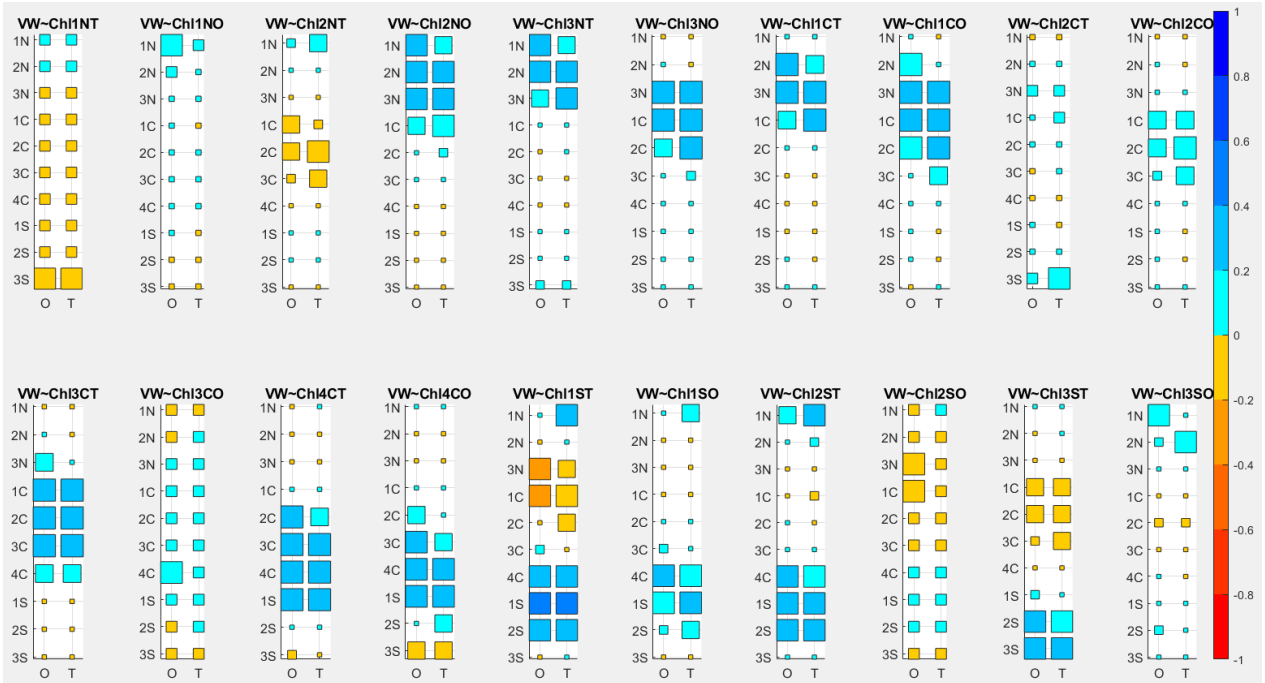
FIGURE A.2.23. VW~CHL CORRELATION IN THE WHOLE SYSTEM. SECTION 4.2.2 AND FIGURE A.2.1 FOR A FULL LEGEND EXPLANATION.
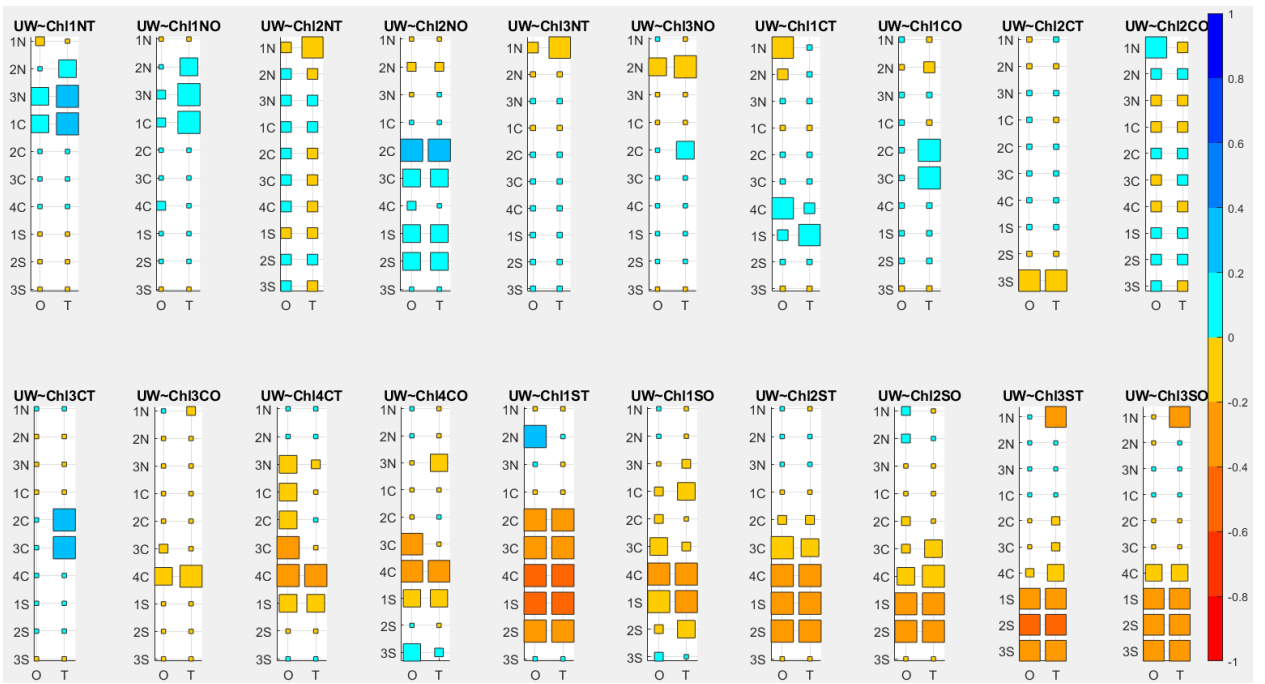
FIGURE A.2.24. UW~CHL CORRELATION IN THE WHOLE SYSTEM. SECTION 4.2.2 AND FIGURE A.2.1 FOR A FULL LEGEND EXPLANATION.

214
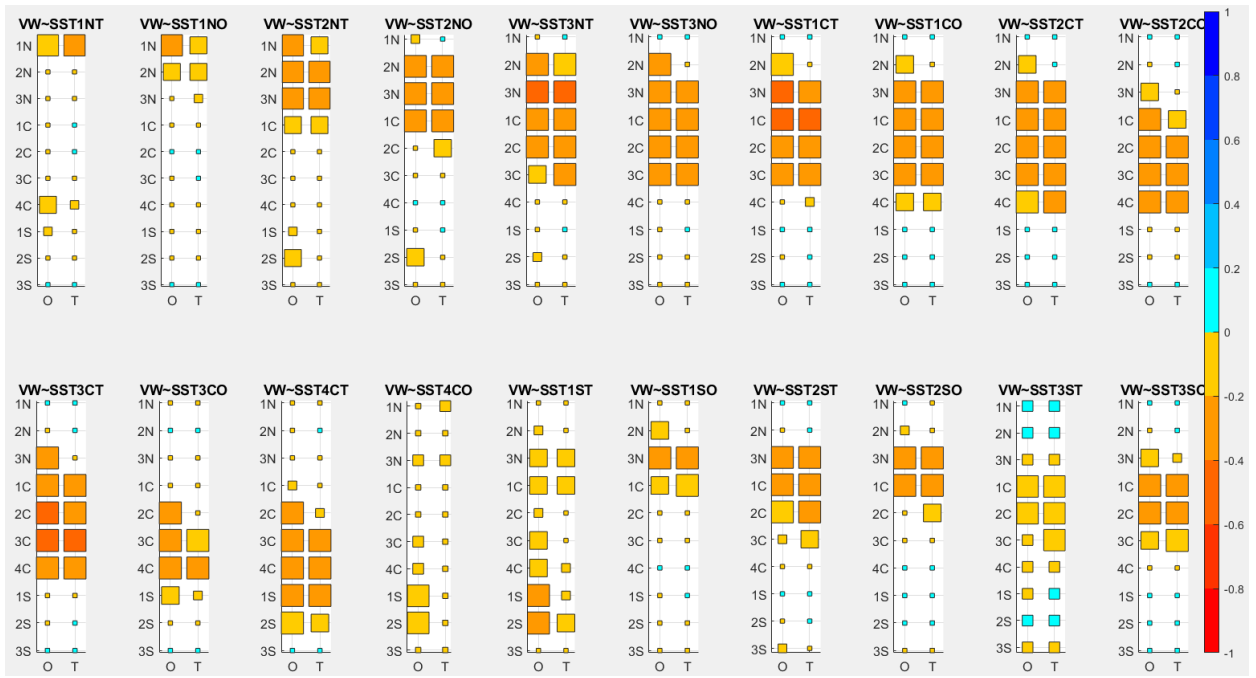
FIGURE A.2.25. VW~SST CORRELATION IN THE WHOLE SYSTEM. SECTION 4.2.2 AND FIGURE A.2.1 FOR A FULL LEGEND EXPLANATION.
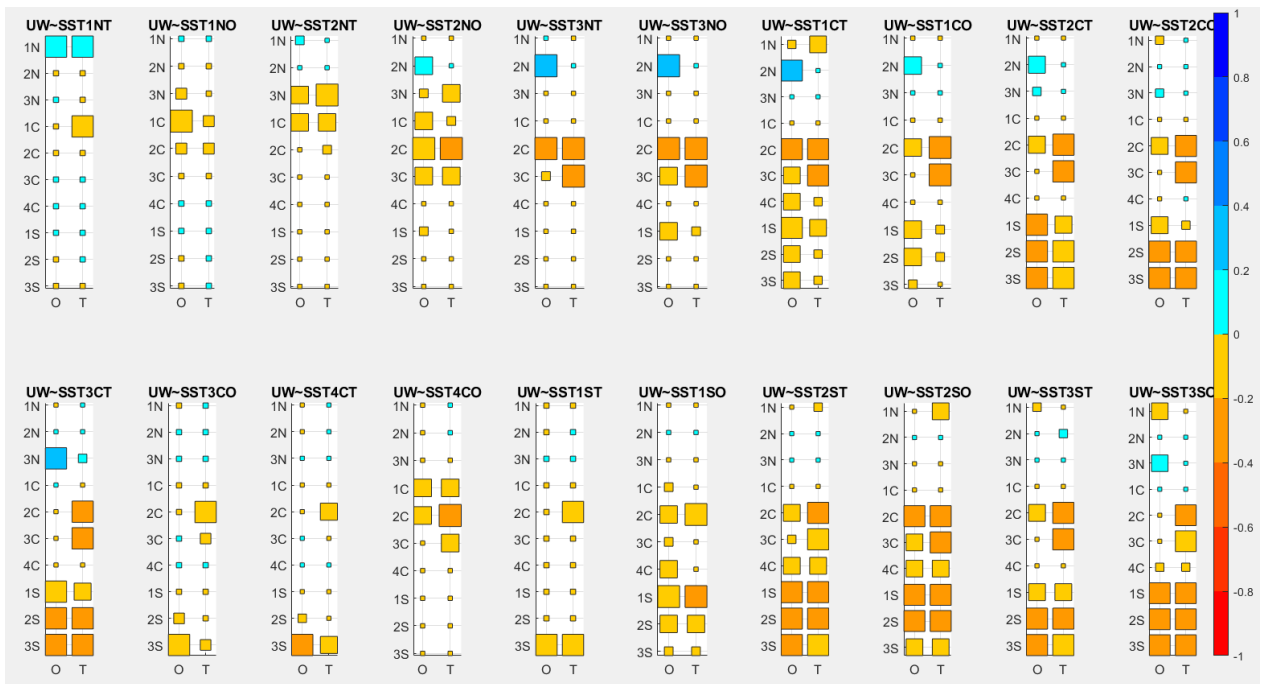
FIGURE A.2.26. UW~SST CORRELATION IN THE WHOLE SYSTEM. SECTION 4.2.2 AND FIGURE A.2.1 FOR A FULL LEGEND EXPLANATION.

215
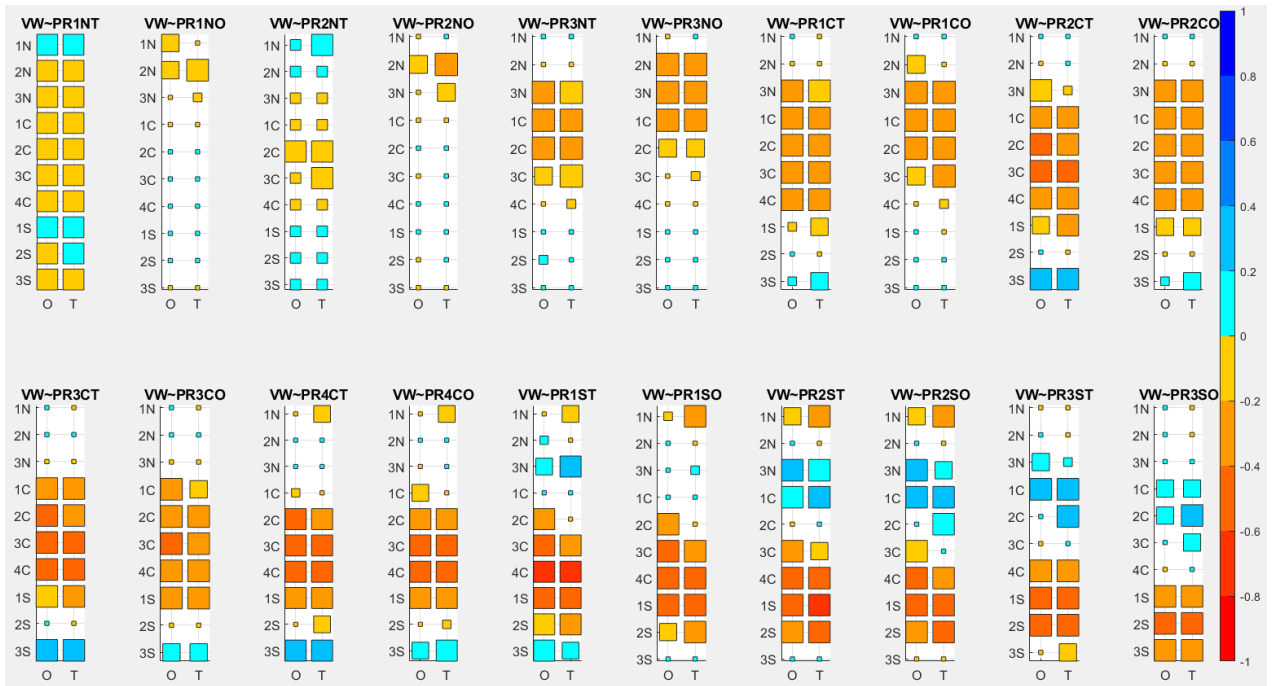
FIGURE A.2.27. VW~PR CORRELATION IN THE WHOLE SYSTEM. SECTION 4.2.2 AND FIGURE A.2.1 FOR A FULL LEGEND EXPLANATION.
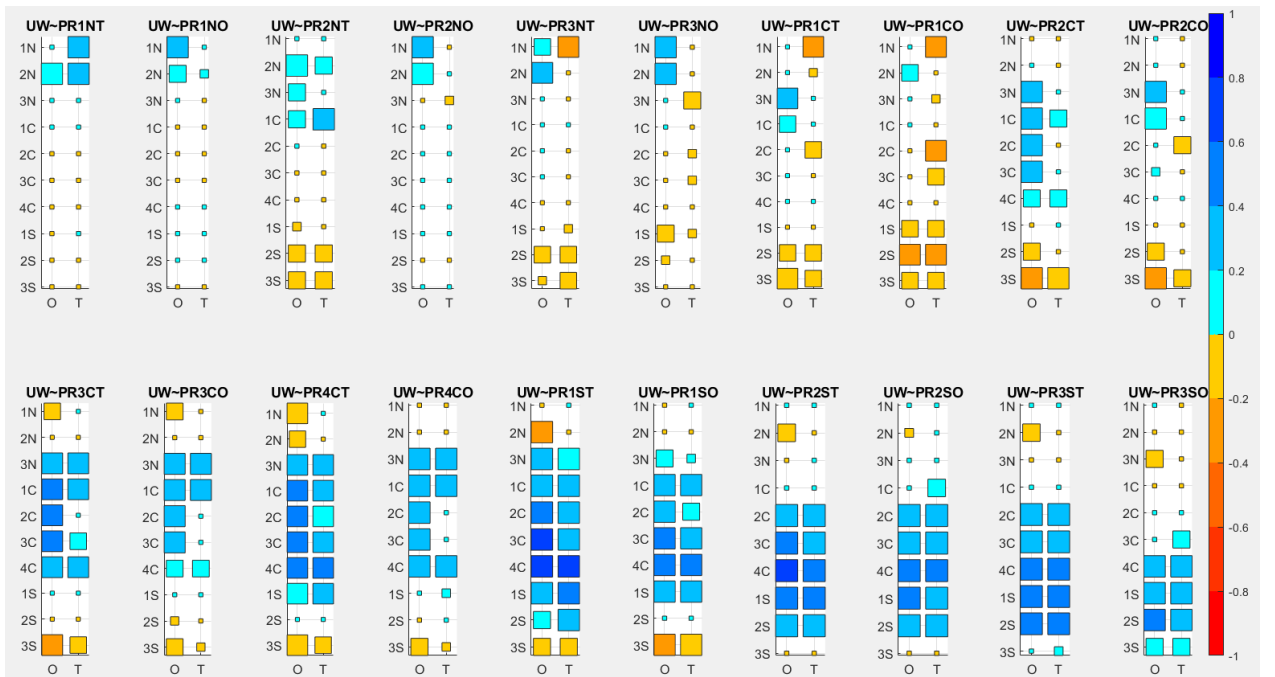
FIGURE A.2.28. UW~PR CORRELATION IN THE WHOLE SYSTEM. SECTION 4.2.2 AND FIGURE A.2.1 FOR A FULL LEGEND EXPLANATION.

216

A.3. Coastal averaged correlation for All cases using only the core period of each case.
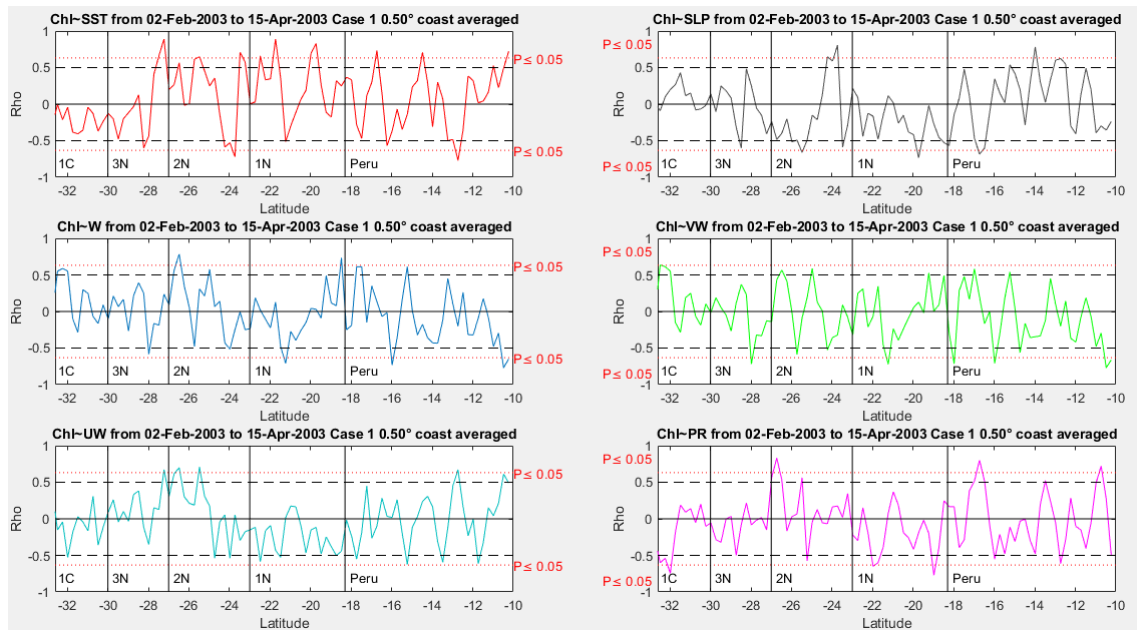
FIGURE A.3.1. CASE 1 COASTAL AVERAGED FROM 0 TO 0.5° CHL CORRELATIONS WITH ALL PHYSICAL VARIABLES USING ONLY THE CORE PERIOD.
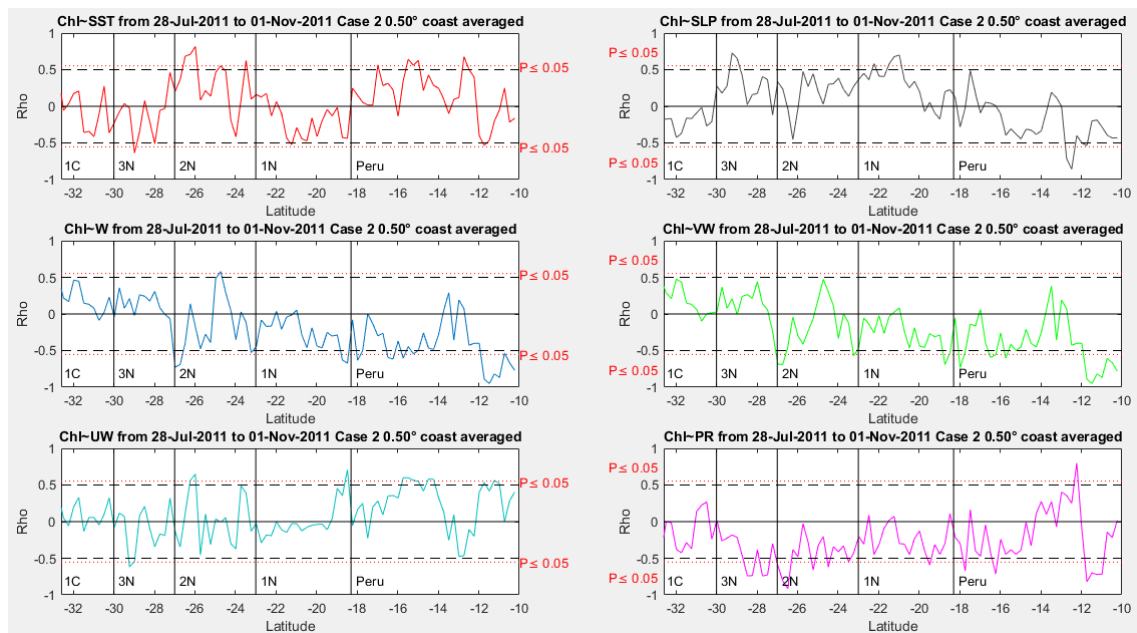

FIGURE A.3.2. CASE 2 COASTAL AVERAGED FROM 0 TO 0.5° CHL CORRELATIONS WITH ALL PHYSICAL VARIABLES USING ONLY THE CORE PERIOD.

217
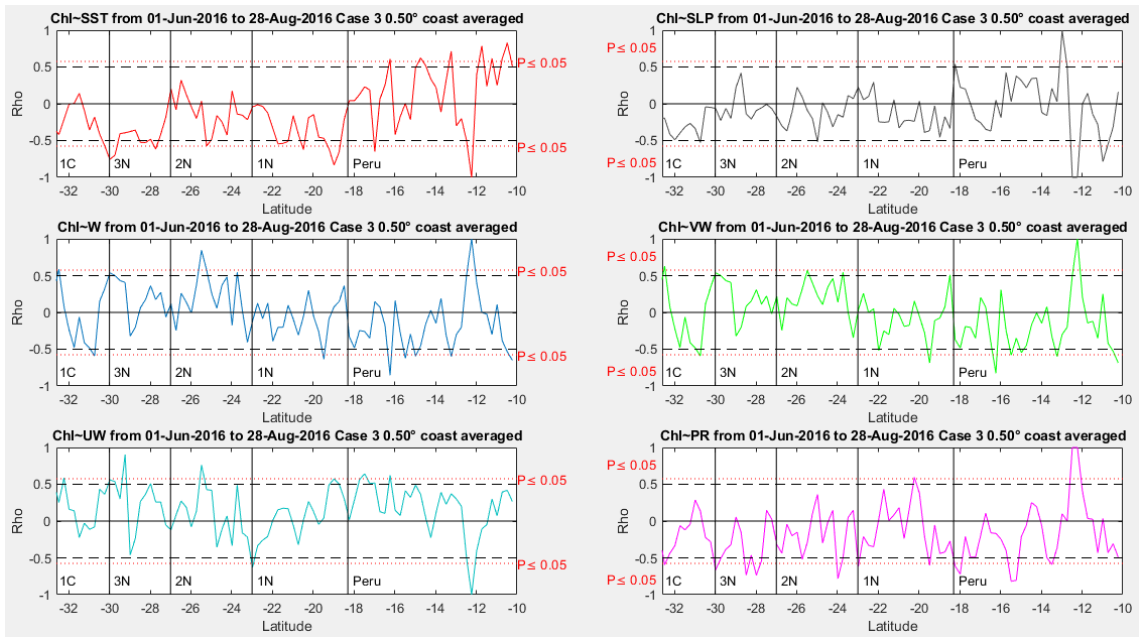
FIGURE A.3.3. CASE 3 COASTAL AVERAGED FROM 0 TO 0.5° CHL CORRELATIONS WITH ALL PHYSICAL VARIABLES USING ONLY THE CORE PERIOD.
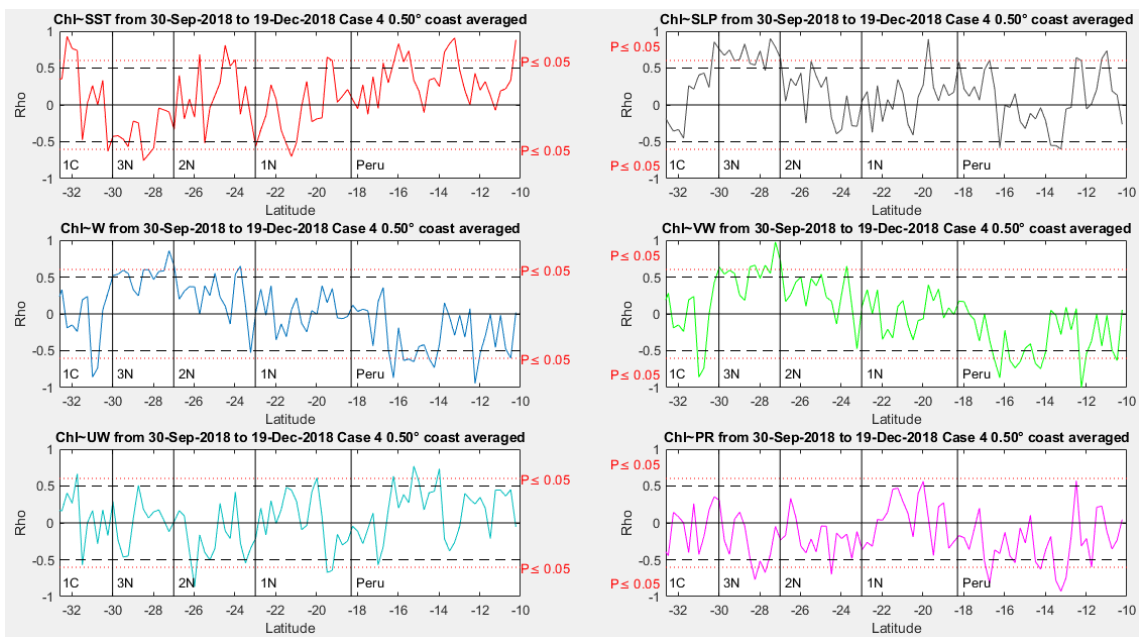
FIGURE A.3.4. CASE 4 COASTAL AVERAGED FROM 0 TO 0.5° CHL CORRELATIONS WITH ALL PHYSICAL VARIABLES USING ONLY THE CORE PERIOD.

218
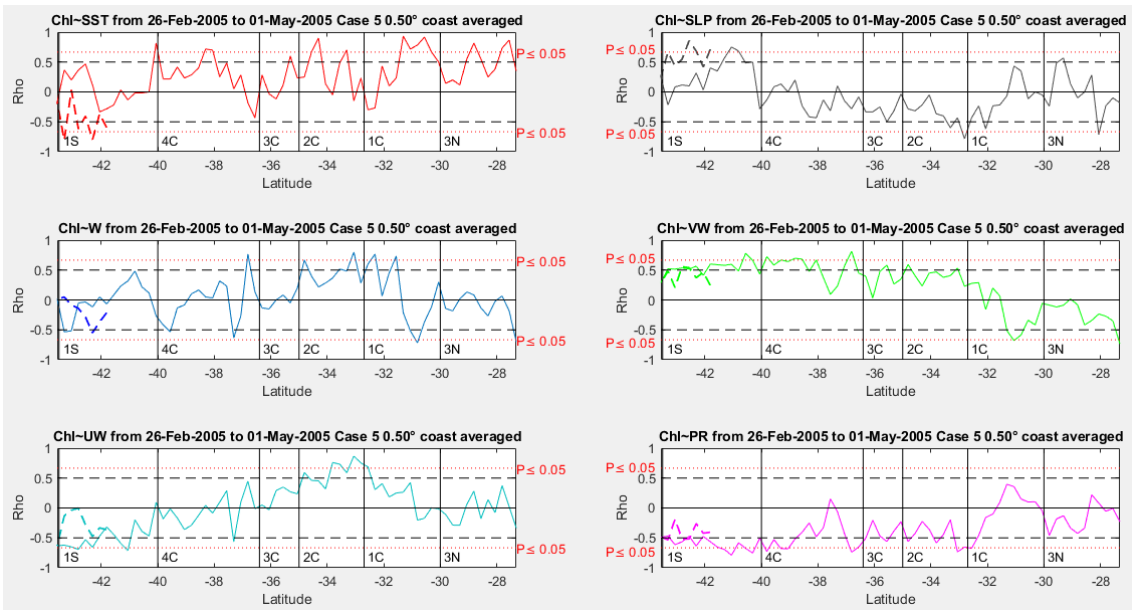
FIGURE A.3.5. CASE 5 COASTAL AVERAGED FROM 0 TO 0.5° CHL CORRELATIONS WITH ALL PHYSICAL VARIABLES USING ONLY THE CORE PERIOD.
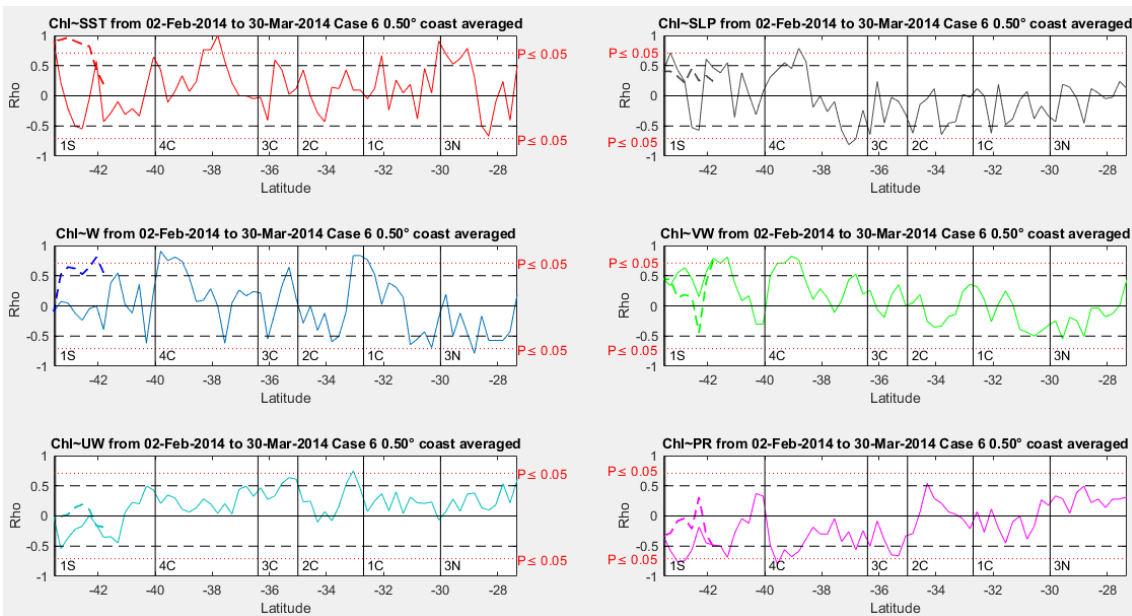
FIGURE A.3.6. CASE 6 COASTAL AVERAGED FROM 0 TO 0.5° CHL CORRELATIONS WITH ALL PHYSICAL VARIABLES USING ONLY THE CORE PERIOD.
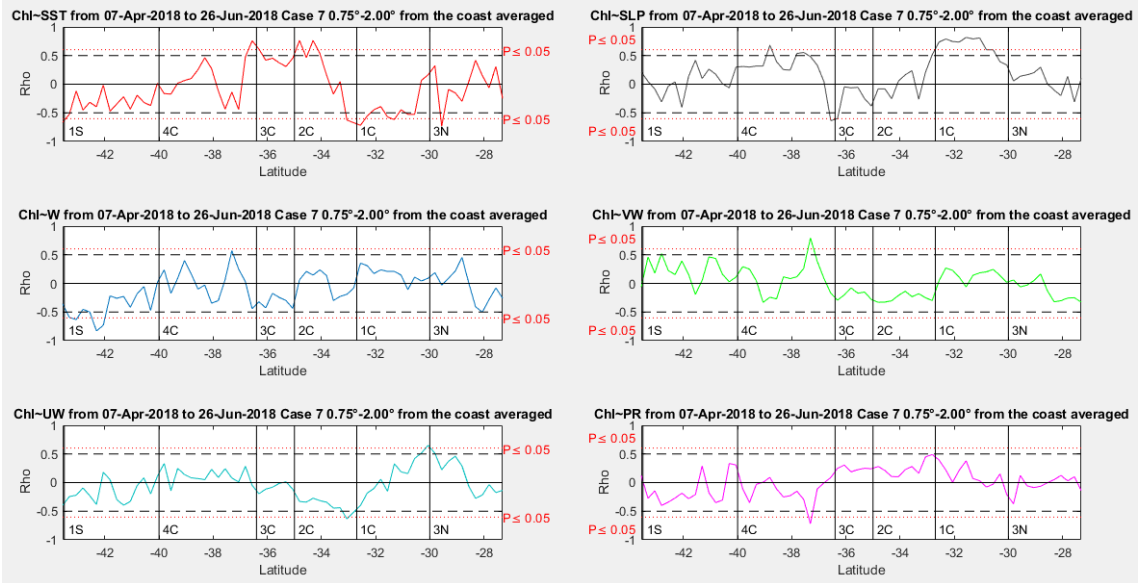
FIGURE A.3.7. CASE 7 OCEAN STRIP AVERAGED FROM 0.75° TO 2.0° PARALLEL TO THE COAST CHL CORRELATIONS WITH ALL PHYSICAL VARIABLES USING ONLY THE CORE PERIOD.
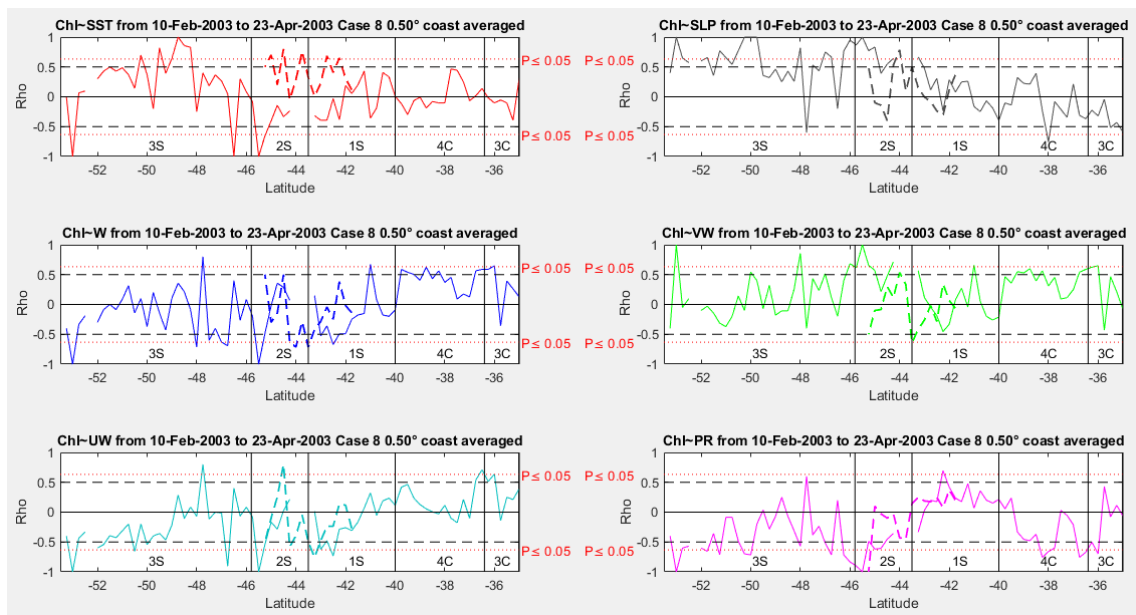

FIGURE A.3.8. CASE 8 COASTAL AVERAGED FROM 0 TO 0.5° CHL CORRELATIONS WITH ALL PHYSICAL VARIABLES USING ONLY THE CORE PERIOD.

220
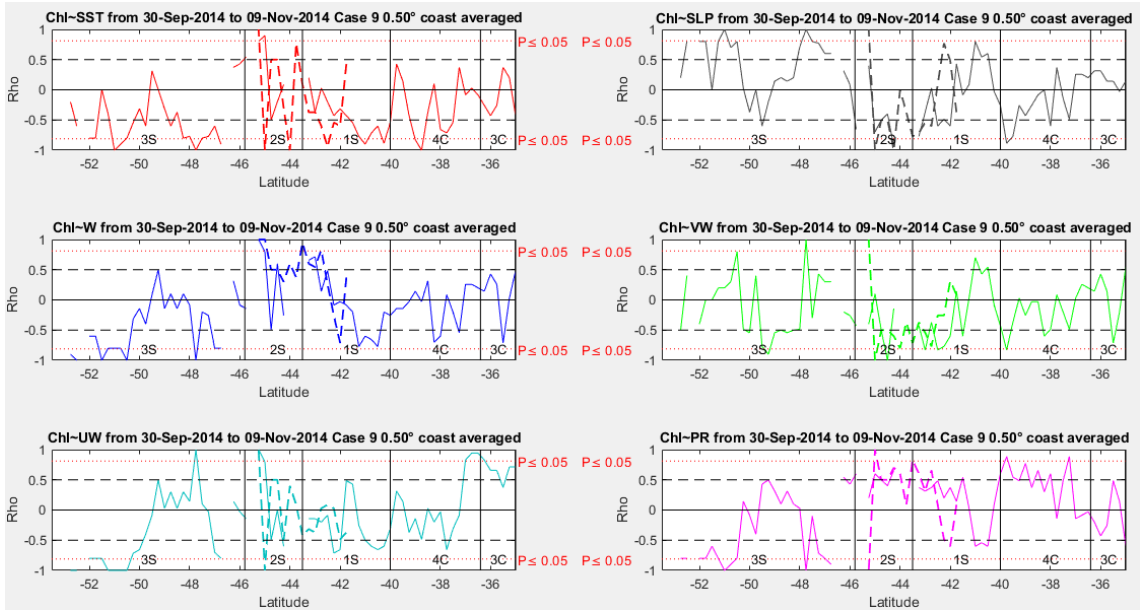
FIGURE A.3.9. CASE 9 COASTAL AVERAGED FROM 0 TO 0.5° CHL CORRELATIONS WITH ALL PHYSICAL VARIABLES USING ONLY THE CORE PERIOD.
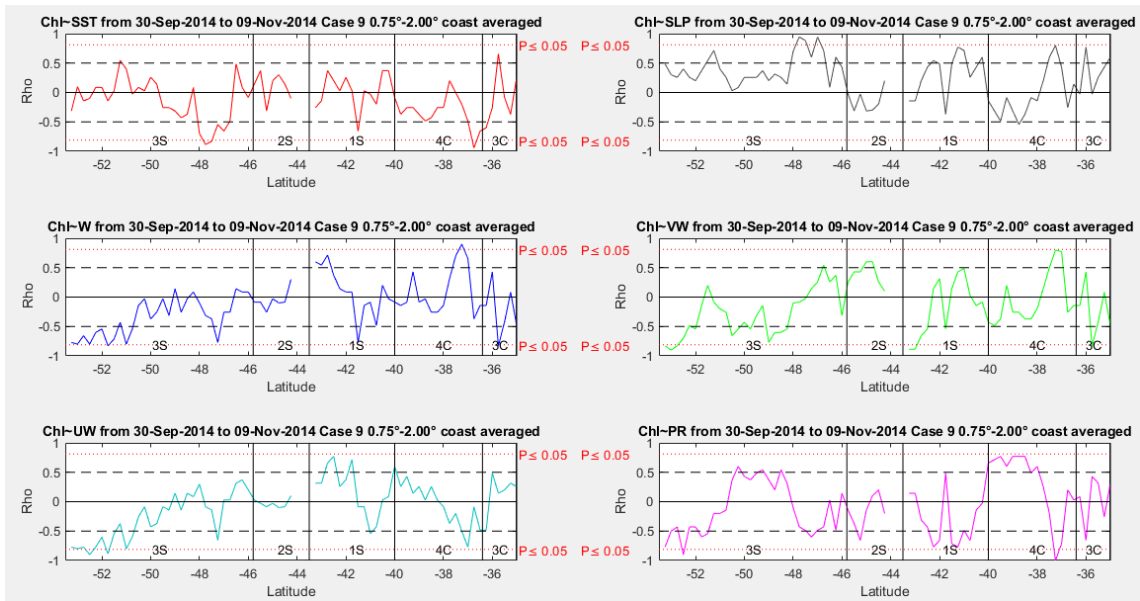
FIGURE A.3.10. CASE 9 OCEAN STRIP AVERAGED FROM 0.75° TO 2.0° PARALLEL TO THE COAST CHL CORRELATIONS WITH ALL PHYSICAL VARIABLES USING ONLY THE CORE PERIOD.

221
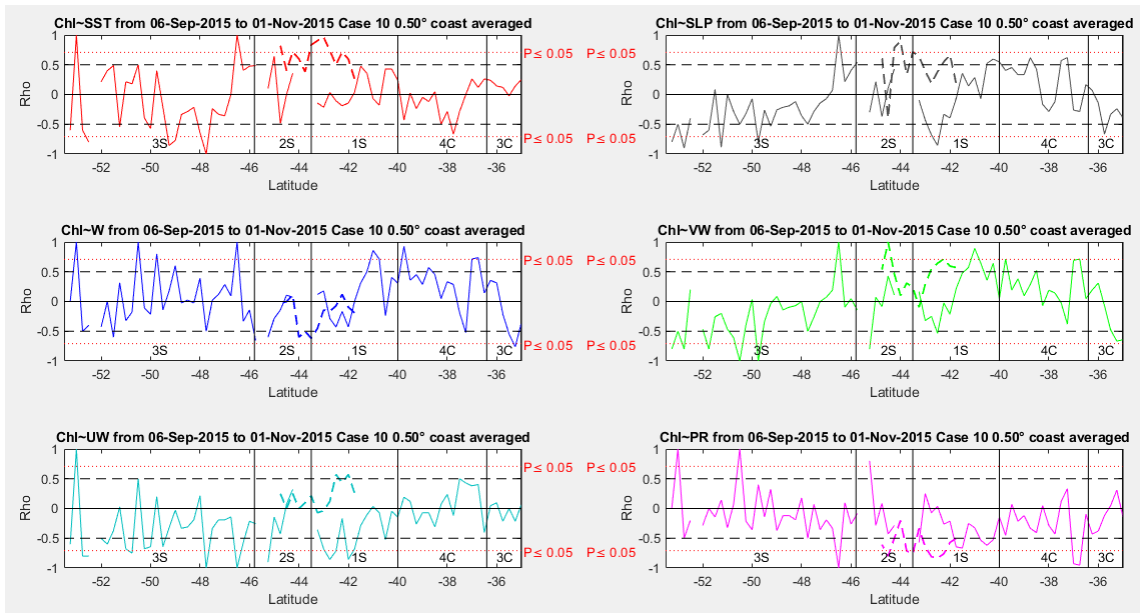
FIGURE A.3.11. CASE 10 COASTAL AVERAGED FROM 0 TO 0.5° CHL CORRELATIONS WITH ALL PHYSICAL VARIABLES USING ONLY THE CORE PERIOD.

A.4. Coastal monthly averaged with WS and PR vs PO$_4^{-2}$ and SiO$_4^{-2}$.
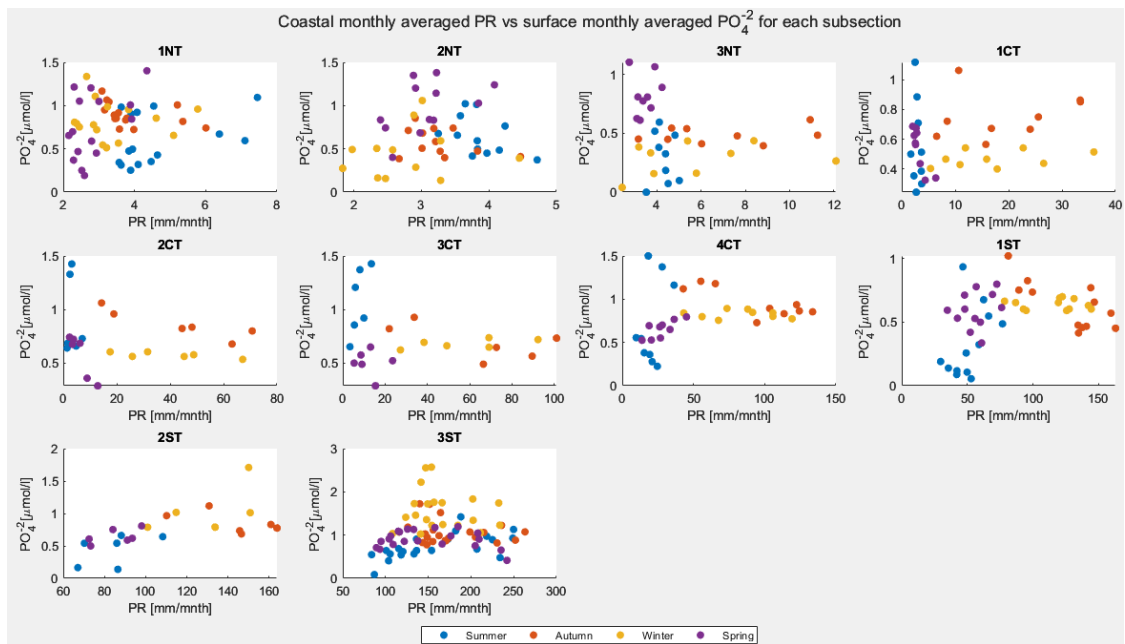

FIGURE A.4.1. COASTAL MONTHLY AVERAGED PR VS SURFACE MONTHLY AVERAGED PO$_4^{-2}$ FOR EACH SUBSECTION WITH 1° DEGREE RESOLUTION. THE MONTHLY DATA ARE COLOURED BY SEASON.
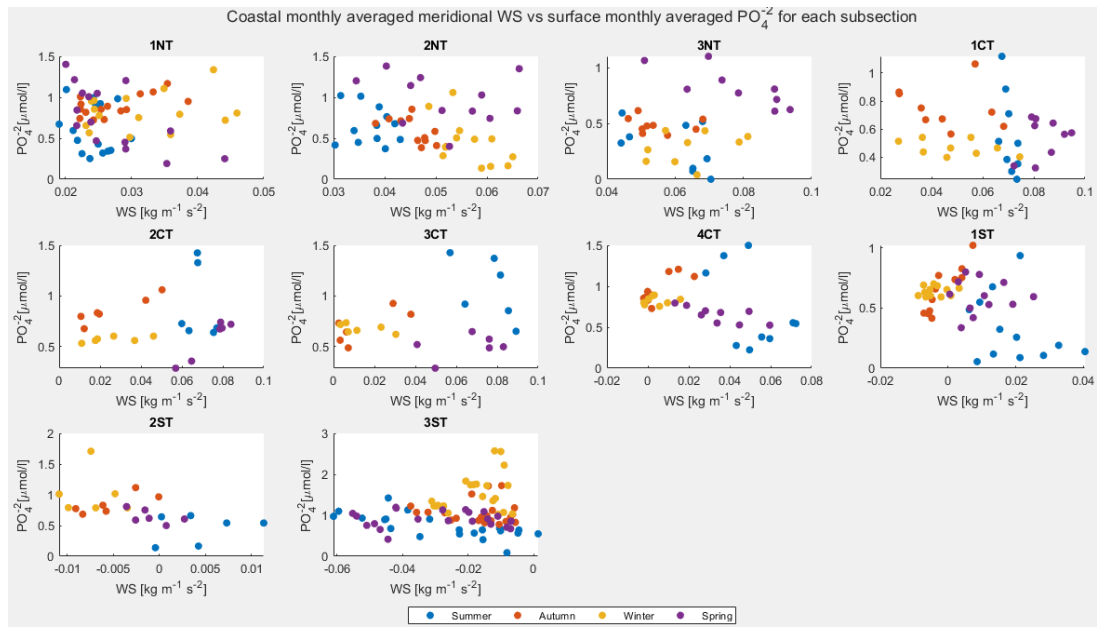
FIGURE A.4.2. COASTAL MONTHLY AVERAGED MERIDIONAL WS VS SURFACE MONTHLY AVERAGED PO_4^{-2} FOR EACH SUBSECTION WITH $1°$ DEGREE RESOLUTION. THE MONTHLY DATA ARE COLOURED BY SEASON.
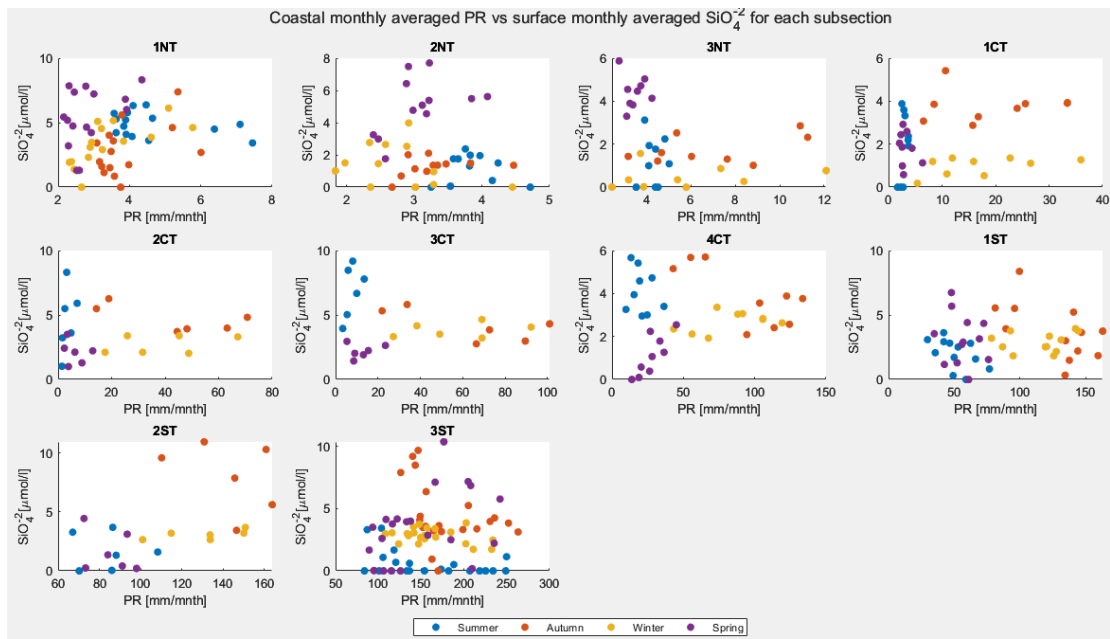
FIGURE A.4.3. COASTAL MONTHLY AVERAGED PR VS SURFACE MONTHLY AVERAGED SiO_4^{-2} FOR EACH SUBSECTION WITH $1°$ DEGREE RESOLUTION. THE MONTHLY DATA ARE COLOURED BY SEASON.

223
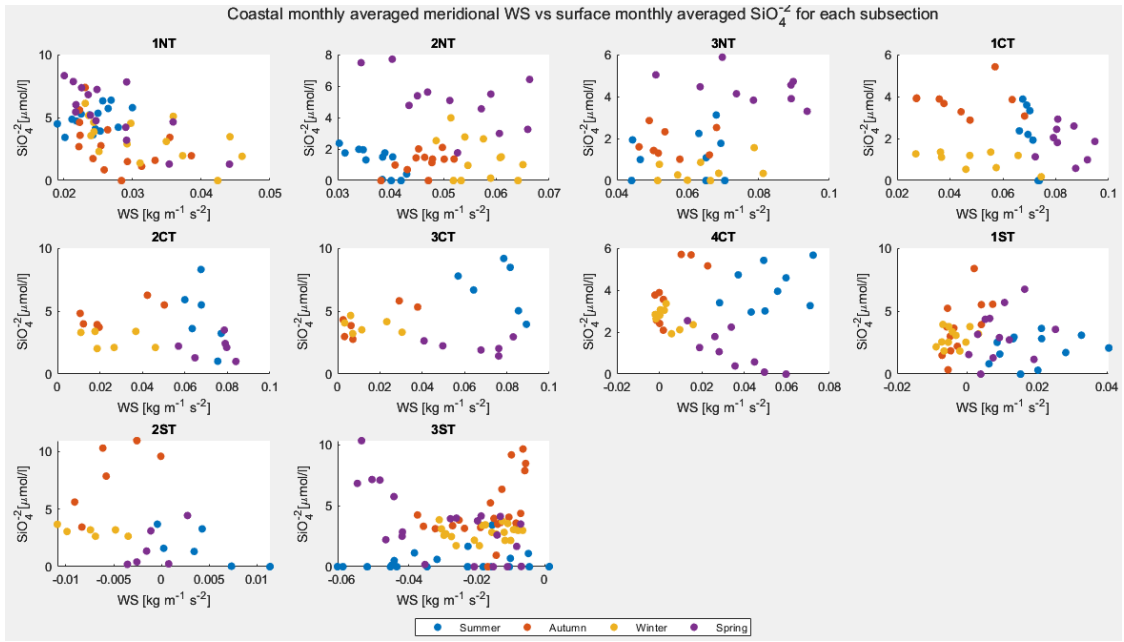
FIGURE A.4.4. COASTAL MONTHLY AVERAGED MERIDIONAL WS VS SURFACE MONTHLY AVERAGED SiO$_4$$^{-2}$ FOR EACH SUBSECTION WITH 1° DEGREE RESOLUTION. THE MONTHLY DATA ARE COLOURED BY SEASON.